PHYSIC V

VOLUME 93

AM

THE PHYSICAL REVIEW

A journal of experimental and theoretical physics established by E. L. Nichols in 1893

Published by the American Institute of Physics
for the
AMERICAN PHYSICAL SOCIETY

Officers

President

H. A. Bethe
Cornell University
Ithaca, New York

Vice-President

R. T. Birge
University of California,
Berkeley, California

Secretary

E. U. Condon
Bell Telephone Laboratories
Office:
Columbia University
New York 27, New York

Treasurer

G. B. Pegram
Columbia University
New York 27, New York

Local Secretary
for the Pacific Coast

J. Kaplan
University of California at Los
Angeles
Los Angeles, California

Managing Editor

S. A. Goudsmit
Brookhaven National Laboratory
Upton, Long Island
New York

The Physical Review

Entered as second-class matter

Acceptance for mailing at special rate of

BOARD OF EDITORS

Associate Editors

1933–1937

W. A. Fowler
Elizabeth Gardner
Charles Kittel
R. E. Marshak
W. C. H. Pandesky
V. F. Weisskopf

1935–1939

F. G. Brickwedde
Gregory Breit
F. J. Dyson
P. Kusch
R. Serber
J. C. Slater

Communications for publication should be submitted to S. A. Goudsmit, Brookhaven National Laboratory, Upton, Long Island, New York. Authors of communications are requested to pay a publication charge of $15 per page. The Physical Review furnishes them to 100 free reprints. Instructions regarding the page charge policy are given

Notices of address changes and all other correspondence concerning papers in the process of publication should be addressed to the Publication Manager, American Institute of Physics, 57 East 55th Street, New York 22, New York.

Subscription Prices

[illegible] Journals.....$20.00
[illegible].....$12.00

Back Numbers

Back numbers of the [illegible] complete year is available:

[illegible] 1929: $25.00
[illegible] 1930: $20.00
[illegible] prior to July, 1929;
$1.[illegible] July, 1929–December, 1941;
$2.00 [illegible] January, 1942–December, 1945;
$1.00 each, thereafter.
[illegible] 1929–1932: $4.00.

Orders, remittances and claims for back numbers should be addressed to the Institute of Physics, 57 East 55 Street, New York 22, New York.

Additional copies in the case of members of the American Physical Society may be obtained from the Treasurer; in the case of other subscribers to the Physical Review

[illegible] Cornell University, Ithaca, New York.

[illegible] Lancaster, Pennsylvania.

[illegible] Pennsylvania, under the Act of March 3, 1879.

[illegible] section 34.87, P. L. & R., of 1938, authorized January 20, 1941.

THE
PHYSICAL REVIEW

A journal of experimental and theoretical physics established by E. L. Nichols in 1893

SECOND SERIES, VOL. 93, NO. 5 MARCH 1, 1954

The Albedo of Various Materials for 1-Mev Photons*

EVANS HAYWARD AND JOHN HUBBELL
National Bureau of Standards, Washington, D. C.
(Received November 16, 1953)

The Monte Carlo method has been used to determine the albedo of 1-Mev photons reflected from semi-infinite slabs of water, aluminum, copper, tin, and lead at various angles of incidence. The case histories of 67 photons were followed. For normal incidence the number albedo varies from 33 percent for water to 0.5 percent for lead, and the energy albedo from 5 percent for water to 0.1 percent for lead.

IN a recent experiment[1] the authors have studied the photons backscattered from semi-infinite media of various Z when the Co^{60} gamma rays were incident upon them. The experiment was slanted to permit a general analysis of the backscattering but did not lend itself to a measure of the albedo, i.e., the fraction of the incident radiation which actually emerged from the target. It occurred to us that a more reliable estimate of this quantity, on which there really existed no information, could be obtained by a "theoretical experiment" using the Monte Carlo technique.

Since only rough answers were required and backscattering events are not too unlikely, it was feasible to do such a Monte Carlo calculation using a desk computer. The results presented here derive from the case histories of 67 1-Mev gamma rays in an infinite medium.

The calculation was carried out for a point monodirectional source in an infinite medium so that various boundary conditions might be applied to it at will. The medium was first treated as a pure Compton scatterer so that the basic calculation was applicable to all elements. Photon absorption by photoelectric effect was included afterwards by calculating the survival probability along the photon's path for five different materials, water, aluminum, copper, tin, and lead. The survival curve is an exponential which changes slope discontinuously at every collision. Each case history was followed until the photon energy was less than 30 kev, beyond which the survival factor S usually fell below 0.1 percent for water and was much smaller for higher Z materials. The details of the calculation are set forth in NBS Report No. 2768.[2]

To determine the backscattering of photons that impinge on a medium with an angle of incidence α the infinite medium of the Monte Carlo problem was sliced with an exit plane drawn through the source so that its normal formed an angle α with the original direction of the photons. Each photon which crossed the exit plane was characterized by a survival factor S_x evaluated for the point where its track first crossed the exit plane. For trajectories that never crossed the exit plane we set $S_x=0$.

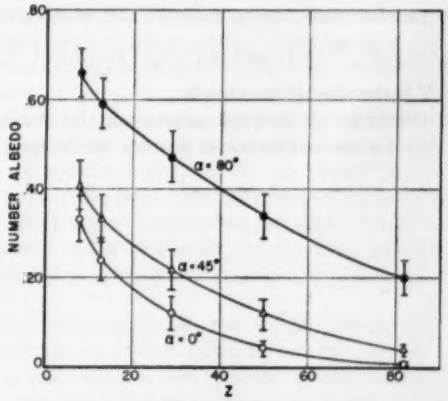

FIG. 1. The number albedo plotted as a function of Z for three angles of incidence, 0°, 45°, and 80°.

* Supported by the U. S. Office of Naval Research and the U. S. Atomic Energy Commission.

[1] E. Hayward and J. H. Hubbell, J. Appl. Phys. (to be published).

[2] E. Hayward and J. H. Hubbell, National Bureau of Standards Report NBS 2768, 1953 (unpublished).

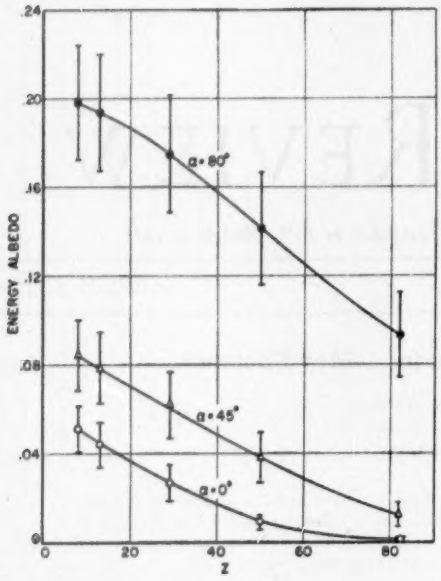

FIG. 2. The energy albedo plotted as a function of Z for three angles of incidence, 0°, 45°, and 80°.

Figures 1 and 2 show different types of albedo as a function of Z for three angles of incidence, defined as follows: (1) The number albedo is S_z averaged over all photons $\langle S_z \rangle$. (2) The energy albedo is the fraction of the incident energy that escapes $\langle S_z \epsilon \rangle$, where ϵ is the fraction of the incident energy carried by the emergent photon. (3) The dose albedo is the energy albedo further weighted to the response of a dosimeter to different photon energies, $\langle S_z \epsilon \sigma_a(\epsilon)/\sigma_a(1\ \text{Mev}) \rangle$, where $\sigma_a(\epsilon)$ is the energy absorption coefficient of air, for photons of ϵ Mev. The dose albedo is not shown as it does not differ significantly from the energy albedo for 1-Mev incident photons. The standard deviations in the number and energy albedos are, respectively,

$$\pm[(\langle S_z^2 \rangle - \langle S_z \rangle^2)/N]^{\frac{1}{2}} \text{ and } \pm[(\langle S_z \epsilon \rangle^2) - \langle S_z \epsilon \rangle^2)/N]^{\frac{1}{2}},$$

where N is the size of the sample.

The albedo for an isotropic source may be obtained from that for monodirectional sources by integration over all angles of incidence α. The number and energy albedos given in Figs. 1 and 2 pertain to $\alpha=0°$, 45°, and 80°. For each atomic number these albedos were plotted against $\cos\alpha$ and a smooth curve drawn from 1 to 0 through the three points. The area under each curve represents the number or energy albedo for the isotropic source. These albedos are shown in Fig. 3 and have errors of about ±10 percent.

The dependence of the albedos on Z and on the angle of incidence can be easily understood because of the increase in the photoelectric absorption with Z and the likelihood of escape with small deflection and small energy loss for grazing incidence. The variation of the albedos with incident energy has not been explored, but we expect the albedo to increase as the photon energy decreases.

General boundary problems are now being coded by other workers for an automatic computer. The computation will be done essentially in the same way, except that the size of the sample will be large enough so that energy and angular distributions may be obtained. It will also be done for a variety of incident energies.

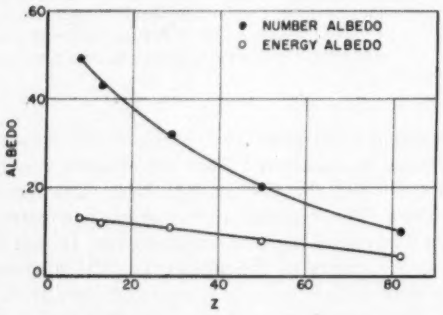

FIG. 3. The number and energy albedos plotted as a function of Z for an isotropic source.

We wish to thank Dr. U. Fano, Dr. M. J. Berger, and Dr. L. V. Spencer for their interest, and to acknowledge the help of Ida Hornstein in calculating many of the case histories.

The Measurement and the Calculation of the Liquid Helium Vapor Pressure-Temperature Scale from 1° to 4.2°K†

R. A. ERICKSON, *University of Tennessee, Knoxville, Tennessee*

AND

L. D. ROBERTS, *Oak Ridge National Laboratory, Oak Ridge, Tennessee*

(Received October 9, 1953)

Measurements between 1.2 and 4.2°K on a paramagnetic salt using a mutual inductance bridge apparatus indicate errors in the presently accepted liquid helium temperature scale amounting to 12 millidegrees at the λ point. These data, together with those of Kistemaker, are found to be in good agreement with a temperature scale calculated from the other thermodynamic properties of helium. The calculated scale is further confirmed by a comparison between the calculated and observed latent heat of vaporization. Accepting as correct the boiling point determination of Keesom and Clusius, the estimated accuracy of the proposed temperature scale is 1.5 millidegrees below the λ point and 3 millidegrees above the λ point.

I. INTRODUCTION

THE presently accepted temperature scale in the liquid helium region was adopted[1] in 1948. Between 1.6 and 4.2°K, this scale is based upon the vapor pressure measurements of Schmidt and Keesom[2] (1937 scale) using a helium gas thermometer calibrated at liquid hydrogen temperatures. Below 1.6°K the scale follows the formula derived by Bleaney and Simon[3] which was experimentally verified by Bleaney and Hull[4] using a magnetic thermometer.

Measurements by Kistemaker and Keesom[5] of the isotherms of helium gas indicated the possibility of errors in the 1937 scale of Schmidt and Keesom. Subsequently Kistemaker[6] extended the range of these measurements and at the same time made measurements of the vapor pressure using a helium gas thermometer. These results were in reasonable agreement with the formula of Bleaney and Simon below 1.6°K but disagreed with the 1937 scale above 1.6°K. A maximum deviation of −0.013°K was found at the λ point. Unfortunately, these measurements were not sufficiently extensive above the λ point and could not, therefore, be conveniently incorporated in the 1948 scale.

In connection with an experiment on the polarization of nuclei in manganese ammonium sulfate hexahydrate (MAS), it was desirable to evaluate the specific heat and Weiss constant of this material. From measurements to determine the latter constant, it became apparent that rather large irregularities in the susceptibility temperature data were present. These could logically arise from a pecularity in the magnetic properties of MAS, instrumental errors, or from errors in the temperature scale. After a series of experiments designed to distinguish these possibilities, we attribute the irregularities to the latter effect and interpret our results as showing essential agreement with Kistemaker's scale below T_λ and that there are in addition small errors in the 1948 scale above the λ point.

These results are shown to be in good agreement with the vapor pressure calculated from the known thermodynamic properties of helium. Finally, the latent heat of vaporization is calculated and found to agree satisfactorily with the experimental measurements.

II. EXPERIMENTAL PROCEDURE AND RESULTS

The vapor pressure of liquid helium was measured with either a mercury or an oil manometer. The manometers were of sufficiently large bore (25 mm) to make the meniscus correction negligible. The column heights were measured with an accuracy of 0.05 mm using a sliding vernier cursor on a steel scale. In the usual practice, the pressure was measured at the top of the cryostat over the helium bath and a small correction was applied for the gas flow pressure gradient in the Dewar flask. In all cases the dimensions of the pressure measuring apparatus were large enough to make thermomolecular pressure corrections negligible. In the helium I region a correction for the hydrostatic pressure gradient was made using the liquid densities measured by Kamerlingh Onnes and Boks.[7] Below the λ point the temperature gradient in the liquid is negligible because of the large thermal transport in helium II, so that the latter correction does not apply. For convenient reference to the 1948 scale, the observed pressures were corrected to a standard gravity (980.7 cm sec^{-2}) and 20°C.

The temperature of the liquid helium bath was varied by controlled pumping of the helium vapor. After the pressure was reduced to the desired value, the pumping speed was adjusted until the temperature was essentially stationary. The usual thermal drift rate while making observations was about 0.5 millidegree

† Presented at the Washington Meeting of the American Physical Society, April, 1953.

[1] H. Van Dijk and D. Shoenberg, Nature **164**, 151 (1949).

[2] G. Schmidt and W. H. Keesom, Physica **4**, 963, 971 (1937).

[3] B. Bleaney and F. Simon, Trans. Faraday Soc. **35**, 1205 (1939).

[4] B. Bleaney and R. A. Hull, Proc. Roy. Soc. (London) **A178**, 74 (1941).

[5] J. Kistemaker and W. H. Keesom, Physica **12**, 227 (1946).

[6] J. Kistemaker, Physica **12**, 272, 281 (1946).

[7] H. Kamerlingh Onnes and J. D. A. Boks, Communs. Kamerlingh Onnes Lab. Univ. Leiden 170b (1924).

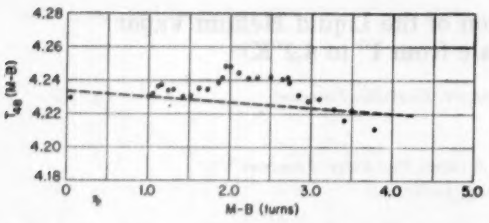

FIG. 1. The relative susceptibility of manganese ammonium sulfate hexahydrate. The straight line corresponds to a Weiss constant of 3 millidegrees.

per minute. To avoid nonequilibrium thermal distributions while in the helium I region, the sequence of observations was always toward lower temperatures. Measurements below the λ point were made from either direction according to convenience.

The temperature of the bath was obtained through the measurement of the magnetic susceptibility of a sample of paramagnetic salt in contact with the bath. This salt in the shape of a 12-mm diam sphere of compressed powder was supported in a plastic holder and located in the central region of a set of mutual inductance coils mounted in the liquid nitrogen bath. In all cases the paramagnetic sample was shielded from high-temperature radiation through the glass apparatus or down the sample tube. The Dewar coils were connected with a variable mutual inductance and a null detector into an alternating-current bridge arrangement in which the dial reading of the variable mutual inductance is proportional to the susceptibility of the sample. The measurements were made at a frequency of either 165 cps or 500 cps with an oscillating magnetic field at the sample of 3-gauss amplitude. The details of the mutual inductance bridge apparatus are reported elsewhere.[8]

With a paramagnetic sample whose susceptibility follows a Curie-Weiss law, the mutual inductance readings M at the bridge box will have the temperature dependence, $M-B=A/(T+\Delta)$, where B is the residual unbalance of the Dewar coils in the absence of a sample, A is proportional to the Curie constant, and Δ is the Weiss constant. Since B changes somewhat with each cooling of the apparatus, it is necessary to infer its value in each experiment. This is most satisfactorily done by measuring M with the sample in equilibrium with the nitrogen bath before helium is transferred. Since $M-B$ is relatively small at 77°K, rather approximate values of A and Δ are then sufficient to accurately determine B.

The results of the first experiment (I) with MAS are shown in Fig. 1. If the salt obeys the Curie-Weiss law and the 1948 vapor pressure-temperature scale T_{48} is correct, then $T_{48}(M-B)$ should be a linear function of $M-B$, with slope Δ and intercept A. This is not the case, but rather there are considerable deviations from a linear behavior.

Since the estimated uncertainties in our measurement of $M-B$ and T_{48} are, respectively, 0.05 and 0.005 percent at 4.2°K and 0.02 and 0.2 percent at 1.2°K, most of the deviation is well outside the limit of normal experimental error. The irregularities might, however, result from the anomalous behavior or errors in the measurement of any of the following: (a) the mutual inductance bridge apparatus; (b) the paramagnetism of MAS; (c) the vapor pressure; (d) the helium temperature scale. To resolve these possibilities, 3 additional experiments were carried out.

The first possibility was ruled out by simply repeating experiment I with the same sample of MAS. Although the values of A in the two runs agreed within 0.15 percent, the values of B differed by about $A/4$. For the same values of $M-B$ and T_{48}, therefore, the bridge reading M was vastly different in the two experiments. The results of experiment II, as shown in Table I, have the same behavior as those in experiment I; so it is concluded that the anomaly does not originate in the electrical measurements. The observed pressures in Table I have been corrected for gravity, temperature, manometer back pressure, and the gas-flow pressure drop in the cryostat. The correction in the second column is for the hydrostatic head of liquid nitrogen or helium over the sample. Additional liquid helium was added after the 2.47°K point, which accounts for the larger correction at the next lower points. The depth corrections in this second experiment were somewhat smaller than in the first, so the agreement of the results has some bearing on the validity of this correction.

Although possibility (b) was deemed quite unlikely in view of the many studies of MAS, it nevertheless seemed desirable to conduct an experiment that would conclusively eliminate this possibility. To this purpose experiment III was performed. The paramagnetic salt was iron alum, $FeNH_4(SO_4)_2\cdot 12H_2O$; the other procedures were identical with those in I and II. The results are shown in Fig. 2. In spite of the relatively large Weiss constant (~0.030°K), the results are seen to be entirely consistent with those of the previous experiments.

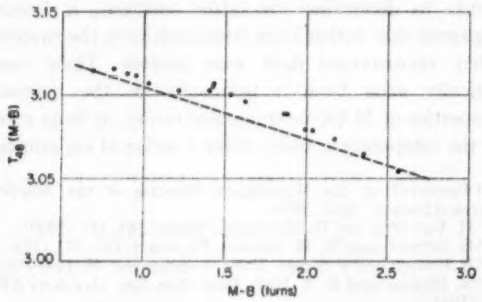

FIG. 2. The relative susceptibility of iron ammonium alum. The indicated Weiss constant is 32 millidegrees.

[8] Erickson, Roberts, and Dabbs, Rev. Sci. Instr. (to be published).

TABLE I. Susceptibility—vapor pressure data for MAS in experiment II. The correction in the second column is for the hydrostatic pressure head.

P_{obs} mm Hg. 20°C	Correction mm Hg	P mm Hg. 20°C	T_{55} °K	M Dial turns	$M-B$	$T_{55}(M-B)$	No. of obs
737.5 N_2	30.0	767.5	77.44	−1.3656	0.0546	4.228	
737.5	2.3	739.8	4.184	−0.4109	1.0093	4.2229	3
542.7	2.1	544.8	3.883	−0.3316	1.0886	4.2270	6
259.5	2.1	261.6	3.263	−0.1232	1.2970	4.2321	5
128.7	2.05	130.75	2.791	0.0930	1.5132	4.2233	3
70.6	2.05	72.65	2.471	0.2917	1.7119	4.2301	4
61.05	2.5	63.55	2.407	0.3373	1.7575	4.2303	2
39.07	2.45	41.52	2.218	0.4888	1.9090	4.2342	1
37.99		37.99	2.182	0.5252	1.9454	4.2449	1
37.70		37.70	2.179	0.5275	1.9477	4.2440	2
10.61		10.61	1.758	0.9900	2.4102	4.2371	2
4.56		4.56	1.552	1.3051	2.7253	4.2297	2
7.50		7.50	1.668	1.1205	2.5457	4.2462	2
5.90		5.90	1.611	1.2120	2.6320	4.2402	3
3.455		3.455	1.492	1.4034	2.8236	4.2128	3
1.936		1.936	1.381	1.6298	3.0500	4.2120	2
1.142		1.142	1.290	1.8361	3.2563	4.2006	2
0.590		0.590	1.192	2.1071	3.5273	4.2045	2
0.410		0.410	1.142	2.2532	3.6734	4.1950	2

There remained the more difficult problem of showing that the pressure measurements and corrections properly described the conditions at the sample. In the customary procedure, as employed in the previous experiments, the salt was enclosed in a glass envelope tube and held in thermal contact with the bath by means of helium exchange gas. As the sample temperature was independent of the amount of exchange gas for pressures greater than 15μ, it seems highly improbable that the sample temperature could have been different from that of the bath. However, the hydrostatic depth corrections were quite large (~0.025°K) in the region immediately above the λ point. Since the simply calculated correction assumes no heat conduction or convection in the helium bath, this was considered a possible source of large error. It must be noted, however, that no change in the depth correction procedure would affect the results below the λ point.

To clarify this situation a fourth experiment was performed using a fresh sample of MAS. Here the capsule tube was again in thermal contact with the bath, but the sample was immersed barely below the surface in helium liquid condensed within the sample tube and the vapor pressure was measured in the sample tube as well as over the bath. The sample tube was large enough (18 mm) so that the pressure gradients due to refluxing condensation in the upper tube should have been negligible. Thus, the capsule tube pressure together with a quite small depth correction should fairly represent the pressure at the sample. The observations in experiment IV demonstrated that the previous technique of pressure measurement and correction is quite appropriate. Thus the observed anomalies must arise from errors in the temperature scale.

Because of the parameters A and Δ, it is not possible with the data available to establish uniquely a temperature scale. To do this it would be necessary to determine these parameters from observations at higher temperatures, e.g., with liquid hydrogen. However, the data do permit of an accurate interpolation (or extrapolation) based on any 2 points in the observed interval of temperature. The validity of the temperature scale resulting will then be determined primarily by the correctness of these adopted points. Following this procedure we have adopted as correct the 1948 scale temperatures at 4.2 and 1.3°K. For each experiment the parameters A and Δ can then be calculated, and with these and $M-B$ a magnetic temperature T_m is obtained. The results are given in Fig. 3 where the difference between the accepted temperature and the magnetic temperature is shown as a function of T_{55}. Kistemaker's suggested correction below the λ point is shown as a dashed curve, and it is seen to be quite consistent with these results. The deviation around 3.5°K indicates that the 1937 correction to the 1932 scale was too large in this region. It is of interest that the values of the Weiss constant for the two different samples of MAS, although very small, were of opposite sign. We conclude that the Weiss constant of a perfectly spherical specimen of powdered MAS is probably negative but very small in this temperature region, and that the measured Weiss constant in any actual sample is determined more by the aggregate state and surface condition than by the intrinsic properties of MAS.

It is noted that in each of these experiments the deviation just above the λ point is greater than that just below the λ point. This apparent discontinuity was consistently 3–5 millidegrees. Since a vapor in thermodynamic equilibrium with its liquid cannot possess such a discontinuity, this behavior must originate in some dynamic mechanism, e.g., a slight superheating of the boiling liquid in the He I region.

According to the usual criterion for the determination of the λ point, the vanishing of thermal gradients in the liquid, we observe the λ pressure to be 38.05

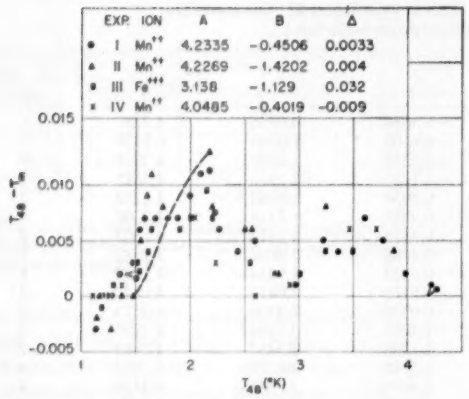

FIG. 3. The deviation of the magnetic temperature data from the 1948 temperature scale. Kistemaker's proposed correction is given by the dashed curve.

±0.05 mm Hg (20°C), in agreement with the result reported by Long and Meyer.[9]

III. CALCULATION OF THE VAPOR PRESSURE AND LATENT HEAT

From the thermodynamic properties of liquid helium and a knowledge of the virial coefficients of the vapor, it is possible to calculate the vapor pressure and latent heat as a function of the temperature. Calculations of this type have been made by Bleaney and Simon[3] and by Kistemaker.[6] We repeat these calculations using more recent data on the liquid specific heat and the fundamental atomic constants, and employing a more exact evaluation of the virial correction terms.

If a liquid and its vapor are in equilibrium, then their Gibbs free energies are equal. Thus[10]

$$RT\left\{\ln\frac{P}{T^{5/2}}-i_0-\phi(v)\right\}-L_0 = \int_0^T V_l\left(\frac{dP}{dT}\right)dT-\int_0^T S_l dT, \quad (1)$$

where $i_0=\ln(2\pi m)^{3/2}k^{5/2}h^{-3}$ is the chemical constant; $\phi(v)=2B/v+3C/2v^2-\ln(Pv/RT)$ is the virial correction in which $Pv/RT=1+B/v+C/v^2$; L_0 is the latent heat of vaporization at $T=0$; V_l and S_l are, respectively, the volume and entropy of the liquid.

For the values of atomic constants given by Bearden *et al.*,[11] $m=6.6456\times10^{-24}$ gram, $k=1.38039\times10^{-16}$ erg/deg, $h=6.62509\times10^{-27}$ erg sec, whence $i_0=12.244$ cgs, or with P in mm Hg at 20°C, $i_0'=2.1940$. This is somewhat smaller than the previous value of the chemical constant for helium.

Kistemaker and Keesom[6] have measured the virial coefficients of helium below 2°K and have found them to be consistent with the adopted values[12] for higher temperatures. The second virial term is conveniently described by $B=15.31-386.5/T$ cm³/mole; the third virial coefficient has been taken from a graphical plot of the measured values. Having values for the virial coefficients, it is then a simple matter to solve the cubic equation for the mole volume of the vapor at a given pressure and temperature and then to evaluate the correction term $\phi(v)$.

The liquid volume is obtained from the data of Kamerlingh Onnes and Boks,[8] and dP/dT from the 1948 temperature scale.[1] The liquid entropy is evaluated from an integration of a smooth curve through the specific heat data of Dana and Kamerlingh Onnes,[13] Keesom and Clusius,[14] Keesom and Miss Keesom,[15] Hull, Wilkinson, and Wilks,[16] and Kramers, Wasscher, and Gorter.[17]

There is insufficient knowledge of the interatomic forces in liquid helium to make an accurate calculation of L_0 from first principles. L_0 must therefore be derived either from Eq. (1), using observed $T-P$ data, or from an expression equivalent to (1) involving the measured latent heat of vaporization. Since the latent heat measurements are not sufficiently extensive nor accurate for this determination, we use the smoothed T_m-P data and calculate L_0 values from Eq. (1). The validity of the T_m scale is then demonstrated by the consistency of the L_0 values.

The results from this calculation are summarized in Table II. Values of L_0 derived from the 1948 scale are also given, and it is seen that they are much less consistent than the values obtained with T_m. Considering the T_m data around 2°K and those above 3°K as most valid, the suggested value of L_0 is 59.50 joules/

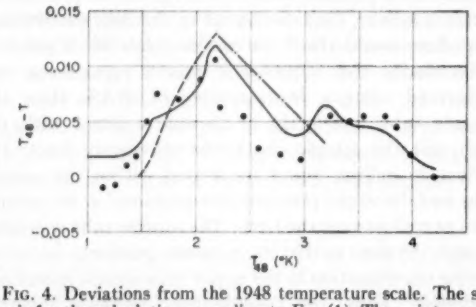

FIG. 4. Deviations from the 1948 temperature scale. The solid line is for the calculation according to Eq. (1). The points are the averaged data shown in Fig. 3. The broken line represents the correction consistent with the measurements of Kistemaker and of Abraham, Osborne, and Weinstock.

[9] E. Long and L. Meyer, Phys. Rev. **83**, 860 (1951).
[10] See J. E. Mayer and M. G. Mayer, *Statistical Mechanics* (John Wiley and Sons, Inc., New York, 1940), p. 292.
[11] Bearden, Earle, Minkowski, and Thompsen, "Values of the Atomic Constants as of April 1953" (unpublished).
[12] W. H. Keesom, *Helium* (Elsevier Press, Amsterdam, 1942), p. 49.
[13] L. I. Dana and H. Kamerlingh Onnes, Communs. Kamerlingh Onnes Lab. Univ. Leiden. 179d (1926)
[14] W. H. Keesom and K. Clusius, Communs. Kamerlingh Onnes Lab. Univ. Leiden 219e (1932).
[15] W. H. Keesom and Miss A. P. Keesom, Physica **2**, 557 (1935).
[16] Hull, Wilkinson, and Wilks, Proc. Phys. Soc. (London) **A64**, 379 (1951).
[17] Kramers, Wasscher, and Gorter, Physica **18**, 329 (1952).

TABLE II. Calculated values of the latent heat of varpoization at $T=0$.

P mm Hg. 20°C	T_m °K	T_α °K	v cc/mole	$-RT\phi(v)$ joules/mole	$\int_0^T SdT$ joules/mole	$\int_0^P Vdp$ joules/mole	L_0 joules/mole T_m	T_α
751.7	4.2	4.200	234.2	9.02	22.91	2.95	59.52	59.52
617.0	4.0	4.002	291.1	7.70	20.20	2.38	59.50	59.57
501.0	3.8	3.805	358.2	6.55	17.65	1.90	59.47	59.63
400.0	3.6	3.605	443.5	5.50	15.25	1.50	59.50	59.65
314.3	3.4	3.405	552.3	4.57	12.99	1.16	59.50	59.67
242.3	3.2	3.206	694.3	3.77	10.86	0.90	59.53	59.73
181.5	3.0	3.001	895	3.00	8.86	0.67	59.61	59.65
133.2	2.8	2.802	1162	2.42	6.99	0.49	59.59	59.67
93.6	2.6	2.602	1573	1.85	5.25	0.34	59.68	59.77
63.4	2.4	2.406	2190	1.36	3.65	0.23	59.64	59.88
40.4	2.2	2.207	3214	0.95	2.22	0.14	59.69	60.01
38.00	2.17	2.182	3382	0.88	2.02	0.13	59.47	60.00
31.65	2.1	2.110	3955	0.76	1.63	0.11	59.53	59.99
24.00	2.0	2.008	5007	0.61	1.18	0.08	59.50	59.89
12.65	1.8	1.807	8684	0.35	0.58	0.05	59.46	59.83
5.80	1.6	1.607	1.70×10^4	0.19	0.26	0.02	59.42	59.79
2.175	1.4	1.402	4.03×10^4	0.08	0.10	0.01	59.55	59.68
0.626	1.2	1.200	12.0×10^4	0.03	0.03		59.64	59.64
0.120	1.0	1.000	51.7×10^4	0.01	0.01		59.58	59.58

mole. This is a somewhat lower value than that given by Bleaney and Simon[3] or by Kistemaker,[6] the difference resulting primarily from the smaller chemical constant employed here. Adopting $L_0=59.50$ joules/mole, one calculates a $P-T$ relation from Eq. (1). The deviation of this calculated temperature from the 1948 scale is shown as the solid line in Fig. 4; also shown are the average data points from Fig. 3, and Kistemaker's correction is shown by the broken line. The dashed curve above the λ point is that which Abraham, Osborne, and Weinstock[18] have taken from Kistemaker's data, and which seems reasonably confirmed by their measurements of the vapor pressure of He^3.

The latent heat of vaporization can now be evaluated on a basis consistent with the calculated $P-T$ function according to the expression,

$$L/T=-R\{\ln(P/T^{5/2})-i_0-5/2\}-R\phi(v)-RT(\partial\phi/\partial T)_P-S_l, \quad (2)$$

where the second and third terms are the viral corrections to the ideal gas entropy. The results for this calculation are given in Table III, and compared with the experimental observations of Dana and Kamerlingh Onnes[19] in Fig. 5. Kistemaker's calculation of the latent heat function is given by the broken line in Fig. 5.

IV. DISCUSSION

Below the λ Point

In this region the calculated $P-T$ and latent heat functions agree very well with the observations and with Kistemaker's results. The disagreement at the lowest temperatures between the observed and calculated temperatures, as shown in Fig. 4, results of course from the adoption of the 1.3°K point on the 1948 scale. According to the calculated scale, this point is in error by about −1.5 millidegrees. Renormalizing the T_m data to this new low-temperature point would give a correction to the T_m points amounting to 0.0005° at 3°K, 0.001° at 2.2°K, and 0.0017° at 1.0°K. This would in general give an even better agreement between the T_m points and the calculated curve.

Up to the λ point the gas and liquid corrections to the ideal vapor pressure are sufficiently small to be represented by simple analytic expressions. The vapor pressure is then described by the formula,

$$\log P_{mm}(20°C)=-\frac{3.1071}{T}+2.5\log T+2.1940-5.00\times10^{-4}T^6+\frac{0.0522}{T}\int_0^T \exp[-20(2.20-T)^2]\times dT+0.448T^{\frac{1}{2}}e^{-7.16/T}. \quad (3)$$

TABLE III. Calculated values of the latent heat of vaporization of liquid helium as a function of temperature.[a]

T °K	S_g joules/mole deg S_{ideal}	Virial correction	S_g	S_l joules/mole deg	L joules/mole
4.2	37.56	4.07	33.49	13.97	81.98
4.0	38.19	3.41	34.78	13.13	86.60
3.8	38.94	2.95	35.99	12.38	89.72
3.6	39.61	2.56	37.05	11.65	91.44
3.4	40.43	2.24	38.19	10.98	92.51
3.2	41.24	1.97	39.27	10.31	92.67
3.0	42.35	1.70	40.65	9.67	92.94
2.8	43.50	1.46	42.04	9.04	92.40
2.6	44.85	1.18	43.67	8.37	91.78
2.4	46.44	0.92	45.52	7.58	91.06
2.2	48.35	0.66	47.69	6.56	90.49
2.17	48.68	0.64	48.04	6.15	90.90
2.1	49.49	0.55	48.94	5.06	92.15
2.0	50.78	0.45	50.34	3.90	92.88
1.8	53.94	0.25	53.69	2.23	92.63
1.6	58.01	0.14	57.87	1.13	90.78
1.4	63.30	0.06	63.24	0.52	87.81
1.2	70.38	0.02	70.36	0.18	84.22
1.0	80.29	0.01	80.28	0.06	80.22

[a] S_g is the gas entropy, given by the first three terms on the right-hand side of Eq. (2).

[18] Abraham, Osborne, and Weinstock, Phys. Rev. **80**, 366 (1950).

[19] L. I. Dana and H. Kamerlingh Onnes, Communs. Kamerlingh Onnes Lab. Univ. Leiden 179c (1926).

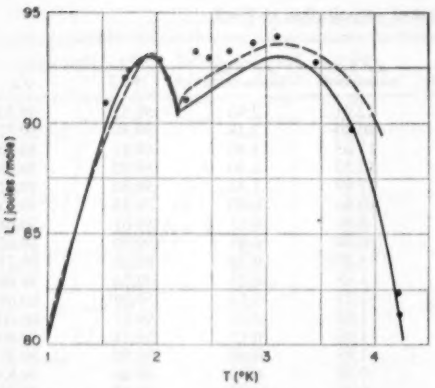

FIG. 5. The latent heat of varpoization of liquid helium. The data points are the measurements of Dana and Kamerlingh Onnes. The solid curve is calculated from Eq. (2), and the dashed curves follows the calculation of Kistemaker.

The fourth and fifth terms in this formula result from the liquid entropy integral, and the last term represents the virial correction and liquid volume integral. In this formula the λ pressure of 38.05 mm corresponds to the temperature 2.170°K.

We estimate the uncertainty in the last 3 terms of Eq. (3) to be one percent, and in L_0 to be ± 0.05 joule/mole. This gives rise to an uncertainty in the calculated temperature scale amounting to 1.5 millidegrees at T_λ and 0.7 millidegrees at 1°K.

Above the λ Point

Although the calculated and observed functions agree quite satisfactorily in this region also, it is interesting to note the seemingly consistent departures in both the $P-T$ and latent heat function in the interval 2.2–3.2°K. The largest potential source of error in these calculations results from the scatter of the specific heat measurements above the λ point. However, it is not possible to modify the liquid entropy in such a manner as to improve the agreement of the calculation with both the $P-T$ and latent heat data, and yet be consistent with the measured specific heat. Since these departures barely exceed the experimental uncertainty of the data, and there seems to be no methodical way of improving the agreement, it is difficult to assess the possible origin or significance of the disagreement.

If the error in the liquid and gas correction terms is again taken to be one percent then the resulting uncertainty in the calculated *absolute* temperature amounts to 11 millidegrees at 4.2°K and 5 millidegrees at 3°K. The T_m data have, therefore, a somewhat greater significance than the calculated scale in this region, for, if the susceptibility data are corrected according to the calculated scale below the λ point, then an extrapolation of T_m according to a Curie-Weiss law for the paramagnetic salt determines the 4.2°K point within 5 millidegrees of the accepted value. Since this is not so precise as the determination of the normal boiling point by Schmidt and Keesom we prefer to continue the adoption of their point on the absolute scale. The calculated scale is then of the nature of an interpolation between the λ temperature of 2.170°K and the normal boiling temperature of 4.216°K. The adoption of the latter point considerably reduces the uncertainty in the liquid entropy determination, and as a result the *relative* temperature is given by the calculated scale with an estimated accuracy of 3 millidegrees. As shown in Fig. 4, this is in agreement with the magnetic temperature data as well as the correction curve adopted by Abraham, Osborne, and Weinstock.[18] It seems reasonable, therefore, to propose that the temperature interpolation given by the calculated scale is correct to 3 millidegrees in the region above the λ point.

The validity of the calculated scale is further demonstrated by the agreement between the calculated and observed latent heat of vaporization at the higher temperatures, as shown in Fig. 5. Whereas Kistemaker's calculation of the latent heat suggested rather large errors in the experimental observations around 4°K, the results here are in good agreement with the data. The discrepancy in the two calculations originates in the manner of evaluating the virial corrections in Eq. (2). We have calculated $\phi(v)$ and $d\phi/dT$ in a manner exact through the third virial coefficient, whereas the more usual procedure is to expand the virial correction as a power series of the pressure and use only the first few terms.

We gratefully acknowledge the technical assistance of Mr. J. B. Capehart.

Nonsingle Scattering of Electrons at Oblique Incidence

MORTON HAMERMESH AND JAMES MONAHAN
Argonne National Laboratory, Lemont, Illinois
(Received October 27, 1953)

A detailed calculation shows that effects of plural scattering of electrons are adequately described by the method of Goertzel and Cox.

GOERTZEL and Cox[1] have pointed out that for electrons at oblique incidence there exists an asymmetry between the number of electrons scattered through a fixed angle from a foil in the reflection and transmission positions. As shown in Figs. 1 and 2, in these standard experimental arrangements, the incident and scattered electrons make definite angles with the plane of the foil. In the "reflection" position both beams are on the same side, while in the "transmission" position, the beams are on opposite sides of the foil. By assuming that the principal deviation from single scattering is that due to the combination of two deflections of the same order of magnitude and considering only those regions of the foil in which such events are most likely to take place—roughly about one-half of the total volume of the scattering foil—they have obtained expressions for the minimum contribution of nonsingle scattering for electrons incident at an angle of 45° to the normal of the foil. Recent experiments,[2] however, suggest an asymmetry several times greater than is indicated by this calculation.

The asymmetry caused by nonsingle scattering of electrons obliquely incident on a thin foil is reinvestigated in the present calculation. Contributions from the entire volume of the foil are considered. Numerical results are given for the case of 1.7-Mev electrons incident at an angle of 45° on an aluminum foil 7 mg/cm² thick. These values were chosen to conform with the parameters of Waldman's experiments. While the result of this calculation indicates that the asymmetry may be much as three times greater than the value obtained by Goertzel and Cox, it is still considerably less than Waldman's data seem to indicate.

In Fig. 1 the foil is shown in the reflection position. The direction of incidence **AO** makes an angle δ with the normal **OZ**; the scattering angle α is in the plane of incidence. The electron is considered first to be deflected through an angle θ along **OC** to an arbitrary point P within the foil where it suffers a second deflection through an angle ψ into the collecting chamber at B'. **OC'** is the projection of **OC** on the plane of the foil. In the reflection position the foil is oriented such that

$$\alpha=\pi-2\delta\geq\pi/2. \tag{1}$$

The distribution of the deflections produced by the scatterer is assumed to be

$$P(\xi,t)=G(\xi,t)+S(\xi,t), \tag{2}$$

where G represents a Gaussian distribution based on the statistical theory of Williams,[3] and S is the single-scattering tail; more specifically S is given by the McKinley-Feshbach[4] approximation formula. ξ is the spatial scattering angle, and t is the length of the path within the foil of the undeflected electron.

If h represents the thickness of the foil, the distribution about the center of the foil, O, is then $P(\theta, h/2\cos\delta)$, and the probability that an electron, initially deflected

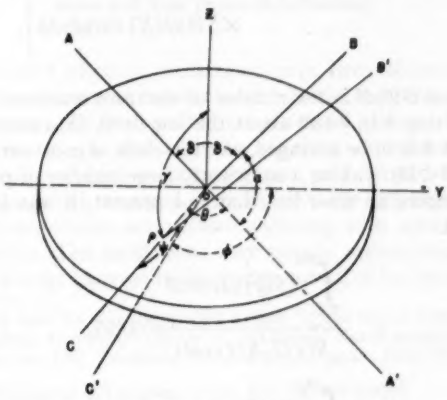

FIG. 1. Reflection position of the foil.

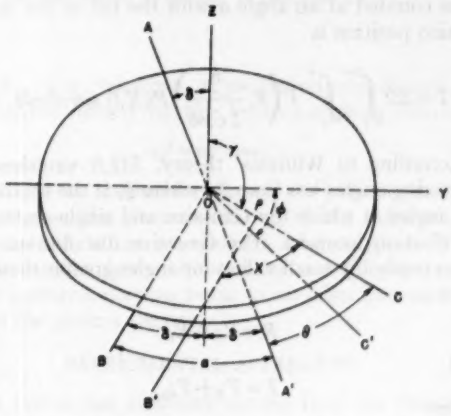

FIG. 2. Transmission position of the foil.

[1] G. Goertzel and R. T. Cox, Phys. Rev. **63**, 37 (1943).
[2] B. Waldman (private communication).
[3] E. J. Williams, Phys. Rev. **58**, 292 (1940).
[4] W. A. McKinley and H. Feshbach, Phys. Rev. **74**, 1759 (1948).

through an angle θ, suffers a second collision through an angle ψ necessary to bring it to the collector is $P(\psi,t)\Delta\Omega$, where

$$t=\begin{cases} h/2|\cos\gamma| & \text{for } h<2\lambda|\cos\gamma| \\ \lambda & \text{for } h>2\lambda|\cos\gamma|. \end{cases} \tag{3}$$

$\Delta\Omega$ is the element of solid angle subtended by the collector at the foil, γ is the integration variable defined in Fig. 1, and

$$\lambda=-\int_{E_0}^{E_1}\frac{dE}{p},$$

where p is the stopping-power, E_0 the energy of the incident electron, and E_1 the minimum energy necessary to activate the counter. The total number of electrons deflected through an angle α from a foil in the reflection position, and counted in the chamber at B is then

$$R=\Delta\Omega\int_0^{2\pi}\int_0^{\pi}P\left(\theta,\frac{h}{2\cos\delta}\right)P(\psi,t)\sin\gamma d\gamma d\varphi, \tag{4}$$

where

$$\begin{aligned}\cos\theta&=\sin\gamma\cos\varphi\sin\delta-\cos\gamma\cos\delta,\\ \cos\psi&=\sin\gamma\cos\varphi\sin\delta+\cos\gamma\cos\delta.\end{aligned} \tag{5}$$

In the transmission position (Fig. 2) the foil is oriented in a manner such that

$$\alpha=2\delta\leqslant\pi/2. \tag{6}$$

In this position the initial distribution about the point 0 is again $P(\theta, h/2\cos\delta)$; however, the probability of a second deflection which will bring the electron to the collecting chamber is now $P(X,t)\Delta\Omega$, where

$$\cos X=-\cos\psi. \tag{7}$$

t is again defined by Eq. (3). Thus the number of electrons counted at an angle α with the foil in the transmission position is

$$T=\Delta\Omega\int_0^{2\pi}\int_0^{\pi}P\left(\theta,\frac{h}{2\cos\delta}\right)P(X,t)\sin\gamma d\gamma d\phi. \tag{8}$$

According to Williams' theory, $S(\xi,t)$ vanishes for scattering angles less than ξ_2, where ξ_2 is the smaller of the angles at which the Gaussian and single-scattering distribution intersect. The Gaussian distribution falls off to negligibly small values for angles greater than $2\xi_2$. Thus

$$R=R_S+R_G \tag{4'}$$

and

$$T=T_S+T_G, \tag{8'}$$

where

$$R_S=\Delta\Omega\int_0^{2\pi}\int_0^{\pi}S\left(\theta,\frac{h}{2\cos\delta}\right)S(\psi,t)\sin\gamma d\gamma d\phi \tag{9}$$

and

$$T_S=\Delta\Omega\int_0^{2\pi}\int_0^{\pi}S\left(\theta,\frac{h}{2\cos\delta}\right)S(X,t)\sin\gamma d\gamma d\phi. \tag{10}$$

R_G and T_G are defined by Eqs. (13) and (14). Equations (9) and (10) represent the contributions to the electron intensity at an angle α due entirely to double scattering.

The integrals R_S and T_S have been evaluated numerically for the following parameters:

$$E_0=1.7\text{ Mev};\quad h(\text{Al})=2.5\times10^{-3}\text{ cm};\quad \lambda=2.96h;\quad \alpha=90^\circ. \tag{11}$$

Neglecting fourth- and higher-order differences of the integrand in a double application of Simpson's rule, the following results were obtained:

$$\frac{R_S}{S(\pi/2,\,h/2\cos\delta)}=0.050;\qquad \frac{T_S}{S(\pi/2,\,h/2\cos\delta)}=0.005. \tag{12}$$

The integration mesh on a unit circle about the point 0 was made sufficiently fine that the principal error did not exceed one percent.

The remaining terms, R_G and T_G, include the so-called direct scattering; these terms are slightly asymmetrical due to the Gaussian distribution about the direction of incidence.

$$R_G=\Delta\Omega\left\{\int_0^{2\theta_2}\langle S(\psi)\rangle_{\theta}G(\theta)d\theta+\int_{-2\theta_2}^{2\theta_2}\int_{\frac{1}{2}(\pi-\alpha)-2\theta_2}^{\frac{1}{2}(\pi-\alpha)+2\theta_2}\times S(\theta)G(\psi)\sin\gamma d\gamma d\phi\right\}, \tag{13}$$

$$T_G=\Delta\Omega\left\{\int_0^{2\theta_2}\langle S(X)\rangle_{\theta}G(\theta)d\theta+\int_{\pi-2\theta_2}^{\pi+2\theta_2}\int_{\pi-\frac{1}{2}\alpha-2\theta_2}^{\pi-\frac{1}{2}\alpha+2\theta_2}\times S(\theta)G(X)\sin\gamma d\gamma d\phi\right\}, \tag{14}$$

where $G(\theta)d\theta$ is the number of electrons scattered into the ring θ to $\theta+d\theta$ about the line $\theta=0$. $\langle S\rangle_{\theta}$ indicates that S is to be averaged over the circle of constant θ for $0<\theta<2\theta_2$. Taking a sufficiently large number of points to insure an error less than one percent, it was found that

$$\frac{\int_0^{2\theta_2}\langle S(\psi)\rangle_{\theta}G(\theta)d\theta}{S(\pi/2,\,h/2\cos\delta)}=0.495;\qquad \frac{\int_0^{2\theta_2}\langle S(X)\rangle_{\theta}G(\theta)d\theta}{S(\pi/2,\,h/2\cos\delta)}=0.489. \tag{15}$$

The second integrals in the expressions (13) and (14) can be shown to be equal; thus they can introduce no asymmetry between the scattered intensities for the two positions of the foil. Further, if G is assumed to be a delta function about the direction of scattering, then

$$2\int_{-2\theta_2}^{2\theta_2}\int_{\frac{1}{2}(\pi-\alpha)-2\theta_2}^{\frac{1}{2}(\pi-\alpha)+2\theta_2} S(\theta)G(\psi)\sin\gamma d\gamma d\phi = S\left(\frac{\pi}{2}, \frac{h}{2\cos\delta}\right). \tag{16}$$

In view of the results of Eq. (15) it seems reasonable to assume that this approximation introduces an error of at most five percent in the absolute scattering intensity. Although this is sufficiently large to mask any double-scattering contribution to the number of electrons scattered through a given angle, it introduces a comparatively small error in the asymmetry ratio R/T, the contribution of the two integrals being entirely symmetric.

Adding these contributions, one obtains the ratio

$$R/T = 1.05 \pm 0.01. \tag{17}$$

Comparing Eqs. (12) and (15) it is obvious that for electrons at oblique incidence the only serious deviation from single scattering is that due to double scattering. This is essentially the condition for the validity of the approximation made by Goertzel and Cox. Using Rutherford's formula with relativistic electron mass for the single-scattering distribution, $S(\xi)$, they obtain an asymmetry ratio slightly less than 1.02 for the parameters considered above; the discrepancy is due almost entirely to the choice of different single-scattering distributions. The accuracy, apart from any assumptions as to scattering distributions, of the Goertzel-Cox approximation permits an essential simplification in calculations of this type.

Note added in proof.—A calculation similar to that of Goertzel and Cox has been published by Norio Ryu, J. Phys. Soc. Japan **5**, 423 (1950).

PHYSICAL REVIEW VOLUME 93, NUMBER 5 MARCH 1, 1954

The Excitation of Plasma Oscillations*

DUNCAN H. LOONEY,† AND SANBORN C. BROWN
Research Laboratory of Electronics and Department of Physics, Massachusetts Institute of Technology, Cambridge, Massachusetts

(Received November 24, 1953)

A beam of high-energy electrons, injected into the plasma of a dc discharge from an auxiliary electron gun, excited oscillations in the plasma at the plasma electron oscillation frequency given by the Tonks-Langmuir equation. A movable probe showed the existence of standing-wave patterns of the oscillatory energy in the region of the plasma in and around the electron beam. Nodes of the patterns coincided with the electrodes which limited the region of the plasma traversed by the beam. The standing-wave patterns were independent of the frequency of the oscillation. At any particular frequency, the standing wave was determined by the thickness of the ion sheaths on the bounding electrodes. The mechanism of the energy transfer from the electron beam to the oscillation of the plasma electrons was established as a velocity-modulation process by the detailed behavior of the frequency of oscillation and the transitions in the standing-wave patterns as the sheath thickness was varied. Experimental attempts to produce plasma oscillations as predicted by Bohm and Gross proved to be fruitless.

PLASMA electron oscillations have been observed in a number of experiments[1–4] in which a beam of high-energy electrons penetrated a neutral plasma of a low-pressure gas discharge. In all these experiments the beam of high-energy electrons was formed by electrons which emerged from the cathode fall region of a low-pressure arc without colliding with neutral gas atoms. The oscillations were usually accompanied by an abrupt increase in the energy spread of the beam particles. The frequency of oscillation was related to the electron density by the Tonks-Langmuir relation,

$$\omega_p^2 = ne^2/m\epsilon_0, \tag{1}$$

where ω_p is the radian frequency of the plasma electron oscillation, n the electron density, m the mass of an electron, and ϵ_0 the permittivity of free space. The experimental evidence indicated that energy was transferred from the electron beam to an organized oscillation of the plasma electron.

EXPERIMENTAL APPARATUS

The use of fast electrons coming from the cathode region of an arc as a beam to excite plasma oscillations has several disadvantages. One of the most obvious drawbacks is that the plasma itself is controlled by the

* This work has been supported in part by the Signal Corps, Air Materiel Command, and the U. S. Office of Naval Research.
† Now at Bell Telephone Laboratories, Murray Hill, New Jersey.
[1] L. Tonks and I. Langmuir, Phys. Rev. **33**, 195 (1929).
[2] H. J. Merrill and W. Webb, Phys. Rev. **55**, 1191 (1939).
[3] T. R. Neill and K. G. Emeleus, Proc. Roy. Irish Acad. **A53**, 197 (1951).
[4] G. Wehner, J. Appl. Phys. **22**, 761 (1951).

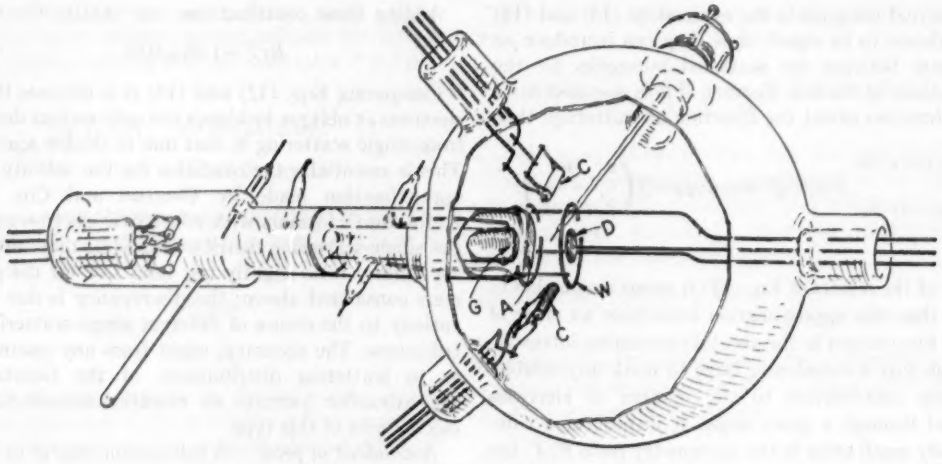

FIG. 1. Sketch of the experimental tube.

density and energy of the beam electrons since these electrons maintain the plasma. In addition, neither the density of electrons in the beam nor their energy is easily varied. The use of a beam of high-energy electrons from an auxiliary source rather than from the cathode of the arc eliminates these difficulties, and the present apparatus was designed with this object in view.

A glass tube was constructed in which a controlled electron beam was injected into the plasma of a low-pressure (about three microns) mercury arc. The main plasma was drawn from two large oxide-coated cathodes, marked *C-C* in Fig. 1. A second discharge in the side arm acted as a source of electrons for an electron gun. A beam of electrons was drawn from a 1-mm hole in the anode of the gun discharge, *G* of Fig. 1, accelerated through several hundred volts, and injected into the plasma through a 1-mm hole in the accelerating anode marked *A* in Fig. 1. The electron beam finally impinged on an anode disk *D*, which was electrically connected to the accelerating anode and 1.5 cm away from it. The geometry of the tube and the electrical circuits controlling the arc were arranged to give large ion sheaths on the accelerating electrode and the anode disk. These two electrodes could be biased negatively with respect to the wire ring anode, *W*, of the main discharge through a range of 200 volts. This allowed the thickness of the ion sheaths to be changed. A probe, attached to the tube by a stainless steel bellows, could be moved through the interaction region of the plasma and the electron beam. The probe was a wire 3 thousandths of an inch in diameter and 5 mm long; its position was measured by a cathetometer to an accuracy of ± 0.1 mm.

Oscillations were detected by a superheterodyne receiver capacitatively coupled to the movable probe. The probe picked up the oscillation whether it was in or near the electron beam. The selectivity of the receiver determined the frequency of the oscillation to ± 5 Mc/sec whereas the band width of the oscillation was usually less than 10 Mc/sec.

EXPERIMENTAL RESULTS

The behavior of the plasma oscillation was studied by varying the electron density of the beam (controlled by the electron gun discharge current) and the thickness of the ion space-charge sheath (controlled by the sheath bias voltage). The electron density of the beam was so large that the density of the plasma region around the beam was determined by the density of the beam particles. Probe measurements showed that the plasma electron density varied as a linear function of the gun discharge current if the energy of the beam particles was kept constant. The variation of the thickness of the sheath on the beam electrodes had no effect on the plasma electron density until the sheath thickness was comparable to the plasma length—AD.

The frequency of oscillation was observed to vary in a discontinuous manner with the gun discharge current. The frequency would remain nearly constant over small variations of the gun discharge current and then jump abruptly to a new frequency. Along one of these frequency plateaus, the intensity of the oscillation would rise to a maximum and then fall to a much lower value before a jump to a new frequency occurred. It was observed that the frequency corresponding to the strongest signal for each frequency range was consistent with the predictions of Eq. (1). Since the plasma electron density was a linear function of the gun discharge current, the square of the frequency of the oscillation at each intensity maximum was a linear function of the gun discharge current. Equation (1) was used to determine a conversion factor, relating the electron density and the gun discharge current, from two observed points of the plot of gun discharge current *versus* the square of the frequency. The electron density was then calculated from the observed gun

discharge current. The measured frequency of oscillation as a function of this normalized electron density is shown in Fig. 2.

With the electron density held constant, motion of the probe (coupled to the high-frequency receiver) through the plasma, showed that the entire plasma between the accelerating anode and the anode disk was oscillating in a standing wave. As the electron density was varied so that the tube oscillation jumped from one frequency plateau to another, the standing-wave pattern changed, each frequency plateau corresponding to a given wave pattern. The standing-wave pattern associated with each range of frequency is also shown in Fig. 2. In general, the standing-wave pattern had an integral number of half-waves between the two beam electrodes with nodes at these electrodes.

The standing-wave patterns were measured as the thickness of the plasma sheaths on the accelerating anode and anode disk was varied, keeping the electron density constant. The results of these measurements are illustrated in Fig. 3. As the two beam electrodes were made more negative with respect to the wire ring anode of the main discharge, the plasma sheaths became thicker. Sudden transitions in the frequency of oscillation occurred as the sheath thickness was varied. These transitions were accompanied by abrupt changes in the wavelength of the plasma oscillations. As in the case of the sudden frequency transitions with changes in density, small changes in frequency occurred over a certain change in sheath thickness, and then a major jump in oscillation frequency occurred as the wavelength of the standing wave changed. The positions of the visible sheath edge show that both the frequency of oscillation and the transitions in the standing wave patterns were associated with this edge. The abrupt changes in the wavelength adjusted the standing-wave pattern to keep a node of the pattern near the visible sheath edge.

The thickness of the sheath, X_s, may be calculated

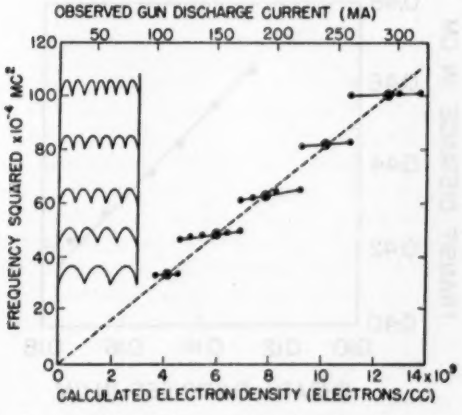

FIG. 2. Oscillation frequency as a function of the gun discharge current and electron density.

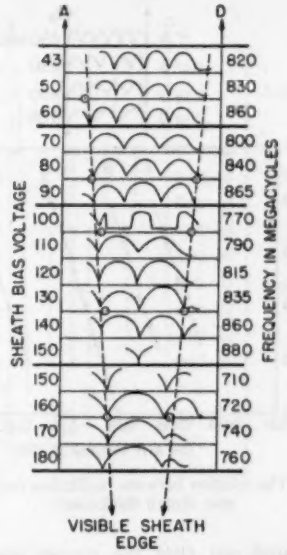

FIG. 3. Standing-wave pattern as a function of the thickness of the plasma sheath keeping the electron density constant. A and D represent the positions of the accelerating anode and anode disk as shown in Fig. 1.

from the space charge law for an infinite plane to give

$$X_s = 375 V_s^{\frac{1}{2}}/n^{\frac{1}{2}},$$

where V_s is the sheath bias voltage and a directed ion velocity of 1.7×10^6 cm/sec was assumed. The electron density may be eliminated by using Eq. (1) to give

$$X_s = 3.4 V_s^{\frac{1}{2}}/f_0, \qquad (2)$$

where f_0 is the average frequency in Mc/sec of a given frequency range. The variation of the measured frequency of oscillation as a function of the sheath thickness calculated from Eq. (2) is shown in Fig. 4. In each frequency range, the frequency is a linear function of the sheath thickness. The standing-wave pattern of each frequency range is also shown in the figure.

MECHANISM OF EXCITATION

An explanation of an experimental plasma oscillator has been given by Wehner.[4] The mechanism of energy transfer from the electron beam to the oscillation of the plasma electrons is described by him as a transit time process similar to that controlling a klystron. The frequency of the oscillation is determined fundamentally by the resonant properties of the plasma given by Eq. (1). The electron beam enters the plasma through an ion sheath and is velocity-modulated at a point near the sheath edge of the plasma. As the beam traverses the plasma, the velocity modulation of the beam causes the electrons to bunch. An electric field of the proper phase for retarding the bunched electrons, and thus extract energy from the beam, must be assumed.

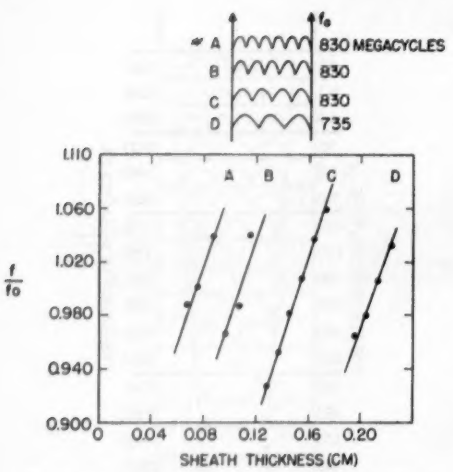

FIG. 4. The relation between oscillation frequency and sheath thickness.

Wehner pointed out that the proper phase relation between the electric field where the beam is modulated and where the energy is extracted from the beam requires that the average transit time t of a beam electron across the distance X_t between the modulation and extraction points be

$$t = X_t/v_0 = [(4k+1)/4]/f, \qquad (3)$$

where $k=0, 1, 2, \cdots$; v_0 is the average velocity of the beam electrons calculated from the accelerating voltage of 500 volts and the sheath bias voltage; and f is the frequency of oscillation. If the distance X_t is assumed constant, Eq. (3) may be written as $\lambda\sqrt{V}=$constant, where λ is the free-space wavelength of the oscillation and V is the voltage accelerating the beam. This relation has been observed by Neill and Emeleus[3] and by Wehner.[4]

In the present experiment, the actual point in the plasma where the beam was modulated was not detected since the probe did not have sufficient motion to pass through the sheath. If the modulation point is assumed to be at the sheath edge and the extraction point is assumed to be fixed by the standing-wave pattern, the deviations of the measured frequency from the frequency predicted by Eq. (1) may be understood by considering Eq. (3). If X_s is the sheath thickness on the accelerating anode and X_t is the distance from the modulation point at the sheath edge to the extraction point, then the extraction point is fixed at a distance X_s+X_t from the accelerating anode, or $X_s+X_t=$constant. If the sheath thickness X_s increases, and the plasma density remains constant, X_t must decrease and the frequency of oscillation increase to satisfy the transit time relation. This is shown in Fig. 4. If the sheath voltage is held constant and the plasma density is increased, the frequency of the oscillation should increase according to Eq. (1), as was discussed above. However, the increase in the plasma density decreases the sheath thickness and consequently increases X_t. To satisfy Eq. (3), the frequency should decrease. As a result of these two opposing effects the increase in the measured frequency is less than the increase predicted by Eq. (1). This effect accounts for the frequency plateau curves of Fig. 2.

If the transit-time mechanism is correct, the sheath thickness X_s must be linearly related to thet ransit distance X_t. By use of the measured frequency of oscillation and the velocity of the beam determined by the applied potentials, the distance X_t can be calculated from Eq. (3). For every case where sufficient data were taken and the plasma density remained constant, X_s varied linearly with X_t. An example of these data is illustrated in Fig. 5. The slope of the X_t *versus* X_s line is equal to minus one, indicating that the extraction point was fixed and the sheath thickness varied as assumed above.

The modulation of the electron beam occurs in the large fields at the sheath edge, whereas the beam may be demodulated in any region where the field has the opposite sign. This means that the modulation and the extraction points must always be separated by a node in the standing wave pattern. Both the sheath thickness and the transit distance can be calculated from the observed data. The distance X_s determines the location of the modulation point with respect to the accelerating anode, and the sum of X_s and X_t determines the location of the extraction point with respect to the accelerating anode. Superimposing the calculated sheath and extraction points on a diagram indicating the positions of the nodes of various standing waves observed, we find this phase relation is indeed met, as illustrated in Fig. 6. The transitions in the standing-wave patterns occur as the plasma oscillation adjusts itself to satisfy both the condition expressed by Eq. (1) and that expressed by Eq. (3) by keeping the extraction point and the modulation point separated by a node in the standing-

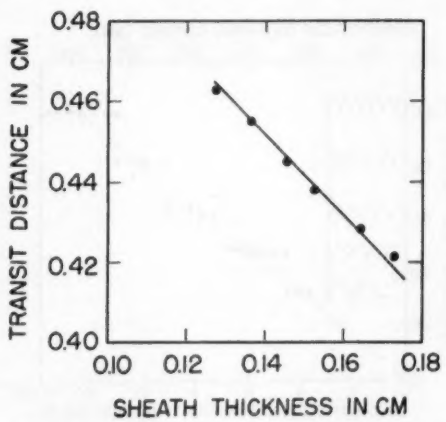

FIG. 5. Relation between the sheath thickness and the transit distance keeping the electron density constant.

wave pattern while oscillating in the frequency range required by the Tonks-Langmuir equation. The amplitude of the observed oscillation increased as the extraction region approached the maximum of the standing wave and decreased on approaching a node.

DISCUSSION

In 1949 Bohm and Gross[5] published a theory of plasma electron oscillations based on a one-dimensional analysis of a uniform infinite plasma. The theory postulated that a traveling longitudinal potential field could be excited by a beam of high-velocity electrons in the plasma and that this could be used to explain the energy transfer from a beam of high-energy particles to the oscillation existing in the plasma. A large portion of our experimental effort was devoted to injecting an electron beam into a discharge plasma so as to generate a plasma oscillation by the mechanism proposed by Bohm and Gross. The electron beam injected into a uniform plasma from an electron gun did not excite observable plasma oscillations in any of the experimental tubes constructed to satisfy the conditions of the Bohm and Gross theory. However, as soon as the discharge in the tube shown in Fig. 1 was modified by introducing large sheaths on the beam electrodes, oscillations were immediately found at the same plasma density where they were not observed in the "infinite" plasma.

All previous experimental investigations of plasma oscillations are consistent with the interpretation of the excitation process suggested by these present experiments. However, none have established the existence of an organized oscillation throughout the plasma region

[5] David Bohm and E. P. Gross, Phys. Rev. **75**, 1851 and 1865 (1949); Phys. Rev. **79**, 992 (1950).

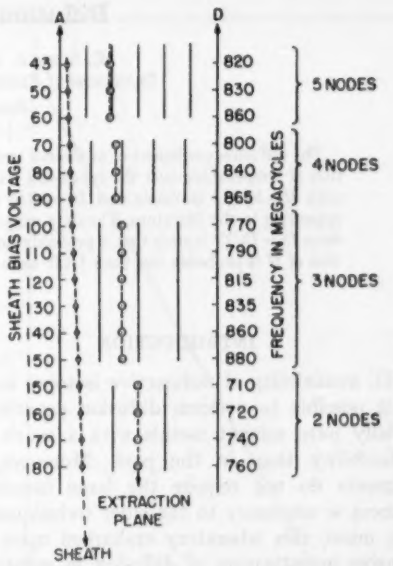

FIG. 6. Calculated positions of the sheath and extraction planes superimposed on a diagram of the positions of the nodes of various standing waves observed.

which modulated and demodulated the electron beam and provided a feedback mechanism to sustain the oscillation. Our experiments indicate the existence of a standing wave, set up in the plasma, which provides the necessary mechanism for maintaining the oscillations. It is apparent from calculation of the phase velocity of the components of the standing wave that it is not electromagnetic in origin. The experimental evidence indicates the oscillation is a longitudinal pressure wave set up in the plasma electrons.

Diffusion of Antimony in Silver*

E. SONDER, L. SLIFKIN, AND C. T. TOMIZUKA
Department of Physics, University of Illinois, Urbana, Illinois
(Received November 20, 1953)

The diffusion coefficient of antimony tracers in single crystals of pure silver has been measured as a function of temperature over the range 468–942°C. The relation $D=D_0\exp(-H/RT)$ was found to be obeyed with $H=38\,320$ cal/mole and $D_0=0.169$ cm²/sec. These values are in marked disagreement with those appearing in the literature. The data suggest, in addition, that any variation with temperature in D_0 of the form $D_0=D_0'T^n$ is such that n probably lies in the range 0 to $+\frac{1}{2}$. This implies that any temperature variation of H is probably less than 1 cal/mole deg.

I. INTRODUCTION

THE availability of radioactive isotopes has made it possible to perform diffusion experiments in essentially pure solvent metals with a much greater reproducibility than in the past. Moreover, tracer experiments do not require the large concentration differences so necessary to the older techniques.[1] With this in mind, this laboratory embarked upon a comprehensive investigation of diffusion in substitutional alloys, one aim being to obtain a comparison of diffusion in the silver lattice of tracers of those elements neighboring silver in the periodic table. The present experiment, preliminary results of which have been reported earlier,[2] represents part of this program. It was felt that careful measurements with single crystals, over as large a temperature range as possible, would be of basic importance in assessing the applicability of the equation $D=D_0\exp(-H/RT)$, in which the activation energy H is taken to be temperature independent.

EXPERIMENTAL

Specimens were prepared from 99.99 percent Handy and Harmon silver, melted, degassed, and grown in vacuum into single crystals of diameter $\frac{3}{4}$ in. These were then cast in plaster of Paris and cut into half-inch long cylinders with a cut-off wheel.[3] The worked layer was removed, simultaneously flattening the surface, by polishing on emery paper, followed by electropolishing. The electropolishing bath was the type employed by Francis and Colner.[4] Current was supplied as pulsating dc from a simple rectifier. The crystals were next annealed for 24 hours, the temperature rising slowly from 200°C to 700°C, to remove any residual strains. A subsequent cyanide etch[5] served to show whether the specimen were still a single crystal. The good specimens were then each plated with about 1 microcurie of high specific activity antimony (layer about 100A thick), sealed off in evacuated vycor tubes, and placed in the diffusion annealing furnaces. A description of the annealing, the sectioning of the specimens on a lathe, and the analysis of these sections has been previously published.[6]

RESULTS

A total of 13 diffusion runs were performed, ten on single crystals and three, for comparison, on polycrystals (grain size about 0.1 mm). The two higher temperature measurements on polycrystals involved only volume diffusion; not until 550°C (the third polycrystalline run) did any contribution from grain boundary diffusion appear. Of the single crystal measurements, the previously reported[2] run at 935°C was discarded because of an excessive deviation: when all four runs in the range 935°C–942°C were normalized to a common temperature, the deviation of the suspect measurement was 70 times that of the other three from their average; moreover, this point differs from the best fit of all the data by more than seven times the standard deviation. The discrepancy is explainable by a possible error of one hour in recording the time of diffusion.

The penetration curves for all volume diffusion runs showed a strict proportionality between the logarithm of the activity and the square of the penetration depth. The plots were similar to those previously published[2] and hence are not repeated here.

The diffusion coefficients calculated from these plots are given in Table I. These diffusion coefficients were not "corrected" for the fact that all distances were measured at room temperature rather than at the temperature of diffusion. Since the fundamental process of diffusion should be described in terms of atomic jumps rather than the length of each jump, such a "correction" would actually introduce an extraneous variation of D with temperature. Figure 1 shows the data plotted as $\log D$ *versus* the inverse of the absolute temperature. The straight line that best fits the data

* Supported in part by the U. S. Atomic Energy Commission.
[1] A. D. LeClaire, in *Progress in Metal Physics*, edited by B. Chalmers (Butterworth Scientific Publications, London, 1949 and 1953), Vols. I and IV; F. Seitz, in *Phase Transformations in Solids*, edited by J. Smoluchowski *et al.* (John Wiley and Sons, Inc., New York, 1951).
[2] Slifkin, Lazarus, and Tomizuka, J. Appl. Phys. **23**, 1405 (1952).
[3] We are indebted to Dr. J. Marx, now of Phillips Petroleum Company, for the suggestion of this method of protecting the crystals while being cut.
[4] H. Francis and W. Colner, J. Electrochem. Soc. **97**, 237 (1950).
[5] G. Kehl, *Principles of Metallographic Laboratory Practice* (McGraw-Hill Book Company, Inc., New York, 1949).
[6] Slifkin, Lazarus, and Tomizuka, J. Appl. Phys. **23**, 1032 (1952).

is given by the equation

$$D=0.169\exp(-38\,320/RT)\ \text{cm}^2/\text{sec}.$$

The individual diffusion measurements are good to ±2 percent. This precision, together with the large number and range of the measurements, statistically determines the activation energy to 0.001 percent, a figure probably negligible relative to possible systematic errors of unknown origin. Statistically, D_0 is precise to 2 percent; this, too, seems overly optimistic.

DISCUSSION

The present results differ greatly from earlier measurements made on the same system by Seith and Peretti.[7] These workers reported an activation energy of 21 700 cal/mole and a D_0 equal to 5.3×10^{-5} cm²/sec. The discrepancy cannot lie in the fact that they used polycrystals since our polycrystal runs agree with measurements on single crystals down to reasonably low temperatures (about 600°C). Moreover, their low value of the activation energy cannot be ascribed to some other "short-circuiting path," as suggested by Nowick,[8] since near the melting point their value of the diffusion coefficient is considerably less (by a factor of 5) than ours. It seems probable, then, that the discrepancy may lie in the fact that Seith and Peretti, having no tracers, observed the diffusion of antimony from a 2-percent alloy into pure silver. The effects of both the larger concentration of antimony and the presence of an appreciable gradient of the concentration are now being investigated.

TABLE I. Summary of data.

D(cm²/sec)	Temperature (°C)	Specimen
2.15×10^{-8}	942.4	Single crystal
2.07×10^{-8}	940.2	Single crystal
2.06×10^{-8}	940.0	Polycrystal
1.44×10^{-8}	908.2	Single crystal
4.92×10^{-9}	838.6	Single crystal
1.14×10^{-9}	754.9	Single crystal
4.12×10^{-10}	698.3	Polycrystal
1.34×10^{-10}	648.5	Single crystal
1.70×10^{-11}	564.9	Single crystal
2.53×10^{-12}	500.5	Single crystal
8.50×10^{-12}	468.5	Single crystal

That these concentration effects may quite generally have been a dominant factor in much of the older work is borne out by recent tracer experiments on the diffusion of Cd, In, and Sn in silver.[9] In these new measurements, as in the present case, the activation energies are found to be much closer to the 45 500 cal/mole for self-diffusion than given by the earlier, nontracer experiments. The theory of solute-vacancy complexes[10] has been the basis for the interpretation of the former results that in a given metal almost all solutes diffused with an activation energy much smaller (by about 50 percent) than that for self-diffusion. It now appears, however, that the binding energy between a solute atom and a vacancy may be much less than previously considered. A theory to explain the 7200-cal/mole difference in activation energy between that for self-diffusion and for antimony in silver, as found in this work, has been formulated by Lazarus.[11]

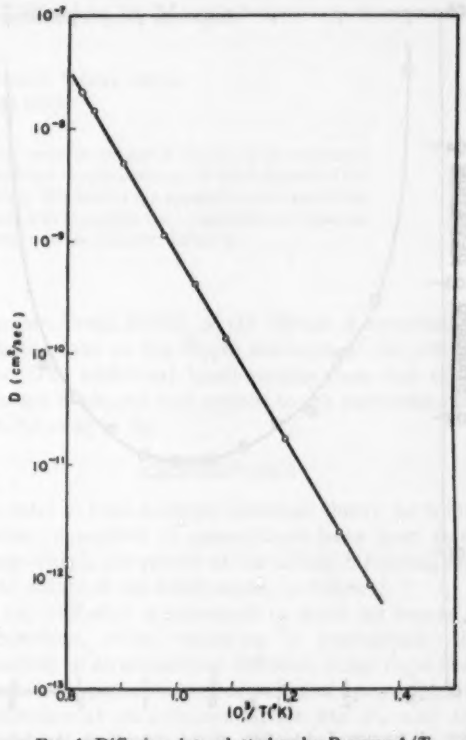

FIG. 1. Diffusion data plotted as log$D$ *versus* $1/T$.

Another marked disagreement between our work and that of Seith and Peretti lies in the value of D_0. It has been predicted[12] that the reported values of the order of 10^{-5} cm²/sec would be revised upwards about four or five powers of ten; the present results are consistent with this prediction.

In order to obtain information concerning the temperature dependence of D_0 (H being assumed to be constant over the range of temperature), expressions of the form

$$D=D_0'T^n\exp(-H'/RT)$$

have been tested by computing the best H' and D_0' for a given n and then evaluating the standard deviation

[7] W. Seith and E. Peretti, Z. Elektrochem. **42**, 570 (1936).
[8] A. S. Nowick, J. Appl. Phys. **22**, 1182 (1951).
[9] C. T. Tomizuka, Bull. Am. Phys. Soc. **28**, No. 6, 18 (1953); C. T. Tomizuka and L. Slifkin (to be published).
[10] C. Wagner, Z. physik. Chem. **B38**, 325 (1938); R. P. Johnson, Phys. Rev. **56**, 814 (1939).
[11] D. Lazarus, following paper [Phys. Rev. **93**, 973 (1954)].
[12] C. Zener in *Imperfections in Nearly Perfect Crystals*, edited by W. Shockley *et al.* (John Wiley and Sons, Inc., New York, 1952).

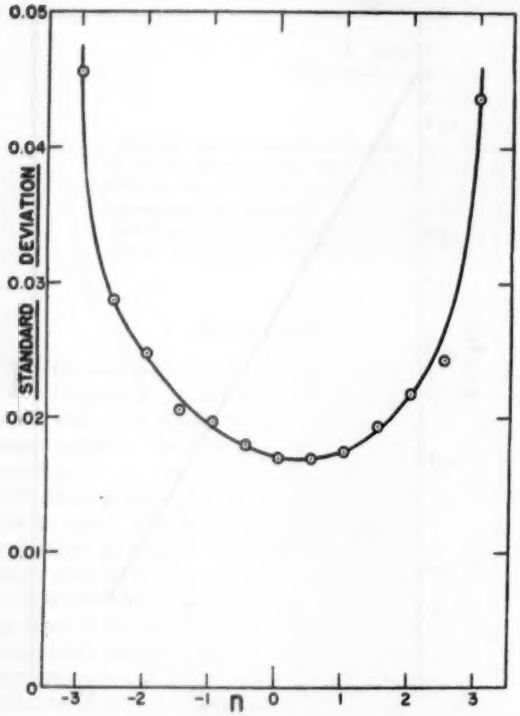

FIG. 2. Standard deviation of the data from the relations $D=D_0'T^n\exp(-H'/RT)$ as a function of n. *Note added in proof.*—The ordinate in this figure is actually the probable error rather than the standard deviation.

of the data. The probable error thus obtained is shown as a function of n in Fig. 2. These results rule out any strong dependence of D_0 on T and, in fact, indicate that n probably does not lie far from the range 0 to $+\frac{1}{2}$. Values of H', D_0', and the probable error for $-\frac{1}{2}\leq n\leq+1$ are given in Table II.

From this limitation on the temperature dependence of D_0, information can be obtained concerning the possible temperature variation of the enthalpy of activation H. One can write[1]

$$D=a^2\nu e^{S/R}e^{-H/RT},$$

where a is the lattice parameter, ν is a lattice vibration frequency, and S and H refer to the activation process of the elementary diffusion act. If one expands H as a power series in T, all terms higher than the linear one may be neglected since no curvature appears in Fig. 1:

$$H=H_0+H_1T.$$

Employing the relation

$$(\partial H/\partial T)_p=T(\partial S/\partial T)_p,$$

one obtains

$$S=S_0+H_1\ln(T/T_0),$$

where S_0 is the entropy of activation at some reference

TABLE II. Best values of H' and D_0' for various values of n.

n	H'(cal/mole)	D_0'(cm²/sec-deg^n)	Probable error in ln$D$
$-\frac{1}{2}$	39 270	0.274	0.0180
0	38 320	0.169	0.0170
$+\frac{1}{2}$	37 380	0.104	0.0170
1	36 420	0.064	0.0174

temperature T_0. Then,

$$D=a^2\nu\left(\frac{T}{T_0}\right)^{H_1/R}\exp\left(\frac{S_0-H_1}{R}\right)\exp(-H_0/RT).$$

Since we have not corrected our D's for temperature variation of the lattice parameter, the a^2 term is constant. Also, if one assumes ν to be independent of temperature, the only term in D_0 dependent on T is $T^{H_1/R}$. Referring to the previous paragraph H_1/R must be equated to n. Thus, $0\leq H_1\leq R/2$ and H varies by no more than 1 cal/mole degree.

We wish to thank Dr. F. Seitz and Dr. D. Lazarus for many valuable discussions.

Effect of Screening on Solute Diffusion in Metals*

DAVID LAZARUS
Department of Physics, University of Illinois, Urbana, Illinois
(Received November 25, 1953)

A simple atomistic theory of solute diffusion in metals for cases of negligible chemical concentration gradients is discussed. Calculations are made, using a Thomas-Fermi approximation, of the influence of the presence of impurity atoms on the Fermi electrons of the lattice. The results are applied to the case of diffusion of Sb in Ag, and indicate that the screening terms are sufficient to explain the magnitude and direction of the observed deviation from self-diffusion in Ag for a vacancy mechanism for diffusion.

INTRODUCTION

THE recent work of Sonder, Slifkin, and Tomizuka[1] on the diffusion of Sb^{124} into pure monocrystalline Ag has demonstrated conclusively that the solute Sb atoms diffuse at a rate markedly different from the rate of self-diffusion[2] of Ag under conditions of negligible chemical concentration gradients. The magnitude of the effect proved much smaller than that previously reported.[3] The previous work had been the basis for a considerable amount of speculation on the nature of the solute diffusion process, and a number of mechnisms[4] had been proposed to explain the large differences between the rates of solute diffusion and self-diffusion in metals, which required the assumption of strong coupling forces between a diffusing solute atom and a lattice imperfection.

It is apparent from a consideration of the kinetics of the diffusion process[5] that the true diffusion characteristics of relatively isolated solute atoms in a lattice can easily be masked by large unidirectional currents of imperfections which result from gradients in chemical composition. Such currents give rise to the measurable volume changes and porosity associated with the Kirkendall effect.[6] Since all of the original work on solute diffusion[7] was done under conditions of strong chemical gradients, the interpretation of much of the old data is open to question.

In the present paper, an attempt is made to adopt an atomistic approach to the diffusion problem, in contrast to some of the current thermodynamic theories,[8] in order to account quantitatively for the observed effects. The computations are confined to a consideration, using a Thomas-Fermi model, of the effects of screening of the solute ions on the Fermi electrons of the solvent lattice. The additional terms arising from this interaction are evaluated and applied to the particular case of Sb diffusing in Ag.

CALCULATIONS

In order to form a simple atomistic theory for solute diffusion, a number of assumptions have been made dealing with I, the nature of the diffusion process, and II, the nature of the solute atom, as follows:

I. (A) Diffusion is presumed to occur by means of imperfections, either vacancies or interstitials; the probability of an elementary diffusion jump P_D is then related to the probability of existence of an appropriate imperfection at an adjacent lattice site P_E and the probability of jump of the diffusing atom into the imperfection P_J by the relation $P_D=(P_E)(P_J)$.

(B) Thermal equilibrium is presumed to be established at all stages of the diffusion process, the formation and destruction of imperfections being effected at dislocations or surfaces by mechanisms not of immediate concern which represent an infinite potential reservoir of imperfections. One may then assume that the above probabilities may be treated using Boltzmann statistics, and that the diffusion process is adequately described by the relation

$$D=r_0^2\nu\exp[-(E_f+E_m)/kT], \qquad (1)$$

where D is the diffusion coefficient, r_0 the interatomic distance, ν the vibrational frequency of the atom in the lattice, E_f the energy required to form an imperfection (analogous to P_E), E_m the energy required for motion of an atom into an adjacent imperfection (analogous to P_J), k Boltzmann's constant, and T the absolute temperature.

II. (A) The assumption is made that a solute atom may be represented as a solvent atom differing only in nuclear charge and numbers of valence electrons, that is inserted into the lattice in place of a solvent atom. The limitations of this assumption are considered later.

(B) It is assumed that the change in energy of the lattice resulting from replacement of a solvent atom by an isolated solute atom is small compared to the binding energy of the solvent atom in the lattice. This assump-

* Supported in part by the U. S. Atomic Energy Commission and the U. S. Office of Naval Research.
[1] Sonder, Slifkin, and Tomizuka, this issue [Phys. Rev. 93, 970 (1954)].
[2] Slifkin, Lazarus, and Tomizuka, J. Appl. Phys. 23, 1032 (1952).
[3] W. Seith and E. Peretti, Z. Elektrochem. 42, 570 (1936).
[4] R. P. Johnson, Phys. Rev. 56, 814 (1939); G. Wyllie, Proc. Phys. Soc. (London) 59, 694 (1947).
[5] E.g., F. Seitz in *Phase Transformations in Solids* (John Wiley and Sons, Inc., New York, 1951).
[6] A. Smigelskas and E. Kirkendall, Trans. Am. Inst. Mining Met. Engrs. 171, 130 (1947).
[7] E.g., W. Seith, *Diffusion in Metallen* (Julius Springer, Berlin, 1939); C. J. Smithells, *Metals Reference Book* (Butterworth Scientific Publications, London, 1949).
[8] E.g., C. Zener, J. Appl. Phys. 22, 372 (1951); G. J. Dienes, Phys. Rev. 89, 185 (1953); A. D. LeClaire, Acta Metallurgica 1, 438 (1953).

tion is shown to lead to self-consistent results. The calculations will therefore be confined to a consideration of the changes in the various quantities of Eq. (1) by insertion of the solute atom into the lattice.

The procedure follows that developed by Mott[9] in a calculation of the effect of impurities on electrical resistivity. The solvent atom is assumed to be monovalent, while the solute atom has $1+Z$ valence electrons. The limits on the electrostatic potential $\phi(r)$ around the solute atom are

$$\phi \to Ze/r \quad \text{as } r \to 0,$$
$$\phi \to 0 \quad \text{as } r \text{ becomes infinite.}$$

A Thomas-Fermi model is assumed, the density of the electron gas being given by

$$N(r) = (8\pi/3h^3)[2me(\phi+\phi_0)]^{\frac{3}{2}},$$

where $e\phi_0$ is the maximum energy of electrons in the Fermi gas

$$e\phi_0 = (h^2/2m)(3N_0/8\pi)^{\frac{2}{3}}.$$

The density of the negative charge is then

$$\rho(r) = -eN(r),$$

and the total excess charge density is $e(N_0-N)$. Poisson's equation can be written as

$$\nabla^2\phi = -4\pi e(N_0-N) = \alpha[(\phi+\phi_0)^{\frac{3}{2}} - \phi_0^{\frac{3}{2}}],$$

where $\alpha = 2^{13/2}\pi^2 m^{3/2} e^{5/2}/3h^3$.

Under the conditions $\phi \ll \phi_0$, the expression can be expanded to first terms only. Then,

$$\nabla^2\phi = \tfrac{3}{2}\alpha\phi_0^{\frac{1}{2}}\phi = q^2\phi,$$

where $q^2 = 4me^2(3N_0/\pi)^{\frac{1}{3}}/h^2$. Solving, one obtains a value for $\phi(r)$,

$$\phi(r) = \frac{Ze}{r}\exp(-qr).$$

Using this value of the electrostatic potential, one may estimate the additional Coulomb energy, E_c, considering dipole terms only, as

$$E_c(r) = e\phi(r) = \frac{Ze^2}{r}\exp(-qr). \tag{2}$$

E_c is a repulsive contribution to the total lattice energy, so that the change in energy of formation of an imperfection at the nearest-neighbor distance r_0 will be given by

$$\Delta E_f = \pm E_c(r_0), \tag{3}$$

where the positive sign applies to formation of an interstitial and the negative sign for formation of a vacancy.

In evaluating the change in energy of motion E_m it will be assumed that this barrier can be represented entirely in terms of the elastic shear strain energy involved during the jump of the diffusing atom into the imperfection site. Following the method of Fuchs,[10] two shear deformations will be considered. The first of these is equivalent to an equal and opposite tension and compression on two orthogonal axes of the unit cell, such that the volume of the cell remains unchanged. The modulus of this deformation, A, is related to the macroscopic (110) shear modulus $\frac{1}{2}(C_{11}-C_{12})$ by

$$A/V_0 = (C_{11}-C_{12}),$$

where V_0 is the volume of the unit cell. The second deformation is the familiar "pure shear," the atomic modulus B being related to the macroscopic (100) shear modulus by

$$B/V_0 = \tfrac{1}{2}C_{44}.$$

The atomic moduli A and B are defined in the usual way in terms of the second derivatives of the lattice energy E with respect to the appropriate shear strain, evaluated at r_0, the equilibrium interatomic distance. They can be written for a face-centered cubic lattice in terms of derivatives with respect to distance as

$$A = \tfrac{1}{2}r^2d^2E/dr^2 + (7/2)rdE/dr,$$
$$2B = \tfrac{1}{2}r^2d^2E/dr^2 + (3/2)rdE/dr. \tag{4}$$

The changes in these moduli due to the additional term $E_c(r)$ defined by Eq. (3) can be calculated by substitution of E_c for E in Eq. (4). Then

$$\Delta A_c = \tfrac{1}{4}E_c(q^2r^2 - 5qr - 5),$$
$$\Delta B_c = \tfrac{1}{4}E_c(q^2r^2 - qr - 1). \tag{5}$$

For many metals, and in particular for Ag, the (110) shear modulus $\frac{1}{2}(C_{11}-C_{12})$ is much smaller than the (100) modulus C_{44}. For such materials one may assume that the strain energy of motion E_m arises almost entirely from (110) strains, and that E_m should be about equal to $A/2$ (the factor of 2 entering because Fuch's moduli are energies per ion *pair*). Using experimental values of the elastic constants for Ag, E_m for self-diffusion in Ag would then be 0.84 ev/atom, which is about the value expected from other theoretical considerations.[11]

For such anisotropic materials, one may then directly relate ΔA_c with ΔE_m, the change in energy of motion, by

$$\Delta E_m = \tfrac{1}{2}\Delta A_c. \tag{6}$$

In estimating the other factors which would be expected to change for diffusion of solute atoms compared to self-diffusion, one must consider the usual thermodynamic expression for the diffusion coefficient

$$D = D_0\exp(-H/RT), \tag{7}$$

where the frequency factor D_0 and enthalpy or heat of activation H are assumed to be temperature-independent, and R is the gas constant. This relation is obeyed

[9] N. F. Mott, Proc. Cambridge Phil. Soc. **32**, 281 (1936).

[10] K. Fuchs, Proc. Roy. Soc. (London) **151**, 585 (1935); **153**, 622 (1936); **157**, 444 (1936).

[11] H. B. Huntington and F. Seitz, Phys. Rev. **61**, 315, 325 (1942).

experimentally to high precision,[1] any residual temperature dependence of D being negligible within the limits of error. In correlating Eq. (7) with the atomistic diffusion Eq. (1), it is obviously sufficient to define

$$(E_m+E_f)=H/N_0+Td(E_m+E_f)/dT,$$
$$D_0=r_0^2\nu\exp[-d(E_m+E_f)/kdT], \quad (8)$$

where N_0 is Avogadro's number. Higher derivatives of E_m and E_f with respect to temperature are assumed negligible because of the observed consistency of the experimental measurements with Eq. (7).

One must consider the energies E_m and E_f as functions of temperature both explicitly and implicitly through the distance parameter r, as shown in previous work[12] on a study of the variation of elastic constants of cubic materials with pressure. The derivatives in Eq. (8) may then be expanded as

$$d(E_m+E_f)/dT=[\partial(E_m+E_f)/\partial r]_T dr/dT+[\partial(E_m+E_f)/\partial T]_r. \quad (9)$$

The second term on the right of Eq. (9) is not amenable to analytical solution without a complete knowledge of $E(r,T)$, but might be presumed to arise from the variation in amplitude of the lattice vibrations with temperature. Such a variation might be expected to produce a large effect in E_m but a negligible change in E_f. It will be assumed that the explicit temperature dependence of E_m is proportional to the implicit term, as indicated by the high-pressure measurements for shear moduli. Then, the temperature variation may be written as

$$d(E_m+E_f)/dT=r_0\alpha[(\partial E_f/\partial r)_T+C(\partial E_m/\partial r)_T], \quad (10)$$

where α is the linear thermal expansion coefficient and the constant C will be evaluated from the observed value of D_0 for self-diffusion.

In evaluating C the assumption is made that the dominant terms in $(\partial E/\partial r)_T$ for self-diffusion arise from the closed-shell repulsion energy, W_r, given by the Born-Mayer approximation

$$W_r(r)=k\exp(-r/\rho), \quad (11)$$

and, as above, that E_m will be equal to $A/2$, as defined by Eq. (4) with W_r in place of E. Then

$$r_0(\partial E/\partial r)_T=r_0(\partial E_m/\partial r)_T=-r_0E_m/\rho. \quad (12)$$

The value of the constant C can now be estimated by comparison of the observed value of D_0 for self-diffusion with that defined by Eq. (8). Using the same value for C for the case of solute diffusion, one can then easily compute the change in D_0, from Eqs. (3), (5), and (6), since

$$r_0(\partial\Delta E_f/\partial r)_T=-(qr_0+1)E_c(r_0),$$
$$r_0(\partial\Delta E_m/\partial r)_T=-\tfrac{1}{4}E_c(r_0)[2q^2r_0^2-5qr_0-(qr_0+1)(q^2r_0^2-5qr_0-5)]. \quad (13)$$

[12] D. Lazarus, Phys. Rev. **76**, 545 (1949).

RESULTS AND DISCUSSION

By substituting appropriate parameters for Ag and Sb, the changes in D_0 and H for diffusion of Sb in Ag compared with self-diffusion in Ag can now be calculated. The following values are assigned to the parameters:

$r_0=2.88$A (from x-ray data),

$\nu=0.9\times10^{13}$ sec^{-1} (from ratio of velocity of sound to r_0),

$q=1/0.58$A (from Mott[9]),

$\rho=0.345$A (from Fuchs[10]),

$\alpha=1.9\times10^{-5}$ deg C^{-1} (from *Handbook of Chemistry and Physics*),

D_0(self-diffusion of Ag)$=0.72$ cm^2/sec (from reference 2),

H(self-diffusion of Ag)$=45.5$ kcal/mol (from reference 2).

The excess valence of Sb, Z, is taken as 4, and E_m for self-diffusion in Ag is taken as 0.84 ev from the (110) shear modulus. The constant C, from Eqs. (12) and (8) and the observed value of D_0 for self-diffusion, is evaluated as 3.

If a vacancy mechanism for diffusion is assumed, ΔE_f is defined by using the negative sign in Eq. (3), and the calculated expression for diffusion of Sb in Ag is

$$D_{\text{calc}}=0.16\exp(-38\,100/RT)\text{ cm}^2/\text{sec},$$

while the experimental value[1] is

$$D_{\text{exp}}=0.167\exp(-38\,320/RT)\text{ cm}^2/\text{sec}.$$

If an interstitial mechanism is assumed, the calculated value of H is 44.7 kcal/mol, in substantial disagreement with the observed value.

The extremely close agreement between the calculated and observed results can only be regarded as fortuitous, particularly in the case of the D_0 term, where a considerable approximation has been made in estimating the numerical constant in the exponent. However, it is noteworthy that the screening effects alone appear to be sufficient to explain the magnitude and direction of the measured effect, without requiring the introduction of any detailed models.

The derived dependence of the terms D_0 and H of Eq. (7) on the excess valency Z and screening parameter q is given by:

$$D_0(\text{solute})=D_0(\text{solvent})\exp\left\{-\frac{\alpha E_c}{k}[(qr_0+1)+(\tfrac{1}{4}C)(-q^3r_0^3+6q^2r_0^2+5qr_0+5)]\right\},$$

$$H(\text{solute})=H(\text{solvent})-[1-\tfrac{1}{4}(q^2r_0^2-5qr_0-5)]N_0E_c,$$

where E_c is $(Ze^2/r_0)\exp(-qr_0)$.

The functional form of these relationships is strongly influenced by the approximations made in the Thomas-Fermi model. Friedel[13] has recently shown by a more exact Hartree-Foch calculation of screening that the Thomas-Fermi model is approximately correct for large even values of Z, but that a relatively larger screening effect would probably be observed for $Z=1$, and possibly also for $Z=3$.

One of the most questionable approximations made in the present treatment is II(A), concerning the nature of the solute atom. One can estimate the magnitude of terms neglected by ignoring the possible difference in closed-shell radii of solute and solvent atoms by writing the closed-shell repulsion energy as

$$W_r(r)=K' \exp[(r_1+r_2-r)/\rho],$$

where r_1 and r_2 are radii of the solvent and solute ions, respectively. The calculated value of ΔE_f will be approximately unchanged since the exponent vanishes for $r=r_0$ in a close-packed lattice. The calculated value of ΔE_m, however, will be modified by the addition of a repulsive term ΔA_r given by

$$\Delta A_r=W_r(r_0)[(r_2-r_1)/\rho](r_0/\rho-7/2).$$

The sign of this term is that of r_2-r_1, since $r_0/\rho>7/2$. For an atom such as Sb of intrinsically larger size than Ag, ΔA_r might be presumed to be small and positive, tending to decrease the magnitude of the calculated value of ΔE_m.

In considering the motion of the solute atom into the imperfection site, the degree of randomness of the process must be evaluated, as shown by Bardeen and Herring.[14] It will be sufficient here to consider the difference in probability of return P_r of the atom to its initial position after a second jump for self-diffusion and solute diffusion. For the former case, P_r is of the order of the reciprocal of the number of nearest neighbors. For solute diffusion, one must consider as especially favored in the second jump both the solute atom and the solvent atoms which are nearest neighbors of both the imperfection and the solute atom. The energy required for motion of any of these atoms will be changed by an amount ΔE_m because of the symmetry of the Coulomb potential. Thus for a face-centered cubic lattice the probability of return P_r is of the order $b/5(1+b)$, where $b=(5/7)\exp[-(\Delta E_m/kT)]$. For the case of Sb in Ag, this probability is about 0.16, which is only a factor two larger than that for self-diffusion. The increase in correlation arising from the change in P_r should be expected to change the calculated effect by only a few percent, and can be neglected in the present approximation.

It is also evident that a solute-vacancy complex, in the sense of the Johnson mechanism,[4] is not expected to play an important role in the solute diffusion process, since the probability that a vacancy will remain as a nearest neighbor of the solute atom after a second jump is $b/(1+b)=0.8$ for the present case. The mean lifetime of the complex is thus only about 5 jump times. However, this effect should produce an appreciable change in the rate of self-diffusion of the solvent atoms if the solute is present as an impurity of the order of one percent concentration.

The author wishes to express his sincere thanks to Professor D. Pines, Professor F. Seitz, and Professor L. Slifkin for several stimulating conversations.

[13] J. Friedel, Phil. Mag. 43, 153 (1952).

[14] J. Bardeen and C. Herring, in *Imperfections in Nearly Perfect Crystals* (John Wiley and Sons, Inc., New York, 1952), p. 281 ff.

Infrared Absorption, Photoconductivity, and Impurity States in Germanium*

W. KAISER AND H. Y. FAN
Purdue University, Lafayette, Indiana
(Received October 19, 1953)

Infrared absorption and photoconductivity in p-type germanium with gold and copper impurities have been investigated at different temperatures. Photoconductivity in gold-doped germanium at liquid nitrogen and liquid helium temperatures shows a long wavelength tail beyond the fundamental absorption edge, which falls off sharply at about 6 microns corresponding to 0.21 ev. This value agrees well with the acceptor activation energy determined by electrical measurements. For copper-doped germanium at low temperatures both absorption and photoconductivity show a maximum at about 22 microns corresponding to 0.055 ev. This value also agrees with the acceptor activation energy given by Hall effect measurements. At room temperature more absorption is found in the region 2 to 5 microns as compared to p-type germanium doped with indium and aluminum. This is likely to be due to photoionization from a deeper level 0.25 ev above the valence band.

OPTICAL excitation of electrons or holes from impurity states was found in silicon from absorption measurements.[1] Later, photoconductivity associated with such processes was reported, with maximum at a wavelength corresponding to several hundredths of an electron-volt for the ionization energy.[2] In the case of germanium it is known from resistivity and Hall effect measurements that the ionization energy for commonly used acceptor and donor impurities is much smaller than in the case of silicon, $\lesssim 0.01$ ev. The threshold of photoionization should be >100 microns, which is difficult to reach. Furthermore, anomalous behavior of Hall coefficient at low temperatures makes the determination of free carrier concentration ambiguous. On account of this complication, low-temperature absorption measurements have not as yet given conclusive evidence of photoexcitation of impurities.[3] This has been found for germanium with two special acceptor impurities: gold and copper.

GOLD-DOPED GERMANIUM

The study of gold-doped germanium at this laboratory was initiated by Lark-Horovitz some time ago.[4] Gold added to high-resistivity germanium gives p-type semiconductors. The activation energy of the acceptor state has been determined from electrical measurements to be ~ 0.2 ev. Figure 1 gives the curves of absorption coefficient for two temperatures. The specimen has a resistivity $\rho = 1.3$ ohm cm and a hole concentration $n_h \sim 6\times 10^{15}$ cm^{-3} at 300°K, and $\rho = 1.5\times 10^{6}$ ohm cm, and $n_h \sim 10^{9}$ cm^{-3} at 77°K. Thus very few holes are left at the lower temperatures, most of them having settled in the acceptor states. At 300°K the strong absorption beyond 7 microns agrees with other p-type germanium of same hole concentration, whereas at 77°K only lattice absorption (dotted curve) remains. This provides a strong evidence that the long wavelength absorption at 300°K (aside from the lattice bands) is due to the presence of free holes. For shorter wavelengths, 7 to 2 microns, the absorption at 300°K does not show distinctly two peaks as observed in other p-type germanium and is generally higher in magnitude. Furthermore the almost flat absorption at 77°K from 4 to 14 microns is higher than in other high-resistivity germanium. This is very likely true because of the scattering by islands of precipitated gold in the specimen, which are clearly visible on the surface.

Figure 2 gives the spectral response of photoconductivity at liquid nitrogen and liquid helium temperatures. Coming from the short wavelength side there is a sharp drop near 2 microns corresponding to the edge of the fundamental absorption, electron excitation across the energy gap. This is followed by a flat response up to about 6 microns, corresponding to ~ 0.21 ev, where it again drops sharply. The response beyond 2 microns is evidently associated with photoionization of holes on

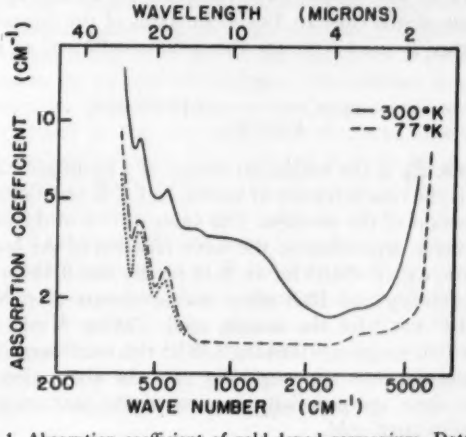

FIG. 1. Absorption coefficient of gold-doped germanium. Dotted line gives lattice absorption.

* Work supported by a Signal Corps Contract.
[1] H. Y. Fan and M. Becker, Phys. Rev. 78, 178 (1950).
[2] Burstein, Oberly, and Davisson, Phys. Rev. 89, 331 (1953).
[3] Kaiser, Collins, and Fan, Phys. Rev. 91, 1380 (1953).
[4] Single crystals with gold additions were first made by W. L. Taylor (1950) and later by L. M. Roth; Benko, Fan, and Lark-Horovitz, Purdue Semiconductor Research Progress Report, June, 1952 (unpublished); M. Nisenoff, Master's thesis, Purdue University, 1952 (unpublished); R. Dreyfus, Master's thesis, Purdue University, 1953 (unpublished); see also W. C. Dunlap, Jr., Phys. Rev. 91, 1282 (1953).

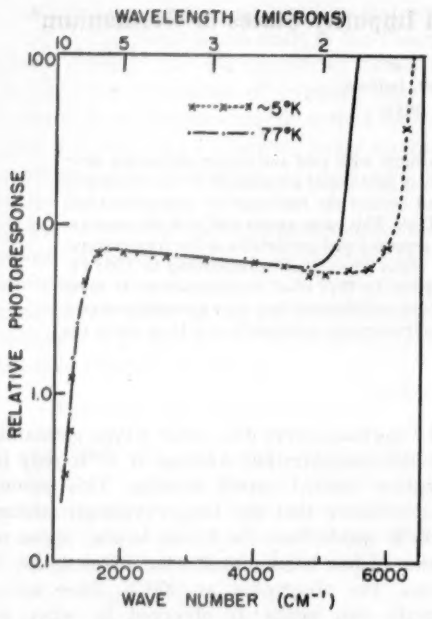

FIG. 2. Photoconductive response (increment of conductance for constant incident energy) of gold-doped germanium at 77°K and ~5°K. The values are given on arbitrary scales which are not the same for the two temperatures.

acceptor states, the threshold 0.21 ev agreeing closely with the activation energy determined electrically. The absorption due to this process did not however show up in the absorption curve at 77°K. According to the theory of photoionization of atoms,[5] the absorption coefficient is given approximately by

$$\mu_i \propto (1/\nu)^{\alpha}, \tag{1}$$

where α depends on the wave function of the bound state and has somewhat different values for frequencies near the threshold ν_0 and frequencies much smaller than ν_0. For simple wave functions $1s$, $2s$, and $2p$ the value of α is close to 3 or 4. In terms of the ionization energy E the maximum absorption coefficient at ν_0 is

$$\mu_i = C\frac{N}{K(E/E_H)}\times 10^{-17}\ \text{cm}^{-1}, \tag{2}$$

where E_H is the ionization energy of a hydrogen atom, N is the concentration of atoms, and K is the dielectric constant of the medium. The value of C is of the order of unity depending on the wave function of the bound state, e.g., $C=0.63$ for $1s$, 0.37 for $2s$, and 0.34 for $2p$. Resistivity and Hall effect measurements give $N=6\times10^{15}$ cm^{-3} for the sample used. Taking $K=16$ and $C=0.63$ we get $\mu_i=0.64$ cm^{-1}. With this small magnitude expected, it is not surprising that the absorption did not show up, especially in view of the scattering by precipitated gold.

[5] H. Hall, Revs. Modern Phys. 8, 358 (1936).

The photoresponse per unit incident energy should be

$$\Delta\sigma \propto \frac{\mu_i}{\mu}\frac{W}{h\nu}, \tag{3}$$

where μ is the total absorption coefficient and W is the power absorbed in the sample. W can be estimated from the absorption coefficient and the thickness of the sample. For the sample used μ and W are practically constant over the range 2 to 14 microns at 77°K. Therefore we should expect $\Delta\sigma \propto \mu_i/\nu$ giving a fairly large frequency dependence. The measured photoresponse is, however, practically flat. This might be caused by a tail in the photoconductivity due to fundamental absorption which decreases with increasing wavelength.

Figures 1 and 2 show that the edge of the fundamental absorption and its associated photoconductivity shifts to shorter wavelengths with decreasing temperature. This has been interpreted as variation of energy gap with temperature.[6] The threshold of photoconductivity, on the other hand, shows no shift at liquid helium from that at 77°K. This indicates that the acceptor energy level remains fixed relative to the valence band while the energy gap is changed.[7]

COPPER-DOPED GERMANIUM

It is known that copper diffuses readily into germanium at elevated temperatures and that it acts as acceptors. A sample of n-type germanium 26-ohm cm with a layer of copper deposited on its surfaces was heated to 900°C and rapidly quenched to room temperature. It became p type with resistivity 0.2-ohm cm. Table I gives the results obtained from Hall effect measurements.[8] An identical sample of n-type germanium was heat-treated in the same way but without surface deposit of copper. The sample became p type of 1.5-ohm cm at room temperature. The results of Hall effect measurement are also given in Table I. The concentration of introduced acceptors is about ten times smaller than in the sample with added copper. Thus in the first sample at least most of the acceptors are due to copper. The acceptor activation energy is the same for the two samples. Furthermore, absorption

TABLE I. Data for quenched germanium from electrical measurements.

Sample	Resistivity ohm cm 300°K	77°K	~5°K	Hole concentration 10^{15} cm^{-3} 300°K	77°K	Acceptor activation energy ev
Quenched only	1.5	0.43	$\sim10^6$	2.3	1.0	0.050
Copper added	0.2	0.19	$\sim10^7$	20	3.3	0.051

[6] H. Y. Fan, Phys. Rev. 82, 900 (1951).

[7] Attention was drawn to this interesting point by K. Lark-Horovitz.

[8] We are indebted to D. L. Waldorf for making these measurements.

and photoconductivity measurements also give similar results for the two samples. It has been reported recently[9] that quenching from 900°C introduces into germanium only $\sim 10^{14}$ cm^{-3} acceptors if special care is taken to remove any trace of copper from the surfaces before heat treatment. Thus it seems that the sample quenched without copper addition had nevertheless enough copper to determine its observed behavior.

The absorption curves for three temperatures are shown in Figs. 3(a) and 3(b) for the two samples. Consider first the long-wavelength region, beyond 5 microns. The room temperature curves have the same shape and agree reasonably well in magnitude with results on other p-type samples. The absorption is thus due to free holes. The low-temperature curves on the other hand are quite different from those of other samples and drop sharply at the long-wavelength end. The liquid helium curve of Fig. 3(a) is replotted in Fig. 4 (curve A beyond 5 microns) after subtracting the lattice bands. It shows a maximum around 22 microns corresponding to 0.055 ev. The close agreement between this value and the acceptor activation energy determined by Hall effect measurement indicates that the absorption is due to photoionization of neutral acceptors. The data in Table I show that practically all acceptors became neutral at helium temperature. Thus this curve in Fig. 4 gives the cross section for photoionization of an acceptor. The liquid helium curve of Fig. 3(b) gives values about 30 percent lower. These results are less reliable as the proportion of lattice

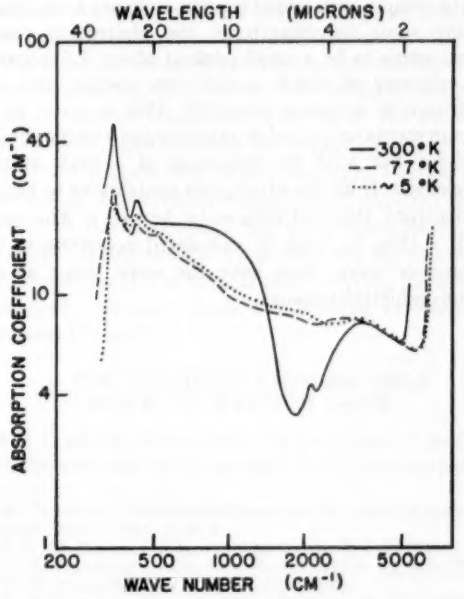

FIG. 3. (a) Absorption coefficient at different temperatures for germanium quenched with added copper.

[9] R. A. Logan, Phys. Rev. **91**, 757 (1953).

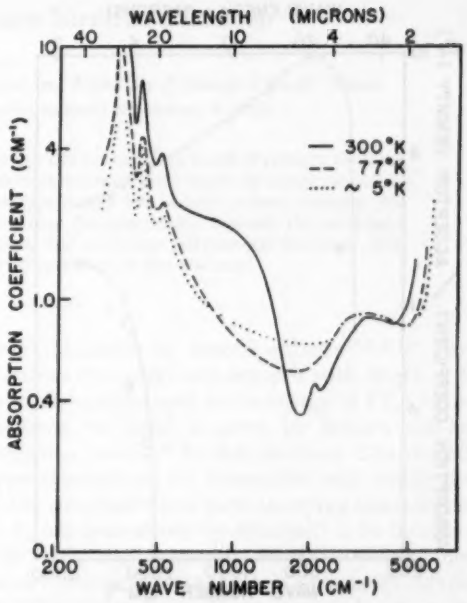

FIG. 3. (b) Absorption coefficient of germanium quenched without adding copper.

absorption which has to be subtracted from the measured curve is much higher in this case. Also, there may be in this sample a significant proportion of acceptors other than copper. The difference between the liquid helium curves and the corresponding liquid nitrogen curves can be explained by the fact that at the higher temperature the absorption of free holes was not negligible and not all the acceptors were neutral.

Consider now the short-wavelength region, 2 to 5 microns. At room temperature the absorption in this region relative to the long-wavelength absorption is higher than in "ordinary" p-type samples, doped, for example, with indium or aluminum.[3,10] Curve B, Fig. 4, gives the "excess" absorption coefficient divided by the acceptor concentration. Both samples give the same curve indicating that the excess absorption is proportional to the number of acceptors. For ordinary p-type germanium the absorption in this region becomes a sharp band at low temperatures.[3] However, the low temperature curves in Fig. 3(a) and 3(b) do not show a sharp band. On the other hand the curves in Fig. 3(b), especially the liquid nitrogen curve, do show a rise at about 5 microns. The following hypothesis is proposed to explain these behaviors. The absorption is assumed to consist of two parts. One component is the same as observed in other p-type germanium, but it becomes very small at low temperatures instead of merely sharpening up as in other samples. One difference between these and other samples is that the hole

[10] This has been observed independently by D. H. Rank and D. C. Cronemeyer, Phys. Rev. **90**, 202 (1953).

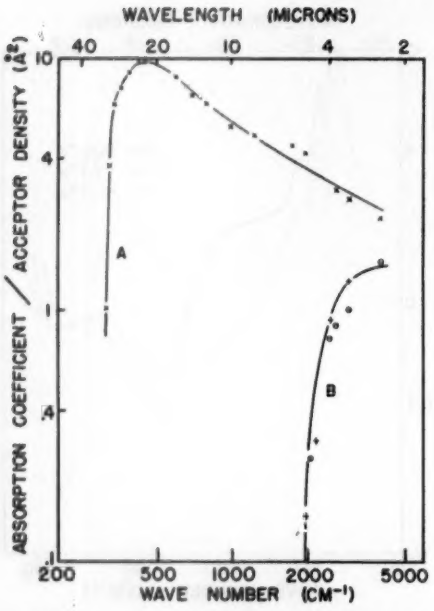

FIG. 4. Absorption coefficient per acceptor concentration. The crosses are points obtained from data in Fig. 3 (a), and the circles are points obtained from data in Fig. 3 (b). Curve B gives excess absorption over absorption in indium-doped germanium, at room temperature. Curve A gives absorption at liquid helium temperature after subtracting the lattice bands and curve B.

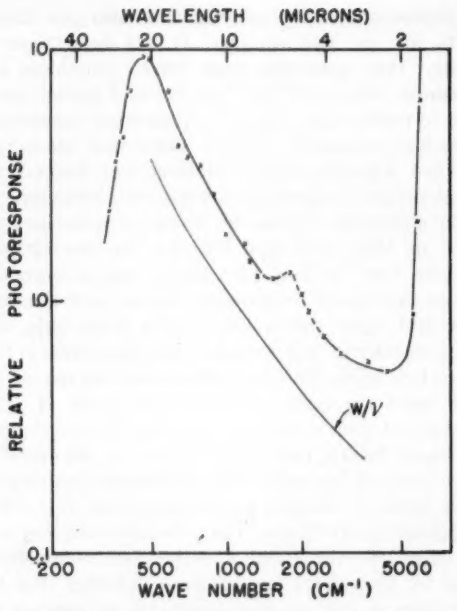

FIG. 5. Photoconductive response of copper-doped germanium at ~5°K. The curve W/ν is calculated by using the absorption curve to estimate W.

concentration here definitely becomes very small at low temperatures. The other component is given then by curve B, Fig. 4, at room temperature and is assumed to be independent of temperature. It might be photoionization of a deeper level associated with copper, about 0.25 ev from the valence band. On this basis we get for both samples a smooth curve of absorption due to photoionization of acceptors by subtracting curve B, Fig. 4, from the measured absorption curve at helium temperature. The part of curve A, Fig. 4, for wavelength <5 microns is obtained in this way for the sample with added copper.

The decrease of absorption from the maximum toward shorter wavelength, as shown by curve A in Fig. 4, seems to be also not as fast as might be expected. However, the maximum absorption gives $C=1.2$ according to (2), which is a reasonable value.

Figure 5 gives the observed photoconductive response for the sample with added copper. It shows a maximum at the same wavelength as the absorption curve. There seems to be a small peak at about 5.5 microns, the existence of which is not very certain with the experimental accuracy involved. This is more so as measurements on the other sample gave a curve similar in shape but with no indication of a peak at this wavelength. If all the absorption contributes to photoconductivity then (3) reduces to $\Delta\sigma \propto W/\nu$. The curve of W/ν (Fig. 5), with W calculated according to the absorption curve, does have the same shape as the photoconductive response.

The Mechanism of Secondary Electron Emission

A. O. Barut
Swiss Federal Institute of Technology, Zurich, Switzerland, and University of Chicago, Chicago, Illinois
(Received July 24, 1953; revised manuscript received Novermber 9, 1953)

It is shown that a simple theory based on the constant energy loss per unit path length of primary electrons accounts quantitatively for the variation of secondary electron emission yield below its maximum value. The theory can be extended formally to include a Bethe-type energy loss at high primary energies. An attempt was made to clarify the present situation concerning the relationship between the secondary electron emission and the atomic structure of the elements, and some new relations are indicated. The mechanism of the secondary emission of insulators and semiconductors is also discussed.

1. INTRODUCTION

THE secondary electron emission of solids when bombarded by electrons (of moderate energies) is a complex phenomenon involving several single events: (1) the slowing down of primary electrons (PE) in the solid, (2) the production of excited "internal secondary electrons (SE)" through the interaction of PE with the lattice electrons, (3) absorption of internal SE within the solid or the possible production of tertiary electrons by energetic SE, (4) the escape of internal SE from the surface of the solid, and (5) the reflection and backscattering of PE.

There exist in the literature various assumptions and calculations for these single processes,[1–9] but a satisfactory quantitative agreement with the experiments on secondary emission has not yet been reached.

The interaction of PE with the electrons of the solid, which is the fundamental process, depends strongly upon the energy E_p of PE. For small energies it is clear that only an interaction with the outermost electrons of the atoms of the solid or with the free electrons of a metal is possible. If, however, the primary energy is greater than the ionization potential of the electrons of the K shell, then the atom as a whole takes part in the interaction process and absorbs energy. Furthermore there are for these higher energies other types of radiations from the solid under electron bombardment and therefore the proportionality between energy loss of PE and the production of SE will depend on E_p. This is the reason why we have made a distinction between the processes (1) and (2).

2. THE SECONDARY EMISSION YIELD BELOW ITS MAXIMUM VALUE

The Coulomb interaction of a fast primary electron with the electrons in the periodic field of the lattice has been calculated by several authors.[10,3–5,7,8] For free electrons the energy loss per unit path length of PE is inversely proportional to the energy of PE;[4] for bound electrons the result is given by Bethe's well-known ionization formula[10] for fast electrons. The Wooldridge approximation of the interaction with weakly bound lattice electrons[3] which gave an energy loss independent of E_p has been shown by Marshall[9] to be incorrect for sufficiently high energies. Marshall showed that a correct treatment yields Bethe's formula for sufficiently high primary energies. There seems to be at present no other information concerning the energy loss and the production of internal SE by low-energy primaries, which is of prime interest here.

It has been found that a constant energy loss can explain quantitatively, for all elements, the variation of secondary emission yield up to its maximum value. A constant energy loss in the form

$$-dE/dx=A \tag{1}$$

gives, for the penetration depth of PE,

$$X=E_p/A. \tag{2}$$

Such a linear increase of the penetration depth for slow PE has been observed experimentally by Copeland.[11] It will be assumed that the production of SE per unit path length is proportional to Eq. (1) (i.e., that it is also constant and equal to KA) and that the absorption of SE in the solid is according to an exponential law. If p denotes the probability that an internal SE will escape the surface of the solid (p is nearly independent of x, where x is the coordinate in the direction of the primary beam normal to the surface), then the true secondary emission yield can be expressed as

$$\Delta=\int_0^X KAe^{-\alpha x}dx=\frac{KAp}{\alpha}[1-\exp(-\alpha E_p/A)]. \tag{3}$$

This is the same as the result obtained by Baroody in a paper correcting Wooldridge's result.[5] The observed secondary electron emission yield can then be written

$$\delta=\Delta(E_p)+\eta, \tag{4}$$

[1] H. Bruining, *Sekundarelektronenemission fester Körper* (J. Springer, Berlin, 1942) p. 60 ff.
[2] J. L. H. Jonker, Philips Research Repts. **7**, 1 (1952).
[3] D. E. Wooldridge, Phys. Rev. **56**, 562 (1939); **58**, 316 (1940).
[4] E. M. Baroody, Phys. Rev. **78**, 780 (1950).
[5] E. M. Baroody, Phys. Rev. **83**, 857 (1951), **86**, 915 (1952).
[6] O. Hachenberg, Ann. Physik **2**, 404 (1948).
[7] H. Schlechtweg, Naturwiss. **31**, 204 (1943).
[8] A. J. Dekker and A. van der Ziel, Phys. Rev. **86**, 775 (1952).
[9] J. F. Marshall, Phys. Rev. **88**, 416 (1952).
[10] H. Bethe, Ann. Physik **5**, 325 (1930).
[11] P. L. Copeland, Phys. Rev. **58**, 604 (1940).

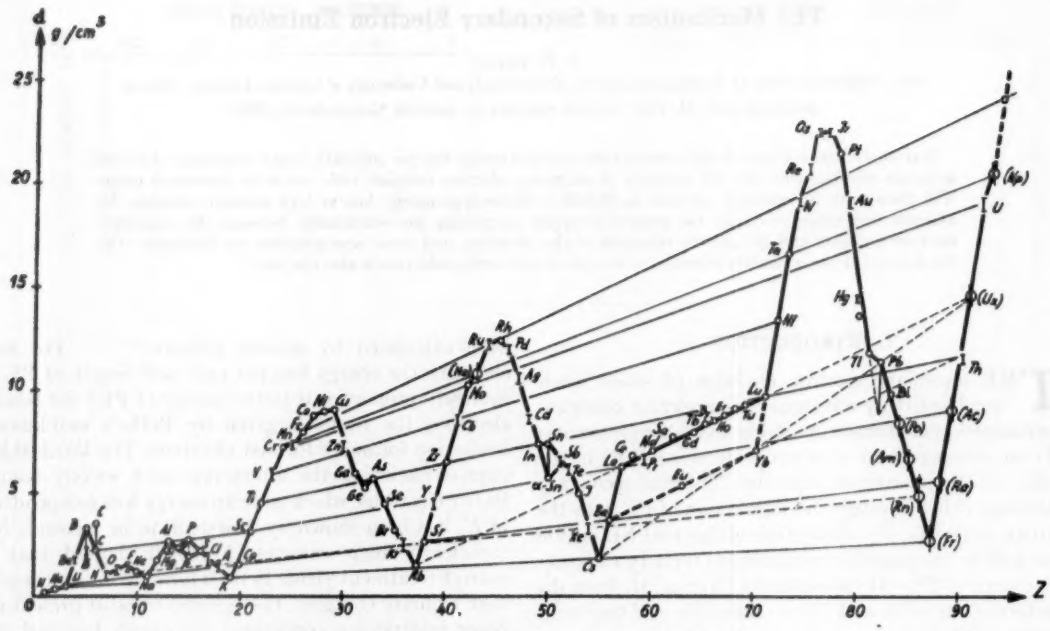

FIG. 1. Plot of the density d *versus* the atomic number Z.

where η is the proportion of reflected and backscattered PE and is only very slowly dependent on E_p for the range considered.

Experimentally it has been found that one obtains a universal secondary emission yield curve by plotting the yield relative to its maximum value, namely δ/δ_m *vs* E_p/E_m.[4] Identifying Δ_m with $\Delta_\infty = KA\rho/\alpha$, one gets

$$\delta/\delta_m \approx \Delta/\Delta_\infty = 1-\exp[(-\alpha E_m/A)E_p/E_m]; \quad (5)$$

this expression is exactly the experimental universal curve if one puts

$$E_m = 5A/\alpha. \quad (6)$$

Then

$$\Delta_m = \Delta_\infty = K\rho E_m/5 = K\rho A/\alpha. \quad (7)$$

The right-hand side of Eq. (5) has only two constants, the absorption coefficient α and the "energy loss constant" A. In the constant K, on the other hand, the possible production of tertiary electrons is included; if all internal SE have the same initial energy E_0, then $K \cong 1/E_0$.

Geyer[12] had found empirically that the logarithm of the derivative of the yield curve below its maximum, considered as a function of the primary energy, gives a straight line for all elements and has tried to give physical meanings to the slope and the intersection of this line with the ordinate. From Eq. (3) it follows that

$$\log(\partial\Delta/\partial E_p) = \log K_p - \frac{\alpha}{A}E_p = \log\frac{5\Delta_m}{E_m} - \frac{5}{E_m}E_p, \quad (8)$$

or, from Eq. (5),

$$\log[\partial(\Delta/\Delta_m)/\partial(E_p/E_m)] = \log 5 - 5E_p/E_m. \quad (8')$$

Geyer's empirical relations find here their natural analytical form. We shall turn now to a discussion of the absolute value of the yield and of the constants.

3. SECONDARY ELECTRON EMISSION AND PERIODIC SYSTEM OF ELEMENTS

According to Eq. (7) the ratio of Δ_m to E_m does not depend on the ratio A/α. It will be shown, by examination of the changes of Δ_m and E_m in practical measurements that the separation of Δ_m into two factors $(K\rho)$ and (A/α) is of real interest. An examination of the experimental values shows that, in general, to large values of δ_m (or Δ_m) there correspond large values of E_m (this is seen by simply plotting δ_m *vs* E_m); this shows that $(K\rho)$ varies slowly, as one should expect. $K\rho$ (essentially equal to Δ_m/E_m) is almost the same in each period of the atomic table and decreases linearly with the quantum number of the outermost electron shell, n.

It is seen furthermore from Eq. (6) that E_m has a simpler physical meaning than δ_m; it is, apart from the factor 5 which arose from the mathematical approximation, the ratio of the two constants A and α [also the slope of Eq. (8)]. Unfortunately the experimental values of E_m have been determined up to now only very roughly. It is believed that an exact determination of E_m might give important new information. However, even with the known less reliable values of E_m one obtains a well-defined periodic curve if one plots E_m

[12] K. H. Geyer, Ann. Physik 42, 337 (1942–43).

vs atomic number Z. It must be pointed out that there are many ways of correlating the secondary electron emission with the atomic structure; in fact, attempts have been made to compare δ_m or some related quantity of the δ curve with the atomic number Z,[13,14] or with other properties of solids such as work function[4,15] or density.[15] Many investigations, especially those on complex targets,[16] indicate that the depth to which primary electrons penetrate is the most important factor for the secondary emission; in fact a close relation has been found to exist between density on one hand and the secondary emission constants on the other. Figure 1 shows the density of the elements as a function the atomic number Z. The previously mentioned $E_m=f(Z)$ curve (not given here) has a very similar shape to this curve.

If one further plots either δ_m or Δ_m against the density d, a striking proportionality is found for the elements in the first half of each period (Fig. 2). Comparing Figs. (1) and (2), it follows that in each period where the density increases linearly with Z, Δ_m (or δ_m) increases linearly with density and therefore also linearly with Z. No simple correlation is found for the other elements from the existing data. This fact explains partly the correlation reported by Sternglass,[13] where Δ_m increases linearly with Z in each half-period. However, it must be remarked that there is no reason to assume that Δ_m also increases linearly with Z for the elements of the second half of each period (where d decreases with Z), namely elements $Z=30$–36, 48–54, and 79–86, as Sternglass implicitly did. Moreover, the values of Δ_m for Au, Sb,[17] and the recent values for Pb, Hg, Ga, and Bi [18] would not agree with his representation.

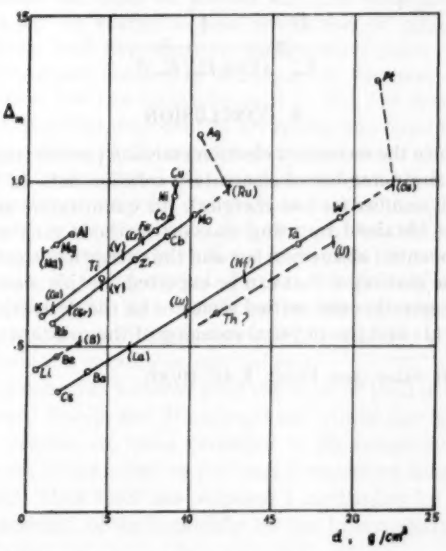

FIG. 2. Plot of the maximum true secondary-emission yield Δ_m *vs* the density d. The circles represent experimental points; the vertical bars give predicted values.

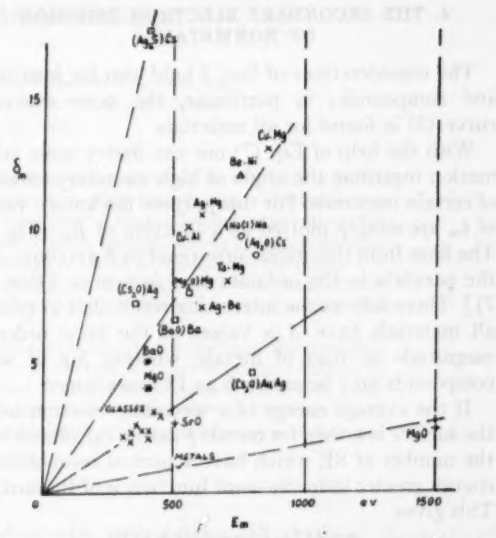

FIG. 3. The secondary emission yield δ_m of different materials as a function of E_m, the primary energy at which δ_m occurs. × H. Salow, Z. tech. Phys. **21**, 8 (1950); ○ G. Maurer, Z. Physik **118**, 122 (1941); △ Gille, Mathes, Z. tech. Phys. **22**, 228, 232 (1941); □ Timofeew, Physik. Ber. **23**, 1070, 1071 (1942); + K. H. Geyer, Ann. Physik **42**, 241 (1942); ✳ H. Bruining and J. H. de Boer, Physica **5**, 17 (1938).

Similar curves to those in Fig. 2 are obtained in each period, if Δ_m is plotted against the work function φ instead of d (though these have larger deviations from straight lines). This is because φ is also related to the density of the elements.[19] However, a universal relationship between δ_m and φ[4,15] does not seem to exist.

If the constants introduced here turn out to be useful, the best way of expressing the above relationships would be in terms of these constants like one considers the variation of the work function or the ionization potential with the atomic number Z. There are two ways of determining the constants (A/α) and (Kp): one from the maximum values Δ_m and E_m according to Eqs. (6) and (7), and the other from the δ curve $\delta=f(E_p)$ according to Eq. (8). If further the penetration depth can be determined, then A and α can be separated. If the factor p can be calculated approximately (Sec. 4) then the constant K can be evaluated. It must be remarked that other factors like the surface conditions or deviations from ideal crystal structure have not been treated explicitly here; their effect is included in the other constants.

[13] E. J. Sternglass, Phys. Rev. **80**, 925 (1950).
[14] P. L. Copeland, Phys. Rev. **46**, 167 (1934).
[15] K. G. McKay, *Advances in Electronics* (Academic Press, Inc., New York, 1948), Vol. 1, p. 69.
[16] P. L. Copeland, Phys. Rev. **48**, 96 (1935); R. Truell, Phys. Rev. **62**, 340 (1942).
[17] P. Görlich, Physik. Z. **43**, 121 (1942).
[18] J. J. Brophy, Phys. Rev. **83**, 534 (1951).
[19] F. Rother and H. Bomke, Z. Physik **86**, 231 (1933).

4. THE SECONDARY ELECTRON EMISSION OF NONMETALS

The considerations of Sec. 2 hold also for insulators and compounds; in particular, the same universal curve (5) is found for all materials.

With the help of Eq. (7) one can derive some information regarding the origin of high secondary emission of certain materials. For this purpose the known values of δ_m are simply plotted as a function of E_m (Fig. 3). The lines from the origin correspond to $Kp=$ const. and the parallels to the ordinate to $A/\alpha=$ const. [Eqs. (6, 7)]. There follows the interesting result that in general all materials have A/α values of the same order of magnitude as that of metals, whereas Kp of some compounds may be as much as 15 times larger.

If the average energy of a secondary electron below the surface is $\bar{\epsilon}$, then for metals p can be calculated from the number of SE which have a normal component of energy greater than the work function φ of the surface. This gives

$$p=\tfrac{1}{2}\{1-[(\varphi+\xi)(\bar{\epsilon}+\xi)]^{\frac{1}{2}}\}, \tag{9}$$

where ξ is the Fermi-energy; p does not depend strongly on ϵ, so that the average over the distribution function of ϵ can be replaced by $\bar{\epsilon}$.

In the case of insulators and semiconductors, electrons which have been excited to the conduction band can only escape the surface if the conduction band lies higher than the vacuum level. In this case, if W denotes the breadth of the conduction band and χ the energy difference between the lower end of conduction band and the vacuum level, then p is essentially given by the following expression:

$$(1-\chi/W). \tag{10}$$

This factor is responsible for the high Kp values found experimentally. One can see now why the intrinsic semiconductors B, Ge, Si or the defect semiconductors (e.g., SnO_2, Cu_2O, Ag_2O, MoO_2, $\cdots$) with χ of the order of 4 ev are poor secondary emitters in comparison with, for example, alkali halides with $\chi\approx 0-1$ ev. This consideration strongly supports the qualitative view of Bruining and deBoer[20] concerning the mechanism of the secondary emission of compounds rather than the other view that the high secondary emission is due to the absence of absorption of internal SE due to the conduction electrons.[21] Furthermore it follows that for excess semiconductors (e.g., activated semiconducting layers) the enhanced secondary emission is not due to the emission of active centers itself but due to the decrease of χ by these centers.

5. HIGH PRIMARY ENERGIES

For high primary energies, Eq. (1) does not hold and one should have [8-10]

$$-dE/dx=(B/E)\log(E/E_i), \tag{11}$$

where B and E_i are characteristics of the medium. The variation of the logarithmic term is very slow and one gets a penetration depth which tends to a quadratic curve with increasing E_p in accordance with experiment.[11] Also the initial energies of the internal SE are different than in low-energy region.

Formally, taking a combination of (1) and (11) and writing the total number of SE in the form

$$dn/dx=kA/(1+D^2E_p^2)^{\frac{1}{2}}, \tag{12}$$

one obtains exactly the entire experimental curve by adjusting only the constant D. However, because of its empirical character, this calculation is not given here. For $E_p>E_m$ the result has the simple form

$$\frac{\delta}{\delta_m}\cong\frac{4}{(15+E_p/E_m)^{\frac{1}{2}}}. \tag{13}$$

6. CONCLUSION

Since the secondary electron emission process consists of a finite number of elementary collision acts (a very small number for low energies), the quantitative agreement obtained by using classical methods such as an exponential absorption law and the energy loss equation is the maximum that can be expected. In this sense the only question not settled seems to be the derivation of Eq. (1) and the physical meaning of the constant A.

[20] H. Bruining and J. de Boer, Physica 6, 834 (1939).

[21] H. Salow, Ann. Physik. 5, 417 (1950).

X-Ray Coloration of Alkali Halides*

D. L. DEXTER
Institute of Optics, University of Rochester, Rochester, New York, and Metallurgy Division, U. S. Naval Research Laboratory, Washington, D. C.

(Received November 23, 1953)

Processes of importance in the coloration of solids by x-radiation are discussed on the basis of Seitz's hypothesis that vacancies are created at jogs on dislocations or at other imperfections. The interaction between F centers and dislocations is calculated, and it is shown that F centers located within about 50A of edge-type dislocations would experience measurable broadening and perhaps shifting of their absorption peaks, in contradiction of experiment. From the available energy in the form of point thermal pulses, it is shown that most vacancies freed from jogs or other sources probably make less than a thousand atomic jumps during x-irradiation at He temperatures and hence are unable to diffuse more than about 100A from their sources.

The tunneling of F-center electrons to positive-hole centers is calculated, and it is concluded that tunneling can occur with high probability over a distance of ~30A by an electron in its ground state, ~40A in its first excited state. Such tunneling is important in limiting local F- and V-center concentrations even at He temperature in the dark. Crystals achieving macroscopic concentrations of the order 10^{18} cm^{-3}, it is concluded, must contain very high densities of vacancy sources to be consistent with the requirements of both the large tunneling range and the small diffusion distance.

I. INTRODUCTION

IN the past year or so a number of speculations have been made regarding the role of dislocations in the formation of F centers by x-irradiation at He temperatures.[1,2] The general argument is as follows: An x-ray is absorbed by the crystal, thus giving rise to a single fast photoelectron of, let us say, 50-kev kinetic energy. Such an electron has insufficient momentum to displace a lattice ion from its normal site and consequently gives up its energy in the production of phonons, excitons, and free electrons and positive holes. The electrons and holes may subsequently combine with whatever few free vacancies exist at this low temperature, and thus color centers are readily produced from the positive- and negative-ion vacancies already present in the crystal. The excitons also can aid in the production of the color centers,[3] but none of these light particles (electrons, holes, and excitons) has sufficient momentum to increase by direct interaction the number of vacancies in the crystal. Further, the probability is negligibly small that a sufficient number of phonons will meet in a small region to contribute enough energy to produce a vacancy-interstitial pair.

It is generally believed from the work of Dutton and Maurer,[4] Duerig and Markham,[5] and others that more color centers are being produced at He temperatures than can be explained on the basis of vacancies initially present. Thus Seitz[2] has proposed a mechanism for the enhancement of darkenability by the intermediary of jogs[6] on edge-type dislocations: the ionic character of the alkali halides gives rise to effective charges on the jogs, or on their associated incipient vacancies; Mott and Seitz independently demonstrated that the magnitude of the effective charge is $e/2$.[7] Hence, according to Seitz, the free electrons and holes are attracted to the incipient negative- and positive-ion vacancies, respectively, and are trapped in localized energy states with the production of heat. Until recently it was assumed that the increased density of phonons made possible the escape of the incipient F and V centers by diffusion.[8] This interpretation was not entirely satisfactory because of the known low jump frequencies for diffusion[9] and because it is not at all evident that the energy of the system would be lowered by the escape of the centers. Seitz[2] has suggested a modification of this picture, namely, that many of the incipient vacancies occur as nearby positive-negative pairs because of the Coulomb attraction. Thus when an electron is trapped by the incipient negative-ion vacancy, the incipient F center has an effective charge of $-e/2$ and repels the nearby incipient positive-ion vacancy. The latter's

* This research has been supported in part by funds from the U. S. Air Force under a contract monitored by Headquarters, Air Research and Development Command, P.O. Box 1395, Baltimore 3, Maryland.

[1] J. J. Markham, Phys. Rev. **88**, 500 (1952).
[2] F. Seitz, Phys. Rev. **89**, 1290 (1953).
[3] D. L. Dexter and W. R. Heller, Phys. Rev. **84**, 377 (1951).
[4] D. Dutton and R. J. Maurer, Phys. Rev. **90**, 126 (1953).
[5] W. H. Duerig and J. J. Markham, Phys. Rev. **88**, 1043 (1952).

[6] Let the dislocation line lie along the Z direction in a cubic crystal, and let ZX represent the slip plane so that the YZ plane is parallel to the "extra plane" of atoms. If for $z>0$ the dislocation line is given by $x=y=0$, and if for $z<0$ the dislocation line is $x=0$, $y=\pm a$, where a is a crystal unit length, we say that a jog exists on the dislocation line at $z=0$. That is, a jog occurs at the terminus of an extra half line of atoms added to the extra half plane. F. R. N. Nabarro [Conference on the Strength of Solids (The Physical Society, London, 1948), p. 75] was apparently the first to recognize that diffusion of atoms to this jog could take place relatively easily for geometrical reasons. F. Seitz [Phys. Rev. **80**, 239 (1950)] has extended this concept with particular emphasis on the vacancies left behind by such diffusion and has given the name "incipient vacancy" to the immediate vicinity of the jog.
[7] F. Seitz, Revs. Modern Phys. **23**, 341 (1951).
[8] D. L. Dexter, Science **115**, 199 (1952); see, also, reference 1.
[9] See F. Seitz, Revs. Modern Phys. **18**, 384 (1946), for a review of the data on diffusion of vacancies. See also G. J. Dienes, J. Chem. Phys. **16**, 620 (1948), with regard to diffusion of vacancy pairs.

diffusion is aided by the liberation of heat when the electron is trapped. When the incipient positive-ion vacancy is filled by a positive ion, the jog moves over one lattice distance, that is, there is created in an adjacent site an incipient negative-ion vacancy. Thus at this stage there would be an incipient negative-ion vacancy and an incipient F center. The latter would subsequently trap a positive hole, presumably, and the point thermal spike following recombination would allow the diffusion away of the incipient negative-ion vacancy. Thus there would finally be, as initially, a positive-negative pair of incipient ion vacancies and in addition a positive-negative pair of free vacancies (not necessarily associated). Similar arguments may apply for the trapping of holes, but probably the specific processes are somewhat different. (For example, it is probable that the incipient negative-ion vacancy does not diffuse away when a positive hole is trapped, unless the incipient vacancies are very close together, since the activation energy for diffusion of the relatively large negative-ion is large.) By this process, according to Seitz, vacancies of both signs, both clustered and isolated, will come to exist in high concentrations near the dislocations. Other electrons and holes will be attracted to these vacancies to form F and V centers. The relative strength of the α band to that of the F band in crystals x-rayed at low temperatures and the high bleachability of such crystals are explained by the unusual closeness of the F and V centers to each other, since both are close to the dislocations.

It seems an inescapable conclusion that if additional vacancies are created during x-irradiation, they must be generated near imperfections such as dislocations. Qualitatively, then, one would expect that if dislocations interact appreciably with F centers, such interaction should be most important in crystals having been colored by irradiation at low temperatures, where diffusion frequencies are extremely low. In crystals heavily cold-worked at room temperature the dislocation concentrations are expected to be large, and appreciable broadening of the F band is observed. The crystals are so distorted that it is not clear how the observations can be quantitatively related to "good" crystals, but at least the existence of an interaction between F centers and dislocations is strongly indicated.

The purpose of this note is to investigate more quantitatively some of the processes believed to be important in the coloration of the alkali halides, in particular, the influence of dislocations on the position and width of the F band, the processes important for the diffusion of the free vacancies, and the extent to which tunneling of F-center electrons can be expected to occur.

II. INTERACTION OF F CENTERS WITH DISLOCATIONS

The lattice surrounding an imperfection is of course in a state of strain, and intuitively it is clear that the energy of the F band must be dependent on this distortion. One of the most effective imperfections for modifying the optical behavior of an F center we would expect to be an edge-type dislocation, since there is associated with it a long range strain pattern. Vacancies, interstitials, impurity atoms, and screw-type dislocations would have much less effect, and we shall ignore them in most of the following.

Surrounding an isolated edge dislocation in a medium of Poisson ratio ν, the density variation at a point P is given by

$$\frac{\Delta\rho}{\rho_0}=\frac{\lambda}{2\pi}\frac{1-2\nu}{1-\nu}\frac{\sin\omega}{r}, \tag{1}$$

where λ is the unit crystallographic slip distance, r the length of the position vector of P measured perpendicularly from the dislocation line, and ω the angle between this vector and the slip plane.[10] This equation is derived on the assumption of an isotropic, homogeneous continuum and is not expected to be valid within a few angstroms of the dislocation axis; it should be fairly accurate for r larger than, say, 5A.

Since the energy E of the optical transition corresponding to the F band is a function of the local density, we may expand it in a Taylor series, and obtain

$$E(\mathbf{r})=E_0(1+\gamma\Delta\rho(\mathbf{r})/\rho_0+\cdots). \tag{2}$$

The dimensionless constant γ can be calculated on the basis of specific models for the F center, and it may also be directly obtained from experiments on the pressure dependence of the F-band energy.[11] Burstein *et al.* find values of 0.87 for KI, 1.14 for KCl, and 1.73 for NaCl. Thus, combining Eqs. (1) and (2), we obtain for the energy of the absorption peak of the F center, as a function of its position with respect to the nearest dislocation, the value

$$E(\mathbf{r})=E_0\left(1+\frac{\gamma\lambda}{2\pi}\frac{1-2\nu}{1-\nu}\frac{\sin\omega}{r}\right). \tag{3}$$

This equation would perhaps be somewhat modified if the dislocation line were not straight. Let $n(\mathbf{r})$ represent the number density of F centers at position $\mathbf{r}$ from the nearest dislocation. Then the absorption coefficient is given as a function of energy E' by the expression

$$\mu(E')=\tau^{-1}\int d\tau n(\mathbf{r})\sigma(E'-E[\mathbf{r}]). \tag{4}$$

In this expression σ, the absorption cross section of an

[10] J. S. Koehler, Phys. Rev. **60**, 397 (1941).

[11] Burstein, Oberly, and Davisson, Phys. Rev. **85**, 729 (1952). The foregoing abstract will be written up in detail in the near future. The writer is indebted to Mr. Burstein for access to his data before publication. See also I. S. Jacobs, Fifth Annual Report to U. S. Office of Naval Research on High Pressure Research, Institute for the Study of Metals, the University of Chicago, July, 1952 (unpublished).

F center for light of energy E' is written as a function only of the difference between E' and E, the energy of maximum absorption. That is, it is assumed here that there is no change in the shape of the absorption cross section of a single center but only in the position of its midpoint. As Markham has pointed out,[1] the presence of a dislocation will probably modify somewhat the spectrum of lattice vibrations with which the given F center interacts, but this effect is assumed small here; Burstein and Jacobs observed no change in width of the F band with changing pressure.[11]

Let us evaluate Eq. (3) numerically for the case of KCl. Here $E_0=2.29$ ev, $\gamma=1.14$, $\lambda=4.44$A,[12] and $\nu=\frac{1}{3}$. Then we obtain

$$E(\mathbf{r})=2.29\text{ ev}+0.92(\sin\omega/r)\text{ ev}, \qquad (5)$$

where r is measured in angstrom units. Thus an F center located 5A from the dislocation may have its peak absorption shifted by as much as ± 0.2 ev, and F centers within about 50A would experience easily measurable shifts.

In a well-annealed crystal additively colored at high temperatures, where the dislocation concentrations are no higher than 10^{10} per cm^2, and where the F centers are expected to be randomly distributed throughout the crystal, the fractional number of F centers within 50A of a dislocation line would be less than one percent, and the smearing associated with the dislocations would not be detectable. On the other hand, if every F center were within 50A of a dislocation line,[13] as one might expect in crystals colored by x-irradiation at He temperatures, the F band would be markedly changed, either broadened, or broadened and shifted. It would appear that the strain energy would be lower if the incipient vacancy exchanged places with an ion on the compression side of the slip plane than if it jumped to the low-density side. Thus it appears that the shift in the F band should be toward higher energy, but perhaps one cannot be certain. The writer has been able to think of no arguments in favor of diffusion preferentially along the slip plane, where $\sin\omega$, and, hence, the energy shift, are zero.

Experimentally no marked effect is observed. The F band produced by x-irradiation at 5°K and measured at this same temperature has the same mid-point as that produced at high temperatures and measured after cooling to 5°K; and, further, the width of the F band is if anything the *lower* in the sample irradiated at He temperatures.[5] Thus we are forced to the conclusion that the F centers are not predominantly located within 50A of edge-type dislocations in good crystals.

Clearly this could be true for either of two reasons: (1) vacancies are not produced at edge-type dislocations in the first place, or (2) the vacancies are able to diffuse much more than 50A away. Seitz has made two interesting comments to the writer in connection with (1). First, he has emphasized that in well-annealed single crystals the long-range elastic fields about edge-type dislocations are reduced as a result of their orientation in the formation of mosaic boundaries. This would decrease the distance over which the F-center dislocation interaction would be detectable. Second, he has cited recent unpublished calculations by Jean Dickey Apker indicating that the energy associated with screw dislocations is lower than that for edge dislocations in NaCl, so that one would expect the former to predominate in good crystals. Now the F-center interaction with screw dislocations would not be detectable for separations greater than a few angstroms, but of course a screw dislocation is not a suitable, low-energy source of vacancies. General dislocations combining the required properties can be readily imagined: for example, a short segment of edge type connecting greater lengths of screw-type dislocation would suffice as a source of vacancies, and, if the segment were sufficiently short, the elastic field at large distances would be greatly reduced. Collapsed vacancy disks of small linear dimensions would also appear to serve as a vacancy source without long-range elastic distortions which could be detected by a modification of the F band. Anticipating the results of the following analysis of possibility (2), we may expect that an interpretation along these lines is in fact correct.

The second possibility mentioned above involves the diffusion of negative-ion vacancies (or F centers). With activation energies for diffusion, W, of at least several tenths of an electron volt (1.1 ev for a negative-ion vacancy, 0.8 ev for a positive-ion vacancy, and 0.4 ev for a pair in KCl[9]), the jump frequencies at 5°K are vanishingly small with the equilibrium number of phonons. Some idea of the magnitude may be obtained from the value $\nu=\nu_0\exp(-W/kT)\sim 10^{-394}$ sec^{-1} for vacancy pairs in KCl. Markham[1] and Seitz[2] have pointed out that when an electron is trapped at an incipient vacancy much of the trapping energy will be released as a point thermal spike, and it is this thermal energy $E\sim 1$ ev which aids in the initial escape of the incipient vacancy. This energy will of course diffuse away as a cloud of phonons, and one may then estimate the excess thermal energy per atom at a distance from the center of the cloud. If the ionic density is n_0, the number of ions within a distance L is $(4/3)\pi L^3 n_0$, so that the energy per ion at distance L is less than $E/(4/3\pi L^3 n_0)$. At a distance 25A in KCl the latter has

[12] The slip planes in the alkali halides are presumably (110) planes with (110) as the slip direction. See F. Seitz, reference 6, for a description of this configuration.

[13] One may ask if it is physically possible to pack all of the centers into such a small volume as is represented by cylinders of 100-A diameter around each dislocation. If dislocation concentrations of 10^{10} cm^{-2} are present under these circumstances, the fractional volume within 50A of the lines is about one percent, so that a macroscopic F-center density of 10^{18} cm^{-3}, as observed by (reference 5) Duerig and Markham, would require local concentrations of 10^{20} cm^{-3}. Such a distribution is not obviously impossible, since macroscopic concentrations of this magnitude have been observed. [R. Hilsch (private communication), and R. Kaiser, Z. Physik 132, 482 (1952). See also reference 3 and the papers by Apker and Taft cited there.]

a value $\sim 5\times 10^{-4}$ ev which is approximately equal to kT at 6°K. Thus the probability is negligibly small that the initial thermal spike can induce diffusion of vacancies or pairs to this distance.

A mechanism of much greater importance for the diffusion is the local heating produced by recombination of excitons and of free electrons with holes: consider the energy poured into the crystal during x-irradiation. If the tube is operated at 50 kv and 20 ma, if 0.2 percent of this energy is converted into x-radiation, and if the crystal is 4 cm from the target, the energy absorbed in the crystal is equal to $\sim 10^{17}$ ev/cm³ sec. Thus, in 15 minutes of x-ray time, if the energy is absorbed in 0.1 mm,[5] the energy absorbed per cm³ is about 10^{22} ev/cm³. Now most of this energy eventually goes into the production of excitons and of free electrons and holes. If of the order of 10 ev is required for each exciton and electron-hole pair produced, there are about 10^{21} point thermal spikes per cm³ in the 15-minute irradiation, arising from the recombination of the excitons and pairs. If 10^{18} F centers per cm³ are produced by this exposure, about 10^4 ev or 10^3 thermal pulses accompany the creation of each F center. The above figures approximate the data in reference 5. Very similar values have been obtained by Maurer[14a] from the data of reference 4, by Harten, and by Martienssen.[14b] It seems noteworthy that such close agreement should be obtained by different workers on different crystals and with different experimental arrangements, for, if our present views are correct, the efficiency of F-center production should be distinctly structure-sensitive. Several remarks should be made in this connection. (a) First, the recombination of excitons and electron-hole pairs must occur extremely preferentially near imperfections; if the thermal pulses were randomly distributed with respect to the vacancies, then, since the fractional concentration of vacancies is less than 10^{-4}, a recombination would occur on a nearest neighbor of a vacancy less than once on the average. In this event the average vacancy would not be able to diffuse more than one or two atomic distances, and the F band so produced would certainly differ from that produced by additive coloration. It is reasonable that this preferential recombination near imperfections should be observed since phenomena involving "recombination centers" are common in luminescence and semiconductor investigations. (b) Secondly, the constancy of the production rate of F centers should be noted. It is remarkable that for several orders of magnitude change in F-center concentration the production rate is essentially unchanged. This observation could easily be interpreted on a picture involving F-center production at random points in a perfect lattice but in the present theory probably arises from a balancing of two phenomena, namely, the increasing fraction of thermal pulses located next to a vacancy where they can contribute to diffusion and the increasing probability of bleaching by tunneling as the concentration increases. (c) Finally, if we assume that recombinations occur exclusively on atoms adjacent to vacancies, and further assume that the associated thermal spike is sufficient to allow one atomic jump with high probability, we may obtain an estimate for the diffusion length perpendicular to the dislocation line of about 80A. This estimate is almost certainly too large but yet leads to a prediction of a measurable change in the F band, if long segments of edge-type dislocations were the source.

We have tacitly assumed above that diffusion occurs by isolated vacancies, whereas if vacancies of both signs are produced at the same or closely adjacent sources, the vacancies probably associate and diffuse together for part of their journey. This does not change the qualitative picture, except perhaps to improve the assumption that a thermal pulse induces one atomic jump. Eventually the vacancies must dissociate in order to form F and V centers.

Seitz[1,9] has discussed the solvent action of electrons and holes on pairs and clusters of vacancies and suggests that[1] "When a coupled pair of vacancies captures an electron, the positive-ion vacancy is, with the aid of the accompanying thermal spike, expelled for several lattice spacings even at helium temperatures, as a result of the electrostatic repulsion of the electron and the positive-ion vacancy. Hence the F center formed is essentially normal." The writer agrees with this conclusion, but would like to suggest that as a result of charge-dipole interactions the positive-ion vacancy is actually attracted to the F center, so that the thermal spike must overcome binding forces which are important at He temperatures. We may estimate the strength of the binding by computing the second-order perturbation energy associated with the interaction

$$V(\mathbf{R}) = -e^2/(\kappa R) + e^2/\kappa|\mathbf{r}+\mathbf{R}|, \tag{6}$$

where $\mathbf{R}$ is the position vector of the negative-ion vacancy measured from the positive-ion vacancy and $\mathbf{r}$ is the position vector of the F-center electron measured from the negative-ion vacancy. The first term on the right side of Eq. (6) is the interaction energy between the vacancies, and the second is that between the positive-ion vacancy and the electron. In this expression κ is the static dielectric constant, 4.68 for KCl. Taking R along the X axis and expanding, we obtain

$$\Delta E = \frac{-e^2}{2R^4\kappa^2}\left\{2e^2\sum_n \frac{|\langle n|x|0\rangle|^2}{E_n - E_0}\right\}, \tag{7}$$

in terms of the dipole matrix elements between the

[14a] R. J. Maurer, (private communication).

[14b] H. U. Harten, Z. Physik 126, 619 (1949); Nachr. Akad. Wiss. Göttingen, Math.-physik. Kl. 2a, 15 (1950). W. Martienssen, Z. Physik 131, 488 (1952); W. Martienssen and R. W. Pohl, Z. Physik 133, 153 (1952); W. Martienssen, Nachr. Akad. Wiss. Göttingen, Math.-physik. Kl. 2a, 111 (1952). See also F. Seitz (submitted for publication to Revs. Modern Phys.) for a review of this work.

ground and excited states of the F center. The quantity in curly brackets is the polarizability of the F center, α_F, approximately 22×10^{-24} cm^3 in KCl. If the F center at **R** were replaced by a normal negative ion, the interaction energy would be $-e^2/(2R^4\kappa^2)\alpha_I$, where α_I is the polarizability of the halide ion, approximately 3.5×10^{-24} cm^3 for KCl. Thus the net reduction in the energy as a result of the nearness of the positive-ion vacancy to the F center is given by

$$U=\frac{-e^2}{2R^4\kappa^2}(\alpha_F-\alpha_I), \tag{8}$$

which becomes numerically equal to

$$U=-78(a_0/R)^4 \text{ ev}, \tag{9}$$

where a_0 is the Bohr radius. For R equal to the separation between nearest neighbors in KCl, 5.9 a_0, U has the value $U\sim-0.06$ ev, and the binding energy is probably of this order of magnitude. In the absence of thermal spikes, a binding energy this large would be important at He temperatures although not at nitrogen temperatures or above. When an electron is captured by a pair of vacancies, however, the point thermal spike accompanying lattice relaxation will usually be sufficient to overcome the attractive charge-dipole forces and will allow the escape of the positive-ion vacancy from the first shell about the F center.

It seems likely then that under the influence of the initial thermal spike when the electron is captured the positive-ion vacancy may jump from the nearest to one of the second nearest unlike lattice sites. Further diffusion must await the recombination of additional excitons and electron-hole pairs in the vicinity of the positive-ion vacancy. If the positive-ion vacancy traps a positive hole before making about a hundred jumps, the two centers will be annihilated by tunneling, as discussed in the next section. Thus there is a mechanism operating to keep the F centers "normal," and also, of course, the same mechanism tends to keep the efficiency of coloration low.

III. TUNNELING OF F-CENTER ELECTRONS

In view of the short diffusion lengths of vacancies at low temperatures and of observations on the relative strength of the α band and on the bleachability of the F band at low temperatures, it is of considerable interest to investigate the tunneling of an electron from an F center to a V center. The electron is bound to a negative-ion vacancy with a potential energy $U=-e^2/\kappa_0 r$ at large distances, where κ_0 is close to the high-frequency dielectric constant of the crystal. At distance R, let us say, there exists a V_1 center, and associated with it is a positive hole on one of the surrounding halide ions. If the electron should reach one of these ions, it would experience a strong attractive potential and would probably recombine with the hole, since the recombination energy is much larger than the binding energy to the vacancy. Thus we shall make use of a potential for the electron in the ground state which is constant within the negative-ion vacancy, varies as $-e/\kappa_0 r$ at larger distances, and drops abruptly by several volts at a distance $R-a\sqrt{2}$ from the negative ion vacancy, where a is the atomic spacing. Thus the "transmission coefficient" is given by

$$\exp\left(-2\int_{r_n}^{R-a\sqrt{2}}\{(2m/\hbar^2)[U_n(r)-E_n]\}^{\frac{1}{2}}dr\right),$$

reduced by the fractional solid angle subtended by the V center. In this expression r_n is the distance at which the kinetic energy becomes negative and E_n is the energy of the electron in the nth excited state. Multiplying by the electronic frequency $|E_n|/2\pi\hbar$, we obtain the recombination frequency

$$\nu_n(R)=-\frac{E_n}{8\pi\hbar}\frac{a^2}{(R-a\sqrt{2})^2}$$
$$\times\exp\left(-2\int_{r_n}^{R-a\sqrt{2}}\{(2m/\hbar^2)[U_n(r)-E_n]\}^{\frac{1}{2}}dr\right). \tag{10}$$

The potential energy is written with the subscript n to indicate that a different (larger) dielectric constant is to be used in the potential when the electron is in an excited state. This is a result of the relaxation of the surrounding lattice when the negative-ion vacancy no longer contains a large fraction of an electron charge. Equation (10) can be evaluated in closed form, and we find

$$\nu_n(R)=\frac{-E_n a^2}{8\pi\hbar(R-a\sqrt{2})^2}$$
$$\times\exp-2\left\{\frac{R-a\sqrt{2}}{a_0}\left(\frac{-2a_0}{\kappa_n(R-a\sqrt{2})}\frac{-2a_0E_n}{e^2}\right)^{\frac{1}{2}}\right.$$
$$\left.\times\tanh^{-1}\left[1+\frac{e^2}{\kappa_n E_n(R-a\sqrt{2})}\right]^{\frac{1}{2}}\right\}. \tag{11}$$

Equation (11) has been evaluated with the results shown in Fig. 1. In the numerical computation we have used the values $a=3.14$A for KCl, $E_0=-2.9$ ev, and $E_1=-0.3$ ev for the energies of the ground and (relaxed) first excited states, and the values $e/2.5$ and $e/4.0$ for the effective nuclear charges of the negative-ion vacancy in these states.

From Fig. 1 we see that tunneling can occur in an hour to a distance of about 30A when the electron is in its ground state. Thus we conclude that at microscopic concentrations greater than $10^{24}/(4/3\pi30^3)=9\times10^{18}$

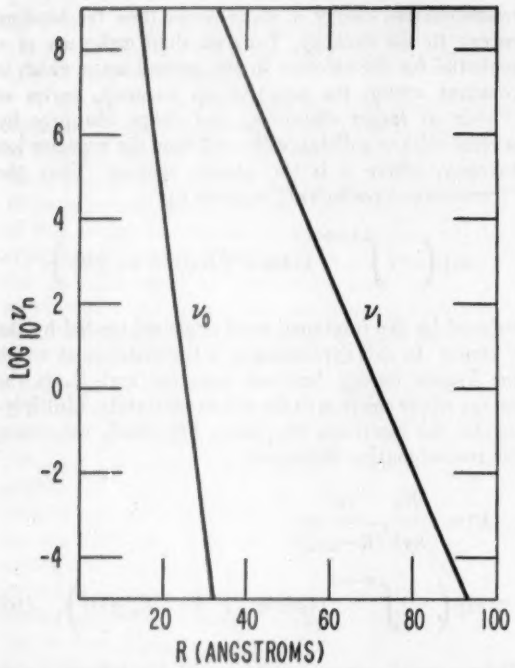

FIG. 1. Dependence of tunneling probability, in units of sec^{-1}, on the separation R between an F center and a hole-center in KCl. The two curves represent tunneling by an electron in the ground state (labeled ν_0) and in the first excited state (ν_1).

cm^{-3} many F and V centers would be destroyed by tunneling in the dark at low temperatures. Since macroscopic concentrations of the order of and greater than 10^{18} cm^{-3} have been observed,[5] it follows that the F and V centers must be distributed throughout much of the crystal. Because of the long tunneling range it is not difficult to understand why sizable α bands should be observed.

If we assume that screw dislocations can effectively act as vacancy sources through short segments of edge-type dislocation and take 80A as the diffusion length for the color centers, then, with local concentrations less than 10^{19} per cm^3, we require a dislocation density of 5×10^{10} line cm per cm^3. This corresponds to a degree of disorder to be expected in cold-worked crystals. If, on the other hand, we assume "point" vacancy sources, we obtain an upper limit for the diffusion length of about 100A and a maximum number of F centers per source of about 40. To explain observed macroscopic concentrations of 10^{18} per cm^3, then, we must imagine a source concentration greater than 2×10^{16} sources/cm^3. Such sources might be collapsed vacancy disks; and, computing the total periphery of these disks, we find an equivalent dislocation concentration of at least 8×10^9 dislocation line cm/cm^3, a considerably higher value than we like to associate with good crystals. It should be emphasized that we are led to this unsatisfactory conclusion by the high efficiency of coloration, which makes the possible diffusion length small, and the large tunneling range, which prevents large interpenetrating concentrations of electron and hole centers. The combination of these two requirements argues for the existence of a high concentration of vacancy sources.

F-center concentrations in excess of 10^{19} cm^{-3} would perhaps not be inconsistent with the tunneling results if the hole centers should preferentially cluster either on an atomic or larger scale. The former is not observed as a growth of other V bands at the expense of V_1 bands at low temperatures, and there seems to be no direct evidence for the occurrence of the latter. However, it is likely that the F- and V_1-center distributions are not identical, but that the F centers are somewhat more dense and compact. This would be expected if the jump probability for negative-ion vacancies in the presence of a thermal pulse were less than unity. In this case the V_1 centers in the inner region occupied by F centers would be somewhat depleted, and qualitatively the distribution might be described as a spherical or cylindrical shell of V_1 centers surrounding a sphere or cylinder of F centers, depending on whether point or line sources are operative. A simple example suffices to show that the total number of color centers near each source may be considerably increased by such a configuration. Suppose that a region τ is uniformly occupied, instantaneously, by a concentration of 10^{20} per cm^3 of both F and V_1 centers. Subsequent tunneling will bleach both concentrations to about 10^{19} per cm^3 and leave 9×10^{19} α centers per cm^3. Now imagine that τ is occupied by 10^{20} per cm^3 of V_1 centers, and $\frac{1}{2}\tau$, contained within it, is filled by 2×10^{20} F centers per cm^3. After tunneling occurs, then, a volume $\tau/2$ will contain 10^{20} V_1 centers per cm^3, and the remaining region $\tau/2$ will contain 10^{20} F centers per cm^3 and 10^{20} α centers per cm^3.

A similar end result would be obtained if the recombination cross sections of positive- and negative-ion vacancies were different. It may be argued that positive ion vacancies easily trap positive holes because of their large effective mass and because of the relatively large interaction (between holes and the surroundings of a positive-ion vacancy) indicated by the extremely low thermal activation energy of V_1 centers. Thus the common recombination process may involve trapping of holes first, followed by annihilation of an electron and hole at the positive-ion vacancy. If this process occurs 80 percent of the time, the volume filled by V_1 centers will be 8 times as large as that filled by F centers, which will be characterized by a diffusion length $\lesssim$65A.

The tunneling range is appreciably larger when the F center is in an excited, bound state. However, it must be recalled that the electron is in an excited state for only a very short time so that this increased range becomes much less significant. One would expect an emission probability from an F center of about 10^8 sec^{-1},

and since the luminescence efficiency is no more than a few percent,[15] the F center probably makes an internal, nonradiative transition in less than 10^{-9} sec. Thus the electron can probably tunnel a distance of about 35A while it remains in the excited state. If the intensity of the exciting light is such that an electron is raised to the first excited state about one hundred times per hour,[16] the average tunneling range is about 40A with a one-hour bleach. The figure 40A is to be compared with the comparable quantity 30A for an electron in the ground state. Thus one would expect appreciable bleaching of the F and V bands with F-band light at He temperatures for concentrations of the order 10^{18} cm^{-3}. Such bleaching has been observed by Markham and co-workers[16] and others. It is interesting to note in Fig. 11 of reference 16 that about half of the initial bleaching of KBr at nitrogen temperatures does not recover. This loss is presumably a result of the tunneling of F-center electrons to hole centers. Markham[16] has suggested that the recoverable part is associated with tunneling of F-center electrons to form F' centers. It should be remarked that the tunneling calculation above is independent of the specific process undergone by the electron after it passes the barrier, and hence one would expect probabilities for formation of F' centers by excited F centers comparable to those for annihilation of V centers at the same distance. Thus the fact that about half the bleaching is not recoverable might be an indication that the F-center and V-center distributions are locally about the same.

Note that the nonrecoverable diminution of the F band should be associated with a growth of the α band. Such a process should occur at He temperatures, where it could not easily be explained by thermal ionization of the F-center electron from its excited state. In the absence of data for KI on the temperature dependence of photoconductivity associated with the F band, it is not clear whether the tunneling mechanism is solely responsible for the growth of the α band observed by Pringsheim and co-workers at nitrogen temperatures.[17]

The statement is sometimes made that crystals x-rayed at higher temperatures bleach less easily than do those irradiated at low temperatures. It may be that this statement is correct only because the F-center concentration in the crystal colored at high temperature is lower than the concentration of centers in a crystal colored at low temperature. (The equilibrium concentration reached at high temperature where V centers are mobile might be depressed because diffusion by a few atomic spacings could result in annihilation by tunneling.) If the statement is true for crystals of the same macroscopic density, less than the final equilibrium value, it is likely that the coloration would be more uniform in the crystal irradiated at high temperature, and bleaching would be less probable. Another known effect is the absence of simple hole centers, i.e., V_1 centers, at high temperatures; if only two-hole centers were present, the effective concentration of hole traps would be reduced by almost a factor of two.

Dutton and Maurer[4] have measured the bursts of charge associated with thermal bleaching of the V_1 band in KCl and KBr and have correlated these currents with changes in the absorption due to F and V_1 centers. The characteristic temperatures are about -150°C. From the magnitude of the burst of charge and the number of V_1 centers destroyed, they conclude that the average distance of drift in the direction of the applied field is equal to 3×10^{-11} cm/(volt/cm) and 1×10^{-11} cm/(volt/cm) for KCl and KBr, respectively. These results are interpreted as indicative of thermal ionization of holes from the V_1 centers; from the temperatures of the current peaks the thermal ionization are estimated to be 0.26 ev and 0.23 ev for KCl and KBr.[4]

Maurer and Teegarden[18] have likewise investigated the photoconductivity in KCl and KBr upon irradiating in the V_1 band at -185°C and also the bleaching of the V_1 bands under these conditions. They find that the optical bleaching yield η_b is about 0.1 V_1 centers destroyed per photon absorbed, but that no appreciable photoconductivity is associated with the bleaching of the V_1 band. If η_h is the quantum yield for the ionization of V_1 centers to produce free holes and if w_h is the average range of the holes in the direction of a unit electric field, they find that $\eta_h w_h$ is probably less than about 10^{-14} cm/(volt/cm). If η_h should be as large as the bleaching yield, 0.1, the average range must be less than about 10^{-13} cm/(volt/cm). Such a hypothesis seems to be ruled out by: (1) the much larger range of holes, $10^{-11}-3\times10^{-11}$ cm/(volt/cm), thermally ionized at -150°C, and (2) the sizable photocurrents from holes optically ionized from V_2 and V_4 centers at -185°C.[18] Thus one is led to the conclusion that the quantum yield for the production of free holes is much less than the bleaching yield, and hence to the hypothesis that tunneling is responsible for the optical bleaching of the V_1 centers. The foregoing arguments have been presented by Maurer and Teegarden.[18]

We have not attempted a quantitative estimate of this tunneling range of holes because of too little knowledge of their energy levels. The personal opinion of the writer is that this range for holes in the ground state of V_1 centers would be less than for electrons in the ground state of F centers. Since nothing at all is known about the energy levels of excited V_1 centers, the difference in probabilities of tunneling of holes and electrons in excited states cannot be estimated even as

[15] C. C. Klick (to be published).

[16] This figure is obtained from the initial slope of the bleaching curve of Fig. 10, J. J. Markham, Preprint of Papers, J. Phys. Chem., Symposium of Impurity Phenomena, June 16–18, 1953 (unpublished).

[17] Delbecq, Pringsheim, and Yuster, J. Chem. Phys. **19**, 574 (1951).

[18] R. J. Maurer (private communication), and K. Teegarden, Report to National Science Foundation from the University of Illinois, August, 1953 (unpublished).

to sign. If the present interpretation based on tunneling should be correct for optical bleaching of V_1 centers, it would probably imply that the tunneling range of holes in excited states is larger than the tunneling range of electrons in the ground state, since, if not, the F and V centers would already have destroyed each other. The implication is not ironclad, however, since the thermal spike following absorption of a photon probably allows some diffusion of the center to positions of smaller separation from F centers.

A possible alternative to the interpretation of the thermal bleaching experiments of Dutton and Maurer,[4] namely, the thermal ionization of the V_1 centers, might be based on a tunneling process. For such a mechanism to be of significance, it would be necessary to assume that V_1 centers become mobile at about -150°C so that they diffuse to relatively small distances, say 25A, from F centers. At these separations tunneling by F-center electrons would occur with high probability, and, if an electric field were present, as in the experiments by Dutton and Maurer,[4] one would expect tunneling to occur preferentially opposite to the direction of the field, thus giving rise to a net current at the time of thermal bleaching. A current would also be expected in optical bleaching experiments for the same reason. If such a process should be responsible for thermal bleaching and the accompanying burst of charge, it would remove the current problem of the high ratio of the optical to the thermal ionization energy of V_1 centers. It is then of interest to examine the effect of an electric field upon the tunneling probability. In the presence of a field $\mathcal{E}$, another term, $-e\mathcal{E}\cdot\mathbf{r}$, must be added to the potential energy of the hole in Eq. (10). Since this term is small in comparison with the sum of the others over almost all of the range of interest, we may obtain the change in the tunneling probability in a simple way by expanding the square root and applying the mean value theorem. In this way we estimate the increased probability for tunneling in the direction of the field, which is larger by a factor of about

$$\{1+(2me^2/\hbar^2)^{\frac{1}{2}}\mathcal{E}R^2\langle(U_n-E_n)^{-\frac{1}{2}}\rangle_{\text{Av}}\}$$

than the probability for tunneling in the opposite direction.

If the average energy difference U_n-E_n for holes in the excited states of V_1 centers is characterized by the value $\langle(U_n-E_n)^{-\frac{1}{2}}\rangle_{\text{Av}}=(0.5\text{ ev})^{-\frac{1}{2}}$, then, for tunneling distances of the order of 30A, the above factor becomes $(1+6\times10^{-6}\mathcal{E})$, where $\mathcal{E}$ is expressed in volts/cm. Hence, the average net motion in the direction of the field is of the order 3×10^{-13} cm/(volt/cm). This is somewhat larger than the approximate upper limit fixed by Maurer and Teegarden[17] of 10^{-13} cm/ (volt/cm) in their optical bleaching experiments.

Tunneling almost certainly has nothing to do with thermal bleaching of V_1 centers even though it is probably responsible for optical bleaching. As we have just seen, the presence of an electric field gives rise to a preferred tunneling in the direction of the field such as to give the excited holes an average *schubweg* of about 3×10^{-13} cm/(volt/cm), about two orders of magnitude less than that observed by Dutton and Maurer[4] for KCl. In the thermal bleaching experiments where the electrons and holes are not in excited states, the average energy-difference term would be larger and the current would be still smaller. Hence, it does not seem possible to explain the thermal bursts of charge on the basis of tunneling, and thermal ionization of the V_1 centers appears essential to explain the observed currents, in agreement with the conclusions of Dutton and Maurer.

A further point that should be at least mentioned is the effect of thermal oscillation itself on tunneling probabilities, in the absence of diffusion. A quantitative account of the effect seems difficult, but qualitatively it is clear that thermal vibration of the lattice must instantaneously change the energy of the bound state of an electron or hole and thus would affect the tunneling probability. It is doubtful that such an effect would be important at -145°C.

IV. ACKNOWLEDGMENTS

The writer is indebted to Professor R. J. Maurer for illuminating discussions of his bleaching results and for access to his data before publication. He is likewise grateful to Dr. C. C. Klick and Dr. J. H. Schulman for helpful criticism of the manuscript. The section on diffusion phenomena benefited directly from helpful discussions and correspondence with F. Seitz, R. J. Maurer, and D. Dutton.

Effect of Pressure on *F*-Center Absorption in Alkali Halides*

I. S. JACOBS†
Department of Physics, University of Chicago, Chicago, Illinois
(Received November 23, 1953)

Measurements are reported for the effect of hydrostatic pressure to 5000 atmospheres on the *F*-center absorption of seven alkali halides. An interpretation is made of the shift of the absorption band maximum with pressure, and of the difference between the shift with pressure and that with temperature. The shift with pressure depends almost entirely on the local interionic distance at the *F* center. The shift with temperature is largely governed by this same factor, but it must be supplemented by a contribution from the interaction of the *F*-center electron with the optical vibrations of the lattice. Effects of the pressure-induced structure transformation in RbCl are described for both photochemically and additively colored crystals.

I. INTRODUCTION

THE problems and phenomena associated with the externally induced colored absorption bands in alkali halide crystals have commanded considerable attention for many years. Both experimental and theoretical investigations of recent years in this field seem to confirm the defect model of the centers responsible for the absorption. This model assumes the presence of electrons in quasi-atomic or molecular states trapped in the vicinity of lattice imperfections in ionic crystals, and attributes the bands to electronic transitions between these states. Excellent reviews of this subject may be found in the work of Pohl,[1] of Mott and Gurney,[2] and of Seitz.[3]

Among these colored bands, the so-called *F* bands of the alkali halides play a very fundamental role. Their absorption spectra, in or near the visible range, are bell-shaped. The peak wave number and width may be made to vary with temperature and pressure. Over the range of alkali halide crystals with the NaCl lattice structure, Mollwo[4] has indicated that, at a given temperature, the peak wavelength of the *F* band is approximately proportional to the square of the interionic distance. More recently, Ivey[5] has made a better representation in this form using the exponent 1.84 instead of 2. This relation is an empirical one. Its successful prediction from theory is bound up with the problem of calculating the wave functions and energy levels of electrons trapped at lattice defects.

Most of the theoretical calculations for *F* centers have treated the crystal as a homogeneous dielectric continuum, with the electron moving in the central field of the halogen ion vacancy which serves as the trapping site. Among the contributors to this approach are Tibbs,[6] Kubo,[7] Simpson,[8] Inui and Uemura,[9] Pincherle,[10] and Krumhansl and Schwartz.[11] An alternative approach employs a molecular orbital model of the *F* center, wherein the wave function of the electron is taken as a linear combination of atomic orbitals, each representing the extra electron in an atomic state on one of the atoms adjacent to the halogen ion vacancy. The first calculations of this type are due to Muto[12] and to Inui and Uemura.[9] The molecular orbital model has received significant support from the electron spin resonance absorption experiment on colored KCl, performed by Hutchison and Noble.[13] Kahn and Kittel[14] have made an interpretation of this work, and additional experiments of this type have been done by Kip, Kittel, Levy, and Portis.[15] At the present time, the work of Inui and Uemura, confined to the lithium salts, is the only quantitative calculation of energy levels with this model.

In recent years considerable attention has been directed toward the explanation of the shift of the absorption peak toward longer wavelengths, and of the increase in the absorption band width, with increasing temperature. In the work of Muto,[12] Huang and Rhys,[16] Lax,[17] and O'Rourke,[18] both the shift and the broadening have been accounted for by considering the interaction of the electron with optical vibrations of the lattice. On the other hand, the temperature shift has been ascribed mainly to the thermal expansion of the lattice by Inui and Uemura,[9] and Nagamiya.[19]

* This paper is based on a thesis submitted in partial fulfillment of the requirements for the degree of Doctor of Philosophy at the University of Chicago. The work was performed in the High Pressure Laboratory of the Institute for the Study of Metals.

† Now at General Electric Research Laboratory, The Knolls, Schenectady, New York.

[1] R. W. Pohl, Proc. Phys. Soc. (London) **49**, 3 (1937).
[2] N. F. Mott and R. W. Gurney, *Electronic Processes in Ionic Crystals* (Oxford University Press, London, 1940).
[3] F. Seitz, Revs. Modern Phys. **18**, 384 (1946).
[4] E. Mollwo, Z. Physik **85**, 56 (1933).
[5] H. F. Ivey, Phys. Rev. **72**, 341 (1947).
[6] S. R. Tibbs, Trans. Faraday Soc. **35**, 1471 (1939).
[7] R. Kubo, J. Phys. Soc. Japan **3**, 254 (1948); **4**, 322, 326 (1949).
[8] J. H. Simpson, Proc. Roy. Soc. (London) **A197**, 269 (1949).
[9] T. Inui and Y. Uemura, Progr. Theoret. Phys. **5**, 252, 395 (1950).
[10] L. Pincherle, Proc. Phys. Soc. (London) **A64**, 648 (1951).
[11] J. A. Krumhansl and N. Schwartz, Phys. Rev. **89**, 1154 (1953).
[12] T. Muto, Progr. Theoret. Phys. **4**, 181, 243 (1949).
[13] C. A. Hutchison, Jr., and G. A. Noble, Phys. Rev. **87**, 1125 (1952).
[14] A. H. Kahn and C. Kittel, Phys. Rev. **89**, 315 (1953).
[15] Kip, Kittel, Levy, and Portis, Phys. Rev. **91**, 1066 (1953).
[16] K. Huang and A. Rhys, Proc. Roy. Soc. (London) **A204**, 406 (1950).
[17] M. Lax, J. Chem. Phys. **20**, 1752 (1952).
[18] R. C. O'Rourke, Phys. Rev. **91**, 265 (1953).
[19] T. Nagamiya, J. Phys. Soc. Japan **7**, 354 (1952).

The last two investigators and Burstein and Oberly[20] have employed an adiabatic approximation to determine the effect of neighboring ion position on the F-center energy, and accordingly the effect of thermal agitation on the width.

Muto has pointed out that, in reality, we have to consider simultaneously not only effects arising from thermal expansion but also those connected with the excitation of lattice vibrations in order to obtain a full knowledge of the phenomena concerned. In an attempt to separate and clarify these effects, an investigation was undertaken to study the dependence on hydrostatic pressure of the F-band parameters. One limited experiment of this type has been reported briefly by Burstein, Oberly, and Davisson.[21] Measurements are reported below on the F-absorption band of seven alkali halides at room temperature up to pressures of 5000 atmospheres. The compounds studied were NaCl, NaBr, KCl, KBr, KI, RbCl, and CsCl. Other compounds were not studied owing to difficulties in procurement or preparation of suitable samples, experimental difficulties in the optical transmission of the pressure chamber, or the instability of their F band at room temperature.

The results of the experiments on the shift of the band peak with pressure are compared with the existing data in the literature on the shift with temperature, in an effort to interpret how the effects mentioned above have to be taken into account to form a consistent picture. For most of the compounds studied, the shift of the peak with pressure is less than that with temperature, when each is considered with respect to the corresponding change in lattice dimensions. In the analysis of the data for these compounds, it is shown that a small part (up to 5 percent) of the pressure shift is due to the interaction of the electron with the optical lattice vibrations. The remainder of the pressure shift is due to the explicit dependence of the F-center energy on local interatomic distance. The additional increment for the temperature shift above the pressure shift is attributed to a further interaction with optical lattice vibrations. An expression is obtained for the band width which combines the two existing theories and is consistent with the analysis of the shift of the band peak with pressure and temperature. The negligible effect of pressure on the band width is in agreement with these considerations.

A subordinate purpose of the present investigation is a study of the effects on the F band of the structure transformation in the rubidium halides. Excepting the fluoride, these salts show a polymorphic transition at room temperature and about 5000 atmospheres pressure, which was first observed by Slater[22] and was measured by Bridgman.[23] Jacobs[24] has shown that the crystal structure changes from the NaCl structure to the CsCl structure in the high-pressure form. Although various difficulties prevented the detection of a new F band in the transformed state, a number of interesting observations are described and discussed.

II. EXPERIMENTAL METHOD

A. Apparatus

A high-pressure system to allow for spectrophotometric measurements was constructed for this investigation. It was used in conjunction with a Beckman Model DU Quartz Spectrophotometer, employing the usual tungsten lamp and phototubes for the visible range. The system is capable of subjecting the sample to 8000 atmospheres pressure, although problems with failure of the windows restricted most of the work to a range of 5000 atmospheres.

The need for compactness and portability gave rise to several special features in this apparatus. The whole system is self-contained, with the pump for generating pressures made in the form of a plug which screws into the high-pressure bomb. To minimize the optical path through the bomb, a search was made for a more compact method of sealing the synthetic sapphire windows[25] than the Poulter[26] packing usually employed. Our experiments have shown that it is feasible to use ordinary synthetic rubber O-rings to seal pressures to at least 8000 atmospheres. With this technique only one O-ring is used to seal both the window and its supporting plug.

The high-pressure apparatus consists of the pump, the bomb, a mounting carriage with wheels, and a baseboard arrangement for positioning the Beckman spectrophotometer. This baseboard provides a track on which the carriage can be rolled so that either the observation hole or the blank reference hole is in position in the light path. A black cloth is fastened over the bomb and photocell units to keep out stray light during measurements. The pump is capable of producing a pressure of 2000 atmospheres. The pump liquid is 20-centistoke DC-200 silicone fluid (Dow-Corning). Figure 1 shows a diagram of the high-pressure bomb. The bomb contains a piston intensifier to magnify the 2000-atmosphere pressure delivered by the pump to a maximum pressure of 8000 atmospheres at the sample. Pressure is determined by measurement of the change in resistance of a manganin resistance gauge which is immersed in the pressure fluid. The gauge calibration procedure has been described previously.[27] The hy-

[20] E. Burstein and J. J. Oberly, National Bureau of Standards Circular No. 519 (U. S. Government Printing Office, Washington D. C., 1952), p. 285.
[21] Burstein, Oberly, and Davisson, Phys. Rev. **85**, 729 (1952).
[22] J. C. Slater, Phys. Rev. **23**, 488 (1924).
[23] P. W. Bridgman, Z. Krist. **67**, 363 (1928).
[24] R. B. Jacobs, Phys. Rev. **54**, 468 (1938).
[25] Purchased from The Linde Air Products Company, Synthetic Gem Division, Chicago, Illinois.
[26] T. C. Poulter, Phys. Rev. **35**, 297 (1930); see also P. W. Bridgman, *The Physics of High Pressure* (G. Bell and Sons, Ltd., London, 1949), p. 58.
[27] D. Lazarus, Phys. Rev. **76**, 545 (1949).

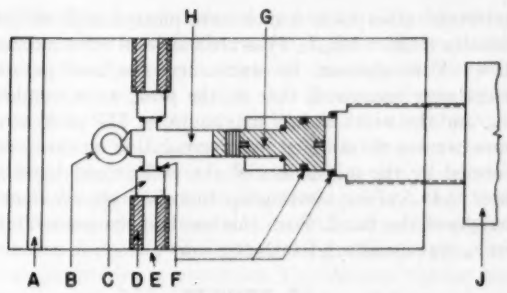

FIG. 1. Diagram of the high-pressure bomb. *A*, reference hole; *B*, gauge plug hole; *C*, synthetic sapphire window; *D*, window plug; *E*, sample observation hole; *F*, O-rings; *G*, piston intensifier; *H*, sample region; *J*, portion of pump.

draulic medium around the sample is 3-centistoke DC-200 silicone fluid, which is sufficiently transparent over the visible range. The sample holder is a split cylinder, with a $\frac{1}{4}$-inch hole transverse to the cylinder axis to permit passage of light. One of the cylinder halves has a recess $\frac{3}{8}$ in.$\times\frac{5}{16}$ in.$\times\frac{1}{16}$ in. for the crystal samples which are cleaved to that size. A coil spring around the cylinder keeps the halves together and provides the necessary friction with the walls to maintain the holder in a fixed position in the bomb.

The Beckman spectrophotometer needs no modification for use with the high-pressure system except for the separation of the photocell housing from the main unit by about 4 inches to accommodate the bomb.

B. Preparation of Samples

The specimens of NaCl, KCl, and KBr used in this work were cleaved from single-crystal blocks obtained from the Harshaw Chemical Company. No analysis of these samples was made, but the work of Duerig and Markham[28] includes a representative analysis of this type of commercial sample. Single-crystal specimens of the other four compounds were grown in the laboratory. The NaBr salt was Mallinckrodt, Analytical Reagent, and the KI salt was Baker and Adamson, Reagent. The CsCl salt used was 99+ percent, 0.5 percent K, 0.02 percent Pb, the two listed impurities having been added for a prior experiment. The RbCl samples were grown from two sources of the salt. One grade was Fairmount, cp, for which spectroscopic analysis showed 5 percent K, 0.5 percent Ba, 0.4 percent Na, 0.1 percent Cs, and lesser quantities of Li, the other alkaline earths and Pb. A purer source was Mackay "99.99 percent" for which spectroscopic analysis showed 0.3 percent K, 0.03 percent Na, and smaller quantities of Cs, and the alkaline earths.

The NaBr, KI, and RbCl crystals were grown in air from a platinum crucible by the Czochralski[29] method, with crystallization occurring on a platinum wire that was slowly withdrawn from the melt surface. The divalent impurities in these salts were reduced in concentration by a factor of two to ten in crystals grown in this manner. The CsCl specimen was grown by slowly lowering through a gradient furnace an evacuated and sealed Vycor tube containing the salt in a small spun platinum crucible with a conical bottom. All samples were annealed after growth for a 12-hour period. The air-grown crystals were readily cleaved to desired sizes. The deliquescent CsCl specimen, which did not cleave, was cut to shape and polished under silicone fluid. Similar handling precautions were taken with those of the other samples whose surfaces tended to fog easily.

The *F* band was produced in the crystals by irradiation with x-rays from a Machlett type A-2 molybdenum target tube with a beryllium window. The irradiations varied from 5 minutes to 90 minutes (40–50 kv, 20 ma) with the sample about one inch from the tube window. The ranges of time correspond to the varying darkenability of the different compounds. X-irradiation was performed in the dark, during which all samples showed a faint green or blue-green fluorescence. This effect has also been observed by Molnar[30] and attributed to impurities because the fluorescence differs in natural and synthetic NaCl. Subsequent handling of colored samples was done in the near-dark or with appropriate filters over the light source to remove *F*-band light.

Samples of KCl and RbCl were also additively colored with excess K or Na metal. A crystal somewhat larger than sample size was sealed in an evacuated Vycor tube with the metal. The metal was previously melted in a rough vacuum to draw off trapped gas. The tube, crystal, and metal were so arranged in the furnace that the crystal was kept at 660°C, while the metal was at about 300°C. After about 20 hours the tube was quenched in a brine solution. Samples suitable for measurement were cleaved from inner regions of the colored crystal.

C. Measurement Procedure

The absorption coefficients of the crystals were measured at each desired pressure, as a function of wave number, over a range embracing the whole *F* band. Readings were taken on a linear wave number scale, 250 cm^{-1} apart. To minimize the bleaching effect of the measuring light, the sensitivity adjustment on the spectrophotometer was set so that minimum slit widths were required. In this way the entire range of pressures could be explored with one x-irradiation of a sample. Such readings measured the transmission of the crystal and associated liquid and windows with respect to the reference hole which presented the same geometrical aperture. To obtain the true color-center absorption curve, a correction had to be applied for the effect

[28] W. H. Duerig and J. J. Markham, Phys. Rev. **88**, 1043 (1952).
[29] See H. E. Buckley, *Crystal Growth* (John Wiley and Sons, Inc., New York, 1951).
[30] J. P. Molnar, thesis, Massachusetts Institute of Technology, 1940 (unpublished).

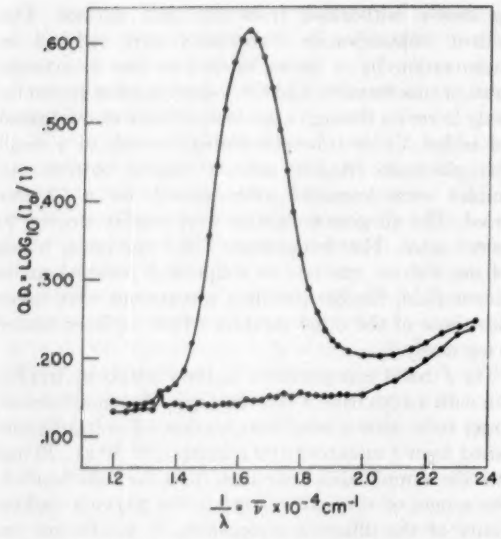

FIG. 2. Typical uncorrected F-band curve and a correction curve for the same sample.

of the blank crystal and associated apparatus. This could be measured by assembling the system with an uncolored crystal or by bleaching the x-ray colored crystal still in the bomb at the end of a pressure run. No significant differences were detected between these alternatives, if the bleaching with an ordinary incandescent lamp were sufficiently long. The latter procedure was usually adopted for the x-rayed specimens, while the former procedure was necessary for the additively colored samples. It was found that these blank absorption curves changed with pressure only by a linear displacement of the ordinate of the curve. This effect arose in part from changes in the interface reflections with the variation of the index of refraction with pressure and in part from irreversible changes in interfacial conditions induced by pressure. From this it follows that one blank absorption curve taken at one pressure was sufficient to make the necessary correction. This curve was linearly displaced to fit the colored absorption curves at one point where the F-band absorption was negligible. Figure 2 shows an uncorrected F-band curve and a correction curve taken on the same sample.

A very slow contamination of the bomb fluid took place at the violet end of the spectral range due to a dissolution of binding agents from the O-rings and piston washer. This resulted in some uncertainty in the height of the F band and gave rise to an uncertainty in the width at half-maximum, γ, of $\pm 0.004 \times 10^4$ cm^{-1}.

To avoid the distortion in the position of the band maximum due to the optical bleaching during the measurements, absorption curves were taken with both increasing and decreasing wavelengths in separate runs on each compound except NaBr and KI. The corrected absorption curves were plotted with optical density (O.D. $= \log_{10} I_0/I$) as ordinate and wave number ($\tilde{\nu} = 1/\lambda$) as abscissa. For each curve the band parameters were measured, that is, the peak wave number, $\tilde{\nu}_m$, and the width at half-maximum, γ. The peak wave number was determined by extrapolation on the curve formed by the mid-points of the bell-shaped band at four O.D. values, starting up from half the maximum height of the band. With this method the uncertainty in $\tilde{\nu}_m$ was usually $\pm 0.002 \times 10^4$ cm^{-1}.

III. RESULTS

A. Pressure Dependence of F-Band Parameters

The data from the measurement of the F-band peak wave number at intervals of about 1000 atmospheres are presented in Table I and in terms of wavelength in Table II. These data represent the average of two or more runs, except in the cases of NaBr and KI for which only one run was made. The experiments were conducted at room temperature, which was constant within 1°C during any single run but which varied during separate runs from 20° to 28°C. The agreement of the atmospheric pressure values in Table II with those listed by Ivey[6] is reasonably satisfactory in most cases. The agreement is even better with the recent values of Gnaedinger[21] for the compounds which he studied. The largest discrepancy from Ivey's tabulation is in the case of CsCl, but a re-examination of the source[1] of this value suggests that our value in Table II is reliable. The values based on a single run are distorted in the direction anticipated from the optical bleaching. It should be pointed out that the reported location of the peak may be affected by the method chosen to fix its location, due to the considerable width of the room temperature bands.

In order to make a more significant physical correlation, the results are considered as a function of the crystallographic unit cell distance, a. This is calculated from the compressibility at 30°C determined by Slater

TABLE I. Pressure dependence of F-band peak wave number.

Pressure bars[a]	Peak wave number[b] 10^4 cm^{-1} NaCl	NaBr[c]	KCl	KBr	KI[d]	RbCl	CsCl
1	2.147	1.865	1.787	1.593	1.446	1.578	1.656
1000	2.161	1.876	1.798	1.604	1.460	1.591	1.666
2000	2.175	1.886	1.810	1.616	1.474	1.604	1.676
3000	2.190	1.897	1.821	1.628	1.489	1.615	1.685
4000	2.203	1.909	1.832	1.640	1.503	1.624	1.693
5000	2.215	...	1.842	1.652	1.517	1.634	1.701
6000	2.226	...	...	...	...	...	...
7000	2.238	...	...	...	...	...	...
8000	2.250	...	...	...	...	...	...

[a] 1 bar $= 10^6$ dynes/cm$^2 = 1.01971$ kg/cm$^2 = 0.98692$ atmos.
[b] $\pm 0.002 \times 10^4$ cm^{-1}.
[c] Measured with increasing wavelength only.
[d] Measured with decreasing wavelength only.

[21] R. J. Gnaedinger, Jr., J. Chem. Phys. 21, 323 (1953).

and Bridgman, as tabulated by Birch,[32] with regard for recent corrections in the value of the compressibility of iron. For the complete data on the compressibility of RbCl, the original article by Bridgman[33] must be consulted. The effect on the elastic constants due to the presence of F centers is negligible for color-center concentrations encountered in usual practice. A calculation of this type has been presented by MacKenzie,[34] in which the correction term is proportional to the relative decrease in density of the material due to the presence of small cavities or vacancies. This density change has been measured in two investigations,[35,36] but it is insignificant in the case at hand. A simple correlation of the pressure data is found by plotting $\log_{10}\tilde{\nu}_m$ *versus* $\log_{10}a$ for each individual compound. The points lie along a straight line whose slope can be measured with an uncertainty of about 5 percent. Figure 3 presents typical curves from individual runs on each of the seven compounds, plotted on reduced scales. The straight lines become more clearly defined when data from several runs are considered, but these are omitted from the figure for the sake of clarity.

The quantity of interest in this method of considering the results is the parameter $n_T(P)$, which is the negative of the slope of the line, i.e., $n_T(P)=-(\partial\ln\tilde{\nu}_m/\partial\ln a)_T$. From the figure it is seen that most of the lines have nearly the same $n_T(P)$, i.e., 3.5, with the exception of NaCl which is high (4.4), and of CsCl which is low (2.8). The specific values are recorded in column 2 of Table III. The slopes did not vary outside the limits of uncertainty on different samples of the same compound, or on samples of different purity obtained from separate sources as in the case of RbCl, or on samples colored by different methods, additively or photochemically (x-ray) as in the cases of KCl and RbCl.

The widths at half-maximum at atmospheric pressure are in good agreement with previously published values, subject to the experimental uncertainties mentioned above. For five of the seven compounds studied, the width of the band does not change with pressure, within a scatter of 2 or 3 percent. For NaBr there appeared to be a decrease in band width amounting to about 10 percent in 4000 atmospheres. The experiment on NaBr left much to be desired because of a tendency of the sample to become fogged, impairing the optical measurements. In view of behavior of the five other compounds of the same structure and similar properties, the validity of this result for NaBr remains in considerable doubt. CsCl also shows a dependence of width on pressure, but in the opposite direction. The amount of the increase is about 5 percent and appeared in each of two runs on the same sample, despite a 5 percent difference in the zero pressure value of the width of the band between the two runs. The average value of this zero pressure width at room temperature is found to be $\gamma=0.295\pm0.009\times10^4$ cm^{-1}. A value for comparison does not appear to be available in the literature. The validity of this width increase with pressure for CsCl is in doubt, as the argument employed above need not apply to a compound of different structure. Further experiments are required to confirm the result.

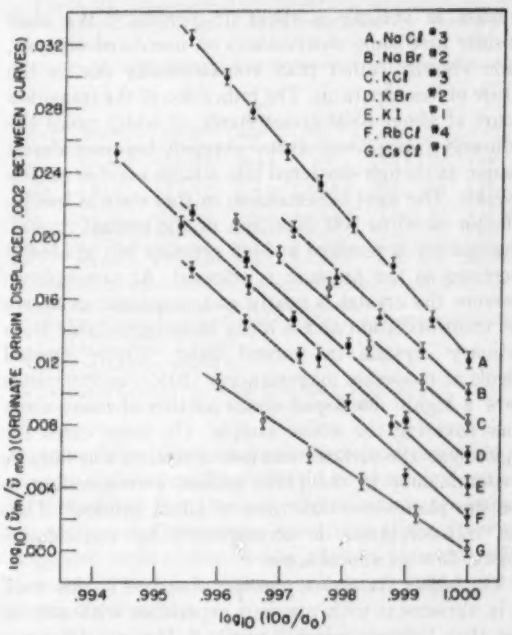

FIG. 3. Experimental curves showing dependence of peak wave number on lattice parameter. The reduced ordinates are referred to their values at atmospheric pressure.

TABLE II. F-band wavelength and shift with pressure.

Crystal	λ_{max}(1 bar) A	$\lambda_{max}(1)-\lambda_{max}(5000)$ A
NaCl	4658±5	143±7
NaBr[a]	5362±6	154±8[c]
KCl	5596±6	167±9
KBr	6277±8	224±11
KI[b]	6916+10	324±14
RbCl	6337±8	217±11
CsCl	6039±7	160±10

[a] See footnote c, Table I.
[b] See footnote d, Table I.
[c] Extrapolated value.

B. Effects of Structure Transformation

Experiments were performed on colored and uncolored crystals of RbCl at pressures in excess of that required to induce the structure transformation mentioned in Sec. I. The equilibrium transition pressure is about 5000 atmospheres and the associated relative

[32] F. Birch *et al.*, *Handbook of Physical Constants* (Geological Society of America, Special Papers, No. 36, 1942), p. 52. See also reference 27.
[33] P. W. Bridgman, Proc. Am. Acad. Arts Sci. **67**, 345 (1932).
[34] J. K. MacKenzie, Proc. Phys. Soc. (London) **B63**, 2 (1950).
[35] Estermann, Leivo, and Stern, Phys. Rev. **75**, 627 (1949).
[36] H. Witt, Nachr. Akad. Wiss. Göttingen, Math-physik Kl. 4, 17 (1952).

decrease in volume is about 15 percent.[23] We shall consider first some observations on uncolored crystals, made visually rather than volumetrically due to the nature of the apparatus. The indication of the transition occurs at about 6500 atmospheres, at which point the ordinarily transparent crystal abruptly becomes almost opaque as though shattered into a large number of tiny crystals. The light transmission in this state is less by a factor of 50 to 100 than that of the normal crystal. The opacity is retained at high pressure but gradually decreases as the pressure is released. At atmospheric pressure the crystal is nearly as transparent as before the transformation and is often indistinguishable from ordinary crystals in normal light. Under crossed Nicols at moderate magnification (20×), such crystals show a highly developed strain pattern of many short lines covering the whole sample. (In some cases the region near the surfaces was free of strain.) The lines lie predominantly in the {110} planes, corresponding to the slip planes and directions of alkali halides.[37] Thus the transformation is accompanied by considerable plastic flow on a local scale.

The higher transition pressure observed in this work is in agreement with previous experience with salts of less than "atomic weight" purity.[24] Thus no difference was noted when the relatively purer RbCl salt was introduced in the present experiment.

The phenomenon of opaque or shattered crystals which regain their transparency is visually similar to that observed by Kraus and Nutting[38] for the low temperature transition in ammonium chrome sulfate and selenate alums.

The crystallographic aspects of this type of structure transformation have been discussed by Buerger.[39] A contraction along a body diagonal of the face-centered cubic cell with an expansion perpendicular to that axis will transform the structure to simple cubic. Since there is no observable macroscopic distortion of the RbCl sample in the high-pressure modification, the transformation must proceed from a large number of nucleation centers, at each of which there is a choice of four possible trigonal axes along which to propagate. Thus there may be some degree of mismatch between adjoining regions characterized by different transformation axes. Associated with this mismatch, or with that between regions which have transformed and those which have not, there should be variations in the index of refraction which give rise to light scattering and to the observation of opacity.

Laue back-reflection x-ray pictures of uncolored RbCl samples which had been through the transformation generally produced patterns of smeared ring segments, if the strain extended throughout the crystal. Annealing at 300°C for one day brought about recrystallization. These results differ somewhat from findings in a recent single-crystal study[40] of the CsCl transformation to the NaCl structure at 469°C.

Observations were made on x-ray colored crystals with the hope, initially, of detecting an F band in the high-pressure form of RbCl. A rough estimate of the expected spectral location of the band can be made by assuming the approximate validity of a Mollwo-like relation for salts of the CsCl structure. The position of the F band at room temperature in CsCl is given in Table II, while the value of λ_{max} for CsBr at room temperature is 6750A, from measurements of Pringsheim.[41] If the peak wavelength is assumed to be proportional to some power of the interionic distance, calculation with these data yields the result that the power is about 2.6. Then, using Bridgman's data for the density of the high-pressure form of RbCl, it is estimated that the F band should be near 5200A.

The features described above for uncolored crystals remain valid for x-ray colored crystals. The optical density of the transformed crystals is about 1.5 to 2.0, which is a very insensitive region for the spectrophotometer. To reduce the light intensity passing through the reference hole, fine mesh screens were used. This reduced the apparent optical density of the crystals, but the measurements obtained were frequently erratic. Frequent development of window cracks around 7000 atmospheres also interfered with the work.

High-pressure absorption measurements taken just after the transformation revealed the F band located in its pretransition position but decreased in height by 40 percent. Returning to one atmosphere, the band retained about 50 percent of its original height. Subsequent experiments of a "before and after" type demonstrated that 85–95 percent of the band could be destroyed by subjecting the colored crystal to the two-way transformation. For these experiments, the crystals were taken to 8000 atmospheres between the two absorption curve measurements.

The explanation of this effect is readily found in the experiments of Smekal[42] and of Schröder,[43] interpreted by Seitz,[44] which show that x-ray darkened crystals are bleached by cold work. As noted above, considerable plastic deformation accompanies the structure transformation. Schröder reduced the F-band height by 20 percent with uniaxial stresses of 40–400 g/mm². A separate experiment in this study confirmed his result by reducing the band height by at least 25 percent after the application of a load of 500 g/mm² on an x-rayed KCl sample in a bath at 0°C. This result makes allow-

[37] E. Schmid and W. Boas, *Plasticity of Crystals* (F. A. Hughes Company, London, 1950), pp. 228, 233.
[38] D. L. Kraus and G. C. Nutting, J. Chem. Phys. **9**, 133 (1941); see also J. Eisenstein, Revs. Modern Phys. **24**, 74 (1952).
[39] M. J. Buerger, "Crystallographic Aspects of Phase Transformations," Chapter in *Phase Transformations in Solids* (John Wiley and Sons, Inc., New York, 1951).
[40] Menary, Ubbelohde, and Woodward, Proc. Roy. Soc. (London) **A208**, 158 (1951).
[41] P. Pringsheim (private communication). The author is indebted to Dr. Pringsheim for providing this information.
[42] A. Smekal, Z. Ver. deut. Ing. **72**, 667 (1928).
[43] H. J. Schröder, Z. Physik **76**, 608 (1932).
[44] F. Seitz, Phys. Rev. **80**, 239 (1950).

ance for the natural thermal bleaching during the period between measurements.

Experiments were also undertaken on additively colored RbCl crystals to study the effect of the structure transformation. For conventional work this type of coloration is relatively stable. In absorption measurements above the transition pressure no new band was observed, but there was evidence of a considerably reduced pretransition F band. "Before and after" experiments on samples colored with excess K metal produced complete destruction of the F band and recrystallization of the sample upon returning to atmospheric pressure. An uncolored but quenched sample did not recrystallize during such an experiment. Its behavior was identical to that of an annealed uncolored specimen.

The effect of plastic flow on additively colored crystals was investigated in an auxiliary experiment. Such work does not appear to have been undertaken in the past. KCl crystals containing excess K metal were subjected to uniaxial loads of from 200 to 500 g/mm², while the samples were kept at 0°C. The decrease in the height of the F band is negligible and there is no detectable growth of subsidiary long-wavelength bands. Compared with the effects in x-ray colored crystals, this result is somewhat surprising. In analyzing this we take note of the suggestion of Tyler,[45] based on the experiments of Gyulai and Boros,[46] that electronic processes may contribute to the enhanced conductivity due to plastic flow.[47] The latter workers, using low stresses of 100 g/mm², observed short decay times (10^{-3} sec) for the enhanced conductivity in alkali halide crystals. The magnitude of the effect was doubled when photochemically or additively colored crystals were studied, but the decay time was unaffected. For the present experiments, the work of Gyulai and Boros implies that the plastic flow causes the evaporation of electrons from the F centers. The conclusion to be drawn from the null effect observed is that the necessary rearrangements of vacancy aggregates to form M or other centers cannot take place in the few seconds during which the dislocations are moving rapidly. Thus the electrons are mostly retrapped in the isolated negative ion vacancies from which they were ejected.

In discussing the effect of plastic flow on x-ray colored crystals, Seitz[44] offered three tentative explanations. Only the first of these is consistent with the observations of Gyulai and Boros and with the null effect of plastic flow on additively colored crystals. This is the suggestion that the region about the vacancies associated with the color centers becomes heated when a dislocation passes very close, and that the electrons and holes evaporate and have an opportunity to recombine. The vacancies involved probably lie close to dislocations,[48] and should be in an ideal position to experience the thermal effects which accompany the motion of dislocations. Variations of the other two suggested explanations would allow a bleaching effect due to cold work in additively colored crystals, contrary to our observations.

[45] W. W. Tyler, Phys. Rev. 86, 801 (1952).
[46] Z. Gyulai and J. Boros, Math. naturw. Anz. ungar. Akad. Wiss. 59, 115 (1940).
[47] See reference 44 for a discussion of the earlier experiments of Gyulai and Hartly on the influence of plastic flow on conductivity.

TABLE III. Experimental and theoretical parameters describing the dependence of the F-band maximum on pressure and temperature.

1 Compound[a]	2 $n_T(P)$	3 $n_P(T)$	4 α_P 10^{-6} deg^{-1}	5 δ/θ (cm deg)$^{-1}$	6 n_Q[b]	7 f[c]	8 n_M[d]	9 f[e]
NaCl	4.4±0.1	4.0±0.2	40±1	~0	1.5	2.9	1.94	2.3
NaCl[f]		4.4±0.2	44±1	~0				
NaBr	3.6±0.2	3.8±0.2	41±1	0.2±0.2	(1.5)	2.4	1.83	2.0
KCl	3.5±0.1	5.0±0.2	35±1	0.9±0.1	1.6	2.1	1.74	2.0
KBr	3.5±0.1	4.5±0.2	41±1	0.7±0.1	(1.6)	2.1	1.66	2.1
KI	3.7±0.1	4.4±0.2	41±1	0.4±0.1	(1.6)	2.3	1.55	2.4
RbCl	3.4±0.1	5.2±0.2	35±1	1.0±0.1	(1.6)	2.1	1.66	2.0
CsCl	2.8±0.2	4.9±0.2[g]	46±1	1.6±0.2	1.76	1.5	2.65[h]	1.0

[a] At room temperature, unless otherwise noted.
[b] Calculated from square well model; values in parentheses estimated.
[c] Using values from column 6.
[d] Derived from plot of $\log_{10}E$ vs a^{-1}.
[e] Using values from column 8.
[f] At 200°C.
[g] Calculated for CsBr; $\lambda_m(-190°C) = 6450$A, reference 41.
[h] Obtained by plotting data from CsCl and CsBr.

IV. THEORY

The theroretical interpretation of the shift of the absorption peak with pressure or temperature must include the effect of the variation of interatomic distance and also the effect of the interaction of the F-center electron with the lattice vibrations. These effects have been considered separately by various investigators, as mentioned in Sec. I, in attempts to account for the temperature shift. There does not appear to have been any attempt to combine both parts into a consistent picture. The reason for this probably lies in the difficulty in making a theoretical estimate of the relative magnitudes of the separate contributions of each effect and in the lack, up to this time, of sufficient experimental data from which to evaluate these relative contributions. The results of the present experiment provide the additional data with which to overcome this obstacle and to make empirical estimates of the magnitudes of the individual effects.

We characterize the results of the pressure experiment in terms of the parameter $n_T(P)$ listed in column 2 of Table III. Along with it we require for comparison the corresponding parameter for the temperature shift, $n_P(T) = -(\partial \ln \tilde{\nu}_m/\partial \ln a)_P$. It is listed in column 3 of the same table and is evaluated for a range around room temperature except as otherwise noted. The data for the dependence of $\tilde{\nu}_m$ on temperature are mainly due to Mollwo,[4] supplemented in various cases by data from

[48] See the recent work of J. J. Markham, Phys. Rev. 88, 500 (1952), and F. Seitz, Phys. Rev. 89, 1299 (1953), for development of the idea that F centers are located near dislocations, as a consequence of their formation at incipient vacancies associated with jogs in Taylor dislocations.

Gnaedinger,[21] Molnar,[20] and Pringsheim.[41] Room temperature thermal expansion data are employed in most cases, because considerable discrepancies often appear in the values from different workers as they depart from room temperature. The values used are listed in column 4. It is seen that for most compounds the "pressure slope," $n_T(P)$, is smaller than the "temperature slope," $n_P(T)$.

We use a high-temperature representation for the F-center energy at the peak of the absorption curve, E, in the form

$$E=E_0[R(a)]-bT/\Theta(a). \tag{1}$$

A suitable modification may be made for the low-temperature region. E_0 is the energy at absolute zero and is a function of the distance parameter, R, which in turn depends on the interionic distance, a, in the bulk crystal. The distance R is the significant parameter in determining the energy E_0, and its interpretation depends on the model employed to calculate the F-center energy levels. In a continuum model R may be the radius of the potential well of the vacancy, or in a molecular orbital model it may be the actual distance of the first neighbor ions from the center of the vacancy after relaxation has taken place. The form of the second term in Eq. (1) has its basis in the work of Huang and Rhys[16] and of Muto.[12] Huang and Rhys assume that the predominant coupling between electron and lattice is produced by the long-range Coulomb interaction between the F-center electron and the electric polarization associated with the single-frequency longitudinal optical vibrations of the lattice. They use this coupling to account for the temperature broadening of the band. They find, however, as has been confirmed in the more general treatments of Lax[17] and of O'Rourke,[18] that this idea does not give rise to any shift of the absorption peak with temperature. To rectify this, they use an idea (previously put forth by Muto) that when an F center changes its state the lattice frequency is altered by a small amount. This small frequency change, proportional to b in Eq. (1), does not appear in the harmonic forces approximation usually used to describe the lattice. Thus the parameter $\Theta(a)$, in our expression for the energy, is the characteristic temperature related to the longitudinal optical vibration frequency of the lattice. This temperature is sufficiently close to the usual Debye temperature that we need not distinguish them.

For the shift of the absorption band peak with pressure we must form the derivative $(\partial \ln E/\partial \ln a)_T$ from Eq. (1). Thus we have:

$$\left(\frac{\partial \ln E}{\partial \ln a}\right)_T = -n_T(P)=\left(\frac{\partial \ln E}{\partial \ln \Theta}\right)_{T,R}\frac{d\ln\Theta}{d\ln a} + \left(\frac{\partial \ln E}{\partial \ln R}\right)_{T,\Theta}\left(\frac{\partial \ln R}{\partial \ln a}\right)_T. \tag{2}$$

From the Grüneisen relation we obtain:

$$d\ln\Theta/d\ln a=-3\gamma_G, \tag{3}$$

where γ_G is the Grüneisen constant. The term $(\partial \ln R/\partial \ln a)_T$, the ratio of the relative change in R to the relative change in a at constant temperature, is equal to the ratio of the effective isothermal compressibility around the F center to the isothermal compressibility of the bulk material. There are several ways of estimating this, but we shall consider it as unknown and designate it by the symbol f_T. The derivative $(\partial \ln E/\partial \ln R)_{T,\Theta}=(d\ln E_0/d\ln R)$ may also be estimated in a number of ways. A particular model may be assumed for the F center, from which the energy levels may be calculated in terms of their dependence on R, and thus the value of the derivative may be calculated. We designate the negative of this derivative by the symbol n_Q. As an alternative the slope of a plot of the experimental values of $\log_{10}E$ *versus* $\log_{10}a$ may be employed, if it is assumed that the factor which relates the equilibrium values of R and a does not vary rapidly from one compound to another. Such a plot should be made using the values of E and a at absolute zero or as an intermediate compromise, using values which correspond to the characteristic temperature, Θ. The negative of the slope of this plot we call n_M, to distinguish it as a different way of estimating n_Q. This matter will be discussed further in the following section.

For the present, we shall use values calculated from an exceedingly simple continuum model, namely that which represents the F center as an electron trapped in a spherically symmetric square potential well. The radius of the well R is chosen equal to the interionic distance a. The depth of the well is chosen so that the energy difference between the ground s state and the excited p state is equal to the observed F-center energy. To evaluate the variation of E_0 with R, it is assumed that the well depth is inversely proportional to its radius R. The results of such a calculation are that the values of n_Q are 1.5, 1.6, and 1.76 for NaCl, KCl, and CsCl, respectively. Thus we obtain for the pressure shift:

$$n_T(P)=3\gamma_G bT/E\Theta+n_Q f_T. \tag{4}$$

The shift of the absorption band peak with temperature is derived in an analogous fashion, by forming $(\partial \ln E/\partial \ln a)_P$. From Eq. (1) we obtain:

$$\left(\frac{\partial \ln E}{\partial \ln a}\right)_P = -n_P(T)=\left(\frac{\partial \ln E}{\partial T}\right)_{\Theta,R}\left(\frac{\partial T}{\partial \ln a}\right)_P + \left(\frac{\partial \ln E}{\partial \ln \Theta}\right)_{T,R}\left(\frac{d\ln\Theta}{d\ln a}+\frac{\partial \ln E}{\partial \ln R}\right)_{T,\Theta}\left(\frac{\partial \ln R}{\partial \ln a}\right)_P. \tag{5}$$

The term $(\partial T/\partial \ln a)_P$ which appears here is the reciprocal of the isobaric linear thermal expansion coefficient, α_P. Similar to its counterpart in the pressure shift, the term $(\partial \ln R/\partial \ln a)_P$ is equal to the ratio of

the effective thermal expansion coefficient around the F center to the bulk value of the thermal expansion coefficient. We designate this factor by the symbol f_P. The expression for the temperature shift is then given by

$$n_P(T)=b/E\Theta\alpha_P+3\gamma_G bT/E\Theta+n_Q f_P. \quad (6)$$

We may consider that the thermal expansion of a solid arises from the effect of an outward thermal pressure set up by the anharmonicity of the vibrations of the atoms of the solid. This thermal pressure acts against the same forces as does the external pressure considered with respect to the compressibility of a solid. Since the thermal expansion is particularly dependent on the nonlinearities in these forces, we may expect that the effective thermal expansion factor, f_P, is at least as large as the effective compressibility factor, f_T, in the neighborhood of the F center. We lack, however, a method of evaluating this difference in detail. Consequently, we may not make too great an error if we assume that the two factors are approximately the same. If we then drop the subscripts from these two factors in Eqs. (4) and (6), we may combine these two expressions to obtain the result:

$$b/E\Theta\alpha_P=n_P(T)-n_T(P). \quad (7)$$

In this way the quantity b/Θ may be calculated from the experimental data on the pressure and temperature shifts of the F-band absorption maximum. These values are listed in column 5 of Table III. Making a substitution back into Eq. (4), the value of the factor f may be obtained. The magnitude of this factor will depend directly on the value used for the term n_Q. Using the calculations from the square well continuum model, the values of f listed in column 7 of Table III are obtained. If values of n_Q obtained from a different method are used, a new set of values for f will result.

In the preceding analysis we have presented a simple approach in which the temperature and pressure dependence of the F-band absorption peak are treated in a unified manner. The conclusion is reached that the shift of band with pressure is due mainly to the dependence of the energy on interatomic distance, with a small contribution, amounting to 5 percent at most, arising from the interaction with optical lattice vibrations. The temperature shift is governed by the same factors as the pressure shift, plus an additional term, as large as 40 percent, arising from a further contribution from this same electron-lattice interaction.

We turn now to a consideration of the width of the F band. This problem is rather unsettled. As pointed out in Sec. I, two explanations have been offered by separate groups of investigators. We have mentioned the long-range electron-optical lattice vibration interaction used by Huang and Rhys. This coupling gives rise to a broadening of the absorption band. Lax and O'Rourke have shown that a simple formula describes this width, in the approximation in which all lattice modes have the same frequency (that of the longitudinal optical vibrations). If we call γ_1 the width at half-maximum due to this mechanism, we have from O'Rourke:[18]

$$\gamma_1=2(2\ln 2)^{\frac{1}{2}}\hbar\omega[S\coth(\hbar\omega/2kT)]^{\frac{1}{2}}, \quad (8)$$

where ω is the frequency just mentioned, S is the net number of vibrational quanta involved at the absorption maximum, and the numerical factor in front converts the root-mean-square value of the distribution to the width at half-maximum, on the assumption that the distribution is approximately Gaussian. The width γ_1 is independent of the parameter b introduced in Eq. (1).

The second contribution to the broadening arises when we consider that the local deformation of the lattice causes variations in the gap between the electronic energy levels. In an adiabatic approximation, we may say that absorption takes place when the wavelength of light coincides with the energy gap determined as a function of the displacement of the surrounding ions. Several versions of this approach have appeared.[9,19,20] Their principal achievement has been the demonstration that the finite width of the F band at low temperatures may be accounted for by the zero-point vibrations of the neighboring ions. The idea which is common to all is that the mean square fluctuation in the F-center energy is determined by the mean square fluctuation in a suitable radius for the vacancy.

A factor which has been overlooked in these versions is the role of shear waves in causing a broadening. When the region of the vacancy is distorted from its spherical shape, it is reasonable to expect a change in the F-center energy, at least through an interaction with the angular momentum of the excited p state. The continuous variation of the nonspherical distortion would then contribute to the band width. Since we lack a detailed calculation of this effect, we may account in a rough way for the two shear modes by multiplying the contribution to the width from the radial distortions by the factor $\sqrt{3}$.

Both explanations of the band width seem to be valid. Consequently, we would like to combine their separate contributions to obtain the total band width. Since they appear to be independent, and assuming, for simplicity, that each gives rise to a Gaussian shape, we must add them as the square root of the sum of the squares of the individual widths.

To be specific, we consider a very simple calculation for the local deformation width. The coupling in this case is to the acoustical modes of the lattice. From the Einstein formula for fluctuations, we may write for the mean square fluctuation in the volume around the F center:

$$\langle(V-V_0)^2\rangle=V_0\chi_{eff}kT, \quad (9)$$

where V_0 is the equilibrium value of this volume, χ_{eff} is the effective compressibility around the F center, and kT is the Boltzmann constant times the absolute

temperature. This expression assumes that the temperature is sufficiently high that equipartition of energy has occurred. This formula gives values differing by only a few percent from a more rigorous formula containing a Debye function and the zero-point energy explicitly. The corresponding fluctuation in the F-center energy is obtained from a Taylor expansion about its mean value. We next consider that the volume is a sphere of radius R, that the effective compressibility χ_{eff} is greater than the bulk compressibility χ_0 by the factor f, that the shear modes are accounted for by the simple factor $\sqrt{3}$, and that the conversion factor from root mean square to width at half-maximum is that for a Gaussian shape. Thus we obtain for γ_2, the deformation width:

$$\gamma_2 = En_Q[(2\ln 2)f\chi_0 kT/\pi R^3]^{\frac{1}{2}}. \quad (10)$$

For KCl at room temperature, using $n_Q = 1.6$, a calculation from Eq. (10) gives $\gamma_2 = 0.20f^{\frac{1}{2}}$ ev.

We are now able to combine γ_1 and γ_2. For KCl under the same conditions, Eq. (8) gives $\gamma_1 = 0.088S^{\frac{1}{2}}$ ev, where S is still undetermined. One possible procedure is to fit these results to the observed total band width, γ, after choosing a suitable value of f, say 2. This produces an estimate of S such that $S = 5.4$. If we had ascribed the full width to the interaction with optical lattice vibrations, with Huang and Rhys, the value of S required would be 16 for KCl. On the other hand, Huang and Rhys estimate from Simpson's wave functions for NaCl that S should be about 4. Thus our simple model for the deformation width, using a value for f consistent with the pressure shift data, enables us to make a reasonable estimate of the parameter S in the Huang-Rhys contribution to the width.

The preceding discussion of the theories of the width of the F band serves principally to illustrate that there is considerable room for a careful theoretical analysis of the problem.

Of particular interest in the present research is the fact that the observed F-band width did not change with pressure for most of the compounds studied. Using the various expressions for the width, either separately or in suitable combination, it may be predicted that the width should increase about 1 or 2 percent in 5000 atmospheres. In view of the uncertainties described in measuring the width, such an increase could not be detected.

V. DISCUSSION

Several points in the preceding section require further consideration. It is not difficult to understand why the term $f_T = (\partial \ln R/\partial \ln a)_T$, in Eq. (2), may be greater than unity.[31] R represents a measure of the radius of a spherical cavity from which matter has been removed, i.e., a halogen ion, while a is the normal interionic distance in the crystal at a great distance from the cavity. The ion which previously occupied this region exerted a repulsive force on the surrounding material. The electron which replaces the negative ion does not exert this repulsion in a first approximation. Thus when the crystal is subjected to an external pressure, it is natural to expect that the cavity will contract more when it is empty than when it is occupied by matter. This line of reasoning suggests that it may be fruitful to consider the crystal as a continuous elastic medium. From this point of view the problem at hand reduces to the simple calculation of the radial strain in a shell bounded by concentric spherical surfaces. The solution of this problem provides an independent estimate of $f_T \approx f$. The details may be obtained from any standard textbook on elasticity, e.g., Love.[49] The radius of the internal sphere is R and the internal pressure is taken to be zero. We let the radius of the external sphere become infinite and equate the pressure on its surface to the pressure applied externally to the crystal. Thus we obtain:

$$(\Delta R/R)/(\Delta a/a) = (\partial \ln R/\partial \ln a)_T = 1 + (3K/4\mu), \quad (11)$$

where the crystal is treated as an isotropic body describable by two elastic constants: K, the bulk modulus, and μ, the shear modulus. The ratio (K/μ) may be calculated from the experimental data,[32] using an average of the two shear moduli c_{44} and $\frac{1}{2}(c_{11}-c_{12})$ for μ. An alternate way to obtain this ratio is to assume that Poisson's ratio is $\frac{1}{4}$ for these crystals, from which we can readily find $(K/\mu) = (5/3)$. In this approximation the result is $f = 2.25$, while the values obtained from the experimental data range from about 2.13 to 2.25. The results of this independent estimate of f are in approximate agreement with those obtained from the pressure-temperature shift theory in the preceding section.

From another point of view we may expect that f should be smaller for CsCl since it has a more closely packed structure than the other compounds. The ions may be treated as hard spheres and the distance that the nearest neighbors can move toward the center of the vacancy without coming into contact may be calculated for the two structures involved. Thus for Cs and Cl ions it is found that they may move nearly twice as far when arrayed in the NaCl structure as when in the CsCl structure. This is a very crude approach, but it does serve to indicate why the f values for CsCl may be lower, as found in Table III.

We now consider in further detail the various ways of estimating the quantity n_Q which appears throughout the theory of the pressure and temperature shift. It was emphasized earlier that the values calculated for f from the theory depend on the values used for this quantity. If some model for the F center is assumed for which the energy levels can be calculated, then n_Q may be computed readily. The various continuum models that have been used lend themselves to an easy calculation of this term. Before adopting the square well model described in the preceding section, calcula-

[49] A. E. H. Love, *The Mathematical Theory of Elasticity* (Cambridge University Press, Cambridge, 1927), p. 142.

tions were made with Simpson's[8] model using the revised potential well depth suggested by Krumhansl and Schwartz,[11] and with Pincherle's[10] model which simplifies the calculations of the Simpson model. In the Pincherle calculation the potential well has a flat bottom out to a radius R and has a simple or slightly modified Coulomb dependence at large distance. In our calculation with this model the well depth was chosen so as to reproduce the experimentally observed energy difference between the two states, as was done in the square well model. In obtaining n_Q, the well depth was assumed to vary inversely with the radius R, again as in the square well model. This assumption is certainly a reasonable one, for the principal contribution to the depth is the Madelung energy which is controlled mainly by the distance to the nearest neighbors, and the secondary contribution is the energy of polarization of the surroundings, which is inversely proportional to the well radius. The result of this calculation for NaCl is $n_Q=1.53$ when the static and high-frequency dielectric constants are held fixed, and 1.50 when they are allowed to vary with pressure. An earlier calculation with Simpson's model with more restricted conditions gave a result of about 1.3. The similarity of these results led to the adoption of the square well model which is the easiest to handle numerically. For the present experiment, involving a relatively large scale effect, it is felt that the continuum represents a suitable approximation with which to treat the problem.

Recent evidence, noted in Sec. I, has pointed to the importance of the molecular orbital model of the F center. This model has found its greatest success in explaining hyperfine interactions in electron spin resonance experiments. The only quantitative calculation[9] of F-center energy levels with this model is not presented in a way which may be readily adapted to the type of calculation just described. It will be seen below, however, that certain conclusions may be drawn from that work.

The alternative to calculating n_Q from a specific model is to obtain it from a plot of experimental data, as mentioned in Sec. IV. We then replace n_Q by n_M in Eqs. (4) and (6). Assuming that a straight line may be drawn through the points on a $\log_{10}E$ *versus* $\log_{10}a$ plot, we might be tempted to adopt Ivey's value for its slope, namely $n_M=1.84$. If the data is plotted corresponding to the Debye temperature for each compound, we find that a better straight line may be drawn for which $n_M=1.6$. Actually, the notion of a straight line on such a plot is more fiction than fact. Plotting the data for the chloride, bromide, and iodide of sodium, potassium, and rubidium, with $\log_{10}E$ and $\log_{10}a$ as ordinates, we find that curves (not straight lines!) having approximately the same shapes may be drawn through the points with a common cation. Without knowing the exact shape of these curves, defined by only three points, some sort of compromise must be adopted to estimate the values of n_M, which change from compound to compound. It would be desirable to find a suitable choice of ordinates on which a straight line could be drawn with some reliability. In attempting to do this, it was found that a plot of $\log_{10}E$ *versus* a^{-1} produces a line which is at least as good as the $\log_{10}E$ *versus* $\log_{10}a$ "straight line." Evaluating the n_M parameters from this plot gives a variation from compound to compound in the same direction as found with the curves above. Considering all these alternatives, it is important to note that they do not differ significantly from one another in the results that they give. Also, these results are not particularly different from those found with the various models. To show approximately how these alternatives vary, we have tabulated values of n_M and f in columns 8 and 9 of Table III as obtained from the plot of $\log_{10}E$ *versus* a^{-1}.

An additional observation may be made in connection with the graphical way of estimating $n_M \approx n_Q$. We may plot the results of the molecular orbital calculation of Inui and Uemura on a $\log_{10}E$ *versus* $\log_{10}a$ graph. Using their model IV with a potential due to 26 neighboring ions, the data for LiCl, LiBr, and LiI fall on a rather good straight line with $n_M=1.43$. This bit of evidence, in general agreement with what has gone before, may be taken as support for our contention that no startling deviation is to be expected from the molecular orbital model, and that the continuum model is a useful approximation for this experiment.

By introducing the factor f, and making use of the lattice interaction constant b, we are able to develop a reasonably consistent account of the behavior of F-center absorption as a function of pressure and temperature. The factor f, as derived in the theory, is in satisfactory agreement with an estimate of its value from elasticity theory. Also, it is used in a simple theory of the band width, which combines the two proposed mechanisms of broadening, in such a way as to give a reasonable value for the number of vibrational quanta involved in broadening by interaction with optical lattice vibrations. The coupling constant b/Θ does not vary too greatly, if we exclude the sodium salts and CsCl. As used by Huang and Rhys and others, it would appear that negative values for b/Θ are inadmissible theoretically. Also, since the errors almost overlap in the case of NaCl, there is no strong experimental evidence that these values are negative. Thus, we say $b/\Theta \sim 0$ for NaCl, when small negative values would result from the calculation. Perhaps some experimental uncertainty, unknown to us, may account for the discrepancy. Another possibility is that the theory has not included some term which, although it may be small, may be sufficient to account for the different behavior of NaCl and NaBr in contrast to the other compounds. The term in b appears to be the only satisfactory suggestion, thus far offered, which is capable of treating the difference in the pressure and temperature shifts. In the Huang and Rhys approxima-

tion this term involves only the optical lattice vibrations. It is possible that future investigation will reveal that a similar contribution involving the acoustical lattice vibrations must be taken into account. In any case, however, such a term would not affect the qualitative conclusions which are made above, but would affect their quantitative interpretation.

VI. ACKNOWLEDGMENTS

The author wishes to express his gratitude to his sponsor, Professor A. W. Lawson, for his advice and encouragement throughout the course of this investigation. Much appreciation is expressed to the members of the Institute for the Study of Metals for many suggestions and discussions, and to the members of the Laboratory of Molecular Structure and Spectra for their cooperation and for making available their experimental facilities. Acknowledgment is also made to Mr. N. D. Nachtrieb and Mr. K. Lindholm for assistance in the design, construction, and maintenance of the high-pressure apparatus. The author is indebted to the Shell Oil Company for the grant of a fellowship during this work. The experiment was supported in part by the U. S. Office of Naval Research.

PHYSICAL REVIEW VOLUME 93, NUMBER 5 MARCH 1, 1954

The Superconductivity of Some Transition Metal Compounds*

GEORGE F. HARDY† AND JOHN K. HULM
Institute for the Study of Metals, University of Chicago, Chicago, Illinois

(Received November 23, 1953)

About eighty transition metal compounds comprising borides, carbides, nitrides, oxides, silicides, and germanides of metals of Groups 4A, 5A, and 6A were tested for superconductivity down to 1.20°K, using a magnetic method. Among the specimens were most of the known compounds of the above type not examined magnetically for superconducting behavior by previous workers, and in all cases the structures were checked by x-ray diffraction analysis. The following eleven new superconductors were discovered, with the transition temperatures (°K) shown in parentheses: W_2B (3.10°), Nb_2C (9.18°), Ta_2C (3.26°), Nb_4N_3 (7.2°), V_3Si (17.1°), V_3Ge (6.01°), Mo_3Si (1.30°), Mo_3Ge (1.43°), α-$ThSi_2$ (3.16°), β-$ThSi_2$ (2.41°), and W_3Si_2 (2.84°). These compounds include the first superconducting germanides, V_3Ge and Mo_3Ge, which, together with V_3Si and Mo_3Si, crystallize in the cubic β-tungsten structure. The transition temperature of V_3Si is apparently the highest known for any binary superconducting compound.

I. INTRODUCTION

IT is well known that there exists a group of compounds of transition metals with nonmetals, typified by the borides, carbides, and nitrides of "A group" transition metals, which possess most of the properties of metals or alloys. These compounds show metallic luster and have thermal and electrical resistivities of the same order of magnitude as those for pure metals, together with a positive temperature coefficient of electrical resistivity. In many cases they are known to have high hardness values, high moduli of elasticity, high melting points, and relatively high strengths at elevated temperatures, properties which cause them to be of considerable technological importance.[1] At the time of the first extensive crystal structure determinations for these substances, carried out by Hägg,[2] it seemed appropriate to call them "interstitial" compounds, implying that the nonmetal atoms merely fit into interstices in the metallic lattice, thereby slightly modifying the properties of the pure metal. More recent investigations have shown that for borides the interstitial picture is inadequate owing to the tendency of the boron to form chains, nets, and three-dimensional networks,[3] while even for carbides and nitrides it is the exception rather than the rule for the lattice of metal atoms in the compound to be identical with the lattice of the pure metal.[4]

Among the typically metallic properties of transition metal compounds one may include the fact that many become superconducting at temperatures of a few degrees absolute. This behavior was first discovered during the extensive investigations of Meissner and his co-workers over twenty years ago.[5–7] Unfortunately, Meissner's results were obtained using electrical resistance measurements, which have since been shown to yield unreliable results with impure specimens. The

* Based on a dissertation submitted by G. F. Hardy in partial fulfillment of the requirements for the degree of Doctor of Philosophy at the University of Chicago.

† Now at the Research and Development Laboratories, The Barrett Division, Allied Chemical and Dye Corporation, Glenolden, Pennsylvania.

[1] The term "hard metals" is often applied to this whole group of materials. See P. Schwarzkopf and R. Kieffer, *Refractory Hard Metals* (Macmillan Company, New York, 1953).

[2] G. Hägg, Z. physik. Chem. **B6**, 221 (1930); **B12**, 33 (1931).

[3] R. Kiessling, Acta Chem. Scand. **1**, 893 (1947); **3**, 90 and 595 (1949); **4**, 146 and 209 (1950).

[4] R. E. Rundle, Acta Cryst. **1**, 180 (1948).

[5] W. Meissner and H. Franz, Z. Physik **65**, 30 (1930).

[6] Meissner, Franz, and Westerhoff, Ann. Physik **13**, 505 (1932); **17**, 593 (1933).

[7] Meissner, Franz, and Westerhoff, Z. Physik **75**, 521 (1932).

problem has recently been taken up by several other investigators[8–10] using more decisive magnetic methods; these experiments have revealed a number of new superconducting compounds, and have corrected several errors in the earlier work.

In spite of the increased interest in this field, the results reported to date have been confined mainly to the borides, carbides, and nitrides of the "A group" transition metals and even here have not covered all of the known compounds. Since these data are important for the light which they may throw on the fundamental chemical and crystallographical conditions favoring the occurrence of superconductivity, we have felt that it would be of value to complete and extend them as far as possible. Using a magnetic method for the detection of superconductivity, we have studied a number of borides, carbides, nitrides, and oxides which have not previously been tested for superconducting behavior, and have reinvestigated several compounds of this type already tested by previous workers. We have also systematically surveyed the occurrence of superconductivity among the silicides and germanides of the "A group" transition metals, since these compounds have been largely neglected in previous superconducting work, although they have received much study from the metallurgical standpoint. While many of our data on the latter compounds have already been briefly reported,[11] the present paper describes the experimental techniques used and the detailed structural and superconducting results so far obtained.

II. EXPERIMENTAL DETAILS

A. Method

Superconductivity is most simply detected by measuring either the electrical resistance or the magnetic permeability of a given specimen. The ideal specimen for both these tests is a long solid rod of pure, homogeneous, strain-free material; for such a specimen the electrical resistivity and magnetic permeability in a small field may both be expected to drop to zero rather sharply as the temperature is lowered through the superconducting transition point.[12] Unfortunately, since most of the compounds with which the present work is concerned exhibit such properties as high melting points, brittleness, and ease of contamination, the fabrication of an ideal specimen of the above type is, with present techniques, a very tedious and difficult task. Thus, in preliminary experiments it is necessary to work with more readily prepared specimens, which, for the refractory compounds, include arc-melted pellets, porous sintered rods, or even fine powders. For these specimens the onset of superconductivity is often smeared out over a range of temperature, but a large drop in resistance or permeability usually gives unmistakable evidence of superconducting behavior.

Some caution is necessary in interpreting the results on inhomogeneous specimens, for the following reasons. It is not infrequent for such specimens, even when carefully prepared, to contain small amounts of superconducting impurities, often as one or more separate phases. Small quantities of the latter will sometimes form a continuous path through the specimen, for example at the grain boundaries, and cause the apparent resistance of the entire specimen to disappear at the transition point of the impurity.[12] Alternatively, the impurity may be deposited in a thin skin around the individual grains or particles of the specimen; if the thickness of this skin exceeds the penetration depth ($\sim 10^{-5}$ cm), the onset of superconductivity in the impurity is accompanied by the exclusion of magnetic flux from the grain or particle as a whole, so that the impurity produces a much greater magnetic effect than one might expect from its actual volume. Thus, in both electrical and magnetic tests for superconductivity it is essential to take account of impurities, even trace amounts, in the specimens. Failure to observe this point in early work led to a number of ambiguities, some of which crop up in the present investigation. However, the difficulties resulted mainly from resistance tests, which are apparently more sensitive to impurities than magnetic tests, presumably because continuous filaments are formed more readily than closed skins. For this reason, and also because of the unsuitability of the resistance method for powdered samples, the magnetic method is preferred in the present work.

B. Apparatus

The magnetic test arrangement used in earlier work[9] was supplemented by a new gas thermometer cryostat in which specimens could be studied not only in the liquid hydrogen and liquid helium ranges, but also at accurately known temperatures in the intervening region. The essential low-temperature parts of this apparatus are shown in cross section in Fig. 1. For simplicity, the surrounding liquid nitrogen Dewar flask and the head of the cryostat with its associated electrical connections and pumping lines are omitted from the diagram.

The six specimens which could be tested during a single experiment were mounted in radial positions just inside the rim of a hollow copper spool, which also served as a gas thermometer bulb *D*. The top and bottom plates of the spool were slotted radially to minimize magnetic disturbance due to eddy currents.

[8] F. H. Horn and W. T. Ziegler, J. Am. Chem. Soc. **69**, 2762 (1947).
[9] B. T. Matthias and J. K. Hulm, Phys. Rev. **87**, 799 (1952).
[10] W. T. Ziegler and R. A. Young, Phys. Rev. **90**, 115 (1953).
[11] G. Hardy and J. K. Hulm, Phys. Rev. **89**, 884 (1953).
[12] See D. Shoenberg, *Superconductivity* (Cambridge University Press, Cambridge, 1952), second edition.
[12] D. Shoenberg, Nature **159**, 303 (1947).

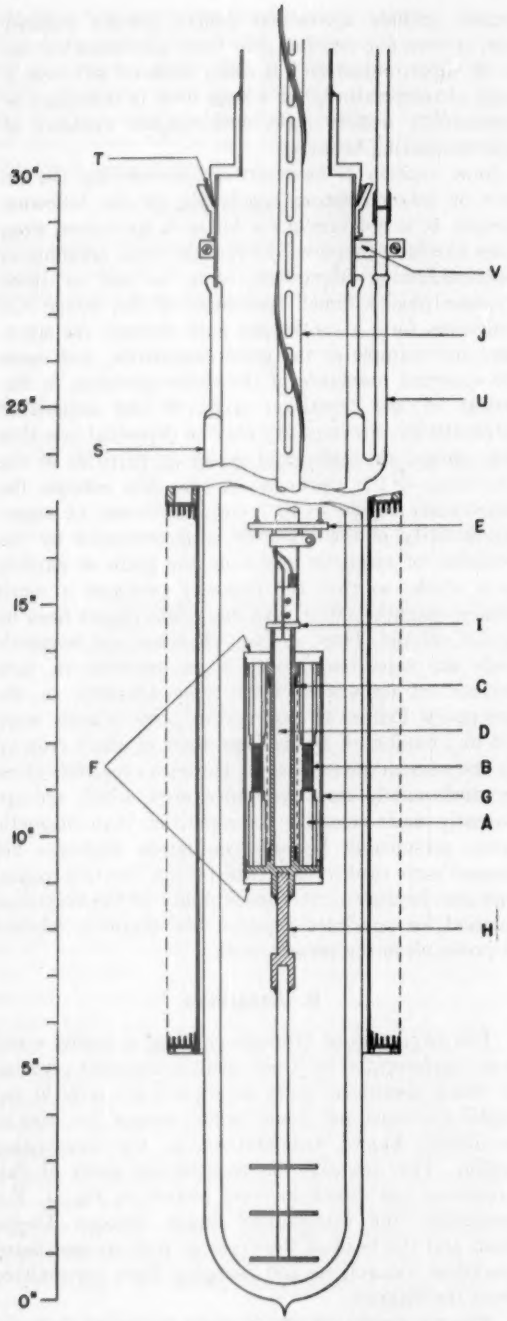

FIG. 1. Gas thermometer cryostat (lower half), liquid nitrogen Dewar flask removed.

Fragmented or powdered specimens and sintered rods were contained in Lucite tubes *A*, each having a thin-walled section upon which a detector coil *B*, consisting of about 250 turns of 40-gauge Formex insulated copper wire, was tightly wound. Melted pellets were held in position in the spool by micarta supports and had detector coils wound directly upon them. Leads from the six coils passed out of the cryostat via the terminals *E* and were connected through a selector switch to an almost critically damped ballistic galvanometer. Uniform magnetic fields up to about 700 oersteds could be applied to the specimens by a liquid-nitrogen-cooled solenoid which was suspended outside the liquid helium Dewar flask *S* but inside the liquid nitrogen flask. The Pyrex helium Dewar was itself attached to the cryostat head by a copper-to-glass seal and an easily disconnected Rose's metal joint *T*, while the interspace could be evacuated through the tube *U* and an external needle valve.

C. Temperature Measurement

For measurements below 4.2°K, the specimen holder was completely submerged in liquid helium; temperatures down to just below 1.2°K could be attained by suitably varying the pumping rate on the liquid helium bath. In this range the specimen temperatures were obtained by measuring the vapor pressure of the bath, using for conversion the 1949 International Scale.[14] A similar procedure was used in the liquid hydrogen range.

For measurements between 4.2°K and 13.9°K the triple point of liquid hydrogen, the helium bath level was allowed to fall below the specimen holder. The temperature of the specimen holder was then raised above that of the bath by means of a heater coil *C* of 30-gauge manganin wire wound noninductively upon the outside of the gas thermometer bulb. Heat from this coil flowed down a brass rod *H* and was dissipated in the helium bath via a copper fin system which extended to the bottom of the Dewar. Owing to the high thermal conductivity of copper relative to that of brass, almost the entire temperature drop occurred in the brass rod and the gradient in the specimen holder was negligible. In addition, the slotted support tube *J* of Supernickel ensured that the heat input from the cryostat head was negligible compared to that generated in the heater coil, while a thin brass envelope *G* and Lucite end plates *F* prevented convection in the helium vapor from disturbing the temperature equilibrium of the specimens.

Specimen temperatures above 4.2°K were measured with the constant volume helium gas thermometer (bulb *D*) which had previously been calibrated when immersed in liquid helium. After corrections for dead-space volume, gas imperfections, and thermomolecular pressure gradient in the capillary tube, specimen temperatures between 4.2° and 13.9°K were known to better than 0.01°K. This accuracy was checked in two ways, first by using the gas thermometer to investigate certain superconducting transition curves which lay

[14] H. Van Dijk and D. Shoenberg, Nature **164**, 151 (1949).

above 13.9°K and which had previously been studied by immersing the specimens directly in liquid hydrogen, and second by comparing our results for a single crystal of lead with those of previous workers.[15] In both cases the specimen temperatures agreed to within one hundredth of a degree, while temperature inequalities within the specimens could be presumed to be even smaller than this value.

D. Magnetic Measurements

Prior to each experiment the magnetic system was calibrated at room temperature by observing the galvanometer throw from each detector coil due to switching off an accurately known solenoid field of a few oersteds. This procedure was carried out first with the coils empty and second with the specimens in place, in order to show up ferromagnetic or other anomalous magnetic properties. In most cases, however, there was no noticeable difference between the "full" and "empty" readings, indicating a specimen permeability close to unity. Morever, the galvanometer throw was quite accurately proportional to the applied field for fields up to a few hundred oersteds.

On cooling to liquid hydrogen or liquid helium temperatures, there was always a small, reproducible increase in deflection per unit change of field, presumably due to small changes in the detector coil dimensions and circuit resistance. When the specimen became superconducting, however, a large decrease in deflection was observed such as shown in Fig. 2. In this diagram the effective permeability μ is the ratio of the actual deflection due to switching off a given field H' to the deflection obtained in the normal region by switching off the same field. Initial tests showed that the deflection given by each coil was unaffected by the presence of superconductors in any of the five remaining coils within the specimen holder.

The onset of superconductivity usually took place over an appreciable range of temperature, as shown in Fig. 2; such transition broadening is thought to be mainly due to inhomogeneities in composition and strain which produce variations of transition temperature from one region of the specimen to another. Thus, as will be seen later, very wide transitions, spread over a degree or more, were observed for certain carbides and nitrides in which quite large variations of carbon and nitrogen content are known to be possible. On the other hand, much sharper transitions were found for most of the silicides and germanides in which far smaller deviations from stoichiometric composition are permitted. Assuming that the variations of composition throughout a specimen are mainly random deviations from an ideal, stoichiometric formula, it seems reasonable to obtain the transition temperature from the mid-point of the transition curve, corresponding to an

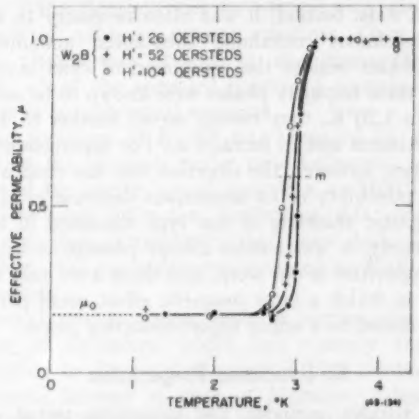

FIG. 2. Temperature variation of effective permeability at various values of measuring field H' arc-melted W_2B specimen.

effective permeability $(\mu_0+1)/2$, where $\mu \to \mu_0$ as $T \to 0$. Most of our data were treated in this fashion, but in a few cases, for example certain nitrides, where most of the spreading was attributable to a specific dissolved impurity which displaced T_c in one direction, the transition temperature was estimated from the point of onset of superconductivity in the purest sample.

A slight broadening of the transition occurs for purely geometrical reasons when the specimen does not have the ideal long, cylindrical shape. Thus, for an ellipsoid of demagnetizing coefficient $4\pi n$ in a measuring field H' small compared to the critical field at absolute zero H_{c0}, it may be shown that the mid-point of the transition T_m and its total breadth ΔT are given by

$$T_m/T_c = 1-\tfrac{1}{4}[(2-n)/(1-n)][H'/H_{c0}] \quad (1)$$

and

$$\Delta T/T_c = \tfrac{1}{2}[n/(1-n)][H'/H_{c0}], \quad (2)$$

respectively. The first equation indicates that T_m always depends upon H', even for an ideal, cylindrical specimen with zero n; a linear dependence of this type was in fact observed for all our specimens (e.g., Fig. 2), and each transition temperature was determined from the value of T_m obtained at several different field strengths by extrapolating to zero field. Since our estimated n values rarely exceeded one-third (the value for a sphere) and H'/H_{c0} could usually be assumed to be less than 0.1, the geometrical transition width was less than $T_c/40$ which was in most cases negligible compared to the broadening due to inhomogeneity. Owing to the nonideal nature of the specimens, no accurate values of H_{c0} were obtained in the present work.

The effective permeability of our specimens in the limit $T \to 0$, μ_0, was never actually zero, for several reasons. First, there was flux leakage between the windings of the detector coil and the specimen and also through the specimen itself in the case of powders or

[15] J. G. Daunt and K. Mendelssohn, Proc. Roy. Soc. (London) **A160**, 127 (1937).

sintered rods. Second, it was often necessary to work with specimens containing substantial amounts of other phases besides the compound of chief interest. Where these impurity phases were known to be normal down to 1.20°K, they merely served further to dilute the specimens and to increase μ_0. For superconducting impurities, however, the situation was less clear owing to the possibility of an anomalous decrease in μ_0 due to magnetic shielding of the type discussed in II A. Fortunately, it was almost always possible to exclude such impurities in our work, and there were only three cases[16] in which a large magnetic effect could perhaps be attributed to a minor superconducting phase.

E. Specimen Preparation

The borides, carbides, and monoxides tested were, in most cases, prepared by the fusion of compressed pellets consisting of appropriate mixtures of the pure powdered metals with boron, carbon, or higher metallic oxide powders in an arc-melting furnace. Melting was carried out in an atmosphere of specially purified argon. The pellets were melted repeatedly, using a tungsten electrode, in a water-cooled copper crucible; spectrographic analyses of representative specimens showed that the copper and tungsten pickup of the arc-melts was considerably less than 0.1 percent in all cases. When phases that formed only at very high temperatures were not under investigation, the specimens were then annealed at about 1500°C for between 20 and 50 hours in an atmosphere of purified helium.

Most of the silicides were prepared by heating compressed pellets of the powdered metals and silicon for several hours at about 1500°C in a furnace heated by "Globar" resistance elements. The pellets were supported by "Alundum" boats placed in the center of the "Sillimanite" furnace tube in which a slight overpressure of pure helium was maintained during heating. Many duplicate silicide specimens were prepared by arc-melting, and gave in most cases superconducting results practically identical with those obtained for sintered specimens of the same composition.

Germanide specimens were also prepared by the sintering technique, compressed pellets of germanium and metal powders being heated at about 1000°C in pure helium gas. Arc-melting preparations were tried for many of these compounds, but were usually unsuccessful due to extensive volatilization of germanium. In particular, we were unable to obtain suitable specimens of the lower niobium and tantalum germanides for this reason; these specimens could not be prepared by sintering even after very extended periods, since the inertness of the metals caused spongy, extremely inhomogeneous specimens to be produced.

Nitride preparations were usually carried out in a second "Globar" furnace in which metal powders could be heated to about 1450°C in carefully purified nitrogen. In one case, vanadium nitride, the compound was obtained by decomposing ammonium metavanadate in a stream of dry ammonia.

The composition of all specimens was checked by by x-ray powder diffraction analysis, and lattice parameter determinations were carried out wherever feasible. The results were for the most part in good agreement with those of earlier workers[17] and need not be discussed in great detail. Our structural data will be mentioned explicitly only in cases of appreciable deviation from earlier work or where new phases were observed. When the exact composition or the very existence of a phase is in doubt, the formula appears in quotation marks.

Spectrographic analyses showed that most of the specimens contained less than 0.1 percent of dissolved metallic impurities, and here again the exceptions are discussed later. Finally, vacuum fusion analyses were performed in an iron bath at about 2100°C for most of the nitrides and proved essential in relating the oxygen and nitrogen contents of these specimens to their superconducting behavior.

III. RESULTS AND DISCUSSION

A. Borides

Of eighteen transition metal borides tested magnetically by Matthias and Hulm,[9] only two, NbB and Mo_2B, were superconducting above 1.28°K. Ziegler and Young[10] reported normal behavior in seven borides down to 1.8°K. Among the remaining borides we have tested the nine compounds TiB, "ThB," "V_2B" (two forms), VB, Ta_2B, Cr_2B, W_2B, and Ru_2B down to a temperature slightly below 1.20°K. The results for these compounds are summarized in Table I (super-

TABLE I. Superconducting nitrides, carbides, and borides of the Groups 4, 5, and 6 transition metals.

TiN	(5.6°)[a]	VN	(8.2°)[a]	None reported for chromium	
ZrN	(8.9°)[a]	Nb_4N_3	(7.2°)[a]	Mo_2N	(5.0°)[d]
["ZrB"	(3.3°)][b]	NbN	(14.7°)[c]	MoN	(12.0°)[d]
		Nb_2C	(9.18°)[a]	Mo_2C	(2.78°)[d]
None reported for		NbC	(6.0°)[a]	MoC	(9.26°)[d]
hafnium or the		NbB	(8.25°)[d]	Mo_2B	(4.74°)[d]
lanthanide and		Ta_2C	(3.26°)[a]	W_2C	(2.74°)[d]
actinide series of metals		[Ta_2B	(3.12°)][a,e]	W_2B	(3.10°)[a]

[a] Transition temperature from present work, magnetic data.
[b] Transition temperature from reference 7, electrical data only.
[c] Transition temperature from reference 8, magnetic data.
[d] Transition temperature from reference 9, magnetic data.
[e] Superconductivity doubtful owing to free tantalum (see text).

[16] Ta_2B, "Nb_2Ge," and "Ta_2Ge" specimens all contained traces of free metal (see later discussion).

[17] The literature on the crystal structure and phase diagram constitution of the transition metal borides, carbides, nitrides, and silicides is very extensive, but, fortunately a comprehensive survey of this field has recently been published (reference 1). The present paper does not, therefore, include an exhaustive list of all the references consulted in connection with our chemical and structural studies, and specific mention is made only of very recent publications or those articles having close bearing on the superconductive investigation.

TABLE II. Nonsuperconducting borides, carbides, nitrides, and oxides of the Groups 4, 5, and 6 transition metals.

TiB[a]	"V_2B" (2)[a]	Cr_2B[a]
TiB_2[b,e]	VB[a]	CrB[b]
TiC[a,e,d]	V_2C[a]	CrB_2[b]
TiO[a]	VC[a,e,d]	Cr_4C[a]
	"V_3N_2"[a]	Cr_7C_3[a]
	VO[a]	Cr_3C_2[a,b]
		CrN[b]
ZrB_2[c]	Nb_3B_4[b]	
ZrC[a,e,d]	NbB_2[b,e]	MoB (2)[b,e]
	Nb_2N[a]	Mo_2B_5[b]
	NbO[a,d]	
HfB[d]		WB[b,e]
HfC[d]	TaB[b]	W_2B_5[b]
	Ta_3B_4[b]	WC[b,e]
"ThB"[a]	TaB_2[b,e]	W_2N[b]
ThB_2[c]	TaC[a,e]	
ThC[a]	Ta_2N[a,e]	UC[a]
Th_3N_4[a]	TaN[a,e]	UN[a]

[a] Tested magnetically down to 1.20°K, present work.
[b] Tested magnetically down to 1.28°K, reference 9.
[c] Tested magnetically down to 1.8°K, reference 10.
[d] Tested electrically down to about 1.2°K, references 5–7.
[e] Tested magnetically down to 1.88°K, reference 8.

conducting) and Table II (normal), together with our data for carbides, nitrides, and oxides of the transition metals discussed in later sections. These tables also show the borides, carbides, and nitrides tested by earlier workers, classified according to the best available evidence.

Of the compounds tested by us, only Ta_2B and W_2B showed superconducting behavior, the latter exhibiting a fairly sharp transition (Fig. 2) centered on 3.10°K. Unfortunately, in common with previous investigators,[3,18] we were unable to prepare a specimen of Ta_2B which did not contain substantial amounts (about 30 percent of each) of free tantalum and TaB, even though a number of different annealing procedures were tried. These specimens all showed superconductivity at about 3.12°K. In spite of the very high flux expulsion from the detector coil (about 80 percent), it was felt, for the reasons discussed in Sec. II, that the magnetic effect could be due to the free tantalum in the specimens. This view was supported by the data for an arc-melted specimen of tantalum saturated with boron, which had a transition temperature of 3.32°K. Thus, although Ta_2B itself may become superconducting close to 3°K, this result is not definitely established.

The normal compounds include the recently reported phase VB;[19] and two new phases which were observed in several specimens of the over-all composition V_2B prepared by arc-melting, followed by prolonged annealing, in some cases, at temperatures of 1500° and 1700°C. These specimens were shown by x-ray diffraction analysis to contain two new compounds of unknown crystal structure. Only one of these phases was present in the unannealed arc-melts; all of the annealed specimens contained both phases in roughly equal amounts.

The specimen of Ru_2B[20] was prepared by melting together the elements under pure helium at 1450°C, followed by twelve hours' annealing at 1100°C. The complex x-ray diffraction pattern of this compound has not been interpreted; the x-ray data showed, however, that our specimen contained no RuB or free ruthenium.

Several attempts were made to prepare the monoboride of zirconium, which has recently been investigated by Post and Glaser.[21–23] This compound is of special interest in view of Meissner, Franz, and Westerhoff's earlier result[7] that the electrical resistance of "ZrB" drops to zero between 3.8° and 2.8°K. Since "ZrB" is reported as forming only between 1000° and 1200°C, our preparations were carried out in a vacuum induction furnace or in the annealing furnace. All of the resulting specimens proved to contain only Zr, ZrB_2, and traces of ZrO_2, so that the superconductivity of zirconium monoboride could not be checked.

Magnetic data are now available for four hemiborides which crystallize in the tetragonal $CuAl_2$[D_{4h}^{18}] type of lattice, namely, Mo_2B and W_2B (superconducting), Ta_2B (doubtful), and Cr_2B (normal to 1.2°K). Including, as it does, two of the three known superconducting borides, this lattice evidently favors superconductivity, perhaps because the individual boron atoms are isolated. One might expect the higher borides to be somewhat less "metallic" in character owing to the progressive increase in the number of covalent linkages between boron atoms with increasing boron content,[24] although it must be admitted that this change does not seem to be accompanied by a systematic increase in electrical resistivity.[1,22] Another interesting feature is that the known superconducting borides are clustered in a single region of the periodic system in which two of the parent metals, molybdenum and tungsten, remain normal down to very low temperatures. This situation will shortly be seen to be repeated, with some variations, in several other classes of compounds.

B. Carbides

Meissner and his co-workers[5,7] observed that the electrical resistance of monocarbide specimens of ZrC, NbC, TaC, MoC, and WC dropped steeply, in some cases to zero, in the temperature intervals 4.07°–3.35°, 10.5°–10.1°, 9.5°–9.3°, 7.8°–7.6°, and 4.2°–2.5°K, respectively. However, in magnetic measurements

[18] Brewer, Sawyer, Templeton, and Dauben, J. Am. Ceram. Soc. 34, 173 (1951).
[19] H. Blumenthal, J. Am. Chem. Soc. 74, 2942 (1952), reported VB as isomorphous with CrB (Orthorhombic D_{2h}^{17}), lattice parameters 3.10, 8.17, and 2.98A. We had independently reached the same conclusion and found the lattice parameters 3.058, 8.026, and 2.971A.
[20] J. H. Buddery and A. J. Welch, Nature 167, 362 (1951).
[21] B. Post and F. W. Glaser, J. Chem. Phys. 20, 1050 (1952).
[22] F. W. Glaser, J. Metals 4, 391 (1952).
[23] F. W. Glaser and B. Post, J. Metals 5, 1117 (1953).
[24] R. Kiessling, J. Electrochem. Soc. 98, 166 (1951).

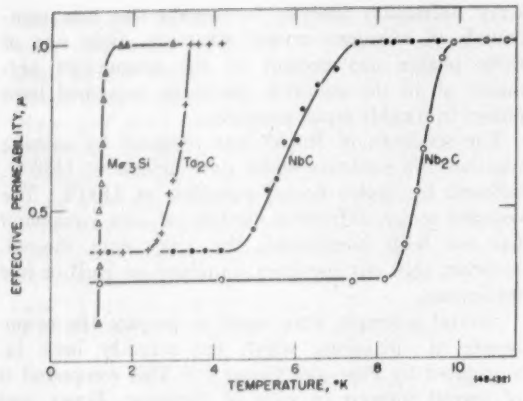

Fig. 3. Temperature variation of effective permeability for arc-melted Nb_2C, NbC, Ta_2C, and sintered Mo_3Si specimens, measuring field 26 oersteds.

Ziegler and Young[10] found no evidence of superconducting behavior in TiC, ZrC, VC, TaC, and WC down to 1.8°K, while Matthias and Hulm[9] reported WC to be normal down to 1.28°K, but MoC as superconducting at about 9.26°K, which is somewhat higher than Meissner and Franz's value.

To check and extend these results we studied the seven monocarbides TiC, ZrC, ThC, VC, NbC, TaC, and UC down to 1.20°K. Most of these compounds were prepared by arc-melting, but the specimen of UC was obtained in a vacuum induction furnace by the reaction at 1800°C of an intimate mixture of U_3O_8 and graphite powder, contained in a graphite crucible.[25,26] This method of preparation might be expected to yield a product containing appreciable amounts of oxygen in solution; unfortunately, the previously reported values[25,26] of the lattice constant of "pure" UC differ by 0.004A, with the result that the lattice paremeter for our specimen (4.952A), while it lay between the two published values, did not provide a very precise indication of the specimen purity. The specimens of ThC and UC, both of which are unstable in air, were handled in a dry-box under argon, and were tested while sealed in thin-walled glass tubes under pure helium.

No evidence of superconducting behavior was found in the monocarbides of titanium, zirconium, thorium, vanadium, tantalum, and uranium, so that we must conclude, in agreement with Ziegler and Young,[10] that the disappearance of electrical resistance found by Meissner and Franz in ZrC and TaC was due to traces of superconducting impurity, possibly the nitride in the former case and free tantalum in the latter. Our NbC specimen showed a rather broad superconducting transition over a range of about 3°K with its mid-point at 6°K (Fig. 3). Since the x-ray diffraction pattern of this specimen contained only monocarbide lines, we presume that the electrical transition which Meissner and Franz[5] found between 10.5° and 10.1°K for "NbC" may have been due to impurities, perhaps Nb_2C (see below) or free niobium.

In addition to the monocarbides, we investigated the lower compounds V_2C, Nb_2C, Ta_2C, Cr_4C, Cr_7C_3, and Cr_3C_2 down to 1.20°K. Since Cr_4C was reported[27] to be unstable above 1530°C, this specimen was annealed at about 1450°C for 50 hours, after arc-melting. Nb_2C and Ta_2C were also subjected to a similar, especially long annealing treatment and their x-ray diffraction patterns contained no lines due to other compounds or to the free metals. It should be mentioned that although the hemicarbides of vanadium and niobium have been reported by several workers,[28–31] some doubt has been expressed regarding their actual existence.[32] However, our x-ray data for these compounds indicated a hexagonal structure, similar to that of Ta_2C, Mo_2C, and W_2C, with the lattice parameters 2.944, 4.608A (V_2C) and 3.105, 4.970A (Nb_2C).

Of the six lower carbides tested, only Nb_2C and Ta_2C became superconducting above 1.20°K; both these compounds exhibited quite sharp transitions centered upon 9.18°K (Nb_2C) and 3.26°K (Ta_2C) (Fig. 3). Neither compound has been investigated for superconductivity in previous work.

C. Nitrides

Electrical resistance transitions similar to those found by Meissner and his co-workers in the monocarbides were also reported by these investigators for the mononitrides TiN (two drops in resistance, at 5.5° and 1.2°K), ZrN (9.6°–9.3°K), and VN (3.2°–1.5°K). More recently, Justi and his co-workers[33] and Horn and Ziegler[8] independently found magnetic evidence of superconductivity in NbN at about 15°K, while the latter workers reported TaN as normal down to 1.88°K.

TABLE III. Influence of oxygen contamination on the superconductivity of TiN.

Specimen	Oxygen content (weight %)	Lattice parameter (A)	T_c (°K)
A	0.4	4.240	5.58
B	0.8	4.240	5.58
C	1.5	4.240	4.86
D	1.6	4.230	2.90

[a] Onset temperature, extrapolated to zero field.

[25] Rundle, Baenziger, Wilson, and McDonald, J. Am. Chem. Soc. **70**, 99 (1948).
[26] Litz, Garrett, and Croxton, J. Am. Chem. Soc. **70**, 1718 (1948).
[27] See M. Hansen, *Der Aufbau der Zweistofflegierungen* (Julius Springer, Berlin, 1936), p. 354.
[28] A. Westgren, Metallwirtschaft **9**, 921 (1930).
[29] M. Oya and A. Osawa, Sci. Repts. Tôhoku Univ. **19**, 95 (1930).
[30] G. Brauer, Z. Elektrochem. **46**, 397 (1940).
[31] J. S. Umanski, Zhur. Fiz. Khim. **14**, 332 (1940).
[32] See reference 1, pp. 104, 110.
[33] Aschermann, Friederich, Justi, and Kramer, Physik. Z. **42**, 349 (1941).

Matthias and Hulm[9] observed a superconducting transition in MoN at about 12°K.

Since the electrical data for several monocarbides were not confirmed by later magnetic tests, it was felt necessary to check the above electrical results for the mononitrides. While our magnetic studies have shown that all three compounds, TiN, ZrN, and VN, are indeed superconducting, the behavior of our specimens of TiN and VN was found to be quite sensitive to variations in the small quantities of oxygen which entered the specimens during preparation.

By heating various samples of titanium for about 8 hours at 1450°C in nitrogen gas subjected to different degrees of purification, we prepared three specimens of TiN (*A*, *B*, and *C*) containing slightly different amounts of oxygen. The oxygen contents determined by vacuum fusion analysis are shown in Table III and the superconducting results in Fig. 4. X-ray evidence ("tailing" off of diffraction peaks at high angles) and slight changes of color from the surface to the interior of these specimens suggested that the oxygen content was somewhat higher in the surface region than at the center. This was also supported by the very wide range of the superconducting transition; the sharp drop in permeability at about 5.5°K for specimen *A* is attributed to a pure central core in which the oxygen content was even less than the 0.4 percent average value for the specimen as a whole. It should be noted that the same lattice parameter was obtained for *A*, *B*, and *C*, 4.240A, which lies between the values 4.242A and 4.235A reported previously for pure TiN.[34,35]

As a further check on the above results, a fourth TiN specimen, *D* (Table III), was prepared by annealing part of specimen *C* under purified helium for twenty hours at 1500°C. The total oxygen content was hardly changed, but, presumably owing to diffusion of oxygen into the purer parts of the specimen, the lattice parameter decreased appreciably and the temperature of onset of superconductivity (not shown in Fig. 4) was depressed to 2.9°K. Replacement of nitrogen by oxygen in the TiN lattice evidently decreases the superconducting transition temperature,

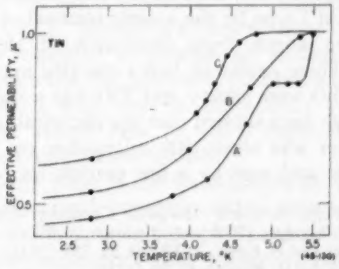

FIG. 4. Temperature variation of effective permeability for sintered TiN samples containing different amounts of oxygen (Table III), measuring field 26 oersteds.

[34] P. Ehrlich, Z. anorg. u. allgem. Chem. **259**, 1 (1949).
[35] A. K. Brager, Acta Physicochim. U.R.S.S. **11**, 617 (1939).

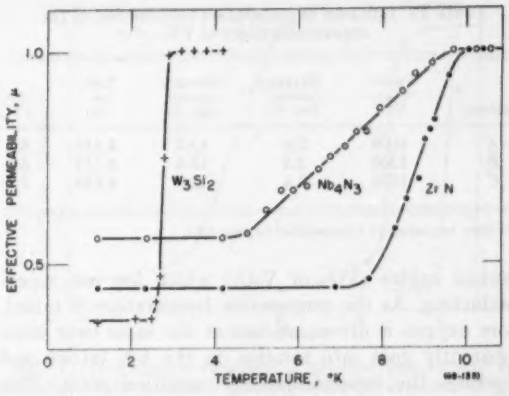

FIG. 5. Temperature variation of effective permeability for sintered ZrN, Nb_4N_3, and W_3Si_2 specimens, measuring field 26 oersteds.

which is not unreasonable in view of the fact that the isostructural monoxide, TiO, is itself normal down to 1.20°K (Sec. III D).

From the temperature of the sudden onset of superconductivity in specimen *A*, extrapolated to zero field, we obtain a value 5.6°K for the transition point of pure TiN. This compares quite favorably with the upper electrical transition observed by Meissner and Franz; their second transition at 1.2°K may have been due to oxygen contamination or perhaps to the presence of impure titanium metal.[36]

Samples of ZrN prepared by the same method as TiN gave quite broad superconducting transitions of the type shown in Fig. 5, with mid-points in all cases close to 8.9°K, in good agreement with Meissner and Franz's electrical data. Oxygen contamination does not seem seriously to affect the superconductivity of this compound, perhaps because the formation of ZrO_2 is preferred to the replacement of nitrogen by oxygen in the nitride lattice; no evidence has been found for the existence of ZrO.[37]

In preparing VN by heating NH_4VO_3 in ammonia, previous investigators [38,39] found that at temperatures high enough to ensure complete reduction of the vanadium oxides (about 1200°C), the VN itself loses appreciable amounts of nitrogen. To see how this affected the superconductivity, we prepared three VN specimens of about the same shape at three different temperatures, with the results shown in Table IV and Fig. 6. Even though specimen *A* contained the most oxygen, it exhibits the sharpest superconducting transition and the lowest effective permeability, probably owing to the fact that the oxygen occurs as

[36] Although the present accepted transition temperature of titanium is 0.53°K, early specimens had transitions at 1.2° and 1.8°K, presumably owing to impurities. See reference 12, p. 223.
[37] D. D. Cubicciotti, J. Am. Chem. Soc. **73**, 2032 (1951).
[38] V. A. Epelbaum and B. F. Ormont, Acta Physicochim. U.R.S.S. **22**, 319 (1947).
[39] H. Hahn, Z. anorg. u. allgem. Chem. **258**, 58 (1949).

TABLE IV. Influence of preparation temperature on the superconductivity of VN.

Specimen	Prepn. temp. (°C)	Oxygen content (wt. %)	Nitrogen content (wt. %)	Latt. par. (A)	T_c* (°K)
A	1000	7.6	13.7	4.135	8.2
B	1200	2.3	18.6	4.132	6.7
C	1350	2.4	11.8	4.130	5.8

* Onset temperature extrapolated to zero field.

residual oxides (VO_2 or V_2O_5) which are not superconducting. As the preparation temperature is raised, more oxygen is driven off but at the same time more apparently goes into solution in the VN lattice and depresses the superconducting transition point. This may have been responsible for the low transition temperature observed by Meissner and Franz; in view of the fact that our specimen *A* was the most completely superconducting and gave a lattice parameter closest to the values reported by previous workers[39–41] for pure VN (4.134A and 4.137A), we regard the temperature of onset of superconductivity in this specimen (8.2°K) as the most reliable transition temperature at present available.

In addition to the above mononitrides we tested the seven compounds Th_3N_4, "V_3N_2," Nb_2N, Nb_4N_3, Ta_2N, TaN, and UN down to 1.20°K. Normal behavior was observed in all cases except that of Nb_4N_3, which became superconducting over a range of 5°K with its mid-point at 7.2°K (Fig. 5); according to Brauer and Jander[42] this compound has a crystal structure based upon a tetragonally deformed NbN (NaCl type) lattice. In view of the high transition points of the vanadium and niobium mononitrides, and of the metals themselves, it is interesting that the hexagonal lower nitrides "V_3N_2" and Nb_2N remain normal down to 1.20°K. Both these compounds involve a close-packed hexagonal metal lattice with nitrogen atoms in the interstices[30,39]; however, as Hahn has pointed out, since the holes in the vanadium lattice are too small for the nitrogen atoms, the compound is formed in the range $VN_{0.37}$ to $VN_{0.43}$ instead of at the ideal composition $VN_{0.50}$.

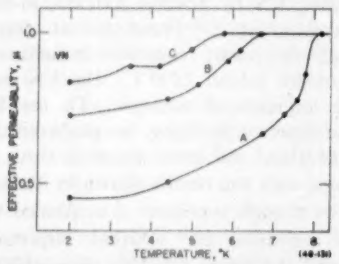

FIG. 6. Temperature variation of effective permeability for "VN" samples containing different amounts of oxygen and nitrogen (Table IV), measuring field 26 oersteds.

The absence of superconductivity in Th_3N_4 is perhaps to be expected, since this compound is usually regarded as a typical "ionic" and nonmetallic nitride.[43] While our particular specimen of TaN showed no trace of superconductivity, its x-ray diffraction pattern did not resemble that reported by Horn and Ziegler[8] for a sample which remained normal down to 1.88°K, and neither of these patterns agree with that given by Becker and Ebert[44] for TaN. On the other hand, our Ta_2N, which was made by heating an intimate mixture of TaN and tantalum at 1450°C, gave a hexagonal pattern similar to that of Nb_2N and identical with the data of van Arkel[45] for a specimen which he called "TaN." Chiotti[46] has shown convincingly that this hexagonal close-packed phase is actually the heminitride of tantalum, but the structures existing around the composition "TaN" remain obscure.

D. Oxides

Arc-melted pellets of the monoxides TiO, VO, and NbO showed no trace of superconductivity down to 1.20°K. The TiO and VO specimens were found to have a sodium chloride structure, with lattice parameters in good agreement with values obtained by earlier workers.[47,48] NbO also gave an x-ray diffraction pattern in good agreement with that previously reported,[49] which apparently corresponds to a structure derived from the NaCl type by the orderly removal of niobium and oxygen atoms from one-fourth of the lattice positions. These oxides all had a metallic appearance; VO and NbO were silvery and TiO was a dull golden color. Rough tests showed that the electrical resistivity of the latter was about 300 micro-ohm cm at room temperature and rose by a few percent on cooling to

TABLE V. Superconducting silicides and germanides of Groups 4, 5, and 6 transition metals (present work).

None found for titanium or zirconium	V_3Si	(17.1°)	None found for chromium
	V_3Ge	(6.01°)	
None tested for hafnium	["Nb_3Ge"	(1.9°)]*	Mo_3Si (1.30°)
			Mo_3Ge (1.43°)
α-$ThSi_2$ (3.16°)	["Ta_3Ge"	(1.6°)]*	W_3Si_2 (2.84°)
β-$ThSi_2$ (2.41°)			

* Doubtful owing to presence of free metal.

[40] A. K. Brager and V. A. Epelbaum, Acta Physicochim. U.R.S.S. **13**, 595 and 600 (1940).
[41] V. A. Epelbaum and B. F. Ormont, Zhur. Fiz. Khim. **21**, 3 (1947).
[42] G. Brauer and J. Jander, Z. anorg. u. allgem. Chem. **270**, 160 (1952).
[43] A. F. Wells, *Structural Inorganic Chemistry* (Oxford University Press, London, 1950) second edition, p. 477.
[44] K. Becker and F. Ebert, Z. Physik **31**, 268 (1925).
[45] A. E. van Arkel, Physica **4**, 286 (1924).
[46] P. Chiotti, J. Am. Ceram. Soc. **35**, 123 (1952).
[47] W. Rostoker, J. Metals **4**, 981 (1952). (Our TiO specimen was obtained from Dr. W. Rostoker.)
[48] W. Klemm and L. Grimm, Z. anorg. u. allgem. Chem. **250**, 42 (1942).
[49] G. Brauer, Z. anorg. u. allgem. Chem. **248**, 1 (1941).

78°K, which suggests semiconducting behavior. It should be remarked that Meissner, Franz, and Westerhoff[6] found a gradual drop in electrical resistance for NbO between about 4.2° and 1.4°K, which, in view of the present results, was probably due to impurities.

E. Silicides

Although the radius of silicon is too large for the extensive formation of interstitial compounds, many of the transition metal silicides have metallic character and their structures have been extensively studied.[50] In the present work all the known silicides of the Groups 4, 5, and 6 transition metals, with the exception of hafnium and uranium, were tested for superconductivity down to 1.20°K. The results of these studies, together with those for similar tests on the corresponding germanides, are summarized in Table V (superconducting) and Table VI (normal).

TABLE VI. Silicides and germanides of Groups 4, 5, and 6 transition metals nonsuperconducting down to 1.20°K (present work).

Ti_5Si_3, Ti_5Ge_3	"V_3Si_2," V–Ge	Cr_3Si, Cr_3Ge
TiSi	VSi_2	Cr_5Si_3, Cr_5Ge_3
$TiSi_2$, $TiGe_2$		CrSi, CrGe
	Nb_5Si_3	$CrSi_2$
Zr_4Si, Zr_5Si	"Nb_2Si"	
Zr_2Si_2, Zr_4Si_3	$NbSi_2$, $NbGe_2$	Mo_3Si_3, Mo_5Ge_3
Zr_6Si_5		$MoSi_2$
ZrSi, Zr–Ge	Ta_5Si, Ta_5Si_2	α-$MoGe_2$
$ZrSi_2$, $ZrGe_2$	Ta_2Si_2	β-$MoGe_2$
	$TaSi_2$, $TaGe_2$	
Th_3Si_3, Th–Ge		WSi_2

Superconducting behavior was observed in the five silicides V_3Si (17.1°K, Fig. 7), Mo_3Si (1.30°K, Fig. 3), α-$ThSi_2$ (3.16°K, Fig. 8), β-$ThSi_2$ (2.41°K, Fig. 8), and W_5Si_3 (2.84°K, Fig. 5), representing four structure types in which the phenomenon has not previously been reported. The most striking feature of these results is the transition temperature of V_3Si, which is the highest known for any binary compound. Since both V_3Si and Mo_3Si crystallize in a cubic structure of the β-tungsten type [O_h^3], it is interesting that a third silicide of the same structure, Cr_3Si, remains normal down to 1.20°K. According to Zener[51] these compounds might be expected to possess an antiferromagnetic spin arrangement, but this point does not seem to have been checked with neutron diffraction; there is at present no known case in which superconductivity and antiferromagnetism coexist.

At an early stage in the investigation of V_3Si it was found that certain impurities often present in commercial vanadium metal, in particular iron, tend to depress the superconducting transition temperature. The transition curves for three specimens prepared from vanadium obtained from three different sources

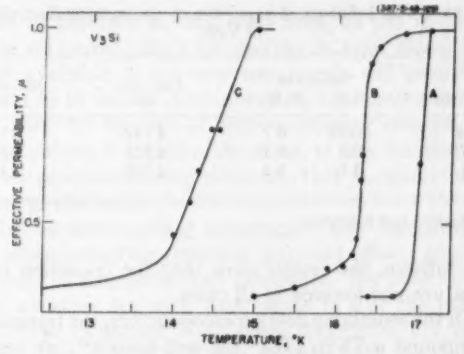

FIG. 7. Temperature variation of effective permeability for arc-melted V_3Si samples containing different amounts of impurity (Table VII), measuring field 8 oersteds.

are shown in Fig. 7; Table VII gives the main impurity content of these specimens and indicates that as little as 0.1 percent of iron lowers the transition temperature by nearly one degree. Since all our specimens contained about the same amount of manganese, it was not possible to decide how much effect this impurity had upon the transition temperature. However, since the neighboring elements iron and chromium (see Table VIII) tend to depress the transition, manganese probably has the same effect and we presume that the transition temperature of extremely pure V_3Si lies somewhat above 17°K.

In an attempt to raise the transition temperature of V_3Si specimens, we investigated the effect of varying the silicon content and also of replacing part of the vanadium or silicon by other elements. Changes up to ±20 atomic percent of silicon produced hardly any change of T_c, probably because the single phase region for V_3Si is rather narrow. The introduction of other elements caused the changes listed in Table VIII; although many of the added elements did not dissolve completely in the V_3Si phase, in spite of melting in the

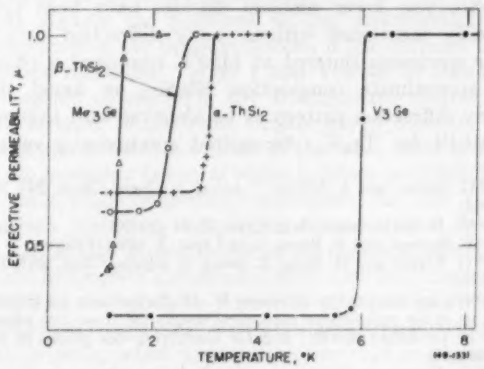

FIG. 8. Temperature variation of effective permeability for arc-melted V_3Ge, Mo_3Ge, and sintered α-$ThSi_2$, β-$ThSi_2$ specimens, measuring field 26 oersteds.

[50] For a detailed list of papers, see reference 1.
[51] C. Zener, Phys. Rev. 81, 440 (1951).

TABLE VII. Influence of impurities on the superconductivity of V_3Si.

Specimen	Impurities % Fe	% Mn	Latt. par. (A)	Mid-point[a] (°K)
A	0.05	0.2	4.722	17.0
B	0.1	0.3	4.723	16.3
C	1.0	0.3	4.720	14.4

[a] Applied field 8 oersteds.

arc furnace, the results show that the transition temperature was lowered in all cases.

Of the remaining new superconductors, the tetragonal compound α-$ThSi_2$ [D_{4h}^{19}] is well known[52]; we tested the isomorphous compounds[53–55] $CeSi_2$, $LaSi_2$, and YSi_2 (distorted), but all three remained normal down to 1.20°K. A series of Th-Si specimens of different silicon contents also yielded, in addition to α-$ThSi_2$, two previously unreported phases,[56] β-$ThSi_2$ [hexagonal (D_{6h}^1) superconducting at 2.41°K] and Th_4Si_3 [tetragonal (D_{4h}^5) normal]. These specimens also contained a good deal of ThO_2, which, however, merely served to increase the effective permeability in the superconducting range.

In a previous paper[11] superconductivity was reported in Mo_3Si_2, which is apparently isomorphous with the superconductor W_3Si_2, both structures being unidentified. This result was an erroneous one due to the presence of Mo_3Si impurities in the original "Mo_3Si_2" specimen. Since the x-ray diffraction pattern of pure Mo_3Si_2 contains all the lines of Mo_3Si, the presence of these impurities remained undetected for some time. However, prolonged annealing of the specimen caused the superconductivity to disappear, presumably owing to the removal of Mo_3Si.

It is of interest to mention some normal phases found by us in silicide systems which have hitherto been incompletely explored. For the vanadium-silicon system a new phase of unknown structure was observed at the approximate composition V_3Si_2. In addition to $NbSi_2$, two lower niobium silicides have been previously mentioned without x-ray diffraction data.[57] Our specimens sintered at 1450°C contained a phase of approximate composition Nb_5Si_3; we found the x-ray diffraction pattern to be identical with that reported[58] for Ta_5Si_3. Arc-melted specimens gave an additional phase of composition Nb_2Si which is apparently formed only at very high temperatures.

Finally, we note that four tantalum silicides[58,59] remained normal down to 1.20°K, which strongly suggests that the disappearance of electrical resistance observed by Meissner, Franz, and Westerhoff[7] in a "TaSi" specimen was due to impurities, probably free tantalum.

F. Germanides

Structural interest in the transition metal germanides is quite recent, and far less information is available than for the silicides. However, the data so far obtained seem to indicate that the silicides and germanides of a given transition metal are much more closely related to each other than to the carbides or nitrides of that metal. Whereas the carbides and nitrides tend to have "interstitial" structures, the silicides and germanides have structures based, to some extent, on bonding of nonmetal atoms to each other,[53] and on equivalence between the roles of metal and nonmetal atoms in the structure, in analogy with the borides.[24]

We tested the known germanides of the Groups 4, 5, and 6 metals down to 1.20°K, with the results given in Tables V (superconducting) and VI (normal). Only two new superconductors were observed, V_3Ge (6.01°K, Fig. 8) and Mo_3Ge (1.43°K, Fig. 8), both of which are isomorphous with V_3Si.[60,61]

In view of our incomplete knowledge of the phase diagrams, it was usual to prepare for each transition metal about eight sintered specimens of different germanium contents in the range M_4Ge to MGe_2, where M is the metal. X-ray studies for the systems Zr-Ge, Th-Ge, and V-Ge indicated the presence of several new phases in addition to the known compounds[60] $ZrGe_2$ and V_3Ge, but since none of these were superconducting above 1.20°K, they were not investigated further. In both arc-melted and sintered specimens of Nb-Ge and Ta-Ge, evidence was found for existence of

TABLE VIII. Effect of added elements on the superconductivity of V_3Si.

Composition	Latt. par. (A)	Trans. range[a] (°K)	Mid-point[a] (°K)
V_3Si	4.722	16.4–17.1	16.8
$V_2Si_{0.9}C_{0.1}$	4.723	15.5–16.7	16.4
$V_2Si_{0.9}Ge_{0.1}$	4.731	13.0–14.4	14.0
$V_2Si_{0.9}B_{0.1}$	4.720	15.0–16.3	15.8
$V_2Si_{0.9}Al_{0.1}$	4.727	13.1–14.9	14.05
$(V_{0.9}Ti_{0.1})_3Si$	4.736	10.0–12.0	10.9
$(V_{0.9}Zr_{0.1})_3Si$	4.724	11.0–15.3	13.2
$(V_{0.9}Nb_{0.1})_3Si$	4.756	12.0–13.5	12.8
$(V_{0.9}Mo_{0.1})_3Si$	4.732	11.5–12.5	11.7
$(V_{0.9}Cr_{0.1})_3Si$	4.697	11.0–11.9	11.3
$(V_{0.9}Ru_{0.1})_3Si$	4.707	2.0– 3.8	2.9

[a] Applied field 26 oersteds.

[52] G. Brauer and A. Mitius, Z. anorg. u. allgem. Chem. **249**, 325 (1942).
[53] W. H. Zachariasen, Acta Cryst. **2**, 94 (1949).
[54] F. Bertaut and P. Blum, Acta Cryst. **3**, 319 (1950).
[55] G. Brauer and H. Haag, Z. anorg. u. allgem. Chem. **267**, 198 (1952).
[56] We are indebted to Professor W. H. Zachariasen for informing us of his unpublished structural results for these two phases (to be published shortly) and for identifying the phases in our specimens.
[57] G. Brauer, in W. Klemm, *FIAT Review of German Science 1939–1946, Inorganic Chemistry*, Part II (1948), p. 105.
[58] Brewer, Searcy, Templeton, and Dauben, J. Am. Ceram. Soc. **33**, 291 (1950).
[59] Nowotny, Schachner, Kieffer, and Benesovsky, Monatsh. Chem. **84**, 1 (1953).
[60] H. J. Wallbaum, Naturwiss, **32**, 76 (1944).
[61] Searcy, Peavler, and Yearian, J. Am. Chem. Soc. **74**, 566 (1952).

the previously reported[60] digermanides, which remained normal down to 1.20°K, and two lower compounds of approximate composition "Nb_2Ge" and "Ta_2Ge" which showed superconducting behavior at about 1.9° and 1.6°K, respectively. However, since free metal was present in all specimens of these hemigermanides, their superconductivity remains in doubt.

In the Ti-Ge, Cr-Ge, and Mo-Ge specimens, only known compounds were present,[60-62] the normal compounds including Mo_3Ge_2 and two forms of $MoGe_2$ upon which x-ray data has recently been published.[62] Just as for Mo_3Si_2, discussed in Sec. III E, the superconducting behavior previously reported[11] for Mo_3Ge_2 disappeared after prolonged annealing and was therefore presumed to have been due to Mo_3Ge impurities. No compounds were found in the W-Ge system.

G. Other Compounds

Since superconductivity was observed in four compounds, V_3Si, V_3Ge, Mo_3Si, and Mo_3Ge, which crystallize in a structure of the β-tungsten type, it was thought worth while to test several intermetallic compounds of this structure. However, four such compounds, Ti_3Pt,[64] Ti_3Au,[64] V_3Co,[65] and Mo_3Zr,[66] remained normal down to 1.20°K.

The lowest known sulphide of niobium, NbS,[67] was prepared by heating the powdered metal and sulphur in a sealed, evacuated "Vycor" tube at about 1000°C until equilibrium was attained. No trace of superconductivity was observed in this compound down to 1.28°K.

IV. CONCLUSION

Excluding the bismuthides,[9] about thirty compounds of metals with nonmetallic elements have now been shown to be superconducting on the basis of quite reliable magnetic evidence. Most of these are listed in Tables I and V, including the eleven new superconductors found in the present work; the others comprise CuS [68] and several compounds of Group 8 metals recently reported superconducting by Matthias.[69] Errors in early work due to reliance upon electrical measurements or due to inadequate knowledge of the specimen composition have now been largely corrected. Most of the compounds of Groups 4, 5, and 6 transition metals with boron, carbon, nitrogen, oxygen, silicon, and germanium have been tested for superconductivity down to about 1°K, but even here, as the detailed phase diagrams (which are lacking in most cases) become available, a few new compounds will probably remain to be tested. Attention should be drawn to the fact that the fraction of superconducting compounds in our tables is roughly the same as the fraction of known superconducting elements, that is, about one-fourth of the total.

The superconducting compounds now outnumber the superconducting elements (21), and offer a greater diversity of structures than heretofore. The most common structure for such compounds is still the cubic NaCl type (5 normal, NbC, NbN, TiN, ZrN, VN, and 3 distorted, Nb_4N_3, Mo_2N, W_2N), but the cubic β-tungsten type (V_3Si, V_3Ge, Mo_3Si, and Mo_3Ge) and the hexagonal structure based upon a close-packed array of metal atoms with nonmetal atoms in the interstices (Nb_2C, Ta_2C, Mo_2C, W_2C, and very distorted NbB) have recently come into prominence. There are also at least ten other important superconducting structure types, ranging in symmetry from the cubic fluorite type[70] ($CoSi_2$) through the tetragonal $CuAl_2$ type (the hemiborides), the tetragonal α-$ThSi_2$ type, the hexagonal NiAs type[69] to the orthorhombic MnP and monoclinic PdBi types.[69] There are several unknown structures, including for example W_3Si_2; this compound is probably closely related to its cubic neighbor Mo_3Si.

It was remarked in a previous paper[9] that superconducting transition temperatures of both cubic elements and compounds tend to be higher than those for hexagonal elements and compounds. This tendency seems to have been confirmed in the present work, in view of the rather high transition points of the β-tungsten structure vanadium compounds and the cubic mononitrides, in contrast to the absence of superconductivity in the hexagonal heminitrides and the low transition points of the hexagonal hemicarbides. It must be admitted, however, that the normal behavior of most of the cubic monocarbides forms an exception to the above hypothesis.

As regards the positions of the superconducting compounds in the periodic system, if one excludes the thorium disilicides, Tables I and V seem to indicate a diagonal character in the arrangement, that is, a displacement to the right (higher group number) as one proceeds down a column of the table. This is due to the persistent failure of either hafnium or chromium to form superconducting compounds; the fact that fourteen chromium compounds remain normal down to 1.28°K may be partly due to the magnetic influence of the incomplete chromium d shell. One may contrast with this the extensive formation of superconducting compounds by the other Group 6A metals, molybdenum and tungsten, which apparently come close to possessing the requisite electronic structure for superconductivity.

[62] P. Pietrowsky and P. Duwez, J. Metals 3, 772 (1951).
[63] A. W. Searcy and R. J. Peavler, Abstracts of papers presented at the 124th annual meeting of the American Chemical Society, Chicago, September, 1953.
[64] P. Duwez and C. B. Jordan, Acta Cryst. 5, 213 (1952).
[65] P. Duwez, J. Metals 3, 564 (1951).
[66] H. Nowotny, in W. Klemm, *FIAT Review of German Science, 1939–1946, Inorganic Chemistry*, Part IV (1948), p. 81.
[67] W. Biltz and A. Köcher, Z. anorg. u. allgem. Chem. **237**, 369 (1938).
[68] See reference 12, p. 229.
[69] B. T. Matthias, Phys. Rev. **87**, 380 (1952); **90**, 487 (1953); **91**, 413 (1953).
[70] B. T. Matthias and J. K. Hulm, Phys. Rev. **89**, 439 (1953).

Recently certain theoretical relationships have been established[71,72] between the occurrence of superconductivity in a metal and the normal properties of the metal, in particular the "ideal" electrical resistivity at room temperature. While in their present form these relations seem to be mainly applicable to metals of rather simple outer electronic structure, nevertheless it would be interesting to test their validity for a few of the approximately one hundred compounds listed in our tables. In particular, the added complication of differences of crystal structure, which are not taken into account in the above free-electron theories, might be removed by working with an isostructural group such as the NaCl structure monocarbides, mononitrides, and monoxides with many superconducting and normal members. Unfortunately, however, little accurate information is available on the normal properties of most of these compounds, chiefly owing to the difficulty of preparing them in stoichiometric, homogeneous, solid form. Various estimates[1] of the room-temperature electrical resistivities of the carbides and nitrides, for example, differ by more than an order of magnitude in some cases, and since hardly any low-temperature data are available, it is impossible to derive accurate values of the "ideal" resistivity. If the most recently obtained resistivity values are assumed to be correct, the nitrides, which include most of the superconductors of NaCl structure, seem to have resistivities predominantly lower than those of the carbides and monoxides, but beyond this little can be said.

A more systematic investigation of the normal electronic properties of transition metal compounds is clearly desirable, not only for the light which may be thrown on their superconducting behavior, but also for the intrinsic interest of the chemical binding in these compounds. Whereas many are known to have metallic character, a few semiconductors, such as titanium monoxide, have also been reported; thus, solid solutions of TiC or TiN with TiO may provide a continuous transition from metallic to semiconducting properties in the same, relatively simple lattice. A similar, but less smooth, transition may occur with increasing nonmetal content in the borides and silicides, since during this increase each boron or silicon atom tends to form step by step a greater number of linkages with its boron or silicon neighbors. Experiments to check these hypotheses through the detailed study of electrical properties are now in progress.

We are grateful to Professor E. A. Long and Professor W. H. Zachariasen for helpful discussions; to Dr. W. Rostoker (Illinois Institute of Technology) for the loan of TiO specimens; to Mr. A. Moskowitz and Mrs. A. R. Tompkins for carrying out vacuum fusion and spectrographic analyses, respectively; to Mr. E. Selmanoff for metallurgical assistance; and to Mr. R. Szara for liquefying helium. Part of the work was carried out during tenure by one of us (G. F. H.) of a U. S. Rubber Company Fellowship at the University of Chicago.

[71] H. Fröhlich, Phys. Rev. **79**, 845 (1950).
[72] J. Bardeen, Phys. Rev. **80**, 567 (1950).

X-Ray-Induced Photostimulated Conductivity in Magnesium Oxide*

ALBERT S. EISENSTEIN†
Department of Physics, University of Missouri, Columbia, Missouri
(Received October 22, 1953)

Single crystals of MgO luminesce under x-ray excitation with a multiband spectrum. The 3.6-ev band exhibits a long-time phosphorescence accompanied by an induced photoconductivity. Photostimulation of crystals previously x-ray-irradiated produces a sizable photoconductivity during the excitation. This, together with the phosphorescence, decays with time. Remote hole trapping may account for these observations.

FURST and Kallmann[1] have studied the storage of energy in silver-activated alkali halides induced by x-ray irradiation and its subsequent release by photostimulation. This energy release was evidenced by a luminescence, the photon energy of which exceeded that of the photostimulation and was observed following this stimulation. Mandeville and Albrecht[2] have recently examined this luminescence during the stimulation as well as its decay following the termination of the photostimulation. They made use of a Geiger counter selected to have a photoelectric threshold providing sensitivity for the ultraviolet luminescence but not for the photostimulation. A similar luminescence effect has been found in x-ray-irradiated MgO crystals, and in addition a photostimulated conductivity has been found in these crystals.

High-purity single crystals[3] of MgO luminescence under x-ray irradiation with a multiband spectrum; however, only the 3.6-ev band shows a long-time phosphorescence, this following approximately a power law decay. The decay of an x-ray-induced photoconductivity could be followed for several hours in the apparatus shown in Fig. 1. Platinum electrodes fired on opposite faces of the crystal were clamped between spring clips which led to the vibrating reed electrometer. Optical irradiation, from above, and x-ray irradiation, from the side, could be used to induce luminescence and conductivity. The luminescence radiation was detected by a photon counter (a 1P28 photomultiplier held at liquid air temperature) and entered this detector through the quartz light pipe located below the crystal. Visible light in the 2.3-ev absorption band[4] and ultraviolet radiation at 3.4 ev, in the 3.7-ev absorption band,[4] were used for photostimulation.

Crystals which were bleached by annealing at 600°K showed no initial conductivity nor luminescence response to irradiation at 2.3 ev and only a slight sensitivity to 3.4-ev radiation.[5] Following an x-ray irradiation at 35 kv (doses of 500 to 4×10^4 roentgens were used) and even though the x-ray-induced luminescence and conductivity had decayed to a low level, the crystals could be photostimulated by both 2.3-ev and 3.4-ev radiation. During this stimulation only conductivity was measured, but following this optical irradiation both luminescence and conductivity were observed to decay. Figure 2 (a,b) shows these effects in a previously x-ray-irradiated crystal. In (a) the luminescence had decayed to the level L_1 and the conductivity current to i_1 before stimulation. Upon exposure to an intensity of 600 μw/cm² of 2.3-ev radiation, the current increased 60-fold and decayed only slightly during the 6-minute irradiation. In the period 6 to 12 minutes, luminescence and conductivity decayed without stimulation; and from 12 to 18 minutes the sample was

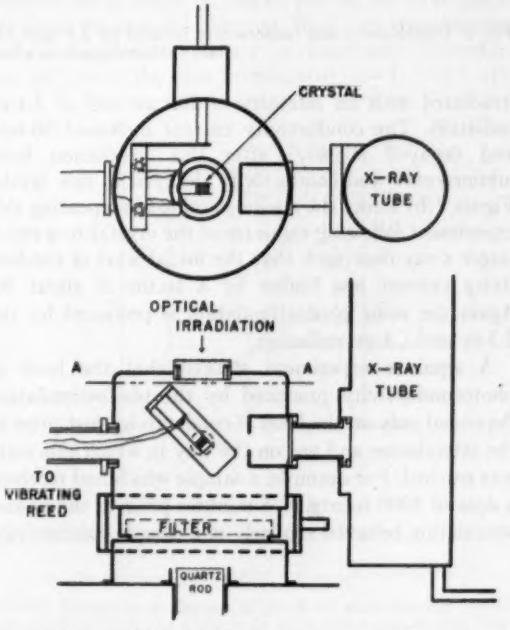

FIG. 1. MgO crystal mounted for simultaneous measurements of conductivity and luminescence.

photon counter with an over-all efficiency of 0.5 percent should detect 200 3.6-ev photons originating in the crystal per second.

* Supported in part by the U. S. Office of Naval Research.
† Deceased, December 16, 1953.
[1] M. Furst and H. G. Kallmann, Phys. Rev. **82**, 964 (1951).
[2] C. E. Mandeville and H. O. Albrecht, Phys. Rev. **91**, 566 (1953).
[3] Grown in an electric arc furnace from high-purity material by Dr. Harold F. John.
[4] H. Weber, Z. Physik **130**, 392 (1951).
[5] The dark current in these crystals was about 10^{-15} amp corresponding to a specific resistivity of 10^{16} ohm cm, and the

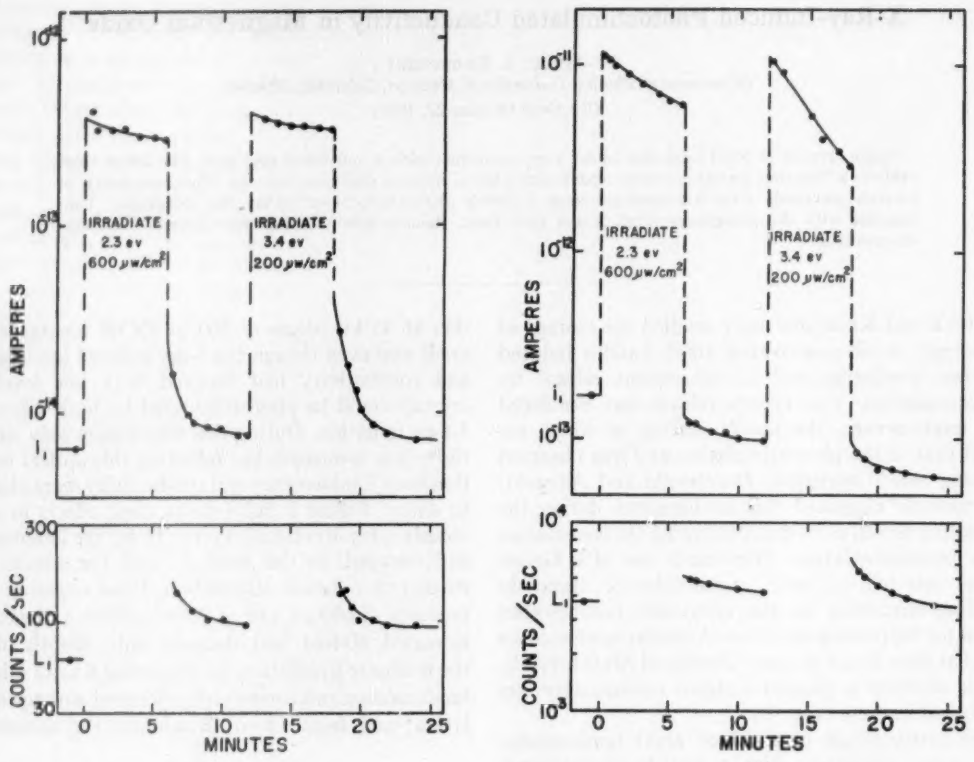

FIG. 2. Conductivity and luminescence induced by 2.3- and 3.4-ev radiation on MgO crystal previously irradiated with x-rays. Case (b) corresponds to a much larger x-ray dose than case (a).

irradiated with an intensity of 200 $\mu w/cm^2$ of 3.4-ev radiation. The conductivity current increased 50-fold and decayed slightly; after this irradiation both luminescence and conductivity decayed to new levels. Figure 2(b) shows the results obtained in repeating this experiment following exposure of the crystal to a much larger x-ray dose such that the initial level of conductivity current was higher by a factor of about 30. Again the same photostimulation is produced by the 2.3-ev and 3.4-ev radiation.

A separate experiment showed that the level of photoconductivity produced by the photostimulation depended only on the level of conductivity just prior to the stimulation and not on the way in which this state was reached. For example, a sample which had received a dose of 5000 roentgens 5 minutes prior to the photostimulation behaved similarly to a sample conductivity had decayed to the same level 180 minutes following a dose of 4×10^4 roentgens.

This photostimulated conductivity effect which is present only in previously x-ray-irradiated crystals is interpretable in terms of remote trapping of holes as proposed by Day.[6] Acceptor levels 2.1 ev above the valence band, normally occupied by electrons in annealed specimens, trap holes as the result of electron excitations produced by the x-ray irradiation. The photostimulated conductivity results from releasing these holes which in turn are annihilated by electrons trapped at higher levels, thus giving rise to the observed luminescence. This process does not differ significantly from the ordinary photoconductivity observed by Day in that a quantum efficiency of 10^{-5} is found as compared with values between 10^{-4} and 10^{-7} which he reported.

[6] Harold R. Day, Phys. Rev. **91**, 822 (1953).

Zeeman Effect and Line Breadth Studies of the Microwave Lines of Oxygen*

ROBERT M. HILL AND WALTER GORDY
Department of Physics, Duke University, Durham, North Carolina
(Received October 13, 1953)

Measurements made at 90°K and at 300°K on the O_2 line breadths show that the line breadth parameter, $\Delta\nu$, varies as T^{-x}, with x ranging in value from 0.76 for the 9₋ line to 0.90 for the 1₋ line. The type of variation of x with the rotational quantum number N indicates that both rotational resonance and quadrupole moment interactions are important factors in determining the line breadths. The Zeeman splittings observed for the 1₋, the 1₊, and the 3₋ lines are in good agreement with the splitting predicted from first-order perturbation theory.

ZEEMAN EFFECT

THE Zeeman effect of the O_2 lines was first investigated by Schmidt, Budo, and Zempler[1] in the optical region, where the "microwave lines" appear as a fine structure superimposed upon the transitions of higher energy. Because of the low resolution obtainable in the optical region, their measurements were of necessity made with very high fields where the internal couplings were partly broken down. Similarly, the microwave paramagnetic resonance measurements on O_2 by Beringer and Castle[2] were made with such high fields that some decoupling of the internal momentum vectors was produced. In contrast, the present investigations were made with extremely weak fields (less than 100 gauss) at which no decoupling effects are expected.

A preliminary measurement of the Zeeman splitting of a single line (the 1₋ line at 2.5-mm wavelength) reported earlier from this laboratory[3] indicated a discrepancy of about 20 percent with the weak-field Zeeman theory. The Zeeman work has been continued, and the more extensive and accurate measurements reported here are in complete agreement with theory.

The level splitting for the weak-field case is easily calculated from the vector model treatment.[3] It is given by

$$E_H = -g\beta H M_J, \tag{1}$$

where

$$g = \frac{J(J+1)+S(S+1)-N(N+1)}{J(J+1)}.$$

In the last expression N represents the quantum number for the end-over-end rotation,[4] S the electronic spin quantum number, and J the quantum number for the total angular momentum. Since for O_2 $S=1$, there are three J values for each value of N,

$$J = N+1, \quad N, \quad N-1.$$

Also,

$$M_J = J, \quad J-1, \quad J-2 \cdots -J.$$

The selection rules are

$$\Delta J = \pm 1, \quad \Delta N = 0, \quad \text{and} \quad \Delta M_J = 0, \quad \pm 1.$$

Because the interaction with the microwave radiation field occurs through the magnetic dipole moment, the $\Delta M_J = \pm 1$ components are observed when the externally imposed H is perpendicular to the magnetic component of the radiation, and the $\Delta M_J = 0$ components when it is parallel to this field component. In our experiment we imposed the dc magnetic field by placing the wave-guide cell along the axis of a solenoid. With this arrangement both the σ and π components are observable. Nevertheless, for two of the lines investigated, the $1_+ (J=2 \rightarrow 1)$

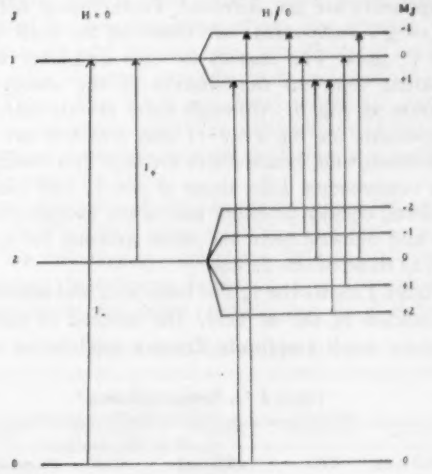

FIG. 1. Energy level diagram of the $N=1$ state showing transitions observed with and without an externally imposed field. The Zeeman splitting is greatly exaggerated.

* This research was supported by the United States Air Force under a contract monitored by the Office of Scientific Research, Air Research and Development Command. The information contained in this paper is part of a thesis submitted by one of the authors, Robert M. Hill, in partial fulfillment of the requirements for the Ph.D. degree at Duke University.

[1] Schmidt, Budo, and Zempler, Z. Physik **103**, 250 (1936).

[2] R. Beringer and J. G. Castle, Jr., Phys. Rev. **81**, 82 (1951).

[3] Gordy, Smith, and Trambarulo, *Microwave Spectroscopy* (John Wiley and Sons, Inc., New York, 1953), Sec. 3.2b.

[4] The symbol K has been conventionally used in the past, but because of possible confusion with symmetric-top notation [see J. H. Van Vleck, Revs. Modern Phys. **23**, 213 (1951)] we have [following Gordy, Smith, and Trambarulo, *Microwave Spectroscopy* (John Wiley and Sons, Inc., New York, 1953)] adopted the notation N as recommended by an international committee on nomenclature headed by Professor F. A. Jenkins [J. Opt. Soc. Am. **43**, 410 (1953)].

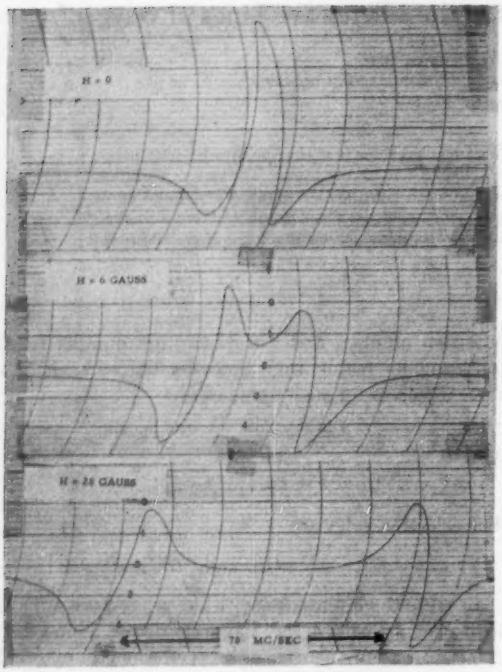

FIG. 2. Recording of the 1_+ line ($J=2\rightarrow1$) with and without magnetic fields.

and $1_-(J=0\rightarrow1)$, no displacement of the $\Delta M_J=0$ component is produced by the field, and with the detection system employed which depends upon modulation by an ac magnetic field these undisplaced components are not detected. Furthermore, only two $\Delta M_J=\pm1$ components are observed for both the 1_+ and 1_- lines. The reasons for this simplicity will be apparent from an examination of the energy level diagram of Fig. 1. Although there are six $\Delta M_J=\pm1$ components for the $J=2\rightarrow1$ line, two sets are triply degenerate, and, hence, there are only two distinguishable components. Like those of the 1_- line these are displaced equally on either side of the unsplit zero-field line and likewise have the same splitting for a given field as those of the 1_- line.

Figure 2 shows the 1_+ line both with and without the application of the dc field. The method of detection employs small amplitude Zeeman modulation and is the same as that previously described.[5] With this method of detection the graph of the unsplit (zero dc field) line represents the second derivative of the actual line contour, whereas that for the individual Zeeman components represents the first derivative of their line contour. For the 3_- line ($J=2\rightarrow3$) there are many components which were incompletely resolved with the low fields employed in our experiments. The outer components were sufficiently separated, however, for measurement. These gave results in good agreement with theory.

Table I gives a comparison of the experimentally measured quantity $2\Delta\nu/H$ for the different lines with the values calculated with Eq. 1. Here $2\Delta\nu$ represents the separation of the observed doublets of the 1_- and 1_+ lines and of the outer Zeeman components of the 3_- line. The theoretical values lie well within the limits of error of the experimental ones. Since the $J=0$ state is not split by an external field, it is possible to evaluate the g factor for the $J=1$, $N=1$ state from the measured splitting of the $J=0\rightarrow1$ line. The result is 0.99 ± 0.01, in agreement with the theoretical value of 1.00. With the observed g factor of the $J=1$ level thus determined, the g factor for the $J=2$, $N=1$ state can then be obtained from the splitting of the $2\rightarrow1$ line. It is 1.00 ± 0.01 as compared with the theoretical value of 1.00.

TABLE I. O_2 Zeeman splitting.[a]

Line	$2\Delta\nu/H$ in (Mc/sec)/gauss Observed	Calculated
1_-	2.78 ± 0.02	2.80
1_+	2.80 ± 0.02	2.80
3_-	5.14 ± 0.04	5.12

[a] The splitting, $2\Delta\nu$, represents the separation of the observed doublet for the 1_- and 1_+ lines and the separation of the two outermost components for the 3_- line.

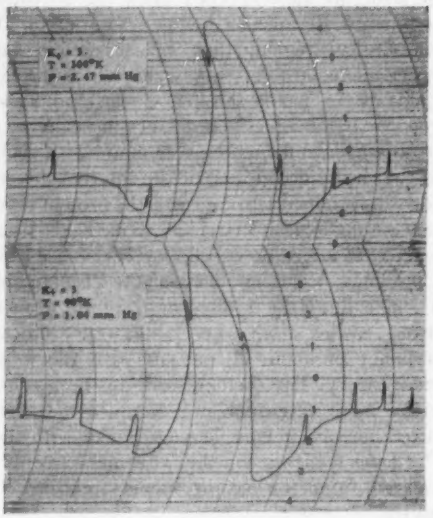

FIG. 3. Recording of the 3_+ line at room and at liquid air temperatures. Pressures are adjusted to give approximately equal line widths at the two temperatures. Small pips represent frequency markers.

[5] Burkhalter, Anderson, Smith, and Gordy, Phys. Rev. **79**, 651 (1950); Anderson, Smith, and Gordy, Phys. Rev. **87**, 561 (1952).

TEMPERATURE DEPENDENCE OF THE LINE BREADTH

The line breadth parameters for individual lines of the O_2 microwave spectrum have now been measured by three groups of investigators. Those measured by Anderson, Smith, and Gordy[5] and by Artmann and Gordon[6] are in good agreement, except that the former observers detected a decrease in the line breadth parameter with increasing N after the maximum of the Boltzmann distribution. This effect was attributed to the influence of rotational resonance on the line widths. One of the purposes of the present investigation is to gain additional information regarding the rotational resonance effect by shifting the Boltzmann maximum through cooling the sample. Another purpose is to obtain information about the other factors which significantly influence the line breadths.

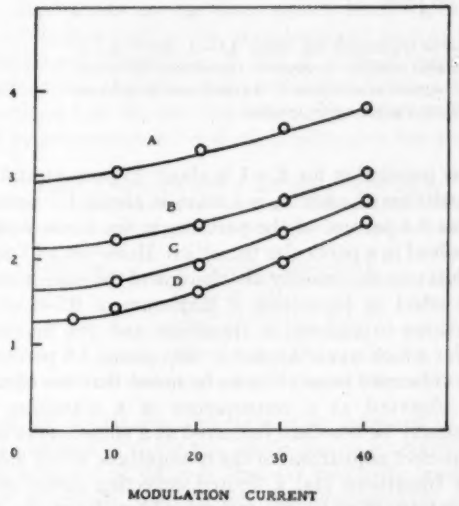

FIG. 4. Plot of measured widths for the 9_ line *versus* ac modulation current in ma. The pressures are, in mm of Hg, 2.62 for Curve *A*, 1.53 for Curve *B*, 0.84 for Curve *C*, and 0.45 for Curve *D*.

Figure 3 shows a line at both liquid air and at room temperature with the relative pressures adjusted to give approximately equal widths. To a first approximation, the observed shapes are second derivatives of the true line contours.[6] This approximation becomes better as the modulation amplitude is decreased. With the superimposed lattice of markers, the separation of the two minima was measured for several values of the modulating field, the lowest value being the lowest for which a usable line strength was obtainable. The mean value of $\Delta\nu$ for three runs at each modulation was plotted against the amplitude of the modulating field, and the best curve through these points was extrapolated to zero modulation, as shown in Fig. 4. This was done at four pressures. The "zero-field" values were then

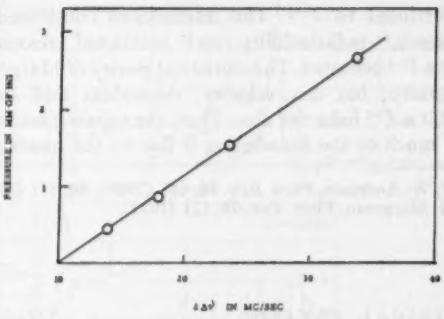

FIG. 5. Plot of zero-field line width, $2\Delta\nu$, *versus* pressure for the 9_ line. The slope yields $\Delta\nu = 4.55$ (Mc/sec) per (mm of Hg).

plotted against pressure, and the best straight line was drawn through the point. Figure 5 shows this plot for the 9_ line. The residual line breadth for zero pressure is due primarily to the broadening from the earth's magnetic field. The slope of the curve, however, is directly proportional to the line breadth parameter.

The results obtained are listed in Table II. The lines for N greater than 9 were so weak at liquid air temperatures that reliable measurements on them could not be obtained. Our results for room temperature are in good agreement with the earlier results of Anderson, Smith, and Gordy,[5] and the average line breadths of all the lines measured 1.95 (Mc/sec)/(mm of Hg) is in good agreement with the average obtained by Artmann and Gordon,[6] 1.94 (Mc/sec)/(mm of Hg). Furthermore, the variation of the line breadth parameter with temperature tends to confirm the contribution of rotational resonance to the line breadth noted by Anderson, Smith, and Gordy. The latter effect is revealed by the comparison of the line breadth ratios at liquid air with those at room temperature (Table II). This ratio increases consistently from the $K=9$ to the $K=5$ line. The $N=3$ and $N=5$ states are near the Boltzmann maximum at the temperature of liquid air, whereas at room temperature the Boltzmann maximum occurs near $N=11$.

The exponents of the temperature-dependence relation, $\Delta\nu/P = CT^{-x}$, given in Table II offer some insight into the broadening mechanism. Mizushima's theory[7] of oxygen broadening, based on a quadrupole-quadrupole interaction only, predicts that $\Delta\nu/P$ should be

TABLE II. O_2 line breadth data.

Line	$\Delta\nu$ in (Mc/sec) per (mm of Hg) $T=300°K$	$T=90°K$	$\frac{(\Delta\nu)_{T=90}}{(\Delta\nu)_{T=300}}$	x $(\Delta\nu = CT^{-x})$
1_	1.97	5.80	2.94	0.90
1+		5.63		
3+	2.07	5.77	2.80	0.85
5+	1.80	5.22	2.90	0.90
7-1	2.01	5.52	2.74	0.84
9_	1.94	4.55	2.35	0.76

[6] J. O. Artmann and J. P. Gordon, Phys. Rev. 87, 227 (1952).

[7] M. Mizushima, Phys. Rev. 83, 94 (1951).

proportional to $T^{-\frac{1}{2}}$. The interactions considered by Anderson,[8] polarizability and rotational resonance, show a T^{-1} behavior. The statistical theory of Margenau[9] is density, but not velocity, dependent and should exhibit a T^{-1} behavior also. Thus, the values found show that much of the broadening is due to the quadrupole interaction. The results of Beringer and Castle[10] for strong-field Zeeman transitions, in agreement with the present work, show temperature dependences between $T^{-\frac{1}{2}}$ and T^{-1}. From the knowledge at hand it seems that the quadrupole-quadrupole and the rotational resonance interactions are both important mechanisms in the broadening of oxygen absorption spectra.

[8] P. W. Anderson, Phys. Rev. **76**, 647 (1949); **80**, 511 (1950).
[9] H. Margenau, Phys. Rev. **76**, 121 (1949).
[10] R. Beringer and J. G. Castle, Jr., Phys. Rev. **81**, 82 (951).

PHYSICAL REVIEW VOLUME 93, NUMBER 5 MARCH 1, 1954

Some Observations of Double- and Triple-Quantum Transitions*

P. KUSCH
Columbia University, New York, New York
(Received November 16, 1953)

Data are presented which show that it is possible to observe transitions for which $\Delta J=0$, $\Delta m_J=\pm 2$ or ± 3 in a molecule characterized by a total angular J. It is also possible to observe transitions for which $\Delta F=0$, $\Delta m_F=\pm 2$ or ± 3 in an atom characterized by a total angular momentum F. In each case the process occurs by the absorption or stimulated emission of two or three equienergetic quanta.

CERTAIN experiments, to be described elsewhere, require the measurement of the frequencies of the lines resulting from the transitions $\Delta J=0$, $\Delta m_J=\pm 1$ in the ground, $^3\Sigma$, state of the O_2 molecule for several values of K, the rotational angular momentum. At low values of the magnetic field, all lines for a particular J value coincide, but at magnetic fields sufficiently high to require terms, quadratic in the field, for the representation of the energy levels, $2J$ lines may be expected to appear for each J value.

The observation of the indicated spectrum presents considerable difficulty. A molecular beam of O_2, issuing from a source of 77°K was detected on a Pirani gauge, and the total deflection of an indicating galvanometer was small. In addition, even at 77°K, a significant number of rotational levels is occupied and the population of each state is small. For example, the total population for $K=1$ is about 15 percent and the population of each J, m_J state is about 1.7 percent. Thus 3.3 percent of the particles in the beam may be involved in a particular transition. However, as Torrey[1] points out, the velocity distribution of the molecules has the effect of permitting a maximum of 0.766 of the particles to undergo a transition and the maximum effect which would appear is then about 2.6 percent of the refocused beam. It is to be noted that the effect to be observed as a consequence of a transition will generally be less than indicated as a consequence of an imperfect adjustment of the rf amplitude which induces the transitions and a limited deflecting power of the apparatus in which the transitions are observed.

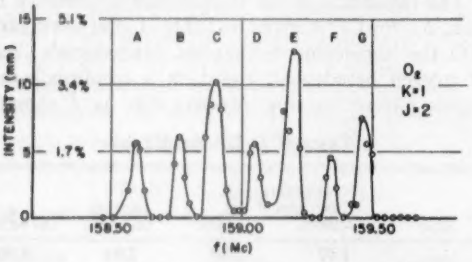

FIG. 1. The spectrum resulting from the transitions $\Delta J=0$, $\Delta m_J=\pm 1$ in the $^3\Sigma$ state of O_2 and for $K=1$, $J=2$ at a field of about 113 gauss. The intensity of the lines is given both as a fraction of the total beam and in absolute magnitude as measured on the apparatus.

In Fig. 1 is shown the spectrum resulting from the transitions which are nominally characterized by $\Delta m_J=\pm 1$ in the state $K=1$, $J=2$. It is at once seen that seven lines appear instead of the four predicted. Five of the lines (A, B, D, F, G) have an intensity of the order of that predicted for a single line, while two of the lines (C, E) have an intensity far greater than that predicted, beyond the range of experimental uncertainty.

We ascribe the observed spectrum to three processes: (1) the absorption or emission of a single quantum to give a transition for which $\Delta m_J=\pm 1$ (the lines A and G are produced by this process exclusively); (2) the absorption or emission of two equienergetic quanta to give a transition for which $\Delta m_J=\pm 2$ (the lines B, D, and F arise from this process); (3) the absorption or emission of three equienergetic quanta to give a transition for which $\Delta m_J=\pm 3$. The lines C and E result from

* This research has been supported in part by the U. S. Office of Naval Research.

[1] H. C. Torrey, Phys. Rev. **59**, 293 (1941).

the superposition of the single-quantum transitions (1) and the three-quantum transitions (3). To the extent to which the energies of the levels can be represented by terms which are linear and quadratic in the field,

$$W = am_J H + bm_J^2 H^2;$$

the lines are all equally spaced and the frequencies of the triple transitions are exactly coincident with those of the single transitions. It should be noted that the triple transition at a particular frequency involves neither of the levels in which the single transition at the same frequency arises, and hence a total intensity, approximately twice that of the single transition, may be expected when the triple transition occurs. Finally it should be noted that a four-quantum transition may contribute to the intensity of the line D.

That the structure of the spectrum does not result from an inhomogeneity of the magnetic field is indicated by observations on the lines arising in $K=1$, $J=1$. The two lines had, at the same magnetic field as that used for the observations in Fig. 1, a mean frequency of about 164 Mc/sec but the separation between them was about 1.50 Mc/sec. The lines had no close satellites, but by an increase in the rf amplitude a new line arising from the double-quantum transition appeared at the mean frequency of the two single-quantum transitions. The intensity of the new line was markedly sensitive to rf amplitude, and the line was unobservable when the single-quantum transitions still had a large intensity. The relative intensities of the lines arising in $J=2$ could also be modified by a change in the rf amplitude, where the lines B, D, and F were preferentially suppressed with decreasing amplitude.

TABLE I. Notation used in describing transition in the spectrum $\Delta F=0$, $\Delta m_F=\pm 1$, of K^{39}.

Line designation	Transition $(F,m \leftrightarrow F,m')$
α	$(2, 2 \leftrightarrow 2, 1)$
β	$(2, 1 \leftrightarrow 1, 0)$, $(1, 1 \leftrightarrow 1, 0)$
γ	$(2, 0 \leftrightarrow 2, -1)$, $(1, 0 \leftrightarrow 1, -1)$
δ	$(2, -1 \leftrightarrow 2, -2)$

An attempt was made to observe the transitions B, D, F as a single-quantum transition for which $\Delta m_J=\pm 2$ by application of an rf field of twice the frequency shown in Fig. 1. No evidence for the occurrence of the transition could be found and the possibility that a second harmonic of the oscillator produced the observed transition is thus excluded.

Since the observation and detailed analyses of the lines is made excessively difficult in the case of O_2 by the small beam intensity, further observations were made on the spectrum associated with the transitions $\Delta F=0$, $\Delta m_F=\pm 1$ in K^{39}. The spectrum was observed with an apparatus previously described.[2] In this apparatus the deflecting fields are very long; in addition the ratio of the gradient of the magnetic field and the field is high $[(\partial H/\partial Z)/H \cong 8]$. Accordingly, the field necessary to give particles with a moment of the order of a Bohr magneton an adequate deflection is sufficiently low so that potassium atoms are characterized by the quantum numbers F and m_F. In this quantization, for an atom with a spin of $\frac{3}{2}$ and in the $^2S_{\frac{1}{2}}$ state, atoms which have the same F but differ by 1 in m_F have moments which differ by $\frac{1}{2}\mu_0$. Hence it is possible to observe all transitions characterized by $\Delta F=0$, $\Delta m_F=\pm 1$. The length of the rf transition field was 2.5 cm. Since $I=\frac{3}{2}$ and the atom occurs in the $^2S_{\frac{1}{2}}$ state, $F=2$ or 1, and four lines appear in the state $F=2$ and two in $F=1$. Each of the two lines arising in $F=1$ forms a close doublet of separation $2g_I\mu_0 H/h$ with one of the lines in $F=2$. In all cases of interest here the doublet separation is much smaller than the natural width of the lines. The notation shown in Table I is used. The double-quantum transitions are designated as $(\alpha+\beta)/2$, etc.

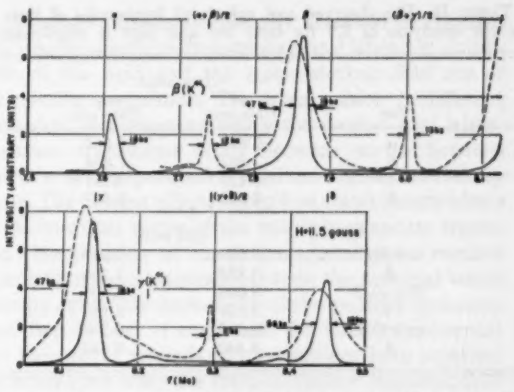

FIG. 2. The spectrum resulting from the transitions $\Delta F=0$, $\Delta m_F=\pm 1$ for K^{39}. The solid line shows the spectrum for low rf amplitude and the dotted line for high rf amplitude.

In Fig. 2 is shown the observed spectrum at a field of about 11.5 gauss for a low rf amplitude (solid line) at which the single-quantum transitions are characterized by their natural half-widths (~18 kc/sec) and the spectrum for a high rf amplitude (dotted line) at which the double-quantum transitions have become prominent. In Table II are given the frequencies of the single-quantum transitions at both low and high rf amplitudes and of the double-quantum transitions at high rf amplitude. It is possible to choose a value of 0.069456 for the field parameter x,

$$x=(g_J-g_I)\mu_0 H/h\Delta\nu,$$

such that the calculated frequencies of the single-quantum transitions at low amplitude and of the double-quantum transitions at high amplitude agree, within experimental error, with the observed frequencies. It thus appears that the double-quantum transitions

[2] P. Kusch and H. M. Foley, Phys. Rev. 74, 250 (1948); H. Taub and P. Kusch, Phys. Rev. 75, 1481 (1949).

TABLE II. The observed and calculated frequencies of lines in the spectrum of K^{39} for both low and high rf amplitudes.

line	obs f(Mc/sec)	calc f(Mc/sec)
	Low ampl.	
α	7.612	7.612
β	7.862	7.864
γ	8.139	8.141
δ	8.449	8.447
	High ampl.	
$(\alpha+\beta)/2$	7.739	7.737
β	7.852	7.864
$(\beta+\gamma)/2$	8.004	8.003
γ	8.129	8.141
$(\gamma+\delta)/2$	8.295	8.293
δ	8.440	8.447

do, in fact, occur at a frequency which is determined from the elementary theory of the energy levels at a known magnetic field. It is evident, however, both from Fig. 2 and the data of Table II that the single-quantum transitions at high rf amplitude are shifted downwards in frequency. The data in the table are given in the sequence in which observations were made. It is very improbable that the indicated discrepancies can be ascribed to a drift in the magnetic field. It is not clear from experimental data alone that the shift is wholly related to the increased rf amplitude, since data exist in which lines are badly distorted at high rf amplitude because of inhomogeneities in the magnetic field in which transitions occur.

The half-widths of all the single-quantum lines agree closely with the predicted width of 18 kc/sec. The double-quantum lines are conspicously narrower, of the order of 12 kc/sec. Substantially similar widths have been observed at a field of about 20 gauss, where, however, the existence of a shift cannot be established because of a field drift.

Observations have also been made of the three-quantum transition which can, of course, occur only in the upper ($F=2$) state. It can be shown from the usual expressions for the energy levels of the states that the frequency f_t of the triple transition and the frequency f_s of the single transition are related by

$$\delta=|f_t-f_s|=x^3\Delta\nu/16$$

to terms in H^3. Since $\Delta\nu=461.7$ Mc/sec, $\delta\cong 100$ kc/sec at $x\cong 0.15$, which corresponds to $H=25$ gauss. The lines should be resolved under these conditions. Figure 3 shows the three transitions $(\alpha+\beta)/2$, β, and $(\alpha+\beta+\gamma)/3$. The rf amplitude was so adjusted that the triple transition was of less than the maximum intensity. A small increase in rf amplitude increased the intensity of the line to about twice the indicated intensity with no significant increase in half-width. The dashes indicate a set of values for the line frequencies calculated directly from the energy level expressions where the frequency of the triple transition is used to determine the field. It is seen that the frequencies of the lines $(\alpha+\beta+\gamma)/3$ and $(\alpha+\beta)/2$ are very nearly consistent, while the line β is shifted to lower frequencies by about 50 kc/sec.

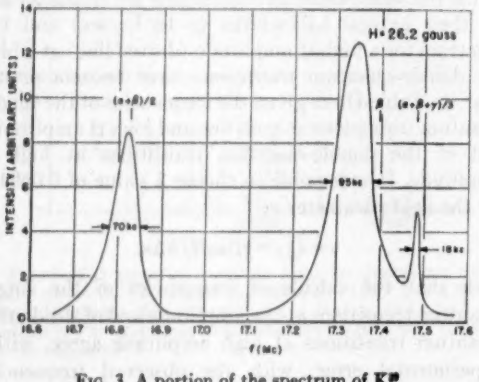

FIG. 3. A portion of the spectrum of K^{39} observed at a high rf amplitude.

The observations recorded in Fig. 3 have been repeated. In Table III are recorded the observed frequencies, in the order of measurement, of the lines β, $(\alpha+\beta)/2$, and $(\alpha+\beta+\gamma)/3$. The first and last measurement indicate the absence of any significant drift in the magnetic field. The data indicate that the double- and triple-quantum transitions at high amplitude have frequencies consistent with the single-quantum transition at low amplitude but that the single-quantum transition at high amplitude is shifted to lower frequencies by 50 kc/sec.

TABLE III. The frequencies of several lines in the spectrum of K^{39}.

Line	Rf ampl.	Obs f(Mc/sec)	Calc f(Mc/sec)	Half-width kc/sec
β	Low	17.168	17.168 (Assumed)	19.5
$(\alpha+\beta+\gamma)/3$	High	17.252	17.251	20
β	High	17.118	17.168	66
$(\alpha+\beta)/2$	High	16.610	16.612	40
β	Low	17.167	17.168 (Assumed)	27

It has not been possible to postulate any instrumental effect or observational procedure which would give rise to the indicated shifts. Particularly impressive are the widths of the single-quantum lines at low rf amplitude, which seem to preclude the existence of large inhomogeneities in the region of the magnet in which the transitions occurred. It is also remarkable, in Fig. 3, that the double-quantum transition with a width of 70 kc/sec is very nearly of the correct frequency relative to that of the triple-quantum transition, while the single-quantum transition with a width of 95 kc/sec is shifted to lower frequencies by 50 kc/sec. Nevertheless, the reality of shifts as atomic phenomena, not related to malfunctioning of the apparatus is not clearly established. The data here presented on the spectrum of potassium were made with a transition field not designed to produce a low and highly homogeneous

magnetic field and which, moreover, has a history which suggests the existence of a considerable and variable inhomogeneity. By the criteria of the data it appears that, by good fortune, the data were taken in a section of the magnet which was homogeneous at the time of the observations. Extensive efforts to obtain lines as narrow as those whose observation is here reported by subjecting the magnet to various magnetizing and demagnetizing procedures have been unsuccessful; ultimately it appeared that the efforts were misdirected, in the sense that even a successful effort would be a rare accident and would not have any inherent criterion of the quality of the field external to the data obtained by use of the field. Apparatus is now being constructed in which the field will have much better inherent properties.[3]

Hughes and Grabner report the occurrence of certain double-quantum transitions in the radio-frequency spectrum of RbF observed by the electric resonance method. These occur between two levels between which a single-quantum transition is also allowed in the presence of a static electric field. They correspond to the absorption or emission of two quanta, which may be equienergetic, whose total energy is equal to that of the single quantum ordinarily absorbed or emitted. The double-quantum transitions occur when the amplitude of the field and the static electric field are of comparable magnitude. The phenomenon is different from that here reported where the double- and triple-quantum transitions occur between states between which a single-quantum transition cannot ordinarily occur. The present effects depend on states intermediate to the terminal states of the multiple-quantum transition; the position of the intermediate states relative to equally spaced intervals between the terminal states strongly affects the probability of the multiple-quantum transition for any rf amplitude. On both experimental and theoretical grounds, the transitions here reported can occur even when the radio-frequency magnetic field has an amplitude small compared to the static field.

A discussion of the theory of multiple-quantum transitions and its application to the present data will be given by Mr. R. Salwen in a forthcoming paper. The theory predicts line widths which are in satisfactory agreement with those here reported. However, no satisfactory explanation of shifts of the order of those presently observed has been obtained.

I am indebted to Mr. Joseph Hendrie and to Mr. A. G. Prodell for their aid in taking the data of these experiments.

[3] V. Hughes and L. Grabner, Phys. Rev. 79, 314 (1950); 79, 829 (1950); 82, 561 (1951).

PHYSICAL REVIEW VOLUME 93, NUMBER 5 MARCH 1, 1954

A Determination of the Energy of Antimony-Beryllium Photoneutrons

RICHARD CULP AND BERNARD HAMERMESH
Argonne National Laboratory, Lemont, Illinois
(Received November 27, 1953)

The effective energy of Sb—Be photoneutrons has been measured by comparison of the transmission cross sections of five elements for the photoneutrons with previously measured cross-section values over a range of energies. The result placed the energy close to 25 kev.

INTRODUCTION

INTENSE gamma radiation from Sb^{124} falling upon Be^{9} provides a copious source of nearly monoenergetic neutrons,[1] and has been used extensively for activation cross-section determinations.[2,3] Degradation by various scattering processes in any source large enough to be useful poses the main difficulty in assigning the proper energy to the Sb—Be photoneutrons.[4] Several measurements by various methods and with different source sizes have been made,[1,5,6] with values being quoted from 25 to 35 kilovolts. The present work concerns the possibility of narrowing the limits of error in the stated energy by a comparison of transmission cross sections for Sb—Be photoneutrons with transmission cross sections measured with the Argonne electrostatic generator in the 20 to 40 kilovolt region.

The specific purpose of this research was to assign a more definite value to the energy of the neutrons from that photoneutron source used by Hummel, Hamermesh, and Kimball[2,3] in their activation cross-section work. A similar source was also used by others[1,4,7] in various experiments involving cross sections, energy, and abundance of Sb—Be photoneutrons. The energy value determined in this experiment will thus provide cross checks on these earlier data.

[1] A. Wattenberg, Phys. Rev. 71, 497 (1947).
[2] V. Hummel and B. Hamermesh, Phys. Rev. 82, 67 (1951).
[3] C. Kimball and B. Hamermesh, Phys. Rev. 89, 1306 (1953).
[4] Fields, Russell, Sachs, and Wattenberg, Phys. Rev. 71, 508 (1947).
[5] G. S. Klaiber and G. Scharff-Goldhaber, Phys. Rev. 67, 733 (1942).
[6] D. Hughes and C. Eggler, Phys. Rev. 72, 902 (1947).
[7] Russell, Sachs, Wattenberg, and Fields, Phys. Rev. 73, 545 (1948).

The method used was a determination of total cross section by transmission measurements of several pure metal samples. The energy was then determined as the intersection of the cross section *versus* neutron energy curve[8] with a constant cross-section line at the experimental cross-section value. Five elements were chosen for their rapid variation of cross section in the 20 to 40 kilovolt region.

It is to be emphasized that the use of this method does not constitute a fundamental measurement, and that the result is dependent upon both the errors in the Van de Graaff curve determinations and experimental errors in the present work. The assumption is made that reproducibility of the energy value from the five independent metallic samples would constitute sufficient evidence for an accurate energy determination.

DISCUSSION

In general, a transmission measurement determines the sum of the cross sections for all processes that attenuate a given beam. In the energy range of the Sb—Be photoneutron source, the absorption cross section for most elements is small in comparison with the total scattering cross section. For the purposes of this experiment, the transmission and scattering cross sections are assumed equal within the range of error of the method used.

In the ideal case a transmission experiment would consist of two measurements: an intensity determination with the detector having unrestricted view of the source, and an intensity measurement with the transmission sample completely hiding the source from the detector. For a beam of neutrons, the situation is usually complicated by the presence of a background arising from incomplete collimation. The effects of small angle and multiple scattering must also be considered.

The background may usually be quantitatively determined, but statistical difficulties are encountered if it represents a major fraction of the total count. It is for this reason that source sizes are chosen as large as possible consistent with good collimation. Theoretical determinations of the small angle scattering have been made.[1] The small angle scattered count results from those neutrons that are deflected by angles so small that they still reach the detector.

Multiple scattering is not correctable by any simple process. For this experiment, the transmission samples were designed to pass more than 60 percent of the beam, thus minimizing the probability of more than one collision per particle.

The use of an omnidirectional source allows two general methods of collimation. The beam may be defined by a system of slits or the uncollimated radial beam may be used with sample eclipsing the detector. Hibdon, Langsdorf, and Holland[8] used a collimated beam in their work with the Van de Graaff accelerator, while Wattenberg[1] chose the "infinite beam" method for his photoneutron sources.

The defining slits for moderately fast neutrons are necessarily massive. A combination of paraffin and cadmium is an effective neutron shield for this energy range. The paraffin slows the neutrons down by successive collisions to a point where cadmium presents a high absorption cross section to them. Such a paraffin-cadmium combination was used in this experiment.

APPARATUS

The threshold for the photoemission of neutrons from beryllium is 1.666 Mev.[9] Meyerhoff and Scharff-Goldhaber proposed 1.7 Mev as the energy of the hard gamma ray from Sb^{124}.[10] NBS-499 reports 1.75 Mev for the same gamma ray.[11] A calculation of the neutron energy from considerations of momentum and energy conservation is not practical since such a calculation would give the neutron energy from a theoretical dimensionless source and could not account for the self-degradation of any real source.

The physical makeup of the source used in this experiment is shown in Fig. 1. The aluminum cylinder containing nearly 100 grams of fused antimony was irradiated in the central thimble of the heavy water pile at Argonne for seven months. The 60-day activity was

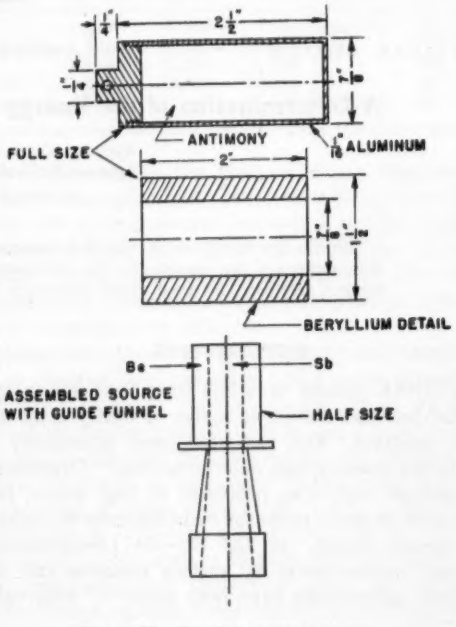

FIG. 1. Sb—Be photoneutron source.

[8] Hibdon, Langsdorf, and Holland, Phys. Rev. **85**, 595 (1952).

[9] R. C. Mobley and R. A. Laubenstein, Phys. Rev. **80**, 309 (1950).

[10] W. E. Meyerhoff and G. Scharff-Goldhaber, Phys. Rev. **72**, 273 (1947).

[11] *Table of Nuclear Data*, National Bureau of Standards Circular 499 (U. S. Government Printing Office, Washington, D. C., 1950).

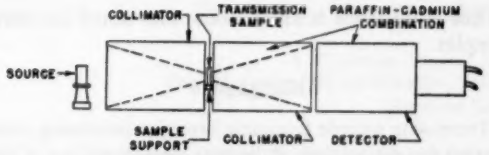

FIG. 2. Platform assembly for transmission measurements.

then about 90 percent saturated. The source was allowed to cool for two weeks after removal from the pile to eliminate possible interference from short-lived activities. The gamma activity at the start of measurements was 40 curies.

The intensity and high energy of the gamma-ray source necessitated remote handling. Upon removal from the pile, the source was strung with a length of wire leader and stored in a 1000-pound lead pot. All subsequent handling was accomplished by means of strings and pulleys from a distance of 50 feet. In practice, the antimony cylinder was pulled into the beryllium annulus through the aluminum funnel by means of a string passing axially through the assembled source.

The pulse ionization chamber used in these experiments was the so-called "long counter." Attached directly to the ionization chamber was a preamplifier designed to increase pulse size for transmission along the 50-foot cable to the final amplifier and scaler. The long cable was necessitated by the intensity of the gamma-ray source. The entire assembly (counter, paraffin thermalizer, and preamplifier) was assembled within a cylindrical aluminum case. A 0.120-in. layer of cadmium sheet shielded the detector from any thermal neutrons that might have been present. The pulse-height selector on the final amplifier was set to discriminate against gamma pulses. No counts from gamma rays resulted even when the 40-curie source was only 12 inches from the detector.

The paraffin-cadmium combination mentioned earlier was arranged as shown in Fig. 2. Two cylindrical paraffin collimators of the same outside diameter as the detector were placed between detector and source. All units were aligned axially by the framework that supported them. The collimators had conical apertures and were placed on the support frame with apexes adjacent. A small paraffin platform was molded on one collimator to support the transmission sample so that it completely covered the opening. The samples were placed by hand after the antimony source was lowered into the lead pot.

METHOD

The collimated beam method was chosen for this experiment for the reason that pure samples of the desired metals were not available in sizes large enough to blanket the detector to prevent it from seeing the source. It was considered desirable to use the same samples as had been used by Hibdon, Langsdorf, and Holland[8] in their transmission measurements. These samples were of various shapes and dimensions, but none was smaller than one inch square in the plane perpendicular to the neutron beam. Collimation by the paraffin cylinders, even in conjunction with the 0.120-in. cadmium shielding the counter, was not perfect. Those neutrons detected after being scattered and degraded by the collimator contributed to a latent counting rate analogous to background. Neutrons scattered by the walls of the room also contributed a fraction of this latent count, though this room scattering was reduced by supporting the transmission apparatus on a light framework 12 feet high in the center of a large quonset building.

The transmission cross sections of the various samples were measured relative to an already well established cross section. The "standard" used was carbon, the cross section of which is known to 1 percent and is independent of energy from 20 to 60 kev.[12] The transmission cross section of carbon is 4.55 barns in this energy region. By designing the carbon plugs to reproduce accurately the geometry of each sample both in transmission and transverse dimensions, it was possible approximately to duplicate the erroneous counts resulting from small angle and multiple scattering. The unknown counting rates arising from these processes in (1) the metallic sample and (2) the carbon duplicator, then canceled in the calculation of sample transmission.

Let N_0 = count observed with no scatterer in place (open beam), N_b = collimator and room scattered count, N_{tb} = true beam (N_0-N_b), N_c = count observed with carbon plug in beam (closed beam), N_s = count observed with metallic sample in beam, T_c = transmission of carbon plug (calculated using 4.55 b cross section), and T_s = transmission of sample. If the carbon plugs are machined so that T_c closely approximates T_s, then to determine the true beam:

$$\begin{aligned} N_0&=N_b+N_{tb},\\ N_c&=N_b+T_c(N_{tb}),\\ N_0-N_c&=N_{tb}(1-T_c),\\ N_{\text{true beam}}&=(N_0-N_c)/(1-T_c). \end{aligned} \tag{1}$$

Similarly, for sample transmission:

$$N_0-N_s=N_{tb}(1-T_s),$$

so that

$$1-T_s=\frac{N_0-N_s}{N_{tb}}=\frac{(N_0-N_s)\times(1-T_c)}{N_0-N_c}. \tag{2}$$

A set of readings consisted of (1) open beam, (2) carbon plug transmission, (3) sample transmission, and (4) open beam. Any run was discarded if the open beam reading varied more than 2 percent from (1) to (4). Each counting period was long enough to achieve 1 percent statistics. Instrumental background was less

[12] *A Compilation of Neutron Cross Sections*, U. S. Atomic Energy Commission Report AECU-2040 (Office of Technical Services, Department of Commerce, Washington, D. C., 1952).

than 1 percent of the lowest counting rate used. The cross section was then calculated from T_s.

One effect which has not been included in the calculations is the so-called hardening of the beam. If cross section decreases with increasing energy in a given region, the more energetic neutrons of the beam will tend to be transmitted more readily than the slower ones. The sample cross section would then appear to decrease with increasing sample thickness. By using samples of transmission greater than 60 percent this effect was reduced sufficiently so as not to affect our Sb—Be energy value.

The thickness of all samples and carbon plugs were machined to within 0.001-in. tolerance. The metals used and the number of samples of each were as follows: Ti (2), V(4), Mn (2), Co (1), and Ni (4).

RESULTS

The cross-section results and their corresponding energy values are given below, element by element. The original cross section *vs* energy curves, from reference 8, were used in order to determine the Sb—Be photoneutron energy.

Titanium

The thickest of the two samples of titanium available exceeded the arbitrary lower limit of transmission. It had a transmission of only 0.335. The cross section determined for this sample was 30.6 barns, 18 percent lower than the 37.2-barn value for the thinner sample. Considering the beam hardening involved, this difference is not excessive. The 37.2-barn cross section was used for the energy determination. (See Fig. 5, reference 8.) The result was 27.0 kev.[13] The other side of a resonance peak in the σ *vs* E_n curve made a value of 22 kev possible, though not probable, since the energy spread in the neutrons would normally blanket as narrow a dip between two resonances as appears in the curve for this metal.

Vanadium

The cross sections obtained from vanadium samples were in excellent agreement. They fell between 23 and 25 barns, which resulted in a 23- to 24-kev value for the neutron energy. (See Fig. 6, reference 8.) The cross-section values were close to a resonance peak. The constant cross-section line also intersected the curve at 19 kev. This value is much below that found for other samples.

Manganese

Increasing sample thickness brought decreasing cross section for manganese, indicating negative slope of the σ *vs* E_n curve at the point of intersection. Energy values on both sides of a resonance were possible. These values were 21 and 25 kev on the low- and high-energy side of the resonance. (See Fig. 8, reference 8.) The 25-kev value is favored in view of the negative slope.

Cobalt

Only cobalt powder was available in pure form. A sample consisting of a section of thin-walled aluminum tubing with end plates 0.001 in. thick was constructed. The density of the packed cobalt powder was determined as the average of six weight and volume determinations. The cross section was 16.7 barns, placing the energy at 28.5 kev or 32 kev. (See Fig. 7, reference 8.)

Nickel

No trend resulting from increasing thickness was indicated for the four samples of nickel metal. The cross sections varied from 19.9 to 22.7 barns, placing the energy at 22.5 kev (see Fig. 4, reference 8). The excellent reproducibility and well-resolved curve for nickel gave much weight to this energy value.[14]

CONCLUSION

The results indicate a probable energy spread of 20 percent or more in the neutrons from this Sb—Be photoneutron source. The average energy value is 24.6 kev. The complexity of possible errors is great enough to make a statement of the energy to closer than 4 kev unwise at this time, though the cross-section values determined in this experiment are accurate to 10 percent. It is proposed that a further study of the energy of this source be made after re-examination, with better resolution, of the variations of cross section *vs* energy. This project is now underway using the improved Argonne Van de Graaff accelerator.

ACKNOWLEDGMENTS

We wish to thank Dr. C. T. Hibdon and the members of the Van de Graaff group for the use of their original cross section *vs* energy curves.

[13] Results of a recent repetition of the cross section *vs* energy curve for titanium suggest an energy value for the Sb—Be photoneutron of 25.5 kev.

[14] Recent results for nickel revise the energy estimate downward to 20.5 kev.

The Half-Life of Yttrium-90

A. CHETHAM-STRODE, JR., AND E. M. KINDERMAN
Hanford Atomic Products Operation, General Electric Company, Richland, Washington
(Received November 5, 1953)

Radioactive yttrium-90 separated from two aged samples of fission product strontium was allowed to decay. The change in activity was followed for more than 650 hours with standard mica-window beta counters. From the observed changes, the mean half-life of yttrium-90 was calculated to be 64.60±0.43 hours.

THE half-life of yttrium-90 has been reported by a number of investigators.[1–5] The reported values fall in two sets, one at 61 hr, the other at 65 hr.

Lawson and Cork[1] first reported a half-life of 60.5±2 hr for yttrium-90, produced by deuteron bombardment of a sample of yttrium nitrate. This was confirmed by Bothe[2] who obtained a value of 61±1 hr for the decay of yttrium activity produced by neutron bombardment of yttrium oxide. Yttrium activity was isolated from among the spallation products from bismuth by Goeckermann and Perlman[3] who identified activities of 10-hr, 62-hr, and 57-day half-lives. The 62-hr activity was assigned to yttrium-90.

Nottorf[4] used strontium produced by uranium fission as a source of active yttrium. His measurements indicated a half-life of 65 hr for yttrium-90. More recently, Schott and Meinke[5] have isolated yttrium activities of 18 min, 3.5 hr, and 65 hr from $Zr(n,p)$ reactions. To resolve the discrepancy, a new determination of the yttrium-90 half-life was made.

Two separate samples of fission strontium-yttrium mixture furnished by the Isotope Division, U. S. Atomic Energy Commission, were used. The samples had aged for 18 months or more since their preparation. Separation and purification of the yttrium-90 daughter from the parent strontium-90 was by TTA (thenoyltrifluoroacetone) extraction. The original solution was buffered with acetate to a *p*H of 4.5 and contacted with 0.5*M* TTA in benzene. The organic phase was removed and contacted with a 0.01*M* HNO_3 solution. This cycle which has proven effective for the separation[6] was repeated four times, and an aliquot of the final aqueous phase was mounted for counting. Examination of the radiations of sample I with a beta spectrometer showed only the characteristic spectrum of yttrium. Counting for each sample was with separate standard mica-window beta counters. The response of the instruments was checked each day with uranium standards and all observed counting rates corrected for the day-to-day variations in response as well as for background activity.

Data for sample I were obtained by measuring the activity from the second-shelf position for 311 hours after separation; beginning at 237 hours and continuing until 743 hours, the activity of the sample was measured on the first shelf. The 15 determinations of activity on the second shelf gave a half-life of 64.57±1.3[7] hr, as determined by a least-squares treatment. The 16 determinations at the first-shelf position gave a value of 65.51±3.4 hr. These were combined to give a value of 64.70±1.2 hr. The total time the sample was under observation was 743 hr or 11.4 half-lives with no detectable deviation from linearity.

Sample II was counted at the second-shelf position only. For the first six determinations of activity (291 hr of decay or 4.5 half-lives) a total of more than 10^6 counts was observed for each determination. No deviation from linearity was observed for 673 hr (10.4 half-lives) at which time the experiment was discontinued. The half-life computed from these data was 64.59±0.59 hr. The weighted mean half-life of samples I and II is 64.60±0.43 hr.

[1] Stewart, Lawson, and Cork, Phys. Rev. **52**, 901 (1937).
[2] W. Bothe, Z. Naturforsch. **1**, 179 (1946).
[3] R. H. Goeckermann and I. Perlman, Phys. Rev. **76**, 628 (1949).
[4] Nottorf, Coryell, and Sugarman, *Radiochemical Studies: The Fission Products* (McGraw-Hill Book Company, Inc., New York, 1951), Paper No. 77, National Nuclear Energy Series, Plutonium Project Record, Vol. 9, Div. IV.
[5] G. L. Schott and W. W. Meinke, Phys. Rev. **89**, 1156 (1953).
[6] A. Chetham-Strode, Jr. (unpublished work).
[7] Precision figures are at the 95 percent confidence level.

Slow Neutron Resonances in Cesium, Palladium, and Gold*

H. H. Landon and V. L. Sailor
Brookhaven National Laboratory, Upton, New York

(Received November 25, 1953)

The slow neutron total cross sections of Cs, Pd, and Au have been measured with a crystal spectrometer using beryllium as a monochromator. A strong resonance was found in Cs at 5.90 ev. The strength of this resonance is $\sigma_0\Gamma^2=144\pm25$ barn ev^2 with $\sigma_0=9500\pm2000$ barns. Pd has a strong resonance at 34.1 ev with weaker ones at 26 and 13.3 ev. The 4.91-ev resonance in Au has been found to have unusual shape. If it is a single resonance, the maximum total cross section is $\sigma_0=31\,000\pm1000$ barns and the total width is $\Gamma=0.175\pm0.01$ ev.

I. INTRODUCTION

THE Brookhaven National Laboratory's crystal spectrometer[1] has been used to study the neutron resonance structure of cesium, palladium, and gold in the energy region from approximately 0.6 ev to 60 ev. Cesium was selected because it had not previously been run, and, on the basis of its large thermal cross section,[2] should have a resonance near thermal energy. Palladium was chosen because of the observation of a resonance by Goldhaber[3] by means of a resonance filter activation. Gold was examined as a continuation of the study of the well-known resonances in a series of elements used commonly as standard absorbers. The resolution that it is possible to achieve with this instrument warrants such a re-examination.

II. APPARATUS

The apparatus and technique of measurement with this instrument have been previously described.[1] When the spectrometer was first put into operation, it was pointed out[4] that a two percent energy discrepancy existed between the results of this instrument and those reported previously for a series of well-known resonances. Since the abstract[5] of a preliminary report of this work was published, the source of this discrepancy has been located. The energy scale is now in good agreement with that of other instruments,[1] and the energy values quoted in this paper supersede those of the preliminary abstract.

In the study of neutron resonances with the resolution available with this instrument, sample preparation becomes important. In general, several different sample thicknesses are necessary, each of which must be of high purity. The gold and palladium samples were in the form of foils, while the cesium samples were prepared as the iodide and the chloride. The gold, whose purity was better than 99.9 percent, was supplied by the J. M. Ney Company. One of the two palladium samples was a spectroscopically pure sample, purchased from the Jarrell-Ash Company. The other sample has been spectroscopically analyzed at this laboratory. The CsCl sample was a "spec pure" Johnson, Matthey and Company sample, the CsI, an A. D. McKay sample.

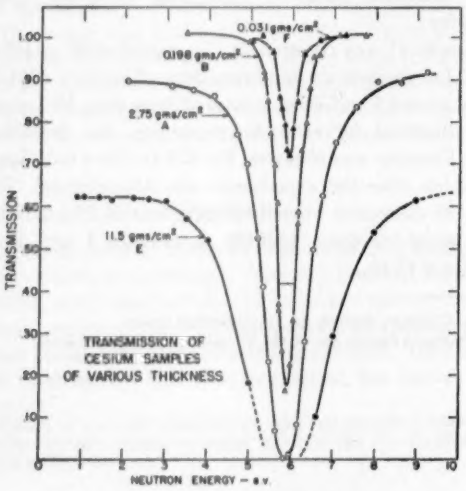

FIG. 1. Transmission *versus* neutron energy of various cesium samples.

III. MEASUREMENTS

Cesium

The initial cesium measurements consisted of a search from 0.6 ev to 20 ev for resonances, using a thick CsI sample. A single, strong resonance at 5.90 ev was found and the transmission data for four different sample thicknesses are shown in Fig. 1, corrected for the iodine and chlorine components. The total cross section is shown plotted in Fig. 2 in the region of the resonance. The instrumental resolution in this region is indicated by the lower triangle.

Since this resonance is an isolated,[6] single level in a monoisotopic element, an analysis in terms of the appropriate Breit-Wigner constants was attempted.

* Under contract with U. S. Atomic Energy Commission.
[1] L. B. Borst and V. L. Sailor, Rev. Sci. Instr. **24**, 141 (1953).
[2] Seren, Friedlander, and Turkel, Phys. Rev. **72**, 888 (1947).
[3] Goldhaber, Lowry, and Sunyar, Phys. Rev. **76**, 189 (1949).
[4] L. B. Borst and V. L. Sailor, Phys. Rev. **85**, 711 (1952).
[5] H. H. Landon and V. L. Sailor, Phys. Rev. **86**, 605 (1952).
[6] R. H. Rohrer, Phys. Rev. **87**, 177 (1952). (Rohrer has reported evidence of a level near 300 ev.)

The difficulties of such an analysis are severe because of the relatively poor resolution of the spectrometer at this energy. One can calculate an upper limit on the strength of this resonance if one assigns all of the observed thermal absorption cross section to this isolated resonance. This gives, using $\sigma_{abs}{}^{thermal}=29$ barns[7] and $E_0=5.90$ ev, a $\sigma_0\Gamma^2$ of 260 ev^2 barns. The evaluation[8] of $\int_{-\infty}^{\infty}(1-T)dE$, which is represented by the area under the transmission curve, was obtained for each of the thick samples after correction for a one percent second-order contamination. A small Doppler correction was also applied to the areas.[9] Difficulty in this measurement is apparent, however, when consideration is made of the contribution to the area of the nonresonant cross section.

An analysis, such as the one reported by Selove,[10] of the variation of the cross section in a region removed

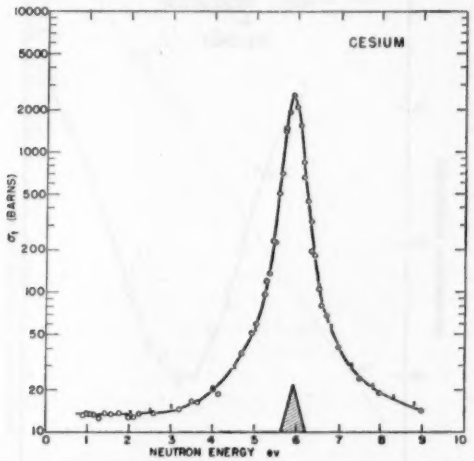

FIG. 2. Cesium total cross section near resonance; open circles are observed points; crosses are calculated using parameters in text.

from the resonance was attempted. This consisted of applying the one-level Breit-Wigner formula to points on the cross-section curve sufficiently far from resonance, so that the cross section could be considered to vary as

$$\sigma_t(E)=b+\left(\frac{E_0}{E}\right)^{\frac{1}{2}}\frac{\sigma_0\Gamma^2}{4(E-E_0)^2},$$

where b is the nonresonant contribution to the cross section and E_0 is the resonant energy. The cross section in this region is varying slowly enough to be essentially independent of spectrometer resolution. A least-squares adjustment of this equation to the data in the region from 3 to 5 ev and 6.5 ev to 7.5 ev then yielded the values shown in Table I.

TABLE I. Resonance parameters from wing data.

Energy (ev)	$\sigma_0\Gamma^2$ (barns ev^2)	b (barns)
3 –5	140	11.0
6.5–7.5	154	12.4

TABLE II. Cesium resonance parameters.

E_0	5.90±0.04 ev
σ_0	9500±2000 barns
Γ	0.12±0.02 ev
$g\Gamma_n$	$2.6\pm0.2\times10^{-3}$ ev
Σ_r	$3.0\pm0.3\times10^{-22}$ cm^2

With this approximation to b, better estimates of the resonant contribution to the area measurement could then be made. An average $\sigma_0\Gamma^2=144\pm25$ ev^2 barns was obtained. The error is estimated from the spread in results of the different methods.

The area measurement was then applied to the very thin CsCl sample and a value of $\sigma_0\Gamma=1170\pm150$ barns ev was obtained. If this is then combined with the $\sigma_0\Gamma^2$ from above, we obtain $\sigma_0=9500\pm2000$ barns and $\Gamma=0.12\pm0.02$ ev.

Finally, with this estimate for σ_0 and Γ, a least-squares adjustment of the data can be made to the Breit-Wigner equation, including resonant scattering and interference terms. The energy region chosen for adjustment was again such as to make the effect of resolution and Doppler broadening negligible. The value for the spin weighting factor, g, was taken as $\frac{1}{2}$. This is a sufficiently good approximation for this adjustment, since I, the spin of the target nucleus, is known to be 7/2. The potential scattering length associated with the resonant spin state was taken to be equal to the nuclear radius. The potential scattering cross section σ_p was taken to be 11 barns, which is 4 barns larger than that measured by Shull.[11] This discrepancy is probably due to the presence of a small amount of water in the CsI sample, but is not serious

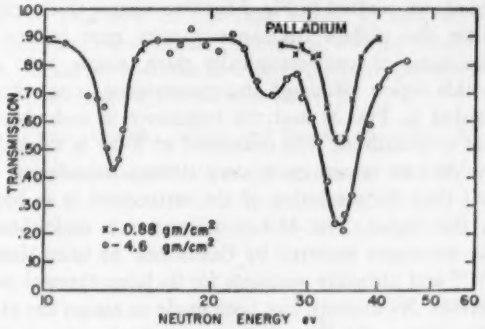

FIG. 3. Transmission of palladium samples.

[7] H. Pomerance, Phys. Rev. **83**, 641 (1951).
[8] W. W. Havens and L. J. Rainwater, Phys. Rev. **70**, 136 (1946).
[9] E. Melkonian, Phys. Rev. **90**, 362 (1953).
[10] W. Selove, Phys. Rev. **84**, 869 (1951).
[11] C. G. Shull and E. O. Wollan, Phys. Rev. **81**, 527 (1951).

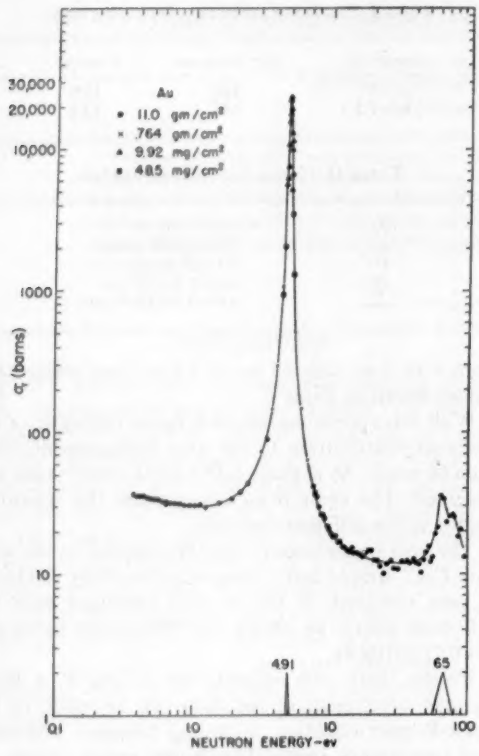

FIG. 4. Gold total cross section.

for the above adjustment. The curve drawn from the parameters resulting from this adjustment is shown plotted on Fig. 2, along with the observed points. A summary of the parameters for this resonance are given in Table II, along with associated derived parameters.

Palladium

Transmission measurements were taken in the usual manner with a thick Pd sample up to 50 ev. Three resonances were found at 13.3, 26, and 34.1 ev, and are shown plotted in Fig. 3 for two sample thicknesses. Since the 13.3-ev resonance is very near to one in platinum, a spectroscopically pure sample was run in this region (although the transmission is not shown plotted in Fig. 3) and the resonance is undoubtedly due to palladium. The resonance at 26 ev is weak, but the 34.1-ev resonance is very strong, considering the fact that the resolution of the instrument is so broad in this region. The 34.1-ev resonance is undoubtedly the resonance reported by Goldhaber[3] as being due to Pd^{108} and probably accounts for its large thermal cross section. No attempt has been made to assign the other two, since activation at these energies is not practical with this instrument and separated isotopes were not available.

Gold

The 4.91-ev resonance in gold has been widely used as a standard[12] and consequently has been widely studied. The level is very strong and is known to be isolated with the nearest observed level 60 ev higher in energy.[13] It was decided to reexamine this important resonance, however, in an attempt to verify the most recent choice[13] of Breit-Wigner parameters, particularly in view of the possible inconsistency of the level assignment with the capture gamma-ray study of Kinsey.[14] The resolution that can be achieved using the 2461 planes of a Be monochromator is higher than any previously used. These planes give a Bragg angle of ten degrees for the 4.91-ev neutrons at the center of the resonance. The resolution of the instrument at this

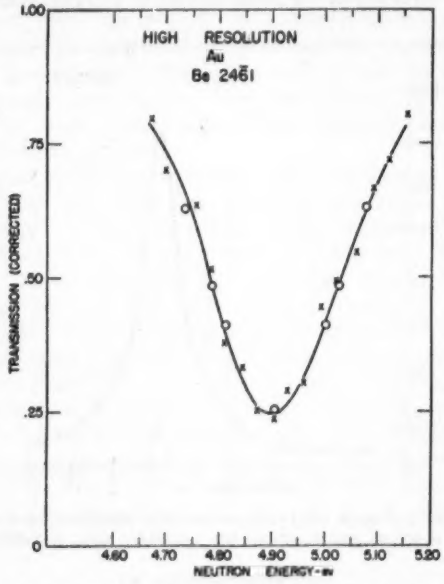

FIG. 5. Transmission of gold sample *H*, 19.8 mg/cm²; crosses are observed points; circles are calculated points using parameters in text.

angle is 2.5 percent, which corresponds to a resolution width of 0.125 ev.

Runs were made with several sample thicknesses and the results are shown plotted as cross section in Fig. 4. The peak of the low-energy resonance was run with three very thin gold foils. The results for sample *H*, the thickest of these, is shown in Fig. 5, plotted as transmission, corrected for a one percent second-order contamination in the monochromatic beam.

If the transmission at the resonance peak is plotted against sample thickness, as in Fig. 6, the slope of

[12] H. Pomerance, Phys. Rev. **77**, 747 (1950); Harris, Muehlhause, and Thomas, Phys. Rev. **79**, 11 (1950).
[13] J. Tittman and C. Sheer, Phys. Rev. **83**, 746 (1951).
[14] B. B. Kinsey, Can. J. Phys. **31**, 1025 (1953).

the resulting curve gives a lower limit to σ_0. This measurement is not independent of resolution or Doppler, but yields for σ_0 a value of 21 800 barns.

A shape analysis of the peak of the resonance using both a resolution and Doppler correction was then attempted, assuming the single level Breit-Wigner formula to apply, neglecting interference terms. The observed width of the line was 0.23 ev and the Doppler width was 0.050 ev, making both of the above corrections appreciable. The method of analysis used has been described by Sailor.[15] Seven points at the peak of the resonance, as observed with sample *H*, were chosen for adjustment, one at the exact peak and three on either side. (See Fig. 5.) The parameters which resulted

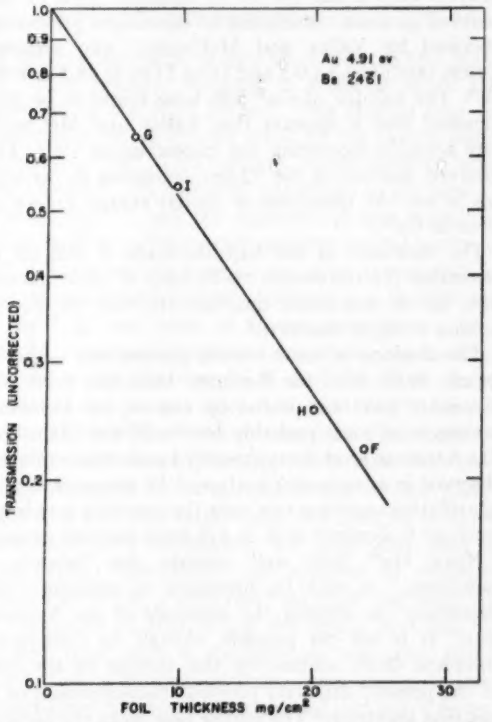

FIG. 6. Transmission *versus* gold foil thickness at 4.91 ev.

from this correction were $\sigma_0 = 31\,000 \pm 1000$ barns and $\Gamma = 0.175 \pm 0.01$ ev. The errors are estimated from the sensitivity of the adjustment.

[15] V. L. Sailor, Phys. Rev. **91**, 53 (1953).

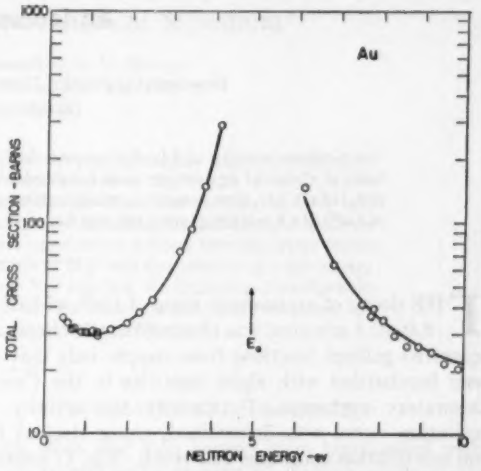

FIG. 7. Gold total cross section in wings of resonance; open circles are observed points; the curve is drawn from parameters obtained by the method of least squares.

The data in the wings of the resonance were then used to give an independent evaluation of the parameters. In the energy region chosen, the resolution and Doppler corrections are no longer important, but resonant scattering and interference terms must be considered in the Breit-Wigner equation. By making a least-squares fit of the data to the single-level formula, the curve of Fig. 7 is obtained. The parameters of the curve shown are $\sigma_0\Gamma^2 = 732$ barn ev^2, $\sigma_p = 10.7$, and $ag\Gamma_n = 1.17 \times 10^{-14}$ cm ev, where a is the scattering length of the resonant spin state. When these parameters are used to evaluate the total cross section at thermal energy, $E = 0.025$ ev, by extrapolation of the single level formula, approximate agreement with the value of 98 barns[16] is achieved. For this calculation the ratio of Γ_γ/Γ as obtained from the shape analysis was used.

There is, therefore, a different set of parameters needed to fit the peak of the resonance from that which fits the wings, if the one-level formula obtains. To resolve this discrepancy a better resolution than is practically available at this time might be necessary. It should be observed that the capture width Γ_γ of the line as calculated from the data near the peak is quite large for this region of the periodic table.[17]

[16] Carter, Palevsky, Myers, and Hughes, Phys. Rev. **92**, 716 (1953).

[17] J. Heidman and H. A. Bethe, Phys. Rev. **84**, 274 (1951).

An Isomeric State of Ga^{65}

BERND CRASEMANN*
Department of Physics, University of California, Berkeley, California
(Received September 28, 1953)

A positron activity of 8.0±0.5 minutes half-life has been assigned to an isomeric state of Ga^{65} on the basis of chemical separation, cross bombardments, and excitation curves. Gamma rays of 52±2, 92±4, and 114±4 kev were measured, which exhibited the 15-minute half-life of the previously known activity of Ga^{65}. No 8-minute gamma ray was found.

THE decay of an isomeric state of Ga^{65}, of half-life 8.0±0.5 minutes, was observed in the chemically separated gallium fractions from copper foils that had been bombarded with alpha particles in the Crocker Laboratory cyclotron. To identify the activity, its excitation curve was determined, using stacked foils and scintillation counting. The result (Fig. 1) indicates that the 8-minute activity, like the known 15-minute activity of Ga^{65}, is produced by an $(\alpha,2n)$ reaction on copper. It could, therefore, be due to Ga^{65} or Ga^{67}. Additional experiments showed that the 8-minute activity was produced by deuteron bombardments of zinc, but not by proton bombardments of zinc. Since Ga^{67} can be produced by the reaction $Zn^{67}(p,n)$, this possibility was eliminated and the 8-minute activity assigned to Ga^{65}.

A search for gamma rays connected with the decay of Ga^{65} was undertaken with a scintillation spectrometer and with a thick-lens beta-ray spectrometer, scanning for internal conversion electrons and for electrons ejected from a gold radiator. K conversion electron peaks were observed, associated with gamma energies of 52±2, 92±4, and 114±4 kev. Each of these peaks decayed with a half-life of 15 minutes. Two of the observed gammas correspond to transitions previously described by Valley and McCreary,[1] who assigned gamma rays of 53.8±0.5 and 117±1 kev to 18.5-minute Ga^{70}. The half-life of Ga^{70} was later found to be 20.3 minutes,[2] and it appears that Valley and McCreary were actually measuring the transitions in Ga^{65}. The observed half-life of the 92-kev transition shows that this is not the transition of similar energy known to occur in Ga^{67}.[2]

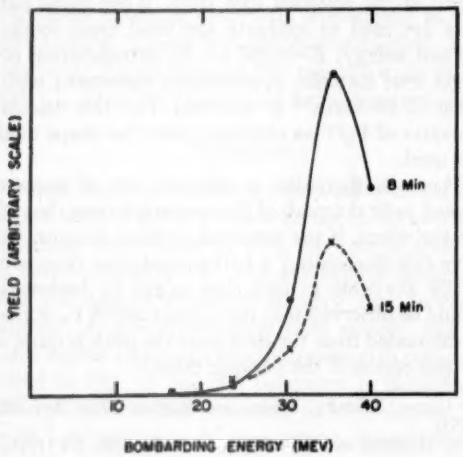

FIG. 1. Excitation curves for the production of 15-minute and 8-minute Ga^{65} in the alpha bombardment of copper.

The shortness of the half-life made it difficult to determine the conversion coefficients of these gamma rays, but it was noted qualitatively that the 52-kev gamma is highly converted.

The absence of an 8-minute gamma ray makes it appear likely that the 8-minute level lies below the 15-minute level and is fed by one of the 15-minute gamma rays, most probably by the 52-kev transition. The 8-minute level decays mostly by positron emission, observed in a trochoidal analyzer.[3] An excess of relative scintillation counting rate over the counting rate in the trochoid is ascribed to K x-rays from electron capture.

Since Ga^{65} falls well outside the "islands of isomerism," it may be necessary to consider "core isomerism" to explain the existence of the 8-minute level. It is not yet possible, though, to construct a complete decay scheme for this isotope on the basis of the present data and previous measurements of its positron spectrum.[4] The author now lacks the facilities for work on such short-lived activities and hopes that study of the decay of Ga^{65} will be continued elsewhere.

The writer wishes to thank Professor A. C. Helmholz for his interest in this work, and the staff of the Crocker Laboratory cyclotron for making the bombardments.

* Now at the University of Oregon, Eugene, Oregon.

[1] G. E. Valley and R. L. McCreary, Phys. Rev. **56**, 863 (1939).
[2] Hollander, Perlman, and Seaborg, Revs. Modern Phys. **25**, 469 (1953).
[3] B. Crasemann, Rev. Sci. Instr. **24**, 470 (1953).
[4] B. Crasemann, Phys. Rev. **90**, 995 (1953).

Gamma Rays from the Proton Bombardment of Sodium*

J. W. TEENER,† L. W. SEAGONDOLLAR, AND R. W. KRONE
Department of Physics, University of Kansas, Lawrence, Kansas

(Received October 22, 1953)

The yield of the (p,γ) capture process in Na^{23} has been studied for proton energies ranging between 0.85 and 1.70 Mev. Resonances were observed corresponding to excited levels of Mg^{24} at 12.71, 12.72, 12.79, 12.86, 12.90, 12.94, 12.97, 13.01, 13.02, 13.08, 13.10, 13.14, and 13.32 Mev. The energies of the γ rays emitted from the most pronounced resonances were measured by photographing the pulse-height spectrum obtained with a single crystal scintillation spectrometer. These experiments indicate two competing modes of decay: the radiative cascade decay leading to the ground state of Mg^{24} and the emission of a low-energy γ ray of energy 1.6 Mev which is attributed to the $Na^{23}(p,\alpha\gamma)$ Ne^{20} reaction. No single-step transitions to the ground state were found in the capture process. Both two- and three-step transitions are observed, but all except one of the γ-ray cascades lead to the well-known 1.37-Mev state in Mg^{24}.

INTRODUCTION

THE present paper is concerned with the first phase of a program designed to study in detail the properties of the Mg^{24} nucleus. This nucleus may be formed in a highly excited state by the proton bombardment of Na^{23}. Two different modes of decay have been reported: the radiative transitions to the ground state of Mg^{24} [1,2] and the emission of two α-particle groups leading to the ground and first excited states of Ne^{20}.[1,3] These reactions are known to be in competition with the elastic and inelastic scattering of the protons by Na^{23}.[3] At least some of the processes show a pronounced resonance structure[4,5] for proton bombarding energies ranging between 0.25 and 2.0 Mev. As a portion of the present work, states in Mg^{24} between 12.55 and 13.35 Mev were re-examined. The measurements have given more detailed information than previously reported. From a combination of the thick-target data and thin-target data, the energies of these states have been calculated. We have also used a single crystal scintillation spectrometer to measure the energies of the γ rays resulting from the decay of the compound nucleus. While the results that can be obtained from such a spectrometer are only semi-quantitative, the measurements were made to see whether the γ rays observed could be fitted into a decay scheme consistent with well-established results of other experiments.[6]

APPARATUS AND PROCEDURE

Both thick and thin targets were bombarded with protons from the University of Kansas electrostatic generator.[7] Considerable difficulties were encountered in trying to prepare thin targets free of contamination. Fluorine contamination in both the target backing material and in the targets themselves was never completely eliminated but was reduced to a low level. Tungsten was found to be the most satisfactory backing material. Thin sodium targets were prepared by two methods: by vacuum evaporation of sodium onto tungsten disks and by electrical heating of tungsten strips in an oxygen atmosphere. Sodium was found in the oxide formed by the last method. Gamma-ray yield curves obtained with the two types of targets revealed that evaporated targets could be made much thinner than the oxidized targets could be made. Such curves also revealed that resonance peaks attributable to the $F^{19}(p,\alpha\gamma)$ reactions[8] were more prominent with the evaporated targets than with the oxidized targets. As a consequence, most of the data were taken with oxidized targets at energy intervals of 5 kev. Those energy regions at which resonances were observed were than re-examined in steps of 1 kev with the use of the evaporated type of targets with which much better resolution could be obtained. Slices of sodium metal were used as thick targets. Whereas sodium carbonate, sodium hydroxide, and oxides of sodium were undoubtedly present in all targets, neither hydrogen nor oxygen (p,γ) resonances have been observed for proton energies less than 2 Mev, and any resonances resulting from carbon (p,γ) reactions should be easily recognizable.[9]

The γ rays were detected with a scintillation counter consisting of an RCA 5819 photomultiplier tube and a NaI(Tl) crystal in an Argonne-type[10] crystal mount.

* This work was supported in part by U. S. Office of Naval Research.

† Now at Naval Research Laboratory, Washington, D. C. Part of the material in this paper was submitted by J. W. T. to the University of Kansas in partial fulfillment of the requirement for the Doctor of Philosophy degree.

[1] Stehlson, Preston, and Goodman, Phys. Rev. **86**, 629 (1952).

[2] H. Casson, Phys. Rev. **89**, 809 (1953).

[3] Donahue, Jones, McEllistrem, and Richards, Phys. Rev. **89**, 824 (1953).

[4] R. L. Burling, Phys. Rev. **60**, 340 (1941).

[5] R. Tangen, Kgl. Norske Videnskab. Selskabs Skrifter, 1946, No. 1 (1947).

[6] For a review of the work done up to 1950, see D. E. Alburger and E. M. Hafner, Revs. Modern Phys. **22**, 373 (1950).

[7] A description of the electrostatic generator, its control and stability, will be published elsewhere.

[8] Chao, Tollestrup, Fowler, and Lauritsen, Phys. Rev. **79**, 108 (1950).

[9] F. Ajzenberg and T. Lauritsen, Revs. Modern Phys. **24**, 321 (1952).

[10] R. K. Swank and J. S. Moenich, Rev. Sci. Instr. **23**, 502 (1952).

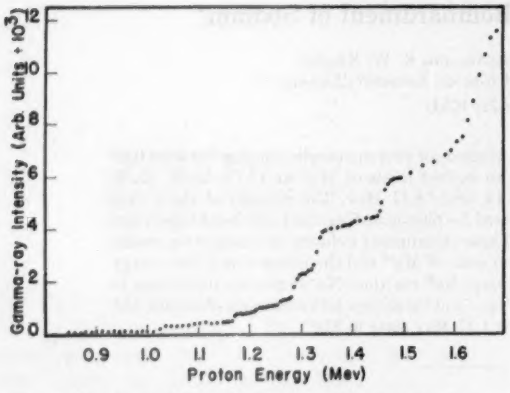

FIG. 1. The γ-ray yield observed when a thick sodium target was bombarded with protons.

The pulses from the photomultiplier were amplified with a linear amplifier, counted by a scale-of-32, and observed simulataneously on a driven-sweep oscilloscope.[11]

The γ-ray yield was measured as a function of proton energy for both thick and thin targets. Since the observed γ-ray yield was very highly dependent upon amplifier setting and the bias of the discriminator in the scaler, a procedure was adopted of counting pulses of height equal to or greater than those produced when a Cs^{137} source was placed near the detector. With this procedure, it was found necessary to shield the counter with several inches of lead in order to decrease the background caused by bremsstrahlung radiation from the electrostatic generator and by radiation induced by ions striking other than target atoms. Even with such shielding, the background radiation was sufficiently large to make it necessary to apply a background correction. The correction was obtained by intercepting the proton beam with a tantalum plate just ahead of the target. All γ-ray yields were normalized to equal numbers of bombarding protons. The relative numbers of protons per run were measured with a current integrator of the type developed by Gittings.[12]

The γ-ray spectrum resulting from the decay of the compound nucleus was obtained by photographing the pulse-height distribution observed on the oscilloscope. To prevent fogging of the film, all pulses smaller than those produced by the γ rays from Cs^{137} were rejected by adjusting the discriminator bias control on the X-axis sweep. This discrimination caused each pulse to appear to start slightly above the true base line. To facilitate the measurement of the pulse height, the edge-lighted grid furnished with this model oscilloscope was illuminated for about one second during each exposure. This procedure superimposed a rectangular coordinate system on all photographs. At the customarily used sweep speed of 1 cm/μsec, the pulses did not recover from overshoot during the 12-cm sweep. For the purpose of aligning the bottom of the coordinate grid with the base line of the pulses, pulses were observed visually at a reduced sweep speed of 0.01 cm/μsec, and the Y-position control of the oscilloscope was adjusted until the trace following the overshoot coincided with the bottom line of the grid.

Gamma-ray energies ranging between 700 kev and 18 Mev were observed. Care was taken that neither the linear amplifier nor the amplifier in the oscilloscope was ever used at such high gain that appreciable nonlinearity of pulse amplification resulted. Two different gain settings were used on the oscilloscope: one for observing γ rays of energy greater than 3 Mev, another for low-energy γ rays. During all runs the high voltage on the photomultiplier tube was maintained at 650 volts, and the linear amplifier gain was kept constant. A 1-cm thick NaI(Tl) crystal was used for the observation of the low-energy γ rays, whereas the high-energy γ rays were detected with a $1\frac{1}{2}$-in. thick crystal.

The system was calibrated by photographing pulse-height distributions corresponding to γ rays of known energy. Cs^{137} and Sb^{124} sources were used at low energies, whereas the γ rays resulting from the proton bombardment of thick targets of lithium and fluorine gave calibration points at high energy. In a typical run, Sb^{124} and Cs^{137} sources were placed, one at a time, near the γ-ray detector and calibration photographs taken for each source. These sources were then removed, and a fresh thin sodium target was bombarded at various energies with a proton beam of about 1 microampere for approximately 2 hours. The target chamber was then opened, and a tantalum calibration disk was inserted just ahead of the target. One side of the calibration disk had been treated with hydrofluoric acid, and a thick slice of lithium was pinned to the other side. Calibration photographs were taken while one side of the disk was bombarded with protons of about 1 Mev; then the disk was reversed, and a calibration was made with the other side in place. The calibration disk and the previously used sodium target were then removed from the target chamber and a fresh sodium target inserted. So that the effects of carbon deposits would be minimized, no targets were ever bombarded for more than two hours.

RESULTS

Gamma-ray yields were obtained as a function of proton bombarding energies varying between 0.85 and 1.70 Mev. Figure 1 shows the results obtained from a typical thick target. Figure 2 summarizes the work done with thin targets. The upper portion of the graph shows the γ-ray yield over the entire energy range as obtained with a target prepared by heating tungsten in an oxygen atmosphere. The individual resonance peaks shown in the lower portion are the results of experiments with very thin evaporated sodium targets. The thicknesses of these evaporated targets were calcu-

[11] Model 514D Tektronix.
[12] H. T. Gittings, Rev. Sci. Instr. **20**, 325 (1949).

lated by the method described by Fowler *et al.*[13] The area under each of several resonances was divided by the height of the corresponding step in the thick target curve. Such calculations were made for the resonances at 1164, 1284, 1330, and 1459 kev, and in each case the target thickness was found to be less than 500 ev.

The resonance peaks in Fig. 2 that are due to sodium are indications of excited levels in Mg^{24}. Since the target thickness was found to be negligibly small, the energies of the excited states in Mg^{24} can be calculated by the equation $E_e = 11.74 + (23/24)E_m$, where E_e is the excitation energy in Mev and E_m is the proton energy in Mev (in the laboratory system) at which a maximum occurs for the γ-ray yield.

The proton energies at which resonance maxima appear and the corresponding values of the excited states in Mg^{24} are listed in Table I. Also shown are the relative intensities of the resulting radiation and the width of the resonances at half-maxima. All values were read from the lower portion of Fig. 2. The two resonance peaks shown at 1.328 and 1.332 Mev on the lower curve may or may not be due to separate energy levels in the Mg^{24} nucleus. Resolution of the two peaks has been obtained only with this particular set of data and therefore must be considered very dubious. The small shoulder shown at 1.320 Mev is quite definite and has been reproduced many times. With the bias of the discriminator set to reject pulses due to photons of energy less than 2 Mev, a small peak is observed at 1.320-Mev proton energy and no peak is observed at 1.328 or 1.332 Mev.

The two peaks labeled *F* on each curve in Fig. 2 are very probably due to fluorine.‡ The proton energies at which these resonances occur, as well as the energy of the γ rays emitted, leave no doubt as to their identification. Pulse-height analysis of the γ-ray spectrum shows that part of the resonance structure above 1.6 Mev is also due to fluorine. In spite of the likelihood of carbon deposits on the targets, no evidence was found that any of the resonances observed could be attributed to carbon contamination.

TABLE I. The proton energies at which resonance maxima appear in the γ-ray yield curve obtained when Na^{23} was bombarded with protons, the corresponding values of excited states in Mg^{24}, the relative intensities of the radiation, and the width of the resonances at half-maxima.

Proton energy at resonance (Mev)	Energy of excited states of Mg^{24} (Mev)	Width at half-max (kev)	Relative peak height	Relative intensity (height × width)
1.009	12.71	4	1.5	6
1.020	12.72	6	1.5	9
1.094	12.79	10	0.8	8
1.164	12.86	4	4.1	16
1.212	12.90	4	3.1	12
1.256	12.94	4	3.6	14
1.284	12.97	8	7.1	57
1.320	13.01			
1.330	13.02	10	10.4	104
1.395	13.08	4	3.0	12
1.417	13.10	4	3.0	12
1.459	13.14	12	9.8	118
1.647	13.32	33	10.7	353

[13] Fowler, Lauritsen, and Lauritsen, Revs. Modern Phys. **20**, 236 (1938).

‡ *Note added in proof.*—Private communication with E. Goldberg, University of California, shows that recent $Ne^{20}(\alpha,\alpha)Ne^{20}$ data indicate we should obtain a sodium resonance near 874 kev. Further investigation here has shown that the first peak labeled *F* is primarily due to fluorine but is also partially due to a small sodium peak at 877 kev. Further details on this measurement will be included in a later paper.

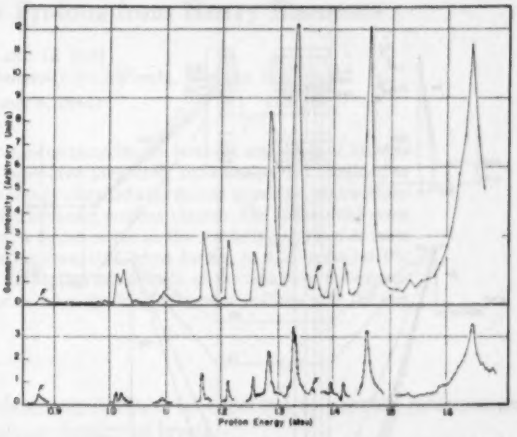

FIG. 2. The γ-ray yields observed when thin sodium targets were bombarded with protons. The upper yield curve was observed using targets prepared by heating tungsten sheet in an oxygen atmosphere. Sodium was found in the oxide layer thus formed. The lower yield curve was observed with use of targets prepared by vacuum evaporation of sodium onto tungsten backing material. The peaks labeled F are primarily the result of slight fluorine contamination of the targets.

Photographs of pulse-height distributions of the γ-ray spectrum observed at several of these resonances reveal that the compound nucleus decays by at least two different processes. Table II gives a summary of the results obtained from the present experiments. The occurrence of γ rays having energy of 1.6 Mev is undoubtedly the result of the well-known process $Na^{23}(p,\alpha)Ne^{20*}(\gamma)Ne^{20}$, whereas the high-energy γ rays observed at several of the resonances can only be understood by assuming transitions that lead ultimately to the ground state of Mg^{24}. With the experimental technique used, no precise determination of the γ-ray energies could be attempted. It was, however, possible to see whether a decay scheme could be established, assuming the existence of the energy levels in Mg^{24} that had been predicted from other experiments. Of those levels, the most accurately known occur at 1.37 and 4.14 Mev. Others have been shown to exist at 1.7, 5.5, 7.5, and 8.5 Mev, respectively.[6] Figure 3 shows an energy-level diagram of Mg^{24} in which the transitions consistent with the results of the present experiments are indicated. For completeness, the results obtained from other experiments are also included.

Many of the pulse-height distributions obtained showed the presence of a γ ray having energy of approximately 6 Mev. Such a γ ray can be attributed,

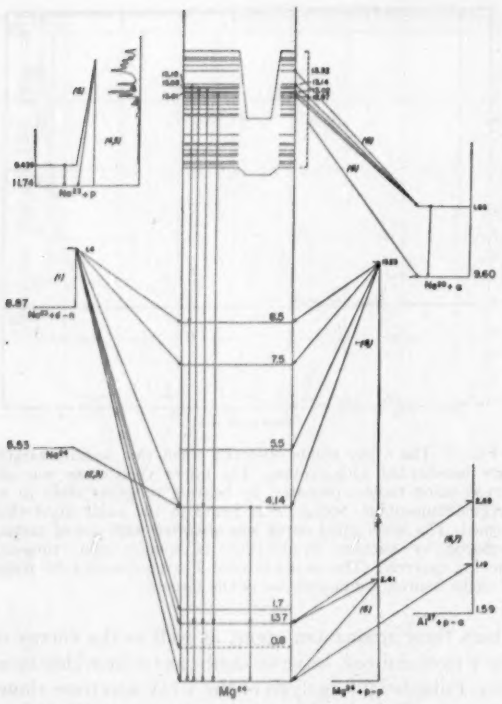

FIG. 3. Energy-level diagram of Mg^{24}. This energy-level diagram has been constructed using the results of the present work as well as published results of other investigations.§ The general form and notation are the same as that employed by F. Ajzenberg and T. Lauritsen, Revs. Modern Phys. 24, 321 (1952). The numbers in parentheses appearing in connection with several of the reactions refer to the following references: (1) C. E. Mandeville, Phys. Rev. 76, 436 (1949); (2) M. L. Wiedenbeck, Phys. Rev. 72, 429 (1947); (3) K. Siegbahn, Phys. Rev. 70, 127 (1946); (4) R. L. Burling, Phys. Rev. 60, 340 (1941); (5) R. Tangen, Kgl. Norske Videnskab. Selskabs Skrifter, 1946, No. 1 (1947); (6) Donahue, Jones, McEllistrem, and Richards, Phys. Rev. 89, 824 (1953); (7) Shoemaker, Faulkner, Bouricius, Kaufmann, and Mooring, Phys. Rev. 83, 1011 (1951); (8) H. W. Fulbright and R. R. Bush, Phys. Rev. 74, 1323 (1948).

within the limits of accuracy, to a transition from the 5.5-Mev state to the ground state of Mg^{24}. The failure to observe simultaneously a 7.5-Mev γ ray is not sufficient evidence to discount the possibility that the 6-Mev γ ray is emitted in a $Na^{23}(p,\gamma)$ process inasmuch as it is conceivable that it partakes in a many-step transition composed of several low-energy γ rays. The very large variation in intensity of this γ ray, obtained with different targets, left, however, little doubt that it was a result of fluorine contamination.

Examinations of many photographs of pulse-height distributions reveal that in no instance does there appear a one-step transition leading directly to the ground state of Mg^{24}. All the γ-ray cascades lead to the 1.37-Mev state with the exception of that from the 1.395-Mev resonance. For this resonance such a mode of decay is still apparent but much less intense than the two-step transition giving rise to the γ rays having energies of approximately 4.5 and 8.5 Mev, respectively. The results of investigations on the β decay of Na^{24} exclude the possibility of a single transition to the ground state from the 4.14-Mev state,[14] and therefore the alternative process indicated on the energy-level diagram is proposed.

It is of interest to note that in all those instances in which the (p,γ) process is operative there appears to be a conspicuous lack of short-range α particles leading to the first excited state of Ne^{20}. To be sure, there is some indication of the 1.6-Mev radiation at all the bombarding energies for which pulse-height distributions were taken, but the intensity is very low except at those particular energies at which this radiation is the only contributor to the resonances observed. This seems to suggest that the spins and parities of some of the compound states make this mode of decay from those states forbidden. With the information available no specific spin and parity assignments are possible. It is hoped that a more detailed study of the yield of the long- and short-range α particles and their angular distributions will lead to the additional information necessary for such assignments. Such a study is now in progress.

TABLE II. Summary of the results of γ-ray energy determinations. Column 1 lists the excited states in Mg^{24} for which γ-ray energy determinations were made. Column 2 lists the energies of the γ rays observed. In calculating these energies from the electron energies of the pulse-height spectrum, it was assumed that all pulses corresponding to electron energies greater than 5 Mev were due to the pair process. The lower-energy γ rays were observed as two peaks, one resulting from the photoelectric process, the other from the Compton process. The γ rays listed in parentheses were extremely weak and should be considered questionable. Column 3 shows the reaction giving rise to the most intense γ rays observed.

Energy of excited states in Mg^{24}(Mev)	γ-ray energies (Mev)	Dominant process
12.97	1.6	(p,α)
13.01	11.6; 1.37[a] (1.6)	(p,γ)
13.02	1.6	(p,α)
13.08	4.5; 8.5 (11.9; 1.37) (1.6)	(p,γ)
13.10	9.0; 2.76; 1.37 (1.6)	(p,γ)
13.14	1.6	(p,α)
13.32	1.6	(p,α)

[a] The energies of 1.37- and 2.76-Mev γ rays could not be determined to the accuracy indicated. The values given for these two energies are in accordance with determinations from other experiments.

We wish to thank Mr. R. K. Smith, Mr. D. H. Byers, Mr. R. A. Moore, and Mr. R. B. Smith for their assistance in much of the experimental work.

§ *Note added in proof.*—Errata in Fig. 3: The left-hand vertical decay line should start at 13.08 Mev. The third from the left verticle decay line should start at 13.10 Mev. See Table II.

[14] M. L. Wiedenbeck, Phys. Rev. 72, 429 (1947).

The Inelastic Scattering of 31-Mev Protons from Heavy Elements

R. M. EISBERG* AND G. IGO†
Radiation Laboratory, Department of Physics, University of California, Berkeley, California
(Received September 8, 1953)

Energy distributions, angular distributions, and total cross sections for the inelastic scattering of 31-Mev protons from four heavy elements, Pb, Au, Ta, and Sn, have been measured. Information was obtained at five scattering angles: 30°, 45°, 60°, 90°, and 135°. The energy distributions do not show the Maxwellian-like behavior which would be predicted on the basis of compound nucleus theory. The differential cross sections are strongly peaked forward, increasing by about a factor of ten as the scattering angle goes from 135° to 30°. The total cross sections all have values ranging from 0.25 barns for Sn, to 0.29 barns for Pb. A model has been proposed which is capable of giving a qualitative explanation of the results of the experiment. According to the model, the inelastic scattering occurs when the incident proton collides with the rim of a target nucleus.

I. INTRODUCTION

INELASTIC scattering of high-energy protons is a technique which has been used extensively in the past decade to investigate the energy structure of nuclei. The procedure involves bombarding thin targets of the element to be investigated with monoenergetic protons and, at some angle with respect to the incident beam, observing the energy distribution of the scattered protons.

When targets of low atomic number are used, the energy spectra of the scattered protons are usually found to consist of an elastically scattered group and several discrete groups of lower energy, corresponding to inelastic scattering.[1] In the center-of-mass system, the energy of the incident proton, less the energy of the inelastically scattered proton, must equal the energy absorbed by the target nucleus. Thus, from the observed laboratory energy spectrum of protons, one may infer information about the spectrum of energy levels of the target nucleus.

The density of energy levels of a nucleus, in the neighborhood of a particular excitation energy, increases as the excitation energy increases. Thus, at sufficiently high bombarding energies, it is found that the spectrum of the lower-energy inelastically-scattered protons is continuous (corresponding to excitation of the target nucleus to its continuum). Furthermore, as the atomic number of a nucleus increases, the average spacing of the energy levels of the nucleus decreases. Thus, using apparatus of moderate resolving power, one would expect that the observed energy spectrum of protons inelastically scattered from a heavy element would consist entirely of a continuous spectrum. The information that one would expect to obtain about the heavy elements from inelastic scattering, consequently, differs from that obtained about light elements. For the light elements, inelastic proton scattering provides the location of discrete energy levels—for the heavy elements, it could be expected to provide information about density of levels.

Most of the inelastic proton scattering experiments performed to date have used bombarding energies in the region of 4 to 8 Mev.[2–4] These experiments are limited to the investigation of the lighter nuclei in which the Coulomb barrier is lower than the bombarding energy. The Berkeley proton linear accelerator, which produces an intense, well-collimated beam of 31-Mev protons, is thus particularly well suited for inelastic scattering experiments with the heavy elements.

The results of several experiments involving the lighter nuclei, performed with 31-Mev protons, can be explained by the compound nucleus theory.[5,6] Consequently it would be reasonable to anticipate that the inelastic scattering of 31-Mev protons from heavy elements would also be a compound nucleus process. For such a compound nucleus process the energy distribution of inelastically scattered protons would be a Maxwellian (modified by the effect of the Coulomb barrier) corresponding to a temperature of the order of 1 Mev.[7,8] The angular distribution would be isotropic, and the total cross section would be very small because only protons in the high-energy tail of the Maxwellian distribution would be able to escape through the high Coulomb barrier of the heavy nucleus. On the other hand, any inelastic proton-scattering process in competition with the compound-nucleus process could easily dominate in this case since the compound-nucleus inelastic proton scattering cross section is so small.

The first experiments on the inelastic proton scattering from heavy elements were done several years ago at the Berkeley linear accelerator by Britten.[9] He observed the energy spectra of protons scattered at 90° from Pt and Pb. The observed energy spectra were

* Now at Brookhaven National Laboratory, Upton, New York.
† Now at Yale University, New Haven, Connecticut.
[1] E. H. Rhoderick, Proc. Roy. Soc. (London) **201**, 348 (1950). This paper contains an extensive bibliography of the earlier work on inelastic proton scattering from the light elements.
[2] Baker, Dodd, and Simmons, Phys. Rev. **85**, 1050 (1952).
[3] H. E. Gove and J. A. Harvey, Phys. Rev. **82**, 658 (1951).
[4] H. W. Fulbright and R. R. Bush, Phys. Rev. **74**, 1323 (1948).
[5] Levinthal, Martinelli, and Silverman, Phys. Rev. **78**, 199 (1950).
[6] S. N. Ghoshal, Phys. Rev. **80**, 939 (1950).
[7] V. Weisskopf, Phys. Rev. **52**, 295 (1937).
[8] L. Wolfenstein, Phys. Rev. **82**, 690 (1951).
[9] R. Britten, Phys. Rev. **88**, 283 (1952).

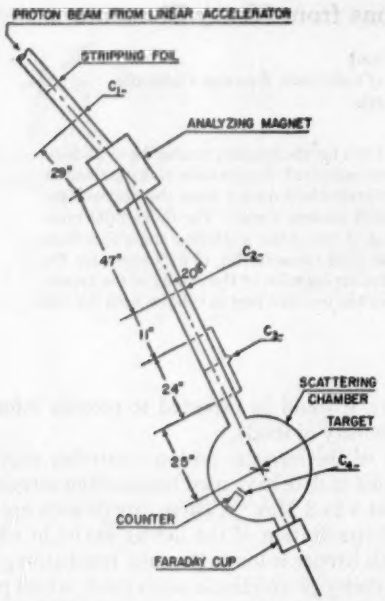

FIG. 1. Schematic diagram of the bombardment geometry.

not of the Maxwellian character predicted by compound nucleus theory, and the measured differential cross sections were at least an order of magnitude larger than the predictions of compound-nucleus theory.

The experiment reported in this paper is an amplification of an earlier experiment performed to confirm the results of Britten.[10] In the present experiment 30.6-Mev protons were scattered from four elements: Sn, Ta, Au, and Pb. Energy distributions of scattered protons were obtained, for each element, at each of six different angles: 15°, 30°, 45°, 60°, 90°, and 135°. The scattered protons were detected by a multiple-counter telescope consisting of three proportional counters and a sodium iodide scintillation counter. The detected particles traverse the three proportional counters, which obtain three samples of the particle's specific ionization and then stop in the scintillation counter, which measures their energy. By correlating the information obtained on the specific ionization with the measurement of the particle's energy, one is able to identify the mass of the detected particle.

II. EXPERIMENTAL TECHNIQUES

A. The Linear Accelerator

The Berkeley linear accelerator is ideally suited as a proton source for heavy-element inelastic scattering experiments. It produces a monoenergetic beam of 31-Mev protons confined to a very narrow bundle of small angular divergence. The beam is emitted in pulses of about 300 microseconds duration at a repetition rate of 15 cps. Thus, it has a very reasonable duty cycle (time "on" per second) of approximately $\frac{1}{2}$ percent. The available time-average beam, for the highly collimated geometry used, is of the order of 10^{-8} ampere, which is somewhat more than could be used in this experiment.

[10] R. M. Eisberg and G. J. Igo, Phys. Rev. 92, 537 (1953).

B. Bombardment Geometry

Figure 1 shows the geometry of collimators, target, counter, and Faraday cup as used in the experiment. The stripping foil consists of a $\frac{1}{4}$-mil aluminum foil which is inserted in the beam ahead of the analyzing magnet. Its purpose is to break up singly-ionized hydrogen molecules, which can be produced at about 16 Mev by the linear accelerator, into two 8-Mev protons which are then removed from the beam by the analyzing magnet. The collimator C_1 is used to control the beam current. It is generally set at about $\frac{1}{8}$ in. by $\frac{1}{8}$ in. After passing through the analyzing magnet, the beam is collimated roughly by C_2, which is set at about $\frac{3}{16}$ in. by $\frac{3}{16}$ in. Collimator C_3 consists of three carbon disks spaced one foot apart. The first disk has a $\frac{1}{8}$-in. hole; the second and the third have $\frac{3}{16}$-in. holes. The collimator is constructed so that the three holes are very accurately coaxial. The first disk gives the beam its final shape. The second and the third disks do not scrape the main beam but act as baffles to remove protons which are scattered from the edges of the first disk. Carbon is used in C_3 because its low Z gives a favorable ratio of stopping power to multiple Coulomb scattering and because its high (p,n) threshold makes it a poor source of background neutrons.

The targets consist of thin foils, $\frac{3}{4}$ in. high and $1\frac{1}{4}$ in. wide, placed at the center of the scattering chamber at 45° to the incident beam. The counter telescope may be set at any desired angle with respect to the incident beam. Particles scattered from the target are required to pass through one more collimator, C_4, before entering the detecting counters. This collimator, which determines the solid angle involved in the calculation of cross sections from the data, is mounted at the front of the counter telescope. It consists of a $\frac{3}{32}$-in. hole in a steel plate at $5\frac{11}{16}$ in. from the center of the target. This defines the solid angle to be 2.13×10^{-4} steradian. To monitor the beam passing through the target, a Faraday cup is mounted on the exit port of the scattering chamber. The Faraday cup, the scattering chamber, and the pipe containing the collimators are all evacuated.

C. The Scattering Chamber

Figure 2 shows a schematic diagram of the scattering chamber. The evacuated volume consists of a circular cylinder 2 ft in diameter and 1 ft high. The incident beam passes through the chamber eight inches above the base. The counters are mounted on a circular table which is capable of rotating through 360° and is driven by a motor. Along the vertical axis of the cylinder is a shaft which supports a frame which can hold eight

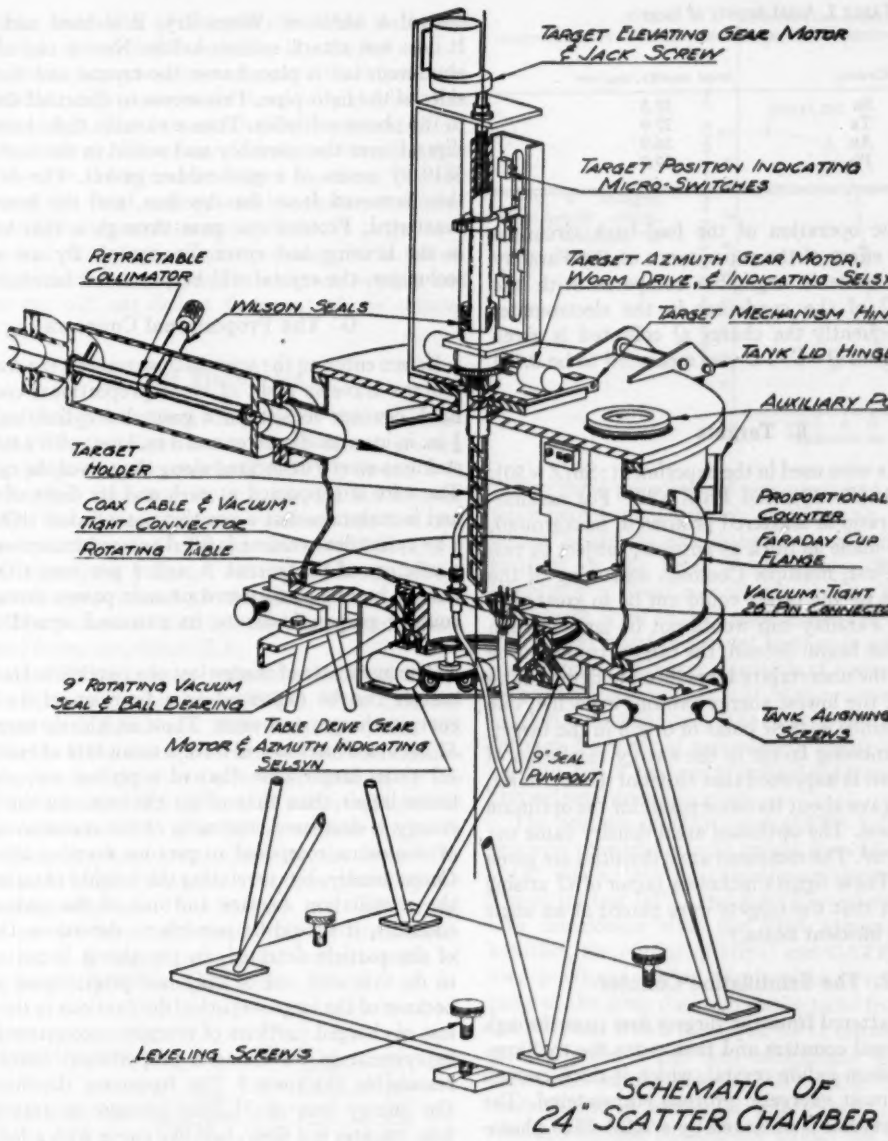

FIG. 2. Schematic diagram of the 24-in. scattering chamber.

targets. Motors drive the shaft up and down and cause it to rotate. The azimuthal and vertical location of the target holder and the azimuthal position of the table are indicated at the remote control panel by a system of selsyns and microswitches. The scattering chamber may be evacuated to a pressure of the order of 10^{-5} mm of Hg by means of a self-contained pump unit.

D. Beam Integration

The beam passing through the target was collected in a Faraday cup mounted on the exit port of the scattering chamber. So that secondary electrons might be prevented from escaping from the Faraday cup, two large Alnico horseshoe magnets were placed to provide a transverse field of several hundred gauss over the surface of the cup struck by the beam. A second pair of magnets placed in front of the Faraday cup served to prevent any electrons that might be in the beam from entering the cup.

The charge collected on the Faraday cup was measured by a feed-back integrating electrometer. The feed-back voltage V is applied to a recording

TABLE I. Areal density of targets.

Element	Areal density, mg/cm²
Sn	37.5
Ta	27.9
Au	36.9
Pb	39.2

voltmeter. The operation of the feed-back circuit is such that the effect of the capacitance of the Faraday cup and the cable is negligible compared with the capacitance C of the condenser in the electrometer circuit. Consequently the charge Q collected is given by the expression $Q=CV$. C was measured to be 0.101 microfarad.

E. Targets

Four targets were used in the experiment: Sn($Z=50$), Ta($Z=73$), Au($Z=79$), and Pb($Z=82$). For maximization of the ratio of scattered protons to background, the foils were made as thick as possible, subject to two restrictions. First, multiple Coulomb scattering of the incident beam by the target could not be so great that the available Faraday cup would not be large enough to intercept the beam. Second, the targets could not be so thick that the uncertainty introduced in determining the energy of the lowest energy protons expected, due to the uncertainty in their point of origin in the target, was the determining factor in the energy resolution of the experiment. It happened that either of these criteria, taken alone, gave about the same result for the optimum target thickness. The optimum areal density came out to be 40 mg/cm². The measured areal densities are given in Table I. (These figures include a factor of $\sqrt{2}$ arising from the fact that the targets were placed at an angle of 45° to the incident beam.)

F. The Scintillation Counter

Protons scattered from the targets first pass through the proportional counters and then enter the thallium-activated sodium iodide crystal, which is thick enough to stop the most energetic protons encountered. The scintillation crystal is observed by a RCA 5819 photomultiplier tube.

The greatest difficulty in using sodium iodide as a scintillator arises from the fact that it is deliquescent. For the purpose of overcoming this difficulty, the following technique was used. A stubby quartz light pipe in the shape of a truncated cone is cemented, in optical contact, to the face of the 5819 photomultiplier. In a dry box, the sodium iodide crystal is cleaved to the shape of a cube, approximately $\frac{3}{4}$ in. on an edge. The crystal is then cemented, in optical contact, to the flat face of the light pipe with a cement known as Bonding Agent R-313 (made by Carl H. Biggs Company, Los Angeles, California). This cement is ideal for the purpose. It dries in several hours after the addition of a hardener. When dry, it is hard and clear. It does not attack sodium iodide. Next a cap of $\frac{1}{4}$-mil aluminum foil is placed over the crystal and the slant sides of the light pipe. This serves to direct all the light to the photomultiplier. Then a vacuum tight housing is slipped over the assembly and sealed to the end of the 5819 by means of a gum-rubber gasket. The device is then removed from the dry box, and the housing is evacuated. Protons can pass through a thin window in the housing and enter the crystal. By use of this technique, the crystal will be preserved indefinitely.

G. The Proportional Counters

Before entering the scintillation counter, the scattered protons traverse a set of three proportional counters. Each counter consists of a grounded cylindrical shell, $\frac{3}{4}$ in. in internal diameter and 3 in. long, with a 0.003-in. stainless-steel wire located along the axis of the cylinder. The wire is supported at each end by disks of Teflon and is maintained at a positive potential of 1800 volts. The cylindrical volume is filled to one atmosphere with a mixture of 96 percent A and 4 per cent CO_2. The narrow bundle of scattered protons passes through the counter perpendicular to its axis and straddling the wire.

The mean rate of energy loss of a particle in traversing matter can be expressed as a function of its kinetic energy, charge, and mass. Thus, at kinetic energies of 31 Mev, a deuteron will have a mean rate of energy loss 1.7 times larger than that of a proton and about 25 times larger than that of an electron. As the kinetic energy is decreased, the ratio of the mean energy loss of deuterons compared to protons remains about 1.7. Consequently, by correlating the heights of pulses from the scintillation counter and one of the proportional counters, it should be possible to determine the mass of the particle detected. In practice it is not possible to do this with use of only one proportional counter because of the large statistical fluctuations in the energy loss of charged particles of energies encountered in this experiment in traversing a proportional counter of a reasonable thickness.[11] The frequency distribution of the energy loss of 31-Mev protons in traversing a $\frac{3}{4}$-in. counter is a skew, bell-like curve with a full width, at half-maximum, of about 50 percent and with a very pronounced tail extending to the high energy losses.[12] This distribution (in particular, the presence of the tail) is too broad to allow adequate resolution of protons and deuterons. However, by use of three proportional counters to sample the ionization of the particle three times, it is possible to achieve a much more accurate estimate of the mean ionization of the particle. This information is treated by sending the three proportional counter pulses into a circuit which selects the smallest pulse. The output of this circuit is then used to represent

[11] B. Rossi, *High Energy Particles* (Prentice-Hall, Inc., New York, 1952), p. 29.
[12] Igo, Clark, and Eisberg, Phys. Rev. 89, 879 (1953).

the mean ionization of the particle. This method is described in detail elsewhere in the literature.[13]

The three proportional counters are machined from a solid block of brass and are evacuated and filled from a common port. The entrace window is a ¼-mil Al foil, ⅛ in. in diameter. There are no foils between the first and second or the second and third counters. The exit window of the third counter and the entrance window of the scintillation counter are sufficiently larger than ⅛ in. so that multiple Coulomb scattering, of the lowest energy particles detected, in the entrance window and counter gas will not deflect them out of the counter telescope.

H. The Electronics

Figure 3 shows a block diagram of the electronic setup used in the experiment. The detected protons traverse proportional counters (PROP) 2, 3, and 4 in succession and then stop in the scintillation counter (XTAL). The pulses from the counters are first fed into shorted delay line clipping units (CLIP) which provide rectangular pulses, 1 microsecond long, whose heights are proportional to the size of the counter pulses. The pulses are then sent through preamplifiers (PA) and linear amplifiers (LA).

The scintillation counter pulses are fed into a one-channel pulse-height analyzer (PHA). This unit has two outputs: integral and differential. A pulse will appear in the integral output whenever the scintillation counter pulse is higher than a level determined by the lower discriminator. The differential output will deliver a pulse whenever the scintillation counter pulse is higher than the level determined by the lower discriminator and lower than the level determined by the higher discriminator. The integral and differential outputs are fed into units containing a discriminator and a circuit giving a rectangular output pulse of variable length (DISC and GATE).

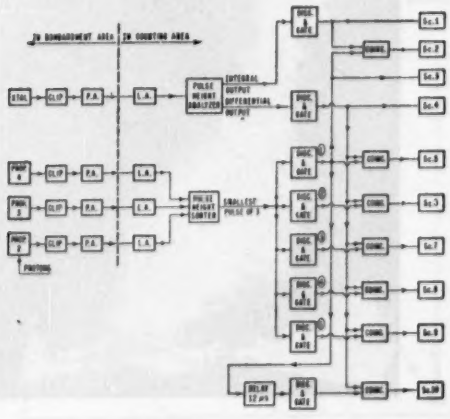

FIG. 3. Block diagram of the electronics.

[13] G. Igo and R. Eisberg, Rev. Sci. Instr. (to be published).

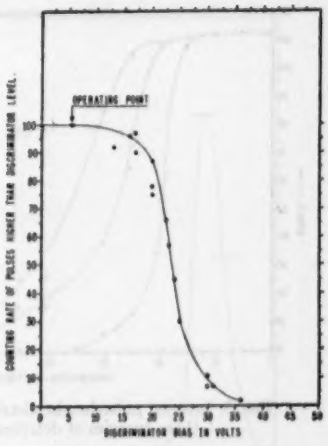

FIG. 4. Integral pulse-height distribution plateau of energy losses.

The three proportional counter pulses are fed into a pulse-height sorter which provides an output pulse whose height is proportional to the height of the smallest of the three input pulses. This device is essentially a Rossi coincidence circuit. The output of this circuit is fed to the inputs of five DISC and GATE units. Unit number 1 is set so that it will produce an output pulse whenever a particle of ionization equal to, or greater than, that of a 31-Mev proton traverses the proportional counters. The discriminators of unit 2 through 5 are set at successively higher levels and are used to run a five-point pulse-height analysis on the proportional counter pulses.

The outputs of DISC and GATE 1 through 5 are put into coincidence with pulses from the PHA differential output in the coincidence circuits (COINC). The output of DISC and GATE number 1 is also put into coincidence with the PHA integral output. In addition, the output of DISC and GATE number 1 is used to trigger a delay circuit which in turn produces a pulse of the same duration as the pulse from DISC and GATE 1 but which is delayed by 12 microseconds. This delayed pulse is put into coincidence with the PHA differential-output pulse and is used to determine the contribution of accidental coincidences to the counts recorded by the coincidence circuit fed by the PHA differential output and the output of DISC and GATE 1. Finally the unmixed differential and integral PHA counts are recorded as well as the counting rate of DISC and GATE 1.

The operation of this circuitry will be further explained in the following sections.

I. Proportional Counter Plateaus

The DISC and GATE number 1 is set so that it will produce an output pulse whenever a heavily ionizing particle traverses the three proportional counters. To do this, the counter telescope is set at some forward angle, where most of the particles entering the telescope are elastically scattered protons. The pulse-height

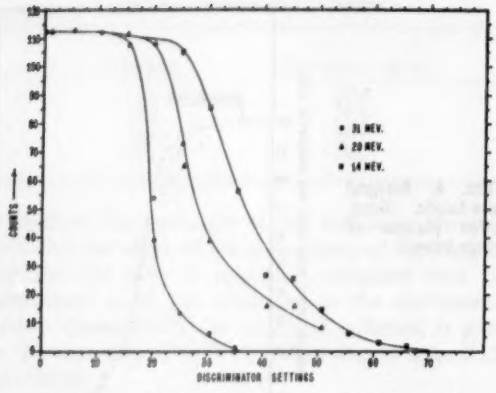

FIG. 5. Integral pulse-height distribution plateaus for three energies of detected particles.

analyzer is set so that it will produce a pulse in its differential output channel when an elastically scattered proton enters the counter telescope. The counting rate of the output pulses of the coincidence circuit fed by DISC and GATE 1 and the PHA differential output is measured as a function of the bias on the discriminator of DISC and GATE 1. When the beam intensity is kept at a reasonable level, a sharply rising plateau is obtained, such as is shown in Fig. 4. This curve, when differentiated, gives the frequency distribution of pulse heights due to 31-Mev protons from the circuit which selects the smallest of the three proportional counter pulses. The derivative is a Gaussian-like curve with a full width at half-maximum of about 30 percent, which is appreciably narrower than what would be obtained using only one counter. The bias of DISC and GATE 1 is set so that the coincidence rate is well up on the plateau, as indicated in Fig. 4. The unit will then produce a gate whenever a 31-Mev proton traverses the proportional counters. Since the specific ionization of a particle increases with decreasing energy and increasing mass, DISC and GATE 1 will also produce a gate whenever a lower-energy proton or deuteron traverses the proportional counters.

III. EXPERIMENTAL RESULTS

A. Search for Deuterons

At each setting of the pulse-height analyzer, corresponding to a particular energy of the detected particles, the biases of the five DISC and GATE units were set at progressively higher levels so as to obtain an integral pulse-height analysis on the ionization pulses. The presence of deuterons would then be distinguished by the presence of a double-step plateau.

Figure 5 shows ionization pulse plateaus for particles of 31 Mev, 20 Mev, and 14 Mev, from a lead target at 60°. The knees of the plateaus can be seen to fall at a pulse height which is inversely proportional to the energy of the particles. Since at 31 Mev all the particles must be protons, then the other plateaus must be due primarily to protons with no large contamination of deuterons. Five-point discriminator plateaus were run on each two-Mev energy channel for each element, at each angle. No deuterons were observed from any of the elements in large numbers. Any peaked distribution of deuterons would have been observed; and if the deuterons were distributed uniformly at all energies, they must not represent more than about 10 percent or 15 percent of all particles counted.

As a qualitative check on the identification of the particles, a photographic method was employed to determine the mass of the particles. The specific ionization is proportional to the ratio of the mass to the energy, so the product of the scintillation counter pulse height and the smallest pulse height of three proportional counter pulse heights is proportional to the mass of the particle. The pulses from the counters were displated on the verticle and horizontal plates of an oscilloscope. The oscilloscope beam was gated on by the proportional counter pulse. This gave a dot of light each time a particle traversed the counter telescope, whose abscissa is proportional to the ionization and whose ordinate is proportional to the energy of the particle. Particles of different masses should fall on separate hyperbolas. Figure 6 shows some of the film data. The elastically scattered protons fall in the prominent spot. No large number of particles lie off the proton hyperbola.

B. Energy Spectra

Figure 7 shows a typical energy spectrum—lead at 90°. The abscissa is particle energy, corrected for window absorption, and the ordinate is counting rate. The large peak at 31 Mev contains the elastically

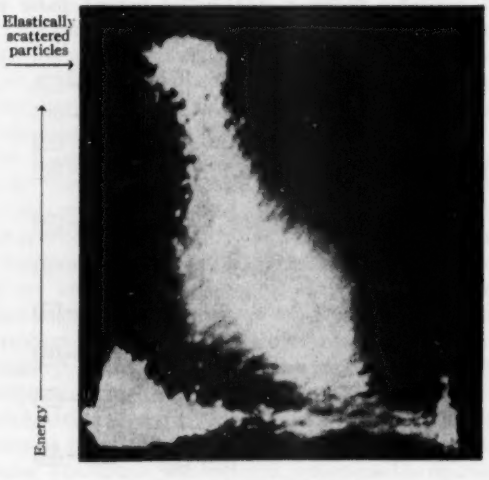

FIG. 6. Photograph of energy losses *vs* energies of particles emitted from a heavy element.

scattered protons. The hump, below the solid line, contains the inelastically scattered protons. Curve *a*, which fuses into the solid curve at about 18 Mev, represents the energy distribution of *all* pulses in the sodium iodide crystal. Curve *b*, which fuses into the solid curve at about 12 Mev, represents crystal pulses which are in time coincidence with a gate from DISC and GATE 1. Thus one sees that below about 15 Mev most of the crystal counts are due to background. The higher-energy background pulses are undoubtedly due to pile-up of the more numerous lower-energy pulses. Curve *c* represents the rate of accidental coincidences between crystal pulses, of a particular energy, and the gates from DISC and GATE 1. The accidentals are measured with the delayed coincidence setup shown in Fig. 3. The solid curve is the difference between curve *b* and curve *c*. It represents the coincident crystal pulses, with accidental coincidences subtracted out—thus the points on the solid curve give the counting rate of real scattered protons.

As the scattering angle decreases towards zero, the cross section for elastic scattering increases very rapidly. Consequently, the complete energy spectra will have a very different appearance at small angles. Figures 8 through 11 show energy spectra for Pb at all the other angles of observation. Figure 12 shows the inelastic spectra of Sn at five angles of observation.

C. Calculation of Cross Sections

Determining the differential cross sections from the energy spectra is simply a matter of counting the total

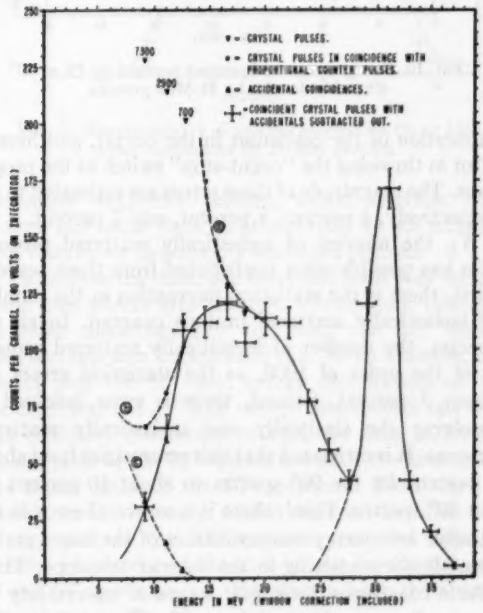
v = CRYSTAL PULSES.
o = CRYSTAL PULSES IN COINCIDENCE WITH PROPORTIONAL COUNTER PULSES.
a = ACCIDENTAL COINCIDENCES.
+ = COINCIDENT CRYSTAL PULSES WITH ACCIDENTALS SUBTRACTED OUT.
7300
2500
700
COUNTS PER CHANNEL (NO VOLTS ON INTEGRATOR)
ENERGY IN MEV (WINDOW CORRECTION INCLUDED)

FIG. 7. Typical energy spectra of protons emitted at 90° from Pb bombarded by 31-Mev protons.

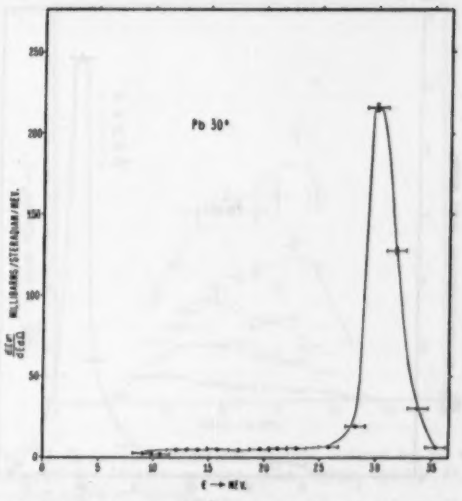

FIG. 8. Energy spectra of protons emitted by Pb at 30° when bombarded by 31-Mev protons.

number of inelastically scattered protons and multiplying by a factor determined by the number of nuclei per cm², the number of bombarding protons, and the solid angle accepted by the counter telescope. To determine the number of inelastically scattered protons it is necessary to take into account the finite resolving power of the scintillation counter for the elastically scattered protons (approximately 8 percent full width at half-maximum). The most reasonable method for doing this involves assuming the resolution curve for the instrument is symmetrical about its maximum point. The upper half of the elastic peak is reflected about its maximum, and the wing of the curve extending into the region of inelastically scattered protons is subtracted out. The reflection process is indicated in Fig. 7.

The differential cross section is defined by the equation

$$N_c = \frac{d\sigma}{d\Omega}\Delta\Omega N_n F,$$

where N_c = number of inelastically scattered protons detected, N_n = number of nuclei/cm² in scatterer, F = number of protons incident upon scatterer, and $\Delta\Omega$ = solid angle accepted by counter telescope. From this we can compute expressions for $d\sigma/d\Omega$, using values for $\Delta\Omega$, N_n, and F given in the last section. The results are

$$(d\sigma/d\Omega)_{Pb} = 6.53\times10^{-28} N_c/V,$$
$$(d\sigma/d\Omega)_{Au} = 6.60\times10^{-28} N_c/V,$$
$$(d\sigma/d\Omega)_{Th} = 8.00\times10^{-28} N_c/V,$$
$$(d\sigma/d\Omega)_{Sn} = 3.91\times10^{-28} N_c/V,$$

where V = voltage to which the Faraday cup electrometer circuit condenser is charged.

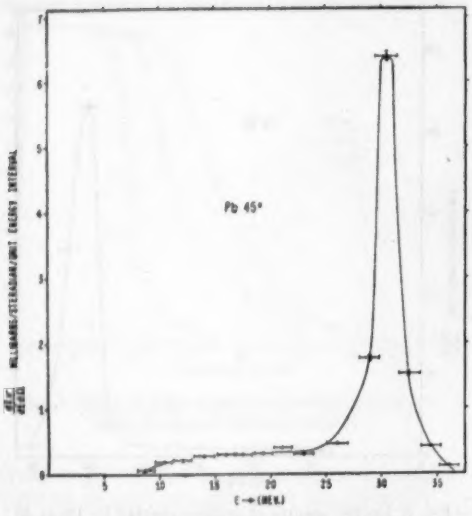

FIG. 9. Energy spectra of protons emitted by Pb at 45° when bombarded by 31-Mev protons.

The total cross section for a particular element may be calculated from the expression

$$\sigma = \int \frac{d\sigma}{d\Omega} d\Omega.$$

Since, in this experiment, information about the differential cross sections is obtained at only six angles, the integral must be approximated by a sum. To do this, the unit sphere is divided into six zones centered about the polar angles at which the differential cross sections were measured. The solid angle of each zone is computed and then the total cross section is calculated from the expression

$$\sigma = \sum_i \left(\frac{d\sigma}{d\Omega}\right)_i \Delta\Omega_i.$$

D. Discussion of Linearity, Errors, and Uncertainties

As a check on the ability of the equipment to provide a linear energy measurement, the energy spectrum of 31-Mev protons scattered from a C target was measured. The observed energy spectrum was in good agreement with the spectrum of Levinthal *et al.*,[5] which was obtained from range measurements. Since the peaks in each spectrum fell at the same energies, the apparatus must be linear.

To arrive at the total uncertainty in the measured cross sections due to the various sources of error, one first considers the formula for the differential cross section

$$\frac{d\sigma}{d\Omega} = \frac{N_e}{\Delta\Omega N_n F}.$$

The solid angle is calculated from the equation: $\Delta\Omega = \pi r^2/R^2$, where r is the radius of the collimator hole and R is the distance of the hole from the target. Both of these distances have a possible error of about 1 percent. Therefore $\Delta\Omega$ is uncertain to about 4 percent.

N_n, the number of target nuclei, is given by the expression: $N_n = (N_{\text{Avogadro}}/A)\sqrt{2}\rho$, where ρ is the areal density of the target. The mean density of the foil is known to about ½ percent, but the density of the region of the foil bombarded by the beam is probably known to only about 2 percent.

F, the number of protons incident upon the scatterer, has uncertainty contributed from three sources: calibration and linearity of the integrating electrometer,

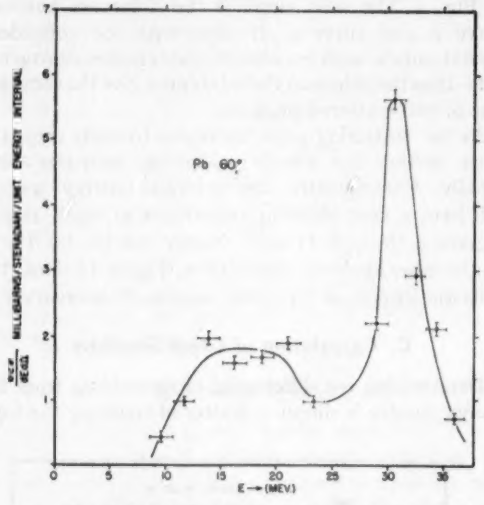

FIG. 10. Energy spectra of protons emitted by Pb at 60° when bombarded by 31-Mev protons.

calibration of the condenser in the circuit, and human error in throwing the "count-stop" switch at the proper time. The magnitude of these errors are estimated to be, respectively, ½ percent, ½ percent, and 1 percent.

N_e, the number of inelastically scattered protons, also has possible error contributed from three sources. First, there is the statistical fluctuation in the number of inelastically scattered protons counted. In all the spectra, the number of inelastically scattered protons is of the order of 1000, so the statistical errors are about 3 percent. Second, there is error involved in resolving the elastically and inelastically scattered protons. It is estimated that this error varies from about 3 percent for the 90° spectra to about 10 percent for the 30° spectra. Third, there is a source of error in the possible low-energy contamination of the beam and in possible slit scattering in the counter telescope. These effects constitute the largest source of uncertainty for the small angle differential cross sections and must be discussed in detail.

Collimator C_3, with all its baffles, was designed to minimize the possibility of slit-scattered protons of degraded energy from remaining in the beam and striking the scattering foil. However, the experiment is, by its very nature, extremely sensitive to beam contamination. This is because any low-energy component of the beam can Coulomb scatter from the target nuclei. At the small angles, the Coulomb scattering cross section becomes very large—and, at low energies, the $1/E^2$ dependence of the Coulomb cross section makes it even larger. Thus, at the forward angles, any low-energy beam contamination will have a high cross section for scattering into the counter telescope where it would be indistinguishable from inelastically scattered protons.

Similar spurious results would obtain if there were any appreciable amount of slit scattering in the collimator C_4 which defines the solid angle accepted by the counter telescope. This is because slit scattering of elastically scattered protons would degrade their energy and cause them to be recorded by the scintillation counter as inelastically scattered protons.

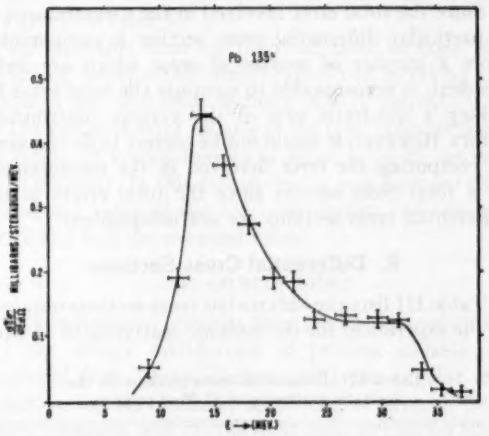

FIG. 11. Energy spectra of protons emitted by Pb at 135° when bombarded by 31-Mev protons.

To analyze the data, one must find some way to take these two effects into account. Fortunately this may be done unambiguously by using the 15° energy distributions as a background run. As an example, one would plot the 15° gold energy distribution on the same axes as the 30° gold energy distribution but with the ordinates contracted so that the area under the elastic peak of the 15° spectrum equals the area under the elastic peak of the 30° spectrum. Then the two curves would be very similar except that the low-energy part of the 15° spectrum contains approximately 50 percent of the area of the low-energy part of the 30° spectrum, i.e., the spectra have the appearance shown in Fig. 13.

Now, if one assumes that all of the low-energy part

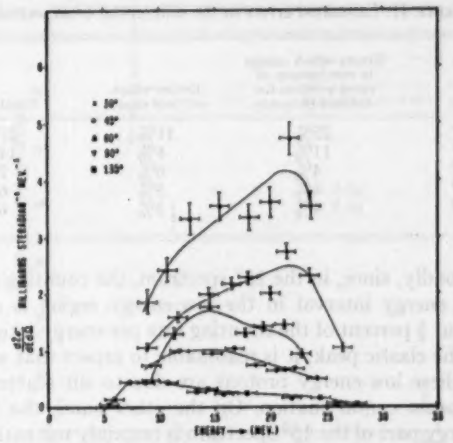

FIG. 12. Inelastically scattered protons emitted by Sn when bombarded by 31-Mev protons. The energy spectra at five scattering angles are shown.

of the 15° spectrum is due to slit scattering or beam contamination, then approximately 50 percent of the low-energy part of the 30° spectrum is due to real inelastically scattered protons, the rest being due to slit scattering or beam contamination. On the other hand, if one assumes that all of the low-energy part of the 15° spectrum is due to real inelastically scattered protons, then there can be no contribution from slit scattering or beam contamination to the 30° spectrum. Thus the true inelastic scattering cross section at 30° is bounded between 50 percent and 100 percent of the value indicated by the raw data.

Now the low-energy part of the 15° spectrum is certainly not all due to real inelastically scattered protons. Firstly, if it were, then the inelastic cross section would increase by about a factor of 20 in going from 30° to 15°. This does not correlate with the behavior of the differential cross section at other angles.

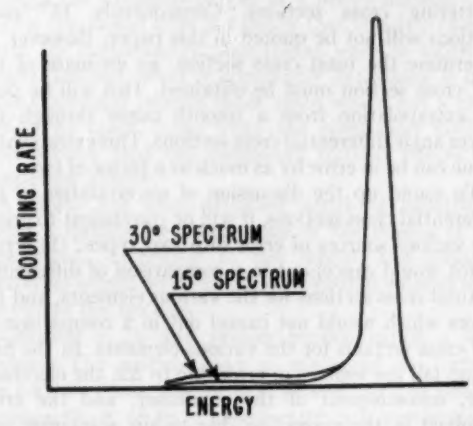

FIG. 13. Energy spectra of protons scattered at 15° and 30° from Au. The counting rates are normalized so that the elastic peaks contain an equal number of detected particles.

TABLE II. Estimated errors in the differential cross sections.

Angle	Errors which cancel in comparison of cross sections for various elements	Errors which will not cancel	Total error
30°	25%	11%	27%
45°	11%	8%	14%
60°	4%	6%	7%
90°	4%	5%	6%
135°	4%	5%	6%

Secondly, since, in the 15° spectrum, the counting rate per energy interval in the low-energy region is only about ½ percent of the counting rate per energy interval in the elastic peak, it is reasonable to expect that some of these low-energy protons are due to slit scattering or beam contamination. On the other hand, the low-energy part of the 15° spectrum is certainly not entirely due to slit scattering or beam contamination. This is true because at 30° these effects give roughly the same contribution to the spectrum as do real inelastically scattered protons and because the cross section for inelastic scattering of protons will be seen to be increasing fairly rapidly with decreasing angle at these angles.

Consequently, a reasonable estimate to make is that the correct value for the inelastic scattering cross section for gold at 30° lies somewhere near the center of the allowed range of 50 percent to 100 percent of the uncorrected value. Consideration of the other elements at 30° gives very similar results whereas at angles greater than 30° these effects are of rapidly decreasing importance.

At 30° the true value of the inelastic scattering cross section is taken to be 75 percent of the value given by the raw data. The limits of error are ±25 percent. At 45° the true value is taken to be 90 percent of the raw data value. The limits of error are ±10 percent. Beyond 45° these effects are negligible.

As is indicated above, the energy spectra taken at 15° are of little value in determining the true inelastic scattering cross sections. Consequently 15° cross sections will not be quoted in this paper. However, to determine the total cross section, an estimate of the 15° cross section must be obtained. This will be done by extrapolation from a smooth curve through the larger angle differential cross sections. This extrapolated value can be in error by as much as a factor of two.

To round up the discussion of uncertainties in the differential cross sections, it will be convenient to group the various sources of error into two types: (1) errors which would cancel out in a comparison of differential or total cross sections for the various elements, and (2) errors which would not cancel out in a comparison of the cross sections for the various elements. In the first group fall the sources of error due to $\Delta\Omega$, the electrometer, measurement of the condenser, and the error involved in the correction due to slit scattering and beam contamination. The second group consists of the errors due to measurement of the density of the scatterer, operation of "count-stop" switch, statistical fluctuations, and the resolving power of the scintillation. Table II gives the quadratic sums of the errors of each type and the quadratic sums of all errors.

The large values of the total probable error for the measurement of the differential cross sections at small angles reflects the fact that it is difficult to obtain information about a relatively small number of inelastic protons in the presence of an overwhelming number of elastic protons.

The error in the total cross section for inelastic scattering is calculated by taking a straight arithmetical average of the suitable weighted errors of the differential cross sections. The weighting factor, for a particular angle, is proportional to the product of the differential cross section and the solid angle for that angle. Since the actual values of the errors in the total cross sections depend on the shape of the differential cross section curve, these errors will not be quoted until the total cross sections are presented.

Since the total error involved in the measurement of a particular differential cross section is compounded from a number of sources of error which are independent, it is reasonable to compute the total error by taking a quadratic sum of the various contributing errors. However, it would not be correct to do the same in computing the error involved in the measurement of a total cross section since the total errors in the differential cross sections are not independent.

E. Differential Cross Sections

Table III lists the differential cross sections obtained in the experiment for the inelastic scattering of 31-Mev

TABLE III. Differential cross sections for the inelastic scattering of 31-Mev protons.

Element	Angle	N_s/V	$d\sigma/d\Omega$ mb/sterad	$d\sigma/d\Omega$ mb/sterad (corrected for slit scattering, etc.)
Pb	135°	644/100	4.2	4.2
	90°	919/40	15.0	15.0
	60°	1144/30	25	25
	45°	1496/20	49	44
	30°	1377/10	90	67
Au	135°	965/100	6.4	6.4
	90°	815/40	13.5	13.5
	60°	1076/30	24	24
	45°	...	...	...
	30°	1360/10	90	67
Ta	135°	698/100	5.6	5.6
	90°	647/40	13.0	13.0
	60°	750/30	20.0	20.0
	45°	1062/20	43	38
	30°	950/10	76	57
Sn	135°	2041/100	7.8	7.8
	90°	1427/40	14.0	14.0
	60°	1838/30	24	24
	45°	1965/20	38	35
	30°	1688/10	66	50

protons. The fourth column contains the data uncorrected for slit scattering and beam contamination. The fifth column is derived from the fourth column by applying the correction for slit scattering and beam contamination described in Sec. 4.

Figures 14 and 15 are plotted from the data contained in the fifth column of Table I. The errors indicated are of the type, described in the last section, which would not cancel out in a comparison of the differential or total cross sections of the various elements.

F. Total Cross Sections

Total cross sections are calculated according to the method described in Sec. 3. In order to do this, one must make estimates for the differential cross section for Au at 45° by interpolation and for the 15° cross sections for all the elements by extrapolation. The estimates are given in Table IV.

The results of the calculation of total cross section are given in Table V.

The probable error for the total cross sections, not including errors which would cancel out in taking the ratios of the total cross sections, is ±10 percent.

The probable error for any of the total cross sections, including all known sources of error, is (+25 percent, −20 percent). In this calculation, it was assumed that the actual value of the 15° cross section lies between twice and half the assumed value.

IV. CONCLUSIONS

This experiment provides three pieces of information: (1) the energy distribution of protons inelastically scattered from heavy elements, (2) the angular distribution for the inelastic scattering of protons from heavy elements, and (3) the total cross section for these

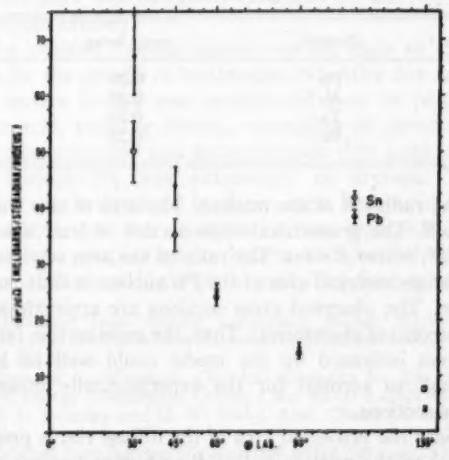

FIG. 14. Differential cross sections for the inelastic scattering of 31-Mev protons from Pb and Sn.

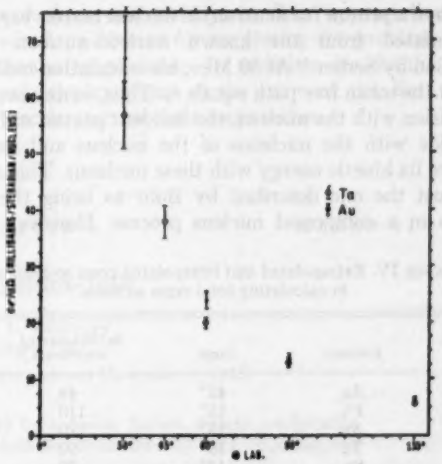

FIG. 15. Differential cross sections for the inelastic scattering of 31-Mev protons from Au and Ta.

inelastic scattering processes. All three point to one easily recognized conclusion—the inelastic scattering process which is taking place has nothing to do with the compound nucleus. The arguments involved in reaching this conclusion are:

(1) The relatively flat energy distributions are very different from the exponential distributions which would characterize the evaporation of nucleons from an excited compound nucleus.

(2) The angular distributions are strongly peaked forward (increasing by about a factor of ten in going from 135° to 30°). This is in contrast to the isotropic distribution one would expect from a compound nucleus process.

(3) The observed total cross sections, which are of the order of 15 percent of geometrical cross section, are at least an order of magnitude larger than the compound-nucleus cross section for boiling off protons through the Coulomb barrier of a heavy nucleus.

This conclusion does not imply that this is a case in which the compound-nucleus theory leads to incorrect results. Instead, what is apparently happening is that some additional process takes place which has a cross section so much larger than the compound nucleus cross section that the compound nucleus effects are completely hidden.

A model has been proposed which is capable of giving a qualitative explanation of the results of the experiment. According to the model, the inelastic scattering occurs when an incident proton collides with the rim of the nucleus.

Consider a 31-Mev proton incident upon a lead nucleus. The nucleus has a radius of $6r_0$, where $r_0=1.4\times10^{-13}$ cm. The incident proton has a de Broglie wavelength, λ, of $\frac{1}{7}r_0$. Consequently, it is legitimate to think of the proton as a small billard ball colliding with a larger billard ball, the nucleus. Now the mean free

path of a proton (or neutron) in nuclear matter has been calculated from the known nucleon-nucleon cross section by Serber.[14] At 30 Mev, his calculation indicates that the mean free path equals r_0. Thus, in any head-on collision with the nucleus, the incident proton will soon collide with the nucleons of the nucleus and rapidly share its kinetic energy with these nucleons. This event is just the one described by Bohr as being the first step in a compound nucleus process. However, in a collision in which the incident proton strikes the diffuse rim of the nucleus, it could collide with one or two nucleons in such a manner that either the incident proton or one of the struck nucleons would escape carrying away a relatively large fraction of the kinetic energy. The diffuse region at the rim of a nucleus, in which the nucleon density decreases from its value inside a nucleus to the external value of zero, is said[15] to have a thickness of the order of r_0. This fuzzy region should behave to some extent like a collection of free nucleons because of the reduced average nucleon density in the region. Consequently, the collision of the incident proton may be considered, approximately, as a collision between free nucleons.

TABLE IV. Extrapolated and interpolated cross sections used in calculating total cross sections.

Element	Angle	$d\sigma/d\Omega$ assumed mb/sterad
Au	45°	44
Pb	15°	110
Au	15°	110
Ta	15°	90
Sn	15°	70

The nucleon-nucleon collisions indicated by the model provide an explanation for the peaked forward character of the observed angular distributions. Consider a collision in which the incident proton strikes a nucleon at rest in the laboratory system. If the differential cross section for scattering is isotropic in the center-of-mass system of the two nucleons (a reasonable approximation for p-p or n-p scattering), then the differential cross section, in the laboratory system, will vanish in the backward hemisphere because of conservation of energy and momentum and will be proportional to the cosine of the scattering angle in the forward hemisphere. If, next, one allows the struck nucleon to have an initial momentum distribution provided by its proximity to the rest of the nucleons in the nucleus, the differential cross section indicated above may well smooth out into something similar to the experimental results shown in Figs. 14 and 15. For instance, the differential cross section would no longer vanish in the backward hemisphere since the incident proton may strike a nucleon with an initial backward component of momentum.

As a simple detailed-balancing argument would indicate, the exponential character of the energy distribution of nucleons emitted from a compound nucleus is essentially due to the exponential form of the energy dependence of the density of states of a nucleon bound to a nucleus. A calculation of the expected energy distribution for the nucleon-nucleon collision process indicated by the model would result in a similar theoretical description. However, in this case, the density of states to be used would probably be closely related to the density of states for a free particle. The density of states for a free particle (the familiar p^2dp factor) varies only slowly with energy. Consequently, the energy distribution would have only a relatively weak energy dependence (compared with an exponential dependence). This checks with the observed energy distribution.

By considering Figs. 7 through 11 one may see that the inelastic parts of the energy spectra are quite similar in shape. Furthermore, as Fig. 12 indicates, the maxima of the spectra shift toward higher energies at smaller scattering angles. These facts are in agreement with what one would expect from a nucleon-nucleon type process since the detailed shape of the energy spectra would not be sensitive to the atomic weight of the bombarded nucleus and since the more energetic particles would be prone to come off in the forward direction.

Finally, the model can be used to predict the magnitude of the total cross section and the dependence of the total cross section on the atomic weight of the nucleus.

The projected area of the diffuse rim is equal to the area of a ring of width r_0 and with a radius about equal to the radius R of the nucleus. The area of this ring is $r_0 \cdot 2\pi R$. The geometrical cross section of lead is equal to πR^2, where $R = 6r_0$. The ratio of the area of the ring to the geometrical area of the Pb nucleus is thus one to three. The observed cross sections are approximately 15 percent of geometrical. Thus, the cross section for the process indicated by the model could well be large enough to account for the experimentally observed cross sections.

TABLE V. Total cross sections for the inelastic scattering of 31-Mev protons.

Element	σ_{total}, barns
Pb	0.29
Au	0.29
Ta	0.25
Sn	0.25

Since the projected area of the diffuse rim is proportional to the nuclear radius R and since nuclear radii are proportional to $A^{\frac{1}{3}}$, the total cross section for the

[14] R. Serber, Phys. Rev. 72, 1114 (1947).
[15] H. A. Bethe and R. F. Bacher, Revs. Modern Phys. 8, 164 (1936).

process predicted by the model might be expected to have an $A^{\frac{1}{3}}$ dependence. In going from Sn to Pb, $A^{\frac{1}{3}}$ increases by 20 percent. This agrees with the experimental evidence that the Pb total cross section is 15 percent greater than the Sn cross section.

The authors wish to express their appreciation to Professor Luis Alvarez for suggesting the problem and for stimulating guidance. In addition, we should like to thank the members of the crew of the Berkeley linear accelerator for their cooperation.

PHYSICAL REVIEW VOLUME 93, NUMBER 5 MARCH 1, 1954

The Half-Life of Lanthanum-140†

H. W. KIRBY AND MURRELL L. SALUTSKY
Mound Laboratory, Miamisburg, Ohio*

(Received September 17, 1953; revised manuscript received November 5, 1953)

Carrier-free lanthanum-140 was separated from barium-140 by a double barium nitrate precipitation from 80 percent nitric acid, using inert barium carrier. The half-life, determined by beta counting, was found to be 40.224±0.020 hours over a period of 574 hours.

IN a separate communication,[1] the authors describe a method for the separation of carrier-free lanthanum-140 from barium-140. A modification of this procedure was used to prepare a high-purity, high-specific activity product which would be suitable for use in a half-life determination.

As a preliminary purification, 0.5 gram of barium nitrate, spiked with approximately one millicurie of barium-140,[2] was precipitated from 80 percent nitric acid, and the filtrate was discarded. To remove possible strontium isotopes, the barium nitrate was redissolved, 10 milligrams of strontium carrier was added, and barium chromate was precipitated from homogeneous solution.[3] The filtrate, containing strontium chromate, was discarded. The barium chromate was redissolved, additional strontium was added, and barium chromate was again precipitated. The barium chromate was converted to barium nitrate (by precipitation from 70 percent nitric acid to remove chromate ion and residual strontium carrier).

The purified barium nitrate was set aside to allow time for the growth of lanthanum-140. After five days, the barium nitrate was precipitated from 80 percent nitric acid, and the filtrate, containing 85 percent of the lanthanum-140 and approximately 0.03 percent of the barium-140, was evaporated to dryness. The residue was redissolved in water, inert barium nitrate was added, and the precipitation was repeated. The filtrate was evaporated to dryness and redissolved in four milliliters of dilute nitric acid. The final solution contained approximately 0.7 millicurie of lanthanum-140, 10^{-7} millicurie of barium-140, and 50 micrograms of inert barium.

Since radium and lead isotopes, if present in the original barium-140, might have passed through the purification process, samples of the purified barium nitrate and the final lanthanum-140 solution were counted in an air-ionization parallel plate alpha counter having a background of less than one count per minute. No alpha counts were detected in either fraction or in any of the samples used for the half-life determination.

The instrument used for beta counting was a 2π proportional counter[4] having a resolution time of 0.1 microsecond. Samples were inserted in the windowless counting chamber, and the chamber was flushed thoroughly with a mixture of 90 percent methane and 10 percent argon. The gas flow was maintained throughout the counting period. The instrument was standardized daily with a plutonium standard sample, and the background, which varied between 50 and 75 counts per minute, was determined before and after each sample was counted. Background and coincidence corrections were made for all counting data. Each measurement was the average of two successive five-minute counts which agreed within one percent.

The upper limit of the instrument was approximately 350 000 counts per minute, and an arbitrary lower limit of approximately 1000 counts per minute was set to avoid loss of counting precision. With these restrictions, no single sample could be counted for more than eight half-lives. Accordingly, a special technique was used by which the lanthanum-140 decay could be followed for a much longer period.

Five samples of the lanthanum-140 solution were mounted on stainless steel disks and evaporated to dryness. The first sample contained approximately

† Abstracted from Mound Laboratory Report MLM-890, July 31, 1953. Available from Technical Information Service, Oak Ridge, Tennessee.

* Operated by Monsanto Chemical Company for the U. S. Atomic Energy Commission, Contract No. AT-33-1-GEN-53.

[1] M. L. Salutsky and H. W. Kirby, Anal. Chem. (to be published).

[2] Obtained from Isotopes Division, Oak Ridge National Laboratory, Oak Ridge, Tennessee.

[3] Salutsky, Stites, and Martin, Anal. Chem. 25, 1677 (1953).

[4] Nuclear Measurements Corporation Model PC-1 alpha-beta-gamma counter.

TABLE I. The half-life of lanthanum-140.

Age of sample[a] (hours)	Starting counts/minute	Half-life (hours)
28–142	6 000	40.2694±0.2754
46–214	106 000	40.1481±0.0276
148–244	59 000	40.2390±0.0552
220–478	316 000	40.1969±0.0341
310–574	308 000	40.2845±0.0226
	Grand mean	40.224 ±0.015 (int. p.e.) 0.020 (ext. p.e.)

[a] Time from final separation to beginning and end of counting.

10 000 counts per minute, and each subsequent sample contained from five to ten times as much lanthanum-140 as the preceding one. The fifth sample contained approximately 50 microcuries of lanthanum-140.

Two samples were counted at the beginning and end of each working day. Whenever a sample decayed below 350 000 counts per minute, it replaced the weaker of the two samples currently being counted. Counting of the final sample was discontinued when it decayed below 1000 counts per minute. Thus, each segment of the decay curve of lanthanum-140 was represented by two separate, overlapping samples. If a long-lived impurity had been present to a significant degree, its presence would have been made evident by a progressive increase in the half-life.

For various practical reasons, it was not found possible to adhere strictly to the plan of counting each sample for eight half-lives, but the technique of overlapping segments made it possible to follow the lanthanum-140 decay with confidence for a period of over 14 half-lives.

The half-life and probable error for each sample was determined by the method of least squares (Table I). The grand mean for the five determinations, weighted inversely as the squares of their probable errors, was 40.224±0.020 hours (external probable error). There was no systematic deviation in any sample, or in the group of five samples, to indicate the presence of a long-lived impurity.

A sixth sample, representing approximately 0.3 millicurie of the original lanthanum-140, was counted beginning 484 hours after purification. The sample had an apparent half-life of 39.8±0.1 hours, but was found to be increasing the counter background by 250 to 900 counts per minute, indicating that the flow of quenching gas through the chamber was causing significant loss of material from the sample mount. On this basis, as well as by Chauvenet's criterion,[5] the sample was excluded from the grand mean.

The currently accepted half-life of lanthanum-140 is 40.0 hours[6] (±0.3 hour,[7] ±0.5 hour,[8] ±0.1 hour[9]), based on work done with neutron- or deuteron-irradiated lanthanum-139. The half-life reported here falls well within the limits of experimental error assigned to two of these determinations.[7,8] In the third case,[9] the data given are insufficient for critical evaluation of the work. However, the authors reported a 2.9-Mev gamma energy which they believed might be caused by an unidentified impurity.

[5] A. G. Worthing and J. Geffner, *Treatment of Experimental Data* (John Wiley and Sons, Inc., New York, 1943), pp. 170–171.
[6] *Nuclear Data, National Bureau of Standards Circular 499* (U. S. Government Printing Office, Washington, D. C., 1950), p. 169, and Supplement I (April 25, 1951), p. 30.
[7] Weimer, Pool, and Kurbatov, Phys. Rev. **63**, 67 (1943).
[8] Ballou, Rubinson, and Glendenin, *Radiochemical Studies: The Fission Products* (McGraw-Hill Book Company, Inc., New York, 1951), Paper No. 165, National Nuclear Energy Series, Plutonium Project Record, Vol. 9, Div. IV.
[9] Bishop, Wilson, and Halban, Phys. Rev. **77**, 416 (1950).

The Internal Conversion Coefficients of Nb^{95}, Zn^{65}, and Sc^{46}†

E. F. STURCKEN, Z. O'FRIEL, O.F.M., AND A. H. WEBER
Saint Louis University, St. Louis, Missouri

(Received November 16, 1953)

The theory of nuclear γ-ray yield determination from Compton electron spectra has been recently developed by Thomas and Lauritsen for interpretation of electron spectra from photoelectric and Compton conversion processes observed with a magnetic lens β-ray spectrometer. The total internal conversion coefficient (N_e/N_γ) is measured by determining N_γ from a high-energy segment of the Compton electron spectrum observed from a thick (140-mg/cm²) aluminum converter and N_e from the internal conversion spectrum of the same source observed without a radiator. The total internal conversion coefficients of two of the isotopes, Mo^{95} (parent, Nb^{95}) and Ti^{46} (parent, Sc^{46}), were also determined by the direct comparison of areas under their internal conversion and beta-spectrum curves and so permitted a check of the new method.

The results of the two methods of determination of Γ are in satisfactory agreement with each other, with other experimental values, and with the predictions of Rose's tables. The results are as follows. Mo^{95} (parent, Nb^{95}) $E_\gamma=0.77$ Mev: by the areas-under-curves method $\Gamma=(2.05\pm0.13)\times10^{-3}$, by the thick-converter Thomas-Lauritsen method $\Gamma=(1.74\pm0.24)\times10^{-3}$. Ti^{46} (parent, Sc^{46}) $E_\gamma=1.12$ Mev; by the areas-under-curves method $\Gamma=(1.34\pm0.15)\times10^{-4}$, by the Thomas-Lauritsen method $\Gamma=(1.00\pm0.06)\times10^{-4}$. Ti^{46} (parent, Sc^{46}) $E_\gamma=0.89$ Mev: by the areas-under-curves method $\Gamma=(2.60\pm0.50)\times10^{-4}$, by the Thomas-Lauritsen method $\Gamma=(1.86\pm0.25)\times10^{-4}$. Cu^{65} (parent, Zn^{65}) $E_\gamma=1.112$ Mev; by the Thomas-Lauritsen method $\Gamma=(2.20\pm0.37)\times10^{-4}$.

INTRODUCTION

A MAGNETIC thin-lens spectrometer of standard design[1] employing a G-M tube as detector has been used to measure the total internal conversion coefficients of certain radioactive isotopes from their Compton electron spectra. The isotope sources were obtained from the Oak Ridge National Laboratory and mounted in the form of circular deposits of about 0.5-cm radius on Lucite disks (0.8-cm radius) fitted to the source holder of the spectrometer. Thus arranged the internal conversion and beta spectra were measured; then a thick (140-mg/cm²) aluminum converter (0.5-cm radius disk) was placed 2 mm in front of the source and the Compton electron spectrum of the secondary electrons emitted by the aluminum was measured. The source arrangements were designed to obtain geometry as nearly identical as possible in the two measurements thus facilitating comparison of the data.

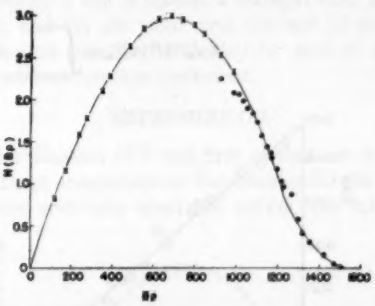

FIG. 1. The beta spectrum of Mo^{95} (parent, Nb^{95}). $N(B\rho)$ is the number of electrons per equal momentum interval, where the magnetic rigidity $B\rho$ is expressed in gauss-cm; circles are experimentally observed data; crosses, values extrapolated from a straight line Fermi-Kurie plot for the observed data. The F-K plot was conveniently drawn by transforming $B\rho$ to $\eta(B\rho=1704.3\eta$ gauss-cm) and employing *Tables for the Analysis of Beta Spectra* [Applied Mathematics Series No. 13, National Bureau of Standards (U. S. Government Printing Office, Washington, D. C., 1952)]. The F-K plot begins to deviate at approximately 75 kev due to source and counter window absorption. The counting statistics are 3.2 percent probable error; the resolution is 2.7 percent.

As is known, the internal conversion coefficient can be measured directly by comparing the areas under the conversion and beta-spectrum curves, yielding the internal conversion coefficient Γ (defined as N_e/N_γ, where N_e is the number of electrons ejected from an atomic shell and N_γ is the number of unconverted nuclear photons). It is simplest and most direct to measure N_γ by the associated continuous β spectrum for isotopes in which a β emission is followed by a γ emission; Nb^{95} (Nb^{95} ejects a β ray, isomeric Mo^{95} then ejects a γ ray to become Mo^{95}) decays in this way.

Thomas and Lauritsen[2] have developed an analysis

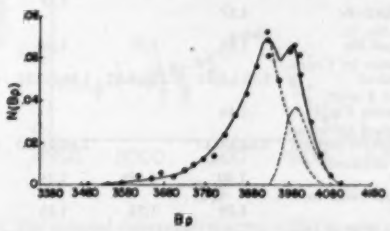

FIG. 2. The internal conversion spectrum of the 0.77-Mev γ ray of Mo^{95} (parent, Nb^{95}). The counting statistics are 2.7 percent probable error at the peak; the resolution is 2.5 percent. The dashed lines suggest the separated K and L peaks which yield a K/L ratio of 2.43. The K and L line shapes follow a line shape calibration employing Hg^{198} (parent, Au^{198}); $B\rho$ in gauss-cm.

† Acknowledgment is made of U. S. Atomic Energy Commission assistance for the construction of the β-ray spectrometer used in this work.

[1] Deutsch, Elliot, and Evans, Rev. Sci. Instr. **15**, 178 (1944).

[2] R. G. Thomas and T. Lauritsen, Phys. Rev. **88**, 969–986 (1952); designated in this paper as T-L.

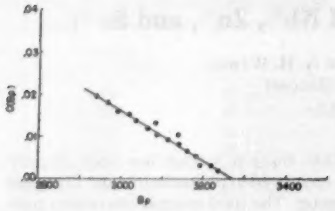

FIG. 3. The high-energy end of the Compton electron spectrum of the 0.77-Mev γ ray of Mo^{95} (parent, Nb^{95}). The source is the same as used for Figs. 1 and 2; the geometry is identical with that in Fig. 1. This spectrum was obtained within 20 hours of the Fig. 2 data. The statistics are 7 percent probable error at the midpoint; $B\rho$ is given in gauss-cm.

yielding the number of unconverted gamma rays in another way, independent of the β-spectrum method, by measuring the absolute number of gamma rays produced in a suitable converter and observing the spectrum of the resulting secondary electrons. In the present experiment it is noted that secondary photoelectrons are negligible because the photoelectric cross section for an aluminum converter is not appreciable above 0.3 Mev.[3] For the thick converter here used, T-L employing the Klein-Nishina cross section for secondary electrons[2] produced in the converter and taking into account the geometry of the spectrometer, obtain for the number of counts per $B\rho$ at a fixed setting $B\rho$ of the spectrometer:

$$C(B\rho)=\tfrac{1}{4}Y\Omega ZNr_0^2m_0c^2\mu_e^{-1}F(x)\epsilon\rho B\rho dx/d(B\rho), \quad (1)$$

where Y is the yield of the γ rays; Z is the atomic number of the converter; N is the number of atoms per cm³ of the converter; ϵ is the shape factor; $r_0=e^2/m_0c^2$; p is the fractional resolution; μ_e is the effective stopping force; Δx is the energy width of the Compton spectrum; and $F(x)$, the number of electrons emerging from the converter into the solid angle Ω, is given by

$$F(x)=2K^{-1}-\tfrac{1}{2}(1+2K)^{-2}+(1+2K)xK^{-2}+\tfrac{1}{2}x^2-K^{-2}x^{-1}+(1-2K^{-2}-2K^{-1})\ln x(1+2K), \quad (2)$$

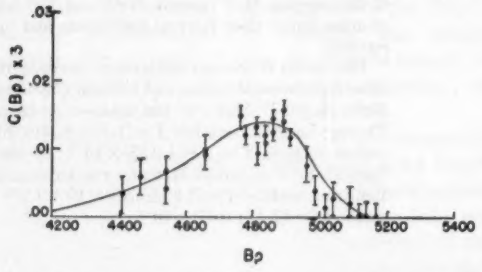

FIG. 4. The internal conversion spectrum of the 1.112-Mev γ ray of Cu^{65} (parent, Zn^{65}). The counting statistics (probable error) are shown by the vertical lines; the resolution of 4.5 percent $B\rho$ is given in gauss-cm.

where

$$K=E_\gamma/m_0c^2, \quad x=(E_\gamma-E_e)/E_\gamma.$$

Integrating (1) yields

$$\int_{(B\rho \text{ at } x_{min})-\Delta B\rho}^{B\rho \text{ at } x_{min}} C(B\rho)d(B\rho)=\tfrac{1}{4}Y\Omega ZNr_0^2m_0c^2 \times\mu_e^{-1}\langle F(x)\rangle_{Av}\epsilon\rho\int_{x_{min}-\Delta x}^{x_{min}}dx, \quad (3)$$

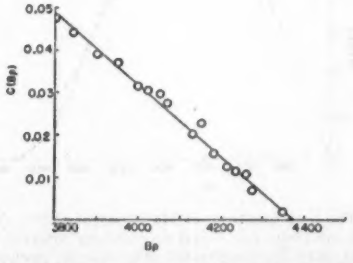

FIG. 5. The high-energy end of the Compton electron spectrum of the 1.112-Mev γ ray of Cu^{65} (parent, Zn^{65}). The geometry is identical with that of Fig. 1. The Compton spectrum was observed immediately following the Fig. 4 experimental run; $B\rho$ is in gauss-cm.

where $\langle F(x)\rangle_{Av}$ is now the average value of $F(x)$ at the midpoint of the Compton spectrum and so is written outside the integral sign. Equation (3) may be solved for the fractional yield observed by the spectrometer, since the area under integral on the left is precisely the area for the small segment of the Compton electron

TABLE I. Summary of total internal conversion coefficients measured by the Compton electron method (Thomas-Lauritsen analysis) and by the areas-under-curves method, and comparison with recent experimental and theoretical values.

Parent nuclide	Nb^{95} (×10³)	Zn^{65} (×10⁴)	Sc^{46} 0.89 Mev (×10⁴)	Sc^{46} 1.12 Mev (×10⁴)
Compton electron method:				
Source No. 1; 1st half-life	1.55	2.51	1.50	0.93
			1.96	1.03
		1.67	1.90	1.10
			2.19	0.95
2nd half-life	1.57			
Source No. 2; 1st half-life	1.98	2.37	1.64	0.99
Mean values by Compton method	1.74±0.24	2.20±0.37	1.86±0.25	1.00±0.06
Estimated K-shell value using Fig. 2	1.16			
Mean values by areas-under-curves method	2.05±0.13		2.60±0.50	1.34±0.15
Recently reported values[a]	1.60	2.28[c]	1.74	0.98
Theoretical value for K shell	1.24	1.75	1.51	0.84
Multipole order of radiation[b]	$E2$	$E2$	$E2$	$E2$

[a] C. V. Fan, Phys. Rev. 87, 252–264 (1952); Waggoner, Moon, and Roberts, Phys. Rev. 80, 420–428 (1950); Moon, Waggoner, and Roberts, Phys. Rev. 79, 905–906 (1950).
[b] Rose, Goertzel, Spinrad, Harr, and Strong, Phys. Rev. 83, 79–85 (1951).
[c] Perkins and Haynes, [Phys. Rev. 92, 687 (1953)] obtain 2.56×10⁻⁴.

[3] C. M. Davisson and R. D. Evans, Revs. Modern Phys. 24, 98 (1952).

spectrum. Hence

$$\frac{Y\Omega}{4\pi}=\frac{\int_{(B\rho \text{ at } x_{\min})-\Delta B\rho}^{B\rho \text{ at } x_{\min}} C(B\rho)d(B\rho)}{\frac{1}{4}ZNr_0^2m_0c^2\mu_e^{-1}\langle F(x)\rangle_{Nu}\epsilon\rho\int_{x_{\min}-\Delta x}^{x_{\min}}dx}. \quad (4)$$

The internal conversion coefficient defined for the present method[4] is

$$\Gamma=\int_{\text{int. conv.}} C(B\rho)d(B\rho)\Big/\left(\frac{Y\Omega}{4\pi}\epsilon\rho\right), \quad (5)$$

where $C(B\rho)$ is the number of counts per $B\rho$, and the integral is over the entire conversion line. Finally, substituting (4) into (5) yields

$$\Gamma=\frac{\int_{\text{int. conv.}} C(B\rho)d(B\rho)}{\int_{(B\rho \text{ at } x_{\min})-\Delta B\rho}^{B\rho \text{ at } x_{\min}} C(B\rho)d(B\rho)\Big/\frac{1}{4}ZNr_0^2m_0c^2\mu_e^{-1}\langle F(x)\rangle_{Nu}\int_{x_{\min}-\Delta x}^{x_{\min}}dx} \quad (6)$$

for the internal conversion coefficient employing the Compton electron spectrum method for the γ-ray yield.

The T-L method permits the separation of two overlapping Compton spectra of two neighboring gamma rays from the same source. Using their formula[5] for the most energetic Compton secondary electron from a given gamma ray,

$$x_{\min}=(1+2K)^{-1}, \quad (7)$$

the end point of the lower-energy γ ray may be located and the corresponding Compton spectrum shape sketched in by noting the shape of the Compton electron spectrum of the higher-energy γ ray. Since the high-energy segment of the Compton spectrum due to the lower-energy γ ray is almost a straight line, Eqs. (1), (2), (4), and (6) are valid over the last 10 percent of the Compton spectrum and may be used to calculate the internal conversion coefficient.

EXPERIMENTAL

A determination of Γ was first carried out with Nb^{95} by the direct comparison of the areas under the internal conversion and beta spectrum curves, the latter area supplying the unconverted γ-ray yield. This direct determination of Γ can be considered as a calibration experiment useful for checking subsequent less direct determinations. Then the T-L analysis was employed, yielding a second determination of Γ in which the γ-ray yield is obtained from the Compton electron spectrum. The two experiments were repeated with different sources, obtained at various times from Oak Ridge, and at different half-life times where sufficient intensity was available. Figures 1–3 show the essential experimental data and the results for Γ are listed in Table I.

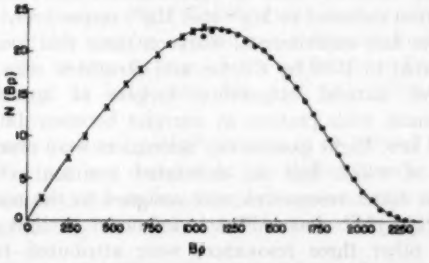

FIG. 6. The beta spectrum of Ti^{45} (parent, Sc^{45}). The circles are the experimentally observed data; the crosses are values extrapolated from a straight line Fermi-Kurie plot as in Fig. 1. The counting statistics are <1 percent probable error; the resolution is 2.7 percent; $B\rho$ is in gauss-cm.

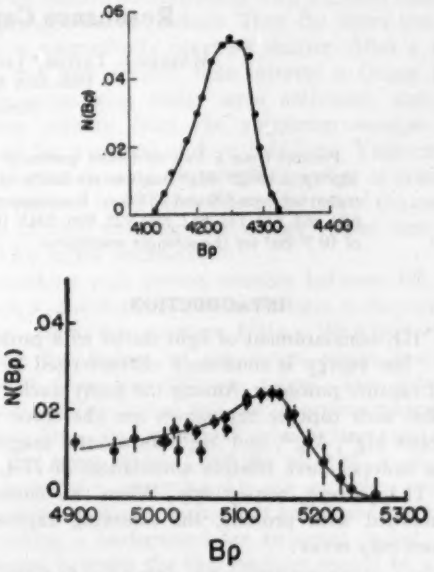

FIG. 7. The internal conversion spectra of Ti^{45} (parent, Sc^{45}) for the 0.89-Mev γ ray (upper curve) and the 1.12-Mev γ ray (lower curve). Because of the thick source necessary for intensity, there was considerable Compton effect within the source. Thus the Compton spectrum of the 1.12-Mev γ ray had to be subtracted out by Eq. (7) and the shape of the Compton spectrum known from Fig. 8. This gave the internal conversion peak of the 0.89-Mev γ ray (upper curve). The counting statistics for these curves was 4.9 percent probable error; the resolution was 2.5 percent; $B\rho$ is in gauss-cm.

[4] Reference 2, p. 973.
[5] Reference 2, p. 970.

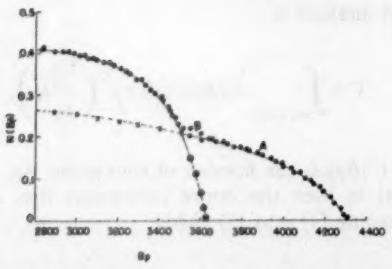

FIG. 8. The high-energy end of the Compton electron spectrum of the 0.89-Mev and 1.12-Mev γ rays of Ti^{46} (parent, Sc^{46}). The experimental data (circles) show clearly the two distinct branches of the different gamma rays. The value of 3628 gauss-cm represents the most energetic secondary electron produced by the 0.89-Mev gamma ray, as calculated from Eq. (7). The points (crosses) were obtained from the log-log extrapolation of the segment AB, which was a straight line on a log-log plot of the data. The points (circle-crosses) were sketched in, following the shape of the experimental curves at the maximum-energy end.

The second kind of experiment employing the T-L Compton electron spectrum method was used for Cu^{65} (parent, Zn^{65}). The first kind of experiment (direct comparison of areas under spectrum curves) was not possible for this isotope. Hence, the usefulness of the T-L method for determining Γ is immediately observed. The essential experimental results are shown by Figs. 4 and 5; the Γ values are listed in Table I.

Both kinds of experiments were carried out for Ti^{46} (parent, Sc^{46}). Thus the T-L method results can again be compared with the direct areas under curves method as has been discussed for the case of Nb^{95}. Experimental results are shown by Figs. 6–8 and Γ values are listed in Table I.

All results and corresponding standard deviations obtained, together with comparison of other experimental results, the theoretical K-shell values of Rose *et al.*[6] are shown in Table I. The overall agreements are quite satisfactory and establish the T-L Compton spectrum method as an additional method of Γ determinations especially for the internal conversion coefficient measurements of isotopes whose beta spectrum is difficult to measure or does not exist, as is the case for Zn^{65}.

The authors are indebted to R. C. Doerner of the Physics Department who drew the figures.

[6] Rose, Goertzel, Spinard, Harr, and Strong, Phys. Rev. **83**, 79–85 (1951).

PHYSICAL REVIEW VOLUME 93, NUMBER 5 MARCH 1, 1954

Resonance Capture of Protons by Mg^{25}†

WARREN E. TAYLOR,* LEONARD N. RUSSELL,‡ AND JOHN N. COOPER
Ohio State University, Columbus 10, Ohio

(Received August 24, 1953)

Protons from a Van de Graaff generator have been used to bombard targets of Mg^{25}. The reaction $Mg^{25}(p,\gamma)Al^{26}(\beta^+)Mg^{26}$ has been studied by observing the positron yield as a function of proton energy in the region between 300 and 1200 kev. Resonance peaks occur for protons with energies of 388, 494, 510, 563, 588, 650, 683, 722, 777, 812, 880, 928, 986, 1043, 1081, 1098, 1132, and 1197 kev. The cross section is of the order of 10^{-27} cm^2 for the stronger resonances.

INTRODUCTION

THE bombardment of light nuclei with protons of low energy is commonly characterized by resonant capture processes. Among the many nuclei which exhibit such capture resonances are the three stable isotopes Mg^{24}, Mg^{25}, and Mg^{26}. In natural magnesium these isotopes have relative abundances of 77.4, 11.5, and 11.1 percent, respectively. When this element is bombarded with protons, the following capture reactions may occur:

(1) $Mg^{24}+H^1 \rightarrow Al^{25*} \rightarrow Al^{25}+2.4$ Mev

(2) $Mg^{25}+H^1 \rightarrow Al^{26*} \rightarrow Al^{26}+5.2$ Mev

(3) $Mg^{26}+H^1 \rightarrow Al^{27*} \rightarrow Al^{27}+8.5$ Mev.

Gamma rays are emitted by the excited aluminum nuclei. Both Al^{25} and Al^{26} are unstable and decay by positron emission to Mg^{25} and Mg^{26}, respectively.

The first experimental work on these reactions was reported in 1939 by Curran and Strothers[1] who bombarded natural magnesium targets of appreciable thickness with protons at energies between 180 and 1000 kev. Eight gamma-ray resonances were observed, five of which had an associated positron activity. These latter resonances were assigned to the reaction $Mg^{25}(p,\gamma)Al^{26}$ since Al^{25} was unknown at that time. The other three resonances were attributed to the reaction $Mg^{26}(p,\gamma)Al^{27}$.

Next Hole, Holtsmark, and Tangen[2] found eight gamma-ray resonances when thin targets of natural

† Supported in part by the U. S. Atomic Energy Commission through a contract with the Ohio State University Research Foundation.

* Now at Sandia Corporation, Albuquerque, New Mexico.
‡ Now at Mound Laboratory, Miamisburg, Ohio.

[1] S. C. Curran and J. E. Strothers, Proc. Roy. Soc. (London) **A172**, 72 (1939).

[2] Hole, Holtsmark, and Tangen, Naturwiss. **28**, 399 (1940).

magnesium were bombarded with protons at energies between 200 and 500 kev. Six years later Tangen[3] investigated the proton capture resonances in this same energy region with greatly improved equipment and techniques. Not only was the gamma-ray yield as a function of energy measured, but also the positron activity. Seven gamma-ray resonances not accompanied by the positron activity and another seven which had associated positron yields were found. By estimating the energy of the gamma rays from absorption measurements, Tangen was able to assign tentatively five of these positron resonances to the reaction $Mg^{25}(p,\gamma)Al^{26}$ and two to the reaction $Mg^{24}(p,\gamma)Al^{25}$. These assignments were confirmed by the work of Grotdahl, Lönsjo, Tangen, and Bergström,[4] who bombarded minute quantities of isotopic Mg^{24} obtained from a mass spectrograph.

In 1950 a preliminary survey[5] of capture reactions in natural magnesium for protons with energies up to 1600 kev revealed the existence of a number of levels, many of which were very close together. The availability of separated isotopes of magnesium suggested a simple way of resolving this complex spectrum. Upon allocation by the Isotopes Division of the U. S. Atomic Energy Commission, small amounts of the oxides of the separated magnesium isotopes were obtained from Carbide and Carbon Chemicals Division, Union Carbide and Carbon Corporation, Y-12 Plant, Oak Ridge, Tennessee. The present paper reports on the yield from proton-capture reactions in one of these isotopes, Mg^{25}.

APPARATUS AND PROCEDURE

Protons at energies between 300 and 1200 kev were separated from the ion beam of a Van de Graaff generator by means of an analyzing magnet and were focused on a $\frac{1}{32}$-in. defining slit. Those protons passing through the slit fell upon a target composed of a very thin layer of Mg^{25} which had been condensed[6] upon a 0.5-mil tantalum backing. This target was placed at the terminal end of a Faraday cage which collected the incident protons. The energy of the protons was determined by measurement of the current in the analyzing magnet. This magnet current was calibrated in terms of proton energy by use of the well-known fluorine resonances[7] at 340.4, 486, 598, 669, 843, 873.5, and 935.3 kev.

Proton capture by Mg^{25} resulted in an excited state of Al^{26} which was detected in two different ways. The first involved the observation of the gamma rays which are emitted by the excited Al^{26} nuclei as they drop to lower energy levels. The second consisted of detecting the positrons emitted as the unstable Al^{26} nuclei decayed to Mg^{26}. The half-life of Al^{26} is approximately 6.5 seconds.[8] Experiments showed that, with the equipment available, the method of detecting positrons was far more sensitive than the gamma-ray method and also permitted greater discrimination against contaminants.

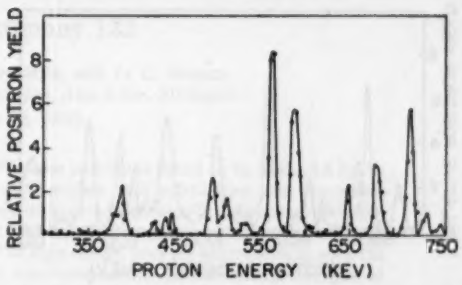

FIG. 1. The relative positron yield from Al^{26} formed by the bombardment of Mg^{25} with protons of energies from 300 to 750 kev. The peaks between 400 and 450 kev are not due to this reaction.

To determine the relative positron yield at each energy the following procedure was followed: the target was bombarded with a constant beam current for 35 seconds, approximately five half-lives of Al^{26}. This insured excitation of 97 percent of the activity which an infinite bombardment with a proton beam of this strength would produce. Then the beam was cut off by a magnetically operated shutter. After a very short, but well defined, time interval a Geiger tube and accompanying scalar were activated, and the positron activity from the aluminum isotope was counted for a period of four half-lives. Yield curves were plotted showing the relative number of positron counts per unit beam current as a function of the energy of the incident protons. The energy values were adjusted for target thickness.

In working with proton energies between 420 and 460 kev, a complication arose in the form of the positron activity from the reaction $C^{12}(p,\gamma)N^{13}(\beta^+)C^{13}$. Presumably the carbon on the target comes from oil molecules from the diffusion pump. The resulting positron activity has a half-life of approximately 10 minutes. Since this length of time is long compared with the seven second half-life of Al^{26}, it is possible to make a correction for the nitrogen activity by counting positrons during four half-lives of Al^{26} and then taking a background for an equal period. The differences between the two readings should be a fair measure of the Al^{26} activity.

EXPERIMENTAL RESULTS

Relative positron yield from the reaction of Mg^{25} $(p,\gamma)Al^{26}(\beta^+)Mg^{26}$ is shown as a function of proton

[3] R. Tangen, Kgl. Norske Videnskab. Selskabs, Skrifter, No. 1 (1946).
[4] Grotdahl, Lönsjo, Tangen, and Bergström, Phys. Rev. **77**, 296 (1950).
[5] Cooper, Taylor, Harris, and Grove, Phys. Rev. **80**, 131 (1950).
[6] Russell, Taylor, and Cooper, Rev. Sci. Instr. **23**, 764 (1952).
[7] Chao, Tollestrup, Fowler, and Lauritsen, Phys. Rev. **79**, 108 (1950).
[8] L. Katz and A. G. W. Cameron, Phys. Rev. **84**, 1115 (1951).

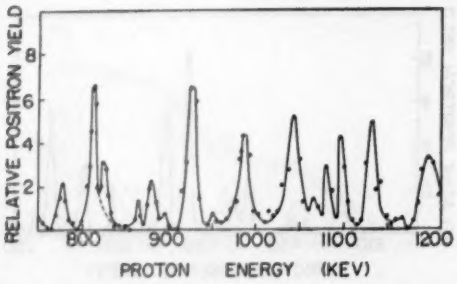

FIG. 2. The relative positron yield from Al^{26} formed by the bombardment of Mg^{25} with protons of energies from 750 to 1200 kev. The peak at 824 kev is not due to this reaction.

energy in Figs. 1 and 2. In each case the curve represents a composite of data taken with several targets on various days. Eighteen levels in the compound nucleus Al^{26} correspond to the following proton energies: 388, 494, 510, 563, 588, 650, 683, 722, 777, 812, 880, 928, 986, 1043, 1081, 1098, 1132, and 1197 kev. The stronger peaks are probably correct to 10 kev in absolute value and the weaker ones to perhaps 15 kev. In addition to these relatively strong resonances there are a number of weaker ones. Over the region covered by the data the cross section for proton capture in Mg^{25} is never greater than a few millibarns. It is estimated that the cross section at the 588-kev resonance is 3×10^{-27} cm^2. A comparison of these results with those of Tangen,[3] whose maximum proton energy was 525 kev, shows excellent agreement. In no case do the energies assigned differ by more than 4 kev.

The other magnesium isotopes were present in appreciable amounts in the Mg^{25} sample, but since the reaction $Mg^{26}(p,\gamma)Al^{27}$ produces a stable nucleus, the only expected activity at these proton energies could come from $Mg^{24}(p,\gamma)Al^{25}(\beta^+)Mg^{25}$, which has a weak resonance at 420 kev and a stronger one at 824 kev. Mg^{24} was present to the extent of 10.7 percent in the Mg^{25} sample, and the yield from this isotope shows clearly in the data with the expected intensity. The dashed lines under the 420- and 824-kev peaks suggest what the yield from pure Mg^{25} might be at these energies.

In addition to the two peaks due to the Mg^{24} impurity, there is a small double peak at 440 kev which has associated with it a half-life considerably longer than that of Al^{26}. This small double peak occurred not only with targets of Mg^{25} but also in targets prepared from Mg^{24}. Since the two peaks appeared in targets of both isotopes and since the activity has a considerably longer half-life than either Al^{26} or Al^{25}, it appears they are not associated with any magnesium isotope. Their origin is not understood.

The position of energy levels of Al^{26} can be determined from the energy available for excitation at each resonance, the masses of the particles involved and the Q of the reaction. If the mass values given by Mattauch and Flammersfeld[9] are used, the Q for the reaction $Mg^{25}(p,\gamma)Al^{26}$ is 5.2 ± 0.25 Mev. Then the levels of the compound nucleus Al^{26} can be calculated and are listed in Table I. Determinations by Tangen[3] and by Curran and Strothers[1] have been modified by using the above value for Q. Energies of levels of Al^{26} lying below 5 Mev have been determined by Swann, Mandeville, and Whitehead[10] through use of the reaction $Mg^{25}(d,n)Al^{26}$. These are also shown in this table.

TABLE I. Energy levels of Al^{26} in Mev.

This research	Swann, Mandeville, and Whitehead[a]	Tangen[b]	Curran and Strothers[c]
	2.00		
	3.63		
	5.13		5.35
		5.48	
5.55		5.56	
5.65		5.65	5.64
5.67		5.67	
		5.68	
5.72			5.73
5.75			
5.81			
5.84			
5.87			
5.93			
5.96			
6.02			
6.07			
6.13			
6.18			
6.22			
6.24			
6.27			
6.33			

[a] See reference 10.
[b] See reference 3.
[c] See reference 1.

ACKNOWLEDGMENTS

The authors are indebted to Dr. J. C. Harris for many excellent discussions and suggestions. They wish to thank the other members of the electrostatic generator group for their assistance in many phases of this research. Both the Ohio State University Development Fund and the Graduate School gave major support which we gratefully acknowledge.

[9] J. Mattauch and A. Flammersfeld, "Isotopic report" (special issue of Z. Naturforsch., 1949).
[10] Swann, Mandeville, and Whitehead, Phys. Rev. 79, 598 (1950).

Radiation from Antimony 122

J. M. Cork, M. K. Brice, G. D. Hickman, and L. C. Schmid
Department of Physics, University of Michigan, Ann Arbor, Michigan

(Received November 30, 1953)

Neutron capture in enriched Sb^{121} yields radioactive Sb^{122} whose half-life is found to be 66.0±0.4 hr. In addition to the two previously observed gamma rays, present studies with scintillation and conversion electron spectrometers indicate the existence of six previously unreported gammas. The energies are 95, 553, 566, 616, 647, 694, 1100, 1200 kev with possibly something at 1.9 Mev. K/L intensity ratios for the conversion lines are observed only for the 553- and 566-kev gammas. The high-energy lines are observed only with the scintillation spectrometer. The beta spectrum is resolved into components with maximum energies at 2.00±0.03, 1.40±0.02, and 0.450 Mev, with possibly some other lower energy present.

Three gamma energies in Sb^{124} are evaluated by their conversion electrons as 603.6, 644, and 727 kev.

IN the early survey of radioactivities induced by slow neutron capture, Fermi *et al.* found[1] a beta-emitting product in antimony, whose half-life was 2.5 days and whose beta energy, as determined by absorption in aluminum, was about 1.6 Mev. Subsequent studies have shown[2] that this activity is undoubtedly in Sb^{122} being formed from Sb^{121} whose natural abundance is 57.2 percent. More recently several reports on the energies of the beta and the gamma radiations have appeared. These exhibit considerable variation in the value of the beta energies. In only one report is more than a single gamma ray mentioned. These results are summarized in Table I.

In the present investigation, antimony enriched in mass 121 up to about 99 percent was irradiated in the Argonne heavy-water pile. The gamma radiations were studied both with photographic magnetic and scintillation crystal spectrometers. The beta radiation has been analyzed by the large double-focusing magnetic spectrometer provided with a thin window counter. The half-life was determined from observation of the decay through several octaves by the use of an ionization electrometer.

BETA ENERGIES

The beta spectrum is found to be complex, consisting of at least three components. The composite Kurie plot is shown in curve *A*, Fig. 1. The curve shape at the upper limit suggests a unique first forbidden transition with ΔI equal to 2 and a change in parity. It is found that the high-energy part of the Kurie plot can be corrected to a straight line by means of the unique first-forbidden, tensor-type correction factor $C\sim(W_0-W)^2L_0+9L_1$, where the factors L_0 and L_1 are obtained from the tables of Rose *et al.*[3] A least squares fit to the corrected Kurie plot gives an upper energy limit of 2.00±0.03 Mev. The remainder after subtraction of this component is shown in Curve *B*. This residual curve is still complex, and its high-energy part does not exhibit the allowed shape. When the same correction factor as used above is applied, an upper energy limit of 1.40±0.02 Mev is found. Subtraction of this component gives a residual curve of maximum energy 450 kev (curve *C*). However, this energy value is influenced appreciably by the type of correction factor applied to curve *B*. The possibility of lower energy beta components is not excluded. The relative abundance of the three beta rays expressed in the order of decreasing energy is 36, 56, and 8 percent. The corresponding log *ft* values in the same order are 8.5, 7.7, and 6.7, respectively.

GAMMA ENERGIES

In the magnetic photographic spectrometers strong K and L electron lines appear with energies of 534.2 and 560.6 kev which, if in tellurium, yield a gamma ray at 566.0 kev. The K to L intensity ratio for the two lines is found to be 7.0±1.5. Weaker K and L lines are observed for a gamma ray of energy 553 kev, with a K/L value of approximately unity. Several additional single electron lines are found and interpreted as K lines in tellurium for gamma rays, following K capture in Sb^{122}. All observed lines died with the same half-life which was found to be 66.0±0.4 hr. The energies of these electron lines are 63.4, 584, 615, and 662 kev, yielding gamma rays with energies of 95.2, 616, 647, and 694 kev. The weakest line is that corresponding to

TABLE I. Previous data relative to Sb^{122}.

Author	Energy in Mev β_1	β_2	γ_1	γ_2
MC[a]	1.36	1.94		
RW[b]			0.57	
K[c]			0.568	
C[d]			0.568	
M[e]	1.19	1.77		
M[f]	1.46			
G[g]	3β's	(No values)	0.56	0.680

[a] L. Miller and L. Curtiss, Phys. Rev. **70**, 983 (1946).
[b] W. Rall and R. Wilkinson, Phys. Rev. **71**, 321 (1947).
[c] Kern, Zaffarano, and Mitchell, Phys. Rev. **73**, 1142 (1948).
[d] C. Cook and L. Langer, Phys. Rev. **73**, 1149 (1948).
[e] C. Mandeville and M. Scherb, Phys. Rev. **73**, 340 (1948).
[f] Macklin, Lidofsky, and Wu, Phys. Rev. **82**, 334 (1951).
[g] M. Glaubman and F. Metzger, Phys. Rev. **87**, 203 (1952).

[1] Amaldi, D'Agostino, Fermi, Pontecorvo, Rasetti, and Segrè, Proc. Roy. Soc. (London) **A149**, 522 (1935).
[2] Mitchell, Langer, and McDaniel, Phys. Rev. **57**, 1107 (1940).
[3] Rose, Perry, and Dismuke, Oak Ridge National Laboratory Report, No. 1459, 1953.

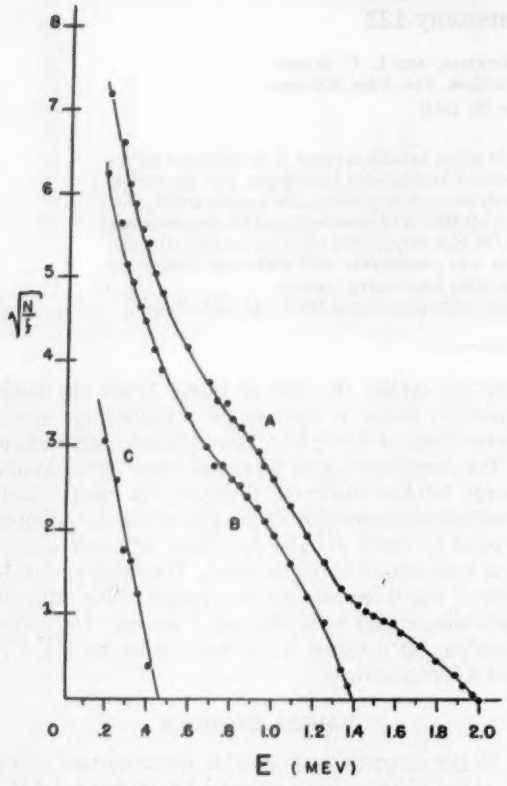

FIG. 1. Resolution of the beta radiation from Sb^{122}.

the gamma ray at 647 kev. A lead radiator giving photoelectrons showed K and L lines only for the strong 566-kev gamma ray.

To insure that none of the observed electron lines could be attributed to Sb^{124}, which has been previously intensively studied,[4] spectrometric exposures were made of a strongly irradiated source of Sb^{122}. The strongest electron line is found to have an energy of 571.8 kev. This is a K line and it is accompanied by an L line of about one-tenth its intensity, at 598.6 kev, so that the energy of the gamma ray is 603.6 kev. Weaker conversion electron lines are observed for gamma rays of energies 644 and 727 kev. Even the very strongest line at 571.8 kev is not observable on the spectrograms obtained with Sb^{122}, hence it seems quite certain that none of the gamma rays attributed to Sb^{122} could be due to Sb^{124}.

Studies have also been made of the activity with a scintillation crystal spectrometer. Due to the increased sensitivity of this method, some slight response is obtained for radiation due to Sb^{124}, particularly at high energies. Peaks are obtained for gamma rays at 1.09 and 1.68 Mev with possibly something at 1.2 Mev and also at a higher energy such as 1.9 Mev, as shown by the singles curve A, in Fig. 2. After a decay of 7 days this trace has dropped to give the relative intensities shown in curve B, thus indicating that the 1.68-Mev gamma ray is in Sb^{124} with its longer half-life, while the 1.10-Mev gamma and possibly the 1.2- and 1.9-Mev transitions are in Sb^{122}. In the low-energy region, peaks are observed only for the gamma rays of energy 694, 566, and 27 kev. The last is due undoubtedly to the K x-rays of tellurium following K capture in antimony. The energy is evaluated by comparison with the known peaks due to Cs^{137} and Co^{60}. For the very strong 566-kev radiation both Compton electron and escape peaks are observed as shown.

COINCIDENCE STUDIES

By placing the radioactive source between two scintillation crystals each with its own output circuit, coincidence events could be observed. For gamma-gamma coincidences both crystals were made of NaI, thallium activated. For beta radiations a crystal of anthracene was employed. The window of one pulse-height analyzer could be adjusted to respond to gamma rays lying between definite energy limits and the other instrument could be swept through all of the gamma peaks in turn. In beta-ray studies the anthracene with its very thin window actuated one of the recording circuits. By interposing successive layers of aluminum between source and crystal the counting rate was reduced so as to obtain a Feather curve. Either the thickness required to reduce the intensity to half-value, or the thickness required to reduce to the gamma background, may be used empirically to give the beta upper energy limit.

In Fig. 2 is also shown a coincidence curve C, when one channel is set to respond only to the 566-kev radiation and the other channel is varied to respond to successive gamma rays. The 566-kev radiation is thus seen to be in sequence with the 694-kev gamma. No evidence could be obtained for the gamma-gamma coincidences except for the tellurium x-ray at 27 kev.

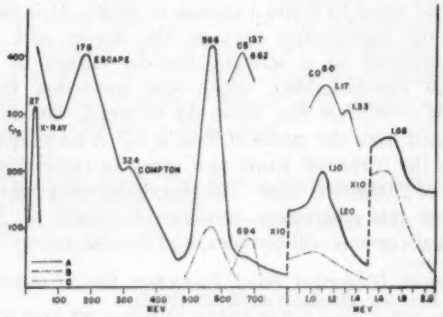

FIG. 2. Energy distribution with the scintillation spectrometer.

[4] Langer, Lazar, and Moffat, Phys. Rev. **91**, 338 (1953); Tomlinson, Ridgeway, and Gohalakrishnan, Phys. Rev. **91**, 484 (1953).

The beta activity as a function of the thickness of aluminum is shown in curve *A*, Fig. 3. The thickness required to reduce the activity to that of the gamma background cannot be sharply determined but it is approximately 0.9 g/cm² corresponding to an energy of about 1.9 Mev. By recording only coincidences between beta response and the 566-kev gamma ray as the absorber is varied in thickness, curve *B* is obtained. The cut-off thickness is now 0.6 g/cm² indicating an energy of 1.4 Mev. This indicates that the 566-kev gamma transition follows in sequence the 1.4-Mev beta decay. Attempts to observe other beta-gamma coincidences were not successful.

The ground level of the even-even $_{52}Te^{122}$ nucleus is undoubtedly a state of zero spin and even parity. If the uniquely forbidden 2.00-Mev beta transition goes directly to the ground state, then the 66-hour $_{51}Sb^{122}$ level is identified as having a spin of two and odd parity. There exists also in Sb^{122} a 3.5-minute isomeric state which has been reported[5] to decay by a 69-kev gamma to the more stable level. The Z^2/W value for the 566-kev radiation is 4.8. In this region a K/L ratio of approximately 7 cannot uniquely determine the type of radiation, and on this basis alone it might be an $E2$ or any type of magnetic transition. The observation of coincidences with beta rays requires a short lifetime which would exclude all magnetic transitions except $M1$, and possibly $M2$. For even-even nuclei the first excited state is usually a level with spin two and even parity, which allows an $E2$ transition to the ground state. The nature of none of the other gamma transitions can be resolved. The low K/L ratio for the 553-kev gamma ray suggests a high-order multipolarity for the transition, such as $E4$ or $M4$. A long lifetime should then be expected which may account for the absence of additional coincidences.

It is possible to arrange a level scheme that will accommodate most of the observed data. Cross-over transitions can be identified from the fact that certain gamma energies have values approximating the sums

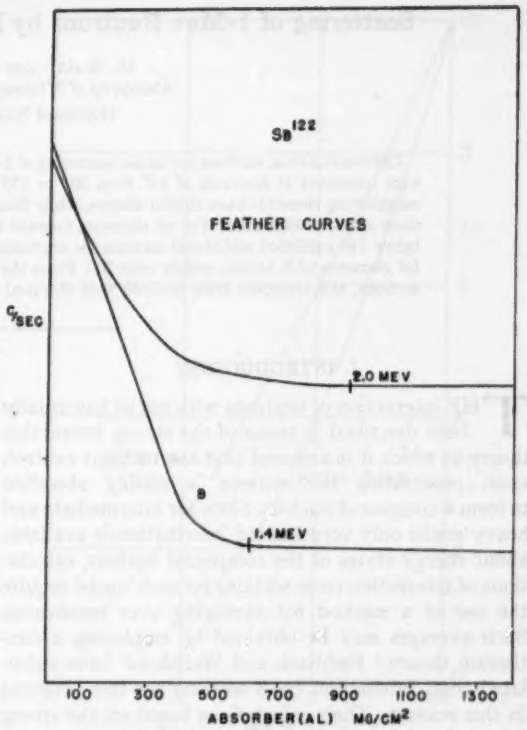

FIG. 3. Absorption of beta radiation observed with scintillation spectrometer.

of others. For example, 566 plus 553, 566 plus 694, and 95 plus 553 will yield 1119, 1260, and 648, respectively, all of which are observed. No trace of positrons could be observed but there might conceivably be K capture leading to Sn^{122}. In this event some of the gamma rays might occur in tin. Level schemes that appear reasonable seem to require an additional low-energy beta ray which is beyond the resolution of the present work.

This investigation received the joint support of the U. S. Office of Naval Research and the U. S. Atomic Energy Commission.

[5] E. derMateosian and M. Goldhaber, Phys. Rev. **82**, 115 (1951); J. H. Kahn, Oak Ridge National Laboratory Report, No. 1089, November, 1951.

Scattering of 1-Mev Neutrons by Intermediate and Heavy Elements*

M. Walt† and H. H. Barschall
University of Wisconsin, Madison, Wisconsin
(Received November 27, 1953)

Differential cross sections for elastic scattering of 1-Mev neutrons from 28 intermediate and heavy elements were measured at intervals of 15° from 30° to 150°. The angular distributions of neutrons scattered by neighboring elements have similar shapes, while those of elements with appreciably different atomic weight show marked differences. For all elements forward maxima were found, and elements with atomic weight below 140 exhibited additional maxima for scattering through 180°. Maxima at about 110° were observed for elements with atomic weight near 200. From the elastic scattering cross sections, inelastic collision cross sections, and transport cross sections were obtained.

I. INTRODUCTION

THE interaction of neutrons with nuclei has usually been described in terms of the strong interaction theory in which it is assumed that the incident neutron upon penetrating the nucleus is readily absorbed to form a compound nucleus. Since for intermediate and heavy nuclei only very limited information is available about energy states of the compound nucleus, calculations of interaction cross sections for such nuclei require the use of a method for averaging over resonances. Such averages may be obtained by employing a continuum theory.[1] Feshbach and Weisskopf[2] have calculated total interaction cross sections for fast neutrons in this manner. Their calculations based on the strong interaction hypothesis predict that total neutron cross sections averaged over resonances should decrease monotonically with energy. On the other hand, recent experiments show that the total cross sections of intermediate and heavy elements measured as a function of neutron energy exhibit broad maxima and minima which shift slowly with atomic weight.[3]

In order to account for these experiments Feshbach, Porter, and Weisskopf[4] have replaced the strong interaction hypothesis by the assumption that the incident neutron is not always absorbed into a compound system but interacts with the average potential produced by the other nucleons. The assumed potential is a complex square well of the form

$$\begin{aligned} V(r) &= -V_0(1+i\zeta), \quad r<R \\ V(r) &= 0, \qquad\qquad\quad r>R, \end{aligned} \tag{1}$$

where the imaginary part of the potential represents absorption corresponding to compound nucleus formation. With values of $R=1.45A^{\frac{1}{3}}\times 10^{-13}$ cm, $V_0=19$ Mev, and $\zeta=0.05$ for the three parameters of the theory, calculated total cross sections are in good agreement with experimental results for neutron energies up to 3 Mev and for elements heavier than iron. The broad maxima and minima in the curves of total cross section as a function of energy and the systematic variation of these curves with atomic weight are reproduced by the theory.

In the theory of Feshbach, Porter, and Weisskopf the neutrons which pass through the nucleus without being absorbed produce a refracted wave which interferes with the incident and the diffracted wave. The angular distributions of elastically scattered neutrons calculated using the complex potential are, therefore, different from those obtained on the basis of the strong interaction model, so that measurements of angular distributions should afford a test of the theory.

Experimental data on the differential cross sections for elastic scattering have previously been published for some neutron energies between 0.2 Mev and 14 Mev.[5–11] In most of these experiments maxima in the forward direction were observed and in some cases additional maxima at larger angles were found. Comparison of the available results with calculated distributions is difficult, however, because either the number of scattering angles employed in the experiments was not sufficient to obtain complete angular distributions or because the detector used did not discriminate adequately against inelastically scattered neutrons.

In the present investigation angular distributions of elastically scattered neutrons were measured for a large number of elements so that one could observe both the shape of the distribution and any systematic change with atomic weight. The quantity measured directly was the cross section for elastic scattering through a given angle per unit solid angle. From a knowledge of this cross section and the total cross section it is possible to deduce the inelastic collision cross section and the transport cross section. The

* Work supported by the U. S. Atomic Energy Commission and the Wisconsin Alumni Research Foundation.
† U. S. Atomic Energy Commission predoctoral fellow. Now at Los Alamos Scientific Laboratory.
[1] H. A. Bethe, Phys. Rev. **57**, 1125 (1940).
[2] H. Feshbach and V. F. Weisskopf, Phys. Rev. **76**, 1550 (1949).
[3] H. H. Barschall, Phys. Rev. **86**, 431 (1952).
[4] Feshbach, Porter, and Weisskopf, Phys. Rev. **90**, 166 (1953).
[5] T. Wakatuki, Proc. Phys.-Math. Soc. Japan **22**, 430 (1940).
[6] H. H. Barschall and R. Ladenburg, Phys. Rev. **61**, 129 (1942).
[7] Amaldi, Bocciarelli, Cacciapuoti, and Trabacchi, Nuovo cimento **3**, 203 (1946).
[8] Barschall, Battat, Bright, Graves, Jorgensen, and Manley, Phys. Rev. **72**, 881 (1947).
[9] A. Langsdorf, Phys. Rev. **80**, 132 (1950).
[10] E. T. Jurney and C. W. Zabel, Phys. Rev. **86**, 594 (1952).
[11] W. D. Whitehead and S. C. Snowdon, Phys. Rev. **92**, 114 (1953).

inelastic collision cross section is given by

$$\sigma_{in}=\sigma_T-\int\sigma(\theta)d\omega,$$

where σ_T is the total cross section, $\sigma(\theta)$ the differential elastic cross section for scattering through an angle θ, and $d\omega$ the solid angle between θ and $\theta+d\theta$. The transport cross section is of interest for some practical applications of diffusion theory and is defined by

$$\sigma_{tr}=\sigma_T-\int\sigma(\theta)\cos\theta d\omega$$

under the assumption that the inelastic scattering is isotropic.

II. EQUIPMENT

A top view of the experimental arrangement is shown in Fig. 1. One-Mev neutrons produced by bombarding a lithium target with 2.7-Mev protons were scattered by a cylindrical sample. Scattered neutrons were observed with a detector which could be moved to various positions on an observation circle in the plane of the figure. The detector was shielded from the neutron source by a paraffin wedge.

A recoil proportional counter, biased to discriminate against inelastically scattered neutrons, was used as the detector. The neutron scattering resonance in helium at about 1 Mev favored the choice of helium as a counter gas and the use of 1-Mev neutrons for the measurements. The maximum in the total cross section at the resonance improved the counting efficiency, and as the angular distribution of 1-Mev neutrons scattered by helium is strongly peaked in the backward direction, a large fraction of the recoiling helium nuclei had close to the maximum possible energy. Below 1 Mev both the total cross section of helium and the differential cross section for scattering at 180° decrease rapidly with decreasing neutron energy, so that the sensitivity of the detector for room-scattered background neutrons was considerably less than the sensitivity for 1-Mev neutrons.

The counter was cylindrical with a 1.9-cm diameter outer wall and a 0.005-in. center wire, 6 cm long. It was operated in the proportional region at a pressure of 17 atmos of helium and a center wire voltage of

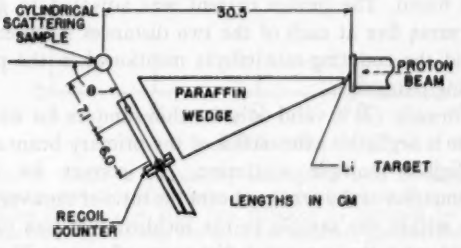

FIG. 1. Top view of the experimental arrangement.

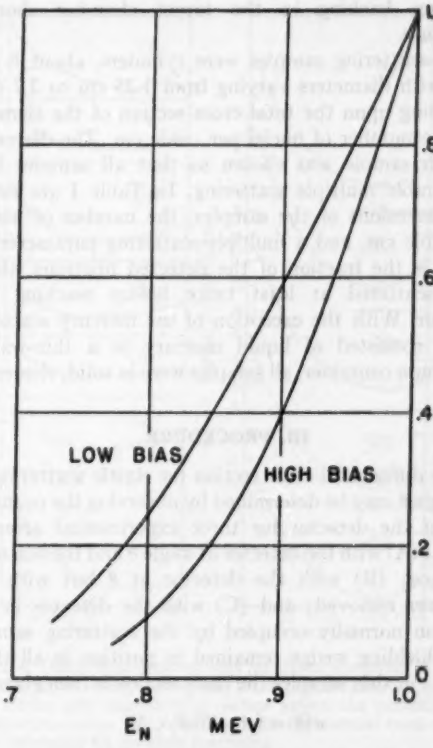

FIG. 2. Counting efficiency of the recoil detector for neutrons of energy E_n divided by the counting efficiency for 1-Mev neutrons.

1700. Pulses from the counter were amplified and fed into two scalers operated in parallel. The discriminators of the two scalers were biased to reject pulses produced by neutrons with energy below about 750 kev and 850 kev, respectively. The energy sensitivity of the counter, obtained by comparing its counting rate with the counting rate of an energy insensitive long counter[12] at several neutron energies, is shown in Fig. 2 where the efficiency relative to the efficiency for 1-Mev neutrons is plotted as a function of neutron energy. At energies below 1 Mev the counter efficiency was different at the two biases, so that the presence of an appreciable number of inelastically scattered neutrons with energies above 750 kev could be recognized by a difference in the values of the cross sections measured at the two biases.

Since the experimental cross sections of intermediate and heavy elements can be easily compared with theory only if the cross sections are averaged over resonances, the lithium target thicknesses were made greater than the spacing between resonances in the elements studied. Four lithium targets, with thicknesses between 90 kev and 160 kev for 2.7-Mev protons, were used during the experiment. Each target was evaporated onto a

[12] A. O. Hanson and J. L. McKibben, Phys. Rev. 72, 673 (1947).

tantalum backing in the target chamber shortly before use.

The scattering samples were cylinders, about 6 cm long, with diameters varying from 1.25 cm to 2.7 cm, depending upon the total cross section of the element and the number of nuclei per cubic cm. The diameter of each sample was chosen so that all samples had comparable multiple scattering. In Table I are listed the dimensions of the samples, the number of nuclei per cubic cm, and a multiple-scattering parameter M which is the fraction of the detected neutrons which were scattered at least twice before reaching the detector. With the exception of the mercury scatterer which consisted of liquid mercury in a thin-walled aluminum container, all samples were in solid, elemental form.

III. PROCEDURE

The differential cross section for elastic scattering at an angle θ may be determined by observing the counting rate of the detector for three experimental arrangements: (A) with the detector at angle θ and the scatterer in place; (B) with the detector at θ but with the scatterer removed; and (C) with the detector in the position normally occupied by the scattering sample. The shielding wedge remained in position in all three cases. For thin samples the cross section is then given by

$$\sigma(\theta)=(A-B)d^2/CN, \qquad (2)$$

where A, B, and C are the counting rates for a constant neutron source strength, observed in the three experimental arrangements, (A), (B), and (C). N is the total number of scattering nuclei, and d is the distance from the scattering sample to the counter.

Counting rates for the three conditions were measured by recording the number of counts obtained in a run during which a fixed number of neutrons was produced at the source. Each of these runs lasted about two minutes and was controlled by a current integrator which ended the run when a fixed proton charge was accumulated at the lithium target. The data were taken in many short runs, the three different arrangements being used in successive runs, so that gradual changes in the target yield or the counter sensitivity would be averaged out. Enough runs were taken at each scattering angle to give a statistical error of about 5 percent in the cross section.

Measurements were made at 15° intervals for angles from 30° to 150°. The background, i.e., the counting rate with the sample removed compared to the counting rate with the sample in place, averaged about 40 percent but depended upon the scattering angle and the scattering element. At 150°, where the shielding was limited by the available space between the counter and source, the background for some elements was as high as 80 percent.

As it was easier to place the counter at 0° on the observation circle rather than in the sample position to observe the direct beam in the arrangement (C), the counting rate measured on the observation circle was multiplied by a constant to give the value which would have been measured at the sample position. This constant was determined experimentally by observing the counting rates with the detector in each of the two positions.

In formula (2) it was assumed that the counter detected primary and scattered neutrons with equal efficiency. The rapid decrease in counting efficiency with decreasing neutron energy resulted, however, in a lower sensitivity for detecting elastically scattered neutrons which had lost some energy in the laboratory system. In addition, the sensitivity of the counter depended on the counting rate. As a result, the direct and scattered neutrons were detected with different efficiency, since the direct flux was 50 to 100 times greater than the flux of scattered and background neutrons. Correction for the energy loss in elastic collisions was made by calculating the energy of the scattered neutrons and using the energy sensitivity of the counter shown in Fig. 2. To estimate the counting-rate effects the counter was placed in the direct beam and the number of counts per run was recorded at two proton currents which produced counting rates roughly equal to those encountered in measuring the direct and the scattered flux. Since the number of neutrons produced during each run was constant, the effect of counting rate upon detector sensitivity was shown by a difference in the number of counts registered during the two runs. The results of this test indicated that the efficiency of the detector decreased by 10 percent in the higher flux.

The distance d in formula (2) was obtained directly by experiment to avoid the necessity of knowing the variation of the sensitivity over the active volume of the counter. At a distance of about 35 cm from the source the lower sensitivity at the ends of the center wire had little effect on the average distance, since the length of the active volume was small compared to the distance from the source. The number of counts per run was recorded with the counter 35 cm from the source and with the counter at a distance from the source equal to its distance from the axis of the scatterer during the cross section determinations. By assuming that the counts per run varied inversely with the square of the distance from counter to source, the value of d was found. The proton current was adjusted to give the same flux at each of the two distances in order to avoid the counting-rate effects mentioned in the preceding paragraph.

Formula (2) is valid only for thin samples for which there is negligible attenuation of the primary beam and negligible multiple scattering. To correct for the attenuation of the primary beam the ratio of the average flux within the sample to the incident flux was computed, and the measured direct counting rate C was

multiplied by this ratio to give an average value of C within the sample.

As the diameters of the scattering samples were about ½ of a mean free path for scattering, some of the scattered neutrons were scattered again before leaving the sample. These multiple-scattering processes tended to diminish the maxima and raise the minima in the angular distributions, so that the observed scattering was more isotropic than the true differential cross section. The procedure followed in computing the correction for this multiple scattering was to assume an initial curve for the differential cross section, then calculate the results of an experiment performed on a scattering sample with the assumed cross section. By adjusting the initial curve until the calculated result coincided with the experimentally measured distribution, the corrected values of the differential cross section were obtained.

To compute the result of an experiment on a sample with a given differential cross section, the following simplifying assumptions were made: (1) no neutron made more than three collisions in the sample; (2) the fraction of the doubly scattered neutrons which suffered a third collision was the same as the fraction of singly scattered neutrons which suffered a second collision; (3) the angular distribution of doubly and triply scattered neutrons leaving the sample was the same as the distribution of doubly and triply scattered neutrons in an infinite medium of the sample material. Methods for computing second- and third-collision distributions in infinite media from a knowledge of the first-collision distributions have been published by several authors.[13,14]

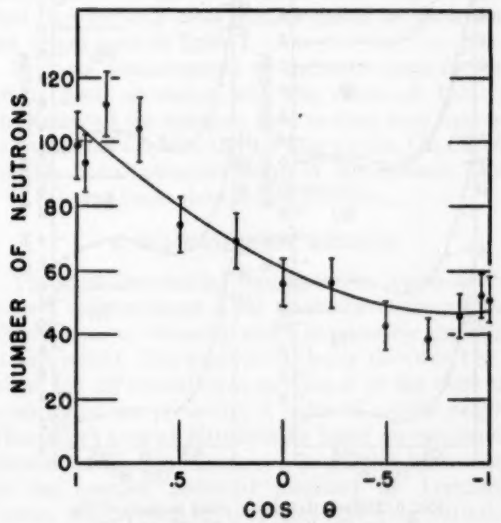

FIG. 3. Check of simplifying assumption used in multiple scattering correction. The circles give the distribution of neutrons reaching the detector after two collisions as obtained by the Monte Carlo calculation. The solid line indicates the distribution of doubly scattered neutrons in an infinite medium of the scattering material.

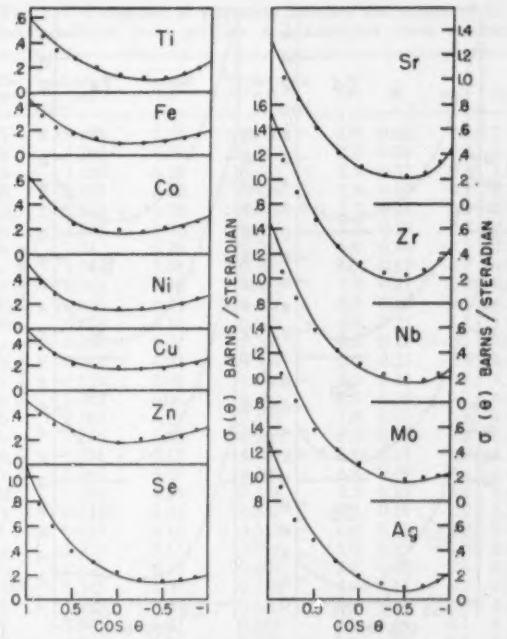

FIG. 4. Differential cross sections for elastic scattering of 1-Mev neutrons from Ti, Fe, Co, Ni, Cu, Zn, Se, Sr, Zr, Nb, Mo, and Ag. The circles give experimental values before the correction for multiple scattering. The solid line is the differential cross section after correction for multiple scattering.

These simplifying assumptions were checked by performing a Monte Carlo calculation on a typical example. About 15 000 scattered neutrons were tracked through a sample having the properties of cadmium. The nature of the event at each step in the path through the sample was selected in sequence from the existing possibilities, each possibility being weighted according to its probability of occurrence. The most critical of the aforesaid assumptions was that the distribution of second-collision neutrons entering the detector was the same as the distribution of second-collision neutrons in an infinite medium. That this assumption does not introduce any large error can be seen from Fig. 3 where the distribution of the second-collision neutrons obtained by the Monte Carlo example is shown with the distribution of second-collision neutrons in an infinite medium. Additional information from the Monte Carlo work indicated that only very small errors are introduced by the other assumptions.

IV. RESULTS

Figures 4 to 6 give the differential cross sections for elastic scattering of 1-Mev neutrons by titanium, iron, cobalt, nickel, copper, zinc, selenium, strontium,

[13] S. Goudsmit and J. L. Saunderson, Phys. Rev. 57, 24 (1940).
[14] J. Blok and C. C. Jonker, Physica 18, 809 (1953).

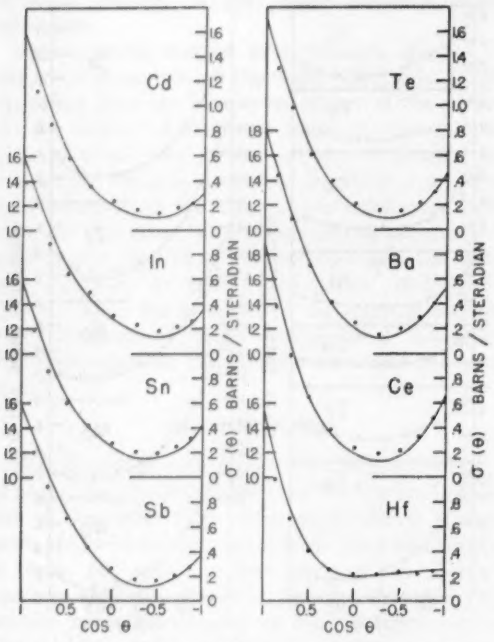

FIG. 5. Differential elastic cross sections of Cd, In, Sn, Sb, Te, Ba, Ce, and Hf.

zirconium, niobium, molybdenum, silver, cadmium, indium, tin, antimony, tellurium, barium, cerium, hafnium, tantalum, wolfram, gold, mercury, radiogenic lead (88 percent Pb^{206}), lead, bismuth, and thorium. The circles give the experimental cross sections uncorrected for multiple scattering and the solid lines give the values of the differential cross sections after the correction for multiple scattering was made. The differential cross sections are plotted as a function of the cosine of the scattering angle, since at 1 Mev it is expected that partial waves of high angular momenta are not involved and that the curves should, therefore, have simpler forms if plotted in this manner. Cross sections for both biases are plotted for wolfram since the results obtained at the two biases did not agree, the higher bias giving the smaller differential cross section. This effect was attributed to the presence of inelastically scattered neutrons with energies greater than 750 kev. The lack of bias effect in all elements except wolfram indicates that the inelastically scattered neutrons lost at least 250 kev in the collision. This might be expected since most of the elements studied do not have known excited states below 250 kev.[15] On the other hand the first excited state of wolfram is at about 100 kev for the isotopes with 106, 108, and 112 neutrons.

From the curves of Figs. 4 to 6 and from previously measured values of the total cross sections,[16–18] the inelastic collision cross sections and the transport cross sections were obtained. In cases where the total cross section varied rapidly with energy near 1 Mev, the transmission measurements were repeated with the lithium target used for the differential cross section experiment to obtain proper averaging over resonances.

The inelastic collision cross sections and the transport cross sections are given in the last two columns of Table I. The lower curve of differential cross section was used to determine the inelastic cross section of wolfram, but since it is possible that inelastically scattered neutrons were detected even with the higher bias, the value of the inelastic collision cross section is only a lower limit.

The over-all error in the differential cross section is about 15 percent for angles between 30° and 150°. The principal uncertainties contributing to this are: statistical errors, 5 percent; the error in the correction for loss of counter sensitivity in the direct flux, estimated to be not more than 5 percent; and the errors in the distances involved in the cross-section determination, 5 percent. The errors in the inelastic collision cross sections are about 15 percent of the value of the integral of the differential elastic cross section, since the error in the total cross section is negligible. As a large part

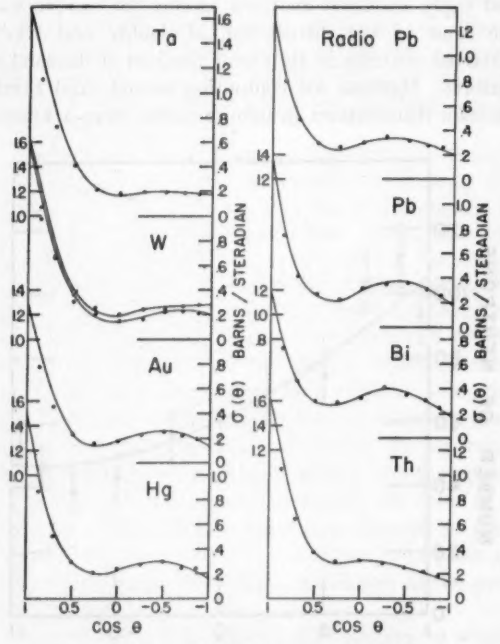

FIG. 6. Differential elastic cross sections of Ta, W, Au, Hg, Radio-lead, Pb, Bi, and Th.

[15] G. Scharff-Goldhaber, Phys. Rev. **90**, 587 (1953).

[16] Miller, Adair, Bockelman, and Darden, Phys. Rev. **88**, 83 (1952).

[17] Walt, Becker, Okazaki, and Fields, Phys. Rev. **89**, 1271 (1953).

[18] Okazaki, Darden, and Walton, Phys. Rev. **93**, 461 (1953).

of this error is common to all elements, the relative values of the inelastic collision cross sections of different elements are, however, probably more accurate than the absolute values. The errors in the transport cross section cannot be easily estimated because the extrapolated values of the differential cross section at angles less than 30° and greater than 150° are heavily weighted in the determination of the transport cross sections.

Previous measurements of angular distributions of elastically scattered neutrons can be compared only qualitatively with the results of the present experiment, because either the energy at which the other investigations were made was higher or the angular and energy resolution was considerably different. Other investigators have observed forward maxima, and Jurney and Zabel[10] as well as Whitehead and Snowdon[11] have found additional maxima at larger angles.

The most extensive measurements of inelastic collision cross sections in this energy region are those of Carter and Beyster,[19] who used fission neutrons and threshold fission detectors. Again the energy was sufficiently different from that used in the present measurement to prevent detailed comparison, but certain features are brought out in both experiments. There is a tendency, more noticeable in the work of Carter and Beyster than in this experiment, for the inelastic cross sections of magic number nuclei to be lower than those of their nonmagic neighbors. Table I corroborates this tendency for bismuth, lead, radiogenic lead, cerium, and barium, although the inelastic cross sections of strontium and tin are not especially low. The fact that no known excited states of the principal isotopes of Sr and Sn occur below 1 Mev might suggest that their inelastic cross sections should be lower than the values given in Table I.

Previous measurements of transport cross sections are in good agreement with the values of Table I. In reference 8 the transport cross sections were reported at energies of 0.6 Mev and 1.5 Mev for Fe, Co, Cu, W, and Pb. For all elements except W the values in Table I lie between those given in the reference.

V. DISCUSSION OF RESULTS

The most outstanding feature in the results of the present measurements is the similarity in the angular distributions of elements which have nearly the same atomic weight. This behavior is clearly shown in Fig. 7 where the differential cross sections of all the elements investigated are presented in order of atomic weight. Theoretical angular distributions based on continuum theories using either the strong interaction hypothesis[2] or the complex potential proposed by Feshbach, Porter, and Weisskopf[4] also show the slow variation with atomic weight, since only parameters which change slowly with nuclear size appear in the continuum formulations.

[19] R. E. Carter and J. R. Beyster, Phys. Rev. **90**, 389 (1953).

TABLE I. Properties of scattering samples and values of inelastic collision cross sections and transport cross sections.

Element	Radius cm	Length cm	Nuclei per $cm^3 \times 10^{-22}$	σ_T[a]	M	σ_{in}	σ_{tr}
Ti	1.194	6.04	0.566	2.9	0.16	0.1	2.1
Fe	1.260	5.99	0.847	2.5	0.20	0.4	2.1
Co	1.168	6.10	0.703	3.5	0.21	0.2	3.0
Ni	0.952	6.02	0.914	2.9	0.19	0.1	2.5
Cu	1.102	6.08	0.845	3.2	0.21	0.3	2.8
Zn	1.115	6.02	0.657	3.6	0.20	0.3	3.3
Se	1.23	6.26	0.310	5.0	0.16	0.7	3.5
Sr	1.11	5.46	0.180	6.7	0.12	0.7	4.8
Zr	0.953	6.08	0.430	7.0	0.21	0.4	4.6
Nb	0.870	6.35	0.491	6.5	0.20	0.7	4.2
Mo	0.788	6.15	0.635	6.8	0.23	1.1	4.6
Ag	0.890	6.02	0.587	6.6	0.23	2.1	4.4
Cd	0.940	6.02	0.463	6.9	0.22	1.4	4.4
In	1.110	6.06	0.386	6.6	0.21	0.4	4.1
Sn	1.269	6.06	0.369	6.8	0.22	0.7	4.6
Sb	1.182	6.11	0.328	7.0	0.20	0.8	4.4
Te	1.276	6.40	0.250	6.5	0.17	0.6	3.9
Ba	1.235	6.13	0.151	6.8	0.11	0.2	4.3
Ce	1.265	6.08	0.287	6.8	0.19	0.1	4.4
Hf	1.270	4.44	0.448	7.2	0.25	2.1	5.4
Ta	0.635	6.05	0.552	7.3	0.19	2.2	5.2
W	0.635	6.15	0.637	6.9	0.21	$\geq$2.2	5.3
Au	1.270	6.17	0.596	5.6	0.25	1.5	4.4
Hg	1.160	6.10	0.408	5.6	0.20	0.9	4.3
Pb^{206}	1.345	6.00	0.330	4.9	0.17	0.2	4.0
Pb	1.350	6.08	0.330	4.9	0.17	0.3	4.1
Bi	1.345	6.02	0.283	4.9	0.15	0.1	4.1
Th	1.268	6.04	0.300	7.1	0.20	1.8	5.3

[a] See references 16, 17, 18.

A comparison of the measured elastic cross sections with calculations is complicated by the fact that at a neutron energy as low as 1 Mev there is an appreciable probability for the decay of the compound nucleus by elastic scattering. In particular, if the bombarded nucleus has no energy level below 1 Mev, as is probably the case for several of the elements investigated, most of the compound nucleus formation will result in elastic scattering. This "compound-elastic" scattering cannot be distinguished experimentally from the "shape-elastic" scattering which is not associated with compound nucleus formation, but the "compound-elastic" scattering is expected to have a different angular distribution from the "shape-elastic" scattering. It is possible to calculate from the theory the cross section for formation of a compound nucleus, but not what fraction of the compound nuclei decays by elastic or inelastic processes. Consequently, only the limits between which the elastic scattering and inelastic collision cross sections should lie can be predicted.

While all the inelastic collision cross sections listed in Table I are smaller than the maxima calculated on the basis of the strong interaction theory, some of the values appear to be larger than the upper limits calculated using the complex potential (1), but the large errors in the experimental values overlap the limits.

If the inelastic collision cross sections were known accurately from the experiments, it would be possible to calculate from the theory definite angular distributions for the elastic scattering. Because of the un-

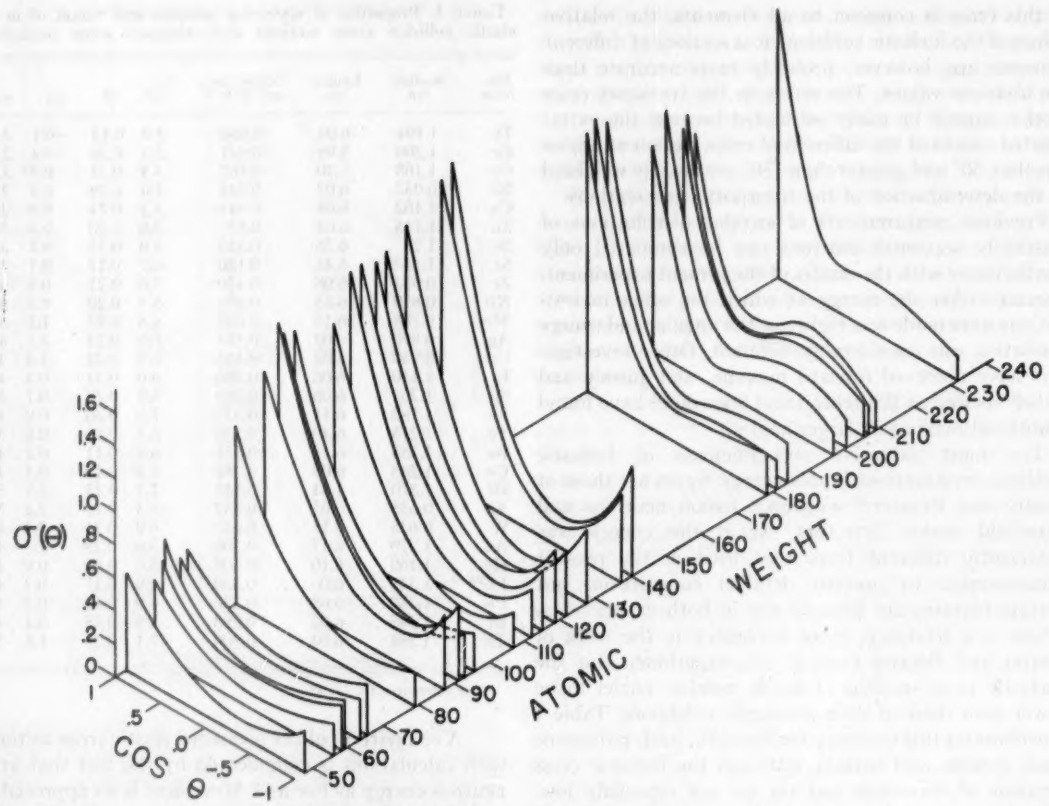

FIG. 7. Differential cross section for elastic scattering of 1-Mev neutrons as a function of the cosine of the scattering angle and of atomic weight.

certainty in the values for the inelastic cross section, however, it is not known how much "compound-elastic" scattering should be added to the calculated angular distributions of "shape-elastic" scattering. Certain characteristic features of the predicted angular distributions are independent of the assumed amount of "compound-elastic" scattering. Distributions calculated on the basis of the strong interaction model[20] have pronounced maxima at 0° in agreement with experiments. This theory does not predict, however, additional maxima at 110° of the magnitude encountered in the heavy elements. On the other hand, the observed maxima at 180° for elements of atomic weight below 160, and maxima around 110° for elements of atomic weight near 200 are characteristic features of the angular distributions calculated from the complex potential (1).[21]

While it is not possible to state that the experiments are definitely in agreement with the recently developed theory of Feshbach, Porter, and Weisskopf, the results appear to agree better with this theory than with the compound nucleus theory.

VI. ACKNOWLEDGMENTS

We wish to thank Professor P. C. Hammer and Mr. J. W. Hollingsworth for coding the Monte Carlo example and performing the calculations on the I.B.M. 604 Card Programmed Calculator. We are grateful to Professor V. F. Weisskopf for valuable discussions and for making the results of reference 21 available to us before publication.

[20] Final Report of the Fast Neutron Data Project, 1951, Atomic Energy Commission Report NYO-636 (unpublished).

[21] Feshbach, Porter, and Weisskopf, Technical Report No. 62, Laboratory for Nuclear Science, Massachusetts Institute of Technology, Cambridge, Massachusetts, 1953 (unpublished).

Gamma Rays from Ne†*

B. P. Foster,‡ G. S. Stanford, and L. L. Lee, Jr.
Sloane Physics Laboratory, Yale University, New Haven, Connecticut
(Received November 5, 1953)

The decay scheme of the low-lying excited states of Ne^{22} has been investigated by means of a proton gamma-ray coincidence study of the $F^{19}(\alpha,p)Ne^{22}$ reaction using a NaI(Tl) gamma-ray scintillation spectrometer. The excitation energies of the second and third excited states were rechecked and found to be 3.3 and 4.9 Mev, respectively. The results cast considerable doubt on the existence of the previously reported level at 0.6 Mev. For the 1.28-Mev excited state a single transition to the ground state was identified. The second excited state was found to decay principally by a cascade transition through the first excited state, although a weaker crossover transition direct to the ground state was also observed. The third excited state was found to decay through transitions to both the first excited and ground states. A discussion of possible spin and parity assignments by means of the Weisskopf relations is presented.

I. INTRODUCTION

THE modes of decay of the lower excited states of Ne^{22} have been investigated by means of a proton gamma-ray coincidence study of the reaction $F^{19}(\alpha,p)Ne^{22}$ using a NaI(Tl) gamma-ray scintillation spectrometer. The experimental method is essentially the same as that used by Allen, May, and Rall[1] on the $Al^{27}(\alpha,p)Si^{30}$ reaction and by May and Foster[2] on the $Na^{23}(\alpha,p)Mg^{26}$ reaction.

II. EXCITED STATES OF Ne^{22}

The ground-state Q value of the $F^{19}(\alpha,p)Ne^{22}$ reaction can be deduced accurately from the work of Mileikowsky and Whaling[3] on the reactions $Ne^{21}(d,p)Ne^{22}$ and $Ne^{21}(d,\alpha)F^{19}$. The result is

$$Q=1.705\pm0.015 \text{ Mev}.$$

The excitation energy of the first excited state of Ne^{22} is known accurately to be 1.277 ± 0.004 Mev from the work of Alburger[4] on the gamma ray following the β decay of Na^{22}. Other information on the low-lying excited states of Ne^{22} has been obtained by several authors[5,6] from the $F^{19}(\alpha,p)Ne^{22}$ reaction using natural α particles.

In the present work a ¼-mil "Teflon" (CF_2—1.4 mg/cm²) foil was bombarded by the 7.6-Mev alpha-particle beam from the Yale cyclotron. Protons from the target were observed at 90° and their ranges measured by means of aluminum absorbers and a "peaked" proportional counter. Figure 1 shows the resulting proton group curve which is essentially that used in the coincidence study. Some resolution was sacrificed to get larger solid angle and higher counting rates.

Figure 2 shows the results of this paper along with those of May and Vaidyanathan and Hjalmar and Slätis. There is essential agreement within the limits of resolution for the levels at 1.28, 3.3, and 4.9 Mev, as Hjalmar and Slätis would not see the latter level because of the low energy of the polonium alpha particles used. Hjalmar and Slätis, however, report a level at 0.57 Mev,

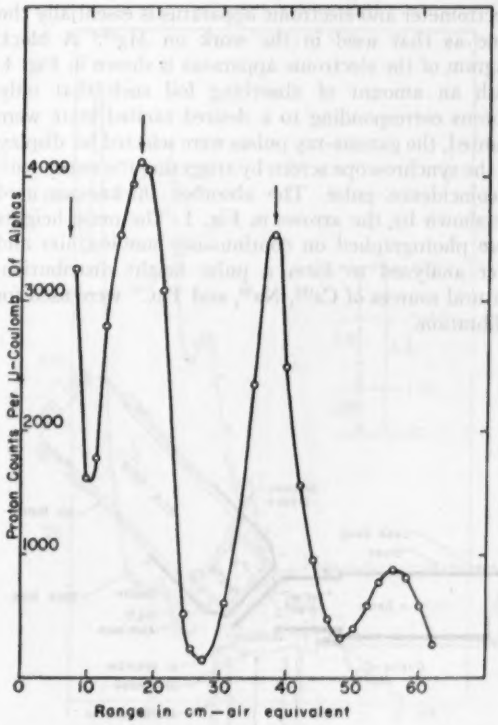

FIG. 1. Proton groups of $F^{19}(\alpha,p)Ne^{22}$ reaction for observation at 90°. Arrows indicate absorber used in coincidence studies.

† Part of a dissertation presented by one of the authors (B.P.F.) to the Faculty of the Graduate School of Yale University, in partial fulfillment of the requirements for the degree of Doctor of Philosophy.

* Assisted by the joint program of the U. S. Office of Naval Research and the U. S. Atomic Energy Commission.

‡ Now at North Texas State College, Denton, Texas.

[1] Allen, May, and Rall, Phys. Rev. **84**, 1203 (1951).

[2] J. E. May and B. P. Foster, Phys. Rev. **90**, 243 (1953).

[3] C. Mileikowsky and W. Whaling, Phys. Rev. **88**, 1254 (1952).

[4] D. E. Alburger, Phys. Rev. **76**, 435 (1949).

[5] A. N. May and R. Vaidyanathan, Proc. Roy. Soc. (London) **A155**, 519 (1936).

[6] E. Hjalmar and H. Slätis, Arkiv. Fysik **4**, 323 (1952).

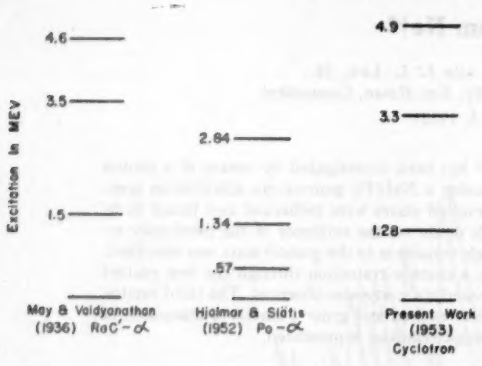

FIG. 2. Energy levels of Ne^{22} determined from present proton group results and those of previous workers.

which was earlier reported by Chadwick and Constable. Their experiment indicates that it is a state of very low yield. The present work, which has better resolution and statistics, gives no evidence for any level between the ground state and the 1.28-Mev excited state. This result, coupled with evidence from the β decay of Na^{22} makes the existence of any such state exceedingly unlikely.

III. COINCIDENCE TECHNIQUE

The detection geometry is shown in Figure 3. The spectrometer and electronic apparatus is essentially the same as that used in the work on Mg^{26}.[2] A block diagram of the electronic apparatus is shown in Fig. 4. With an amount of absorbing foil such that only protons corresponding to a desired excited state were counted, the gamma-ray pulses were selected for display on the synchroscope screen by triggering the sweep with a coincidence pulse. The absorber thicknesses used are shown by the arrows in Fig. 1. The pulse heights were photographed on continuously moving film and later analyzed to form a pulse height distribution. Natural sources of Cs^{137}, Na^{22}, and ThC'' were used for calibration.

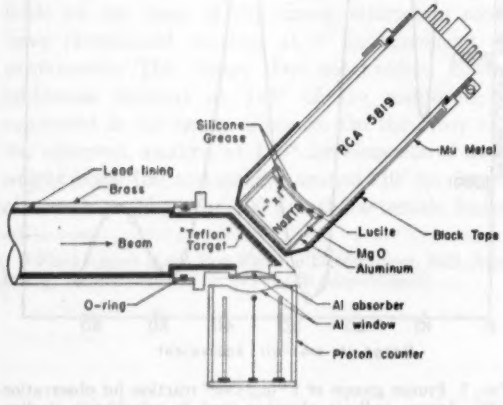

FIG. 3. Diagram of detection geometry.

IV. PULSE-HEIGHT DISTRIBUTION

A. First Excited State

The properties of the first excited state are well known from the β decay of Na^{22}. It was felt, therefore, that a run on this state would be a helpful check on the method and also give a direct quantitative measure of the accidental background above 1.5 Mev. The pulse-height distribution obtained for this state is shown in Fig. 5. The expected 1.28-Mev gamma ray is shown by both its photopeak and Compton edge at about 1.3 and 1.0 Mev, respectively. Spectrometer resolution during this run was 13 percent for the 1.28-Mev photopeak.

B. Second Excited State

Figure 6 shows the pulse-height distribution obtained for gamma rays in coincidence with protons from the second excited state. Two gamma rays are clearly indicated by the presence of their photopeaks at 1.3

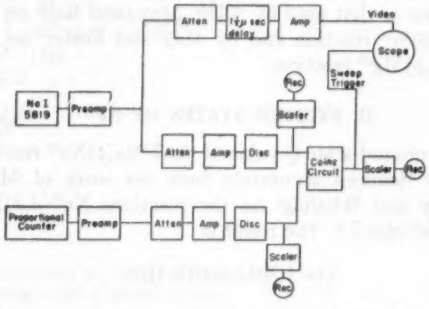

FIG. 4. Block diagram of counting circuits.

and 2.1 Mev, establishing the cascade transition through the first excited state. The Compton edge of the 1.28-Mev gamma ray is shown at 1 Mev, although the other peaks of the 2.1-Mev gamma ray are masked by the 1.28-Mev photopeak and by the rising accidental background. The number of counts above 2.3 Mev is well above the number to be expected from the sum of the background counts and those due to pile-up of the cascade gamma rays in the crystal. This establishes the presence of the 3.4-Mev crossover transition. Comparison of the areas under the curves indicates that the cascade transition is about three times stronger than the crossover. The data shown in Figs. 6 and 7 were taken with a spectrometer resolution of 11 percent for the 1.28-Mev gamma ray.

C. Third Excited State

The pulse-height distribution shown in Fig. 7 was taken for gamma rays in coincidence with protons of seven-cm range. The curve is the smoothest possible curve which can be drawn within the statistics of the points, therefore minimizing the peaks on the curve

because of the poor statistics. The 1.28- and 2.1-Mev gamma rays are indicated by their photopeaks, and the 3.6-Mev transition from the third to the first excited states is shown by the three pair-peaks at about 2.6, 3.1, and 3.6 Mev. The peak at 3.4 Mev may be due to one of the pair-peaks of a weak 3.4-Mev gamma ray. The three higher-energy peaks in the curve may be assigned to the 4.9-Mev transition direct to ground. The pulse heights of these peaks do not fit exactly, but the energy calibration is not very precise in this higher energy region due to the lack of high-energy natural gamma-ray sources.

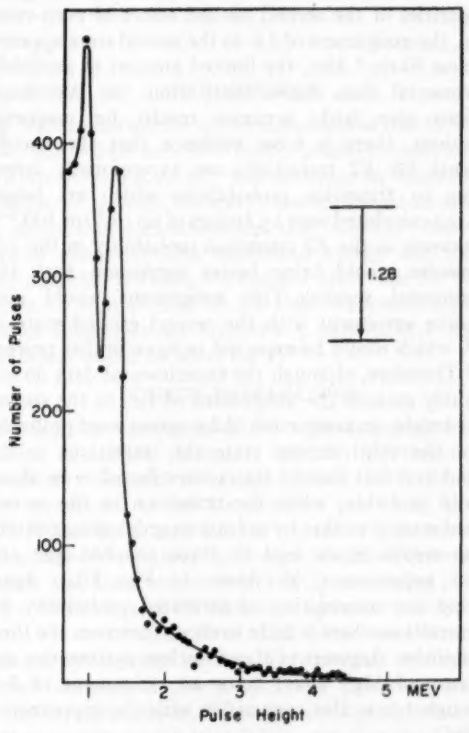

FIG. 5. Gamma rays from 1.28-Mev excited state of Ne^{21}.

In studying this state it was impossible to completely avoid counting some protons from the second excited state, since the absorber used was on the long-range side of the third excited state proton group. Using absorber thicknesses of less than 7-cm air equivalent was impractical because of the presence of elastically scattered alpha particles. Therefore, the pulse, height distribution shown in Fig. 7 comes from both the second and third excited states, and the detection of a gamma ray from the second excited state is not sufficient evidence to establish the presence of a cascade transition through the second excited state. In view of this we can definitely establish the transitions from the third excited state to the ground and first excited states by

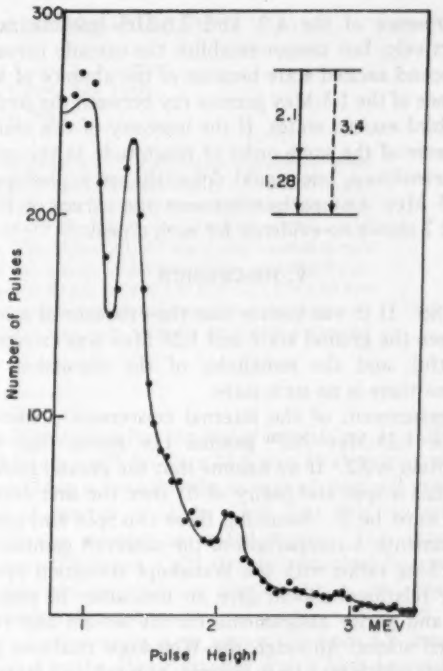

FIG. 6. Gamma rays from the second excited state of Ne^{21}.

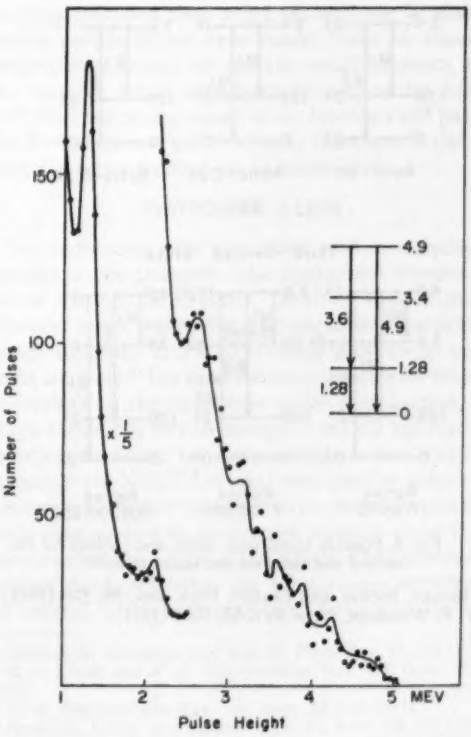

FIG. 7. Gamma rays from the third excited state of Ne^{21}.

the presence of the 4.9- and 3.6-Mev gamma rays, respectively, but cannot establish the cascade through the second excited state because of the absence of any evidence of the 1.5-Mev gamma ray between the second and third excited states. If the intensity of this transition were of the same order of magnitude as the other two transitions, one would definitely see a photopeak at 1.5 Mev. Comparison between the curves of Figs. 6 and 7 shows no evidence for such a peak.

V. DISCUSSION

In Sec. II it was shown that the existence of a level between the ground state and 1.28 Mev was extremely doubtful, and the remainder of the discussion will assume there is no such state.

Measurement of the internal conversion coefficient of the 1.28-Mev Na^{22} gamma ray shows that this transition is $E2$.[7] If we assume that the ground state of Ne^{22} has a spin and parity of 0^+ then the first excited state must be 2^+. Assuming these two spin and parity assignments, a comparison of the observed gamma-ray branching ratios with the Weisskopf transition probability relations[8] should give an indication of possible spin and parity assignments for the second and third excited states. Although the Weisskopf relations give answers which may be in error by as much as a factor of one hundred even such a rough indication can be of some value.

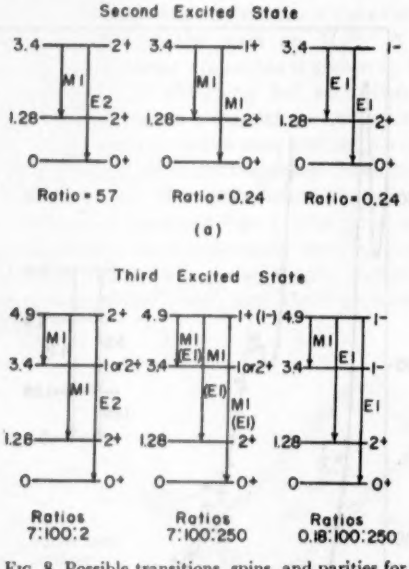

FIG. 8. Possible transitions, spins, and parities for the second and third excited states of Ne^{22}.

The decay of the second excited state was found to involve competition between a 2.1-Mev gamma ray to the first excited state and a 3.4-Mev transition direct to ground, with an intensity ratio of about three to one. The three possible spin and parity assignments which give order of magnitude agreement with this ratio are shown in Fig. 8(a) along with the calculated ratios. The next closest assignments are $2-$, and $3+$ or $4+$ for the second excited state, and give ratios of 10^5 and 10^7, respectively, which can be definitely excluded.

On the basis of the rather limited data on the spins and parities of the second excited states of even-even nuclei, the assignment of $2+$ to the second state appears the most likely.[9] Also, the limited amount of available experimental data shows that, while the Weisskopf relations give fairly accurate results for magnetic transitions, there is some evidence that the matrix elements for $E2$ transitions are exceptionally large, leading to transition probabilities which are larger than the calculated ones by factors of up to 50 or 100.[9-11] An increase in the $E2$ transition probability in the $2+$ assignment would bring better agreement with the experimental results. This assignment would give complete agreement with the second excited state of Mg^{26}, which would be expected to have similar properties.[2] Therefore, although the experimental data do not definitely exclude the assignment of $1\pm$ to the second excited state, an assignment of $2+$ seems most probable.

For the third excited state the transitions to the ground and first excited states were found to be about equally probably, while the transition to the second excited state is weaker by at least an order of magnitude. These results again lead to three possible spin and parity assignments, as shown in Fig. 8(b). Again making our assumption of increased probability for $E2$ transitions there is little to choose between the three possibilities. Arguments about nuclear systematics and the case of Mg^{26} again favor an assignment of $2+$, although $1\pm$ is also compatible with the experimental results.

The authors wish to express their appreciation for the helpful counsel and encouragement of Professor Waldo Rall who suggested this problem and under whose direction the work was completed. We also wish to thank Professor E. C. Pollard for many helpful discussions.

[7] Hinman, Brower, and Leamer, Phys. Rev. **90**, 370 (1953).
[8] V. F. Weisskopf, Phys. Rev. **83**, 1073 (1951).
[9] G. Scharff-Goldhaber, Phys. Rev. **90**, 587 (1953).
[10] J. M. Blatt and V. F. Weisskopf, *Theoretical Nuclear Physics* (John Wiley and Sons, Inc., New York, 1952), p. 633.
[11] M. Goldhaber and A. W. Sunyar, Phys. Rev. **83**, 906 (1951).

Radiations of 13.9-Min Ce^{146} and 24.4-Min Pr^{146}†

W. BERNSTEIN, S. S. MARKOWITZ,* AND S. KATCOFF
Brookhaven National Laboratory, Upton, New York

(Received November 24, 1953)

The radiations of Ce^{146} and Pr^{146} fission products were investigated with a scintillation coincidence spectrometer. The 24.4-min Pr^{146} was shown to decay by two β branches of maximum energy 2.3 ± 0.2 Mev and 3.7 ± 0.2 Mev and of about equal intensity. Gamma rays of 455 ± 13 kev, 750 ± 30 kev, and 1490 ± 40 kev were observed; the 455-kev γ ray was the most intense, and the 750-kev line was shown to consist of two γ rays of about the same energy. A probable decay scheme is given. The 13.9-min Ce^{146} was found to emit β rays of 700 ± 100 kev maximum energy in coincidence with all of the γ rays. Abundant γ rays of 110 ± 5 kev, 142 ± 5 kev, 220 ± 10 kev, 320 ± 10 kev, and weak γ rays of about 50 kev, about 250 kev, and 270 ± 10 kev were observed. The relative intensities and the observed γ-γ coincidences are tabulated, but the data were insufficient to determine a unique decay scheme. Some of the γ rays were partially internally converted giving rise to Pr K x-rays.

INTRODUCTION

THE investigation of the radiations of the 13.9-min Ce^{146}–24.4-min Pr^{146} fission product chain, begun by Caretto and Katcoff,[1] was extended by means of a coincidence scintillation spectrometer. They had shown, by absorption measurements, that the Ce^{146} emits β rays of about 0.9-Mev maximum energy and soft γ rays probably between 0.2 and 0.3 Mev. The Pr^{146} was shown to emit β rays of 3.8-Mev maximum energy. Earlier investigations reported γ rays of 1.4 Mev,[2] 0.49 Mev,[3] and 0.78 Mev[3] for Pr^{146}.

SOURCE PREPARATION

Ce activity was separated from fission products by a solvent extraction procedure recently developed by Glendenin.[4] Samples of uranyl nitrate (10 to 100 mg) were irradiated in the Brookhaven pile at a flux of 4×10^{12} neutrons/cm^2 sec for three to ten minutes and allowed to cool for 5 to 20 minutes. Then the uranyl nitrate was dissolved in $10M$ HNO_3 containing 20 mg of Ce^{+3} carrier, and $NaBrO_3$ was added to oxidize the Ce to the tetravalent form. The latter was extracted with methyl isobutyl ketone. The trivalent rare earths as well as most of the other fission products remain in the aqueous phase. The organic layer containing Ce^{+4} was washed with $10M$ HNO_3 and then the Ce was back-extracted into dilute acid after reduction to Ce^{+3} with H_2O_2. This cycle was repeated two or three more times. The Ce samples were mounted as ceric iodate 15 to 30 minutes after the end of irradiation. In addition to 13.9-min Ce^{146} (and its 24.4-min Pr daughter which was growing in rapidly) the samples contained initially about 2 percent of 33-hr Ce^{143}, but this caused no interference except as noted below. The recently discovered[5] 3.0-min Ce^{145} did not interfere beacuse it had decayed away almost completely by the time the measurements were made.

The Pr^{146} sources were separated from Ce samples prepared in the above manner which had decayed for about 23 minutes. La carrier was used for the Pr^{146}. The Ce was removed by means of three ceric iodate precipitations, and then two LaF_3 and one lanthanum oxalate precipitations were made. Some of these Pr samples were found to contain small amounts of a 6-hr activity which was later shown[5] to be 5.95-hr Pr^{145}. This led to discovery[5] of its 3.0-min Ce^{145} parent. The Pr^{145} does not emit[5] γ rays; therefore it did not affect the measurements on 24.4-min Pr^{146}.

INSTRUMENTATION

The radiations were examined with a coincidence scintillation spectrometer. This instrument consists of a pair of scintillation crystals, DuMont K-1186 photomultiplier tubes, nonoverloading amplifiers,[6] stable high-voltage supplies,[7] and a coincidence gray-wedge pulse-height analyzer.[8] The scintillation crystals were selected appropriate to the radiations under examination. For γ rays above 100 kev in energy, 3 cm×2 cm NaI(Tl) crystals were used; for lower energy γ and x-rays, a 0.2 cm×2 cm NaI(Tl) crystal was used to reduce the sensitivity to higher energy γ rays. Beta-ray measurements were made with anthracene crystals whose thickness exceeded the range of the β rays. The pulse-height analyzer displayed either the total events recorded in one crystal ("singles" spectrum) or events in that

† Work performed under the auspices of the U. S. Atomic Energy Commission.

* Present address: Frick Chemical Laboratory, Princeton University, Princeton, New Jersey.

[1] A. A. Caretto, Jr., and S. Katcoff, Phys. Rev. **89**, 1267 (1953).

[2] R. P. Schuman, Metallurgical Laboratory Report CN-2799, March, 1945 (unpublished), referred to in "Table of isotopes" by Hollander, Perlman, and Seaborg, Revs. Modern Phys. **25**, 469 (1953).

[3] J. D. Knight and D. P. Ames, Los Alamos Laboratory Report WASH-62, December, 1951 (unpublished), referred to in "Table of isotopes" by Hollander, Perlman, and Seaborg, Revs. Modern Phys. **25**, 469 (1953).

[4] L. E. Glendenin (private communication). A similar method was used in this laboratory by J. W. Gryder and R. W. Dodson to separate tetravalent from trivalent Ce [J. Am. Chem. Soc. **73**, 2890 (1951)].

[5] Markowitz, Bernstein, and Katcoff, Phys. Rev. **93**, 178 (1954).

[6] R. L. Chase and W. A. Higinbotham, Rev. Sci. Instr. **23**, 34 (1952).

[7] W. A. Higinbotham, Rev. Sci. Instr. **22**, 133 (1951).

[8] Bernstein, Chase, and Schardt, Rev. Sci. Instr. **24**, 437 (1953); R. L. Chase, Brookhaven National Laboratory Report BNL 263 (T-42), 1953 (unpublished).

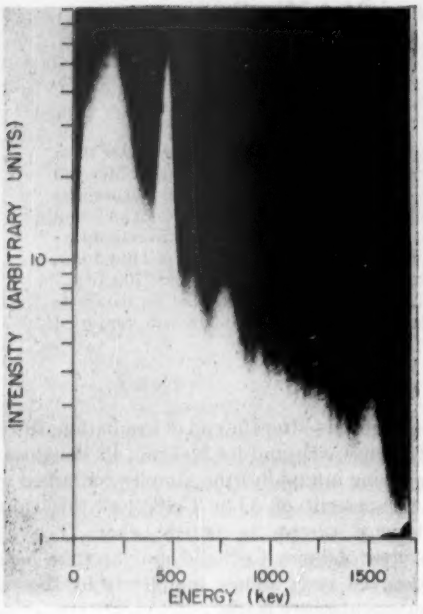

FIG. 1. Gray-wedge photograph of the Pr^{146} γ-ray spectrum.

crystal which occurred in time coincidence with events of a selected amplitude recorded in the other crystal ("coincidence" spectrum). The effective coincidence time was 10^{-7} sec, and accidental coincidence effects were evaluated by the introduction of a 5×10^{-7} sec delay line between the selecting detector and the coincidence circuit. The photographs were taken with a Polaroid Land camera except for the relative intensity measurements which were taken on spectroscopic type *IV-O* 35-mm film. For the γ-ray and x-ray measurements, the β rays were removed with Be absorbers.

RADIATIONS FROM Pr^{146}

The 24.4-min Pr^{146} was investigated first because it could be prepared free of its 13.9-min Ce^{146} parent. Figure 1 is a gray-wedge photograph of the Pr^{146} "singles" spectrum. The following γ rays can be identified: 455 ± 13 kev, 750 ± 30 kev, 1490 ± 40 kev, and possibly another low intensity line at 590 ± 20 kev. Na^{22}, which emits γ rays of 1277 kev and annihilation radiation (511 kev), was used as the calibration source. The width of the 750-kev γ-ray photoline appears to be greater than would be expected from a single γ ray of that energy. No x-rays can be observed above the bremsstrahlung and degraded γ-ray background; thus none of the γ rays are converted to an appreciable extent. The observed relative intensity ratios, calculated from the areas of the photolines after subtraction of the bremsstrahlung background and corrected for the crystal efficiency and the yield in the photoline,[9] were 1.00, 0.22 ± 0.05, and 0.33 ± 0.06 for the 455-kev, 750-kev, and 1490-kev γ rays, respectively.

Coincidence measurements showed that both 1490-kev and 750-kev γ rays were in coincidence with 455-kev γ rays, but they were not in coincidence with each other. However, the 750-kev γ ray was found to be in coincidence with another γ ray of energy approximately 750 kev; this explains the greater width of the 750-kev γ ray in the "singles" spectrum. The weak line at 590 kev could not be found in the "coincidence" spectra.

The β-ray spectrum was compared with that of the 3.58-Mev β rays of K^{42}. By making intense exposures, we could define the end points of the spectra fairly sharply. The "singles" β-ray spectrum and the β rays in coincidence with the 455-kev γ rays both had a maximum energy of 3.7 ± 0.2 Mev. However the β rays in coincidence with the 750-kev and 1490-kev γ rays had a maximum energy of 2.3 ± 0.2 Mev.

From the above data we postulated the decay scheme shown in Fig. 2. Crossover transitions of 1.95 Mev and 1.20 Mev were not observed. The branching ratio for the β rays, as deduced from the measured γ-ray intensities, is 56 percent for the 3.7-Mev β ray and 44 percent for the 2.3-Mev β ray. The log (ft) values are 7.4 and 6.6 for the 3.7-Mev and 2.3-Mev β rays, respectively; this indicates that both transitions are first forbidden. The identification of the 455-kev level in Nd^{146} as the first excited state, with spin and parity assignment of 2+, agrees with the energy predictions and systematics of the first excited states of even-even nuclei.[10] The tentative assignment of (3−) to the spin and parity of the ground state of Pr^{146} was based on the (ft) values and the absence of transitions *from* this level to the 0+ ground state of Nd^{146}, and also *to* this level from the 0+ ground state of Ce^{146}. (See following section.)

RADIATIONS FROM Ce^{146}

After identification of the 24.4-min Pr^{146} radiations, the 13.9-min Ce^{146} was examined in a similar manner. Figure 3 is a gray-wedge photograph of the Ce^{146} γ-ray

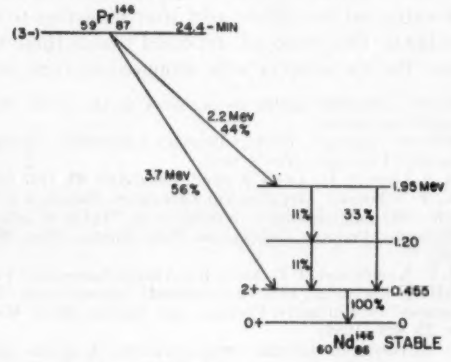

FIG. 2. Probable decay scheme of Pr^{146}.

[9] P. R. Bell (unpublished data).

[10] G. Scharff-Goldhaber, Phys. Rev. **90**, 587 (1953).

"singles" spectrum. The following γ rays were identified in the "singles" γ-ray spectrum: 110±5 kev, 142±5 kev, 220±10 kev, 270±10 kev, and 320±10 kev. The 145-kev γ ray from Ce^{141} and the 320-kev γ ray from Cr^{51} were used as the calibration sources for these energy measurements. An intense line was observed at approximately 36 kev and was identified as a Pr K x-ray by comparison with a known source of Pr K x-rays (Ce^{141}) using a krypton-filled proportional counter.[11] These x-rays are attributed to internal conversion of some of the γ rays. The observed intensity ratios, calculated from the areas of the photolines after subtraction of the bremsstrahlung and degraded γ-ray background and corrected for the crystal efficiency and the yield in the photoline,[9] are shown in column 2, Table I.

The γ-γ coincidence measurements are summarized in column 3, Table I. It is seen that the 110-kev and 142-kev γ rays are in coincidence with 220-kev γ rays but are not in coincidence with each other. In addition it was observed that a shoulder appeared on the high-energy side of the 220-kev γ-ray line when it was displayed in coincidence with the 110-kev γ ray; however the shoulder was absent when the 220-kev line was displayed in coincidence with the 142-kev γ ray. In the converse experiment a 20-kev wide selecting channel was centered at 220 kev and then at 250 kev, and the coincidence spectra were photographed. At the 220-kev channel setting the 142-kev γ-ray intensity was greater than that of the 110-kev γ ray; at the 250-kev channel setting the 110-kev γ ray was more intense. Therefore some of the 110-kev γ rays are in coincidence with a γ ray of approximately 250 kev which was not observed in the "singles" spectrum.

The γ-ray spectrum in coincidence with the x-rays, observed soon after preparation of the source, showed the 110-kev, 142-kev, 220-kev, and 270-kev γ rays. As the source decayed, the 270-kev line broadened, and its intensity decreased more slowly than that of the other γ rays. Eventually its position shifted to 290 kev. This must have been caused by the known coincidences[12]

TABLE I. γ rays observed from 13.9-min Ce^{144}.

Selecting γ ray (kev)	Relative intensity (including efficiency corrections)	γ rays and K x-rays observed in "coincidence" spectrum (kev)
320	1.00	(nothing)
220	0.52±0.10	36, 110, 142
142	0.42±0.08	36, 220
110	0.20±0.05	36, 220, 250
270	0.12±0.03	36, 50
250	low	36, 110
50	low	270
36 (x-ray)	high	36, 110, 142, 220, 270

[11] W. Rubinson and W. Bernstein, Phys. Rev. **86**, 545 (1952).
[12] W. H. Burgus, Phys. Rev. **88**, 1129 (1952).

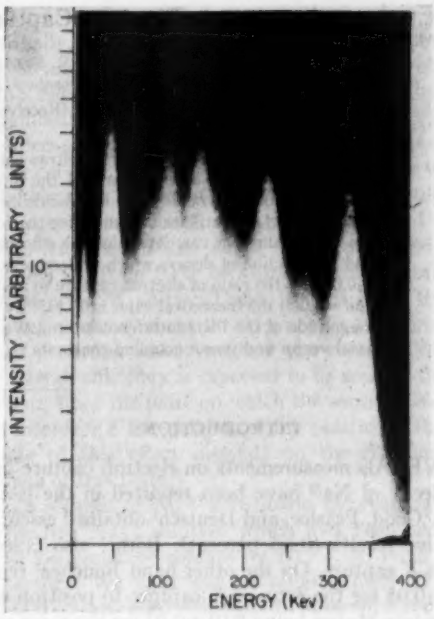

FIG. 3. Gray-wedge photograph of the Ce^{144} γ-ray spectrum.

between x-rays and 289-kev γ rays present in 33-hr Ce^{143}.

A search was undertaken for a 50-kev γ ray which would represent the difference between 320 kev and 270 kev. With the channel set at 270 kev, x-rays and a very weak line at about 50 kev were observed in the coincidence spectrum. Two hours after this observation, these coincidences were still present but in considerably lower intensity. These residual coincidences were attributed mostly to the 289-kev and 57-kev γ rays of Ce^{143}. However, because of the decrease in intensity, some of the coincidences must have been due to the 13.9-min Ce^{144}.

The β-ray "singles" spectrum showed a maximum energy of 700±100 kev when compared in gray-wedge photographs with the 624-kev internal conversion electron line of a Cs^{137} source. The β-ray spectrum observed in coincidence with any of the γ rays was approximately identical with the "singles" spectrum; this shows that no β transitions to the ground state occur. These β-ray energy measurements were less accurate than those of the Pr^{144} because of the presence of the high-energy Pr^{144} β rays in all Ce^{144} samples. If it is assumed that there is only a single β-ray transition of 700 kev, the log (ft) value is 4.0; if other β transitions occur in appreciable intensity, their energy must also be approximately 700 kev with log (ft) no greater than 5. Thus the β decay appears to be allowed and represents transitions from a 0+ to a 1+ state.

The data obtained to date for the Ce^{144} are insufficient for the presentation of a unique decay scheme.

Electron Capture in the Decay of Na^{22}†

R. SHERR* and R. H. MILLER‡
Palmer Physical Laboratory, Princeton University, Princeton, New Jersey
(Received November 27, 1953)

The ratio of electron capture to positron emission in the decay of Na^{22} to the 1.28-Mev level in Ne^{22} has been determined by a comparison of the intensities of positron emission and 1.28-Mev radiation. The measurements were made with a coincidence arrangement employing a 4π beta counter to detect the positrons and a scintillation counter for the γ rays. By varying the bias of a discriminator responding to the γ spectrum, one can determine the efficiency of the 4π beta counter, and the product of this efficiency and the fraction of decays which undergo electron capture. These measurements lead to a value of 0.110 ± 0.006 for the ratio of electron capture to positron emission. If one assumes that the Na^{22} decay is allowed ($\Delta J = 1$, no) the theoretical value is 0.1135. By a comparison of these values, we can make an estimate of the magnitude of the Fierz interference term. We find, subject to the above assumption, that the ratio of the axial vector and tensor coupling constants $C_A/C_T = (-1 \pm 2)$ percent.

INTRODUCTION

SEVERAL measurements on electron capture in the decay of Na^{22} have been reported in the last ten years. Good, Peaslee, and Deutsch[1] obtained essentially negative results (0 ± 5 percent). Bothe[2] also failed to detect K capture. On the other hand Bouchez[3] reports 0.10 ± 0.05 for the ratio of K capture to positron emission, while Major[3] found 0.04 ± 0.03 for the same quantity. The extensive use of Na^{22} for calibrating the efficiency of scintillation counters has led us to attempt a more precise measurement.

Na^{22} decays by positron emission to an excited state of Ne^{22} at 1.28 Mev. [There is a very weak transition (0.06 percent) to the ground state of Ne^{22}; this is too feeble to have any effect on our measurements and we shall ignore it hereafter.] Electron capture to the 1.28-Mev level will also give rise to the 1.28-Mev gamma ray. Our method is essentially the comparison of the relative numbers of positrons and 1.28-Mev quanta.

Suppose a Na^{22} source is placed in the vicinity of a β counter (which we shall assume counts β particles only) and a γ counter shielded in such a way as to count γ's only. The β counter registers the positrons with an efficiency ϵ_β (the efficiency is the number of events detected per event). The γ counter will detect nuclear (1.28-Mev) radiation with an efficiency ϵ_n and annihilation (0.511-Mev) radiation with an efficiency ϵ_a. Since the efficiency depends on geometry as well as on energy, ϵ_a will depend on the place at which the positrons annihilate. We differentiate between that fraction f of the positrons which annihilate after passage through the β counter and those which annihilate elsewhere by designating the γ efficiencies (averaged over geometries) as ϵ_a' and ϵ_a'', respectively. Let P be the average number of positrons per disintegration and K be the average number of electron captures per disintegration ($P+K=1$).

The rate for coincidences between β and γ counts is

$$C = PN_0\epsilon_\beta(2\epsilon_a' + \epsilon_n), \tag{1}$$

where N_0 is the disintegration rate. The counting rate of the γ counter is

$$N = 2PN_0 f\epsilon_a' + 2PN_0(1-f)\epsilon_a'' + N_0\epsilon_n. \tag{2}$$

Since the counter cannot distinguish between the two categories of annihilation quanta, the first two terms on the right are lumped together to give N_a, the counting rate for annihilation quanta and the third term is N_n, the counting rate for the nuclear γ ray.

Let α and β be the fractional γ-counting rates:

$$\alpha = N_n/N = N_0\epsilon_n/N,$$
$$\beta = N_a/N = 2PN_0/N\{f\epsilon_a' + (1-f)\epsilon_a''\}, \tag{3}$$
$$\alpha + \beta = 1.$$

Dividing (1) by N and using (3), we obtain

$$\frac{C}{N} = \epsilon_\beta\left\{\alpha P + \beta\frac{\epsilon_a'}{\epsilon_a'' + f(\epsilon_a' - \epsilon_a'')}\right\}. \tag{4}$$

The physical interpretation of (4) is simply this: if the γ counter can be made to respond only to the nuclear γ ray ($\alpha=1$ and $\beta=0$), then $C/N = \epsilon_\beta P$, which is the probability that the positron will be counted times the probability that a positron was emitted. Similarly if $\beta=1$ and $\alpha=0$, C/N will be the product of the probability that a positron was counted times the probability that the annihilation quantum detected was associated with that positron.

Now in general the γ counter will respond to both γ radiations and in order to obtain P from this type of

† This work was supported in part by the U. S. Atomic Energy Commission and the Higgins Scientific Trust Fund. A preliminary report was presented at the Rochester meeting of the American Physical Society, June, 1952.
* Address for the academic year 1953-1954: W. K. Kellogg Radiation Laboratory, California Institute of Technology, Pasadena, California.
‡ Present address: U.S.S. Howard D. Crow (DE252), Fleet Post Office, New York, New York.
[1] Good, Peaslee, and Deutsch, Phys. Rev. **69**, 313 (1946).
[2] W. Bothe, Z. Physik 123, No. 1E (1944).
[3] Unpublished work referred to by R. Bouchez, Physica **18**, 1171 (1952). This paper is an extensive review of the experimental methods and theoretical interpretation of K capture measurements.

measurement, the other parameters (α, β, ϵ_β, ϵ_a', ϵ_a'', and f) must be determined. Two simplifying conditions are apparent, however. If $f=1$ or $\epsilon_a'=\epsilon_a''$, Eq. (4) reduces to

$$C/N=\epsilon_\beta(\alpha P+\beta). \tag{5}$$

The second condition can be obtained if the β counter is sufficiently small, the source placed close by and all positrons annihilated in the immediate vicinity; if then the γ counter is sufficiently remote, $\epsilon_a'=\epsilon_a''$ since the difference here depends primarily on solid angle. To obtain $f=1$, we can use a 4π beta counter which contains the source within its volume. Actually f cannot be made exactly equal to unity, since the source must be supported and some positrons may enter the support and annihilate there without entering the gas of the counter; however, with care one can achieve $f=0.95$ or better. This is the arrangement which we have used; since the γ counter is perforce exterior to the β counter, ϵ_a' (for positrons annihilated after passage out into the counter) and ϵ_a'' (for positrons annihilating in the source and support) are practically equal.

The condition $f=1$ is desirable for additional reasons. Since f is one of the ingredients of the β counter efficiency ϵ_β, the greater its value, the higher will be the coincidence rate. Also, if f is small because the source is located some distance from an end window counter, γ-γ coincidences may introduce additional corrections. The latter are trivial with the 4π counter.

Once conditions are arranged so that Eq. (5) is applicable, the experimental variables ϵ_β and α (or β) must be determined. If the γ counter is a Geiger counter, α may be measured indirectly, leaving ϵ_β to be separately found. However, by using a scintillation counter one can, by varying the pulse-height selection, change the value of α over a considerable range. It is possible to determine α through an analysis of the pulse spectrum. If one rewrites Eq. (5) using the condition that $\alpha+\beta=1$, one obtains

$$C/N=\epsilon_\beta(1+\alpha K), \tag{6}$$

so that a plot of C/N vs α yields a straight line whose intercept on the C/N axis yields ϵ_β, while at $\alpha=1$, $C/N=\epsilon_\beta(1-K)$. It is therefore possible to determine the desired parameters in one experiment.

EXPERIMENTAL ARRANGEMENT

We have used a 4π counter operating in the high proportional region to detect the positrons. The counter is identical with that described by Borkowski.[4] It consists of two brass pillboxes ($2\frac{3}{4}$ in. i.d. and $1\frac{5}{16}$ in. deep) with the anodes across a diameter. The two counting regions are separated by a thin (1 to 10 mil) aluminum or copper plate. The source is mounted on a zapon film (40 micrograms/cm^2) stretched across a $\frac{1}{4}$-in. hole in the middle of this plate. The anodes (1-mil W wire) of the two halves are connected in parallel externally through isolating condensors to the input of a preamplifier. Additional amplification was obtained with a nonoverloading amplifier designed by Chase and Higginbotham.[5] The gain was set high so that virtually all pulses saturated. By varying the high voltage applied to the counter we found that the counting rate was flat to better than $\frac{1}{2}$ percent from 2.4 to 2.8 kilovolts with a counter filling of methane at a pressure of 1 atmosphere. An integral bias curve of the amplified pulses was also flat from 10 to 64 volts (maximum pulse amplitude was 70 volts). These tests suggest that the counter efficiency must be very nearly 100 percent for those positrons which entered the counter. Actually the overall efficiency is expected to be smaller than 100 percent, since the plate on which the source is mounted can intercept a few percent of the positrons; the magnitude of this effect depends on the thickness and flatness of this plate.

The sources of Na^{22} were made by evaporation of carrier-free NaCl solution which had been separated in an ion exchange column by Dr. T. A. Pond of this laboratory. We used sources ranging from 33 000 to 137 000 counts/min. Attempts to determine the source thickness indicated that on the average it was less than the 40 μg/cm^2 of the supporting foil.

The γ counter was a $1\frac{1}{2}$-in. diam$\times$1 in. high NaI scintillation crystal. It was placed directly under the proportional counter and a house of lead bricks was built around the counters to reduce the background counts. The γ pulses were analyzed with an integral bias discriminator whose output fed a scaler (for N) and a coincidence circuit. Similar apparatus was used in the proportional counter branch. The coincidence circuit resolving time was varied to determine the proper operating region; finally a resolving time of 1 μsec was selected. (With the weak sources used, the random coincidence rate was only a fraction of one percent of the true coincidence rate.)

A typical run consisted in measuring C and N as a function of the bias of the γ-counter discriminator. As expected, the ratio C/N decreases with increasing bias until the bias exceeds the pulse height for annihilation radiation; beyond this it is fairly constant. The integral bias curve for N is then analyzed into two components, one for the 1.28-Mev radiation and one for the 511-kev annihilation radiation. In order to extrapolate the 1.28-Mev spectrum to low amplitudes, a Co^{60} spectrum was taken with a Co^{60} source replacing the Na^{22} source in the 4π counter. The average energy of the two Co^{60} γ rays (1.17 and 1.33 Mev) is sufficiently close to 1.28 Mev so that the shape of Compton spectra below 600 kev should be practically identical. By matching the 1.28-Mev Na^{22} spectrum to the Co^{60} spectrum, the required extrapolation can be carried out.

[4] C. J. Borkowski, Oak Ridge National Laboratory Report ORNL-1056, 1951 (unpublished).

[5] R. L. Chase and W. A. Higginbotham, Rev. Sci. Instr. 23, 34 (1952).

Before describing the experimental results in detail there are two sources of error which must be considered: namely the possibility that the β counter is detecting the K x-rays of Ne^{22} which follow K capture, and secondly, the question of detection of coincident 511-kev and 1.28-Mev quanta in the γ counter.

FLUORESCENT YIELD OF Ne^{22}

Following K capture in Na^{22}, the daughter atom Ne^{22} has an excess energy of about 860 volts corresponding to a vacancy in the K shell. This energy is subsequently liberated in the form of quanta and Auger electrons. If both of these were detected by the β counter the present experiment would lead to the conclusion that there is no K capture. However, the Auger electrons are softer than 840 volts and would be very hard to detect. (According to Ference and Stephenson[6] the range, for example, of a 2-kev electron is about 17 $\mu g/cm^2$.) It would require a great deal of care to make a source sufficiently thin to permit these electrons to escape. This was verified by measurements with 40-$\mu g/cm^2$ zapon films covering both sides of the Na^{22} source. The β-counting rate decreased by approximately 0.3 percent when 4 films were added to each side of the source. This amount of absorber also completely eliminates L radiation of Ne.

On the other hand, K x-rays of Ne would not be appreciably absorbed by 40 $\mu g/cm^2$ of Zapon, while the absorption in the counter gas should be almost complete. We do not know whether our counter would register these x-rays, but it seems highly probable that it would. Counts taken covering the source with ~150 $\mu g/cm^2$ of Zapon and ~150 $\mu g/cm^2$ of aluminum showed a 0.5 percent decrease. These absorbers should reduce the K x-rays by approximately 50 percent. Since some soft positrons were certainly absorbed, this measurement can only set an upper limit of 1 percent for the β-counting rate (without these foils) ascribable to K x-rays. However, consideration of the fluorescent yield indicates that we should expect at most 0.1 percent effect due to the x-rays.

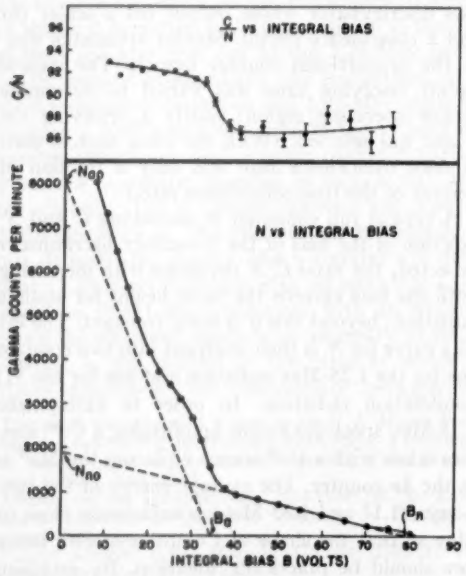

FIG. 1. Lower graph: Integral bias curve for Na^{22} γ rays. The dotted lines show the approximations to the 1.28-Mev and 0.511-Mev spectra used in calculating the spectrum of simultaneous pulses (N_{an}). Upper graph: Integral bias curve for C/N.

While numerous measurements of fluorescent yields have been made throughout the periodic table, very few measurements are available for low Z.[7,8] Locher[9] has measured the fluorescent yield of Ne to be 8.3 percent. (Crone[10] gives a value of 0.81 percent; however, this was not a direct measurement but was obtained by normalizing his data to higher-Z results on the basis of theoretical expectations.) Locher's measurement is considerably in excess of the expected value. The theory of the Auger process is well understood and Burhop[7] gives a calculated value of 1.1 percent. Since theory and experiment are in good accord for higher Z, it seems reasonable to accept Burhop's calculations for Ne. (Locher's experiment is a difficult one involving identification of 800-volt Auger electron blobs at the beginning of a photoelectron track in a cloud chamber.) Since the amount of K capture in Na^{22} is approximately 10 percent, the maximum number of K x-rays which can be detected in the β counter is 0.1 percent of the β^+ count, if we take Burhop's calculated value for the fluorescent yield, and 0.8 percent with Locher's result. Our absorption measurement is consistent with either. If Locher's results are correct, our measurement of the electron capture (K) might require a correction of +8 percent, whereas Burhop's value lead to a maximum correction of +1 percent.

CORRECTION FOR SIMULTANEOUS QUANTA

In writing down Eqs. (1) and (2) we ignored the possibility that an annihilation quantum and a 1.28-Mev quantum might enter (and be absorbed by) the γ crystal simultaneously. Because of the finite solid angle this effect is not trivial, especially near the upper end of the 1.28-Mev spectrum and beyond. Pulses of this type will give coincidences and since they are associated with positrons should be included in β in Eq. (5). Since these pulses can be larger than the 1.28-Mev quanta, α in Eqs. (5) and (7) cannot reach unity. As a function of bias, α increases from a low value (~0.3) to about 0.95 near the end of the 1.28 Mev spectrum and then decreases rapidly to zero beyond this point. (See Fig. 2.)

[6] M. Ference and R. J. Stephenson, Rev. Sci Instr. **9**, 246 (1938).

[7] E. H. S. Burhop, *The Auger Effect* (Cambridge University Press, Cambridge, 1952).

[8] Broyles, Thomas, and Haynes, Phys. Rev. **89**, 715 (1953).

[9] G. L. Locher, Phys. Rev. **40**, 484 (1932).

[10] W. Crone, Ann. Physik **27**, 405 (1936).

Correspondingly the ratio C/N decreases, reaches a plateau, and finally increases to a value ϵ_β. (If it were not for the poor statistics obtained in the last region, this would be a good way to find ϵ_β.)

In order to take these simultaneous quanta into account, we have made the following approximate calculation. Figure 1 shows N *vs* bias for a particular run (after correction for background). N has now three components N_a, N_n, and N_{an}, where the first two correspond to counts resulting from crystal responses to the annihilation quanta and the nuclear γ rays, and N_{an} is the counting rate due to simultaneous responses to these two radiations. Then (in the $f=1$ approximation)

$$\frac{C}{N}=\epsilon_\beta\frac{PN_n+N_a+N_{an}}{N}. \tag{7}$$

If we assume that N_{an} is small, we can decompose N into N_a and N_n as a first approximation. If we approximate these spectra by the straight lines, as shown in Fig. 1, and use these to calculate N_{an}, we find

$$N_{an}=\frac{N_{a0}N_{n0}}{N_0}A_{an}, \tag{8}$$

where N_{a0} and N_{n0} are the extrapolated counting rates at zero bias, and N_0 is the source strength (given with sufficient accuracy by the β count). The quantity A_{an} is given by

$$A_{an}=\begin{cases}1-(B/2B_aB_n) \text{ for } B<B_a\\ (B_a+2B_n-2B)/2B_n \text{ for } B_a<B<B_n,\\ (B_a+B_n-B)^2/2B_aB_n \text{ for } B_n<B<B_a+B_n,\end{cases} \tag{9}$$

where B is the bias setting and B_a and B_n are the upper ends of the straight line approximations to the 0.511- and 1.28-Mev spectra.

This formula was compared with an experimentally determined curve in the region just beyond B_n using a strong source. It was found that our formula gave results about 40 percent high; hence for analysis of the coincidence runs Eq. (8) was multiplied by 0.7. Since this correction is significant only near the end point of the 1.28-Mev spectrum, we feel that this procedure is sufficiently accurate.

The analysis of N to determine α for each bias is carried out as follows. N_{an} is computed as outlined above; its magnitude ($\times 10$) is shown in Fig. 2. These numbers are subtracted from N for biases in excess of 40 volts. This difference is then N_n in this region. To extrapolate to lower bias, we took a Co^{60} spectrum, corrected it for simultaneous pulses, and normalized it to the Na^{22} 1.28-Mev spectrum as shown in Fig. 2. The ratio of the complete 1.28-Mev spectrum to N of Fig. 1 gives α. The latter is also plotted in Fig. 2.

RESULTS

A series of runs were made with several sources to investigate the general features of this experiment.

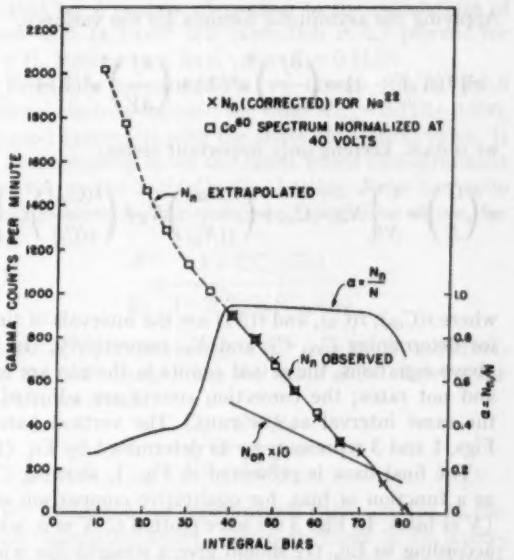

FIG. 2. The 1.28-Mev spectrum (N_n) obtained after correction for simultaneous pulses (N_{an}) and extrapolated to low bias through the use of the Co^{60} spectrum. The scale on the right and the curve labelled α give the fractional counting rate for the 1.28-Mev γ ray.

Analysis of this data gave $\epsilon_\beta=0.995\pm0.007$ and $K=0.101\pm0.011$. The efficiency seemed a bit high (for the source support intercepts some of the positrons) and it was felt that there might have been a systematic error at low γ bias. The electronic equipment was checked carefully and a more extensive set of points were taken. It is these data which we shall discuss. The observed counts (N_{ob} and C_{ob}) had to be corrected for N_b, the background in the γ counter, and C_r and C_b, the random and real (extraneous) coincidences. The last effect is observed with no source in the counter and is probably entirely due to cosmic radiation (7 counts/min) since the rate was insensitive to the bias of the γ counter. The random rate was small (<0.7 percent). The γ background was not negligible amounting to 30 percent at a bias of 80 volts. In calculating the statistical errors, if we ignore these corrections for the moment, we note that while C and N are large numbers and $N-C$ is small, the error in C/N is determined by $N-C$. If there were no K capture and $\epsilon_\beta=1$, $N-C$ would be zero and C/N would be exactly unity, whatever the actual magnitude of C. N_{ob} and C_{ob} are not independent since many of the γ counts are the same counts recorded by the coincidence circuit. Therefore we can break up N_{ob} into two parts, a part which is independent of C_{ob} which we shall call X, and a part directly correlated with C_{ob}, which is just C_{ob}. The same discussion applies to N_b which we write as C_b+N_b'. Then the corrected ratio of C to N is:

$$\frac{C}{N}=\frac{C_{ob}-C_b-C_r}{N_{ob}-N_b}=\frac{C_{ob}-C_b-C_r}{C_{ob}+X-N_b'-C_b}. \tag{11}$$

Applying the asymptotic formula for the variance,

$$\sigma^2\{f(X,Y\cdots)\}=\left(\frac{\partial f}{\partial X}\right)^2\sigma^2(X)+\left(\frac{\partial f}{\partial Y}\right)^2\sigma^2(Y)+\cdots,$$

we obtain, keeping only important terms:

$$\sigma^2\left(\frac{C}{N}\right)=\frac{C^2}{N^4}\left[N_{ob}-C_{ob}+\left(\frac{t(C_{ob})}{t(N_b)}\right)N_b+\left(\frac{t(C_{ob})}{t(C_b)}\right)C_b\right], \tag{12}$$

where $t(C_{ob})$, $t(C_b)$, and $t(N_b)$ are the intervals of times for determining C_{ob}, C_b, and N_b, respectively. (In the above equations, the actual counts in the run are used and not rates; the correction counts are adjusted to the same interval as the runs.) The vertical bars in Figs. 1 and 3 represent $\pm\sigma$ as determined by Eq. (12).

The final data is presented in Fig. 1, showing C/N as a function of bias, for qualitative comparison with (N *vs* bias). In Fig. 3 we have plotted C/N *vs* α, which according to Eq. (7) should give a straight line whose intercept on the (C/N) axis gives ϵ_β, and whose slope is $-K\epsilon_\beta$. The line drawn is a least squares fit to the data and yields $\epsilon_\beta=0.956\pm0.004$ and $K=0.099\pm0.006$.

The efficiency of the counter with this sample was lower than with previous samples. However, it is not unreasonably low for the thin plate which supported the foil was warped and could have intercepted and absorbed a few percent of the positrons. It is precisely effects of this kind which the present method takes care of. On the other hand, the discussion of the theory of this method indicates that if ϵ_a' and ϵ_a'' are not equal a correction arises when f is not unity. We recall that ϵ_a' and ϵ_a'' are, respectively, the γ-counter efficiencies (including solid angle, etc.) for those positrons (the fraction f) which pass into the active volume of the counter, and for those $(1-f)$ which are, in the present case, absorbed in the source and source support. Bias curves were taken with a source uncovered and with the source covered with $\frac{1}{32}$-in. aluminum. These measurements indicate that $\epsilon_a'/\epsilon_a''\lesssim1.08$. If we take the experimental value of ϵ_β, 95.6 percent, and ascribe it entirely to the factor f, and use $\epsilon_a'/\epsilon_a''=1.08$, the above value of K should be decreased by 3 percent. However, ϵ_β will be reduced by other factors, such as counting losses in the electronics and in the counter, and this correction will be smaller than 3 percent. Accepting Burhop's estimate of the fluorescent yield, there may be an additional correction of +1 percent for the K x-rays of Ne^{22} if our counter responded to them. These two corrections partially cancel each other and since they are small compared with statistical errors we shall ignore them. To summarize, our conclusion is that the fraction of electron capture $(K+L)$ in the decay of Na^{22} is 0.099 ± 0.006.

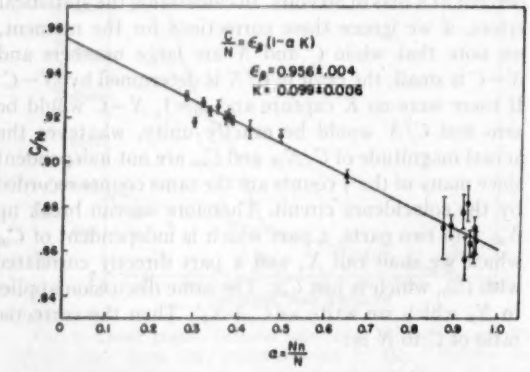

FIG. 3. Plot of C/N *vs* α. The line drawn through the experimental points and the values of ϵ_β and K correspond to a least-squares analysis of the data.

We also performed some experiments setting the β counter in anticoincidence with the γ counter. In this case, the ratio of anticoincidence counts to γ counts is $1-(C/N)$. This gave essentially the same result. Photographs taken of γ pulses in anticoincidence with positrons, showed the 1.28-Mev spectrum with an intensity of $\sim$10 percent of the normal spectrum and an annihilation spectrum with an intensity of $\sim$2 percent of the normal spectrum. No other lines were visible; there was no evidence that levels other than the 1.28 Mev level are involved in the electron capture in the Na^{22} decay.

We feel that the present method can be extended to higher Z decays by using a "4π" scintillation counter for the β counter, for one could bias out Auger and x-ray pulses (providing the β^+ energy is higher than these). The use of a single channel discriminator for the γ pulses would allow a wider range of α to be studied, and would reduce the effect of simultaneous pulses.

DISCUSSION OF RESULTS

To compare our experimental value of the electron capture and positron transition rates with theory, we shall assume that the transitions are allowed. The spin of Na^{22} is known to be 3,[11] and it seems fairly certain that the spin of the Ne first excited state is 2.[12] The parities of both states are most probably even and both the spectrum shape[13] and absence of β-γ correlation[14] are consistent with an allowed transition. On the other hand, $\log(ft)=7.4$ for the Na^{22} decay to Ne^{22*}, a value considerably larger than that usually accepted for a normal allowed transition ($\log ft=4$ to 5.8).[15,16] Therefore this transition,

[11] Davis, Nagle, and Zacharias, Phys. Rev. **76**, 1068 (1949).
[12] G. Scharff-Goldhaber, Phys. Rev. **90**, 587 (1953); Hinman, Brower, and Leamer, Phys. Rev. **90**, 370 (1953).
[13] Macklin, Lidofsky, and Wu, Phys. Rev. **78**, 318 (1950); B. T. Wright, Phys. Rev. **90**, 159 (1953).
[14] D. T. Stevenson and M. Deutsch, Phys. Rev. **83**, 1202 (1951).
[15] E. Feenberg and G. L. Trigg, Revs. Modern Phys. **22**, 399 (1950).
[16] E. J. Konopinski and L. M. Langer, Ann. Rev. Nuc. Sci. **2**, 261 (1953).

allowed by Gamow-Teller selection rules may be slowed down by an accidentally poor overlap of the initial and final wave functions for the nucleons, or it may be l forbidden.[17] In the former case, the electron capture to positron ratio is the same as for normally allowed decays. In the latter case, this ratio may be quite different. Bouchez[3,18] has calculated a value of ~ 0.05 for Na^{22}, assuming that the decay is $\Delta l=2$ forbidden; this value is clearly in disagreement with our measurement. He calculates ~ 0.09 under the assumption that it is first forbidden ($\Delta J=0, 1$ yes); however, it is unlikely that the decay involves a change of parity.

Assuming the decay is allowed, ($\Delta J=1$, no) the transition probabilities P_+ (for positron decay) and P_K (for K capture) are:[19]

$$P_+=\frac{G^2M^2C_T^2}{2\pi^3}\int_1^{E_0} pE(E_0-E)^2F(Z,E)\times\left\{1-\frac{2\gamma}{E}\frac{C_A}{C_T}\right\}dE=\frac{G^2M^2C_T^2f_+}{2\pi^3},$$

$$P_K=\frac{G^2M^2C_T^2}{4\pi^2}(E_0+E_K)^2g_K^2\left\{1+2\frac{C_A}{C_T}\right\}=\frac{G^2M^2C_T^2}{4\pi^2}f_K.$$

The various quantities have their usual meanings: G is the Fermi constant which is a measure of the strength of the β-decay interaction and M is the nuclear matrix element; E and p are the energy and momentum of the positron; $F(Z,E)$ and g_K^2 are determined by the wave functions of the emitted positron and of the K electron respectively; E_K is the total energy of the K electron and is given by $E_K\cong\gamma=(1-\alpha^2Z^2)^{\frac{1}{2}}$. The terms involving C_A/C_T are the Fierz interference terms, where C_AG and C_TG are the coupling constants for the axial vector and tensor interactions. We have assumed that the latter is much larger than the former.[16]

Let R_0 be the ratio of electron capture to positron emission if $C_A/C_T=0$. We have used the *Tables for the Analysis of Beta Spectra*, National Bureau of Standards Applied Mathematics Series No. 13 (U. S. Government Printing Office, Washington, D. C., 1952) to evaluate f_+. The calculation of g_K^2 is straightforward; the effect of screening is included through the use[19] of $Z_{eff}=Z-0.3$. The nuclear matrix element disappears in the ratio. With $E_0=2.061$ (corresponding to a maximum kinetic energy of 542 kev[13] for the positron decay), we find $f_+=0.2722$ and $f_K=0.01865$, giving for R_0 the value 0.1076.

There are a few corrections which should be made;[3] the only important one for the low Z of the Na^{22} decay is that for L capture. According to the calculations of Rose and Jackson[20] this correction is 6.5 percent for $Z=11$, leading to a final value $R_0=0.1135$.

From our measurements we obtain (for 9.9 ± 0.6 percent electron-capture) the value $R_{exp}=0.110\pm0.006$, in good agreement with the above theoretical value. It is now tempting to see the limits which this agreement can set in the ratio C_A/C_T. Letting R be the ratio P_K/P_{β^+} given by the complete expressions above, we find

$$\frac{R}{R_0}=\frac{1+2(C_A/C_T)}{1-2\langle E^{-1}\rangle_{Av}(C_A/C_T)},$$

where $\langle E^{-1}\rangle_{Av}$ is the average of E^{-1} over the β^+ spectrum. For the Na^{22} decay it has the value of 0.7. Solving for C_A/C_T, we obtain

$$\frac{C_A}{C_T}\cong\frac{R-R_0}{3.4R_0}.$$

We take for R our experimental value and for R_0 the value calculated above. However, there is an uncertainty in R_0 due to approximations in the calculations and due to inaccuracy in the measurement of E_0. The uncertainty in E_0 is of the order of 0.5 percent, leading to an uncertainty in R_0 of 1.5 percent. Thus, it seems reasonable to take $R_0=0.1135\pm0.002$. Therefore, $R-R_0=-0.0035\pm0.007$ and $C_A/C_T\cong(-1\pm2)$ percent.

The usual method of determining C_A/C_T is by analysis of the experimental shapes of allowed spectra for those decays which follow Gamow-Teller selection rules. The Fierz terms modify the shape through the factor $[1\pm(2\gamma/E)(C_A/C_T)]$. This will introduce a curvature in the Kurie plot. C_A/C_T is then estimated from the maximum curvature consistent with the Kurie plot which is a straight line for $C_A/C_T=0$. Opinions as to the sensitivity of this type of analysis vary considerably. Konopinski and Langer[16] and Davidson and Peaslee[21] have concluded that $C_A/C_T<2$ percent and 4 percent, respectively, while Winther and Kofoed-Hansen[22] feel that a ratio as large as 20 percent cannot be excluded by an analysis of the published β spectra. It is therefore helpful to have the additional evidence supplied by the present measurement, which indicates that $C_A/C_T<$several percent. However, it must be remarked that the significance of our calculation is somewhat weakened by the lack of knowledge of the precise character of the Na^{22} decay.

We are indebted to Dr. E. Feenberg and Dr. M. E. Rose for illuminating discussions regarding the interpretation of our results, and to Dr. R. Naumann for his assistance in the preparation of sources

[17] L. W. Nordheim, Revs. Modern Phys. **23**, 322 (1951).
[18] R. Nataf and R. Bouchez, J. Phys. Paris **13**, 140 (1952).
[19] S. R. de Groot and H. A. Tolhoek, Physica **16**, 456 (1950).
[20] M. E. Rose and J. L. Jackson, Phys. Rev. **76**, 1540 (1950).
[21] J. P. Davidson and D. C. Peaslee, Phys. Rev. **91**, 1232 (1953).
[22] A. Winther and O. Kofoed-Hansen, Kgl. Danske Videnskab. Selskab, Mat.-fys. Medd. **27**, No. 14 (1953).

Gamma Radiation from Certain Nuclear Reactions*

ROLF M. SINCLAIR†
Rice Institute, Houston, Texas
(Received November 16, 1953)

The gamma radiation from five nuclear reactions has been studied with a single NaI crystal. Three new resonances in the emission of 12-Mev radiation from the reaction $F^{19}(p,\gamma)Ne^{20}$ have been found at 1092-kev, 1324-kev, and 1431-kev bombarding energy. The widths are, respectively, <1.2 kev, 4.0 kev, and 15.7 kev, and the cross sections at resonance are >0.05 mb, 0.081 mb, and 0.19 mb, respectively. The first resonance corresponds to one in the reaction $F^{19}(p,\alpha\gamma)O^{16}$, whereas the last two do not. All the transitions are to the 1.63-Mev level in Ne^{20} or to a nearby level. Possible values of the spin and parity of the excited levels in Ne^{20} are discussed.

A search was made for gamma radiation from the bombardment of lithium by 650-kev deuterons. Upper limits for the production of 5-, 6-, and 7-Mev gamma rays are <2 mb, <1 mb, and <0.5 mb, respectively.

A search was made for the radiative capture of deuterons in the bombardment of deuterium, helium, and oxygen. No capture gamma rays were observed, and upper limits for the cross section for these reactions are: D_2, <0.05 μb at a deuteron energy of 1260 kev; He, <0.1 mb at 1055 kev; and O_2, <0.5 mb at 1100 kev.

I. RADIATIVE CAPTURE OF PROTONS BY FLUORINE

Introduction and Experimental Procedure

IN the proton bombardment of fluorine, a likely mode of decay of the compound nucleus is by the reaction

$$F^{19}+p\rightarrow(Ne^{20*})\rightarrow O^{16}+\alpha. \quad (1)$$

An alternative though less likely reaction is radiative capture of the proton

$$F^{19}+p\rightarrow(Ne^{20*})\rightarrow Ne^{20}+\gamma. \quad (2)$$

Reaction (1) can leave the oxygen nucleus in the ground state, the pair-emitting state, or one of the three gamma-emitting states of excitation energy 6.13, 6.9, and 7.1 Mev. The resonances in the $(p,\alpha\gamma)$ reaction leading to these last three states and in the $(p,\alpha\pi)$ and (p,α) reactions have been the subject of careful study,[1–4] and considerable information concerning the levels in Ne^{20} and O^{16} is now available.[5] Recent work[6] has shown that the level in Ne^{20} formed by incident protons of 669-kev energy decays by reaction (2) about 2 percent of the time. The observed decay[7] is not to the ground state but to the first excited state at 1.634 Mev.[8]

Reaction (2) has been studied in this laboratory, with protons accelerated by the Rice Institute 2-Mev Van de Graaff generator. The energy of the proton beam was measured with a 90° analyzing magnet, and the spread in beam energy was ~0.1 percent of the average proton energy. Targets, together with a blank for background readings, were mounted in a holder so designed that any one of five targets could be rotated into the beam without breaking the vacuum. A single NaI(Tl) crystal, 1½ in. diam.×1½ in. long, was used as the gamma-ray detector and was placed at 0° to the proton beam. Figure 1, curve *A*, shows the differential pulse-height curve obtained with the scintillation spectrometer at the 669-kev resonance. The three gamma rays from reaction (1) are not resolved but appear as a single peak. The 12.1-Mev capture gamma ray appears as a second peak at slightly more than double the pulse height of the first. Excitation curves were then obtained for reactions (1) and (2) by counting the radiation from each reaction separately. The base line and channel width of the pulse-height analyzer were set to cover either the interval marked "high" or that marked "low"; the first interval counted the 12-Mev radiation whereas the second interval detected almost completely the radiation from the $(p,\alpha\gamma)$ reaction. It was necessary to keep the counting rate with the "low" interval below about 320 counts per second to avoid a pileup of counts in the high interval. This was done by placing the crystal further away from the target at the more intense $(p,\alpha\gamma)$ resonances.

A preliminary excitation curve covering the proton energy range 620 kev to 1650 kev detected the pressure of four resonances for the emission of 12-Mev gamma rays. Figures 2 and 3 show the detailed excitation curves obtained in the neighborhood of these resonances for radiative capture at 669 kev, 1092 kev, 1324 kev, and 1431 kev. Results in the region of the 1292-kev resonance (shown for comparison) and the other resonances for 6-Mev radiation showed no capture radiation. Each radiative capture resonance was detected with three different ZnF_2 targets, and data taken showed no evidence of target contamination. Differential pulse-

* This work was supported by the U. S. Atomic Energy Commission.
† Now with Westinghouse Research Laboratories, East Pittsburgh, Pennsylvania.
[1] Bennett, Bonner, Mandeville, and Watt, Phys. Rev. **70**, 882 (1946).
[2] T. W. Bonner and J. E. Evans, Phys. Rev. **73**, 666 (1948).
[3] Chao, Tollestrup, Fowler, and Lauritsen, Phys. Rev. **79**, 108 (1950).
[4] Willard, Blair, Kington, Hahn, Snyder, and Green, Phys. Rev. **85**, 849 (1952).
[5] J. Seed and A. P. French, Phys. Rev. **88**, 1007 (1952).
[6] S. Devons and H. G. Hereward, Nature **162**, 331 (1948).
[7] G. A. Jones and D. H. Wilkinson, Proc. Phys. Soc. (London) **A65**, 1055 (1952).
[8] Donahue, Jones, McElliston, and Richards, Phys. Rev. **89**, 824 (1953).

height curves were obtained at these radiative capture resonances and are shown in Fig. 1. All four curves show the 12-Mev gamma ray. Although the energy of the gamma ray was not measured too accurately, the transition in each case seems to be to the 1.63-Mev level or another level nearby but not to the ground state.

Discussion of Results

The target thickness was taken equal to the experimental width of the very narrow resonance at 1092 kev.[9] The target used to obtain Figs. 2 and 3 was 3.7 kev thick at this energy. The thickness at other energies and the number of fluorine nuclei per cm² were calculated. The efficiency (effective solid angle times probability of a photon interacting in the NaI) of the scintillation spectrometer for 6- and 7-Mev radiation was calculated to be 0.0096, with the crystal 8 mm from the target. This was found from the observed counting rate at the 669-kev resonance and the calculated yield, using the value of 2.5×10^{-26} cm² for the cross section at this energy.[2] The efficiency for detection of the 12-Mev gamma rays was then calculated from the latter by correcting for the greater probability of a 12-Mev photon scattering in the crystal and for the different fraction of the total number of pulses from the crystal that fell within the analyzer window. The yield of 12-Mev gamma rays relative to the yield of gamma rays following alpha emission could then be found from the observed counting rates at each resonance. The absolute cross sections for reaction (2) at the 669-kev and 1092-kev resonances were calculated from the known cross sections for reaction (1) at these energies.[2,9] The cross section in the neighborhood of the 1324-kev and 1431-kev resonances was described by a Breit-Wigner single level formula,[10] and the cross sections at resonance found from the observed widths and target thickness. This treatment assumes that the gamma radiation is emitted isotropically, which is known to be the case at the 669-kev resonance.[6,11] Table I lists the parameters of the four radiative capture resonances. The value of 1.8 percent found for the yield at the 669-kev resonance

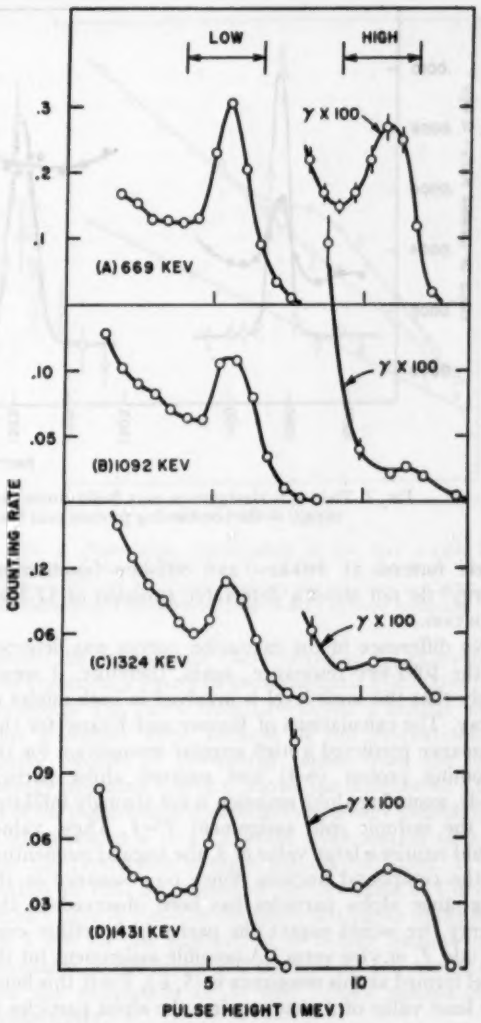

FIG. 1. Pulse-height distributions obtained at the four resonances for radiative capture of protons. Each curve is labeled with the corresponding proton energy.

TABLE I. Resonances in the reaction $F^{19}(p,\gamma)Ne^{20}$.

Proton energy (kev)	Resonance width (kev)	Yield* (percent)	Cross section (mb)
669	7.5	1.8	0.48
1092	<1.2	1.3	>0.05
1324	4.0	>1.5	0.081
1431	15.7	>1.5	0.19

* Yield of 12-Mev gamma radiation relative to yield of 6- and 7-Mev radiation at each resonance.

is in good agreement with the value of 1.72±0.25 percent given by Carver and Wilkinson.[12]

No difference in the excitation curves for the two reactions was detected at the 669-kev resonance, confirming the work of other investigators.[5] It thus seems probable that the same level in Ne^{20} is involved in both reactions. Since this level is (1,+),[5,13] the observed decay scheme is explainable in terms of an $M1$ transition to the (2,+) level at 1.634 Mev.[14] No reason is apparent why this transition is so much stronger than the $M1$ transition to the Ne^{20} ground state or why other (1,+)

[9] F. Ajzenberg and T. Lauritsen, Revs. Modern Phys. **24**, 321 (1952).
[10] G. Breit and E. P. Wigner, Phys. Rev. **49**, 519 (1936).
[11] S. Devons and M. G. N. Hine, Proc. Roy. Soc. (London) **A199**, 56 (1949).
[12] G. H. Carver and D. H. Wilkinson, Proc. Phys. Soc. (London) **A64**, 199 (1951).
[13] C. Y. Chao, Phys. Rev. **80**, 1635 (1950).
[14] J. Seed, Phil. Mag. **44**, 921 (1953).

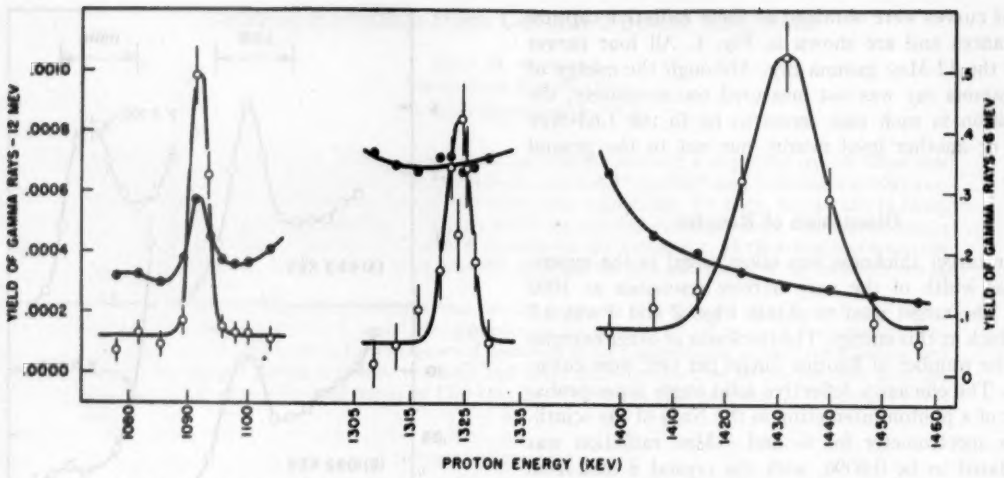

FIG. 2. Yield of 6-Mev gamma rays (solid circles) and 12-Mev gamma rays (open circles) as a function of the energy of the bombarding protons near the resonances at 1092 kev, 1324 kev, and 1431 kev.

levels formed at 340-kev and 935-kev bombarding energy[6] do not show a detectable emission of 12-Mev radiation.

No difference in the excitation curves was detected at the 1092-kev resonance; again, therefore, it seems likely that the same level is involved in both modes of decay. The calculations of Bonner and Evans[2] for this resonance predicted a high angular momentum for the incoming proton (~ 4) and emitted alpha particle (~ 4), assuming alpha emission is not strongly inhibited by the isotopic spin assignment $T=1$. These values would require a large value of J, the angular momentum of the compound nucleus. Since no resonance in the long-range alpha particles has been observed at this energy, we would expect the parity to be either even for odd J, or vice versa.[5] A possible assignment for the level formed at this resonance is $(5,+)$, $T=0$, this being the least value of J that requires the alpha particles to the $(3,-)$ level in O^{16} to carry off three units of angular momentum. If this assignment is correct, it is unlikely the transition to the ground state or to the 1.63-Mev state of Ne^{20} would occur because of the high polarity order of the radiation. On the other hand, radiation to another level with $J \geqslant 4$ would be possible. There is evidence for a level in Ne^{20} at 2.2 Mev,[15,16] and if, for example, it were a $(4,+)$ level, the gamma radiation would be magnetic dipole and might compete with alpha emission. This would be in keeping with the observed trend of even-even nuclei to have the first excited state $(2,+)$ and the second $(4,+)$.[17] If, however, the level formed by 1092-kev protons had $T=1$, J might be much less than the value of five predicted above.

The radiative capture resonances at 1324 kev and 1431 kev do not correspond to known $(p,\alpha\gamma)$ resonances; therefore, the yields of 12-Mev gamma rays given in Table I are lower limits which are calculated from the estimated height of a $(p,\alpha\gamma)$ resonance that would just escape detection. Since these lower limits for the percentage yields are comparable to the observed percentage yield of 12-Mev radiation at the 669-kev resonance, the possibility that weak resonances for alpha-emission occur cannot be ruled out. The alternative conclusion is that either or both of these levels in Ne^{20} cannot emit an alpha particle. A possible assignment for such a level is $(0,-)$ which would forbid alpha emission to all states of O^{16} as well as an electromagnetic transition to the ground state of Ne^{20}. An allowed decay would then be to the 1.63-Mev level, as observed. The observed width of 15.7 kev or 4.0 kev would then be equal to the proton width, which is compatible with the calculations of Christy and Latter[18] and Chao.[13]

II. GAMMA RADIATION FROM DEUTERON BOMBARDMENT

Deuteron Bombardment of Lithium

There is evidence the reaction $Li^7(d,n)Be^{8*}$ leaves the residual nucleus in several excited levels.[19–21] The purpose of the present experiment was to look for gamma emission from any such levels. A combination evaporator-target unit was used to prepare metallic lithium targets (natural isotopic mixture) in the accelerator vacuum system. All parts of the system

[15] C. F. Powell, Proc. Roy. Soc. (London) **A181**, 344 (1942).
[16] Heitler, May, and Powell, Proc. Roy. Soc. (London) **A190**, 180 (1947).
[17] G. Scharff-Goldhaber, Phys. Rev. **90**, 587 (1953).
[18] R. F. Christy and R. Latter, Revs. Modern Phys. **20**, 185 (1948).
[19] H. T. Richards, Phys. Rev. **59**, 796 (1941).
[20] L. L. Green and W. M. Gibson, Proc. Phys. Soc. (London) **A62**, 407 (1949).
[21] W. D. Whitehead, Phys. Rev. **79**, 393 (1950).

struck by the beam were carefully cleaned of carbon and other deposits to reduce spurious sources of gamma radiation. The NaI crystal was placed 4.7 cm from the target, with 1.1 cm of graphite between crystal and target. This absorber, together with the thickness of the target unit, was just sufficient to stop the Li^8 beta rays. A deuteron energy of 650 kev was used to bombard targets about 64 kev thick. At this energy the cross section for the $Li^7(d,n)$ reaction has almost the maximum value obtainable over the available energy range,[22] whereas the 325-kev protons in the weak HH^+ beam will give little high-energy gamma radiation from the reaction $Li^7(p,\gamma)Be^8$ because of the low cross section for this reaction below the 440-kev (proton energy) resonance.[2]

Figure 4, Curve *A*, shows the pulse-height curve obtained with the crystal from the reaction Li+D. There is no indication of gamma radiation between widely separated states of Be^8, which would result in gamma rays of at most several discrete energies. The counting rate immediately after the beam was taken off the target indicated that no more than ~20 percent of the counts above 1.5 Mev were from the effects of 0.9-sec Li^8, and no more than ~0.9 percent of these counts were from the decay of 25-min I^{128} produced by radiative capture of neutrons. The counts in the pulse-height range above 4 Mev can thus be ascribed almost completely to the interaction of neutrons in the crystal and to any gamma radiation from Be^{8*}. The most important means of interaction of the fast neutrons from Li+D will be inelastic scattering.[23] Curve *B*

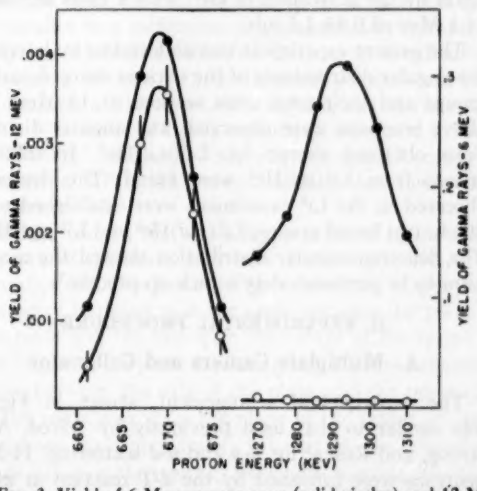

FIG. 3. Yield of 6-Mev gamma rays (solid circles) and 12-Mev gamma rays (open circles) as a function of the energy of the bombarding protons near the resonances at 669 kev and 1292 kev. The 1292-kev resonance for 6-Mev gamma rays is not accompanied by a detectable resonance for 12-Mev gamma rays.

[22] L. M. Baggett and S. J. Bame, Phys. Rev. **85**, 434 (1952).
[23] *Neutron Cross Sections*, U. S. Atomic Energy Commission Report AECU-2040 (Office of Technical Services, Department of Commerce, Washington, D. C., 1952).

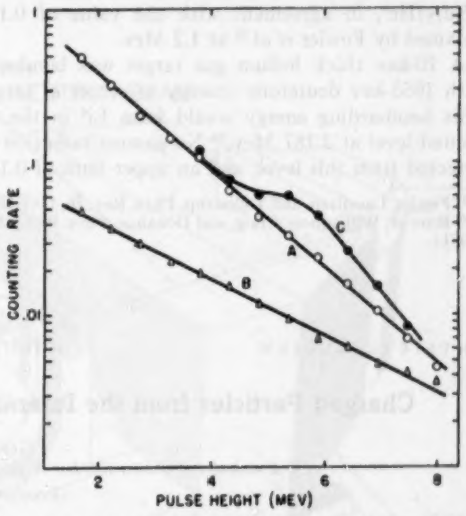

FIG. 4. Pulse-height distributions in the NaI crystal from products of the reaction Li+D (Curve *A*) and from 14-Mev neutrons (Curve *B*). Curve *C* shows the addition to Curve *A* of the pulse-height distribution from 6-Mev gamma radiation.

shows the pulse-height curve obtained by exposure of the crystal to a source of monoenergetic (14.1-Mev) *d*-T neutrons. The curve from Li+D has a similar shape but a steeper slope because of the proportionately larger number of low-energy pulses from the lower energy neutrons. Curve *C* shows the addition to Curve *A* of the pulse-height spectrum from 6-Mev gamma rays, and corresponds to an average cross section of 5 mb for the production of such gamma radiation. It was estimated that 20 percent of the deviation of Curve *C* from Curve *A* could be detected, setting an upper limit of 1 mb for the production of 6-Mev gamma rays. Similarly, upper limits of 2 mb and 0.5 mb can be sent for the production of 5- and 7-Mev gamma rays, respectively.

Earlier experiments[24] reported gamma radiation of 4.9±0.3 Mev, with a cross section of 14 mb for its production at 650 kev. It is now felt that these results were due to 4.47-Mev gamma radiation from C^{12*}, produced by the inelastic scattering of neutrons in the thick graphite absorber which was used.

Radiative Capture of Deuterons

The deuteron beam was admitted to a gas target through a 0.0001-in. nickel foil. The NaI crystal was placed at 90° to the beam, subtending a solid angle of about 1.4 steradians. Bombardment of a 60-kev thick deuterium gas target with 1260-kev deuterons (energy at center of target) gave an upper limit of 0.05 μb for the production of 20-Mev gamma rays from the reaction

[24] Bennett, Bonner, Richards, and Watt, Phys. Rev. **59**, 904 (1941); **71**, 11 (1947).

$H^2(d,\gamma)He^4$, in agreement with the value of 0.1 μb obtained by Fowler *et al.*[25] at 1.2 Mev.

A 70-kev thick helium gas target was bombarded with 1055-kev deuterons (energy at center of target). This bombarding energy would form Li^6 in the first excited level at 2.187 Mev.[26] No gamma radiation was detected from this level, and an upper limit of 0.1 mb was sent on the cross section for the reaction $He^4(d,\gamma)Li^6$.

A 200-kev thick oxygen gas target was bombarded with 1100-kev deuterons (energy at center of target), the energy required to form F^{18} in the 8.5-Mev excited state.[27] Again no capture gamma rays were detected, and an upper limit of 0.5 mb was set on the cross section for the reaction $O^{16}(d,\gamma)F^{18}$.

[25] Fowler, Lauritsen, and Tollestrup, Phys. Rev. **76**, 1767 (1949).
[26] Browne, Williamson, Craig, and Donahue, Phys. Rev. **83**, 179 (1951).
[27] G. Brubaker, Phys. Rev. **56**, 1181 (1939).

PHYSICAL REVIEW VOLUME 93, NUMBER 5 MARCH 1, 1954

Charged Particles from the Interaction of 14-Mev Neutrons with Li^6 and Li^7†

GLENN M. FRYE, JR.
University of California, Los Alamos Scientific Laboratory, Los Alamos, New Mexico

(Received November 24, 1953)

The angular distribution of the charged particles produced in the bombardment of Li^6 and Li^7 by 14-Mev neutrons was observed with nuclear emulsions in a multiplate camera. Metallic targets of enriched Li^6 and Li^7 were used. The following cross sections were measured: $Li^6(n,p)He^6$, 6±2 mb; $Li^6(n,d)He^5$, 89±10 mb; $Li^6(n,d)He^{5*}$, 77±9 mb; $Li^6(n,t)He^4$, 26±4 mb; $Li^7(n,t)He^5$, 55±8 mb. The reaction $Li^7(n,d)He^6$ was also observed but was not well enough resolved to give an angular distribution and total cross section. No evidence was found for the formation of He^7 by $Li^7(n,p)He^7$ with a cross section greater than 5 mb in the range $-1.0>Q>-7.0$ Mev. The angular distributions obtained for $Li^6(n,d)He^5$ and $Li^6(n,d)He^{5*}$ indicate these reactions proceed mainly by an inverse stripping or pick-up process. The energy spectrum of the neutrons from $Li^6(n,d)He^5(n)He^4$ and $Li^6(n,d)He^{5*}(n)He^4$ is calculated using several assumptions for the angular distribution of the He^5 disintegration.

I. INTRODUCTION

THE interaction of neutrons with Li^6 has been studied by many investigators,[1] particularly for neutron energies of 2.5 Mev and below, where only the well-known $Li^6(n,t)He^4$ reaction is energetically possible. Recently Ribe[2] has measured this cross section as a function of energy from 0.88 to 14.2 Mev. Roberts and co-workers[3] have obtained the angular distribution of the tritons for energies up to 2 Mev using Li^6 loaded nuclear track plates. For the other charged particle reactions, Poole and Paul[4] used the formation of 0.8-sec He^6 to establish the $Li^6(n,p)He^6$ reaction for neutrons from 4 to 12 Mev. By the activation technique Battat and Ribe[5] measured the cross section for this reaction at 14.1 Mev as 6.7±0.8 mb. Also at 14 Mev Ribe[6] detected a comparatively large group of deuterons and obtained a value of ~200 mb for the cross section. For Li^7 the $Li^7(n,d)He^6$ process has been observed,[5] again by the activation of He^6, with a cross section at 14.1 Mev of 9.8±1.1 mb.

The present experiment was undertaken to determine the angular distributions of the various charged particle groups and their total cross sections at 14 Mev. The above reactions were observed, and angular distributions obtained except for $Li^7(n,d)He^6$. In addition tritons from $Li^7(n,t)He^5$ were found. The deuterons observed in the Li^6 experiment were established to be due to two broad groups, $Li^6(n,d)He^5$ and $Li^6(n,d)He^{5*}$. The deuteron angular distribution showed the mechanism to be predominately a pick-up process.[7]

II. EXPERIMENTAL PROCEDURE

A. Multiplate Camera and Collimator

The experimental arrangement, shown in Fig. 1, was similar to that used previously by Allred, Armstrong, and Rosen[8] for *n-p* and *n-d* scattering. 14-Mev neutrons were furnished by the *d*-T reaction in which the 250-kev diatomic deuteron beam from the Los Alamos Cockcroft-Walton accelerator was used to bombard a tritium-zirconium target. The neutron flux was monitored by counting the accompanying alpha

† Work performed under the auspices of the U. S. Atomic Energy Commission.
[1] See F. Ajzenberg and T. Lauritsen, Revs. Modern Phys. **24**, 321 (1952), and Hornyak, Lauritsen, Morrison, and Fowler, Revs. Modern Phys. **22**, 291 (1950) for complete references to the earlier work.
[2] F. L. Ribe, Phys. Rev. **91**, 462 (1953).
[3] Darlington, Haugsnes, Mann, and Roberts, Phys. Rev. **90**, 1049 (1953); J. H. Roberts (unpublished report).
[4] M. J. Poole and E. B. Paul, Nature **158**, 482 (1946).
[5] M. E. Battat and F. L. Ribe, Phys. Rev. **89**, 80 (1953).
[6] F. L. Ribe, Phys. Rev. **87**, 205 (1952) and private communication.
[7] S. T. Butler, Proc. Roy. Soc. (London) **A208**, 559 (1951); S. T. Butler and E. E. Salpeter, Phys. Rev. **88**, 133 (1952).
[8] Allred, Armstrong, and Rosen, Phys. Rev. **91**, 90 (1953).

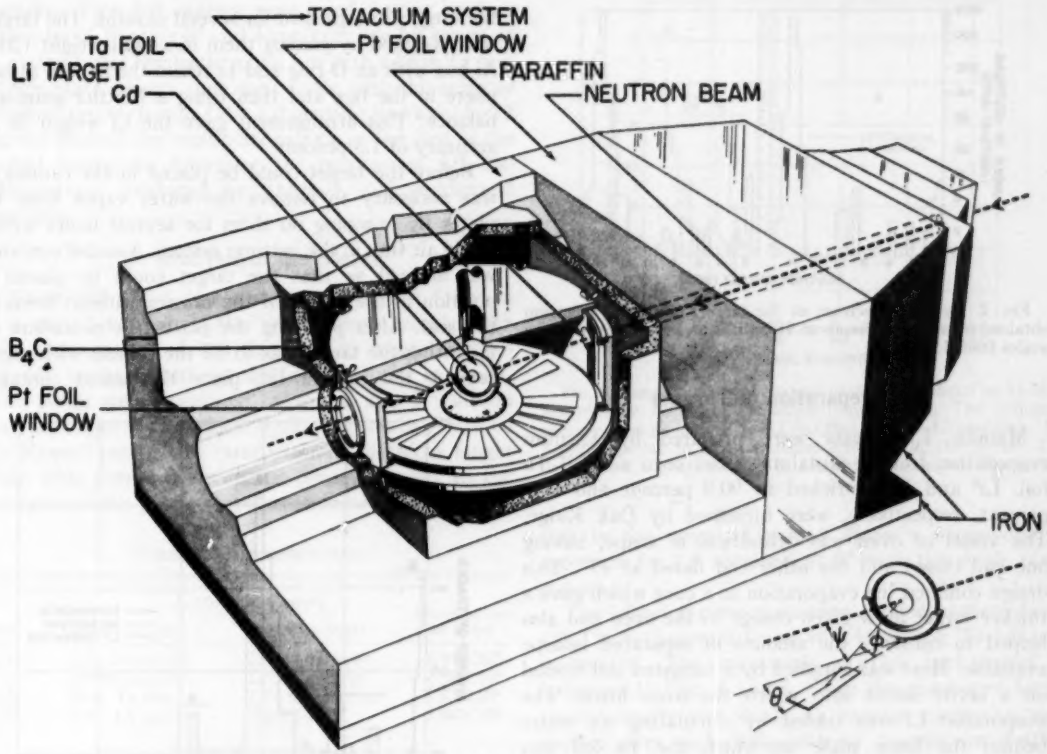

FIG. 1. Perspective view of collimator, multiple camera, and shielding.

particles from the d-T reaction. 18 in. of iron and 8 in. of paraffin in a collimator of approximately pyramidal shape shielded the plates from the source. A cylindrical channel in the iron, $\frac{3}{4}$ in. in diameter, gave a beam 1 in. in diameter at the target. The camera was also shielded by a 1-in. layer of boron carbide powder and a sheet of 0.030-in. cadmium. This was necessary because of the large $Li^6(n,t)He^4$ cross section for low-energy neutrons.

In the camera the plates lay in a plane $1\frac{1}{8}$ in. below the axis of the beam with their inner edges on a circle of radius 3 in. The inset of Fig. 1 shows the target-plate geometry in detail. ϕ is the angle between the plane of the plate and the line from the center of the target to the center of the plate area analyzed. θ is the azimuthal angle between the axis of the plate and the projection of the beam axis upon the plane of the plates. From ϕ and θ one may immediately calculate ψ, the laboratory angle between the neutron beam and particle direction. In this particular geometry, values of ψ from 11° to 169° could be obtained. The plane of the target foil was such that it made an angle of 45° with the beam. Two targets, placed back-to-back, could be used simultaneously. The one facing the collimator will be referred to as the back target and the other as the forward target. The camera was lined with 0.010-in. gold foil to minimize charged-particle production in the walls.

Figure 2 shows the spectrum of the neutron beam which was obtained by measuring the proton recoils from a paraffin target.[8] Figure 2(a) is the spectrum resulting from measurements at a laboratory angle of 15°, while Fig. 2(b) is an average over fifteen angles from 15° to 40°. In each case the intensity of degraded neutrons (1.5 to 12 Mev) is approximately 3 percent of the 14-Mev flux.

B. Single Plate Camera

To obtain data at angles less than 11° a single plate camera was used (Fig. 3). With this arrangement there is no shielding, and the plate is exposed directly to the neutron source. The tracks due to particles coming from the Li target originate on the surface of the emulsion and thus may be distinguished from the much greater number of proton recoils which start within the emulsion. In practice it was found that a neutron flux of $10^9/cm^2$ could be tolerated on the plate. A higher flux resulted in such a "thicket" of recoil tracks down in the emulsion that there was danger that a track originating on the surface could not be followed over its entire range. A typical arrangement was to have the target midway between the source and plate, 8 cm from each.

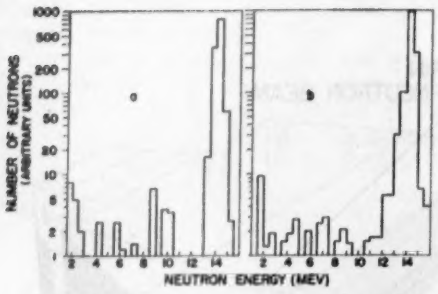

FIG. 2. Neutron spectrum at the target. (a) is the spectrum obtained from proton recoils at 15°. (b) is an average over fifteen angles from 15° to 40°.

C. Preparation of Targets

Metallic Li targets were prepared by vacuum evaporation from a tantalum vessel onto a 4-mil Ta foil. Li^6 and Li^7, enriched to 90.9 percent and 99.9 percent, respectively, were furnished by Oak Ridge. The vessel or oven was cylindrical in shape, having one end closed and the other end flared at 45°. This design confined the evaporation to a cone which gave a thicker target for a given charge in the oven and also helped to conserve the amount of separated isotope available. Heat was supplied by a tungsten coil wound on a lavite sleeve into which the oven fitted. The evaporated Li was cooled by circulating ice water behind the brass plate on which the Ta foil was mounted. A vacuum slide valve[9] between the oven and foil could be closed to separate them during outgassing. The pressure during evaporation was always $<10^{-5}$ mm of Hg. The closed valve and foil were detachable from the evaporating unit so that the foil could be transferred to a dry box without being exposed to air. If metallic Li is exposed to air, Li_3N is the first compound to form. Chemical analysis showed the amount of nitrogen contamination to be less than 0.5 percent by weight. Analysis of the data (see Fig. 4) showed that hydrogen was present to 0.3 percent in the 4-mg/cm² and 0.08 percent in the 10-mg/cm² Li^6 targets, indicating a layer of hydrogenous material. With this system it was possible to make a target having a surface density as great as 10 mg/cm² in one evaporation. Desiccated helium or argon circulated through the dry box kept the targets untarnished for several months. The targets were weighed by placing them in a light-weight (20-g) Al box with an O-ring seal to retain the helium atmosphere in the box and then using a Mettler gram-atic balance. This arrangement gave the Li weight to an accuracy of 1.5 percent.

Before the target could be placed in the camera, it was necessary to remove the water vapor from the plates by pumping on them for several hours with a liquid air trap in the vacuum system. A sealed container was devised so that the target could be placed in position in the center of the camera without breaking the seal. After pumping the plates the procedure for mounting the target was to fill the camera with argon, remove the camera lid, place the sealed container holding the target in the center of the camera, open and remove the container, replace the lid, and start the vacuum pump. This sequence prevented any air from contacting the Li. After completion of a run the procedure was reversed to recover the target. Upon examination in the dry-box, the targets appeared unchanged. The single plate camera could be loaded by placing it in the dry-box. It was necessary to use one Li^6 target (4 mg/cm²) whose surface had darkened slightly during preparation. Data obtained from this target were later compared with that from an untarnished one in the single plate camera. No variation outside that attributable to statistics was found between the two spectra.

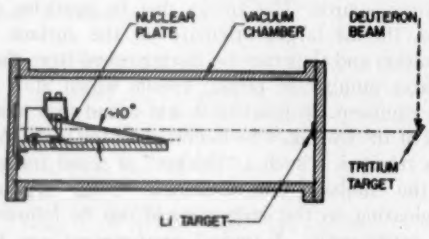

FIG. 3. Single plate camera.

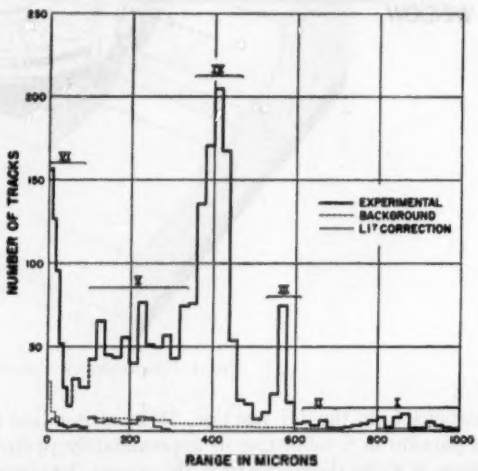

FIG. 4. Range analysis of charged particles produced by 14-Mev neutrons on Li^6 using the multiplate camera. The indicated particle groups are: I—recoil protons, II—$Li^6(n,p)He^6$, III—$Li^6(n,t)He^4$, IV—$Li^6(n,d)He^5$, V—$Li^6(n,d)He^{5*}$, VI—mostly alpha particles from $Li^6(n,t)He^4$, $Li^6(n,d)He^5(n)He^4$ and $Li^6(n,d)He^{5*}(n)He^4$. The data below 60μ are plotted in 10μ intervals; above 60μ in 20μ intervals. The tracks below 100μ came from the analysis of 0.36 cm² of plate; above 100μ from 1.32 cm² of plate.

Table I lists the various experimental runs which were made. Four runs were made with the multiplate

[9] Wahl, Forbes, Nyer, and Little, Rev. Sci. Instr. **23**, 379 (1952).

camera. Two Li^6 targets were used having surface densities of 10 mg/cm² and 4 mg/cm², one Li^7 target of 7 mg/cm², and one background run with a bare Ta foil. Single plate camera runs were made with the same or similar targets. In run *L*-1 a Li^6 loaded plate was placed on the floor of the multiplate camera at the foot of the target holder to determine the number of Li^6 disintegrations produced by thermal and epithermal neutrons.

D. Analysis of the Plates

Ilford 200-μ *E*-1 plates were used except for runs *L*-2 and *L*-4 where 400-μ plates were necessary at laboratory angles of less than 30° to insure that no "good" tracks passed out the bottom of the emulsion. The plates were developed by the *A* and *B* solution cold technique.[10] The optical equipment was as described by Rosen[10] and length measurements of tracks longer than 100μ were made with the precision stage. In the analysis of the plates three measurements were made upon each track: (1) the projected length, i.e., the length in the plane of the emulsion, along the long axis of the plate, (2) the dip angle ϕ_0, and (3) θ_0, the angle between the projected length and the long axis of the plate. Using the experimentally determined shrinkage factor of 2.3 one may compute the true range of each track. Moreover, the angles ϕ_0 and θ_0 made it possible to determine whether or not the particle came from the Li target. Thus limits could be set on ϕ_0 and θ_0 to eliminate background tracks coming from other directions. A check on these criteria was provided by the fact that the number of tracks which lay outside these angular limits was the same with or without a Li target in the camera.

TABLE I. Experimental runs.

A. Multiplate camera

Run	Forward target	Backward target	Neutrons/cm² at target
L-1	Li^7: 6 mg/cm²	Li^6: 10 mg/cm²	4.44×10^9
L-2	Li^6: 10 mg/cm²	Li^7: 6 mg/cm²	4.68×10^9
L-3	Bare Ta foil	Li^6: 4.2 mg/cm²	5.83×10^9
L-4	Li^6: 4.2 mg/cm²	Bare Ta foil	5.84×10^9

B. Single-plate camera

Run	Target	Neutrons/cm² at target
L-5	Li^6: 7 mg/cm²	2.28×10^9
L-6	Li^7: 5.6 mg/cm²	2.28×10^9
L-7	Li^6: 10 mg/cm²	3.98×10^9
L-8	Li^7: 5.6 mg/cm²	3.98×10^9

III. CORRECTIONS AND EVALUATION OF ERRORS

Figure 4 shows a typical range analysis for Li^6 taken at a laboratory angle of 17° with the multiplate camera. The various particle groups from Li^6 are indicated as well as the recoil protons from the hydrogen contamination in the target. Figure 5 shows a corresponding spectrum for Li^7 obtained at 0° with the single plate camera.

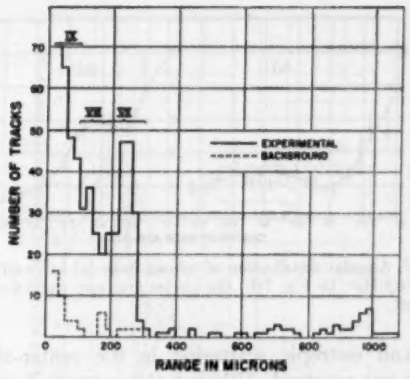

FIG. 5. Range analysis of charged particles produced by 14-Mev neutrons on Li^7 using the single plate camera. The indicated particle groups are VII—$Li^7(n,t)He^5$, VIII—$Li^7(n,d)He^6$, IX—partially due to alpha particles from $Li^7(n,t)He^5(n)He^4$. The data below 60μ are plotted in 10μ intervals; above 60μ in 20μ intervals.

The following corrections were applied to these data: (1) The background found with the blank Ta foil was subtracted. The magnitude of this background is indicated in Figs. 4 and 5. Since the number of background tracks was small, an average correction was applied over each 100μ interval (except for 0–100μ where 20μ steps were taken). At most the background amounted to a few percent of any particle group. (2) A correction was made for the tracks resulting from the hydrogen contamination in the target; for this a total n-p cross section at 14 Mev of 0.685 barn[11] was

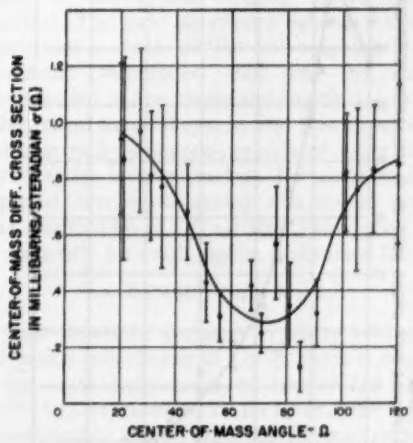

FIG. 6. Angular distribution of protons from $Li^6(n,p)He^6$. In Figs. 6, 7(a), 8, and 9 the crosses are single plate camera points, the squares are data from the 10-mg/cm² Li^6 target, the triangles are from the 4.2-mg/cm² Li^6 target, and the circles are an average of the data from the 10- and 4.2-mg/cm² targets.

[10] L. Rosen, Nucleonics **11**, No. 7, 32 (1953); **11**, No. 8, 38 (1953).

[11] Poss, Salant, Snow, and Yuan, Phys. Rev. **87**, 11 (1952).

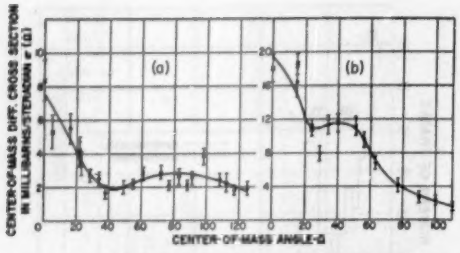

FIG. 7. Angular distribution of tritons from (a) $Li^6(n,t)He^4$ and (b) $Li^7(n,t)He^5$. In Fig. 7(b) the circles are from the 5.6-mg/cm² Li^7 target.

used and isotropic scattering in the center-of-mass system was assumed. Although this correction reduced the $Li^6(n,p)He^6$ and $Li^6(n,t)He^4$ differential cross sections by a maximum of 30 percent (at center-of-mass angles 29° and 49°, respectively), the total cross sections were reduced by less than 5 percent. The deuteron angular distributions were not affected. (3) Lower-energy neutrons present in the 14-Mev beam give triton tracks of the same range as the deuteron tracks produced by the 14-Mev neutrons. Use of Ribe's[2] data for the $Li^6(n,t)He^4$ cross section as a function of energy gives a 2-percent correction to the total deuteron cross sections. (4) The final Li^7 data may be used to correct for the Li^7 present in the Li^6 targets. Since the range of the tritons from Li^7 is less than 300μ, only the $Li^6(n,d)He^{5*}$ deuterons are affected. An average correction over 40μ intervals was applied, amounting at most to 10 percent. Its magnitude is indicated in Fig. 4.

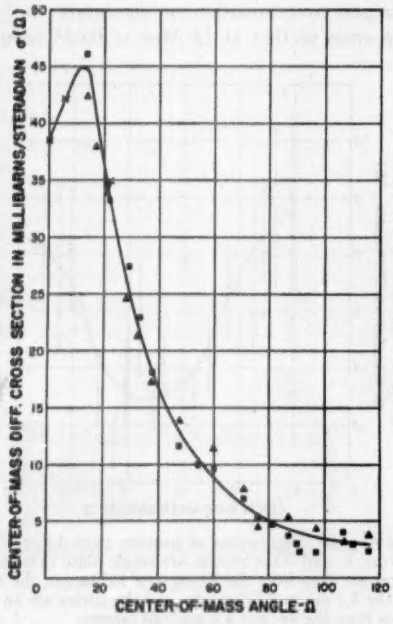

FIG. 8. Angular distribution of deuterons from $Li^6(n,d)He^5$ showing points from the various runs.

(5) Analysis of the number of Li^6 disintegrations in the Li^6 loaded plate enables one to correct the Li^6 data for the number of tracks of range 40μ and under produced by thermal and epithermal neutrons in the target.

In addition to the statistical error the following systematic errors were present: (1) Uncertainty in the neutron flux: 4 percent. (2) Determination of the number of Li atoms in the target: 1.5 percent. (3) Measurements of the camera geometry: 3 percent. (4) Uncertainty as to the exact limits of each particle group (Figs. 4 and 5). The separation between the two deuteron groups is admittedly arbitrary as is discussed further below. It is somewhat difficult to estimate the magnitude of this error for the other reactions as the separation between groups is a function of angle. However, it is felt that 7 percent represents an upper limit.

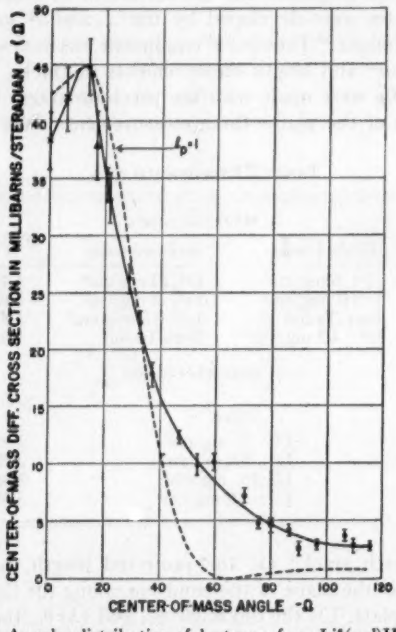

FIG. 9. Angular distribution of deuterons from $Li^6(n,d)He^5$. Here the averaged points and the statistical errors are shown. The solid curve is the same as Fig. 8. The dotted curve is a theoretical Butler curve for $l_p=1$; $r_0=4.5\times10^{-13}$ cm.

Only the statistical errors are shown on the angular distribution curves, Figs. 6–10. The errors on the total cross sections, Table II, include both the statistical and systematic contributions.

IV. RESULTS AND DISCUSSION

A. $Li^6(n,p)He^6$

An angular distribution was obtained for this reaction, Fig. 6, but in view of the poor statistics all that can be said is that there is an asymmetry with a minimum near 70°. The total cross section is 6±2 mb, in good agreement with Battat and Ribe's[5] value of 6.7±0.8 mb.

B. $Li^6(n,t)He^4$

Figure 7 illustrates the triton angular distribution. This single forward maximum is in contrast to the lower-energy data[3] which have maxima at both 0° and 180°. The total cross section is 26±4 mb.

C. $Li^6(n,d)He^5$

There was some question as to whether the group of tracks from 340 to 500μ in Fig. 4 was due to deuterons from $Li^6(n,d)He^5$ or protons from $Li^6(n,p)He^{6*}$, as formation of the 1.71-Mev level[1] in He^6 would give protons of approximately this range. One method of identification was to vary the neutron energy and measure the corresponding change in range of the group. This was done by using the atomic beam of the Cockcroft-Walton at 250 kev which will give 14.8-Mev neutrons at 0° to the deuteron beam and 13.5-Mev neutrons at 150°. Although these neutrons are not monoenergetic, due to the thick tritium-zirconium target employed, the shift in range of this group may be measured relative to the shift of the triton group. The results indicated that the group was predominately deuterons.

TABLE II. Total cross sections.

Reaction	Total cross section in millibarns
$Li^6(n,p)He^6$	6±2
$Li^6(n,t)He^4$	26±4
$Li^6(n,d)He^5$	89±10
$Li^6(n,d)He^{5*}$	77±9
$Li^7(n,t)He^5$	55±8

A more sensitive method of particle identification was the grain counting of individual tracks. For a plate exposed in the single plate camera one had 14-Mev recoil proton tracks in the emulsion and triton tracks from the known triton group for calibration of the grain density characteristics of the emulsion. Moreover, grain counting of recoil protons at various emulsion depths gave a check on uniformity of development. From counting 60 tracks it was found that in the range interval 500–340μ approximately 95 percent of the tracks were deuterons, and in the interval 340–160μ approximately 90 percent of the tracks were deuterons. Below 160μ it was not possible to make positive identification of the tracks. Since the percentage of tracks not identified as deuterons was of the same order as the background, it was assumed for purposes of calculating the angular distribution and total cross section that the two groups of tracks identified in Fig. 4 as $Li^6(n,d)He^5$ and $Li^6(n,d)He^{5*}$ were entirely deuteron.

The separation point for the two deuteron groups was rather arbitrarily taken as the range at which the intensity of the ground state deuterons fell to that of the lower-energy group. The minimum deuteron range was set by the range where alpha particles from $Li^6(n,t)He^4$ would appear. Thus the width of the lower-energy deuteron group is a function of the angle and the group so defined cannot be used as such to obtain an angular distribution. However the total cross section given in Table I for $Li^6(n,d)He^{5*}$ does include all the deuterons with ranges lying between the minimum deuteron range from $Li^6(n,d)He^5$ and the maximum alpha particle range from $Li^6(n,t)He^4$.

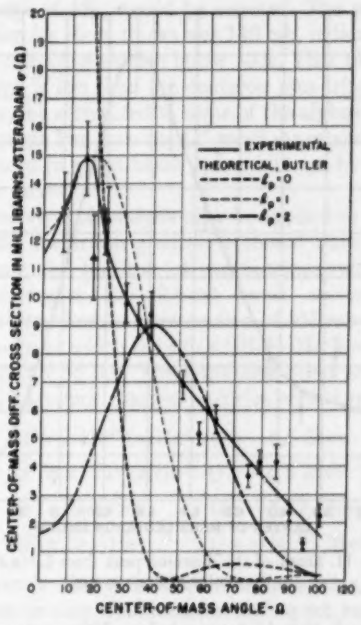

FIG. 10. Angular distribution of deuterons from that part of $Li^6(n,d)He^{5*}$ where $Q=-4.3$ to -6.7 Mev. The dashed curves are Butler curves for $l_p=0$, 1, 2; $r_0=4.5\times10^{-13}$ cm.

Figure 8 shows the angular distribution for $Li^6(n,d)He^5$. The good agreement among the various runs provides a check on the foil weighing and flux measurement techniques, and on the different geometries used in the single and multiplate cameras. The theoretical curve shown in Fig. 9 is for an inverse stripping or pick-up process, calculated using Butler's theory[7] for the inverse reaction $He^5(d,n)Li^6$. By the principle of detailed balancing this should give the angular distribution of $Li^6(n,d)He^5$. Fairly good agreement, especially for small angles, is obtained for

$$r_0=4.5\times10^{-13}\text{cm}; \quad l_p=1.$$

Thus there should be a change in parity between He^5 and Li^6 and a spin change of $\frac{1}{2}$ or $\frac{3}{2}$, which is consistent with the usual assignments to He^5 of $^2P\frac{1}{2}$ and Li^6 of $^3S_1$.[1,12] The total cross section for $Li^6(n,d)He^5$ is 89±10 mb, considerably larger than the $Li^6(n,p)$ or $Li^6(n,t)$ cross sections. This favoritism for the emission of the loosely bound deuteron is difficult to explain by a compound nucleus model and provides further evidence for the reaction proceeding by a pick-up mechanism.

[12] D. R. Inglis, Revs. Modern Phys. **25**, 390 (1953).

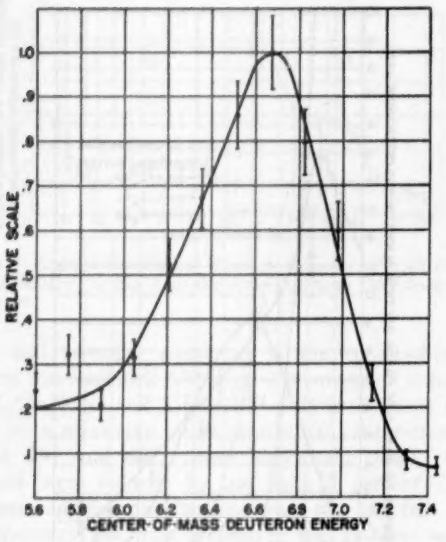

FIG. 11. Shape of the deuteron peak from $Li^6(n,d)He^5$ in the center-of-mass system.

Although the deuterons below 320μ appear to be a continuum rather than a discrete group, it was decided to take the tracks from 320–200μ, which correspond to a $Q=-4.3$ to -6.7 Mev, and treat them as if they were a fraction of a very broad group. (This was the largest fraction that could be taken without including alpha particle tracks from $Li^6(n,t)He^4$ at larger angles.) The resulting angular distribution is shown in Fig. 10. Its shape is similar to the angular distribution of the ground state deuterons. Again the Butler curve[7] for $l_p=1$ seems to give the best fit, although the quantitative agreement is not as good as for $Li^6(n,d)He^5$. If the procedure of using only part of this broad group to determine the angular distribution is valid, the fit for $l_p=1$ is consistent with the result obtained from the analysis of n-He^4 scattering;[13,14] i.e., above the ground state of He^5 lies a very broad $P_{\frac{1}{2}}$ level. Since a fairly sharp level, i.e., one having about the same width as the ground state, had been reported in He^5 at 2.6 Mev,[15] a special search was made in this region (275μ in Fig. 4) using the data from several runs, but no deuteron peak ascribable to this level was seen.

A value for the ground-state energy of He^5 and its width could be found by comparing the peak from $Li^6(n,d)He^5$ with the triton group from $Li^6(n,t)He^4$ for which a $Q=4.780$ Mev has been well established.[1] For this purpose the plate at 17° laboratory angle from run L-3, where the 4-mg/cm^2 target was used, was analyzed over 1.32 cm^2 in an effort to obtain improved statistics. When one obtains the deuteron energy by comparison with the triton energy, only a relative range energy curve for nuclear emulsions is necessary. Also, errors in the target thickness and geometry cancel out, at least in the first approximation. In this manner it was found that the Q for the $Li^6(n,d)He^5$ reaction is -2.57 ± 0.10 Mev or, using the mass table of Li *et al.*,[16]

$$He^5=He^4+n+1.09\pm0.10 \text{ Mev}.$$

It was found that the half-width of the triton group could be explained entirely by the following experimental factors: (1) Target thickness, 0.43 Mev; (2) angular resolution, 0.29 Mev; (3) range straggling in the plate, 0.19 Mev; (4) range measurement errors, 0.05 Mev; and (5) thick target neutron source, 0.05 Mev, giving an rms half-width of 0.5 Mev compared to the experimental value of 0.5 ± 0.1 Mev. When applied to the deuteron group, the same calculation gave a half-width of 0.39 Mev compared to the observed value of 1.10 Mev. After removing the experimental contribution, one obtains a nuclear half-width for the deuteron group in the center-of-mass system of 0.8 Mev. Figure 11 shows the shape of this deuteron group in the center-of-mass system.

D. Energy Spectrum of Neutrons from $Li^6(n,d)He^5(n)He^4$ and $Li^6(n,d)He^{5*}(n)He^4$

Since the He^5 formed in these deuteron reactions has a lifetime only a little longer than the nuclear transit time, the He^5 at once breaks up into He^4 and a neutron. From the observed energy spectrum of the deuterons at

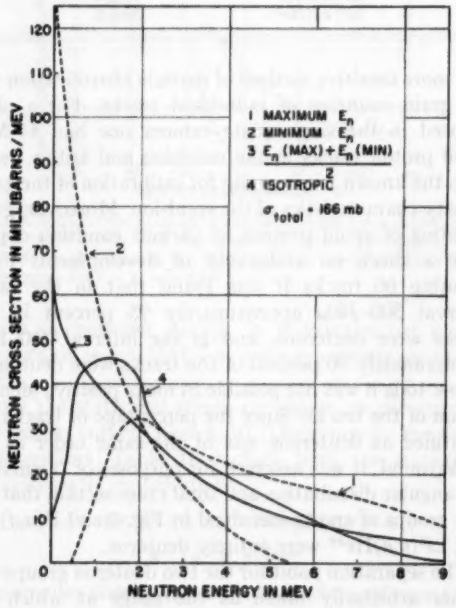

FIG. 12. Neutron energy spectrum from $Li^6(n,d)He^5(n)He^4$ and $Li^6(n,d)He^{5*}(n)He^4$.

[13] D. C. Dodder and J. L. Gammel, Phys. Rev. **88**, 520 (1952).
[14] R. K. Adair, Phys. Rev. **86**, 155 (1952).
[15] W. T. Leland and H. M. Agnew, Phys. Rev. **82**, 559 (1951).
[16] Li, Whaling, Fowler, and Lauritsen, Phys. Rev. **83**, 512 (1951).

each angle, the angular and energy distribution of the He^5's may be calculated. Then if an assumption is made about the angular distribution of the disintegration $He^5 \rightarrow He^4 + n$, the energy spectrum of the neutrons may be calculated. Four different assumptions were made:

(1) The neutron is emitted in the same direction as the He^5 motion. This delta-function angular distribution gives the largest number of high-energy neutrons.

(2) The neutron is emitted in the opposite direction to the He^5, giving the largest number of low-energy neutrons.

(3) Half the neutrons are emitted as in (1) and half as in (2), an approximation to an angular distribution peaked forward and backward in the He^5 center-of-mass system.

(4) The He^5 breakup is isotropic in the He^5 center-of-mass system. The neutron energy distributions resulting from these various assumptions are given in Fig. 12.

Of course (1) and (2) are highly artificial assumptions. The true energy distribution is probably given by (3) or (4) or some combination of them.

E. $Li^7(n,t)He^5$

The angular distribution of this reaction, Fig. 7, is similar to the triton distribution from Li^6. The total cross section is 55 ± 8 mb.

F. $Li^7(n,d)He^6$

This reaction was observed at laboratory angles up to 30° but was not well enough resolved to enable its angular distribution or total cross section to be determined.

G. Other Possible Reactions

The spectrum from Li^6 shows a number of tracks below 100μ which presumably are the result of alpha particles accompanying the triton and deuteron reactions. In addition there may be deuterons of range less than 100μ. To test this possibility the short tracks were integrated over all angles to give a total cross section which should equal the sum of the cross sections for the triton and deuteron groups, 192 mb. A minimum range was set on the short tracks so that no Li recoils, which may have a range of 15μ, would be counted. The resulting cross section for short tracks was 140 mb, indicating no large deuteron cross section below 100μ. That the alpha cross section is less than the deuteron plus triton cross section may be attributed to some of the alphas having an initial range less than the Li^7 recoil range and others being reduced in range below this minimum by energy loss in the target.

The same type of analysis may be applied to the Li^7 data. Below the triton group one should have alphas coming from the breakup of the accompanying He^5. If one subtracts the 9.8-mb cross section[5] for $Li^7(n,d)He^6$ one finds a cross section of 161 mb for the shorter tracks, of which the $Li^7(n,t)He^5 \rightarrow He^4 + n$ alphas can account for 55 mb. There are four other reactions which could produce charged particles of this range:

(1) $Li^7(n,t)He^{5*}(n)He^4$ $\quad Q > -6.6$ Mev

(2) $Li^7(n,n')Li^{7*}(t)He^4$ $\quad Q > -6.6$ Mev

(3) $Li^7(n,2nd)He^4$ $\quad Q = -8.72$ Mev

(4) $Li^7(n,3np)He^4$ $\quad Q = -10.95$ Mev

(4) is barely above threshold. A knowledge of the $(n,2n)$ cross section would enable one to set an upper limit to (3). Possibly (1) and (2) are the most likely since they have the highest Q and the smallest number of particles involved. If all the short tracks were due to (1) and (2) the cross section would be ~50 mb.

H. Search for He^7

To investigate the possibility of the formation of He^7 by the reaction $Li^7(n,p)He^7$, a search was made of the Li^7 data for such a group of protons. Since none was found, the cross section for the formation of He^7 is ≤ 5 mb for $-1.0 > Q > -7.0$.

ACKNOWLEDGMENTS

The author would like to thank the entire microscope group for the analysis of the plates, Mrs. J. Gammel and Mrs. L. Stewart for help in the calculations, Mrs. M. Downs for typing the manuscript, Dr. J. Coon, Mr. R. Davis and Group *P*-4 for use of the Cockcroft-Walton facilities, Dr. A. H. Armstrong and Dr. J. C. Allred for assistance during the experimental runs, and, especially, Dr. Louis Rosen for many helpful discussions.

Theory of Nuclear Level Density

CLAUDE BLOCH
Kellogg Radiation Laboratory, California Institute of Technology, Pasadena 4, California
(Received July 20, 1953; revised manuscript received November 9, 1953)

We have compared the level density of a nuclear model deduced from a statistical analysis with the results of the exact counting of the levels of the same model. The tables of levels of Ne^{20} given by Critchfield and Oleksa have been used as a test of the statistical theory. A new derivation of the level density is presented. It starts, as usual, from the independent-particle model. However, it differs from the previous treatments in two respects: (a) the exact states of the nucleons in the central potential are kept throughout the calculations instead of being replaced by a continuous distribution; (b) the effect of mutual interactions of the nucleons of the Majorana, Bartlett, or Heisenberg type is taken into account in the long-range approximation. With these modifications, the statistical theory agrees very well with the exact counting of the levels, both for the total density and for the density of the levels having a given angular momentum. It is shown that the replacement of the nucleon states by a continuous distribution introduced in most previous derivations, and the neglect of the Majorana forces can produce very large errors. An interpretation is presented of the distribution of angular momentum among nuclear levels in terms of rotations of the whole nucleus as a rigid body.

I. INTRODUCTION

THE theory of nuclear level density was initiated by Bethe[1] many years ago, on the basis of the Fermi gas model of the nucleus. It was soon realized, however, that the pure free-particle model which he used was only a very crude approximation. Moreover, it was not clear to what extent the conventional statistical analysis could be applied to systems containing relatively small numbers of particles. Therefore, a more detailed calculation of the potential energy was introduced, and the statistical analysis was replaced by an explicit counting of the levels of the nuclear model.[2-4] Unfortunately, this procedure is so lengthy that it cannot be repeated for many different values of Z and A. In addition, such a calculation is not feasible for heavy nuclei. It will be shown, however, that after proper modification, the statistical theory yields a reliable and accurate counting procedure even for comparatively light nuclei. It will also be shown that nuclear models, which include a dependence of the potential energy on the symmetry of the wave function, can be treated by statistical methods. The validity of the nuclear model, itself, will not be discussed here.

As usual, the independent-particle model is taken as a basis of the statistical theory. After the energy levels of the individual nucleons in the central potential have been determined, the calculation of the level density of the nucleus can be treated as a purely combinatorial problem, the solution of which is expressed exactly by the Darwin-Fowler integral (3). The main step in the statistical theory is the evaluation of the latter integral by the saddle point method. It will be shown by comparison with the calculations of Critchfield and Oleksa,[4] based on an exact counting of the levels, that this approximation does not introduce large errors even when the number of nucleons is not very large. The standard treatment of statistical mechanics, however, includes additional approximations which lose their validity in systems containing small numbers of particles. Among these is the replacement of the individual nucleon states in the central potential by a continuous distribution. This leads to a very simple expression for the level density, but a comparison with Critchfield's results shows that its accuracy is not very satisfactory. The fact that it does not take into account the shell structure of the ground state of the nucleus is a great weakness of the method of continuous distributions.[5] Thus, for example, if the outer shell has a large angular momentum, and is about half-filled, the outer nucleons can be rearranged in a large number of different ways with very little excitation energy. The level density is, then, larger than it would be in a closed shell nucleus of comparable mass.

In nuclear reactions, the transition probabilities vary so rapidly with angular momentum that only the levels having the appropriate angular momenta are excited with reasonably large probabilities. Therefore, it is important to determine the density of the levels with given angular momentum. More generally, one can compute the density of the levels for which any number of constants of the motion take given values. The isotopic-spin formalism is, then, very convenient for representing Z as a constant of the motion similar to an angular momentum. Another application of these calculations, is the treatment of more complex nuclear models. The determination of the densities of levels with given spin, isotopic spin, or symmetry type is, in fact, the key to an estimation of the effects on the level density of Bartlett, Heisenberg, or Majorana forces.

II. THE CONTINUOUS APPROXIMATION

In the following three sections, we shall consider a nuclear model in which the nucleons move indepen-

[1] H. A. Bethe, Revs. Modern Phys. **9**, 53 (1937).
[2] J. Bardeen and E. Feenberg, Phys. Rev. **54**, 809 (1938).
[3] L. Motz and E. Feenberg, Phys. Rev. **54**, 1055 (1938).
[4] C. Critchfield and S. Oleksa, Phys. Rev. **82**, 243 (1951).
[5] H. Margenau, Phys. Rev. **59**, 627 (1941).

dently in an average central field $V(r)$. For simplicity, we shall assume that V does not depend on the spin and the isotopic spin of the nucleons. The theory can be applied to a j-j model with a few obvious modifications. Let $c_0, c_1, \cdots c_K$ be a set of commuting constants of the motion of a single nucleon. Such constants will be, for instance, the projection along the z axis of the orbital angular momentum l_z, or the spin s_z, or the projection along the ζ axis of the isotopic spin τ_ζ. We shall assume that the values C_k of the constants of the motion for the whole system are the sums of the values of the c_k for the individual nucleons. The states of the nucleons in the potential $V(r)$ can be classified according to their values of the c_k. It will be convenient to call a "component" the set of all nucleon states for which the c_k have the same value. Thus, a component α is defined by the specification of the $m_{k,\alpha}$

$$c_0=m_{0,\alpha}, \quad c_1=m_{1,\alpha}, \quad \cdots, \quad c_K=m_{K,\alpha}. \tag{1}$$

For instance, if we introduce only one constant of the motion s_z, we have two components: the states with $s_z=\frac{1}{2}$, and the states with $s_z=-\frac{1}{2}$. If l_z is taken as one of the constants of the motion, the number of components becomes infinite, corresponding to $l_z=0, \pm1, \pm2, \cdots$.

In what follows, c_0 will always stand for the number of particles. Thus, $m_{0,\alpha}=1$ for all components, and for the whole system $C_0=A$.

We shall denote by ϵ_i the states of a nucleon in the central potential $V(r)$, and by $g_{i,\alpha}$ the statistical weight of ϵ_i in the component α. For simplicity, we shall assume that each of the constants of the motion $c_1, c_2, \cdots c_K$ is similar to the projection on an axis of an angular momentum. Hence, the statistical weights $g_{i,\alpha}$ associated with two components which differ only through the signs of the $m_{k,\alpha}$ are identical.[6]

The central problem in the statistical theory is that of finding the density $\rho(E,M_k)$ of the levels for which the total C_k have given values:

$$C_0=M_0=A, \quad C_1=M_1, \quad \cdots, \quad C_K=M_K. \tag{2}$$

The exact solution to this problem is given by the well-known Darwin-Fowler integral.[7,8]

$$\rho(E,M_k)=(2\pi i)^{-K-2}\int\cdots\int dl dx_0\cdots dx_K \times\exp(El-\textstyle\sum_k x_kM_k+\sum_\alpha \Phi_\alpha), \tag{3}$$

where

$$\Phi_\alpha(l,x_k)=\textstyle\sum_i g_{i,\alpha}\log[1+\exp(\sum_k x_km_{k,\alpha}-\epsilon_i l)]. \tag{4}$$

In (3) the integrals are taken along contours going from $-i\infty$ to $+i\infty$. It is customary in statistical mechanics to replace the distribution of states ϵ_i by a continuous distribution. Let then $\rho_\alpha(\epsilon)$ be the density of nuclear states in the component α. We can replace (4) by

$$\Phi_\alpha(l,x_k)=\int_0^\infty d\epsilon\rho_\alpha(\epsilon)\log[1+\exp(\textstyle\sum_k x_km_{k,\alpha}-\epsilon l)]. \tag{5}$$

We shall first describe the continuous approximation which is based upon the Eqs. (3) and (5).

In the terminology of thermodynamics, the variable l in (3), (4), (5) would be the inverse of the temperature. It is well known that for all excitation energies of interest, a nucleus is a highly degenerate system. Thus, the important values of l in the integral (3) are the large ones. For l large the integrand in (5) falls off very rapidly as ϵ becomes larger than the "Fermi energy of the component α":

$$\epsilon_\alpha=(\textstyle\sum_k x_km_{k,\alpha})/l. \tag{6}$$

This permits an asymptotic estimation of the integrals for $\epsilon_\alpha l\gg1$. According to Sommerfeld,[9,10]

$$\Phi_\alpha=l(\epsilon_\alpha N_\alpha-W_\alpha)+(\pi^2/6l)\rho_\alpha(\epsilon_\alpha), \tag{7}$$

where

$$N_\alpha(\epsilon_\alpha)=\int_0^{\epsilon_\alpha} d\epsilon\rho_\alpha(\epsilon)$$

is the total number of nucleons which can be accommodated in the component α, when all states are filled up to the energy ϵ_α, and

$$W_\alpha(\epsilon_\alpha)=\int_0^{\epsilon_\alpha} d\epsilon\epsilon\rho_\alpha(\epsilon)$$

is the corresponding total energy.

The next step is the evaluation of the integral (3) by the many-variables saddle point method.[7] This yields

$$\rho(E,M_k)=(2\pi)^{-(K+2)/2}D^{-1/2}e^S, \tag{8}$$

where the "entropy" S is the value at the saddle point of

$$S=El-\textstyle\sum_k x_kM_k+\sum_\alpha\Phi_\alpha,$$

and D is the determinant formed with the values at the saddle point of the second derivatives of $\Phi=\sum_\alpha\Phi_\alpha$ with respect to $l, x_0, x_1, \cdots, x_K$. The coordinates of the saddle point are given by

$$E=-\partial\Phi/\partial l, \quad M_k=\partial\Phi/\partial x_k. \tag{9}$$

[6] This assumption is introduced in order to decrease the number of terms in the expansions and could be removed easily. It excludes parity, which can be represented, for instance, by a constant of the motion such that $m_\alpha=0$ for the even nuclear states and $m_\alpha=1$ for the odd states. The density of the even nuclear levels would then be the sum of the densities of the levels for which $C=0, \pm2, \pm4$, etc. The density of the odd levels would be the sum of the densities of the levels such that $C=\pm1, \pm3, \pm5$, etc. In general, the level density will be a smooth function of C, and the densities of levels of both parities will be equal in the first approximation.

[7] R. H. Fowler, *Statistical Mechanics* (Macmillan Company, New York, 1936).

[8] G. E. Uhlenbeck and C. Van Lier, Physica 4, 531 (1937).

[9] A. Sommerfeld, Z. Physik 67, 1 (1928).

[10] This expression is the beginning of an asymptotic expansion. However, the following terms depend on the derivatives of the $\rho_\alpha(\epsilon)$, and therefore have little meaning in nuclear problems, where the replacement of the discrete energy levels of the nucleons by continuous distributions is quite ambiguous (see Sec. 4).

Substitution of (7) into these equations yields

$$E=\sum_\alpha[W_\alpha+(\pi^2/6t^2)(\rho_\alpha+\epsilon_\alpha\rho_\alpha')],$$
$$M_k=\sum_\alpha m_{k,\alpha}[N_\alpha+(\pi^2/6t^2)\rho_\alpha], \tag{10}$$

where all functions of ϵ are taken at $\epsilon=\epsilon_\alpha$ as defined by (6).

The lowest energy level satisfying the conditions (2) is obtained from (10) by putting $t=\infty$. The energy E^1 and the Fermi energies of this state are given by

$$E^1=\sum_\alpha W_\alpha(\epsilon_\alpha^1), \quad M_k=\sum_\alpha m_{k,\alpha}N_\alpha(\epsilon_\alpha^1). \tag{11}$$

The ground-state energy, on the other hand, is the minimum of E^1 for $M_0=A$ and arbitrary $M_1, \cdots M_K$. It is easily seen that in the ground state of the model $M_1, \cdots M_K$ vanish and that the Fermi energies ϵ_α are all equal to a value ϵ^0 defined by

$$\sum_\alpha N_\alpha(\epsilon^0)=A.$$

We shall now assume that the excitation energy $U^1=E-E^1$, measured above the energy E^1 of the lowest level having the given values of the constants of the motion, is sufficiently small so that $1/t^2$ and the variations $\epsilon_\alpha-\epsilon_\alpha^1$ can be considered as infinitesimal quantities. Then, from (10) we get in the first approximation

$$U^1=(\pi^2/6t^2)\sum_\alpha\rho_\alpha(\epsilon_\alpha^1).$$

Moreover, if $M_1, M_2, \cdots M_K$ are small, the ϵ_α^1 do not differ very much from ϵ^0, and we have

$$\sum_\alpha\rho_\alpha(\epsilon_\alpha^1)\approx\sum_\alpha\rho_\alpha(\epsilon^0)=1/\delta. \tag{12}$$

Here $1/\delta$ is the total density of states available to a single nucleon at an energy equal to the Fermi energy ϵ^0 of the ground state. It can be easily shown that the difference,

$$\sum_\alpha\rho_\alpha(\epsilon_\alpha^1)-\sum_\alpha\rho_\alpha(\epsilon^0)=\sum_\alpha(\epsilon_\alpha^1-\epsilon^0)\rho_\alpha'(\epsilon^0),$$

which is neglected in (12) vanishes in the first order in M_k. A short calculation finally yields for the level density in the first approximation

$$\rho(E,M_k)=[(2\pi)^{K/2}(\sqrt{48})U^1\sigma_1\sigma_2\cdots\sigma_K]^{-1}\times\exp[\pi(2U^1/3\delta)^{\frac{1}{2}}], \tag{13}$$

where the σ_k are defined by

$$\sigma_k^2=(1/\pi)\langle m_k^2\rangle_{\text{av}}(6U^1/\delta)^{\frac{1}{2}}. \tag{14}$$

In (14) we have written

$$\langle m_k^2\rangle_{\text{av}}=\sum_\alpha m_{k,\alpha}^2\rho_\alpha(\epsilon^0)/\sum_\alpha\rho_\alpha(\epsilon^0) \tag{15}$$

for the quadratic mean of m_k at the top of the Fermi distribution. A remarkable property of this result is that the level density *depends on the M_k only through U^1*.

We must now compute the energy difference E^1-E^0. The relations (11) yield

$$\epsilon_\alpha^1-\epsilon^0=\delta\sum_{k=1}^K m_{k,\alpha}M_k/\langle m_k^2\rangle_{\text{av}},$$
$$E^1-E^0=U-U^1=\delta\sum_{k=1}^K M_k^2/2\langle m_k^2\rangle_{\text{av}}. \tag{16}$$

Here we have introduced the excitation energy U measured from the ground state. By substitution of the value of U^1 given by (16) into (13), we get the Gaussian distribution law:

$$\rho(U,M_k)=\rho(U)[(2\pi)^{K/2}\sigma_1\sigma_2\cdots\sigma_K]^{-1}\times\exp(-\sum_1^K M_k^2/2\sigma_k^2), \tag{17}$$

where

$$\rho(U)=(U\sqrt{48})^{-1}\exp[\pi(2U/3\delta)^{\frac{1}{2}}] \tag{18}$$

is the well-known expression for the total level density.[1,8] In deriving (18) we have introduced the difference U^1-U only into the exponential which is the rapidly varying factor. Similarly, in the expression (14) defining σ_k, U^1 may be replaced by U. It is seen from (17) that σ_k is the *dispersion* of M_k among the levels.

The results obtained for the continuous model can be summarized as follows: *The density of the levels with given values of $C_1, \cdots C_K$ is proportional to the total level density* (18) *at an energy $U-(E^1-E^0)$, where E^1 is the energy of the lowest of all the considered levels, and E^0 the energy of the ground state. The constant of proportionality is independent of the values of C_k, and can be obtained by normalization of the total density at each energy.*

III. MORE ACCURATE TREATMENT

The calculation of the level density of a highly degenerate gas starts from the assumption that only levels near the top of the Fermi distribution are involved. The replacement of the distribution of the nucleon states by a continuous distribution, on the other hand, requires that the number of nucleon states in the relevant energy interval around the top of the Fermi distribution is large. Moreover, the distribution of these states should be fairly regular so that an equivalent smooth density function could be defined. These conditions are not well satisfied in nuclei, especially in the lighter ones. Actually, the number of relevant energy values of the nucleon states is usually rather small, and some of the states are highly degenerate due to spin, isotopic spin, and angular momentum. The density functions are then not well defined. A more accurate treatment should start from the exact definition of Φ_α given in (4).

Let us assume, for example, that in the ground state of the nucleus, the states $\epsilon_1, \epsilon_2, \cdots \epsilon_{n-1}$ are filled, that ϵ_n is partially filled, and that $\epsilon_{n+1}, \epsilon_{n+2}, \cdots$ are empty. We have seen in the preceding section that as $t\to\infty$, the value of ϵ_α at the saddle point tends to ϵ^0, the energy of

the top of the Fermi distribution. In other words $x_0 \to t\epsilon^0$, and the x_k remain finite. Similarly, in the present case we can expect that x_0 will have the limit $t\epsilon_n$ for large t. Hence, let us write

$$x_0 = t\epsilon_n + a + \delta x_0, \tag{19}$$

where a is a constant which must be adjusted in such a way that

$$\delta x_0 \to 0 \quad \text{as} \quad t \to \infty .$$

We have also seen in the continuous treatment that the x_k ($k=1, \cdots K$) at the saddle point are proportional to M_k. Consequently, for a certain range of values of M_k, we can consider the x_k as small quantities. For convenience, we shall write $x_k = \delta x_k$ for $k=1, \cdots K$. Thus,

$$\sum_k x_k m_{k,\alpha} = t\epsilon_n + a + \sum_{k=0}^{K} \delta x_k m_{k,\alpha}.$$

The method we shall use here consists in treating exactly the dependence of Φ_α on t and a, and in using a power series expansion for the dependence on the δx_k. Thus,

$$\Phi_\alpha = \sum_{i,p} \frac{g_{i,\alpha}}{p!} \Big[\sum_{k=0}^{K} \delta x_k m_{k,\alpha}\Big]^p f^{(p)}[t(\epsilon_n - \epsilon_i) + a], \tag{20}$$

where

$$f(x) = \log(1+e^x),$$
$$f'(x) = 1/(1+e^{-x}),$$
$$f''(x) = \tfrac{1}{4}\,\mathrm{sech}^2(x/2),$$
$$f^{(3)}(x) = -\tfrac{1}{4}\tanh(x/2)\,\mathrm{sech}^2(x/2), \text{ etc.}$$

In the sum (20), the main contributions at low excitation energy come from the state ϵ_n and the states which are close to it. This follows from the rapid decrease of the functions $f^{(p)}$ with $|\epsilon_n - \epsilon_i|$ for large t. The terms involving f or f' do not decrease with $|\epsilon_n - \epsilon_i|$ when $\epsilon_i < \epsilon_n$. These terms, however, can be written

$$f[t(\epsilon_n - \epsilon_i) + a] = t(\epsilon_n - \epsilon_i) + a + f[-t(\epsilon_n - \epsilon_i) - a],$$
$$f'[t(\epsilon_n - \epsilon_i) + a] = 1 - f'[-t(\epsilon_n - \epsilon_i) - a],$$

where the remaining functions f or f' now have the proper behavior. It is convenient to introduce the notation

$$f_i^{(p)} = f^{(p)}[t(\epsilon_n - \epsilon_i) + a] \qquad \text{for } \epsilon_i \gtrsim \epsilon_n,$$
$$f_i^{(p)} = (-)^p f^{(p)}[-t(\epsilon_n - \epsilon_i) - a] \text{ for } \epsilon_i < \epsilon_n. \tag{21}$$

The distinction $\epsilon_i \gtrless \epsilon_n$ is, of course, relevant only for $p=0$, 1, since

$$f^{(p)}(-x) = (-)^p f^{(p)}(x) \text{ for } p \geq 2.$$

If we assume, as above, that $C_1 \cdots C_K$ are such that the numbers $g_{i,\alpha}$ of states with given values of the constants of the motion depend only on the absolute magnitudes of these values and not on their signs, then only terms containing even powers of $\delta x_1, \cdots \delta x_K$ appear in (20).[11] Thus, we get an expansion of the type

$$\Phi = (t\epsilon_n + a + \delta x_0)N_{n-1} - tW_{n-1} + F + F'\delta x_0 + \tfrac{1}{2}\sum_0^K F_k''\delta x_k^2 + \tfrac{1}{6}F^{(3)}\delta x_0^3 + \tfrac{1}{2}\sum_1^K F_k^{(3)}\delta x_k^2\delta x_0 + \frac{1}{24}\sum_0^K F_{kk}^{(4)}\delta x_k^4 + \tfrac{1}{8}\sum_{k\neq l} F_{kl}^{(4)}\delta x_k^2\delta x_l^2 + \cdots, \tag{22}$$

where N_{n-1} is the number of nucleon states of energy less than ϵ_n, W_{n-1} is the corresponding total energy, and the coefficients F are given by

$$F^{(p)} = \sum_{i,\alpha} g_{i,\alpha} f_i^{(p)},$$
$$F_k^{(p)} = \sum_{i,\alpha} g_{i,\alpha} m_{k,\alpha}{}^2 f_i^{(p)},$$
$$F_{kl}^{(p)} = \sum_{i,\alpha} g_{i,\alpha} m_{k,\alpha}{}^2 m_{l,\alpha}{}^2 f_i^{(p)}, \text{ etc.}$$

These coefficients are expressed by elementary functions in terms of the parameter t, and are easily computed, especially since at small excitation energy, only the terms associated with the state ϵ_n and its close neighbors contribute appreciably. We shall further need the following coefficients:

$$G^{(p)} = \sum_{i,\alpha} (\epsilon_i - \epsilon_n) g_{i,\alpha} f_i^{(p)},$$
$$G_k^{(p)} = \sum_{i,\alpha} (\epsilon_i - \epsilon_n) g_{i,\alpha} m_{k,\alpha}{}^2 f_i^{(p)}, \text{ etc.}$$

and

$$H^{(p)} = \sum_{i,\alpha} (\epsilon_i - \epsilon_n)^2 g_{i,\alpha} f_i^{(p)}, \text{ etc.}$$

The latter coefficients are related to the coefficients F by

$$\partial F_k^{(p)}/\partial t = -G_k^{(p+1)}, \quad \partial G_k^{(p)}/\partial t = -H_k^{(p+1)}, \text{ etc.}$$

Equations (9) defining the saddle point read, now,

$$A = N_{n-1} + F' + F''\delta x_0 + \tfrac{1}{2}\sum_{k=0}^{K} F_k^{(3)}\delta x_k^2 + \cdots, \tag{23}$$

$$M_k = F_k''\delta x_k + F_k^{(3)}\delta x_k\delta x_0 + \cdots. \tag{24}$$

The equation in E can be written after some simple transformations

$$U = G' + G''\delta x_0 + \tfrac{1}{2}\sum_{k=0}^{K} G_k^{(3)}\delta x_k^2 + \cdots, \tag{25}$$

where U is the excitation energy measured above the ground state

$$E^0 = W_{n-1} + \epsilon_n(A - N_{n-1}).$$

[11] When S_σ, T_ξ, Y_τ are introduced at the same time, the three corresponding m values for a single nucleon are related by $m_\sigma m_\xi m_\tau = \frac{1}{8}$. From this correlation, it follows that the expansion (20) will contain additional terms such as, for example, a term in $\delta x_\sigma \delta x_\xi \delta x_\tau$, which will yield terms in $S_\sigma T_\xi Y_\tau$ in the final level density formula. This minor correction will be omitted.

The limit of F' for large t is given by the contribution of the level ϵ_n, which is the only term independent of t. Thus, we see from (23) that for large t, δx_0 is proportional to $A-N_{n-1}-F'(t=\infty)$. Consequently, the condition that δx_0 should go to zero for large t reads

$$A-N_{n-1}=F'(t=\infty)=f_n'\sum_a g_{n,a}.$$

This condition defines a. As $f_n'=1/(1+e^{-a})$, we have

$$e^a=[A-N_{n-1}]/[\textstyle\sum_a g_{n,a}-(A-N_{n-1})]. \quad (26)$$

The quantity $A-N_{n-1}$ is the number of nucleons of energy ϵ_n in the ground state, and $\sum_a g_{n,a}$ is the total number of nucleon states of energy ϵ_n. Thus, e^a is equal to the number of nucleons occupying the level ϵ_n in the ground-state configuration divided by the number of holes in that same level.

We must now solve Eqs. (23), (24), and (25) giving t, δx_0, δx_k in terms of U, A, and M_k, and compute the entropy $S=Et-\sum_k x_kM_k-\Phi$, and the determinant D. The calculation is quite straightforward, and the resulting value of the entropy can be written

$$S=S_0+S_1-\sum_1^K M_k^2/2\sigma_k^2-\sum_1^K\sum_1^K B_{kl}M_k^2M_l^2, \quad (27)$$

where the two first terms depend only on U and give the general level density, the third term gives the Gaussian law already obtained in the continuous theory and the fourth term gives the deviations from this simple law.

The term S_0 is a constant equal to the value of S in the limit $t\to\infty$, $M_k=0$; it is given by

$$S_0=a(N_{n-1}-A)+f_n\sum_a g_{n,a}.$$

Upon introducing the values of f_n and of a this becomes

$$S_0=(m+n)\log(m+n)-m\log m-n\log n, \quad (28)$$

where m and n stand for the number of particles and of holes in the level ϵ_n in the ground-state configuration. In what follows, we shall give the first approximations only of the various quantities occurring in the level density formula. More complete expansions are given in the appendix.

The term S_1 is given by

$$S_1=Ut+\bar{F}-\bar{F}'^2/2F'', \quad (29)$$

where

$$\bar{F}=\sum_a\sum_{i\neq n} g_{i,a}f_i, \quad \bar{F}'=\sum_a\sum_{i\neq n} g_{i,a}f_i'$$

are identical with F and F' except that the term coming from ϵ_n is omitted. The ratio $\bar{F}'/F''$ is a small quantity at low energy; it vanishes in the limit of $U\to 0$. Thus, terms proportional to the successive powers of $\bar{F}'/F''$ are correction terms of increasing order. The dependence of the excitation energy on t is given by

$$U=G'-G''(\bar{F}'/F''), \quad (30)$$

and the dispersion coefficients by

$$\sigma_k^2=F_k''-F_k^{(3)}(\bar{F}'/F''). \quad (31)$$

The coefficients B_{kl} of the fourth-order terms are very small in practical cases; their expression is given in the appendix.

The determinant D is readily computed because the off-diagonal terms are much smaller than the diagonal terms. One finds in the first approximation:

$$D=(1-G'^2/H''F'')(H''-H^{(3)}\bar{F}'/F'')\prod_{k=0}^K\sigma_k^2. \quad (32)$$

The preceding derivation does not apply when the outer shell is complete in the ground state, since in this case (26) gives $a=+\infty$ or $a=-\infty$ depending on whether ϵ_n is the last filled level, or the first empty one. Let ϵ_n be the first empty level. It is natural, then, to replace (19) by

$$x_0=t\epsilon^0+a+\delta x_0,$$

where ϵ^0 is some energy between ϵ_{n-1} and ϵ_n, to be determined by the condition that $\delta x_0\to 0$ as $t\to\infty$. We have $A=N_{n-1}$, and the relation (23) giving δx_0 becomes

$$0=F'+F''\delta x_0+\cdots.$$

In the limit of large t we have

$$F'\approx\textstyle\sum_a g_{n,a}\exp[-t(\epsilon_n-\epsilon^0)-a] - g_{n-1,a}\exp[-t(\epsilon^0-\epsilon_{n-1})+a],$$

$$F''\approx\textstyle\sum_a g_{n,a}\exp[-t(\epsilon_n-\epsilon^0)-a] + g_{n-1,a}\exp[-t(\epsilon^0-\epsilon_{n-1})+a].$$

Consequently, if we choose ϵ^0 and a according to

$$\epsilon^0=(\epsilon_n+\epsilon_{n-1})/2, \quad e^{2a}=\textstyle\sum_a g_{n,a}/\sum_a g_{n-1,a},$$

F' goes to zero much faster than F'', and δx_0 goes to zero. In conclusion, ϵ^0 has to be taken halfway between ϵ_n and ϵ_{n-1}, and e^{2a} is the ratio of the weight of ϵ_n to the weight of ϵ_{n-1}. With this modification, all the formulas given above apply, provided that in the definition (21) of the $f_i^{(p)}$ ϵ_n is replaced by ϵ^0. Of course, in the present case, all the functions F go to zero as $U\to 0$. In particular, $S_0=0$.

We shall finally mention the modifications which have to be made, if one wishes to calculate the number $N(E,M_k)$ of levels of energy less than, or equal to, E.

This quantity is immediately derived from (3):

$$N(E,M_k)=(2\pi i)^{-K-2}\int\cdots\int(dt/t)dx_0dx_1\cdots dx_K \times\exp(Et-\sum_0^K x_kM_k+\Phi).$$

This integral can be evaluated by the saddle point method, and the calculation is identical with that of the level density, except that Φ has to be replaced by

$\Phi - \log t$. The result is

$$N(U,M_k)=(2\pi)^{-(K+2)/2}D^{-\frac{1}{2}}t^{-1}e^{S}, \qquad (33)$$

where S is identical with the expression (27). However, the relation (30) between energy and temperature is replaced by[12]

$$U=1/t+G'-G''(F'/F''); \qquad (34)$$

and in the calculation of D, H'' has to be replaced by $H''+1/\ell^2$.

As an example, let us compute the total number of levels of excitation energy $U=0$ in a system of A nucleons. The exact value is given by the binomial coefficient $\binom{m+n}{m}$, where m and n are the numbers of particles and of holes in the level ϵ_n in the ground-state configuration. On the other hand, we apply (33) taking $K=0$. In the limit $U\to 0$ we have

$$S=S_0+t(1/t+G'+\cdots)\to S_0+1,$$
$$D=(1/\ell^2+H''+\cdots)\sigma_0^2\to(1/\ell^2)F''(t=\infty).$$

From the definition of F'' we have

$$F''(t=\infty)=\sum_a g_{n,a}f_n''$$
$$=\tfrac{1}{4}\sum_a g_{n,a}\,\mathrm{sech}^2(a/2)=mn/(m+n),$$

where the value (26) for a has been used. Finally we get, after substitution of (28) for S_0,

$$N(0)=[e/(2\pi)^{\frac{1}{2}}]\times\text{Stirling approximation for }\binom{m+n}{m}$$
$$=1.084\times\text{Stirling approximation for }\binom{m+n}{m}.$$

It is seen that even in this extreme case the error introduced by the saddle point method is very small. The integration with respect to x_0 has had the effect of replacing the binomial coefficient by its Stirling approximation, whereas the integration with respect to t has introduced an error of the order of 8 percent.

IV. ANGULAR MOMENTA

In this section, we shall study the distribution of angular momenta among the nuclear levels.

The present experimental knowledge of the spins of the nuclear-excited states is very scarce except for a few low-lying states to which the statistical theory does not apply. Therefore, it is not possible to verify directly the theoretical predictions. It is, however, interesting to check the accuracy of the statistical treatment by comparing its results with those obtained by a direct counting of the levels performed on the same model. Thus, the discussion of the validity of the model itself will be left entirely aside. Critchfield and Oleksa[4] have given a complete account of the levels of energy less than 25 Mev for the nuclei with $A=20$, which permits an excellent test of the statistical method. Their model actually includes Majorana forces, but it will be shown in the next section that these forces do not change appreciably the distribution of angular momenta.

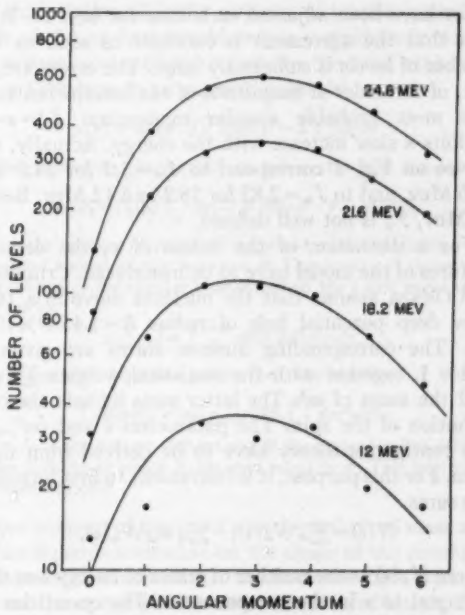

FIG. 1. Number of levels with a given angular momentum and an energy less than a given value. The dots represent the results of Critchfield and Oleksa corresponding to four different energies. The curves represent the function (36) with parameters adjusted for best fit at each energy.

The number N_J of the levels with total angular momentum J and energy less than E is given in terms of the number $N(M)$ of the levels with angular momentum M along the z axis by

$$N_J=N(J)-N(J+1). \qquad (35)$$

The dependence on M of the number of the levels with the angular momentum M along the z axis is given in the first approximation by a Gaussian law $N(M)\sim\exp(-M^2/2\sigma^2)$ [see (17) or (27) and (33)]. Hence, we have for the dependence on J of the number of levels with angular momentum J and energy up to a given value

$$N_J\sim(2J+1)\exp[-(J+\tfrac{1}{2})^2/2\sigma^2]. \qquad (36)$$

First, we shall verify that Critchfield's results obey this law.

The numbers[13] of levels of given angular momentum and of energy less than a given value have been plotted on Fig. 1 as functions of the angular momentum for four different energies together with the curves defined by (36). The parameter σ in (36) and the proportionality

[12] Note here that the relation between energy and temperature depends on the integral which is computed.

[13] These numbers have been taken from Table IV in Critchfield and Oleksa (see reference 4).

factor have been adjusted each time for best fit. It is seen that the agreement is excellent as soon as the number of levels is sufficiently large. The errors are, in fact, of the order of magnitude of random fluctuations. The most probable angular momentum $J_m=\sigma-\frac{1}{2}$ exhibits a slow increase with the energy. Actually, the curves on Fig. 1 correspond to $J_m=3.0$ for 24.8 and 21.6 Mev, and to $J_m=2.82$ for 18.2 and 12 Mev. Below 12 Mev, J_m is not well defined.

For a discussion of the values of σ, the detailed features of the model have to be introduced. Critchfield and Oleksa assume that the nucleons move in a 16.8-Mev deep potential hole of radius $R=1.45A^{\frac{1}{3}}\times10^{-13}$ cm. The corresponding nucleon states are given in Table I, together with the statistical weights $\sum_\alpha g_{i\alpha}$ and the sums of m^2. The latter sums include the contribution of the spin. The parameters δ and $\langle m^2\rangle_{\text{Av}}$ of the continuous theory have to be derived from these data. For this purpose, it is convenient to first introduce the sums

$$N(\epsilon)=\sum_\alpha N_\alpha(\epsilon), \quad \sum_\alpha m_\alpha^2 N_\alpha(\epsilon), \tag{37}$$

where $N_\alpha(\epsilon)$ is the number of states of energy less than or equal to ϵ in the component α. The quantities $1/\delta$ and $\langle m^2\rangle_{\text{Av}}/\delta$ are then the derivatives of the expressions (37) with respect to ϵ at $\epsilon=\epsilon^0$. The sums (37) can be deduced from the data of Table I when ϵ is equal to the energy ϵ_i of one of the nucleon states. For other values of ϵ, an interpolation procedure should be used. Moreover, there is some arbitrariness in the definition of the sums (37) even at the energies ϵ_i. A procedure which yields smooth plots consists in taking the sum of the contributions of the states below ϵ_i, plus half of the contribution of the state ϵ_i. Thus, we get five points for each function, through which we have to draw continuous curves (Fig. 2). The Fermi energy ϵ^0 is the value of ϵ at which $N(\epsilon)$ is equal to $A=20$. The values of $1/\delta$ and $\langle m^2\rangle_{\text{Av}}/\delta$ are then given by the slopes of the two curves at ϵ^0. Clearly, the definition of the latter quantities is not very precise, and this shows one of the weaknesses of the continuous approximation for light nuclei. Measurement of the slopes on Fig. 2 yields[14]

$$1/\delta=1.40\ \text{Mev}^{-1}, \quad \langle m^2\rangle_{\text{Av}}/\delta=2.36\ \text{Mev}^{-1}. \tag{38}$$

With these values, the relation (14) gives for the most probable angular momentum J_m

$$J_m=1.24U^{\frac{1}{2}}-\tfrac{1}{2}.$$

The plot of this function on Fig. 3 (curve a) shows that the values of J_m obtained by the present approximation are significantly smaller than the values deduced from the curves of Fig. 1.[15] The reason for this is easy to understand. The nuclei with $A=20$ have an incomplete d shell with four particles. This is a very favorable situation for producing large angular momenta. An almost empty, or almost filled shell, or an outer shell of small angular momentum, would, on the contrary, yield exceptionally small angular momenta. The continuous theory, which ignores these peculiarities of the nuclei, must deviate one way or the other, depending on the ground state configuration. However, it predicts correctly the order of magnitude of J_m.[16]

We shall now discuss the values of J_m given by the theory of Sec. 3. This theory introduces directly the nucleon states described in Table I. Thus, the functions $F, G, \cdots$ become sums of five terms which are easily computed numerically. The energy ϵ_n is that of the $1d$ state. The outer shell has 4 particles and 16 holes. Hence, $\epsilon^0=\frac{1}{4}$. In the limit $U=0$, $\bar{F}'$ vanishes. Therefore, the limit of σ is simply given by the contribution of the $1d$ state to F_J''. Thus,

$$\sigma^2(0)=\sum_\alpha m_\alpha^2 g_{n,\alpha}(e^{\alpha/2}+e^{-\alpha/2})^{-2}.$$

For the present nuclei, $\sigma^2(0)=7.2$ and $J_m(0)=2.3$. The values at higher excitation energies are easily computed by means of the expansions given in the appendix. The correction terms in σ^2 have three different origins and it is necessary to take the first few terms in the expansions of each kind of correction. These expansions are rapidly convergent. The final results are represented by the curve c on Fig. 3. They are in excellent agreement with the values corresponding to the four energies con-

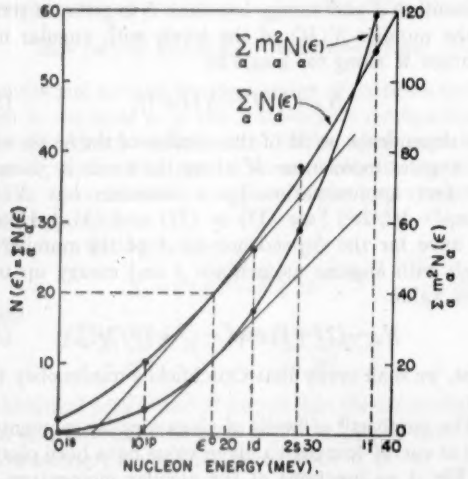

FIG. 2. Determination of the parameters of the continuous theory from the nucleon states. The dots indicate the values of the functions $N(\epsilon)$ and $\sum_\alpha m_\alpha^2 N_\alpha(\epsilon)$ at the energies of the five nucleon states given in Table I. The curves are interpolated between these points.

[14] Modifications of the procedure used in plotting the curves of Fig. 1, do not usually alter these values by more than 10 percent.

[15] Everywhere in the present discussion we have neglected the fact that the most probable angular momentum among the levels of energy less than or equal to E, is not exactly the same as the corresponding quantity for the levels of energy equal to E. However, the difference between the two quantities is very small because of the rapid increase of the level density with energy, and the slow variation of J_m.

[16] It has often been stated incorrectly in the literature that the statistical theory predicts much too many levels with very large angular momentum.

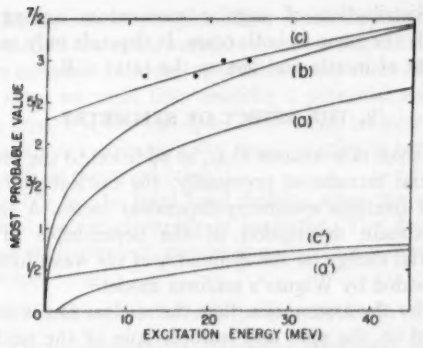

FIG. 3. The most probable angular momentum and spin or isotopic spin among the levels having an energy less than a given value. The dots indicate the values corresponding to Fig. 1. Curves (a) and (b) give the most probable angular momentum derived from the continuous theory, with the values of the parameters determined directly from the nucleon states and by means of the B.W.K. approximation, respectively. Curve (c) gives the values obtained from the method of Sec. 3. The curves (a') and (c') give the corresponding values of the most probable spin or isotopic spin. The curve (b') would be very close to (c'), and, therefore, has been omitted.

sidered above. It should be noted that $J_m(0)$ is an important fraction of J_m in the interesting range of energy. The value of $J_m(0)$ depends entirely on the outer shell. It vanishes for a closed shell, and reaches a maximum when the outer shell is half-filled ($a=0$). For the $1d$ shell, the maximum value which occurs at $A=26$ is equal to $J_m=2.85$.

The coefficient B in (27), which gives the deviation of the distribution of the angular momenta from the Gaussian law, is easily computed by means of the expression given in the appendix. One finds that B has a very slow variation with energy, and is of the order of 10^{-6} at 25 Mev. Therefore, the predicted deviations from the Gaussian law are less than 2 percent for $J \leqslant 6$.

Finally, we shall return to the continuous theory for a more general discussion of the distribution of angular momenta among the nuclear levels. The discussion will be restricted here to nuclear models involving a spin-independent central potential $V(r)$. Then, the projections along the z axis m_l and m_s of the orbital momentum and of the spin of the nucleons are independent, and we have for the projection of the total angular momentum m the relation

$$\langle m^2\rangle_{Av}=\langle m_l^2\rangle_{Av}+\langle m_s^2\rangle_{Av}=\langle m_l^2\rangle_{Av}+\tfrac{1}{4}. \quad (39)$$

In the heavy nuclei, the contribution of the spin is small compared with the orbital term, since large orbital momenta occur near the top of the Fermi distribution. On the other hand, the orbital term is very simply related to the moment of inertia I of the nucleus[17] by

$$\langle m_l^2\rangle_{Av}/\delta=\sum_{m_l} m_l^2\rho(\epsilon^0,m_l)=I/\hbar^2. \quad (40)$$

[17] This relation is implicitly given by Bethe (see reference 1) for the special case of an infinite square-well potential.

In this relation, I is the moment of inertia around an axis of the nucleus considered as a rigid body with a mass density at each point given by the usual expression for a Fermi gas in an external potential:

$$\mu(r)=4(4\pi/3)[2M(\epsilon^0-V)]^{\frac{1}{2}}Mh^{-3}.$$

The proof of the relation (40) starts from the B.W.K. formula,[18]

$$N_l(\epsilon^0)=(4/\pi)\int_{r_0}^{r_1} dr[(2M/\hbar^2)(\epsilon^0-V)-l^2/r^2]^{\frac{1}{2}},$$

giving the number of states of a nucleon with the angular momentum l and an energy less than ϵ^0. The density of states with a projection of the angular momentum on the z axis equal to m_l is given by

$$\rho(\epsilon^0,m_l)=\int_{|m_l|}^{l_{max}} dl(d/d\epsilon^0)N_l(\epsilon^0).$$

An elementary integration yields, then, the identity

$$\int dm_l m_l^2\rho(\epsilon^0,m_l)=(2/3\hbar^3)\int_0^R d\tau r^2\mu(r);$$

where $d\tau$ is the volume element and R the nuclear radius defined as the distance at which V becomes equal to ϵ^0. This relation is equivalent to (40).

The moment of inertia of a nucleus of given mass and radius depends somewhat on the shape of the potential V. Potentials which attract the nucleons more strongly toward the center yield smaller moments of inertia. For example, the harmonic oscillator potential and the infinite square-well yield for I the values $\frac{1}{4}MR^2A$ and $\frac{2}{5}MR^2A$, respectively.

The same procedure gives for the parameter $1/\delta$ the value $1/\delta=(d/d\epsilon^0)N(\epsilon^0)$, where

$$N(\epsilon^0)=4(4\pi/3)\hbar^{-3}\int_0^R d\tau[2M(\epsilon^0-V)]^{\frac{1}{2}}.$$

It is interesting to compare the values of the parameters of the continuous theory deduced from the B.W.K. approximation for $A=20$ with the values (38). One finds with the B.W.K. approximation $J_m=1.5U^{\frac{1}{3}}-\frac{1}{2}$ for the infinite square well, and $J_m=1.24U^{\frac{1}{3}}-\frac{1}{2}$ for the harmonic oscillator potential[19] (contribution of the spin included). The values corresponding to a finite well should lie between the later values. This shows that the B.W.K. approximation overestimates J_m, and, therefore, in the present case, it corrects to some extent the errors introduced by the continuous approximation. It follows that the values of J_m corresponding to an infinite well (curve b on Fig. 3) are more accurate than the values obtained with the parameters determined directly

TABLE I. Independent particles states for $A=20$.

State	$1s$	$1p$	$1d$	$2s$	$1f$
Energy ϵ_i (Mev)	0	10.3	23.1	28.5	37.6
$\sum_a g_{i,a}$	4	12	20	4	28
$\sum_a m_a^2 g_{i,a}$	1	11	45	1	119

[18] L. I. Schiff, *Quantum Mechanics* (McGraw-Hill Book Company, Inc., New York, 1949), Sec. 28.

[19] The parameter of the potential is determined by the condition $V(R)=\epsilon^0$, where R is the nuclear radius.

from the nucleon states. This conclusion, however, does not hold for all values of A.

For the heavy nuclei, the contribution of the spin in (39) can be neglected in the first approximation. A simple physical interpretation of the relation (40) can then be obtained by introducing the quantity U^1 defined in Sec. 2. This quantity here is the excitation energy measured above the lowest nuclear level having an angular momentum M along the z axis. From (16) and (40) we obtain for the difference between U and U^1:

$$U^1-U=-M^2\hbar^2/2I. \tag{41}$$

Thus U^1 is the remaining excitation energy when the kinetic energy due to the rotation of the nucleus as a rigid body around the z axis is subtracted from the total available excitation energy U.[20] It follows that although we have considered a pure independent-particle model, the distribution of angular momentum among the energy levels is the same as it would be for a rigid body. More specifically, this distribution could be obtained in the following manner: (a) we determine all the levels with $J=0$ (states of internal motion); (b) we deduce the levels with angular momentum J by adding the kinetic energy $J(J+1)\hbar^2/2I$ to each energy level with $J=0$.

This property, of course, does not imply that the Hamiltonian can be split into two nearly independent parts, one involving only the internal coordinates of the system, and one involving only the coordinates determining the position of the system in space. Such a separation is possible only in the case of an actual rigid body, and the detailed level scheme is then very different from that of an independent-particle model. This can easily be shown by considering a system consisting, for example, of four particles (α-particle model of O^{16}). For suitable kinds of interactions, the particles will form a tetrahedron which can rotate and vibrate. The behavior of the system depends, then, essentially on two parameters, its radius R, and the amplitude a of the zero-point vibrations. The spacing of the vibrational levels is of the order of $\hbar^2/Ma^2$, and that of the rotational levels of the order of $\hbar^2/MR^2$. In the case $a\ll R$, the system has a well-defined shape; it is a rigid body to a good approximation. The spacing of the vibrational levels is then very much larger than that of the rotational levels. Consequently, we shall observe well-separated groups of levels corresponding to the same vibrational state and different angular momenta. In the other extreme case where $a\approx R$, the particles are nearly independent. The spacing of the vibrational levels and of the rotational levels are then of the same order. Therefore, the groups of levels which existed in the case of the rigid body now overlap in such a way that it becomes actually impossible to distinguish between rotation and vibration. However, the statistical distribution of angular momentum among the levels is the same in both cases. It depends only on the moment of inertia and not on the ratio a/R.

[20] J. H. Jensen (private communication) has proposed to take this simple property as a starting point for the calculation of the distribution of angular momenta in statistical theory.

V. THE EFFECT OF SYMMETRY

We shall now assume that, in addition to the central potential introduced previously, the nuclear potential energy contains symmetry-dependent terms. A simple approximate description of the dependence of the potential energy on the symmetry of the wave function is provided by Wigner's uniform model.[21]

Under the assumption that the nuclear forces do not depend on the spin and isotopic spin of the nucleons (pure Majorana and Wigner forces), the symmetry of the wave function of every nuclear level is characterized by three "partition quantum numbers"[22] $P\geqslant P'\geqslant|P''|$, and the symmetry-dependent part of the potential energy is given by

$$V_M=a_M[P(P+4)+P'(P'+2)+P''^2]. \tag{42}$$

From the discussion of the binding energies,[23] one finds for the value of the parameter a_M:

$$a_M=20/A\,(\text{Mev}).$$

It is reasonable to assume that the same expression gives approximately the potential energy of the excited states.

Spin and isotopic spin-dependent forces can also be considered. Their contribution to the potential energy of the nucleus depends on the total spin or isotopic spin of the levels according to[21]

$$V_S=a_SS(S+1),\quad V_T=a_TT(T+1). \tag{43}$$

The first effect to be considered, is the displacement of the ground state. Since the excitation energy is measured from the ground state, one must in all formulas replace U by

$$U'=U+V^0, \tag{44}$$

where V^0 is the part of the potential energy of the ground state which is not included in the central potential. With the uniform model, for example,

$$V^0=a_M[P^0(P^0+4)+P'^0(P'^0+2)+(P''^0)^2].$$

A consequence of this effect is the fact that among isobar nuclei, the level density increases with T_z for small T_z.[24] In Secs. 2 and 3, we have found that the level density was decreasing with T_z according to a Gaussian law. However, U' increases with T_z, and this results in an increase of the level density which for small T_z overbalances the Gaussian factor.

[21] E. Feenberg and E. P. Wigner, Phys. Rev. **51**, 95 (1937).
[22] E. P. Wigner, Phys. Rev. **51**, 106 (1937).
[23] E. P. Wigner, *University of Pennsylvania Bicentennial Conference* (University of Pennsylvania Press, Philadelphia, 1941).
[24] See, for example, Table VI in Critchfield and Oleksa (reference 4).

The second, more complex effect is the displacement of the excited states by variable amounts depending on their symmetry. In order to illustrate the method followed here, we shall first consider a potential energy of the type V_S, for example. The more realistic expression V_M is mathematically more complex to handle, and it will be discussed later.

Let $\rho(U')$ be the total level density when the spin-dependent potential energy is neglected. The density of states with given S_z can be expressed by a formula of the type

$$\rho(U',S_z)=(2\pi)^{-\frac{1}{2}}\sigma^{-1}\rho(U')\exp(-S_z^2/2\sigma^2), \quad (45)$$

where σ is an appropriate dispersion coefficient to be determined by the methods of Secs. 2 or 3. The density of states of spin S is then

$$\rho_S(U')=\rho(U',S)-\rho(U',S+1), \quad (46)$$

$$=(2\pi)^{-\frac{1}{2}}\sigma^{-3}(S+\tfrac{1}{2})\rho(U')\exp[-(S+\tfrac{1}{2})^2/\sigma^2]. \quad (47)$$

Under the influence of the spin-dependent forces, the energy of the states of spin S is increased by V_S. Consequently, the density of states of spin S at the excitation energy U becomes

$$\rho_S'(U')=\rho_S(U'-V_S). \quad (48)$$

If we want now the density of states of given S_z, we have to compute the sum

$$\rho'(U',S_z)=\sum_{S=|S_z|}^{\infty}\rho_S(U'-V_S), \quad (49)$$

and for the new total level density we get

$$\rho'(U')=\sum_{S=0}^{\infty}(2S+1)\rho_S(U'-V_S). \quad (50)$$

These summations can be carried out very simply in the first approximation. We shall assume that $\log\rho(U')$ is a sufficiently smooth function over the interval V_S so that we can write[25]

$$\log\rho(U'-V_s)=\log\rho(U')-V_s d\log\rho(U')/dU'. \quad (51)$$

Actually, V_S becomes arbitrarily large with increasing S. However, if a_S is sufficiently small, the approximation (51) fails only for values of S so large that the density of the corresponding levels is practically zero. Thus, the condition for the validity of (51) is that the third term in the Taylor expansion should be very small for $S+\frac{1}{2}\approx\sigma$. This reads

$$a_S^2\sigma^4|(d/dU')^2\log\rho(U')|\ll 1.$$

Substitution of (51) into (48) yields

$$\rho_S'(U')=(2\pi)^{-\frac{1}{2}}\sigma^{-3}(S+\tfrac{1}{2})\rho(U')\times\exp[-(S+\tfrac{1}{2})^2/2\sigma^2-a_S S(S+1)d\log\rho(U')/dU']$$
$$=(2\pi)^{-\frac{1}{2}}\sigma^{-3}(S+\tfrac{1}{2})\rho(U')C\exp[-(S+\tfrac{1}{2})^2/2\sigma'^2], \quad (52)$$

where the new dispersion coefficient σ' is given by

$$\sigma'=\sigma(1+2a_S\sigma^2 d\log\rho(U')/dU')^{-\frac{1}{2}}, \quad (53)$$

and where C is the correction factor

$$C=\exp[(a_S/4)d\log\rho(U')/dU']. \quad (54)$$

This factor which originates in the replacement of $S(S+1)$ by $(S+\frac{1}{2})^2$ is usually very near unity. Since the expression (52) for ρ_S' has the same dependence on S as ρ_S, we can immediately go back to the total level density and to the density of states of given S_z. One finds immediately from (45) and (47) that

$$\rho'(U')=C(1+2a_S\sigma^2 d\log\rho/dU')^{-3/2}\rho(U'),$$
$$\rho'(U',S_z)=(2\pi)^{-1/2}\sigma'^{-1}\rho'(U')\exp(-S_z^2/2\sigma'^2). \quad (55)$$

It should be noted that σ is a function of U', and that strictly speaking U' should be replaced by $U'-V_S$ also in σ. However, σ is a very slowly varying function of the energy and this would only introduce a very small correction. The above expressions simplify if we use the results of the continuous theory. We have then, roughly:

$$\sigma^2=(1/4\pi)(6U'/\delta)^{\frac{1}{2}},$$
$$d\log\rho(U')/dU'\cong\pi(6U'\delta)^{-\frac{1}{2}}.$$

Hence,

$$1+2a_S\sigma^2 d\log\rho/dU'=1+a_S/2\delta, \quad (56)$$

which is independent of the energy. Thus, it is seen from (53) and (55) that in the present approximation the dispersion coefficient and the total level density are simply multiplied by constant factors, except for the small additional correction of the latter quantity due to C.

In the case of the Majorana forces we have to consider the constants of motion S_z, T_t, Y_t. The density of levels with given values of these quantities can be written

$$\rho(U',S_z,T_t,Y_t)=(2\pi)^{-\frac{1}{2}}\sigma^{-3}\rho(U')\times\exp[-(S_z^2+T_t^2+Y_t^2)/2\sigma^2]. \quad (57)$$

The problem of deducing from (57) the density of levels with given symmetry character has been treated by Bardeen and Feenberg.[26] The result is more conveniently expressed in terms of the partition numbers $\Lambda_1,\Lambda_2,\Lambda_3,\Lambda_4$. These numbers are related to the partition quantum numbers by

$$2P=\Lambda_1+\Lambda_2-\Lambda_3-\Lambda_4,$$
$$2P'=\Lambda_1-\Lambda_2+\Lambda_3-\Lambda_4,$$
$$2P''=\Lambda_1-\Lambda_2-\Lambda_3+\Lambda_4,$$
$$A=\Lambda_1+\Lambda_2+\Lambda_3+\Lambda_4. \quad (58)$$

Similarly, we replace S_z, T_t, Y_t by λ_1, λ_2, λ_3, λ_4 such

[25] The validity of this approximation is clearly shown by the fact that the curves on Fig. 4 are almost straight lines over large intervals of energy.

[26] J. Bardeen and E. Feenberg, Phys. Rev. **54**, 809 (1938).

that

$$2S_s=\lambda_1+\lambda_2-\lambda_3-\lambda_4,$$
$$2T_t=\lambda_1-\lambda_2+\lambda_3-\lambda_4,$$
$$2Y_t=\lambda_1-\lambda_2-\lambda_3+\lambda_4,$$
$$A=\lambda_1+\lambda_2+\lambda_3+\lambda_4.$$

With the new notation, the relation (57) reads

$$\rho(U',\lambda_1,\lambda_2,\lambda_3,\lambda_4)=(2\pi)^{-\frac{1}{2}}\sigma^{-3}\rho(U')\exp[(\tfrac{1}{4}A^2-\sum_1^4\lambda_i^2)/2\sigma^2]. \quad (59)$$

Let E_i $(i=1,2,3,4)$ be a set of operators which increase the variables λ_i by one unit according to

$$E_1^n f(\lambda_1,\lambda_2,\lambda_3,\lambda_4)=f(\lambda_1+n,\lambda_2,\lambda_3,\lambda_4), \text{ etc.}$$

The density of levels with the symmetry defined by the partition numbers $(\Lambda)=(\Lambda_1,\Lambda_2,\Lambda_3,\Lambda_4)$ is then given by[27]

$$\rho_{(\Lambda)}(U')=\begin{vmatrix}1 & E_2^{-1} & E_3^{-2} & E_4^{-3}\\ E_1 & 1 & E_3^{-1} & E_4^{-2}\\ E_1^2 & E_2 & 1 & E_4^{-1}\\ E_1^3 & E_2^2 & E_3 & 1\end{vmatrix}\times\rho(U',\Lambda_1,\Lambda_2,\Lambda_3,\Lambda_4). \quad (60)$$

This relation is the generalization of (46). It involves a sum of 24 terms, and hence it is not very easy to handle in general. To a good approximation, however, if the function in the right-hand side of (60) is sufficiently smooth, we can replace the operators E_i by differential operators according to

$$E_i^n=1+n(\partial/\partial\lambda_i)+(n^2/2!)(\partial/\partial\lambda_i)^2+\cdots. \quad (61)$$

For greater accuracy, it is desirable to transform the determinant (60) in such a way as to make the arguments n in the Taylor series as small as possible. Therefore, we rewrite the determinant as follows:

$$E_1^{\frac{1}{2}}E_2^{\frac{1}{2}}E_3^{-\frac{1}{2}}E_4^{-\frac{1}{2}}\begin{vmatrix}E_1^{-\frac{1}{2}} & E_2^{-\frac{1}{2}} & E_3^{-\frac{1}{2}} & E_4^{-\frac{1}{2}}\\ E_1^{-\frac{1}{2}} & E_2^{-\frac{1}{2}} & E_3^{-\frac{1}{2}} & E_4^{-\frac{1}{2}}\\ E_1^{\frac{1}{2}} & E_2^{\frac{1}{2}} & E_3^{\frac{1}{2}} & E_4^{\frac{1}{2}}\\ E_1^{\frac{1}{2}} & E_2^{\frac{1}{2}} & E_3^{\frac{1}{2}} & E_4^{\frac{1}{2}}\end{vmatrix}.$$

We now replace in the new determinant the E_i by the expansions (61). After a few algebraic manipulations, we obtain as the first nonvanishing term in the density of states of given symmetry character:

$$\rho_{(\Lambda)}(U')=E_1^{\frac{1}{2}}E_2^{\frac{1}{2}}E_3^{-\frac{1}{2}}E_4^{-\frac{1}{2}}\begin{vmatrix}1^{\frac{1}{2}}_{\frac{1}{2}}0 & 1^{\frac{1}{2}}_{\frac{1}{2}}0 & 1^{\frac{1}{2}}_{\frac{1}{2}}0 & 1^{\frac{1}{2}}_{\frac{1}{2}}0\\ \partial_1^1 & \partial_2^1 & \partial_3^1 & \partial_4^1\\ \partial_1^2 & \partial_2^2 & \partial_3^2 & \partial_4^2\\ \partial_1^3 & \partial_2^3 & \partial_3^3 & \partial_4^3\end{vmatrix}\times\rho(U',\Lambda_1,\Lambda_2,\Lambda_3,\Lambda_4),$$

where ∂_i^m stands for $(\partial/\partial\lambda_i)^m$. If we use for $\rho(U',\lambda_1,\lambda_2,\lambda_3,\lambda_4)$ the expression (59), we get[28]

$$\rho_{(\Lambda)}(U')=(2\pi)^{-\frac{1}{2}}\sigma^{-15}E_1^{\frac{1}{2}}E_2^{\frac{1}{2}}E_3^{-\frac{1}{2}}E_4^{-\frac{1}{2}}(\Lambda_1-\Lambda_2)(\Lambda_1-\Lambda_3)(\Lambda_1-\Lambda_4)(\Lambda_2-\Lambda_3)(\Lambda_2-\Lambda_4)(\Lambda_3-\Lambda_4)\times\rho(U')\exp[(\tfrac{1}{4}A^2-\sum_1^4\Lambda_i^2)/2\sigma^2].$$

By transforming this expression back into the notation of the partition quantum numbers, we finally obtain

$$\rho_{PP'P''}(U')=(2\pi)^{-\frac{1}{2}}\sigma^{-15}[(P+4)^2-(P'+1)^2]\times[(P+2)^2-P''^2][(P'+1)^2-P''^2]\rho(U')\times\exp\{-[(P+2)^2+(P'+1)^2+P''^2]/2\sigma^2\}.$$

This expression is the required generalization of (46). It gives the distribution of symmetry types among the levels.

The Majorana forces increase the energy of levels with the partition quantum numbers P, P', P'' by the amount V_M given by (42). Hence, the density of these levels becomes

$$\rho'_{PP'P''}(U')=\rho_{PP'P''}(U'-V_M). \quad (63)$$

The density of the levels with given S_s, T_t, Y_t is now

$$\rho'(U',S_s,T_t,Y_t)=\sum_{P,P',P''}N_{PP'P''}(S_s,T_t,Y_t)\times\rho_{PP'P''}(U'-V_M), \quad (64)$$

where $N_{PP'P''}(S_s,T_t,Y_t)$ is the number of states with given values of S_s, T_t, Y_t in the supermultiplet P, P', P''. The total level density is similarly

$$\rho'(U')=\sum_{P,P',P''}N_{PP'P''}\rho_{PP'P''}(U'-V_M), \quad (65)$$

where $N_{PP'P''}$ is the total number of states in the supermultiplet P, P', P''. For a very accurate calculation, the sums (64) or (65) should be carried out numerically. However, if $\rho(U')$ and a_M are such that an expression similar to (51) can be used, the dependence of $\rho'_{PP'P''}$ on $P,P'P''$ is the same as that of $\rho_{PP'P''}$. Hence, we can immediately deduce $\rho'(U',S_s,T_t,Y_t)$ and $\rho'(U')$. The new coefficient of dispersion is given by

$$\sigma'=\sigma[1+2a_M\sigma^2 d\log\rho(U')/dU']^{-\frac{1}{2}}, \quad (66)$$

and the total level density becomes

$$\rho'(U')=C[1+2a_M\sigma^2 d\log\rho(U')/dU']^{-15/2}\rho(U'), \quad (67)$$

where C is now

$$C=\exp[(5a_M/2)d\log\rho(U')/dU']. \quad (68)$$

[27] This relation is to be compared with Eq. (13) of Bardeen and Feenberg (reference 26) where the expansion of the determinant given here is written explicitly.

[28] Each term of the determinant is the product of a first-order derivative, a second-order derivative, and a third-order derivative with respect to the λ_i. These derivatives introduce the factors σ^{-2}, σ^{-4}, σ^{-6}, respectively. A factor σ^{-3} is present in the expression (59) for $\rho(U',\lambda_1,\lambda_2,\lambda_3,\lambda_4)$. Thus, altogether one gets the factor σ^{-15}.

Finally, the density of levels with given S_z, T_f, Y_f is

$$\rho'(U', S_z, T_f, Y_f) = (2\pi)^{-\frac{1}{2}}\sigma'^{-3}\rho'(U') \times \exp[-(S_z^2+T_f^2+Y_f^2)/2\sigma'^2]. \quad (69)$$

If the continuous approximation is used, the above expressions become

$$\sigma' = \sigma(1+a_M/2\delta)^{-\frac{1}{2}},$$
$$\rho'(U') = C(1+a_M/2\delta)^{-15/2}\rho(U'), \quad (70)$$
$$C = \exp[(5\pi a_M/2)(6U'\delta)^{-\frac{1}{2}}],$$

and the relation (69) remains unchanged.

It should be mentioned that the three kinds of forces considered above can be introduced simultaneously. The procedure consists then in taking into account first the Majorana forces, and in introducing the effect of the spin and isotopic spin-dependent forces into the formulas (67) or (70). As a result, the level density is multiplied by three factors corresponding to the three kinds of forces. The dispersion occuring in the factors (55) caused by the spin and isotopic spin-dependent forces has to be replaced by the expression (66).

As a first application, we can estimate the effect of Majorana forces, for example, on the distribution of angular momentum. It is clear that, instead of computing directly as in Sec. 4 the density of the levels having a total angular momentum M along the z axis, one can proceed in two steps. First, one determines the density of the levels having an orbital momentum M_L and a spin M_S along the z axis. This yields a two-variables Gaussian distribution with two dispersions σ_L and σ_S. The second step consists in deducing from the two-variables distribution law the density of the levels for which M_L+M_S has a given value M. The result is a Gaussian law with a dispersion σ_J given by

$$\sigma_J^2 = \sigma_L^2 + \sigma_S^2. \quad (71)$$

This procedure gives, of course, the same result as the method of Sec. 4. If Majorana forces are introduced, the Gaussian distribution law of M_L and M_S remains valid, with the only change that σ_S is replaced by σ_S' according to (66) or (70). However, the spin contribution σ_S to the dispersion of the total angular momentum is usually much smaller than the orbital term σ_L. Therefore, the substitution of σ_S' into (71) introduces only a small correction of σ_J. For the nuclei of mass $A=20$, the continuous theory yields

$$\sigma_L^2/\sigma_S^2 = \langle m_L^2\rangle_{Av}/\langle m_S^2\rangle_{Av} = 6.7,$$

when the values (38) of the parameters are used. With $a_M=1$, we get from (70):

$$\sigma_S^2/\sigma_S'^2 = 1.7.$$

One finds then:

$$(\sigma_J-\sigma_J')/\sigma_J = 0.03. \quad (72)$$

The level density computed by means of the method of Sec. 3, increases more slowly with energy than that obtained from the continuous theory (see, for example, Fig. 4). It follows from (66) that the correction to σ_J due to the Majorana forces, is somewhat smaller in the more exact treatment than expressed by (72). Actually, it is of the order of 2 percent at 25 Mev.

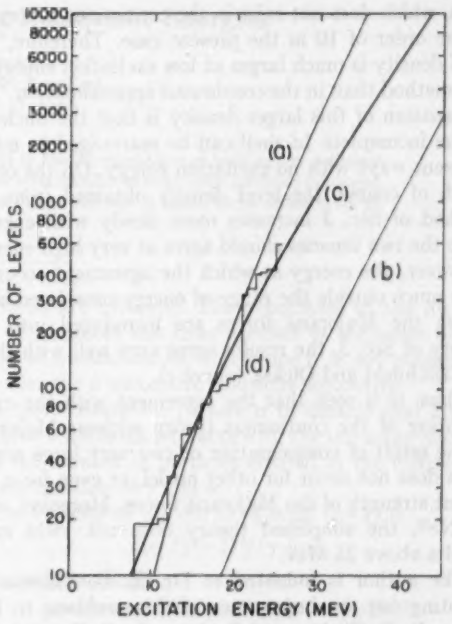

FIG. 4. The number of levels having an energy less than a given value and the most probable angular momentum. Curves (a), (b), and (c) correspond to the continuous theory neglecting the Majorana forces (Bethe), to the continuous theory with Majorana forces included, and to the theory of Sec. 3 with Majorana forces included. The results of Critchfield and Oleksa are represented by (d).

Finally, we have to discuss the absolute values of the level density. Therefore, the numbers of levels of energy less than a given value and *having the most probable angular momentum* corresponding to each energy have been plotted on Fig. 4. These numbers refer to levels of Ne^{20} only, i.e., with $T_f=0$. The corresponding theoretical expression is

$$(2\pi)^{-\frac{1}{2}}\sigma_J^{-2}\sigma_T^{-1}N(U)e^{-\frac{1}{2}}, \quad (73)$$

where $N(U)$ is the total level density computed according to the procedure indicated at the end of Sec. 3, σ_J and σ_T are the dispersion coefficients of angular momentum and isotopic spin, respectively. For the present case $U'=U$. The results obtained from the continuous theory, without taking into account the Majorana forces (curve *a*), are in good agreement with the results of the explicit counting as was already mentioned by Critchfield and Oleksa.[4] The Majorana forces, however, according to (70) and (73) reduce the number of levels by a factor of the order of $(1.7)^7 \approx 40$, and the resulting level density is then completely wrong (curve *b*). The method of Sec. 3, however, gives very much larger level densities than the continuous theory. This is essentially due to the term S_0 in the entropy. This

term, which does not exist in the continuous theory, is of the order of 10 in the present case. Therefore, the level density is much larger at low excitation energy in this method than in the continuous approximation. The explanation of this larger density is that the nucleons in the incomplete $1d$ shell can be rearranged in many different ways with no excitation energy. On the other hand, of course, the level density obtained from the method of Sec. 3 increases more slowly with energy, since the two theories should agree at very high energy. However, the energy at which the agreement occurs is very much outside the range of energy considered here. When the Majorana forces are introduced into the theory of Sec. 3, the results agree very well with those of Critchfield and Oleksa (curve *c*).

Thus, it is seen that the agreement with the exact counting of the continuous theory without Majorana is the result of compensation of two very large errors. This does not occur for other nuclei, or even for a different strength of the Majorana forces. Moreover, even in Ne^{20}, the simplified theory does not yield exact results above 25 Mev.

The author is indebted to Dr. R. G. Thomas for pointing out the importance of this problem, to Professor R. F. Christy and Professor R. P. Feynman for their interest in this work and for many stimulating discussions, and to Dr. A. Rich for his help in preparing the manuscript.

APPENDIX

For accurate calculations, additional terms in the expansions of Sec. 3 are necessary. These are easily obtained from (22) by the derivation outlined in the latter section. Thus one gets for S_1, U, and D:

$$S_1=Ut+\bar{F}-(\bar{F}'^2/2F'')-(\bar{F}'^3/6F''^3)-(\bar{F}'^4F^{(3)2}/8F''^5)+(\bar{F}'^4F^{(4)}/24F''^4)+\cdots, \quad (29')$$

$$U=G'-(\bar{F}'G''/F'')+(\bar{F}'^2/2F''^2)(1+\bar{F}'F^{(3)}/F''^2)\times(F''G^{(3)}-F^{(3)}G'')-(\bar{F}'^3/6F''^4)\times(F''G^{(4)}-F^{(4)}G'')+\cdots, \quad (30')$$

$$D=[1-(G''-\bar{F}'G^{(3)}/F''^2)^2/(F''-\bar{F}'F^{(3)}/F'')\times(H''-\bar{F}'H^{(3)}/F'')][H''-(\bar{F}'/F'')\times(1+\bar{F}'F^{(3)}/2F''^2)H^{(3)}+(\bar{F}'/F'')^2(H^{(4)}/2)]\times\prod_{k=0}^{K}\sigma_k^2. \quad (32')$$

The expansion of σ_k^2 includes terms of different kinds. The terms of the first kind are the coefficients of the terms in M_k^2 appearing in the entropy when this quantity is computed as a function of t and M_k. The corresponding expression for σ_k is

$$\sigma_k=F_k''-(\bar{F}'F_k^{(3)}/F'')(1+\bar{F}'F^{(3)}/2F''^2)+\bar{F}'^2F_k^{(4)}/2F''^2+\cdots. \quad (31')$$

However, the entropy should be computed as a function of U and not of t. Since t is a function of U and M_k, it is seen that the entropy depends also implicitly on M_k through t. This yields the following correction which should be added to (31'):

$$\delta\sigma_k=(\bar{F}'G''/F''^2H'')(F''G_k^{(3)}-G''F_k^{(3)})+\cdots.$$

In an accurate calculation one finds that the determinant D depends also on the M_k. We can then write the determinant as

$$D(1-\sum_1^K\alpha_kM_k^2+\cdots),$$

where the α_k are small. The final formula for the level density is multiplied by the power $-\frac{1}{2}$ of the determinant. This introduces the factor

$$(1-\sum_1^K\alpha_kM_k^2)^{-\frac{1}{2}}\cong\exp(\sum_1^K\alpha_kM_k^2/2),$$

which can be considered as producing an additional correction $\delta^{(1)}\sigma_k$ of σ_k. This correction is given by

$$(\sigma_k+\delta\sigma_k+\delta^{(1)}\sigma_k)^{-2}=(\sigma_k+\delta\sigma_k)^{-2}-\alpha_k,$$

or

$$\delta^{(1)}\sigma_k=(\alpha_k/2)(\sigma_k+\delta\sigma_k)^3.$$

The α_k are given by

$$\begin{aligned}F_k''^2\alpha_k&=F_k^{(3)}H^{(3)}/2(H''F''-\bar{F}'H^{(3)})\\&+\sum_{l=1}^K(F_k^{(3)}F_l^{(3)}/F''-F_{kl}^{(4)})/2(F_l''-\bar{F}'F_l^{(3)}/F'')\\&+[F_k^{(3)}(1+\bar{F}'F_k^{(3)}/F''F_k'')-\bar{F}'F_k^{(4)}/F''^2]/\\&\times(F_k''-\bar{F}'F_k^{(3)}/F'')(F''-\bar{F}'F^{(3)}/F'')\\&+[G_k^{(3)}(1+\bar{F}'F_k^{(3)}/F''F_k'')-\bar{F}'G_k^{(4)}/F''^2]/\\&\times(F_k''-\bar{F}'F_k^{(3)}/F'')(H''-\bar{F}'H^{(3)}/F'')\\&-2(G''-\bar{F}'G^{(3)}/F'')[(F_k^{(3)}G^{(3)}/F'')-(G_k^{(4)}/2)]/\\&\times(F''-\bar{F}'F^{(3)}/F'')(H''-\bar{F}'H^{(3)}/F'').\end{aligned}$$

Here, the two first lines are the contributions from the diagonal terms in the determinant, the other lines are the contributions of the terms $\partial^2\Phi/\partial x_0\partial x_k$, $\partial^2\Phi/\partial t\partial x_k$, $\partial^2\Phi/\partial x_0\partial t$, respectively. It should be mentioned, finally, that a very small correction is produced by the dependence of D on M_k implicitly through t.

The coefficients B_{kl} in (27) are given in the first approximation by

$$F_k''^2F_l''^2B_{kl}=-(1/8F'')F_k^{(3)}F_l^{(3)}+\begin{cases}F_{kl}^{(4)}/8 & \text{if } k\neq l,\\ F_{kk}^{(4)}/24 & \text{if } k=l.\end{cases}$$

Nucleon-Nucleus Collisions at Relativistic Energies

GIUSEPPE COCCONI
Cornell University, Ithaca, New York
(Received November 27, 1953)

The Fermi theory of multiple meson production is utilized in the interpretation of high-energy collisions between nucleons and complex nuclei. A relation between the total number of relativistic particles produced, their angular spread, and the number of nucleons involved in the collision is found to be satisfied by all the cases of relativistic showers published thus far.

THE showers of relativistic particles produced by the nucleonic component of the cosmic radiation, as observed in photographic plates, present radical differences in their angular distribution and in their relative proportion of light and heavy tracks.

This has usually been interpreted as due to the fact that one is dealing, in general, not with single nucleon-nucleon collisions, but rather with composite collisions, i.e., events in which the primary nucleon hits several of the nucleons present in the nucleus involved.

Composite collisions are not the ones most suited for the study of the peculiarities of the nucleon-nucleon interaction, so the experimenters have tried to select the cases which could be thought of as those in which only one of the nucleons in the nucleus is hit (single collisions).

Often considered as examples of single collisions have been the cases in which zero or very few slow particles are observed in addition to the relativistic particles, the argument being that, while in composite collisions the nucleus is strongly excited and boils out many charged particles of small energy, in single collisions the nucleon involved supposedly lies at the periphery of the nucleus and the remaining nucleons can be left practically unexcited.

However, the argument can be wrong in many cases, especially at very high energies, since in a composite collision, when the velocity of the center of mass (c.m.) is quite large, all the particles produced in the first nucleon-nucleon encounter are strongly collimated forward, and in going through the nucleus produce a tunnel[1] which can leave the nucleus not strongly excited. In going through a nucleus of $A=100$, no more than 4–5 nucleons can be hit by the primary nucleon and the breaking of this number of bonds can give an excitation of less than 100 Mev; few neutrons can be emitted and no or few charged particles.[2]

In this note an attempt is made to establish on a different basis a criterion for distinguishing composite from single collisions.

Consider a composite collision at very high energy (primary nucleon with $\gamma=E/Mc^2>200$) in which n nucleons are involved. The n nucleons in the nucleus are at distances one from another of the order of the range of nuclear forces, and hence it is not possible to consider the n successive collisions separately.

A more reasonable picture is to assume that all the lump of n nucleons interacts with the incoming nucleon and the number of particles created in the collision is thus a function of γ and n.

The velocity of the center of mass ($c=1$) is

$$\beta_c=(\gamma^2-1)^{\frac{1}{2}}/(\gamma+n),$$

and correspondingly

$$\gamma_c=(\gamma+n)/(2n\gamma+n^2+1)^{\frac{1}{2}} \underset{\gamma\gg n}{\longrightarrow} (\gamma/2n)^{\frac{1}{2}}.$$

The total energy available in the c.m. system ($Mc^2=1$) is:

$$W_c=(2n\gamma+n^2+1)^{\frac{1}{2}} \underset{\gamma\gg n}{\longrightarrow} (2n\gamma)^{\frac{1}{2}}.$$

To obtain the number of particles produced in the collision, it is necessary to assume a model.

It appears that the Fermi model[3] can give the most reasonable results. The multiplicity N of the charged particles produced in the interaction will be given by an expression similar to that given by Fermi (extreme relativistic case)

$$N=K\gamma^{\frac{1}{4}}f(n);$$

$f(n)$ represents the effect of the composite collision and becomes equal to unity for $n=1$.

The form of $f(n)$ depends on the assumptions about the volume Ω inside which the equilibrium of the meson-nucleon gas takes place. It seems reasonable to put

$$\Omega=n\Omega_0/\gamma_c=\Omega_0(2n^3/\gamma)^{\frac{1}{2}},$$

where

$$\Omega_0=(4/3)\pi(\hbar/\mu c)^3.$$

The factor $1/\gamma_c$ represents the relativistic contraction in the direction of motion, and the factor n comes from the fact that n nucleons are involved. Since the n nucleons are not aligned, it is not possible to define an impact parameter, and the correction for the conservation of momentum does not have to be considered (the correction, a factor $\frac{1}{2}$ in the multiplicity, stands when $n=1$, single collisions). With these assumptions, the dependence of N on n is easily found.

The density of energy in the volume Ω is

$$\delta=W_c/\Omega\propto\gamma n^{-\frac{1}{2}}.$$

[1] M. F. Kaplon and D. M. Ritson, Phys. Rev. **88**, 386 (1952). F. C. Roesler and C. B. A. McCusker, Nuovo cimento **10**, 127 (1953).

[2] This problem has been considered by W. Heitler and C. Terraux in Proc. Phys. Soc. (London) **A66**, 929 (1953).

[3] E. Fermi, Progr. Theoret. Phys. **5**, 570 (1950).

TABLE I. Summary of all the showers reported in the literature, produced either by a single ionizing particle or by a neutral particle, with (a) $\eta<0.10$; (b) $\eta<0.20$. The rows give the numbers of cases with $N\eta^{\frac{1}{2}}$ comprised between 0 and 1 (row 0), between 1 and 2 (row 1), etc. In the columns the cases are subdivided according to the number N_h of heavy tracks accompanying the shower. The subscript "*nb*" refers to unbiased samples, i.e., those cases published by the authors without discarding the showers accompanied by a large number of heavy prongs (references k and q). The subscript "all" refers to all cases reported, most of them biased in favor of events with a few heavy prongs. Column "?" refers to showers originated in thin sheets of brass and detected in nearby plates, for which there is no information about N_h (reference j).*

$N\eta^{\frac{1}{2}}$ \ N_h	0		1–2		3–5		6–10		>10		?	Totals	
	nb	all	*nb*	all	*nb*	all	*nb*	all	*nb*	all		*nb*	all
(a) $\eta<0.10$													
0		1		2									3
1	3	4	2	3	2	3	1	1	1	1	6	9	18
2	1	4	1	2				1			4	2	11
3											8		8
4				1	1	1					2	1	4
5	1	1				1		1		1	2	1	6
6			1	1	1	1						2	2
12							1	1	1	1		2	2
(b) $\eta<0.20$													
0		1		2									3
1	3	4	2	3	2	3	1	1	1	1	6	9	18
2	1	4	1	3	1	3		1			4	3	15
3			2	3	1	3					8	3	14
4	1	1		3	1	2		1			2	2	9
5	1	1	1	1	1	2		1		2	2	3	9
6		1	1	1	1	1						2	3
7						1							1
8		1			2	2						2	3
9													
10													
11			1	1	1	1			1	1		3	3
12							1	1	1	1		2	2
13							1	1				1	1
14					1	1						1	1
23									1	1		1	1

* Papers from which the cases were taken are:
[a] Bertolino, Debenedetti, Lovera, and Vigone, Nuovo cimento **10**, 991 (1953).
[b] Bradt, Kaplon, and Peters, Helv. Phys. Acta. **23**, 24 (1950).
[c] Brown, Camerini, Fowler, Heitler, King, and Powell, Phil. Mag. **40**, 862 (1949).
[d] Camerini, Fowler, Lock, and Muirhead, Phil. Mag. **41**, 413 (1950).
[e] K. Gottstein and M. Teucher, Z. Naturforsch. **8a**, 120 (1953).
[f] Hopper, Biswas, and Darby, Phys. Rev. **84**, 457 (1951).
[g] S. Biswas and V. D. Hopper, Phys. Rev. **86**, 209 (1952).
[h] Lal, Pal, Peters, and Swami, Proc. Indian Acad. Science **36**, 75 (1952).
[i] Kaplon, Peters, and Ritson, Phys. Rev. **85**, 900 (1952).
[j] M. F. Kaplon and D. M. Ritson, Phys. Rev. **88**, 386 (1952).
[k] Kaplon, Ritson, and Walker, Phys. Rev. **90**, 716 (1953).
[l] Lord, Fainberg, and Schein, Phys. Rev. **80**, 970 (1950).
[m] L. S. Osborne, Phys. Rev. **81**, 239 (1951).
[n] E. Pickup and L. Voyvodic, Phys. Rev. **84**, 1190 (1951).
[o] Demeur, Dilworth, and Schönberg, Nuovo cimento **9**, 92 (1952).
[p] A. Gerosa, and R. Levi Setti, Nuovo cimento **8**, 601 (1951).
[q] Daniel, Davies, Mulvey, and Perkins, Phil. Mag. **43**, 753 (1952).
[r] T. F. Hoang, J. phys. et radium **14**, 395 (1953).

The temperature, proportional to $\delta^{\frac{1}{2}}$, is then:

$$T\propto\gamma^{\frac{1}{2}}n^{-\frac{1}{2}}$$

and the total number of charged particles, proportional to W_e/T, is:

$$N=K\gamma^{\frac{1}{2}}n^{\frac{1}{2}}.$$

$K=2.1$ if only π mesons are produced; $K=2.4$ if π mesons and nucleons are produced.[3] Also for a composite collision it is plausible to admit that the particles are emitted, in the c.m. system, symmetrically with respect to the plane normal to the direction of the incoming particle; the observed shower will then satisfy the condition

$$\gamma_e=1/\tan\eta\approx 1/\eta$$

where η is the polar angle, in the laboratory system, which contains $\frac{1}{2}$ of the emitted particles.

Combining this expression of γ_e with that obtained for N, it follows that

$$1.2Kn=N\eta^{\frac{1}{2}}.$$

If the assumptions are reasonable, no relativistic shower observed in emulsions could have

$$N\eta^{\frac{1}{2}}>\sim 1.2\times 2.2\times 5=13.$$

For all the relativistic showers thus far described in the literature (54 cases), the maximum value found for $N\eta^{\frac{1}{2}}$ is 12.

A more detailed analysis of this survey is given in Table I. Table I(a) refers to the cases where $\eta<0.10$, Table I(b) to cases where $\eta<0.20$. Though the relation derived before could be applied only to the cases of Table I(a) the cases of Table I(b), statistically more significant, will also be analyzed in the same manner.

From the columns "all" of both tables it appears that several of the events with number of heavy tracks $N_h=0$ or 1 (i.e., the events previously believed to be due to single collisions) give values of $N\eta^{\frac{1}{2}}$ well above the value expected for a single collision, which is: $1.2\times(2.2/2)\times 1=1.3$. These events are probably composite collisions which leave the nucleus not strongly excited and emitting only neutrons.[4] On the other hand, several of the events with $N_h>3$, and actually also one event with $N_h=15$, should be considered as single collisions according to our criterion. Events of this kind could happen when the collision is single, but one or more other nucleons recoil with relatively high energy and are absorbed by the nucleus.

It is worth pointing out that a picture of the composite collision as given in this paper could not be possible assuming the model proposed by Heisenberg[5] instead of the Fermi model. In fact, according to Heisenberg, the production of mesons takes place in nucleons up to a distance

$$r\simeq(\hbar/\mu c)(0.8+\log_{10}\gamma)$$

from the incoming nucleon; if this is the case, at relativistic energies, when the nucleus is hit centrally, nearly all nucleons would be involved in the collision and it would be much less probable for the nucleus to be left with low excitation.

Actually, this large value of the radius of influence at high energies makes it quite difficult to understand how single collisions with no strong excitation of the nucleus can happen at all. Since after all these collisions are observed quite frequently, this can be considered as an argument in favor of the Fermi model, or of other models in which the radius of action does not extend beyond $\sim\hbar/\mu c$.

[4] Arguments in favor of this conclusion are given also by C. B. A. McCusker and F. C. Roesler, Phys. Rev. **91**, 769 (1953).
[5] W. Heisenberg, *Kosmische Strahlung* (Springer, Berlin, 1953), p. 148.

Bound State Corrections in Two-Body Systems*

THOMAS FULTON,† *Harvard University, Cambridge, Massachusetts*

AND

ROBERT KARPLUS,‡ *University of California, Berkeley, California*

(Received November 16, 1953)

Available expressions for two-body equations contain an interaction kernel which treats particles in intermediate states as free. In situations where the binding is important, such as the calculation of low-energy electrodynamic corrections, a more accurate treatment is necessary. A satisfactory formalism is developed for systems in which an instantaneous interaction is responsible for the binding. The procedure may then be used to evaluate the effects of small retarded perturbations. It consists of summing those binding interactions which occur during the retarded perturbations and which never should have been expanded as "small" effects. The result is expressed in terms of the two-body Green's function of the instantaneously interacting system. This function occurs to describe the propagation of the two particles in the intermediate state. The relative time coordinate does not appear explicitly in the formulas. The method is applied to the calculation of the hyperfine structure of positronium. The infrared divergences which occurred in a previous investigation of this effect are eliminated by the new approach.

I. INTRODUCTION

SEVERAL recent treatments[1–4] of the two-body system have used the techniques developed by Schwinger[5] to derive rigorous functional differential equations for the Green's functions of various two-body systems. These equations include an implicitly defined interaction operator. By various techniques of iteration, an expansion of the operator in powers of the coupling constant is developed to the order desired. The equations that have been obtained in this way are called Bethe-Salpeter[6,7] equations. They are deficient in that all intermediate states that occur during the interaction are expanded about free-particle states by the Born approximation. This fact certainly requires serious examination when the method is applied to strongly interacting bound nucleon systems. The weak electrodynamic coupling, on the other hand, should lead to no difficulties were it not for the fact that photons of arbitrarily long wavelength can occur in radiative corrections. In bound atomic states, therefore, the shape of the wave function will enter significantly into the results of a correct calculation. Methods that neglect this natural cutoff at the atomic radius lead to the familiar infrared catastrophes.

It is the purpose of this paper to correct the equation that describes the bound state of two oppositely charged fermions by taking into account the binding in intermediate states. Because of the weakness of the electric forces, the bound system is essentially nonrelativistic. For the calculation of energy displacements of the order of magnitude $\alpha^5 m$ it is therefore sufficient to provide for the binding in those intermediate states in which the relative momentum of the two particles and the virtual energy are small. The procedure begins with an examination of the terms in the interaction operator that comprise the Born expansion of the Coulomb interaction. It is observed that these constitute a formal expansion of the two-particle Coulomb Green's function. The free-particle Green's functions that occur in certain low-order interactions are then replaced by the correct Green's function with the proviso that the terms including the Coulomb energy explicitly are to be omitted from higher-order interactions. The features of electrodynamic systems mentioned earlier simplify this task greatly. It is, for instance, unnecessary to make the correction in states that contain virtual pairs. Since the manifest covariance is lost as soon as the instantaneous Coulomb interaction is separated and given special treatment, there is no particular disadvantage in making further noncovariant distinctions.[8]

In an application, it is of course impossible to calculate with the complete Coulomb Green's function. A separation into high- and low-energy phenomena as measured by the frequency of the virtual quanta leads to the further simplification that the Born approximation to the Green's function is valid for the high-energy effects whereas a nonrelativistic treatment is adequate in the low-energy region. This separation is identical to the one made in the early calculations of the level shift

* A paper that discusses these same ideas, by R. J. Eden, Proc. Roy. Soc. (London) **219**, 516 (1953), appeared as this manuscript was being submitted for publication. It is hoped that the computational details described here will extend the usefulness of the formalism that is developed.

† Harvard National Scholar.

‡ On leave of absence from Harvard University for the fall semester, 1953–1954.

[1] R. Karplus and A. Klein, Phys. Rev. **87**, 848 (1952), hereafter referred to as KK III. The notation of this paper and of reference 5 is used.

[2] R. Arnowitt, Pnys. Rev. **92**, 1002 (1953).

[3] S. Deser and P. C. Martin, Phys. Rev. **90**, 1075 (1953).

[4] A. Klein, Phys. Rev. **90**, 1101 (1953).

[5] J. Schwinger, Proc. Nat. Acad. Sci. U.S. **37**, 452, 455 (1951).

[6] E. E. Salpeter and H. A. Bethe, Phys. Rev. **84**, 1232 (1951); M. Gell-Mann and F. Low, Phys. Rev. **84**, 350 (1951).

[7] E. E. Salpeter, Phys. Rev. **87**, 328 (1952); G. E. Brown, Proc. Roy. Soc. (London) **A215**, 371 (1952).

[8] Julian Schwinger and Paul C. Martin have privately described to us a completely covariant treatment of binding in intermediate states.

in an external Coulomb field.[9] The method of obtaining high-energy corrections is illustrated by an examination and elimination of the infrared catastrophes that were encountered in the corrections to the fine structure of positronium.

II. PERTURBATION THEORY

A perturbation formalism for obtaining the effects of a time-dependent interaction on the energy of a system bound by an instantaneous interaction has been developed by Salpeter.[7] After some introductory definitions, his results are adapted to the present requirements.

The Green's function for two nonidentical fermions of equal mass with no external field present satisfies the equation[1]

$$[F_1(11')F_2(22')-I(121'2')]G(1'2'34)=\delta(13)\delta(24), \quad (2.1)$$

where

$$F_{1,2}=\gamma^{1,2}p_{1,2}+m=-i\gamma^{1,2}\partial_{1,2}+m=[G_0^{1,2}]^{-1}.$$

I is the interaction operator. The two-particle wave function is a solution of the corresponding homogeneous equation. After renormalization of the mass and the coupling constant, the equation for the wave function becomes[1]

$$[\bar{F}_1(11')\bar{F}_2(22')-\bar{I}(121'2')]\psi(1'2')=0, \quad (2.2)$$

or, in relative coordinates,

$$[F_K(x,x')-I_K(xx')]\varphi_K(x')=0, \quad (2.3)$$

where

$$F_K(x,x')=\int d^4X' e^{-iK(X-X')}\bar{F}_1(11')\bar{F}_2(22'), \quad (2.4)$$

and I_K arises similarly from $\bar{I}$. The wave function is an eigenfunction of total energy-momentum K_μ and is, for renormalized charge and coupling,

$$\psi(12)=e^{iKX}\varphi_K(x) \quad [X=\tfrac{1}{2}(x_1+x_2),\ x=x_1-x_2]. \quad (2.5)$$

The experimental charge and coupling constant appear in all terms of Eqs. (2.3), (2.4), and (2.5).

We next consider such I, or such energy values of our system, for which we can write:

$$\left.\begin{aligned}\bar{I}(1234)&=\bar{I}^C(1234)+\bar{I}'(1234)\\ I_K(x,x')&=I^C(x,x')+I_K'(x,x')\end{aligned}\right\}, \quad (2.6)$$

where I^C is one or a number of irreducible interactions which represents the main part of the total interaction (for example, the Coulomb potential in the case of the electron-positron system) and I_K' represents small corrections to this. We restrict ourselves to the consideration of I^C's local in relative time and in the space time of each particle:

$$I^C(x,x')=-\delta(x-x')\delta(x_0)f(\mathbf{r})\gamma_0^1\gamma_0^2. \quad (2.7)$$

Next we rewrite Eq. (2.3):

$$[F_K(x,x')-I^C(x,x')]\varphi_K(x')=I_K'(x,x')\varphi_K(x'). \quad (2.3')$$

The unperturbed system is described by the total energy momentum K_μ^C and the wave function $\varphi^C(x)$ in relative coordinates. It satisfies the equation

$$[F_{K^C}(x,x')-I^C(x,x')]\varphi^C(x')=0, \quad (2.8)$$

whereas the corresponding bound-state Green's function satisfies

$$[\bar{F}_1(11')\bar{F}_2(22')-\bar{I}^C(121'2')]G^C(1'2'34)=\delta(13)\delta(24). \quad (2.9)$$

By following the steps leading to Salpeter's Eq. (13),[7] one may rearrange both Eqs. (2.1) and (2.8) in such a way that the instantaneous nature of the binding interaction can be explicitly used to simplify the problem in a coordinate system in which the total momentum is zero, $K_\mu=(\mathbf{0},K_0)$, $K^C=(\mathbf{0},K_0^C)$. In this manner one obtains the equations involving the Dirac Hamiltonian $H(\mathbf{p})$:

$$[K_0-H^1(\mathbf{p})-H^2(-\mathbf{p})]\varphi_K(\mathbf{r},0)+\int\Lambda(\mathbf{r}\mathbf{r}')f(\mathbf{r}')\varphi_K(\mathbf{r}',0)d\mathbf{r}'+\int d^4x'd^4x''\Lambda_K(\mathbf{r}0,x')\gamma_0^1\gamma_0^2I_K'(x'x'')\varphi_K(x'')=0, \quad (2.10)$$

and

$$[K_0^C-H^1(\mathbf{p})-H^2(-\mathbf{p})]\varphi^C(\mathbf{r},0)+\int\Lambda(\mathbf{r}\mathbf{r}')f(\mathbf{r}')\varphi^C(\mathbf{r}',0)d\mathbf{r}'=0, \quad (2.11)$$

where

$$\begin{aligned}\Lambda_K(xx')=\int d^4X' e^{-iK(X-X')}&[G_0^1(11')\gamma_0^1\delta(22')+G_0^2(22')\gamma_0^2\delta(11')]\\ =i(2\pi)^{-3}\int d\mathbf{k}e^{i\mathbf{k}\cdot(\mathbf{r}-\mathbf{r}')}&\{e^{-i(E-\frac{1}{2}K_0)|t-t'|}\\ &\times[\Lambda_+^1(\mathbf{k})\theta(t-t')+\Lambda_+^2(-\mathbf{k})\theta(t'-t)]\\ &-e^{-i(E+\frac{1}{2}K_0)|t-t'|}[\Lambda_-^1(\mathbf{k})\theta(t'-t)\\ &+\Lambda_-^2(-\mathbf{k})\theta(t-t')]\},\end{aligned} \quad (2.12)$$

$$[\theta(t)=1,\ t>0;\ =\tfrac{1}{2},\ t=0;\ =0,\ t<0],$$

and

$$\Lambda(\mathbf{r}\mathbf{r}')=-i\Lambda_K(\mathbf{r}t,\mathbf{r}'t)=(2\pi)^{-3}\int d\mathbf{k}e^{i\mathbf{k}\cdot(\mathbf{r}-\mathbf{r}')}\times[\Lambda_+^1(\mathbf{k})\Lambda_+^2(-\mathbf{k})-\Lambda_-^1(\mathbf{k})\Lambda_-^2(-\mathbf{k})]. \quad (2.13)$$

[9] H. A. Bethe, Phys. Rev. 72, 339 (1947); N. M. Kroll and W. E. Lamb, Phys. Rev. 75, 388 (1949); J. B. French and V. F. Weisskopf, Phys. Rev. 75, 1240 (1949); R. P. Feynman, Phys. Rev. 74, 1430 (1948) and 76, 709 (1949); J. Schwinger, Phys. Rev. 76, 790 (1949).

In Eq. (2.12) the numbered variables must be expressed in terms of the X and x according to Eq. (2.5). The $\Lambda_\pm$ are the usual projection operators

$$\Lambda_\pm{}^i(\mathbf{k})=[E(k)\pm H^i(\mathbf{k})]/2E(k). \quad (2.14)$$

In terms of the function $\chi^C(\mathbf{r})$ which is the solution of the Salpeter's[7] equation,

$$[K_0{}^C-H^1(\mathbf{p})-H^2(-\mathbf{p})]\chi^C(\mathbf{r})+f(\mathbf{r})\varphi^C(\mathbf{r},0)=0, \quad (2.15)$$

the functions $\varphi^C(x)$ and $\varphi^C(r,0)$ are expressible as follows:

$$\varphi^C(x)=-i\int\Lambda_K(x,\mathbf{r}'0)\chi^C(\mathbf{r}')d\mathbf{r}';$$
$$\varphi^C(\mathbf{r},0)=\int\Lambda(\mathbf{r}\mathbf{r}')\chi^C(\mathbf{r}')d\mathbf{r}'. \quad (2.16)$$

The normalization is taken to be

$$\int\chi^{C*}(\mathbf{r})\varphi^C(\mathbf{r},0)d\mathbf{r}=1. \quad (2.16')$$

Reference to Eq. (2.12) shows that the relative time behavior of the two-particle wave function is described by free-particle Green's functions. It implies that the one particle propagates to the correct relative time in a a positive energy state if its time is later or in a negative energy state if its time is earlier. One is interested in the wave function at unequal times because the two particles may experience interactions at different times. The difficulty in the use of Eq. (2.16) occurs because this relationship ignores the existence of a binding interaction of the particle which propagates to the later time with the other particle that has made a transition out of the initial state by undergoing an interaction at the earlier time. Of course, these effects are not omitted completely; they occur, expanded in a Born approximation series, in the interaction operator. The rearrangement to be made and illustrated later will overcome this difficulty.

Salpeter[7] now defines a hybrid wave function

$$\varphi^{C'}(x)=-i\int\Lambda_K(x,\mathbf{r}'0)\chi^C(\mathbf{r}')d\mathbf{r}',$$
$$\varphi^{C'}(\mathbf{r},0)=\varphi^C(\mathbf{r},0), \quad (2.17)$$

and its adjoint whose time dependence is determined by K, but whose space dependence is determined by K^C. This function has the property that

$$\gamma_0{}^1\gamma_0{}^2[F_K(xx')-I^C(x,x')]\varphi^{C'}(x')=i(K_0-K_0{}^C)\delta(x_0)\chi^C(\mathbf{r}). \quad (2.18)$$

When Eq. (2.3) is multiplied by $\bar\varphi^{C'}=(\varphi^{C'})^*\gamma_0{}^1\gamma_0{}^2$, we can use the conjugate of Eq. (2.18) to show that

$$K_0-K_0{}^C=\Delta E=-i\int\bar\varphi^{C'}(x)I_K'(x,x')\varphi_K(x')d^4xd^4x'$$
$$\times\int\chi^C(\mathbf{r})\varphi_K(\mathbf{r}0)d\mathbf{r}. \quad (2.19)$$

This expression merely serves as the beginning of an iteration procedure because it depends on the wave function φ_K. The small difference between φ_K and $\varphi^{C'}$ can be neglected in lowest order; for greater accuracy φ_K may be calculated from ΔE by solving the equation for $\varphi_K(x)-\varphi^{C'}(x)$ that can be obtained from Eqs. (2.3) and (2.18):

$$\varphi_K(x)=\varphi^{C'}(x)+\int G_K(x,x')[\gamma_0{}^1\gamma_0{}^2I_K'(x'x'')\varphi^{C'}(x'')dx''$$
$$-i\Delta E\chi^C(\mathbf{r}')\delta(x_0')]d^4x'. \quad (2.20)$$

Here $G_K(x,x')$ is the Green's function in relative coordinates

$$G_K(x,x')=\int d^4X'e^{-iK(X-X')}G(121'2')\gamma_0{}^1\gamma_0{}^2. \quad (2.21)$$

This Green's function should be understood as a power series in I_K' with the Coulomb Green's function as its leading term.

Because the relative time dependence of all the wave functions on the RHS of Eq. (2.20) is known, this expression may be inserted into Eq. (2.10) to yield an equation which has no explicit relative time dependence

$$[K_0-H^1(\mathbf{p})-H^2(-\mathbf{p})]\varphi_K(\mathbf{r}0)+\int\Lambda(\mathbf{r}\mathbf{r}')f(\mathbf{r}')\varphi_K(\mathbf{r}',0)d\mathbf{r}'$$
$$+i\int\mathcal{K}_K(\mathbf{r}\mathbf{r}')\chi^C(\mathbf{r}')d\mathbf{r}'=0. \quad (2.22)$$

The kernel $\mathcal{K}_K$ is given by

$$\mathcal{K}_K(\mathbf{r}\mathbf{r}')=$$
$$-\int\Lambda_K(\mathbf{r}0,x^\alpha)\gamma_0{}^1\gamma_0{}^2I_K'(x^\alpha x^\beta)\Lambda_K(x^\beta,\mathbf{r}'0)d^4x^\alpha d^4x^\beta$$
$$-\int\Lambda_K(\mathbf{r}0,x^\alpha)\gamma_0{}^1\gamma_0{}^2I_K'(x^\alpha x^\beta)G_K(x^\beta x^\gamma)$$
$$\times I_K'(x^\gamma x^\delta)\Lambda_K(x^\delta,\mathbf{r}'0)d^4x^\alpha d^4x^\beta d^4x^\gamma d^4x^\delta$$
$$+i\Delta E\int\Lambda_K(\mathbf{r}0,x^\alpha)\gamma_0{}^1\gamma_0{}^2I_K'(x^\alpha x^\beta)$$
$$\times G_K(x^\beta,\mathbf{r}'0)d^4x^\alpha d^4x^\beta. \quad (2.23)$$

One can look upon Eq. (2.22) as describing the behavior of the compound particle in the nonlocal potential Λf with radiative corrections. The equation is still exact.

An explicit expression for ΔE may be obtained by substituting φ_K, Eq. (2.20), into Eq. (2.19) and solving for ΔE. In electrodynamic problems the energy change and normalization change are usually so small that they can be neglected on the right-hand side. This also implies that $\varphi^{C'}\sim\varphi^C$. We therefore obtain

$$\Delta E=-i\int\bar{\varphi}^C(x)\Big[I'_K{}^c(xx')+\int d^4x''d^4x'''I'_K{}^c(xx'')\times G_K{}^c(x''x''')\gamma_0{}^1\gamma_0{}^2I'_K{}^c(x'''x')\Big]\varphi^C(x')d^4xd^4x', \quad (2.24)$$

$$\Delta E=-i\int\chi^{C*}(\mathbf{r})\mathcal{K}_K{}^c(\mathbf{r}\mathbf{r}')\chi^C(\mathbf{r}')d\mathbf{r}d\mathbf{r}', \quad (2.25)$$

which is the basis for Eq. (3.6) in KK III.

III. PRESCRIPTION FOR BOUND STATE CORRECTIONS

We turn next to the rearrangement that must be carried out in the interaction $I'(1234)$ which we consider given as a power series expansion in the coupling constant. Let us consider a term T which arises from a particular virtual process P. P is restricted in that it must include no interaction I^C between the two particles (it may contain this interaction as a self-interaction of one of the particles); P is irreducible[6] because it occurs in I_K'. We shall further distinguish with a subscript on P and T among the different possible orderings in time of the elementary interactions of which P is composed. For an nth order interaction $P_\alpha(n)$ there will then be $n-1$ time intervals or, in the language of conventional perturbation theory, $n-1$ intermediate states. In each of these the particles are described by noninteracting Green's functions. Now consider in addition the collection $P_\alpha{}^C$ of all those processes that differ from P_α only in that interactions I^C take place during time intervals in which no more than two particles are present. As described in the introduction, the sum,

$$\mathcal{T}_\alpha=T_\alpha+T_\alpha{}^C, \quad (3.1)$$

of the corresponding terms then represents the contribution to the interaction operator of a P_α whose two-particle intermediate states are states of the unperturbed system governed by Eq. (2.8). Of course Eq. (3.1) must be understood in a formal sense only, because the infinite sum on the RHS will usually not converge under the circumstances we contemplate.

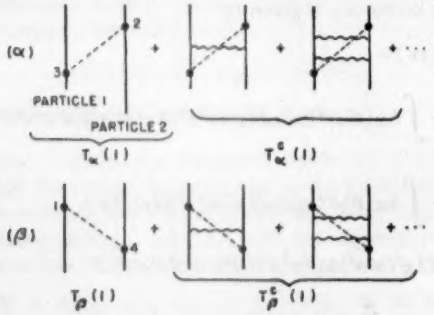

FIG. 1. Coulomb corrections to the exchange of a transverse quantum. Solid lines refer to elecrrons, broken lines to quanta, and wavy lines to the instantaneous Coulomb interaction.

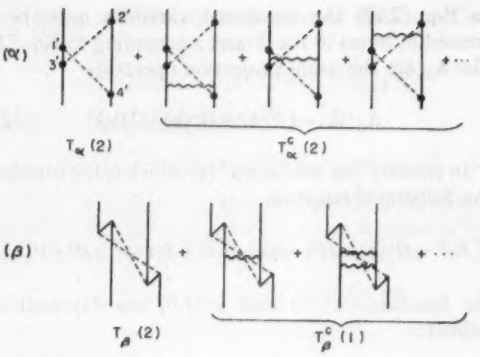

FIG. 2. Coulomb corrections to the exchange of two transverse quanta; pairs are present in some intermediate states.

In a practical case, Eq. (3.1) is recognized to describe the expansion of the Green's function G^C in a Born approximation about the noninteracting $G_0{}^1G_0{}^2$. In order to accomplish the summation, one must replace the free Green's functions in T_α by the functions G^C that describe the propagation of the system in each time interval. This will now be done for the P's illustrated in the Feynman diagrams Figs. 1 and 2. The T's and $\mathcal{T}$'s are given in Eqs. (3.2) to (3.9):[10]

$$T_\alpha(1)=ie^2\sum_{i=1}^{2}\gamma_i{}^2\mathcal{G}_+(23)\gamma_i{}^1\delta(13)\delta(24), \quad t_2<t_2; \quad (3.2)$$

$$\mathcal{T}_\alpha(1)=ie^2\sum_{i=1}^{2}\gamma_i{}^2F_1(11')G^C(1'234')F_2(4'4)\gamma_i{}^1\mathcal{G}_+(23); \quad (3.3)$$

$$T_\beta(1)=ie^2\sum_{i=1}^{2}\gamma_i{}^1\mathcal{G}_+(14)\gamma_i{}^2\delta(13)\delta(24), \quad t_4<t_1; \quad (3.4)$$

$$\mathcal{T}_\beta(1)=ie^2\sum_{i=1}^{2}\gamma_i{}^1F_2(22')G^C(12'3'4)\times F_1(3'3)\gamma_i{}^2\mathcal{G}_+(14); \quad (3.5)$$

$$T_\alpha(2)=(ie^2)^2\sum_{i,j=1}^{2}\gamma_i{}^2\gamma_j{}^1\delta(11')G_0{}^1(1'3')G_0{}^2(24)\times\gamma_j{}^2\gamma_i{}^1\delta(3'3)\mathcal{G}_+(1'4)\mathcal{G}_+(3'2), \quad t_4<t_3'<t_1'<t_2; \quad (3.6)$$

[10] The $\Sigma_{i=1,2}$ represents the sum over transverse components with respect to the Fourier transform momentum of the photon Green's functions.

$$\mathcal{T}_a(2)=(ie^2)^2\sum_{i,j=1}^{2}\gamma_i^1F_1(11'')G^C(1''21'2'')\times\gamma_j^1F_2(2''2')G^C(1'2'3'4')F_2(4'4'')\times\gamma_i^1G^C(3'4''3''4)F_1(3''3)\times\gamma_j^2\mathcal{G}_+(1'4)\mathcal{G}_+(3'2); \quad (3.7)$$

$$T_\beta(2)=(ie^2)^2\sum_{j,i=1}^{2}\gamma_i^1G_0^1(11')\gamma_j^1\delta(1'3)\delta(24')\times\gamma_j^2G_0^2(4'4)\gamma_i^2\mathcal{G}_+(14)\mathcal{G}_+(1'4'), \quad t_4'<t_4<t_1<t_1'; \quad (3.8)$$

$$\mathcal{T}_\beta(2)=(ie^2)^2\sum_{i,j=1}^{2}\gamma_i^1G_0^1(11')\gamma_j^1F_2(22')G^C(1'2'3'4')\times F_1(3'3)\gamma_j^2G_0^2(4'4)\gamma_i^2\mathcal{G}_+(14)\mathcal{G}_+(1'4'). \quad (3.9)$$

In these expressions it was unnecessary to refer explicitly to the times of all the successive events because the Coulomb Green's function at nonvanishing relative times is related to its values at zero relative time by free-particle Green's functions. The free-particle operators F_i applied to it therefore lead to the delta functions in relative time that reduce the above expressions to the result referring to the time intervals one would expect from the discussion leading to Eq. (3.1). This property of G^C is evident when its defining equation is rewritten symmetrically:

$$G^C(1234)=G^0(1234)+G^0(121'2')[I^C(1'2'3'4')+I^C(1'2'56)G^C(5678)I^C(783'4')]G^0(3'4'34). \quad (3.10)$$

It arises from the instantaneous character of the binding interaction I^C.

In this manner the entire interaction operator $\bar{I}'$ is rewritten as an operator $\mathcal{I}'$ from which a relative coordinate transform $\mathcal{I}_K'$ can be obtained by Eq. (2.4). Feynman diagrams may still be used to list the interaction terms; one must take those diagrams that contain no I^C and those that contain it only in intermediate states in which pairs created by a lower-order contribution to $\mathcal{I}_K'$ are present. The Fermion lines are then represented by interacting Green's functions as in Eqs. (3.2)–(3.9) and the quantum lines by the quantum Green's functions.

One encounters a difficulty with the above prescription. This will now be resolved. It has to do with those processes $P_a{}^C$ that contain only interactions I^C between the two particles. These represent the self-energy of each particle in the presence of the other. The corresponding T_a is not contained in I' but has been included in F_1F_2, Eq. (2.1), to facilitate renormalization. One may "borrow" the necessary term and carry out the rearrangement—in other words, rewrite Eq. (3.1):

$$T_a{}^C=(T_a+T_a{}^C)-T_a=\mathcal{T}_a-T_a. \quad (3.1')$$

One must observe the customary precautions for handling the difference between the two usually divergent quantities in the right-hand side.

The effective interactions appearing in the second and third terms of Eq. (2.23) present no new problems. For convenience the Green's function appearing there may be expanded in the Born approximation series. The resulting expression is then very similar to I' itself; all terms in it, however, are reducible. Now, the irreducibility mentioned earlier played no role in the discussion. The prescription can therefore be applied without further argument.

IV. APPLICATION TO THE HYPERFINE STRUCTURE OF POSITRONIUM

As a test for the technique developed in Sec. III, Part IV of KK III was re-examined critically. In this part, infrared divergences which arise in the calculation of the hfs of positronium from the consideration of terms of the direct interaction are shown to cancel when the photon momenta are cut off at a small value. We have recalculated these effects and confirmed the numerical results of KK III by showing that the low-energy terms that were omitted actually do vanish.

To illustrate the formalism, we shall carry out the calculation as it relates to the contributions from a single transverse quantum. The perturbation considered is therefore the one stated in Eqs. (3.3) and (3.5) and illustrated in Fig. 1. It should be pointed out that this includes both I_{K1B} and the Coulomb-transverse terms, of $I_{K2B}{}^{(2)}$.[1] The explicit second-order terms, which we shall not discuss here, involve two transverse quanta. The energy change to be investigated is that derived from Eq. (3.3) by taking the center-of-mass transform,

$$\mathcal{T}_K(x,x')=ie^2\int e^{-iK(X-X')}d^4X'd^4x_1'd^4x_2'd^4x_3'd^4x_4'\times\sum_{i=1}^{2}\gamma_i^2F_1(11')\delta(22')G^C(1'2'3'4')\delta(3'3)\times F_2(4'4)\gamma_i^1\mathcal{G}_+(23)\theta(t_2-t_1)\theta(t_4-t_3)\theta(t_2-t_3), \quad (4.1)$$

and introducing the functions $\theta(t_2-t_1)$ and $\theta(t_4-t_3)$ to exclude the contributions from processes of unwanted time ordering. The positive energy part of the associated function $\mathcal{K}_K(\mathbf{rr}')$, Eq. (2.23), whose matrix element between equal-times wave functions gives the energy change, Eq. (2.25), is

$$\mathcal{K}_K(rr')=-i\alpha(2\pi)^{-9}\int d\mathbf{k}d\mathbf{p}d\mathbf{p}'dK_0'd\mathbf{x}d\mathbf{x}'\times k^{-1}(k+K_0'-K_0)^{-1}e^{i\mathbf{p}\cdot(\mathbf{r}-\mathbf{x})}e^{-i\mathbf{p}'\cdot(\mathbf{r}'-\mathbf{x}')}\times e^{-\frac{1}{2}i\mathbf{k}\cdot(\mathbf{x}+\mathbf{x}')}\sum_{i=1}^{2}\alpha_i^2\Lambda_+^1(\mathbf{p})\times G^C{}_{-\mathbf{k},K_0'}(\mathbf{x}0,\mathbf{x}'0)\Lambda_+^2(-\mathbf{p}')\alpha_i^1, \quad (4.2)$$

which, of course, depends only on the Coulomb Green's function between states at equal time. The integrations

over $\mathbf{x}$ and $\mathbf{x}'$ define a Fourier transform of this Green's function. The momenta involved are $\mathbf{p}$ and $\mathbf{p}'$ of the order of the Bohr momentum αm, and $\mathbf{k}$, the photon momentum. Clearly, the function G^C may be approximated nonrelativistically for values of $k \lesssim \alpha m$, whereas a free-particle expansion is valid for $k > \alpha m$. This separation according to $k \gtrless k_m \approx \alpha m$ will then permit us to take into account the effects of the binding where necessary and to handle the high-energy contributions correctly. We therefore define

$$\mathfrak{K}_{K>}(\mathbf{r}\mathbf{r}') = \int_{k>k_m} d\mathbf{k} \cdots; \quad \mathfrak{K}_{K<} = \int_{k<k_m} d\mathbf{k} \cdots. \tag{4.3}$$

The appropriate expressions for the Green's functions are the expansion about free-particle states:

$$\begin{aligned}
&\Lambda_+^1(\mathbf{p}) \int G^C{}_{-\mathbf{k},K0'}(\mathbf{x}0,\mathbf{x}'0)\Lambda_+^2(-\mathbf{p}')e^{-i\mathbf{p}\cdot\mathbf{x}} \\
&\quad \times e^{i\mathbf{p}'\cdot\mathbf{x}'} e^{-\frac{1}{2}i\mathbf{k}\cdot(\mathbf{x}+\mathbf{x}')} d\mathbf{x}d\mathbf{x}' \\
&\quad \to (2\pi)^3 i \frac{\Lambda_+^1(\mathbf{p})\delta(\mathbf{p}-\mathbf{p}'+\mathbf{k})\Lambda_+^2(-\mathbf{p}')}{E(p)+E(p')-K_0'} \\
&\quad + 4\pi i\alpha \Lambda_+^1(\mathbf{p}) \frac{\Lambda_+^2(-\mathbf{p}-\mathbf{k})}{E(p)+E(\mathbf{p}+\mathbf{k})-K_0'} \\
&\quad \times (\mathbf{p}-\mathbf{p}'+\mathbf{k})^{-2} \frac{\Lambda_+^1(\mathbf{p}'-\mathbf{k})}{E(p')+E(\mathbf{p}'-\mathbf{k})-K_0'} \Lambda_+^2(-\mathbf{p}'),
\end{aligned} \tag{4.4}$$

and the sum over nonrelativistic Pauli wave functions, $\varphi_n(\mathbf{x})$:[11]

$$\begin{aligned}
&G^C{}_{-\mathbf{k},K0'}(\mathbf{x},0,\mathbf{x}'0) \\
&= i\sum_n \left(1+\frac{\boldsymbol{\alpha}^1\cdot(\bar{\mathbf{p}}-\frac{1}{2}\mathbf{k})}{2m}\right)\left(1-\frac{\boldsymbol{\alpha}^2\cdot(\bar{\mathbf{p}}+\frac{1}{2}\mathbf{k})}{2m}\right)\varphi_{-\mathbf{k},n}(\mathbf{x}) \\
&\quad \times \varphi_{-\mathbf{k},n}{}^*(\mathbf{x}')\left(1+\frac{\boldsymbol{\alpha}'\cdot(\bar{\mathbf{p}}'-\frac{1}{2}\mathbf{k})}{2m}\right) \\
&\quad \times \left(1-\frac{\boldsymbol{\alpha}^2\cdot(\bar{\mathbf{p}}'+\frac{1}{2}\mathbf{k})}{2m}\right)\frac{1}{K_n'-K_0'},
\end{aligned} \tag{4.5}$$

where $i\bar{\mathbf{p}}$ and $i\bar{\mathbf{p}}'$ stand for the gradients with respect to $\mathbf{x}$ and $\mathbf{x}'$. The presence of the photon momentum arises from the fact that the system described by the Green's function has a total momentum $-k$ because of recoil. The wave equation satisfied by these wave functions is

$$\begin{aligned}
&[E(\bar{\mathbf{p}}+\tfrac{1}{2}\mathbf{k})+E(\bar{\mathbf{p}}-\tfrac{1}{2}\mathbf{k})-\alpha/|\mathbf{x}|]\varphi_{-\mathbf{k},n}(\mathbf{x}) \\
&\qquad = K_n'\varphi_{-\mathbf{k},n}(\mathbf{x}),
\end{aligned} \tag{4.6}$$

[11] R. J. Eden, Proc. Roy. Soc. (London) **A215**, 133 (1952), has used similar Green's functions of compound particles without, however, explicitly referring to the structure of the system.

or

$$\begin{aligned}
&\left[2m+\frac{\bar{p}^2}{2m}+\frac{k^2}{4m}-\frac{\alpha}{|\mathbf{x}|}\right]\varphi_{-\mathbf{k},n}(\mathbf{x}) \\
&\qquad = \left[\mathfrak{K}(\bar{p})+\frac{k^2}{4m}\right]\varphi_{-\mathbf{k},n}(\mathbf{x}) = K_n'\varphi_{-\mathbf{k},n}(\mathbf{x}),
\end{aligned} \tag{4.7}$$

in a nonrelativistic expansion. $\mathfrak{K}$ is the hydrogenic Hamiltonian with reduced mass $\frac{1}{2}m$ and eigenvalues $2m-\alpha^2 m/4n^2$. The only other quantity that enters the perturbation energy, Eq. (2.25), is the ground-state wave function $\chi^C(\mathbf{r})$, which also may be approximated in terms of a Pauli wave function, $\varphi_0(\mathbf{r})$:

$$\begin{aligned}
\chi^C(\mathbf{r}) &\cong \left(1+\frac{\boldsymbol{\alpha}^1\cdot\mathbf{p}}{2m}\right)\left(1-\frac{\boldsymbol{\alpha}^2\cdot\mathbf{p}}{2m}\right)\varphi_0(\mathbf{r}) \\
&= (2\pi)^{-3}\int d\mathbf{p}e^{i\mathbf{p}\cdot\mathbf{r}}\left(1+\frac{\boldsymbol{\alpha}^1\cdot\mathbf{p}}{2m}\right)\left(1-\frac{\boldsymbol{\alpha}^2\cdot\mathbf{p}}{2m}\right)\varphi_0(\mathbf{p}).
\end{aligned} \tag{4.8}$$

The high-energy contribution,

$$\Delta E_> = -i\int \chi^{C*}(\mathbf{r})\mathfrak{K}_{K>}(\mathbf{r}\mathbf{r}')\chi^C(\mathbf{r}')d\mathbf{r}d\mathbf{r}', \tag{4.9}$$

can be calculated by the methods of KK III. The spin matrix element, denoted by $\langle\ \rangle$, from the first term of Eq. (4.4) gives

$$\begin{aligned}
&\sum_{i=1}^{3}\left\langle\left(1+\frac{\boldsymbol{\alpha}^1\cdot\mathbf{p}}{2m}\right)\left(1-\frac{\boldsymbol{\alpha}^2\cdot\mathbf{p}}{2m}\right)\Lambda_+^1(\mathbf{p})\alpha_i^1\alpha_i^2\right. \\
&\qquad \left.\times\Lambda_+^2(-\mathbf{p}')\left(1+\frac{\boldsymbol{\alpha}^1\cdot\mathbf{p}'}{2m}\right)\left(1-\frac{\boldsymbol{\alpha}^2\cdot\mathbf{p}'}{2m}\right)\right\rangle \\
&\to [E(p)+m][E(p')+m]\langle\boldsymbol{\sigma}^1\times(\mathbf{p}-\mathbf{p}') \\
&\qquad \cdot\boldsymbol{\sigma}^2\times(\mathbf{p}-\mathbf{p}')\rangle/16m^2E(p)E(p') \\
&\to [E(p)+m][E(p')+m] \\
&\qquad \times\tfrac{2}{3}k^2\boldsymbol{\sigma}^1\cdot\boldsymbol{\sigma}^2/16m^2E(p)E(p'),
\end{aligned} \tag{4.10}$$

where we have made use of momentum conservation and spherical symmetry. The resulting expression can be reduced to the first terms of Eq. (4.8), KK III,

$$\begin{aligned}
&\frac{\alpha}{6m^2}\frac{\langle\boldsymbol{\sigma}^1\cdot\boldsymbol{\sigma}^2\rangle}{(2\pi)^5}\int_{k>k_m} d\mathbf{k}d\mathbf{p}d\mathbf{p}'\varphi_0{}^*(\mathbf{p}) \\
&\times\frac{[E(p)+m][E(p')+m]}{4E(p)E(p')}\frac{k\delta(\mathbf{p}-\mathbf{p}'+\mathbf{k})}{k+E(p)+E(p')-K_0}\varphi_0(\mathbf{p}'),
\end{aligned} \tag{4.11}$$

by carrying out the contour integral over K_0'. The factor of one-half of this contribution compared with the formula in KK III is accounted for by the existence of an equal energy change due to the $\mathcal{T}_\beta$ in Eq. (3.5). By the approximations described in KK III the result,

accurate to α(hfs) under the assumption that $k_m \sim \alpha m$, is obtained:

$$\frac{\alpha}{6m^2}\frac{\langle\sigma^1\cdot\sigma^2\rangle}{(2\pi)^2}\int_{k>k_m}\varphi_0(\mathbf{r})e^{-i\mathbf{k}\cdot\mathbf{r}}\varphi_0(\mathbf{r})d\mathbf{r}d\mathbf{k}$$
$$-(2\alpha^2/3m^2)\langle\sigma^1\cdot\sigma^2\rangle|\varphi_0(0)|^2\{1+\ln(m/k_m)\}. \quad (4.12)$$

For the second term in Eq. (4.4), it is sufficient to set

$$\chi^C(\mathbf{r})\cong\varphi_0(0). \quad (4.13)$$

The resulting spin matrix elements are of the form

$$\sum_{i=1}^{3}\langle\alpha_i^2\Lambda_+^2(-\mathbf{k})\Lambda_+^1(-\mathbf{k})\alpha_i^1\rangle\to\tfrac{2}{3}k^2\langle\sigma^1\cdot\sigma^2\rangle/4E^2. \quad (4.14)$$

The integration over K_0' may be carried out as before and yields the expression

$$\frac{\alpha^2}{3m^2}\frac{\langle\sigma^1\cdot\sigma^2\rangle}{2\pi}|\varphi_0(0)|^2\int_{k>k_m}\frac{d\mathbf{k}}{k}\frac{m^2}{E^2}\frac{1}{(E+k-m)^2}, \quad (4.15)$$

which corresponds to a part of Eq. (4.13), KK III. The integration of k gives:

$$(2\alpha^2/3m^2)\langle\sigma^1\cdot\sigma^2\rangle|\varphi_0(0)|^2\{-\tfrac{1}{4}\pi+\ln(m/k_m)\}, \quad (4.16)$$

which is added to Eq. (4.12) for $\Delta E_>$,

$$\Delta E_>=(\alpha/24m^2\pi^2)\langle\sigma^1\cdot\sigma^2\rangle$$
$$\times\int_{k>k_m}\varphi_0^*(\mathbf{r})e^{-i\mathbf{k}\cdot\mathbf{r}}\varphi_0(\mathbf{r})d\mathbf{r}d\mathbf{k}$$
$$-(2\alpha^2/3m^2)\langle\sigma^1\cdot\sigma^2\rangle|\varphi_0(0)|^2(1+\tfrac{1}{4}\pi). \quad (4.17)$$

The low-energy contribution,

$$\Delta E_<=-i\int\chi^{C*}(\mathbf{r})\mathcal{K}_{K<}(\mathbf{r}\mathbf{r}')\chi^C(\mathbf{r}')d\mathbf{r}d\mathbf{r}', \quad (4.18)$$

is evaluated by using Eqs. (4.5) and (4.8) to simplify the expression. The spin matrix elements that occur are

$$\left\langle\left(1+\frac{\boldsymbol{\alpha}^1\cdot\mathbf{p}}{2m}\right)\left(1-\frac{\boldsymbol{\alpha}^2\cdot\mathbf{p}}{2m}\right)\Lambda_+^1(\mathbf{p})\alpha_j^2\left(1+\frac{\boldsymbol{\alpha}^1\cdot\mathbf{p}}{2m}\right)\right.$$
$$\left.\times\left(1-\frac{\boldsymbol{\alpha}^2\cdot(\mathbf{p}+\mathbf{k})}{2m}\right)\right\rangle\to i\frac{(\sigma^2\times\mathbf{k})_j}{2m}\left\{1+\frac{E(\mathbf{p})-m}{2m}\right.$$
$$\left.+\frac{(E(p)-m)p^2}{8m^2E(p)}\right\}\to i(\sigma^2\times\mathbf{k})_j/2m, \quad (4.19)$$

and

$$\left\langle\left(1+\frac{\boldsymbol{\alpha}^1\cdot(\mathbf{p}'-\mathbf{k})}{2m}\right)\left(1-\frac{\boldsymbol{\alpha}^2\cdot\mathbf{p}'}{2m}\right)\alpha_j^1\Lambda_+^2(-\mathbf{p}')\right.$$
$$\left.\times\left(1+\frac{\boldsymbol{\alpha}^1\cdot\mathbf{p}'}{2m}\right)\left(1-\frac{\boldsymbol{\alpha}^2\cdot\mathbf{p}'}{2m}\right)\right\rangle\to-i(\sigma^1\times\mathbf{k})_j/2m, \quad (4.20)$$

where the omitted terms are quadratic in the momenta and therefore of order α^2(hfs). Thus,

$$\Delta E_<=(\alpha/16m^2\pi^2)\sum_n\int_{k<k_m}d\mathbf{k}e^{-\frac{1}{2}i\mathbf{k}\cdot(\mathbf{r}+\mathbf{r}')}k^{-1}d\mathbf{r}d\mathbf{r}'$$
$$\times(k+K_n'-K_0)^{-1}\sum_{i=1}^{3}\varphi_0^*(\mathbf{r})(\sigma^2\times\mathbf{k})_i$$
$$\times\varphi_{-k,n}(\mathbf{r})\varphi_{-k,n}^*(\mathbf{r}')(\sigma^1\times\mathbf{k})_i\varphi_0(\mathbf{r}'). \quad (4.21)$$

In order to eliminate the wave functions of the excited states occurring in Eq. (4.22), we may replace K_n' by $3\mathcal{C}+k^2/4m$, Eq. (4.7), acting on $\varphi_{-k,n}(\mathbf{r})$. The sum over n now yields a δ function between $\mathbf{r}$ and $\mathbf{r}'$:

$$\Delta E_<=(\alpha/16m^2\pi^2)\int_{k<k_m}d\mathbf{k}\varphi_0^*(\mathbf{r})(\sigma^2\times\mathbf{k})\cdot(\sigma^1\times\mathbf{k})$$
$$\times e^{-\frac{1}{2}i\mathbf{k}\cdot\mathbf{r}}k^{-1}(k+3\mathcal{C}-K_0+k^2/4m)^{-1}$$
$$\times e^{-\frac{1}{2}i\mathbf{k}\cdot\mathbf{r}}\varphi_0(\mathbf{r})d\mathbf{r}. \quad (4.22)$$

This expression may be evaluated approximately if one recognizes that the energy level differences in the denominator are of order $\alpha^2 m$ whereas the momentum k is of order αm. It is therefore sufficiently accurate to retain only the first two terms in the expansion

$$k^{-1}(k+3\mathcal{C}-K_0+k^2/4m)^{-1}=k^{-2}-k^{-3}(3\mathcal{C}-K_0+k^2/4m)$$
$$+k^{-3}(3\mathcal{C}-K_0+k^2/4m)^2(k+3\mathcal{C}-K_0+k^2/4m)^{-1}. \quad (4.23)$$

The spherical symmetry of the ground state implies that one may average over angles with the result

$$\langle\sigma^2\times\mathbf{k}\cdot\sigma^1\times\mathbf{k}\rangle\to\tfrac{2}{3}k^2\langle\sigma^1\cdot\sigma^2\rangle. \quad (4.24)$$

With these two observations, the first term of Eq. (4.23) inserted into Eq. (4.22) gives

$$(\alpha/24m^2\pi^2)\langle\sigma^1\cdot\sigma^2\rangle\int_{k<k_m}\varphi_0^*(\mathbf{r})e^{-i\mathbf{k}\cdot\mathbf{r}}\varphi_0(\mathbf{r})d\mathbf{r}d\mathbf{k}, \quad (4.25)$$

whereas the second one gives

$$-(\alpha/24m^2\pi^2)\langle\sigma^1\cdot\sigma^2\rangle\int_{k<k_m}\varphi_0^*(\mathbf{r})e^{-\frac{1}{2}i\mathbf{k}\cdot\mathbf{r}}k^{-1}$$
$$\times[3\mathcal{C}(p)-K_0+k^2/4m]e^{-\frac{1}{2}i\mathbf{k}\cdot\mathbf{r}}\varphi_0(\mathbf{r})d\mathbf{r}d\mathbf{k}. \quad (4.26)$$

Now,

$$(3\mathcal{C}(p)-K_0+k^2/4m)e^{-\frac{1}{2}i\mathbf{k}\cdot\mathbf{r}}\varphi_0(\mathbf{r})$$
$$=[3\mathcal{C}(\mathbf{p}+\tfrac{1}{2}\mathbf{k})-K_0-\mathbf{p}\cdot\mathbf{k}/m]e^{-\frac{1}{2}i\mathbf{k}\cdot\mathbf{r}}\varphi_0(\mathbf{r})$$
$$=-(\mathbf{p}\cdot\mathbf{k}/m)e^{-\frac{1}{2}i\mathbf{k}\cdot\mathbf{r}}\varphi_0(\mathbf{r})+e^{-\frac{1}{2}i\mathbf{k}\cdot\mathbf{r}}[3\mathcal{C}(p)-K_0]\varphi_0(\mathbf{r})$$
$$=-(\mathbf{p}\cdot\mathbf{k}/m)e^{-\frac{1}{2}i\mathbf{k}\cdot\mathbf{r}}\varphi_0(\mathbf{r}). \quad (4.27)$$

Since, furthermore, the ground-state wave function is

real, the integrand of Eq. (4.26) may be rewritten

$$-(\varphi_0(\mathbf{r})e^{-\frac{1}{2}i\mathbf{k}\cdot\mathbf{r}})\frac{\mathbf{k}\cdot\mathbf{p}}{m}(e^{-\frac{1}{2}i\mathbf{k}\cdot\mathbf{r}}\varphi_0(\mathbf{r}))k^{-1}$$
$$=-\frac{1}{2}\frac{\mathbf{k}\cdot\mathbf{p}}{m}[e^{-i\mathbf{k}\cdot\mathbf{r}}(\varphi_0(\mathbf{r}))^2]k^{-1}, \quad (4.28)$$

which becomes a vanishing surface integral when integrated over $\mathbf{r}$. Consequently $\Delta E_<$ is equal to the expression given in Eq. (4.25). When this simple result is added to the high-energy contribution, Eq. (4.17), the total energy change from the perturbation Eq. (4.1) is equal to

$$\Delta E=(\alpha/24m^2\pi^2)\langle\sigma^1\cdot\sigma^2\rangle\int_{\text{all }k}\varphi_0^*(\mathbf{r})e^{-i\mathbf{k}\cdot\mathbf{r}}\varphi_0(\mathbf{r})d\mathbf{r}d\mathbf{k}$$
$$-(2\alpha^2/3m^2)\langle\sigma^1\cdot\sigma^2\rangle|\varphi_0(0)|^2(1+\tfrac{1}{4}\pi) \quad (4.29)$$
$$=(\pi\alpha/3m^2)\langle\sigma^1\cdot\sigma^2\rangle|\varphi_0(0)|^2\{1-(2\alpha/\pi)(1+\tfrac{1}{4}\pi)\}.$$

It is clear that this result is precisely the one that would have been obtained for these terms by the use of artificial cutoffs at small momenta for the divergent contributions. It is a consequence of the fact that the low-energy correction Eq. (4.25) contained no corrections of relative order α to the hyperfine structure. The same procedure, with a similar result, can be applied to the corrections coming from the exchange of two transverse quanta in Eq. (4.11), KK III. The remaining contributions present no difficulties at low energies and need not be examined.

We may point out now that the ideas discussed here are just the ones that were used to evaluate the Lamb shift in hydrogen. The formalism therefore provides the correct connection for joining a nonrelativistic perturbation result such as Eq. (4.21) to a relativistic treatment of the radiation interaction that permits the removal of divergences. The method is being applied to situations where the low-energy contributions that depend on the bound state will not vanish.

We have enjoyed conversations about this subject with Julian Schwinger, Abraham Klein, Malvin Ruderman, and Paul Martin.

Letters to the Editor

PUBLICATION of brief reports of important discoveries in physics may be secured by addressing them to this department. The closing date for this department is five weeks prior to the date of issue. No proof will be sent to the authors. The Board of Editors does not hold itself responsible for the opinions expressed by the correspondents. Communications should not exceed 600 words in length and should be submitted in duplicate.

Energy Transfer from Solvent to Solute in Liquid Organic Solutions Under Ultraviolet Excitation

S. G. COHEN AND A. WEINREB
Department of Physics, Hebrew University, Jerusalem, Israel
(Received December 28, 1953)

AGENO *et al.*[1] and Kallmann *et al.*[2] have shown that when certain organic liquid solutions are irradiated with γ rays a transfer of excitation energy from solvent to solute molecules takes place, giving rise to a very efficient conversion of absorbed energy into fluorescent quanta emitted by the fluorescent solute. Such solutions have an important use as scintillation media. There is still much discussion on the mechanism of energy transfer.[3]

In this work the possibility that a similar transfer occurs when the organic solutions are excited by ultraviolet has been examined. The existence of such a transfer would in itself be interesting, and moreover a detailed investigation of such a process might throw new light on the transfer mechanism, since the primary exciting process is much simpler in the case of ultraviolet excitation than in the case of excitation by ionizing radiations.

In a series of preliminary experiments, it was found that a considerable transport of energy from solvent to solute does indeed occur in many organic solutions when excited by light of wavelength 2537A.

For a convincing demonstration of this process, it is necessary that the solvent absorb most of the primary exciting radiation and that the solute absorb very little; on the other hand, the solute concentration should be sufficient to produce detectable fluorescence after transfer. These conditions are satisfied by a dilute solution of *p*-terphenyl (1 g/liter) in benzene, toluene, or xylene, for an exciting wavelength of 2537A. For a particular solute concentration the fraction of primary excitation energy absorbed by the solute was calculated (this was never greater than a few percent) from the relative absorption coefficients of solute and solvent at 2537A. The fluorescence of terphenyl in the aforementioned solvents when excited at 2537A was compared with the fluorescence obtained from a thin layer of solid terphenyl (for which the fluorescent yield is very high) deposited on a quartz slide at the same wavelength. As a further check a comparison was also made with the fluorescence produced by a solution of terphenyl in chloroform, a solvent which does not absorb significantly at 2537A.[4] It was found that the terphenyl fluorescence obtained in the solutions containing the strongly absorbing solvents was very much greater than that expected on the assumption that fluorescence is produced only through direct absorption by the terphenyl. For example, a solution of terphenyl in toluene at a concentration of 1 g/liter showed a fluorescence twenty times as great. The high fluorescent efficiency must be ascribed to transfer of energy from excited molecules of the solvent to molecules of the fluorescent solute. Although most of the measurements have so far been made with terphenyl, qualitative experiments show that transfer effects are obtained if other organic fluorescent materials are used as solutes.

Ageno *et al.*[5] has found evidence showing that fluorescent emission takes place over a region within a few millimeters from a polonium α-particle source immersed in a solution of terphenyl in xylene, and therefore have suggested that energy transfer takes place via long-range secondary radiation emitted by the solvent and absorbed by the solute. In order to see whether such radiative processes are significant in the case of uv excitation, a solution of terphenyl and xylene was placed in a Hilger quartz cell of variable thickness, and the fluorescence measured as a function of the thickness of the cell down to very small thicknesses, for a primary exciting radiation of 2537A. The results show that there is no appreciable radiative transfer over distances greater than 0.01 mm.

A detailed investigation of the dependence of transfer on various parameters such as wavelength and concentration in different liquid systems is being carried out.

[1] Ageno, Chiozzotto, and Querzoli, Phys. Rev. **79**, 720 (1950).
[2] H. Kallmann and M. Furst, Phys. Rev. **79**, 857 (1950).
[3] For a recent discussion of different points of view see J. B. Birks, *Scintillation Counters* (Pergamon Press, London, 1953).
[4] A reduction of the intensity of the terphenyl fluorescence in chloroform occurs due to partial quenching by the solvent. This reduction, relative to terphenyl in toluene, was found to be about 35 percent, by comparing the two solutions at longer exciting wavelengths, where *both* solvents exhibit negligible absorption relative to the solvent. This quenching was also found to be independent of the exciting wavelength and was taken into account in the comparison at 2537A.
[5] M. Ageno and R. Querzoli, Nuovo cimento **9**, 282 (1932).

Radiation Damage in SiO_2 Structures

M. WITTELS AND F. A. SHERRILL
Oak Ridge National Laboratory, Oak Ridge, Tennessee
(Received December 28, 1953)

FAST-NEUTRON irradiation of solids in the silicon-oxygen system have produced some interesting results.[1-3] Four phases of this system: (1) quartz, (2) low cristobalite, (3) low tridymite, and (4) glass have been irradiated with fluxes up to 2×10^{20} neutrons/cm^2 at this laboratory and the investigation is still in progress. This is a brief report on some of the results of the investigation.

After a total bombardment of 2×10^{20} neutrons/cm^2, the density of single crystals of quartz are reduced by 14.7 percent. It is somewhat unusual that these crystals reveal no macroscopic defects. The change in density has been traced following progressive irradiations and shows a pronounced structure dependence. The rate of change of density (Fig. 1) is initially small and may be

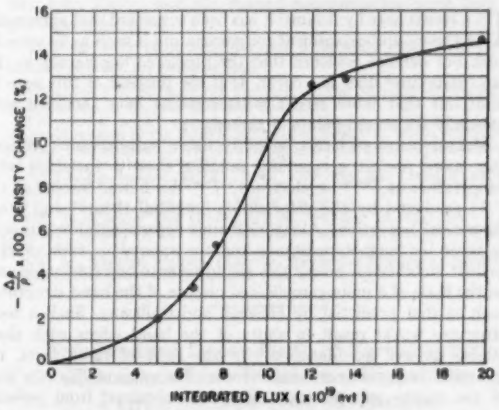

FIG. 1. Density change of quartz as a function of fast neutron bombardment.

due to the early filling of the *c*-axis interstitial channels with displaced atoms. Long-range order is maintained in single crystals but is gradually diminished until they have suffered a bombardment of approximately 1.2×10^{20} neutrons/cm^2. Following this irradiation the single-crystal x-ray reflections disappear. It is believed that permanent damage is induced in the single-crystal lattice at an early stage $\sim2\times10^{19}$ neutrons/cm^2, since at this

point the c/a ratio is lowered below that value which β quartz[6] exhibits at 1000°C. Thermal and electrical evidence supports this view. Crystals bombarded by 5×10^{19} neutrons/cm^3 fail to exhibit the latent heat at the α-β inversion point and piezoelectric crystals no longer resonate after this irradiation.

Heavy dosages of fast neutron flux reduce all four of these solids to a common phase. This highly disordered material has an x-ray diffraction pattern of a glass, is optically isotropic, and has a density of 2.26. This material was recrystallized by annealing at 930°C for 16 hours and resulted in the formation of polycrystalline α quartz. Debye-Scherrer diffraction patterns taken using monochromatic radiation from a Cu target gave x-ray reflections at angles up to $2\theta=90°$. The fact that x-ray reflections were not observed at larger Bragg angles may be due to incomplete recrystallization, particle-size broadening, or strain. The contributions of each of these factors are being determined.

It appears that the bombardment of any of the above-mentioned phases produces a silica glass, with a density and average refractive index near that of normal low tridymite, which can then be transformed into α quartz in a solid-state reaction. Further annealing studies are necessary to confirm this view unambiguously. Such behavior would be of major interest since investigators[6] have been unsuccessful in their attempts to transform any of the complex silica phases into α quartz by means of a solid-state transformation in the absence of chemical aids.

A detailed report on the results of this investigation will be submitted for publication at an early date.

[1] R. Berman, Proc. Roy. Soc. (London) **A208**, 90 (1951).
[2] R. Berman, Advances in Physics **2**, 5, 103 (1953).
[3] M. Wittels, Phys. Rev. **89**, 3, 656 (1953).
[4] M. Wittels, Unpublished post-deadline paper, Washington D. C. Meeting, American Physical Society, May 2, 1953.
[5] Primak, Fuchs, and Day, Phys. Rev. **92**, 1064 (1953).
[6] R. B. Sosman, *The Properties of Silica* (Chemical Catalogue Company, Inc., New York, 1927).

Experimental Evidence Concerning Degeneracy in Germanium

ESTHER M. CONWELL*
Sylvania Electric Products, Bayside, New York
(Received January 14, 1954)

IN a recent note by Adams[1] it has been suggested that agreement of theory and experiment for germanium is such as to provide weak but definite evidence that the predicted degeneracy in the band structure[2] does not occur. It is the purpose of this note to point out that more recent measurements have modified substantially the stated points of agreement.

Measurements of lattice mobility taken on purer and presumably more prefect germanium samples show a variation with temperature as $T^{-1.6}$ for electrons,[3] $T^{-2.3}$ for holes,[4] instead of the $T^{-1.5}$ predicted by the deformation-potential theory[5] and other theoretical derivations. Along with other experimental results such as those for magnetoresistance and the anomalous ratio of Hall to drift mobility for holes,[3] this would seem to be explainable only on the basis of a more complicated picture of the band structure,[6] such as that predicted by Herman and Callaway. Such a band structure would result in shifts of the band edges with shear strains as well as dilatation.[5] In the light of these facts, the quantitative agreement found between the value of $E_{1\sigma}$ (the shift of the energy gap per unit dilatation) obtained from pressure experiments and that predicted by the deformation-potential theory for germanium would seem largely fortuitous. For silicon, it is worth noting, agreement was considerably poorer.

Agreement also apparently existed between values of β, the change in energy gap per degree change in temperature, determined from a few different types of experiment. The significance of this agreement is also open to question. One value of β was calculated from the experimental $E_{1\sigma}$ under the assumption that the change in energy gap with temperature was due entirely to thermal expansion. Another value of β is obtained from comparison of the theoretical formula

$$n_i^2=np=4\left(\frac{2\pi m_n^{\frac{1}{2}}m_p^{\frac{1}{2}}kT}{h^2}\right)^3 e^{-E_0/kT} \qquad (1)$$

with n_i^2 calculated from measurements of intrinsic conductivity. With a $T^{-\frac{3}{2}}$ dependence for the lattice mobility and effective masses equal to the free electron mass, this led to a value of 1×10^{-4} ev/°K for β, in good agreement with the value calculated from $E_{1\sigma}$.[5] Incorporating the changed temperature dependences of the lattice mobilities will change this value and worsen the agreement unless, of course, the effective masses used in (1) are changed. There is, however, a fundamental question as to whether or not these two values of β should agree; it has been shown by Fan[7] that the shift in the energy gap with temperature arises in part from the changing interaction of the electrons with the lattice vibrations.

If the band structure is not the simple kind usually assumed, Eq. (1) must be modified. It may well be that for some particular band structure the modification consists of the insertion of statistical weight factors for the conduction and valence bands as suggested by Adams.[1] The effective masses in the formula for n_i^2 should then represent suitable averages of effective masses over different bands or different directions. Unfortunately, however, the effective mass in other formulas may not be represented by the same average. Thus it appears that, in general, detailed knowledge of the band structure may be required for the determination of β from n_i^2.

A different value of β, 4×10^{-4} ev/°K, is obtained from measurements of infrared absorption.[7] If the band structure of germanium is that calculated by Herman and Callaway, it is not to be expected that this value of β agree with that obtained from thermal transitions.

* On leave from Brooklyn College, Brooklyn, New York.
[1] E. N. Adams, II, Phys. Rev. **92**, 1063 (1953).
[2] F. Herman and J. Callaway, Phys. Rev. **88**, 1210 (1952).
[3] M. B. Prince, Phys. Rev. **92**, 681 (1953).
[4] W. C. Dunlap, Phys. Rev. **79**, 286 (1950).
[5] J. Bardeen and W. Shockley, Phys. Rev. **80**, 72 (1950).
[6] Pearson, Haynes, and Shockley, Phys. Rev. **78**, 295 (1950).
[7] H. Y. Fan, Phys. Rev. **82**, 900 (1951).

"Closed" Fountain Effect in Liquid Helium II*†

CHARLES A. REYNOLDS
University of Connecticut, Storrs, Connecticut
(Received January 4, 1954)

THE rise in the liquid level of a closed system of helium II through which a heat current is passing has been observed. The rise is attributed to a stress which is the difference between

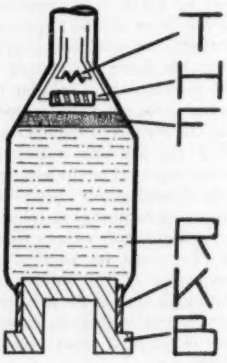

FIG. 1. Diagram of the closed, rouge-packed, glass-metal system.

the thermomechanical tension given by H. London's equation, $\Delta p=\rho S\Delta T$,[1] and a Hooke's law type stress.

Figure 1 is a diagram of the apparatus used. It consists of a glass tube which was packed with rouge powder (R) and which

was surrounded by a bath of liquid helium II. Sealed to the bottom of the glass is a Kovar tube (K) into which was soldered a brass plug (B). The purpose of the glass frit (F) was to serve as a porous barrier against which the rouge could be packed. Above this frit are a heater (H) and a carbon resistance thermometer (T). At the top the system is joined to a small-diameter glass tube which extends up through the helium flask.

Helium gas from an outside supply was condensed in the inner system in such an amount that the liquid level at zero heater power in the helium II temperature range was in and near the bottom of the small-diameter glass tube. The bath temperature was held constant in the liquid helium II range and the height and temperature of the liquid above the frit were observed as a function of heater power.

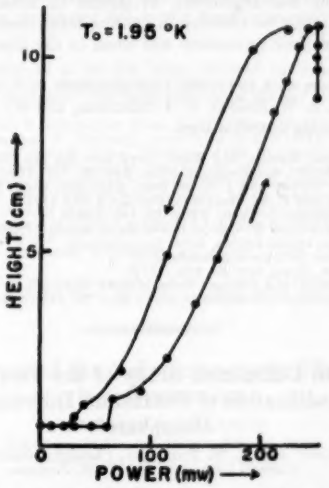

FIG. 2. Plot of the height of the inner liquid helium level above an arbitrary zero as a function of heater power input in milliwatts.

Figure 2 is a typical plot of the height of the inner helium level as a function of heater power (milliwatts). As the power was increased from zero there was at first a slight decrease in level which one would expect as the density of helium II increases with increasing temperature. At a certain power (here 61 mw) the level suddenly rose and continued to rise with increasing power until the temperature of the liquid above the frit exceeded the λ point. Here bubbling and a geyser effect took place. On decreasing the power it was found that the level was higher than on increasing power for the same value of power. However, at low powers the level returned to its original height.

The following results were found. (1) There is a linear relationship between power and temperature difference at low powers. The relationship becomes nonlinear in the power region in which the level begins to rise. (2) In the region of the level rise, the height is proportional to the temperature difference. (3) The level rise for a given temperature difference is much less than for the normal fountain effect.[2,3]

It might be reason that the rise in level follows from the formation of a gas bubble in the gaps between the rouge particles. There are two points which tend to rule out this possibility. One is that there is no drastic change in the thermal conductivity and the other is that no bubbles were ever seen in the gap which eventually developed between the frit bottom and the top of the rouge. To eliminate the possibility that the frit was responsible for the effect and to demonstrate the necessity of the small channels in the rouge, a run was made with a similar apparatus minus the rouge. The only level change observed in this case was a continual decrease in height with increasing power and temperature difference as one would expect from the density-temperature dependence.

To test the hypothesis that this effect was less than the normal thermomechanical effect because of a downward Hooke's law type tension, runs were made with the identical apparatus except that the glass tube above the frit was replaced by one of different cross-sectional area. It was found then that it was more nearly the volume increase in the tube which corresponded to a given temperature difference rather than the height (or pressure).

The "difference" forces acting on a cross-sectional area of the channels in the rouge are considered to be (1) a downward hydrostatic force resulting from the level rise, (2) a downward force resulting from the increase in temperature and hence an increase of vapor pressure of the liquid above the frit, (3) an upward thermomechanical force ($\rho S\Delta T\times$area), and (4) a downward force proportional to the ratio of the elevated volume to the volume of liquid in the rouge (volume strain). The first two are small compared to the last two. A "compressibility" is then calculated.

TABLE I. Summary of data.

Run	Bath temperature (°K)	Tube cross-section area (cm²)	Slope height vs temp. diff. $H/\Delta T$ (cm/°K)	Compressibility (atmos^{-1})
1	2.001	0.128	121	0.30
2	1.950	0.128	115	0.29
3	1.946	0.398	59	0.46
4	1.821	0.128	100	0.30
5	1.817	0.398	43	0.35

Table I is a summary of some of the data. Comparing runs 2 and 3 which were made at about the same temperature, it is seen that the value of $H/\Delta T$ is less for the run with the wider tube; the same comparison may be made for runs 4 and 5. The last column lists the calculated "compressibility." The order of magnitude is to be noted—the normal compressibility of liquid helium is approximately 1.3×10^{-6}/atmos.[4] Thus this "compressibility" is about 25 times the normal compressibility.

The "open" fountain effect was measured after a hole was drilled in the brass plug; the experimental result agreed substantially with that calculated from H. London's equation.

The author wishes to express his appreciation to Professor P. R. Zilsel for many interesting discussions and to Mr. Harold Forstat, Mr. John Reppy, and Mr. Russell Southwick for much help with the experiments.

Further work is in progress and a detailed paper will be submitted shortly for publication.

* Sponsored by the Research Corporation, the National Science Foundation, and the U. S. Office of Naval Research.

† An earlier report was given as a ten-minute paper before the New England Section of the American Physical Society at Storrs, Connecticut, Nov. 7, 1953 and at the Third International Low Temperature Conference at the Rice Institute, Dec. 17–22, 1953.

[1] H. London, Nature **142**, 612 (1938); Proc. Roy. Soc. (London) **A171**, 484 (1939).

[2] P. L. Kapitza, J. Phys. U.S.S.R. **5**, 59 (1941).

[3] W. H. Keesom and G. Duyckaerts, Physica **13**, 153 (1947); J. H. Mellink, Physica **13**, 180 (1947); L. Meyer and J. H. Mellink, Physica **13**, 197 (1947).

[4] W. H. Keesom, *Helium* (Elsevier Publishing Company, Amsterdam-London-New York, 1942), pp. 236, 243.

Temperature Dependence of Ferromagnetic Resonance Line Width in a Nickel Iron Ferrite: A New Loss Mechanism

J. K. GALT, W. A. YAGER, AND F. R. MERRITT
Bell Telephone Laboratories, Murray Hill, New Jersey

(Received January 13, 1954)

WE have measured the ferromagnetic resonance line width in the [111] direction on two single-crystal spheres of a nickel-iron ferrite at 24 000 Mc/sec as a function of temperature from the boiling point of helium to approximately 400°K. The composition of these crystals, which were obtained from the Linde Air Products Company, was approximately $(NiO)_{0.72}(FeO)_{0.28}$

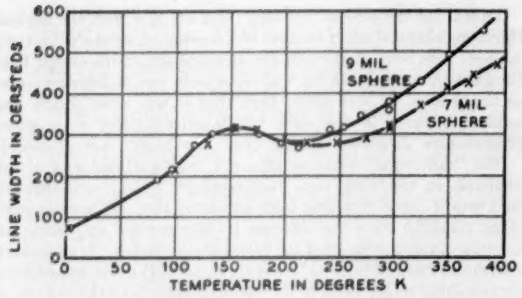

FIG. 1. Ferromagnetic resonance line width *vs* temperature for $(NiO)_{0.72}(FeO)_{0.28}Fe_3O_4$. Frequency 24 000 Mc/sec.

Fe_2O_3. The crystals were not fixed rotationally, but were oriented crystallographically by the dc magnetic field required for resonance. The method used was otherwise similar to one previously described.[1] The experiments will be described in more detail in a later publication.

The width of the line at half-power points is plotted in Fig. 1 for both spheres as a function of temperature. The rise at high temperature is due to the loss arising from the increasing conductivity of these crystals at high temperatures. This is confirmed by the fact that the size dependence characteristic of the relatively high conductivity ferrites[2] is observed in this region, and by the fact that the material from which these spheres are cut has a resistivity of only about 1 ohm-cm at room temperature. The high-temperature end of the curves may therefore be understood at least qualitatively in terms of a loss mechanism (eddy currents) which is not new and not of primary importance in understanding the losses in ferrites generally. If we ignore the contribution of conductivity, the data leads to a damping constant λ of approximately 2×10^7 at room temperature.

The low-temperature portion of the curves in Fig. 1 (below room temperature), however, is quite another matter. The bulk of the loss on this region is clearly due to a mechanism whose effectiveness is a maximum in the neighborhood of 160°K. We suggest that these losses arise from a relaxation in short-range order among the divalent and trivalent iron ions. Order-disorder of this sort was suggested by Verwey and his co-workers as the explanation of the low-temperature transition in Fe_3O_4.[3] This relaxation is the same mechanism as that suggested by Wijn and van der Heide to explain observations at much lower frequencies in other ferrites.[4] The existence of some remnant of the Fe_3O_4 transition in our case is established by the results of ultrasonic measurements of elastic constants made on other crystals of the same composition by Fine[5] of these Laboratories.

Since the magnetization is coupled to the lattice by the magnetostriction, motion of the magnetization produces varying stresses in the lattice. These variations in stress cause the arrangement of the divalent and trivalent iron ions to vary, but with a time lag which causes a loss of energy.

We have made a preliminary calculation of the losses in the crystal lattice due to the phase lag between stress and strain which arises from this mechanism. It gives the right temperature dependence if we calculate the relaxation time from the activation energy associated with conductivity, but it is too small by about an order of magnitude (damping constant $\lambda\cong10^8$ at room temperature). A more accurate calculation may make it possible to explain the whole effect this way, but at present it appears that other aspects of the mechanism are involved.

Domain wall motion experiments of the sort previously reported at room temperature in Fe_3O_4[6] have been carried out on crystals of this composition as a function of temperature by one of us (J.K.G.). The above mechanism should also largely determine the losses observed in these experiments, and the data obtained bear out this expectation. There is a large increase in the viscous damping of domain walls at low temperatures. We mention these results since Wijn does not indicate clearly that this mechanism will contribute to domain wall damping as well as to losses associated with domain rotation processes. This mechanism also explains, of course, why domain wall damping in Fe_3O_4[6] is much larger than that in a nickel-iron ferrite.[7] We agree with Wijn and van der Heide that it also explains the permeability *vs* frequency observations of Galt, Matthias, and Remeika.[8]

We wish to emphasize the fact that the width of the low-temperature maximum is such that the mechanism produces significant losses over a very large range in temperature. This suggests to us that a major contribution to the losses in many or even perhaps all ferrites is due to the relaxation associated with this and other crystallographic transitions characterized primarily by electronic rearrangements. It should be noted that such transitions might be effective in causing losses even though the likelihood of their occurrence was small in the absence of large stresses.

The authors wish to express their gratitude to A. M. Clogston, C. Herring, A. N. Holden, B. T. Matthias, and W. T. Read, Jr., for enlightening conversations.

[1] Yager, Galt, Merritt, and Wood, Phys. Rev. **80**, 744 (1950).
[2] Yager, Merritt, and Guillaud, Phys. Rev. **81**, 477 (1951).
[3] E. J. W. Verwey and J. H. de Boer, Rec. trav. chim. **55**, 531 (1936); E. J. Verwey and P. W. Haayman, Physica **8**, 979 (1941); Verwey, Haayman, and Romeijn, J. Chem. Phys. **15**, 181 (1947).
[4] H. P. J. Wijn and H. van der Heide, Revs. Modern Phys. **25**, 99 (1953); H. P. J. Wijn, thesis, Leiden, 1953, (unpublished).
[5] M. E. Fine (private communication).
[6] J. K. Galt, Phys. Rev. **85**, 664 (1952).
[7] Galt, Andrus, and Hopper, Revs. Modern Phys. **25**, 93 (1953).
[8] Galt, Matthias, and Remeika, Phys. Rev. **79**, 391 (1950).

Neutron Diffraction Study of the Ferroelectric Modification of Potassium Dihydrogen Phosphate*

HENRI A. LEVY AND S. W. PETERSON, *Chemistry Division, Oak Ridge National Laboratory, Oak Ridge, Tennessee*

AND

S. H. SIMONSEN,† *University of Texas, Austin, Texas*

(Received January 18, 1954)

THE ferroelectric modification of KH_2PO_4 which exists at temperatures below 121°K has been examined by single-crystal neutron diffraction techniques at 113°K. Complete data from the (*hkl*) zone of a cylindrical specimen cut parallel to this zone axis were collected at neutron wavelength 1.062A to $\sin\theta/\lambda=0.77$. The data were analyzed by the Fourier synthesis method after applying a modification function[1] $\exp[-3.5(\sin\theta/\lambda)^2]$ to ameliorate termination-of-series errors. Initial phases were computed from the parameters reported by Frazer and Pepinsky[2] with the hydrogen atoms placed 1.08A from oxygen atoms O_1 along the hydrogen bonds. A total of four Fourier projections were prepared from the experimental structure factors. At each stage, correction was made by the back-shift method[3] for residual termination-of-series errors, the correction being based on the initial model of the structure for the first three stages of refinement and on essentially final parameters for the last stage. The final parameters,[4] which are doubly shifted[5] from the corrected output of the fourth Fourier map (maximum shift 0.0005), are listed in Table I. The

TABLE I. Atomic parameters for ferroelectric KH_2PO_4.[a]

	O_1	O_2	H	K
x	0.1160	−0.0345	0.1880	0
y	0.0345	0.1160	−0.0375	0
z	0.1310	−0.1235	0.1355	0.512

[a] Based on orthorhombic space group *Fdd2*, $a_0=10.53$A, $b_0=10.44$A, $c_0=6.90$A (reference 2). Parameters are relative to P at (000). Equivalent positions are (xyz), $(\bar{x}\bar{y}z)$, $(\frac{1}{4}-x, \frac{1}{4}+y, \frac{1}{4}+z)$, $(\frac{1}{4}+x, \frac{1}{4}-y, \frac{1}{4}+z)$, face centered for O and H; $(00z)$, $(\frac{1}{2}, \frac{1}{2}, z+\frac{1}{2})$, face centered for K and P. Temperature factor coefficients in A^2 are: O and P, 0.6; K, 0.4; H, 2.0.

discrepancy factor $\Sigma||F_{obs}|-|F_{calc}||/\Sigma|F_{obs}|$ was 9.4 percent for the initial parameters and 5.9 percent for the final ones.

The results show conclusively that the arrangement of hydrogen atoms is ordered. The hydrogen atoms are situated 1.07A from oxygen atoms O_1, nearly along the hydrogen bonds. The length of the phosphorus-to-hydroxyl-oxygen link is 1.56A, while that of the other P−O link is slightly shorter, 1.53A. The length of the hydrogen bond, O−H···O, is 2.50A. All of these distances are close to those existing in the tetragonal room-temperature modification, where the hydrogen atoms are probably disordered.[6]

Some of the parameters for oxygen derived here differ by small but possibly significant amounts from those given by x-ray diffraction.[2] Should these differences prove to be real, they may indicate that some of the atomic nuclei are displaced away from the centroids of the extranuclear-electron clouds. Such displacements might play a significant role in the ferroelectric behavior of this crystal.

* Work performed at the Oak Ridge National Laboratory under the auspices of the U. S. Atomic Energy Commission.
† Research participant, Oak Ridge Institute of Nuclear Studies, summer of 1952.

[1] J. Waser and V. Schomaker, Revs. Modern Phys. **25**, 671 (1953).
[2] B. C. Fraser and R. Pepinsky, Acta Cryst. **6**, 273 (1953).
[3] A. D. Booth, Proc. Roy. Soc. (London) **A188**, 77 (1946).
[4] Because of overlapping peaks, the (*hkl*) projection cannot yield all the atomic parameters independently. Throughout this treatment, the assumption was made that $x+y$ for O_1 is equal to $y-x$ for O_2, in agreement with the x-ray result (reference 2) and that $x+y$ for H has the same value. The latter assumption places H in a plane parallel to c passing through the hydrogen-bonded oxygen atoms.
[5] Shoemaker, Donohue, Schomaker, and Corey, J. Am. Chem. Soc. **72**, 2328 (1950).
[6] Peterson, Levy, and Simonsen, J. Chem. Phys. **21**, 2084 (1953); G. E. Bacon and R. S. Pease, Proc. Roy Soc. (London) **A220**, 397 (1953).

Theory of the Galvanomagnetic Effects in *n*-Germanium

S. MEIBOOM AND B. ABELES
Weismann Institute of Science, Rehovot, Israel
(Received December 21, 1953)

SEITZ[1] has computed the galvanomagnetic constants of germanium, assuming spherical energy surfaces in momentum space and a relaxation time with cubic symmetry. His results, however, do not fit the published experimental data.[2,3] Shockley[4] has suggested that the energy surfaces may be degenerate, but has not presented any explicit calculations.

We have carried through calculations for *n*-type germanium, based on the following assumptions: (1) The relaxation time is given by $\tau=L/\sqrt{E}$, where E is the energy and L a constant. (2) The energy as function of momentum (**P**) has a number of minima; electrons near each of these minima contribute to the conductivity; and the energy surfaces, near the minima, can be approximated by quadratic functions of **P**.

For brevity, we shall refer to these quadratic functions as ellipsoids. The ellipsoids must be arranged in the Brillouin zone so as to obtain the cubical symmetry of the germanium crystal. We have considered the two simplest models which fulfill this requirement: (a) three rotational ellipsoids, with rotational axes perpendicular to each other; (b) four rotational ellipsoids, with their rotational axes along the body diagonals of a cube.

Model (a) may result when the energy minima are situated at the center of the small faces, and model (b), when they are situated on the large faces, of the first Brillouin zone of the face-centered cubic lattice.[5]

Our calculations are based on the series expansion of the distribution function [e.g., Wilson,[6] Eq. (8.551.3)]. This equation is written in tensor form; terms in H^3 and higher are neglected. On our assumptions, the integrals giving the current [Wilson, Eq. (8.551.4)] can then be computed for each ellipsoid. The total current I is obtained by summing over all the ellipsoids. By inversion, we obtain an expression for E, as function of I and H, in which the coefficients are the galvanomagnetic constants. It was found that the experimental results for *n*-germanium cannot be explained on the basis of model (*a*). Calculations based on this model result in zero longitudinal magnetoresistance effect in the (100) direction. However, a good fit can be obtained, using model (*b*). The only parameter appearing in the results is the ratio K of the effective masses, $K>1$ corresponding to prolate energy ellipsoids and $0<K<1$ to oblate. The results are:

$$R_H=(3\pi/8)[3K(K+2)/(2K+1)^2](1/nec),$$
$$L_{(100)}=(8/3\pi)R_H^2\sigma^3(2K+1)(K-1)^2/K(K+2)^2,$$
$$T_{(100)(010)}=(1/3\pi)R_H^2\sigma^3[K^2(16-3\pi)+K(16-6\pi)+4]/K(K+2),$$
$$L_{(110)}=(1/2)L_{(100)},$$
$$T_{(110)(1\bar{1}0)}=(1/2)L_{(100)}+T_{(100)(010)},$$
$$T_{(110)(001)}=T_{(100)(010)},$$

where the Hall coefficient is denoted by R_H; the conductivity by σ; the number of electrons in the conduction band by n; the longitudinal magnetoresistance coefficient by $L_{(ij)}$ (the indices giving the crystallographic direction of I and H); and the transverse coefficient by $T_{(ij)(mp)}$ (the first set of indices giving the direction of I, and the second set, the direction of H).

TABLE I. Comparison of theoretical and experimental magnetoresistance coefficients (in gauss^{-2}).

Coefficient	Calc[a]	Exp[b]
$L_{(100)}$	$1.91\cdot10^{-9}$	$1.92\cdot10^{-9}$
$T_{(100)(010)}$	0.91	0.90
$T_{(110)(001)}$	0.91	1.03
$T_{(110)(1\bar{1}0)}$	1.86	1.68
$L_{(110)}$	0.95	0.99

[a] Calculated for $K=20$; values for R_H and σ as found by Pearson and Suhl (reference 3) for their *n*-germanium sample at 300°K.
[b] Measurements of Pearson and Suhl on above sample.

Table I shows that the values obtained from these equations for $K=20$ compare closely with the measurements of Pearson and Suhl.[3]

In the equation for R_H, the numerical coefficient gives the ratio of Hall- to drift-mobility. Inserting $K=20$, the value of $0.79(3\pi/8)$ is obtained for this ratio.

Calculations were also made for the sample measured by Pearson and Suhl at 77°K. Agreement was somewhat less satisfactory. However, a better fit can be obtained by taking impurity scattering into account.

[1] F. Seitz, Phys. Rev. **79**, 372 (1950).
[2] I. Esterman and A. Foner, Phys. Rev. **79**, 365 (1950).
[3] G. L. Pearson and H. Suhl, Phys. Rev. **83**, 768 (1951).
[4] W. Shockley, Phys. Rev. **78**, 173 (1950).
[5] L. Brillouin, *Wave Propagation in Periodic Structures* (McGraw-Hill Book Company, Inc., New York, 1946), Fig. 37.11.
[6] A. H. Wilson, *The Theory of Metals* (Cambridge University Press, Cambridge, 1953), second edition.

Origin of Retrograde Motion of Arc Cathode Spots

A. E. ROBSON AND A. VON ENGEL
Clarendon Laboratory, Oxford, England
(Received December 29, 1953)

MINORSKY discovered that if a transverse magnetic field acts on the cathode region of a mercury arc, under certain conditions the cathode spot will move contrary to Ampere's rule.[1] The positive column necessarily remains attached to the spot but is always deflected in the Ampere direction. If the pressure is sufficiently low, the motion is retrograde, but changes to the Ampere direction if the pressure exceeds a critical value which is the greater the lower the current and the stronger the magnetic field. Hitherto no explanation of this effect has carried great conviction.[2] We believe that it can be understood as a classical electrodynamic problem.

Using a tube similar to Gallagher's, at a vapor pressure of $\approx$20 mm Hg and a current of $\approx$10 amp, we observed for moderate

magnetic fields that the spot moved in the Ampere direction and that the constricted positive column immediately above the spot was only slightly deflected. However, in a large field, this part of the column was deflected up to 90° and the movement of the spot reversed.

In the cathode fall region, probably within 10^{-3} cm from the cathode,[2] the electric field is high, but in the constricted column above it, the electric field is very much smaller. An applied magnetic field can therefore cause considerable deflection of the constricted column only and little deflection of the fall region so that the column is sharply curved at the junction. We believe that at the junction of the fall region and the constricted column, the vapor from the spot is excited and ionized. The direction of the resultant electromagnetic force in this region thus determines the direction in which the arc moves, since the location of the spot on the cathode depends on the position of this region in space.

The resultant horizontal force in this region consists of two components. One, proportional to iH, is in the Ampere direction; the other is of order i^2/ρ in the retrograde direction, because of the self-magnetic field of the curved current path consisting of the bent column and the deflected lines of current in the liquid (illustrated by the observed electromagnetic pumping). Here i is the current, H the applied magnetic field, and ρ an equivalent radius of curvature at the junction of the fall region and the constricted column. When $H=10^3$ oersted and $i=10$ amp, the two forces will be equal if $\rho\approx10^{-2}$ cm, which is comparable with the dimensions of the fall region.

If H is increased ρ decreases and the retrograde component is the larger one, and vice versa. If the vapor pressure is increased, the column is constricted along a greater length and it becomes "stiffer" in the given magnetic field. Hence ρ increases and the motion becomes "Ampere." All this agrees with observations.

Retrograde motion is observed for both metal and carbon cathodes provided there is a cathode spot of high current density. If the entire cathode is heated to a temperature at which thermionic emission occurs, the current densities are too low for the self-magnetic field to be significant and retrograde motion ceases.[4]

This letter is published by permission of the Director of the Electrical Research Association, the sponsor of this work. A more detailed account will follow shortly.

[1] M. N. Minorsky, J. phys. et radium 9, 127 (1928).
[2] C. G. Smith, Phys. Rev. 62, 48 (1942); R. L. Longini, Phys. Rev. 71, 642 (1947); G. J. Himmler and G. I. Cohn, Elec. Eng. 67, 1148 (1948); C. J. Gallagher, J. Appl. Phys. 21, 768 (1950).
[3] C. G. Smith, Phys. Rev. 69, 96 (1946).
[4] C. G. Smith, Phys. Rev. 73, 543 (1948).

Short-Lived Metastable States of W^{182}†

A. W. Sunyar
Brookhaven National Laboratory, Upton, New York
(Received January 8, 1954)

THE β decay of Ta^{182} (111 days) is followed by the emission of many gamma rays. The continuous β spectrum, the γ-ray spectrum, and the spectrum of internal conversion electrons have been investigated[1] by several workers. In spite of the fact that the energies of the most prominent gamma rays are known to a high degree of precision,[2] no complete decay scheme has as yet been formulated. An early search for short-lived nuclear isomers by other workers[3] has yielded negative results with an upper limit of 5×10^{-9} sec for the lifetime of any excited state in W^{182} formed by the β decay of Ta^{182}.

The lifetimes of two short-lived metastable states of W^{182} have now been measured by fast-coincidence techniques. The coincidence arrangement used in these measurements is similar to those described by other workers.[4–6] *Trans*-stilbene phosphors on RCA 5819 photomultipliers were used as electron and gamma-ray detectors. Delays were introduced into the appropriate channel by inserting lengths of RG7/U cable. The resolving time used in these measurements was $2\tau\simeq3\times10^{-9}$ sec. Pulse-height selection was imposed upon the pulse distribution from each counter. The outputs of the fast-coincidence circuit and the two pulse-height selectors were mixed in a slow triple-coincidence arrangement in the usual way. As emphasized previously,[4] the precaution of pulse-height selection is necessary to minimize changes in the resolution curve of the coincidence circuit due to differences in input pulse size. The variation in pulse size allowed by the pulse-height selector channel widths was about 12 percent. Prompt-coincidence resolution curves were taken with identical pulse distributions within the limits allowed by the channel widths of the pulse-height selectors. The two lifetimes were found in the following ways:

(1) A typical time distribution of coincidences taken between a portion of the continuous β spectrum and a portion of the Compton distribution arising from hard γ rays is shown in Fig. 1 as $F(t)$.

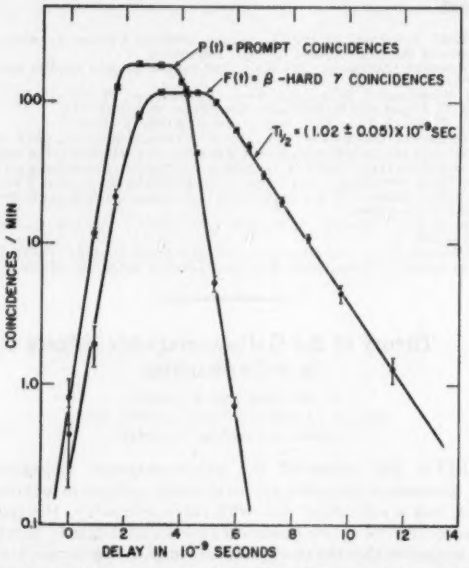

FIG. 1. Time distribution of β—hard γ-ray coincidences. $F(t)$ and $P(t)$ are normalized to the same included area. $F(t)$ has been derived from the experimentally observed $F(t)$ by subtraction of a 17-percent prompt-coincidence component. Narrow window energy selection imposed upon both counters.

$P(t)$ is the prompt resolution curve normalized to the same included area. The $F(t)$ shown is not precisely the experimentally obtained $F(t)$. We shall return to this point later. A centroid analysis[7,8] of $F(t)$ and $P(t)$ leads to the following value for the lifetime of the delayed state: $T_{\frac{1}{2}}=0.98\pm0.07\times10^{-9}$ sec. The lifetime obtained from the exponential tail of $F(t)$ [several runs] is $1.05\pm0.07\times10^{-9}$ sec. We adopt $1.02\pm0.05\times10^{-9}$ sec as the half-life.

The $F(t)$ shown in Fig. 1 was obtained from the experimental $F(t)$ by subtracting a curve of the form of $P(t)$. The subtracted area was 17 percent of the original area. This subtraction was necessary because of an $\sim$17 percent prompt-coincidence component in the Ta β—hard γ delay curve. This prompt component may arise because not all of the hard γ rays following β emission by Ta^{182} are delayed. The presence of low-intensity γ rays of intermediate energy following a different β branch may also contribute to this prompt-coincidence component.

The fact that nearly all hard γ rays are delayed relative to β's does not necessarily mean that all the hard γ rays are the lifetime-determining ones. It is quite possible that a low-energy transition at the top of the decay scheme is responsible for the lifetime entirely, or is in competition with one or more of the γ rays above 1 Mev in energy. It is interesting to note that an $M2$ transition of

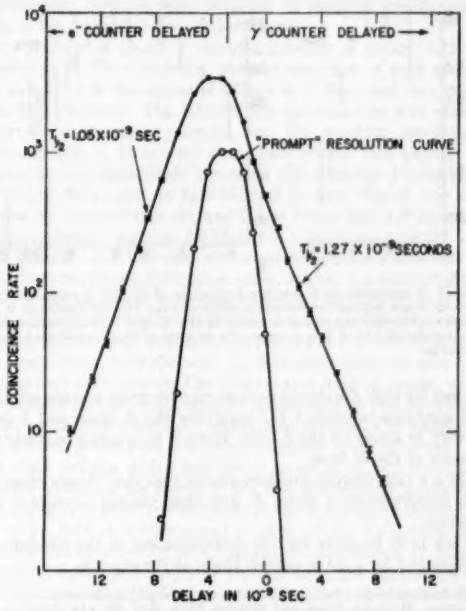

FIG. 2. Time distribution of β^+ conversion electron—hard γ-ray coincidences. Lower-edge energy discrimination imposed upon both counters.

~1.2-Mev energy in W^{182} would be expected to have a half-life of $\sim 1.6\times10^{-8}$ sec (based on the 9×10^{-7} sec half-life[9] for the 513-kev $M2$ transition in Rb^{85}).

(2) A similar coincidence experiment involving coincidences between hard γ rays and soft electrons has shown that conversion electrons of a well-converted low-energy γ ray are delayed with respect to hard γ rays with a half-life of $1.27\pm0.10\times10^{-9}$ sec. It is not possible to obtain the hard γ-conversion electron delay curve free of interference from the β—hard γ lifetime of 1.02×10^{-9} sec even with narrow window energy selectors because of the continuous β-ray spectrum. We therefore show in Fig. 2 the time distribution of coincidences between the electron and hard γ-ray counter taken with lower-edge energy discriminators. The results were checked with narrow-window energy selectors and agreement was obtained with the results shown in Fig. 2.

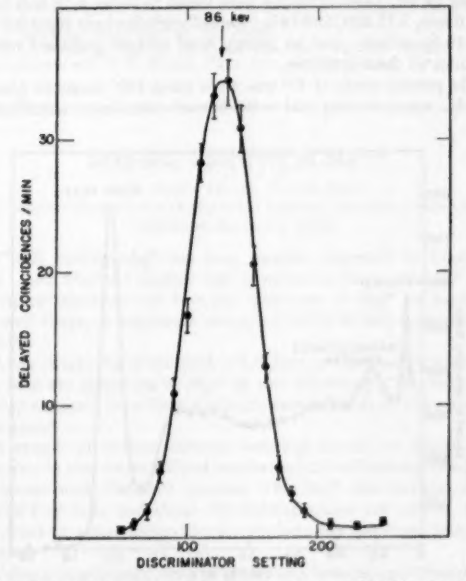

FIG. 3. Pulse-height spectrum of conversion electrons following the decay of the 1.27×10^{-9} sec delayed state.

A pulse-height spectrum of the conversion electrons which show the 1.27×10^{-9} sec lifetime is given in Fig. 3. The spectrum was measured with the hard γ counter delayer by about 6×10^{-9} sec relative to the electron counter. The energy scale was established by pulse-height analysis on the conversion electrons of the 104-kev γ ray in Eu^{152}. We interpret the peak at ~86 kev as the L conversion electron peak of a γ ray of 98 ± 6 kev and identify this with the intense well-converted 100.0-kev γ ray occurring in the decay of Ta^{182}. The 100-kev transition has been shown to be an $E2$ transition[10] and the 1.27×10^{-9} sec lifetime is appropriate for a fast 100-kev $E2$ transition of the "cooperative" type[11,12] in this region of the periodic table. From the fact that no other radiation appears to follow the hard γ rays with this lifetime, we infer that the 100.0-kev state represents the first excited state in W^{182}. This interpretation is in agreement with the energy-systematics of the first excited states of even-even nuclei.[13,14] Further proof of the interpretation that the 100-kev state is the first excited state of W^{182} has been furnished by Coulomb excitation of W.[15]

† Work done under the auspices of the U. S. Atomic Energy Commission.

[1] For a complete list of references see National Bureau of Standards Circular 499 (U. S. Government Printing Office, Washington, D. C., 1950) and its supplements, as well as Hollander, Perlman, and Seaborg, Revs. Modern Phys. **25**, 469 (1953).

[2] Muller, Hoyt, Klein, and Dumond, Phys. Rev. **88**, 775 (1952).

[3] F. K. McGowan, Oak Ridge National Laboratory Report ORNL-952 (1951).

[4] Bell, Graham, and Petch, Can. J. Phys. **30**, 35 (1952).

[5] F. K. McGowan, Oak Ridge National Laboratory Report ORNL-952 (1951).

[6] S. de Benedetti and H. J. Richings, Revs. Modern Phys. **23**, 37 (1952).

[7] T. D. Newton, Phys. Rev. **78**, 490 (1950).

[8] Z. Bay, Phys. Rev. **77**, 419 (1950).

[9] Sunyar, Mihelich, Scharff-Goldhaber, Goldhaber, Wall, and Deutsch, Phys. Rev. **86**, 1023 (1952).

[10] J. W. Mihelich (private communication). The conversion in the various L subshells follows that for $E2$ transitions.

[11] M. Goldhaber and A. W. Sunyar, Phys. Rev. **83**, 906 (1951).

[12] A. Bohr and B. R. Mottelson, Kgl. Danske Videnskab. Selskab, Mat.-fys. Medd. **27**, No. 16 (1953).

[13] G. Scharff-Goldhaber, Phys. Rev. **90**, 587 (1953).

[14] P. Preiswerk and P. Stähelin, Nuovo cimento **10**, 1219 (1953).

[15] T. Huus and J. H. Bjerregaard, Phys. Rev. **92**, 1579 (1953); McClelland, Mark, and Goodman, Phys. Rev. **93**, 904 (1954).

Relative Intensities of π and μ Meson X-Rays of The K and L Series in Low Z Elements*

M. B. STEARNS, S. DEBENEDETTI, M. STEARNS, AND L. LEIPUNER
Carnegie Institute of Technology, Pittsburgh, Pennsylvania
(Received January 15, 1954)

THIS is a preliminary account of work in progress on the x-rays emitted when π and μ mesons[1,2] are captured in light elements. The mesons from a 450-Mev synchrocyclotron are slowed down by a copper absorber and brought to rest in the target of the element investigated (Fig. 1). The stopped mesons

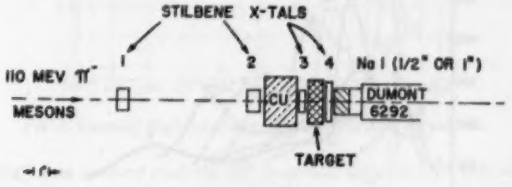

FIG. 1. Detection apparatus.

are detected with an anticoincidence telescope (1+2+3−4) and the resultant x-rays give a pulse in the NaI counter. The NaI pulses are analyzed with a 24-channel pulse-height selector

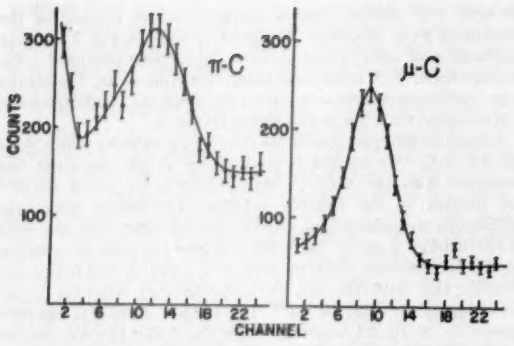

FIG. 2. Typical pulse-height distribution curves of x-rays from the $2p$ to $1s$ transition in C. The first curve corresponds to 400 000 stopped π mesons and the second to 50 000 stopped μ mesons.

whenever they are in coincidence (10^{-7} sec) with the output of the meson telescope.

Meson x-rays from the K, L, and M series have been observed. Typical examples of the curves obtained are shown in Figs. 2 and 3. The width of the peaks is mainly instrumental. Part of this width is due to the statistical fluctuations in the NaI phototube, which are considerable at low energies, and part to the effects of the high singles counting rate. The positions of the peaks agree within our present errors of 10–15 percent with the energies computed in an elementary way.

For the measurements of relative intensities the targets used had the same surface density and linear thickness. After subtracting the background estimated visually from the shape of the curves (this procedure introduces one of the largest errors in the measurement) the counts of all channels within each peak were added together, and then divided by the number of counts in the meson telescope. The relative intensities thus obtained were corrected for (1) absorption of the x-rays in the target and intervening material, (2) chemical effects, (3) NaI detection efficiency, (4) detection efficiency of coincidence circuits. Adequate tests proved that (4) was practically 100 percent down to 25 kev. When compounds were used (N_2H_4 for N, H_2O for O, LiF for F, and LiCl for Cl) it was assumed that each atom, except H, captured in proportion to Z. The intensities from C and CH_2 were found to be the same within 10 percent.

The results for π x-rays are shown in Fig. 4. The small intensity at low Z is believed to be due to competition with the Auger effect. However, if this is the sole contribution to the decreased intensity, our data agree with the approximate estimates of Fermi and Teller[3] but disagree with the calculations of Burbidge and deBorde.[4] The

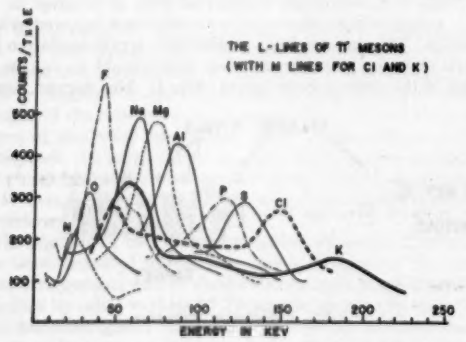

FIG. 3. Pulse-height distribution curves for $\pi - L$ radiation. All curves reduced to the same scale by dividing each reading by telescope counts and by pulse-height-selector channel width. The points have been omitted for clarity. $\pi - M$ radiation appears in Cl and K curves.

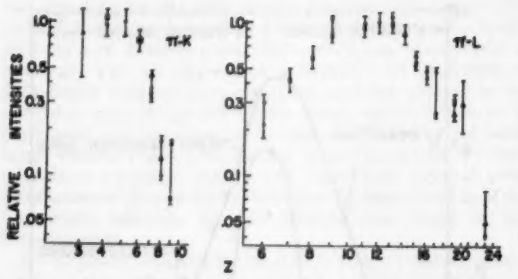

FIG. 4. Z dependence of relative intensities of K and L radiation from π mesons. Each symbol represents a different run. The intensities of B and Mg were arbitrarily set equal to unity in the K and L plots, respectively. The intensity of Li $-K$ line is uncertain because of large corrections due to low energy.

decrease for high Z is due to nuclear capture from mesonic orbits of total quantum number 2 ($2p$ state) for the K lines, and 3 (presumably $3d$ state) for the L lines. Work is in progress to study the behavior of the M lines.

The μ x-rays behave similarly except that the "Auger effect" is more important at a given Z, and that nuclear capture is not observed.

Work is in progress for the determination of the absolute intensities and for a more careful study of the energies.

* Supported in part by the U. S. Atomic Energy Commission.

[1] Camac, McGuire, Platt, and Schulte, Phys. Rev. **88**, 134 (1952).
[2] V. L. Fitch and J. Rainwater, Phys. Rev. **92**, 789 (1953).
[3] E. Fermi and E. Teller, Phys. Rev. **72**, 399 (1947).
[4] G. R. Burbidge and A. H. deBorde, Phys. Rev. **89**, 189 (1953).

Decay of V^{52}

J. M. LEBLANC, J. M. CORK,* S. B. BURSON, AND W. C. JORDAN
Argonne National Laboratory, Lemont, Illinois
(Received January 14, 1954)

THE irradiation of normal V with thermal neutrons has been reported to produce three activities[1] which have been assigned to V^{52}. These activities were found to decay with half-lives of 2.6 min, 3.75 min, and 16 hr. Recent work has been reported[2] on the 16-hr activity and an energy level scheme proposed which includes all three activities.

The present study of V^{52} was made using 180° magnetic photographic spectrometers and a 10-channel coincidence scintillation

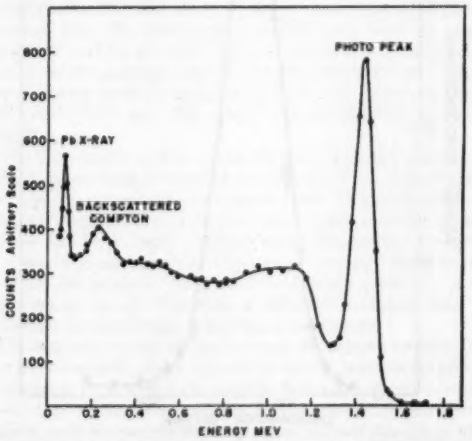

FIG. 1. Gamma-ray pulse-height distribution resulting from V^{52} (3.7 min).

spectrometer. Sources were obtained by neutron irradiation of V_2O_5 in the Argonne heavy water reactor.

Irradiations of about 5 minutes produce a strong 3.75-min activity in V. The conversion electron spectrum of such samples was examined in the region of 10 kev to 2 Mev, and no electron lines were detected. The scintillation spectrometer was used to study the unconverted photons, and the resulting spectrum is shown in Fig. 1. It is clear that there is only one gamma ray present to any appreciable extent in this activity. Its energy is 1.44±0.02 Mev, and its half-life is 3.75 min. The β rays were studied by absorption in Al, and it was found that a β ray whose maximum energy is about 2.6 Mev is in coincidence with the 1.44-Mev gamma ray. The coincidence Al absorption curve did not differ from the singles absorption curve, so that it is concluded that most, if not all, of the beta rays feed the 1.44-Mev level in Cr^{52}.

An attempt was made to detect the 2.6-min activity reported by Renard. Sources were irradiated for periods of 1, 3, and 10 minutes and their decay followed with an ionization chamber and a vibrating reed electrometer. The decay curves were all simple, with a half-life of about 3.7 min. Other investigators[3] also find no evidence for the metastable state in V^{52} reported by Renard. The assignment of a 2.6-min activity to V is thus considered to be doubtful.

A weak activity with a half-life of about 15 hr was found in V samples irradiated for about 15 hr. The scintillation spectrum of this activity, however, corresponds to the spectrum obtained from the 15-hr Na^{24}. A spectroscopic analysis of the V_2O_5 established that Na was an impurity with 0.05 percent abundance. In order to determine if any of the activity was due to V, the Na was chemically separated from the V after irradiation. Both the Na and the V fractions were then counted with the scintillation spectrometer. It was found that the activity of the Na fraction was more than 100 times that of the V fraction, and that the V fraction was only two times the background.

The results of this study indicate that V^{52} decays with a 3.75-min half-life by the emission of a single beta ray of energy 2.6 Mev followed by a gamma ray of energy 1.44 Mev. Neither the 2.6-min nor the 16-hr activity previously reported in V^{52} was found.

The authors wish to thank P. R. Fields, R. F. Barnes, and J. K. Brody of the Argonne National Laboratory for kindly making the chemical separation and spectroscopic analysis.

* University of Michigan, Ann Arbor, Michigan.

[1] E. Amaldi *et al.*, Proc. Roy. Soc. (London) **A149**, 522 (1935); G. A. Renard, Ann. phys. **5**, 385 (1950); Cork, Keller, and Stoddard, Phys. Rev. **76**, 575 (1949); L. A. Turner, Phys. Rev. **58**, 679 (1940).
[2] T. Wiedling, Phys. Rev. **91**, 767 (1953).
[3] J. E. Schwager and L. A. Cox, Phys. Rev. **92**, 102 (1953); G. A. Bartholomew and B. B. Kinsey, Phys. Rev. **89**, 386 (1953).

Beta-Ray Spectrum of Mg^{28}†

J. L. Olsen and G. D. O'Kelley
California Research and Development Company, Livermore, California
(Received January 5, 1954)

THE nuclide Mg^{28} has been recently reported by Lindner[1] and Sheline.[2] Sheline also proposed a decay scheme,[2] and Marquez[4] reported the beta-ray spectrum of Mg^{28} to have an allowed shape, a maximum energy of 418±10 kev, and a logft of 4.25.

As an outgrowth of the work of Lindner, it was possible to study the beta-ray spectrum of Mg^{28} in this laboratory. The beta-ray energy obtained from these measurements differs from the value of Marquez.[4]

A sample of sodium chloride weighing about five grams was wrapped in aluminum foil and bombarded in the Berkeley 184-inch cyclotron with 340-Mev protons. The Mg^{28} was isolated in a carrier-free state and about 10^6 disintegrations per minute were mounted on a thin zapon film for the beta-ray spectrum determinations.

Using a ring-focused, long magnetic lens beta-ray spectrometer,[5] an examination of the electron spectrum was made in the energy range 100 to 3500 kev. A Fermi plot of the data shows two transitions, as may be seen in Fig. 1.

The high-energy component is from Al^{28} whose beta decay has been reported by Motz[6] to have an allowed shape and a maximum energy of 2865±10 kev. He also set a limit of less than two percent for the high-energy beta-ray transition to the ground state.

In the present work the high-energy component from Al^{28} had an allowed shape beyond the Mg^{28} activity, and a least-squares fit of the Fermi plot gave an end point of 2878±14 kev, which within our error is in agreement with the reported values. Also an upper limit of less than 0.8 percent can be set for the high-energy beta-ray transition to the ground state.

The lower-energy component from Mg^{28} was then resolved from the Al^{28} transition by subtracting from the observed activity the

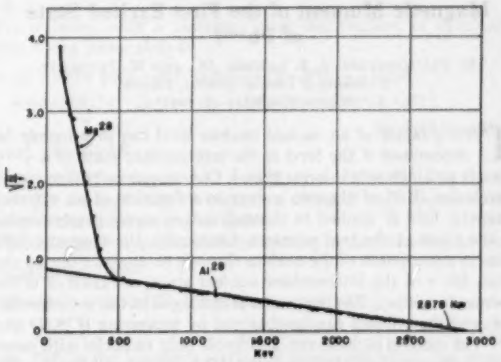

FIG. 1. Fermi analysis of the $Mg^{28}-Al^{28}$ beta-ray spectra.

extrapolated activity of the Al^{28} for a given momentum. The resulting Mg^{28} Fermi plot shows an allowed shape from 100 kev to the end point. By using a least-squares fit, a maximum energy of 459±2 kev was obtained. From the graphs given by Moszkowski[7] the logft value is determined as 4.45.

A check on the Fermi analysis of the low-energy data was made using a carrier-free sample of Cs^{137}, mounted in the same way as the $Mg^{28}-Al^{28}$ mixture. The Cs^{137} Fermi plot, corrected for the forbidden factor a, extrapolated to an energy of 523±2 kev, in excellent agreement with the published values.[8] Figure 2 shows the

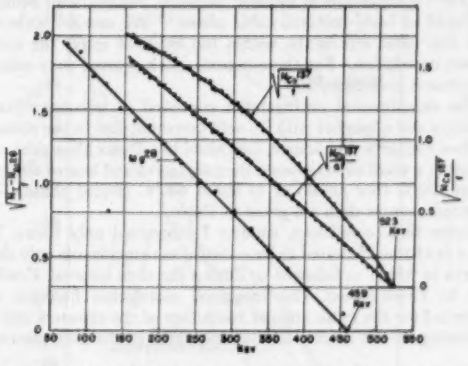

FIG. 2. Resolved Mg^{28} Fermi plot, with Cs^{137} data for comparison.

Mg^{28} data resolved from the Al^{28} spectrum, with the Cs^{137} plot on the same energy axis.

These observations, which agree with the Al^{28} energy, and give a nine percent increase over the Mg^{28} energy previously reported, were reproduced on four spectrometer runs using two separate Mg^{28} samples.

The authors wish to express their thanks to the crew of the 184-inch cyclotron of the University of California Radiation Laboratory and to Dr. M. Lindner for the carrier-free Mg^{28} samples.

* This work was performed under the auspices of the U. S. Atomic Energy Commission.

[1] M. Lindner, Phys. Rev. **89**, 1150 (1953).
[2] R. K. Sheline and N. R. Johnson, Phys. Rev. **89**, 520 (1953).
[3] R. K. Sheline and N. R. Johnson, Phys. Rev. **90**, 325 (1953).
[4] L. Marquez, Phys. Rev. **90**, 330 (1953).
[5] G. D. O'Kelley and J. L. Olsen, California Research and Development Report MTA-38 (unpublished).
[6] H. T. Motz and D. E. Alburger, Phys. Rev. **86**, 165 (1952).
[7] S. A. Moszkowski, Phys. Rev. **82**, 35 (1951).
[8] Hollander, Perlman, and Seaborg, Revs. Modern Phys. **25**, 553 (1953).

Magnetic Moment of the First Excited State of Pb^{204}†

H. Frauenfelder, J. S. Lawson, Jr., and W. Jentschke
University of Illinois, Urbana, Illinois
(Received January 11, 1954)

THE g factor of an excited nuclear level can in principle be determined if the level is the intermediate state of a $\gamma-\gamma$ cascade and if its spin is larger than $\frac{1}{2}$. One measures the directional correlation $W(\theta)$ of the two γ rays as a function of an external magnetic field H applied to the radioactive source perpendicular to the plane of the two counters. Classically, the magnetic field induces a precession of the nucleus through an angle $\omega\tau$ during the mean life τ of the intermediate nuclear state; $\omega=g\mu_N H/\hbar$ is the Larmor frequency. The precession is displayed in the $\gamma-\gamma$ correlation and the g factor can be obtained by measuring $W(\theta,H)$ and τ.[1,2] The method is, however, applicable only to nuclei with mean lives between about 10^{-9} sec and 10^{-6} sec. Consequently, the selection of available nuclides is very restricted and the g factor of only one excited state (Cd^{111}) has been measured to date.[3] We report here a second case, the determination of the g factor of the first-excited state of the even-even nucleus Pb^{204}.

The isomer Pb^{204*} ($T_{\frac{1}{2}}=65$ min) decays through a $\gamma-\gamma$ cascade [$E(\gamma_1)=0.905$ Mev, $E(\gamma_2)=0.374$ Mev]; the intermediate state has a spin 2 and a mean life $\tau=4.3\times10^{-7}$ sec[4] (Fig. 1). We have shown in a previous paper[5] that the directional correlation between γ_1 and γ_2 is strongly perturbed in almost all types of sources by the interaction between the nuclear quadrupole moment and electric field gradients of the surroundings. We found, however, that the anisotropy $A=[W(180°)/W(90°)]-1$ is highest when the Pb^{204} is imbedded in metallic thallium, the thallium being in its liquid or body-centered cubic phase.[5,6] We moreover showed that this value represents, within the limits of error, the undisturbed correlation.[5] For these reasons, such sources were used in the present investigation.

The experimental arrangement consisted of two scintillation counters and a magnet with its field perpendicular to the plane of the two counters. The source, contained in a Pyrex glass tube, was placed in a small oven between the pole pieces and heated either to about 270°C (bcc phase) or to about 400°C (liquid phase). The essential counter data are given in Table I.

Under these conditions, counter I responded only to γ_1. The delay in channel I caused to be recorded as coincidences only those decays in which γ_2 followed γ_1 during the time interval $T_1=0.08$ μsec to $T_2=0.66\mu$sec. The measured correlation function was corrected for the finite angular resolution of the counters and for scattering in the source, in the oven, and in the pole pieces by comparing the zero-field anisotropy with the anisotropy determined in an experiment with much less scattering material around the source and with known geometry.[5]

TABLE I. Characteristics of the counting system.

Counter	Lead shielding Lateral	Lead shielding Front	Discriminator level	Delay	Resolving time
I	1.5 cm	none	0.60 Mev	0.37μsec	0.290μsec
II	1.5 cm	0.2 cm	0.25 Mev	none	

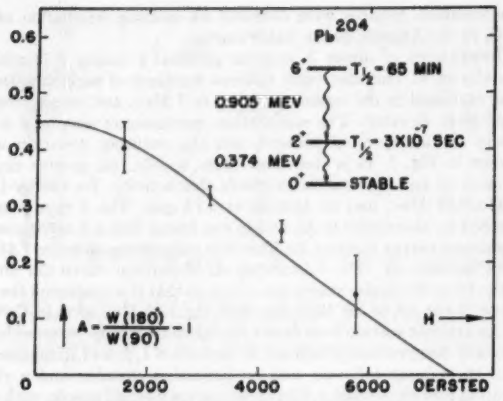

FIG. 1. Decay scheme of Pb^{204} and anisotropy A of the Pb^{204} $\gamma-\gamma$ cascade as a function of an external magnetic field H. The solid line represents the theoretical curve for a g factor with an absolute value of 0.07.

We have performed two sets of experiments. In the first set, we determined the anisotropy A as a function of the field strength H. The results are shown in Fig. 1. Such a measurement clearly yields the magnitude but not the sign of g. In the second set, we measured the correlation function at the angles $\theta=75°$, 105°, 140°, 180°, and 220°, for two different field strengths H. Without field, the correlation function assumes the same values for 75° and 105° and for 140° and 220°. With field, the correlation function shifts and at the same time decreases in amplitude (Fig. 2). The direction of the magnetic field and the sense of the angular shift immediately determine the sign of g. For Pb^{204*}, g was found to be positive.

In order to calculate g from the experimental data, we integrated the theoretical expression for the delayed correlation function $W_d(t)$ [Eq. (127) of reference 2] from T_1 to T_2, inserted the experimental values, and solved the resulting lengthy expression numerically. The final result (solid line in Fig. 1 and dotted line in Fig. 2) is

$$g\ (Pb^{204},\ \text{first-excited state}) = +\left(0.07^{+0.06}_{-0.03}\right).$$

The main contributions to the symmetric part of the error, ±0.03, arise from statistics and from uncertainties in magnetic field, lifetime, delay time, and resolving time. The asymmetric part, $+0.03$, stands as an insurance against possible perturbations from remaining electric field gradients, which tend to lower the measured g factor.[7]

With the known spin 2 of the first-excited state of Pb^{204}, the magnetic moment becomes

$$\mu\ (Pb^{204},\ 2^+) = \pm\left(0.14^{+0.12}_{-0.06}\right)\mu_N.$$

Even though this is only a preliminary value, the following conclusions can be drawn.

The small magnetic moment supports Bohr and Mottelson's supposition[8] that the 2^+ state in Pb^{204} is not a rotational state, but is due to pure neutron excitation (Pb is proton magic). Ford has calculated the excitation energy of the first, excited state in Pb^{204} in a strong-coupling approximation and gets best agreement with the experimental value for the states $[(i_{13/2})^{-4}]_N$ and $[(p_{1/2})^{-2}(i_{13/2})^{-2}]_N$.[9] A mixture[10,11] of these two states would probably yield a moment in agreement with our experimental value.

The small g factor also supports the, perhaps questionable,[10] mass assignment 204 to the 65-min activity, because both Pb^{200} and Pb^{206} are expected to have a larger g factor. We have more-

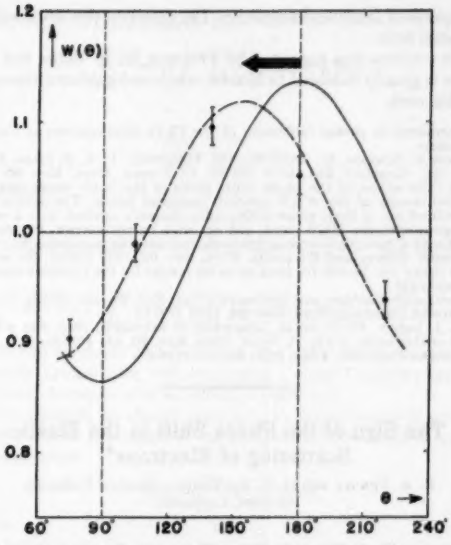

FIG. 2. Angular shift of the directional correlation function $W(\theta)$ of the Pb^{204} $\gamma-\gamma$ cascade in an external magnetic field H. The solid line represents the zero-field correlation; the dotted line is the theoretical curve for $g=+0.07$ and $H=4300$ oersteds. The arrow indicates the classical precession angle of a magnetic dipole.

over shown by simultaneous irradiation of natural Tl and of Tl enriched in Tl^{203} with deuterons, that the 65-min activity is produced from Tl^{203} and therefore cannot be Pb^{204}.

† Assisted by the joint program of the U. S. Office of Naval Research and the U. S. Atomic Energy Commission.

[1] K. Alder, Helv. Phys. Acta **25**, 235 (1952).
[2] L. C. Biedenharn and M. E. Rose, Revs. Modern Phys. **25**, 729 (1953).
[3] Aeppli, Albers-Schönberg, Frauenfelder, and Scherrer, Helv. Phys. Acta **25**, 339 (1953).
[4] Sunyar, Alburger, Friedlander, Goldhaber, and Scharff-Goldhaber, Phys. Rev. **79**, 181 (1950).
[5] Frauenfelder, Lawson, Jentschke, and DePasquali, Phys. Rev. **92**, 1241 (1953).
[6] Frauenfelder, Lawson, Jentschke, and DePasquali, Phys. Rev. **92**, 513 (1953).
[7] A. Abragam and R. V. Pound, Phys. Rev. **92**, 943 (1953).
[8] A. Bohr and B. R. Mottelson, Kgl. Danske Videnskab. Selskab, Mat.-fys. Medd. **27**, No. 16, 117 (1953).
[9] K. W. Ford, Phys. Rev. **90**, 29 (1953).
[10] P. Stähelin and P. Preiswerk, Nuovo cimento **10**, 1219 (1953).
[11] A. De-Shalit and M. Goldhaber, Phys. Rev. **92**, 1211 (1953).

Scattering of High-Energy Electrons by Heavy Nuclei*

ELIZABETH UREY BARANGER
California Institute of Technology, Pasadena, California
(Received January 5, 1954)

THE elastic scattering of high-energy electrons is a tool which can be used to obtain information on the radius and charge distribution of nuclei. There have been several numerical calculations of this process.[1,2] Although the numerical method will undoubtedly remain the most accurate, it may be thought that an analytical solution, even if approximate, would help in the understanding of the physical happenings and would show more clearly the dependence on the various parameters involved. The Born approximation is such an analytical method; however, it cannot be trusted for such heavy nuclei as gold or lead, because $Ze^2/\hbar c$ is too large.

The purpose of this letter is to report on some results obtained with the WKB method. This method is applicable if the potential varies slowly over distances of the order of the electron wavelength. This is the case if $kR\gg1$, where R is the radius of the nucleus and $k=\lambda^{-1}$ is the electron wave number. At the energies at which the experiments of Hofstadter, Fechter, and McIntyre[3] have been done (~125 Mev), kR is about 5 for heavy nuclei. This is about the lower limit of the energy region where the WKB method can be considered valid.

We start from the Dirac equation and neglect the mass of the electron. In that case the phase shift η depends only on the angular momentum j, and not on the parity.[4] We apply the WKB method in the form given by Bessey and Uhlenbeck,[5] with the result

$$\eta_j=\lim_{r\to\infty}\left\{\int_{r_0}^{r}Q(r')dr'-kr-\alpha\ln 2kr+l\frac{\pi}{2}\right\}, \tag{1}$$

where $Q(r)=[(k-V(r)/\hbar c)^2-l^2/r^2]^{\frac{1}{2}}$; $V(r)$ is the potential energy; r_0 is the turning point, i.e., $Q(r_0)=0$; $\alpha=Ze^2/\hbar c$; and l is *defined* as $j+\frac{1}{2}$.

For instance, with a uniform charge distribution, of external radius R, the phase shift is

$$\eta_j=\alpha(1-x^2)^{\frac{1}{2}}+\tfrac{1}{2}\alpha(1-x^2)^{\frac{1}{2}}-\alpha\ln[1+(1-x^2)^{\frac{1}{2}}]-\alpha\ln kR$$
$$+(\alpha^2/2kR)[x^{-1}\sin^{-1}x-(1-x^2)^{\frac{1}{2}}+\tfrac{2}{3}(1-x^2)^{\frac{1}{2}}x^2(4-x^2)],$$
$$\text{for } l<kR; \tag{2}$$
$$\eta_j=\eta_j^c, \quad \text{for } l>kR,$$

where $x=1/kR$, and η_j^c is the Coulomb phase shift. In going from (1) to (2), we kept only the first two terms of the expansion in powers of the small parameter α/kR.

The cross section is conveniently written in the following form:

$$d\sigma/d\Omega=\sec^2\tfrac{1}{2}\theta\,|f(\theta)|^2,$$
$$f(\theta)=f^c(\theta)+(2ik)^{-1}\sum_l l[\exp(2i\eta_l)-\exp(2i\eta_l^c)]$$
$$\times[P_l(\cos\theta)+P_{l-1}(\cos\theta)], \tag{4}$$

where $f^c(\theta)$ is the Coulomb scattering amplitude which has been calculated, at high energies, by Feshbach,[6] and more recently by Yennie *et al.*[7]

The number of terms in the summation in (4) is of order kR. Doing this sum exactly, but using the WKB phase shifts, we obtain the results shown in Figs. 1, 2, 3. It should be noted that the cross section depends only on the combination kR, except for a factor $1/k^2$. In Fig. 1, it is seen that the result compares favorably with the numerical one of Yennie *et al.* There is no agreement between this calculation and the Born approximation. The maxima

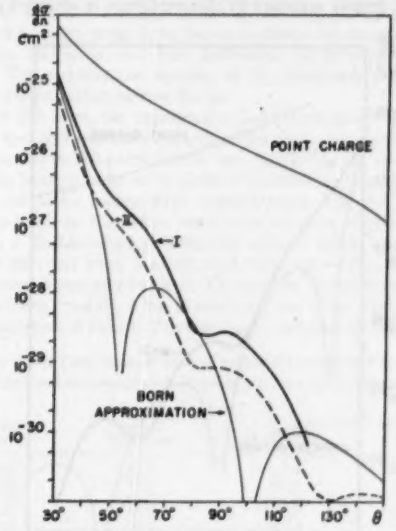

FIG. 1. The differential scattering cross section for a uniform charge distribution. Curve I is the result of the WKB method for $Z=80$, with $kR=5$, $R=1.4A^{\frac{1}{3}}\times10^{-13}$ cm. Curve II is the result obtained by Yennie *et al.* for $Z=79$, $kR=5.4$, $R=1.22A^{\frac{1}{3}}\times10^{-13}$ cm.

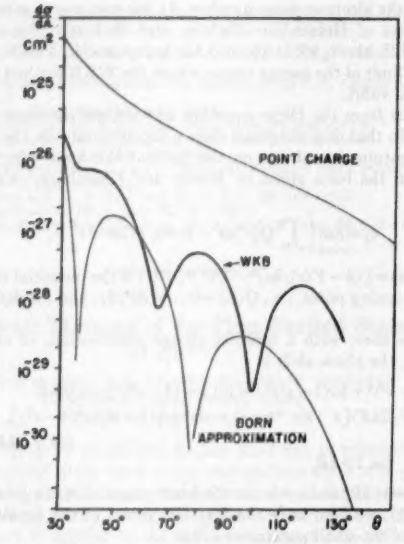

FIG. 2. The differential scattering cross section for a shell distribution with $Z=80$, $kR=5$, and $R=(3/5)^{\frac{1}{2}}\times 1.4A^{\frac{1}{3}}\times 10^{-13}$ cm.

and minima of the Born approximation are greatly smoothed out, especially the first one, and shifted to smaller angles.

However, for reasons given at the beginning of this letter, it would be more interesting to do the summation by an analytical method. We are at the moment working on such a method, involving the replacement of the sum over j by an integral and $P_l(\cos\theta)+P_{l-1}(\cos\theta)$ by $2J_0(2l\sin\frac{1}{2}\theta)$. It then becomes evident that most of the $f^c(\theta)$ part cancels against the Σ part, leaving a result much smaller than the Coulomb amplitude. The method also shows that the Born approximation is only one of several terms which must be taken into account, and not always the largest. By including a sufficient number of corrections to our integral, it is possible to reproduce exactly the curves of Figs. 1–3. However, greater accuracy in this procedure is obtained only at the expense of analytical simplicity. The details of this work will be published later.

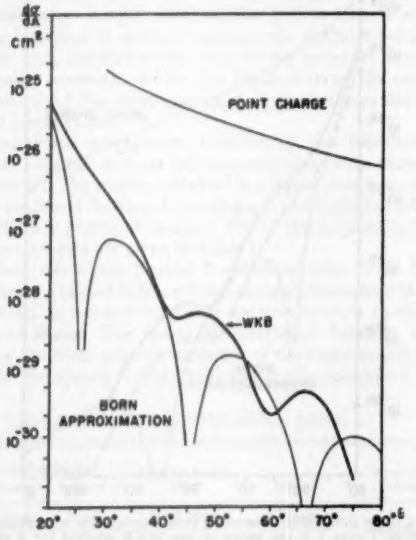

FIG. 3. The differential scattering cross section for a uniform distribution with $Z=80$, $kR=10$, $R=1.4A^{\frac{1}{3}}\times 10^{-13}$ cm.

This problem was suggested by Professor H. A. Bethe and the author is greatly indebted to him for continued guidance throughout this work.

* Submitted in partial fulfillment of the Ph.D. requirements at Cornell University.

[1] Louis K. Acheson, Jr., Phys. Rev. **82**, 488 (1951); L. R. B. Elton, Proc. Phys. Soc. (London) **A63**, 1115 (1950); G. Parzen, Phys. Rev. **80**, 355 (1950). The values of the phase shifts given in the latter paper disagree with the results of the WKB method, discussed below. The author has recalculated one of these phase shifts, using Parzen's method, with a result that agrees with the WKB value, and not with Parzen's result. Parzen has since found a numerical error in his work (private communication).

[2] Yennie, Wilson, and Ravenhall, Phys. Rev. **92**, 1325 (1953). We would like to thank Dr. Yennie for sending us his results for the Coulomb scattering amplitude.

[3] Hofstadter, Fechter, and McIntyre, Phys. Rev. **91**, 422 (1953).

[4] Herman Feshbach, Phys. Rev. **84**, 1206 (1951).

[5] R. J. Bessey, Ph.D. thesis, University of Michigan, 1942. For a brief report of this work, see R. H. Good, Phys. Rev. **90**, 131 (1953).

[6] Herman Feshbach, Phys. Rev. **88**, 295 (1952).

The Sign of the Phase Shift in the Elastic Scattering of Electrons*

D. R. YENNIE AND D. G. RAVENHALL, *Stanford University, Stanford, California*

AND

E. BARANGER, *California Institute of Technology, Pasadena, California*

(Received January 7, 1954)

IN the phase-shift analysis of the scattering of electrons from a nuclear charge distribution, the total phase shift can be expressed as the sum of two terms:

$$\eta_l=\eta_l^c+\delta_l. \tag{1}$$

η_l^c is the phase shift of the lth partial wave for a pure Coulomb field and δ_l is the additional phase shift due to the modification of the Coulomb field inside the nucleus. It is the purpose of this note to point out an error in the literature,[1] in which it is asserted that for large l, δ_l approaches zero through positive values. It will be shown for all reasonable charge distributions inside the nucleus that $\delta_l<0$. For simplicity we neglect the rest energy of the electron compared to the total energy; with a slight modification the proof can be carried through in the more general case. In dimensionless form, the equations giving the radial wave functions are

$$\begin{aligned}(d/dx)F_{l,v}+[(l+1)/x]F_{l,v}-(1-v)G_{l,v}=0,\\ (d/dx)G_{l,v}-[(l+1)/x]G_{l,v}+(1-v)F_{l,v}=0,\end{aligned} \tag{2}$$

with

$$x=Er/\hbar c, \quad v=V/E.$$

For large x, $G_{l,v}$ has the asymptotic form

$$G_{l,v}\sim\sin(x+\gamma\ln 2x-\tfrac{1}{2}l\pi-\eta_l^c+\delta_{l,v}). \tag{3}$$

According to Elton,[1] the difference in the phase shifts due to two different potentials v and v' is given by

$$\sin(\delta_{l,v'}-\delta_{l,v})=-\int_0^\infty (v'-v)(F_{l,v'}F_{l,v}+G_{l,v'}G_{l,v})dx. \tag{4}$$

Our proof is based on the fact that the potential can be varied continuously from the pure Coulomb potential to the final value in such a way that for each small change in v the corresponding change in δ_l is negative. For example, we may define a one-parameter family of potentials:

$$v_\epsilon(x)=\epsilon^{-1}v(x/\epsilon), \quad 0\leqslant\epsilon\leqslant 1; \tag{5}$$

(v_ϵ is the same function of x as v is for an energy ϵE). As ϵ approaches zero, v_ϵ approaches the pure Coulomb potential; at the other limit v_ϵ approaches the potential given by the charge distribution. Explicitly:

$$v_\epsilon=-(\gamma/x)\int_0^{x/\epsilon}\rho x^2dx-(\gamma/\epsilon)\int_{x/\epsilon}^\infty \rho x dx, \tag{6}$$

with

$$\gamma=Ze^2/\hbar c, \quad \int_0^\infty \rho x^2dx=1. \tag{7}$$

Using (4), it is readily shown that

$$\frac{d\delta_l(\epsilon)}{d\epsilon}=-\int_0^\infty\left(\frac{dv_\epsilon}{d\epsilon}\right)(G_{l\epsilon}^2+F_{l\epsilon}^2)dx. \tag{8}$$

But

$$\frac{dv_\epsilon}{d\epsilon}=\frac{\gamma}{\epsilon^2}\int_{x/\epsilon}^\infty \rho x dx. \tag{9}$$

Therefore

$$\delta_l<0, \tag{10}$$

providing ρ is positive everywhere. Rewriting (8) with the aid of (9),

$$\frac{d\delta_l(\epsilon)}{d\epsilon}=-(\gamma/\epsilon^2)\int_0^\infty \rho(x')x'\left\{\int_0^{x'}[G_{l\epsilon}^2(x)+F_{l\epsilon}^2(x)]dx\right\}dx'. \tag{11}$$

From this it seems plausible that the phase shifts tend monotonically toward zero with increasing l, since the inner integral probably decreases with increasing l (fixed x').

In conclusion, we should point out the actual source of error in Elton's paper. He estimates the phase shifts (for large l) by the approximation

$$\delta_l\cong-\int_0^\infty (V_l/\alpha)G_l^2dx, \tag{12}$$

where

$$V_l=(v_E-v_P)(2-v_E-v_P)+x^{-1}(l+1)[(\alpha_P'/\alpha_P)-(\alpha_E'/\alpha_E)]$$
$$+\tfrac{1}{4}[(\alpha_E'/\alpha_E)^2-(\alpha_P'/\alpha_P)^2]-\tfrac{1}{2}[(\alpha_E''/\alpha_E)-(\alpha_P''/\alpha_P)], \tag{13}$$
$$\alpha=1-v.$$

The subscript P refers to the point charge and E to the extended charge. Elton considers the term in $(l+1)$ to be dominant for large l, leading to $\delta_l\to+0$. The fallacy in the argument lies in neglecting the fact that G_l depends on l. This can be seen by carrying out an integration by parts in the term involving the second derivatives of α_E and α_P. The result is a contribution which cancels the term which Elton considered to be dominant.

* Supported in part by the Office of Scientific Research, Air Research and Development Command.

[1] L. R. B. Elton, Proc. Phys. Soc. (London) **A65**, 481 (1952). In a private communication, Dr. Elton concurs that his paper is in error.

[2] L. R. B. Elton, Proc. Phys. Soc. (London) **A66**, 806 (1953). In deriving (4), Elton takes one of the two potentials to be the Coulomb potential, but the proof is also valid for any two potentials so long as the integral converges.

Further Production of Transcurium Nuclides by Neutron Irradiation

BERNARD G. HARVEY, STANLEY G. THOMPSON, ALBERT GHIORSO, AND GREGORY R. CHOPPIN
Radiation Laboratory and Department of Chemistry, University of California, Berkeley, California

(Received January 14, 1954)

IN a continuation of the work previously reported,[1] we have succeeded in producing and chemically identifying an isotope of the element with atomic number 100 through neutron irradiation of the heavy californium isotopes in the Materials Testing Reactor. The method of chemical isolation consisted of precipitation and ion exchange procedures,[1] and the atomic number identification depends on the position in the elution sequence in the ion exchange adsorption-elution method of separation of the actinide elements.[2]

Alpha particles of roughly 7.2-Mev energy and about 3-hour half-life were found in the ion exchange column fraction corresponding to the eka-erbium position immediately preceding the 6.6-Mev alpha particles[1] due to element 99 which eluted in the eka-holmium position immediately preceding the californium alpha activity.[1] Although the amount of activity was small, the identification of atomic number is regarded as definite.

The isotope of element 100 emitting the approximately 7.2-Mev alpha particles is tentatively assigned[3] as 100^{254}, and a possible reaction sequence leading to its production might be the following:

$$Cf^{253}(n,\gamma)\ Cf^{253}\xrightarrow{\beta^-} 99^{253}(n,\gamma)99^{254}\xrightarrow{\beta^-} 100^{254}.$$

Because of the existence of unpublished information on element 100 the question of its first preparation should not be prejudged on the basis of this paper.

It is a pleasure to acknowledge that this work was accomplished with the helpful guidance of Professor Glenn T. Seaborg. Special thanks are due Almon E. Larsh for his valuable assistance with some of the measurements. We wish to acknowledge the help of Dr. W. B. Lewis and the entire Phillips MTR staff for aid in the irradiation of the sample. The continued interest and encouragement of Professor Ernest O. Lawrence and the support of the U. S. Atomic Energy Commission are gratefully acknowledged.

[1] Thompson, Ghiorso, Harvey, and Choppin, Phys. Rev. (to be published).

[2] See, e.g., G. T. Seaborg, *Transuranium Elements: Survey*, edited by G. T. Seaborg and J. J. Katz (McGraw-Hill Book Company, Inc., New York, 1954), National Nuclear Energy Series, Plutonium Project Record, Vol. 14A, Div. IV, Chap. 17 (to be published).

[3] G. T. Seaborg, University of California Radiation Laboratory Report UCRL-1942, March, 1952 (unpublished). (Ohio State University Third Annual Phi Lambda Upsilon Lecture Series.)

Total Cross Sections of 135-Mev to 250-Mev Negative Pions in Hydrogen*

J. ASHKIN, J. P. BLASER, F. FEINER, J. GORMAN, AND M. O. STERN
Carnegie Institute of Technology, Pittsburgh, Pennsylvania

(Received January 13, 1954)

TRANSMISSION measurements yielding the total cross section for the interaction of negative pions with protons have been reported by Anderson *et al.*[1] at Chicago and by Yuan and Lindenbaum[2] at Brookhaven. The Chicago measurements showed a rapid increase of the cross section above 80 Mev with a leveling off or perhaps a maximum at 66±6 millibarns in the region of 150 to 200 Mev. The Brookhaven measurements above 265 Mev gave values well below the maximum Chicago value, thus confirming the existence of a maximum in the cross section in the energy range of the Chicago experiments. The work reported here with the 450-Mev Carnegie Institute of Technology cyclotron covers the energy range from below to above the maximum with the same technique and with somewhat better accuracy than before. This permits the location of the maximum of the cross section within rather narrow limits.

Up to 220 Mev, the experiments have been made with quite intense and well-collimated beams of negative pions with intensities from 300 to 500 particles/cm² sec. At the highest energy, 260 Mev, the beam is reduced to about 3 particles/cm² sec, but this is readily usable for transmission measurements. The pions emerge from channels in the 8-foot magnetite concrete shielding, pass through a double-focusing deflecting magnet which bends them through 45°, and enter a monitoring telescope which determines the number of particles incident. The monitor telescope consists of three stilbene crystals, 4 cm in diameter and ½ cm thick, with a total separation of 115 cm. The beam next traverses the absorber, a

TABLE I. Total cross sections of negative pions in hydrogen.

Energy Mev	Cross section 10^{-27} cm²	Error (10^{-27} cm²) Statistical	Total
133±7	46.9	±1.3	±2.4
157±8	62.9	±1.0	±2.4
179±8	65.9	±1.2	±2.5
194±7	64.6	±1.2	±2.5
195±7	63.1	±1.3	±2.5
215±8	55.5	±1.0	±2.2
236±7	46.1	±1.7	±2.4
240±7	43.5	±1.6	±2.3
258±9	38.2	±3.0	±3.4

column of liquid hydrogen, 4.7 inches long in the beam direction, contained in a styrofoam box.[3,4] The mesons that are not absorbed are detected by a 4-inch diameter liquid scintillation counter in coincidence with the monitor, with mid-plane 22 cm from the center of the hydrogen and 42 cm from the third monitor counter. A dummy target with total thickness of 6 inches of styrofoam in the beam direction was used to obtain the effect of the styrofoam on the transmission. From the ratio of the transmissions (fourfold to threefold coincidences) with and without hydrogen, one obtains directly the total cross section.

In Table I, we have listed the cross sections obtained after the necessary corrections have been applied. Corrections have been made for the following effects:

(1) The incident beam is diluted by the presence of muons to the extent of 5 to 10 percent. The muons are assumed to traverse the hydrogen with no absorption. The percentage of muon contamination is estimated from the range curve for the incident beam (taken with copper absorber) and is probably uncertain to ± 2 or 3 percent. The electron contamination of the beam was shown to be unimportant.

(2) Accidental coincidences in the last detecting counter give an occasional apparent transmission when the meson is really absorbed. These accidentals range from 1 to 3 percent and are considered uncertain to ± 0.5 or ± 1 percent.

(3) Mesons scattered forward into the solid angle defined by the last counter are not recorded as scattered. In addition, a meson scattered sufficiently backward gives a recoil proton which may be detected and thus give a false transmission. Corrections for these events were made on the basis of the Chicago angular distributions of negative pion scattering in hydrogen.[5] They amount to about 3 millibarns with an uncertainty of perhaps ± 1 millibarn.

(4) Effects caused by the angular spread of the beam. From the geometry used and from the measured divergence of the beam, the divergence effects can be shown to be negligible.

The last two columns of Table I contain estimates of the errors in the results. Since we feel that a systematic error which varies strongly with the meson energy is unlikely in view of the fact that all measurements were taken with the same equipment, we have given the error due to counting statistics alone as a measure of the relative error in the measurements. The last column contains an estimate of the total error, taking account of the uncertainties already mentioned. The first column gives the mean meson energy in the center of the hydrogen and the combined energy spread due to the beam inhomogeneity and the energy loss in the hydrogen.

The total cross sections are also shown graphically in Fig. 1 with a smooth curve drawn through the points. It is of some

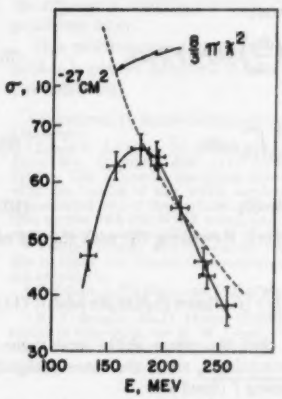

FIG. 1. Total cross sections of negative pions in hydrogen.

theoretical interest[6] to compare the measured values with $(8/3)\pi\lambda^2$, the maximum possible negative meson cross section for the $P_{\frac{3}{2}}$ state of isotopic spin $\frac{3}{2}$. If there is a resonance in this state, the data would indicate that it lies somewhere near 200 Mev and that in this region the other states of angular momentum and isotopic spin contribute surprisingly little to the total cross section. From the total cross section measurements alone it is not possible to decide whether the resonance is real. Measurements of the angular distribution of the scattered mesons in this energy range have been performed at Chicago, but the analysis is so far not complete.[7]

It is a pleasure to express our thanks to S. Friedberg and J. Zimmerman of the Carnegie Institute of Technology Low Temperature Laboratory for expert advice in the production and handling of liquid hydrogen.

* Research partially supported by the U. S. Atomic Energy Commission.
[1] Anderson, Fermi, Long, and Nagle, Phys. Rev. **85**, 934 (1952).
[2] L. Yuan and S. J. Lindenbaum, Bull. Am. Phys. Soc. **28**, No. 6, 13 (1953); Phys. Rev. **92**, 1578 (1953).
[3] We wish to thank L. Marshall for information about the styrofoam target for liquid hydrogen which was used in connection with the proton-proton scattering experiments at Chicago.
[4] The styrofoam box containing the hydrogen was lined with a one-mil copper form to keep the hydrogen from having direct contact with the plastic and to better define the geometrical volume occupied by the hydrogen. Nevertheless, we consider that we do not know the thickness of hydrogen in the beam direction to better than ± 2 percent. This is taken into account in the final error quoted on the cross sections, but should not affect the relative values at different energies.
[5] Fermi, Glicksman, Martin, and Nagle, Phys. Rev. **92**, 161 (1953).
[6] K. A. Brueckner, Phys. Rev. **86**, 106 (1952).
[7] See, however, R. L. Martin, Bull. Am. Phys. Soc. **29**, No. 1, 28 (1954), where a phase shift analysis showing a resonance is reported.

CONTENTS

THE PHYSICAL REVIEW SECOND SERIES, VOLUME 92, NO. 5 MARCH 1, 1953

Albedo of Various Materials for 1-Mev Photons . . . . . Evans Hayward and John Hubbell 905

Measurement and the Calculation of the Liquid Helium Vapor Pressure-Temperature Scale from 1° to 4.2°K . . . . . R. A. Erickson and L. D. Roberts 907

Nonsingle Scattering of Electrons at Oblique Incidence . . . . Morton Hamermesh and James Monahan 913

Excitation of Plasma Oscillations . . . . . Duncan H. Looney and Barbara C. Brown 915

Diffusion of Antimony in Silver . . . . . R. Sauder, L. Slifkin, and C. T. Tomizuka 919

Effect of Screening on Solute Diffusion in Metals . . . . . David Lazarus 923

Infrared Absorption, Photoconductivity, and Impurity States in Germanium . W. Kaiser and H. Y. Fan 927

Mechanism of Secondary Electron Emission . . . . . A. O. Baroni 931

X-Ray Coloration of Alkali Halides . . . . . D. L. Dexter 939

Effect of Pressure on F-Center Absorption in Alkali Halides . . . . . I. S. Jacobs 943

Superconductivity of Some Transition Metal Compounds . . . . George F. Hardy and John K. Hulm 1003

X-Ray-Induced Photostimulated Conductivity in Magnesium Oxide . . . . . Albert S. Eisenstein 1017

Zeeman Effect and Line Breadth Studies of the Microwave Lines of Oxygen . . . . . Robert M. Hill and Walter Gordy 1019

Some Observations of Double- and Triple-Quantum Transitions . . . . . E. Kusch 1022

Determination of the Energy of Antimony-Beryllium Photoneutrons . . . . . Richard Culp and Bernard Hamermesh 1025

Half-Life of Yttrium-90 . . . . . A. Chatham-Strode, Jr., and E. M. Kinderman 1029

Slow Neutron Resonances in Cerium, Palladium, and Gold . . . . . H. H. Landon and V. L. Sailor 1030

Isomeric State of Ga^{68} . . . . . Bernd Crasemann 1034

Gamma Rays from the Proton Bombardment of Sodium . . . . . J. W. Tunnicliffe, L. W. Seagondollar, and R. W. Krone 1035

Inelastic Scattering of 31-Mev Protons from Heavy Elements . . . . . R. M. Eisberg and G. Igo 1039

Half-Life of Lanthanum-140 . . . . . H. W. Kirby and Murrell L. Salutsky 1043

Internal Conversion Coefficients of Pb^{203}, Zn^{65}, and Se^{75} . . . . . E. P. Steinberg, Z. O'Friel, O.S.M., and A. H. Weber 1053

Resonance Capture of Protons by Mg^{25} . . Warren E. Taylor, Leonard N. Russell, and John N. Cooper 1056

Radiation from Antimony 122 . . . . . J. M. Cork, M. K. Brice, G. D. Hickman, and L. C. Schmid 1059

Scattering of 1-Mev Neutrons by Intermediate and Heavy Elements . . . M. Walt and H. H. Barschall 1062

Gamma Rays from Ne . . . . . R. F. Foster, G. S. Stanford, and L. L. Lee, Jr. 1068

Radiations of 13.9-Min Co^{57} and 24.6-Min Fe^{59} . . . . W. Bernstein, S. S. Markowitz, and S. Katcoff 1073

Electron Capture in the Decay of Ho^{163} . . . . . R. Sher and R. H. Miller 1076

Gamma Radiation from Certain Nuclear Reactions . . . . . Rolf M. Sinclair 1082

Charged Particles from the Interaction of 14-Mev Neutrons with Li^6 and Li^7 . . . . Glenn M. Frye, Jr. 1086

Theory of Nuclear Level Density . . . . . Chanda Bloch 1094

Nucleon-Nucleus Collisions at Relativistic Energies . . . . . Giuseppe Cocconi 1107

Bound State Corrections in Two-Body Systems . . . . . Thomas Fulton and Robert Karplus 1109

(continued on cover three)

LANCASTER PRESS, INC., LANCASTER, PA.